THE DEPTHS AND LOCATIONS OF MAGMA RESERVOIRS AND THEIR CONSEQUENCES FOR THE BEHAVIOR OF SULFUR AND VOLCANIC DEGASSING

by

ALLAN HENRY LERNER

A DISSERTATION

Presented to the Department of Earth Sciences
and the Graduate School of the University of Oregon
in partial fulfillment of the requirements
for the degree of
Doctor of Philosophy

September 2020

DISSERTATION APPROVAL PAGE

Student: Allan Henry Lerner

Title: The Depths and Locations of Magma Reservoirs and their Consequences for the Behavior of Sulfur and Volcanic Degassing

This dissertation has been accepted and approved in partial fulfillment of the requirements for the Doctor of Philosophy degree in the Department of Earth Sciences by:

Paul J. Wallace	Chairperson and Advisor
Mark H. Reed	Core Member
Leif Karlstrom	Core Member
Peter J. Kelly	Outside Member
Ramesh Jasti	Institutional Representative

and

Kate Mondloch	Interim Vice Provost and Dean of the Graduate School

Original approval signatures are on file with the University of Oregon Graduate School.

Degree awarded September 2020

DISSERTATION ABSTRACT

Allan Henry Lerner

Doctor of Philosophy

Department of Earth Sciences

September 2020

Title: The Depths and Locations of Magma Reservoirs and their Consequences for the Behavior of Sulfur and Volcanic Degassing

Interpreting volcanic behavior is challenging because the phenomena controlling volcano eruptibility occur at substantial crustal depths. However, volcanic gases are a measurable surface expression of subterranean magmatic processes. Consequently, tracking changes in rates and types of gas emissions is a principle method of monitoring volcanic unrest. The solubility and degassing of magmatic sulfur and other volatiles depend on physical (pressure, temperature) and geochemical parameters (melt composition, oxidation state) that vary widely among volcanoes and are often poorly constrained. Therefore, to better utilize gas emissions as a volcano monitoring tool, the physical and geochemical conditions of the magmatic system must be well characterized to create robust degassing models. My dissertation research aims to improve the physical and geochemical understanding of volcanic systems and how these properties affect volatile behavior.

In chapter two, I compile a global database of geophysically imaged magma reservoirs at arc volcanoes. I assess the depth distribution of inferred magma bodies and their lateral locations relative to associated volcanic edifices. In chapter three, I present new techniques for correcting beam damage in silicate glasses during F-e and S-XANES

measurements. These techniques enable more accurate measurements of redox states of a variety of melt compositions. In chapters four and five, I combine geophysical and petrologic data to better understand the behavior of magmatic volatiles at Kilauea (HI, USA), Augustine (AK, USA), and Mount St. Helens (WA, USA) volcanoes. I derive petrologic degassing frameworks for these volcanoes from analyses of major elements, volatiles, redox states, and sulfur isotopes that are measured in melt inclusions, matrix glasses, re-entrant channels, and silicate minerals. Petrologic gas budgets and degassing models for these volcanoes are compared to independently observed gas emissions, and will aid in the interpretation of future degassing signals at these active volcanoes.

This dissertation includes both previously published and unpublished co-authored material. Supplemental data tables, a collection of volcanic edifice maps, and a Google Earth visualization database for Chapter II are available at the UO Libraries Scholars' Bank (https://doi.org/10.7910/DVN/LHD1HY).

CURRICULUM VITAE

NAME OF AUTHOR: Allan Henry Lerner

GRADUATE AND UNDERGRADUATE SCHOOLS ATTENDED:

University of Oregon, Eugene
Oregon State University, Corvallis
Amherst College, Amherst

DEGREES AWARDED:

Doctor of Philosophy, Earth Sciences, 2020, University of Oregon
Master of Science, Geology, 2015, Oregon State University
Bachelor of Arts, Geology, 2010, Amherst College

AREAS OF SPECIAL INTEREST:

Volcanology
Petrology
Geochemistry
Volcanic gas geochemistry

PROFESSIONAL EXPERIENCE:

Graduate Teaching and Research Fellowship, Department of Earth Sciences, University of Oregon, 2015 – 2020

Physical Science Technician, U.S. Geological Survey Cascades Volcano Observatory, 2019 – 2020

Intern, U.S. Geological Survey Cascades Volcano Observatory, 2016 – 2020

Graduate Teaching and Research Fellowship, Department of Earth, Ocean, and Atmospheric Sciences, Oregon State University, 2013 – 2015

Research Assistant, Centro de Intercambio y Investigación en Vulcanología, University of Colima, 2013

Intern, U.S. Geological Survey Hawaiian Volcano Observatory, 2012 – 2013

Research Assistant, Earth and Environmental Sciences, Los Alamos National Laboratory, 2011 – 2012

Teaching Assistant, Geology Department, Amherst College, 2008 – 2009

GRANTS, AWARDS, AND HONORS:

Graduate Research Fellowship, National Science Foundation (NSF-GRFP), 2015 – 2019

Graduate Research Internship Program (GRIP), National Science Foundation and U.S. Geological Survey, 2016 – 2019

General University Scholarship, University of Oregon, 2019

Special "OPPS" Travel and Research, University of Oregon, 2018

Staples Scholarship for Research and Emeritus Faculty Tribute Fund awards, University of Oregon Department of Earth Sciences, 2016, 2017, 2019

Mineralogy/Petrology Research Award, Mineralogical Society of America, 2017

Graduate Research Grant, Mazamas, 2014, 2017

Graduate Research Grant, Geological Society of America, 2014, 2017

Jack Kleinman Memorial Fund for Volcano Research, U.S. Geological Survey, 2016

Provost's Distinguished Graduate Fellow, Oregon State University, 2013

Undergraduate awards: Walter F. Pond Prize, Belt-Brophy Prize, Richard M. Foose Award, Amherst College Geology Department, 2007 – 2010

PUBLICATIONS:

Lerner, A.H., O'Hara, D., Karlstrom, L., Ebmeier, S.K., Anderson, K.R., Hurwitz, S., (2020). The prevalence and significance of offset magma reservoirs at arc volcanoes. *Geophysical Research Letters.* DOI: 10.1029/2020GL087856.

Kern, C., **Lerner, A.H.,** Elias, T., Nadeau, P., Holland, L., Kelly, P.J., Werner, C.A., Clor, L.E., Cappos, M.J. (2020). Quantifying gas emissions associated with the 2018 rift eruption of Kīlauea Volcano using ground-based DOAS measurements. *Bulletin of Volcanology*. 82, 55. DOI: 10.1007/s00445-020-01390-8.

Lanzirotti, A., Lee, L., Head, E., Sutton, S., Newville, M., McCanta, M., **Lerner, A.**, Wallace, P. (2019). Direct Measurements of Copper Speciation in Basaltic Glasses: Understanding the Relative Roles of Sulfur and Oxygen in Copper Complexation in Melts. *Geochimica et Cosmochimica Acta*. 267, 164-178.

Primulyana S., Kern C., **Lerner A.**, Saing U.B., Kunrat S.L., Alfianti H., Marlia M. (2019). Gas and ash emissions associated with the 2010-present activity of Sinabung Volcano, Indonesia. *Journal of Volcanology and Geothermal Research*, 382, 184-196.

Neal, C.A., Brantley, S.R., Antolik, L., Babb, J.L., Burgess, M., Calles, K., Cappos, M., Chang, J.C., Conway, S., Desmither, L., Dotray, P., Elias, T., Fukunaga, P., Fuke, S., Johanson, I.A., Kamibayashi, K., Kauahikaua, J., Lee, R.L., Pekalib, S., Miklius, A., Million, W., Moniz, C.J., Nadeau, P.A., Okubo, P., Parcheta, C., Patrick, M.R., Shiro, B., Swanson, D.A., Tollett, W., Trusdell, F., Younger, E.F., Zoeller, M.H., Montgomery-Brown, E.K., Anderson, K.R., Poland, M.P., Ball, J.L., Bard, J., Coombs, M., Dietterich, H.R., Kern, C., Thelen, W.A., Cervelli, P.F., Orr, T., Houghton, B.F., Gansecki, C., Hazlett, R., Lundgren, P., Diefenbach, A.K., **Lerner, A.H.**, Waite, G., Kelly, P., Clor, L., Werner, C., Mulliken, K., Fisher, G., Damby, D. (2019). The 2018 rift eruption and summit collapse of Kīlauea Volcano. *Science.* 363, 367–374.

Lerner A.H., Crowley P.D., Nicolaysen K.P., Hazlett R.W. (2018). Stratigraphy, distribution, and evidence for mafic triggering of the ca. 8.5 ka Driftwood Pumice eruption, Makushin Volcano, Alaska, U.S.A. *Journal of Volcanology and Geothermal Research*. 357, 362-377.

Damby D.E., Peek S., **Lerner A.H.**, and Elias T. (2018). Volcanic ash leachate chemistry from increased 2018 activity of Kīlauea Volcano, Hawaii: *U.S. Geological Survey data release.*

Lerner A. (2015). MSc Thesis: Insights into the Geochemical Evolution of the Youngest Toba Tuff (Sumatra, Indonesia) Magma Chamber Through the Lens of Zircon-hosted Melt Inclusions. *Oregon State University, Scholar's Archives.*

Cassidy M., Cole P.D., Hicks K.E., Varley N.R., Peters N., **Lerner A.H.** (2015). Rapid and slow: Varying magma ascent rates provide the mechanism for small Vulcanian eruptions. *Earth and Planetary Science Letters.* 460: 73-84.

Wang P., Hudak M.R., **Lerner A.H.**, Grubbs R.K., Wang S., Zhang Z., Karapetrova E., Hickmott D.D., Majewski J. (2014). X-ray scattering of calcite thin films deposited by atomic layer deposition: Studies in air and in calcite saturated water solution. *Thin Solid Films.* 565: 277-284.

Wang P., **Lerner A.H.**, Taylor M., Baldwin J.K., Grubbs R.K., Majewski J., Hickmott D.D. (2012). High-pressure and High-Temperature Neutron Reflectometry Cell for Solid-Fluid Interface Studies. *European Physics Journal Plus* 127: 76, 1-15.

ACKNOWLEDGMENTS

A life devoted to geologic pursuits is not what I had in mind growing up, but I am thankful to the many teachers in my life for igniting my interest in understanding the workings of this planet. I am incredibly fortunate to have spent the last decade pursuing my passion for discovery, melt inclusions, sulfur, and most of all, volcanology. I am forever grateful to my main advisor, Paul Wallace; his extreme patience, thoughtfulness, and sly wit made my Ph.D. experience immensely rewarding. I am amazed by your breadth of understanding of (seemingly) all aspects of igneous petrology, and your uncanny ability to ask perfect questions. Thank you for instilling in me the importance of careful observations, thorough investigation, and scientific integrity and collaboration.

Thank you Mark Reed for having your door constantly open and sharing endlessly enjoyable banter about mineral-fluid-gas equilibria. Thank you Leif Karlstrom for opening my eyes to how landscapes and scaling relations encode information about magmatic systems. I owe a huge debt of gratitude to my external committee member, Peter Kelly, who taught me that the best way to survive in the field and lab is with a smile. Thank you for sharing your wealth of knowledge of volcanic gases, soldering, helicopter comms, and field safety, and for being the secret mastermind behind much of my dissertation. I also thank my U.O. external committee member, Ramesh Jasti. My Ph.D. work involved a multitude of U.S. Geological Survey colleagues, and universities and institutions across the world. Thank you to my many collaborators for the years of support and for your scientific insights and mentorship in lab, field, and human skills.

I am extremely grateful to the U.O. Department of Earth Sciences for building a vibrant and collaborative environment bristling with motivation and dedication. I am

particularly thankful to have overlapped with enthusiastic peers of all backgrounds and research interests that opened me up to new geologic and life perspectives. I am incredibly thankful for my far-flung family and friends, who provided me with laughter and encouragement over the years. I am fortunate to have such a wonderful foundation, and weathering a lifetime of rock puns is a price happily paid. Finally, I owe a huge debt of gratitude to Samara Haver for endless support and unfathomable patience. I most certainly could not have done this without her, and I am amazed that she has been able to excel in own Ph.D. program while basically keeping me alive for the past five years.

This research was partially supported by the National Science Foundation (NSF) Graduate Research Fellowship Program (grant 1309047) and Graduate Research Internship Program. Analyses were supported by research grants to Allan Lerner from the University of Oregon, Mineralogical Society of America, Geological Society of America, Mazamas climbing organization, and Jack Kleinman Award for Volcano Research (U.S. Geological Survey). Additional support was provided by NSF grant EAR-1834959 (Paul Wallace). This research utilized the Advanced Photon Source, a U.S. Department of Energy Office of Science User Facility operated by Argonne National Laboratory under Contract No. DE-AC02-06CH11357.

I additionally thank the staff of the U.S. Geological Survey's Hawaiian Volcano Observatory, S. Weaver, D. Johnston, and J. Watkins (University of Oregon), and the Smithsonian Institution's Department of Mineral Sciences for access to some of the samples analyzed in this work. I thank Mike Poland, two anonymous reviewers, and editor Chris Huber for constructive comments that significantly improved Chapter II of this dissertation.

For all my teachers

TABLE OF CONTENTS

Chapter Page

Chapter Page

Chapter Page

Chapter Page

Chapter Page

LIST OF FIGURES

Figure Page

Chapter II

Chapter III

Figure Page

Figure Page

Chapter IV

Figure Page

Figure Page

Chapter V

Figure Page

LIST OF TABLES

Table Page

CHAPTER I

PREAMBLE

Interpreting volcanic behavior is challenging because the phenomena controlling volcano eruptibility occur at substantial crustal depths. However, volcanic gases, which are released from rising or cooling magma and percolate upwards through fractures, are a measurable surface expression of subterranean magmatic processes. Consequently, tracking changes in rates and types of gas emissions is a principle method of monitoring volcanic unrest. Volcanic gas geochemistry is a rapidly emerging field, with measurement capabilities often outpacing our understanding of what observed gas signals actually represent in volcanic systems. Our ability to fully utilize sulfur dioxide and other gas emissions to elucidate key volcanic processes, such as the depth of degassing magma and the specific timing or magnitude of future eruptions, remains limited by an incomplete understanding of volatile behavior in volcanic systems.

The behavior of sulfur is particularly challenging to constrain because sulfur is a multivalent element that occurs in multiple oxidation states depending on the properties of the host magma. The solubility and degassing of magmatic sulfur depends on physical (pressure, temperature) and geochemical parameters (melt composition, oxidation state) that vary widely among volcanoes and are often poorly constrained. Therefore, to better utilize sulfur gas emissions as a volcano monitoring tool, the physical and geochemical conditions of the magmatic system must be rigorously characterized to create robust degassing models (i.e., how sulfur and other volatile elements exsolve from magmas into gases with changing temperature, pressure, or magma composition).

This works seeks to answer the following questions:

1. *Where are magma reservoirs located beneath volcanoes?*
2. *What is the depth of sulfur degassing?*
3. *Are there temporal changes in sulfur degassing, and what do these mean for the potential eruptibility of the system*?

To begin addressing these questions, I integrate geophysical observations of magma reservoir locations (Chapter II) with petrologic datasets and geochemical data

(Chapters III, IV, V). Petrologic measurements rely primarily on analyses of melt inclusions, which are pockets of melt trapped within growing phenocrysts that preserve records of volatiles within magmatic systems. Other petrologic measurements involve re-entrant melt channel, matrix glasses, and mineral phases.

Chapter II presents a geophysical compilation of magma reservoir locations, and was coauthored with Daniel O'Hara and Leif Karlstrom (University of Oregon), Susanna Ebmeier (University of Leeds), and Kyle Anderson and Shaul Hurwitz (U.S. Geological Survey), and published in *Geophysical Research Letters* in June 2020.

Chapter II revisits the conceptual framework of volcano architecture that assumes magma reservoirs are located directly beneath their associated volcanic edifices. This "central reservoir" paradigm dominates our physical modeling, and importantly, volcanic monitoring efforts. However, no systematic analyses of large, multidisciplinary datasets have been undertaken to determine the distribution of magma reservoirs detected below volcanic centers. To address this, I assemble a database of geophysically detected magma reservoirs at arc volcanoes (from seismic and magnetotelluric tomography and ground deformation modeling), and quantify their locations relative to associated volcanic edifices. I find that magma reservoirs are vertically distributed throughout the upper 2.5 – 15 km of the crust. While the majority of volcanic systems are centralized, a substantial number of volcanoes have magma reservoirs laterally offset multiple kilometers from their volcano's centers. Additionally, magma reservoirs are more laterally offset at small volcanoes, but more centrally aligned at large volcanoes. I propose that increased magma flux at large volcanoes thermally overprints crustal faults and heterogeneities, leading to progressively more centrally focused magmatic systems. Recognizing the prevalence of laterally offset magmatic systems may revise paradigms of volcano modeling and may help design volcano monitoring networks.

Chapter III focuses on accurately measuring redox states in silicate glasses. This chapter is co-authored with Michelle Muth and Paul Wallace (University of Oregon), Antonio Lanzirotti and Matthew Newville (University of Chicago), Glenn Gaetani (Woods Hole Oceanographic Institution), and Proteek Chowdhury and Rajdeep Dasgupta (Rice University), and is in preparation for submission to *American Mineralogist*.

Chapter III introduces new techniques to improve Fe- and S-XANES measurements of silicate glasses by identifying and correcting for X-ray induced beam damage. I apply these techniques to melt inclusions from the 2018 fissure eruption of Kīlauea Volcano (HI, USA). Lavas from this eruption were subaerially transported long distances, during which, some magma parcels underwent atmospheric oxidation. Melt inclusions in these oxidized magma parcels have re-equilibrated with the external melt over relatively short timescales (hours to days) of lava channel flow. This rapid redox re-equilibration cautions against assuming that olivine-hosted melt inclusions record melt redox conditions at the time of melt inclusion entrapment. The implications of rapid redox re-equilibration apply to redox studies of olivine-hosted melt inclusions in all high temperature volcanic systems.

In Chapter IV, I apply further petrologic and geochemical analyses to understand volatile behavior in magmas from the 2018 fissure eruption of Kīlauea Volcano. This chapter is co-authored with Paul Wallace (University of Oregon), Thomas Shea and Adrien Mourey (University of Hawai'i – Mānoa), Peter Kelly, Patricia Nadeau, Tamar Elias, Christoph Kern, Laura Clor, Lopaka Lee, and Cynthia Werner (U.S. Geological Survey), Cheryl Gansecki (University of Hawai'i – Hilo), and Lowell Moore (Virginia Tech). This chapter is in preparation for submission to a special topical volume of the *Bulletin of Volcanology* focused on the 2018 eruption of Kīlauea.

Chapter IV provides some of the first petrologic insights into the behavior of volatiles during the historic 2018 fissure eruption of Kīlauea Volcano. By measuring major elements, volatiles, redox states, and sulfur isotopes in melt inclusions, matrix glasses, and re-entrant melt channels, I was able to constrain magma source depths and mixing relations among the diverse melt compositions that were produced in this eruption. I compared petrological measurements of sulfur, H_2O, and CO_2 to independently measured gas emissions and lava extrusion rates to derive a volatile budget and estimate eruptive volumes. Finally, through volatile measurements in melt inclusions and considerations of lava lake activity, I emphasize the importance of the recycling of partially degassed magma within the Kīlauea system.

Finally, in Chapter V, I apply petrologic and geochemical analyses to compare volatile behavior at Augustine (AK, USA) and Mount St. Helens (WA, USA) volcanoes.

This chapter is co-authored with Paul Wallace (University of Oregon) and Peter Kelly, Mary Benage, Michelle Coombs, Charles Mandeville, and Carl Thornber (U.S. Geological Survey). This chapter is in preparation for submission to the *Bulletin of Volcanology*.

In Chapter V, I follow a similar petrologic approach of measuring major elements, volatiles, redox states, and sulfur isotopes in melt inclusions, matrix glasses, and re-entrant melt channels in material from the 2006 eruption of Augustine and the 1980 – 1986 and 2004 – 2008 eruptions of Mount St. Helens. These two arc volcanoes share many similarities with one another, but Augustine is a more oxidized system that is frequented by sulfur-rich basaltic intruding magmas (olivine-hosted melt inclusions contain up to 3500 ppm sulfur). In contrast, Mount St. Helens is a relatively more reduced system and S-poor, and lacks significant evidence for basaltic recharge. Combining the multivariate framework developed in Chapter IV, I constrain the effects of sulfur degassing on melt redox and isotopic fractionation at Augustine and Mount St. Helens.

CHAPTER II

THE PREVALENCE AND SIGNIFICANCE OF OFFSET MAGMA RESERVOIRS AT ARC VOLCANOES

This chapter has been published in *Geophysical Research Letters* as of June 2020 (DOI: 10.1029/2020GL087856). I was lead author on the paper, which involved project conception, developing methodology, analysis, database synthesis, and writing the manuscript. Daniel O'Hara (University of Oregon) led the analysis of volcanic edifice topography and aided in manuscript editing. Leif Karlstrom (University of Oregon) served as my main advisor, aiding in project conception, data interpretation, and manuscript editing. Susanna K. Ebmeier (University of Leeds), Kyle R. Anderson (U.S. Geological Survey), and Shaul Hurwitz (U.S. Geological Survey) aiding in project conception and manuscript editing.

Overview

Determining the spatial relations between volcanic edifices and their underlying magma storage zones is fundamental for characterizing long-term evolution and short-term unrest. We compile centroid locations of upper crustal magma reservoirs at 56 arc volcanoes inferred from seismic, magnetotelluric, and geodetic studies. We show that magma reservoirs are often horizontally offset from their associated volcanic edifices by multiple kilometers, and the degree of offset broadly scales with reservoir depth. Approximately 20% of inferred magma reservoir centroids occur outside of the overlying volcano's mean radius. Furthermore, reservoir offset is inversely correlated with edifice size. Taking edifice volume as a proxy for long-term magmatic flux, we suggest that high flux or prolonged magmatism leads to more centralized magma storage beneath arc volcanoes by overprinting upper crustal heterogeneities that would otherwise affect magma ascent. Edifice volumes therefore reflect the spatial distribution of underlying magma storage, which could help guide monitoring strategies at volcanoes.

1. Introduction

Volcano monitoring strategies and models of magma transport in the shallow crust often implicitly assume that magma storage occurs directly under topographic highs of the volcanoes they feed (Moran et al., 2008; Pinel & Jaupart, 2003; Sparks et al., 2012). With an increasing quantity and quality of seismic and magnetotelluric (MT) data, it has been recognized that some magmatic storage zones (hereafter "magma reservoirs") are laterally offset from their associated volcanic edifices (Aizawa et al., 2014; Syracuse et al., 2015; Vargas et al., 2017). Geodetic observations have similarly demonstrated that a substantial proportion of deformation signals occur relatively distant to volcanic edifices (Lu & Dzurisin, 2014; Ebmeier et al., 2018). Lateral offsets are also commonly observed at analog systems such as geysers (Hurwitz & Manga, 2017). However, a systematic compilation and study of offset magma reservoirs at volcanic systems is lacking.

The best available means to assess the locations of magma reservoirs at volcanoes is through geophysical imaging techniques such as seismic and MT tomography, and from inversion of geodetic data. Seismic tomography measures variations in seismic velocities arising from spatially varying lithology, fluid and melt fraction, temperature, and crystallographic alignment (Lees, 2007). MT is sensitive to properties controlling electrical conductivity, namely fluid fraction, melt fraction, lithology/fluid composition, and fluid connectivity (Chave & Jones, 2012). Geodesy (e.g., InSAR, GPS, leveling) measures displacement of the ground surface due to processes such as magma injection or withdrawal, cooling and crystallization of magma bodies, accumulation of magmatic gases, or pressure changes in shallow hydrothermal systems (Dzurisin & Lu, 2007). These techniques are thus sensitive to different, but contemporaneous, aspects of subsurface magma storage and transport.

Quantifying the global pervasiveness of laterally offset magma reservoirs and their depth distributions relative to volcanic edifice volumes and morphologies (Castruccio et al., 2017; Pinel & Jaupart, 2003), magma compositions and degassing rates (Wallace, 2005), stress states of volcanic arcs (Chaussard & Amelung, 2012; Pinel & Jaupart, 2000) and host rock lithologies (Maccaferri et al., 2011; Taisne & Jaupart, 2009) is critical for identifying the key physical processes that control magma transport in the

upper crust. In order to address such questions, we compile a database containing topographic characterizations of volcanic edifices and of geophysically inferred subsurface locations of associated magma reservoirs. We restrict our study to arc volcanoes to limit the potential tectonic variability of hotspot and rift systems. The high threat of many arc volcanoes further motivates the need to better understand these systems.

2. Methods

2.1 Database of geophysically inferred magma reservoir locations

We include in our database magma storage locations from studies published between 2000 and 2018 in which authors explicitly locate a reservoir at depths of 2.5 to 15 km below the local mean ground surface, and where the spatial resolution is sufficiently high (kilometers-scale). Shallower reservoirs are excluded to avoid the preponderance of hydrothermal features, which are difficult to distinguish from magmatic features using geophysical methods. This necessarily excludes a number of published studies, but the resulting database still contains 77 inferred magma reservoirs at 56 arc volcanoes. Forty-seven reservoirs are from geodetic inversions and 30 are inferred from seismic and/or MT tomographic models (Figure 1). Owing to the challenges of maintaining consistency between the diverse datasets, we utilize only the magma reservoir centroid positions (latitude, longitude, and depth of the center of tomographic anomalies and modelled deformation sources) rather than attempting to identify the geometry and spatial extent of magma storage. While tomography can identify crustal anomalies with low seismic velocities or high electrical conductivities that may be related to either dynamic or static magma reservoirs, geodetic signals indicate active magmatic processes. Therefore, the centroid of a modelled deformation source is not necessarily the center of a magma reservoir, but rather a region where detectable deformation at depth (commonly attributed to pressure changes) is occurring. Conversely, magmatic tomographic anomalies do not necessarily imply potentially mobile magma, as there is seldom sufficient resolution to identify particular areas of high melt concentration.

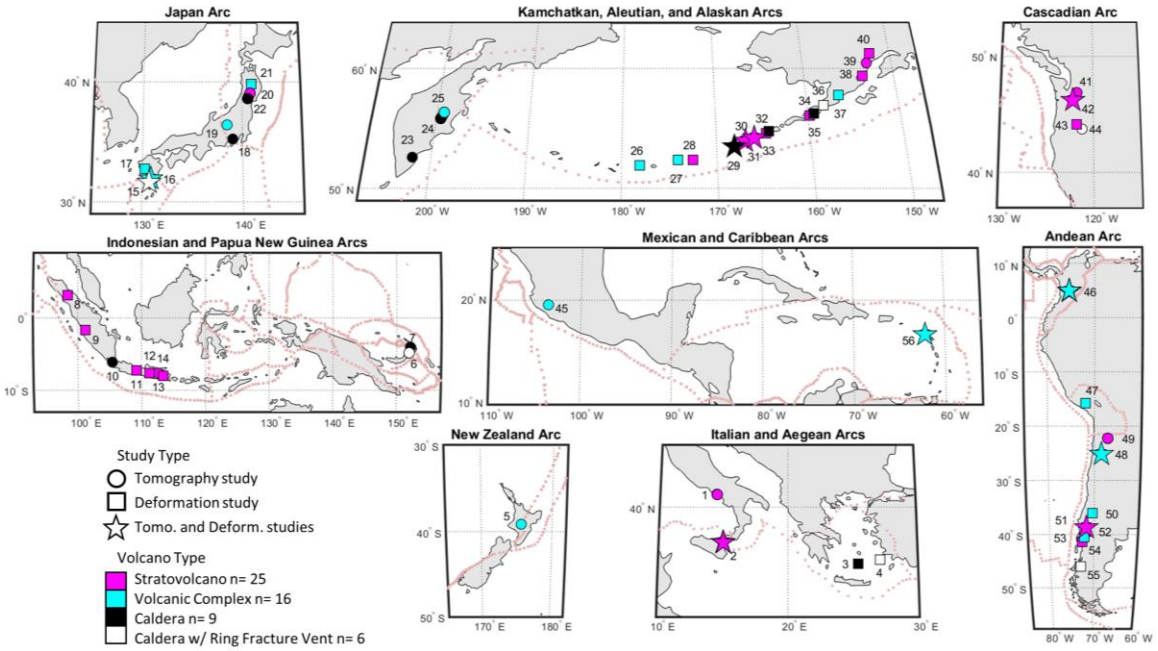

Figure 1. Global distribution of arc volcanoes with geophysically inferred magma reservoirs used in this study. Symbol colors indicate volcanic edifice type and symbol shapes indicates the type of geophysical method. Plate boundaries are mapped in red dashed lines. Volcano numbers relate to information in Tables S1, S2 and Figure A1.

2.2 Coupling geophysical observations with surface topography

Assessing the spatial relation between magma reservoirs and associated volcanic landforms requires a consistent method of characterizing volcanic edifice topography. Most volcanoes are constructed through repeated, localized eruptions and intrusions so that overall volcanic edifice size and shape is a better indicator of the time-averaged locus of volcanic output than the location of an individual vent or volcanic peak. We therefore examine the spatial relations between edifice centroids (the geometrical center of topography, largely determined by low-lying basal area) and magma reservoir centroids. In topographically complicated volcanic settings with flank or nested vents and domes, or where vents have formed along caldera-bounding faults, we consider features of similar age and petrologic character (chemical and isotopic compositions) to be related as an overall volcanic complex. We then treat each complex as a single edifice. Often there is an age progression of structures within volcanic complexes or post-caldera eruptive features, so in viewing volcanic complexes as single edifices we are effectively using a longer timeframe to define the surface expression of a volcanic system. We therefore

classify some volcanoes differently than in the Smithsonian Institution database (2013) (Text A2, Tables S1, S2).

We characterize the topography of each edifice using a closed contour algorithm (Bohnenstiehl et al., 2012), which fits an adjusted basal contour around a volcano, accounting for background slope and the presence of nearby topographic features. Once the bounds of an edifice are defined, the volume, relief, mean radius, and topographic centroid are calculated (Text A2). This method generally produces a conservative estimate of basal contour and therefore edifice volume. By using this mapping algorithm, coupled with a global 30 m digital elevation model (DEM) (NASA JPL, 2013) and a bathymetry database for subaqueous locations (Amante & Eakins, 2009), we maintain a consistent approach for quantifying edifice geometry.

Based on geophysical data quality (e.g., number of stations, ray path coverage, duration of measurement, goodness of model fits, author-stated confidence) and corroborating datasets (earthquake locations, petrologic geobarometry, observed co-eruptive linkages between reservoir locations and edifices), we assign confidence values of low, high, and near-certain (reservoirs with co-eruptive links to edifices) to reservoir locations and to their associations with particular volcanoes. Mount St. Helens (USA) provides an example where the location of the syn-eruptive deformation source is consistent with earthquake locations, leading to high confidence in the modelled geodetic source location and connection to the edifice (Figure 2a). In comparison, a reservoir location to the southwest of the volcano that is inferred from seismic tomography does not share such evidence and is assigned a lower confidence factor. However, filtering the dataset by this confidence value does not greatly affect the results. A more extensive discussion of methods, data sources, and assessment of confidence is presented in supplemental Text A1 – A4. Edifice and magma reservoir location parameters can be found in data sets S1 (edifice bounds maps) and S2 (Google Earth database). All data sets are openly available at https://doi.org/10.7910/DVN/LHD1HY (Lerner, 2020).

3. Results and Discussion

3.1 Distribution of magma reservoirs beneath arc volcanoes

We define reservoir “lateral offset” as the horizontal distance from a magma

reservoir centroid to an associated volcanic edifice centroid (Figure 2a). As the spatial scale of volcanic edifices varies widely (mean radii range from 2 to 16 km), it is also useful to define reservoir "scaled offset" as the magma reservoir lateral offset relative to the mean edifice radius (Figure 3). Considering these metrics, we find the following relations:

3.1.1 Central and offset reservoirs

Although the majority of magma reservoir centroids underlie their respective edifices, more than one third (34%) are offset by ≥ 4 km from their edifice centroids (Figure 2b, Table S3, Figure A5). 18% of the reservoir centroids are outside the "footprint" of their associated edifice, defined as > 1 mean radius distance from the edifice centroid (Figure 3). Basalt-dominated systems have somewhat more centrally aligned reservoirs compared to more silicic volcanoes (Figures A9, A15). The degree of reservoir offset has no apparent relation to arc stress regime, subduction convergence direction, or SO_2 degassing rate (Figures A2, A3, A12, A13). Overall, magma reservoirs are slightly more aligned with edifice centroid locations than with recent eruptive vents or summit locations (Figures A8, A9).

3.1.2 Reservoir depths

Magma reservoirs occur throughout the entire 2.5 – 15 km depth range considered in the dataset (Figure 2b). However, the sensitivity of geophysical techniques generally decreases with depth, so it is probable that deeper magma reservoirs are under-recorded. Noting this caveat, we find that magma reservoirs in the full dataset have a mean depth of 7.4 ± 3.4 km (6.9 km median). Reservoirs with observed co-eruptive links have a similarly large depth range of 7.1 ± 3.4 km (Table S3). Assuming an upper crustal density of 2.75 g/cm^3, the 7.4 ± 3.4 km mean depth of the full dataset translates to storage pressures of 2.0 ± 0.9 kbar. This pressure range encompasses most of the upper crust and is nearly double the range of magma storage pressures of 2.0 ± 0.5 kbar proposed by Huber et al. (2019). Within the granularity of our compilation, volcanoes with dacitic and rhyolitic compositions tend to have shallower reservoirs than more mafic systems (Figures A9, A16). We find no apparent correlation between reservoir depth and the regional stress regime, in contrast to previous interpretations (Chaussard & Amelung, 2012) (Figure A2).

Larger lateral offsets are more commonly observed when magma reservoirs are deeper (Figure 2b): 49% (n=38) of reservoirs occur within an area beneath edifices defined by the 1:2 slope of offset to reservoir depth, whereas 83% (n=64) occur within a 1:1 contour and 99% (n=77) occur within a 2:1 contour. This implies a distributed catchment area for rising magma beneath edifices (Ebmeier et al., 2018; Karlstrom et al., 2009). Arc volcanoes with calderas are more commonly associated with shallower, central magma reservoirs (Figure 2b, Figures A15, A16), consistent with models of collapse calderas involving relatively shallow evacuated magma reservoirs (Acocella, 2007; Lipman, 1997). Geophysical observations of many calderas with ring fracture vents in the database suggest the presence of multiple reservoirs, typically with a shallow reservoir close to the post-caldera ring fracture vent and a deeper reservoir more centrally located under the caldera (Tables S1, S2).

3.2 Relations between magma reservoir locations and edifice volumes

We find that magma reservoirs beneath smaller edifices are generally more offset, both in absolute and scaled distances (Figure 3a, b). Edifice volumes form a continuum over > 3 orders of magnitude (Grosse et al., 2014; Karlstrom et al., 2018), and range from 6 to 730 km3 in our database, with a relatively continuous distribution (Figures A4, A14). At volcanoes with edifice volumes ≤ 43 km3 (for reference, the volume of Mount St. Helens [Figure 2a]), 50% of reservoir centroids are located > 4 km from the edifice centroid (n=10 of 20), whereas only 23% of reservoir centroids at larger volcanoes are offset > 4 km (n=10 of 44). Similarly, 45% of reservoirs at volcanoes with edifice volumes ≤ 43 km3 are laterally offset beyond their edifice radii (scaled offset > 1), but only 7% of reservoirs at larger volcanoes are offset to this degree (Figure 3a; Figure A5). Most volcanoes with reservoir scaled offsets > 1 are small volume andesitic stratovolcanoes or volcanic complexes (Figure A4). There are no notable differences in reservoir depths beneath small and large volcanoes within the upper 15 km of crust (Figure 2b, Figure A16), in contrast to some model predictions (Castruccio et al., 2017). Lastly, we note that magma reservoir locations inferred from tomographic models and from inversions of geodetic data conducted at the same volcano often differ substantially, diverging up to 4 – 10 km horizontally and 2 – 8 km vertically (Text A1, Figure A7).

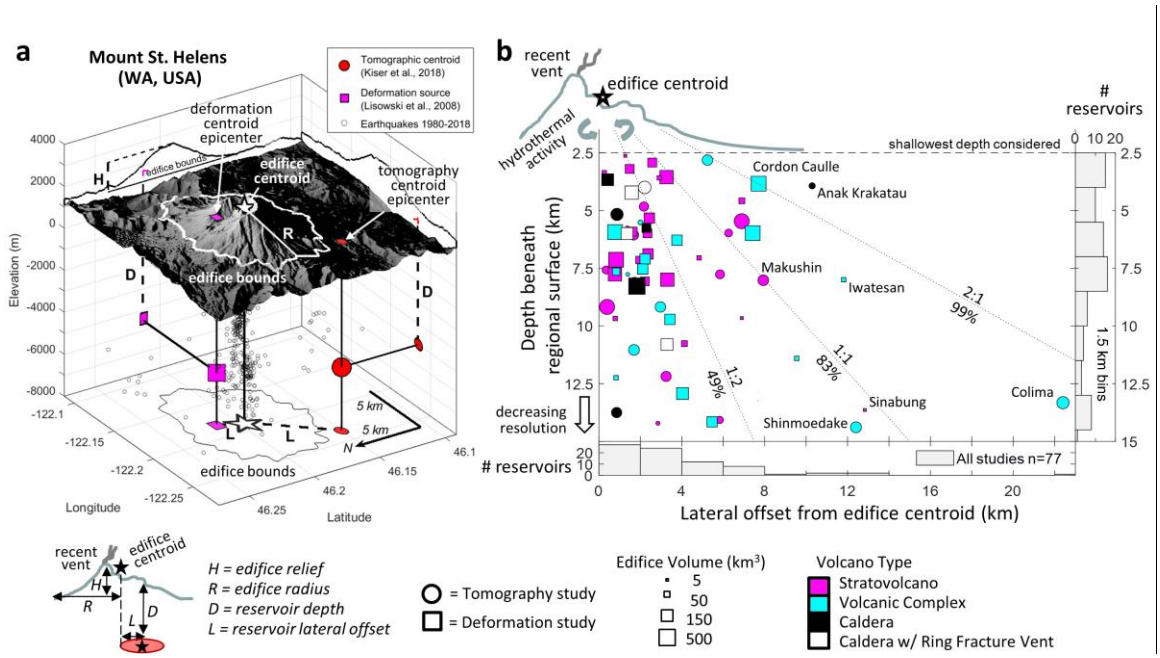

Figure 2. *(a)* Inferred magma reservoir locations and the volcanic edifice of Mount St. Helens, with the key parameters used in this study labeled. Edifice bounds calculated from surface topography (measured February 2000) are shown in white and projected to the figure base, the star is the calculated edifice centroid, R denotes the mean edifice radius from the centroid, and H is edifice height. The centroids of magma reservoirs are inferred from seismic tomography (Kiser et al., 2018) and from co-eruptive deformation between 2004 and 2006 (Lisowski et al., 2008). L is the lateral offset of magma reservoir centroid from edifice centroid, D is magma reservoir centroid depth relative to local surface elevation (Text A1, A3). Earthquake locations for reviewed events larger than magnitude 1 between 1980 and 2018 are shown for context (n=10508; Pacific Northwest Seismic Network) (University of Washington, 1963). *(b)* Lateral offset and depth distribution of magma reservoir centroids relative to their associated volcanic edifices for the global dataset. The percentages of magma reservoirs occurring within different lateral offset to depth ratios are shown. Symbols are classified by volcano type (color), and whether the magma reservoirs were inferred tomographically (circles) or geodetically (squares). Symbol size scales with edifice volume. Thirteen magma reservoirs at volcanoes with unquantified edifice volumes are included in the vertical and horizontal histograms but are not shown in the main plot.

Such differences are likely a result of surface displacements being generated by pressure changes in only a part of a larger reservoir system, as well as differences in the sensitivities of the geophysical techniques (Dzurisin & Lu, 2007; Ebmeier et al., 2018; Lees, 2007).

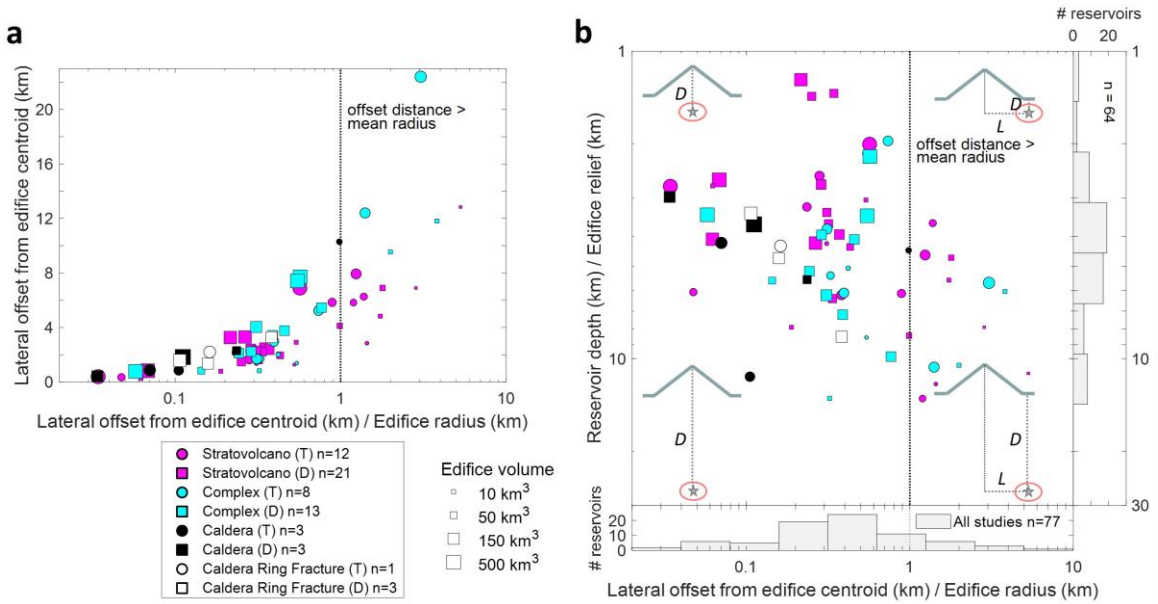

Figure 3. *(a)* Magma reservoir absolute offsets compared to scaled offsets. Edifice centroids with scaled offsets > 1 fall outside the "footprint" of the edifice. Most magma reservoirs with substantial absolute and scaled offsets occur under smaller volcanoes. *(b)* Non-dimensional view of reservoir offset relative to depth, showing that when scaled to edifice height and radius, magma reservoirs at smaller edifices are relatively deeper and more offset, as schematically depicted (*D* is depth; *L* is lateral offset). The database is limited to reservoirs between 2.5 and 15 km depth, which may explain the general lack of reservoirs in the lower left quadrant. Symbol shape, color, and size are as defined in Figure 2. *(T)* and *(D)* indicate tomography and deformation studies, respectively. Thirteen magma reservoirs at volcanoes with unquantified edifice volumes are included in the horizontal histogram but are not shown in the other plots.

3.3 Controls on magma reservoir geometry

The established relation between edifice volumes and the degree to which magma storage is located beneath arc volcanoes has significant implications for modeling magma transport and for volcano monitoring. For example, more laterally offset reservoirs at smaller volcanoes suggests that volcano size encodes some geometrical aspects of the subsurface transport network. Smaller volcanoes are indicative of low-flux or thermally immature systems with shorter histories of volcanic effusion. We infer that low-flux and/or young systems have less centralized magma storage and transport networks than systems with higher magma flux or longer durations of magmatic activity. Further, we propose that this observed relationship is related to a loss of crustal heterogeneity due to

the degree of heating, changes to deviatoric stress, and lithologic replacement of host rock by magma intrusions (Figure 4). Such homogenization is a function of the magnitude and the duration of mass and heat input into the shallow crust (Annen & Sparks, 2002; Karlstrom et al., 2017). In systems with more limited magma flux into and through the shallow crust, pre-existing structural and stress heterogeneities may more significantly influence ascending magma. For example, horizontal or inclined faults (Galland et al., 2007) and lithologic contacts (Magee et al., 2016) facilitate lateral magma transport and the development of laterally offset reservoirs, as do pre-existing background stresses (Maccaferri et al., 2011). Indeed, a number of volcanoes with laterally offset reservoirs occur near major crustal faults (Jay et al., 2014; Lundgren et al., 2015; White & McCausland, 2016).

In contrast, systems with a high magma flux and/or long histories of volcanism alter the shallow crust through cycles of repeated heating, stress changes and intrusion. Deviatoric stresses associated with transient magma storage and volcanic edifice loads may focus dike propagation (Maccaferri et al., 2011; Pinel & Jaupart, 2004; Roman & Jaupart, 2014) and concentrate heat at shallow depths beneath volcanoes. This transport eventually replaces the crustal column and establishes the lateral region of thermomechanically focused magma ascent beneath volcanoes. As crustal impediments to vertical dike ascent are overprinted, eruption locations may become more aligned with the underlying reservoir, causing the volcanic edifice position to progressively migrate. The load of this evolving edifice contributes to further focusing dike ascent, and the magma reservoir may similarly migrate in adjustment to the changing thermal state of the shallow crust (Figure 4b). We propose that, over time, these self-reinforcing mechanisms at high-flux magmatic systems result in larger volcanic edifices being centered above their magma storage zones.

The nature of mechanical coupling between edifice loads and magma reservoirs depends on the wavelength of edifice topography compared to reservoir depth. In the database, all reservoir centroid depths are within an order of magnitude of their edifice diameters (Figure A6), implying that the elastic stress and deformation fields associated with the edifice load and reservoir should interact (McTigue & Segall, 1988). Scaling reservoir depths by edifice relief, which sets the magnitude of the surface load, we find

that reservoirs are generally deeper relative to the overlying edifice as they become more offset (Figure 3b), consistent with a distributary region of magma supply.

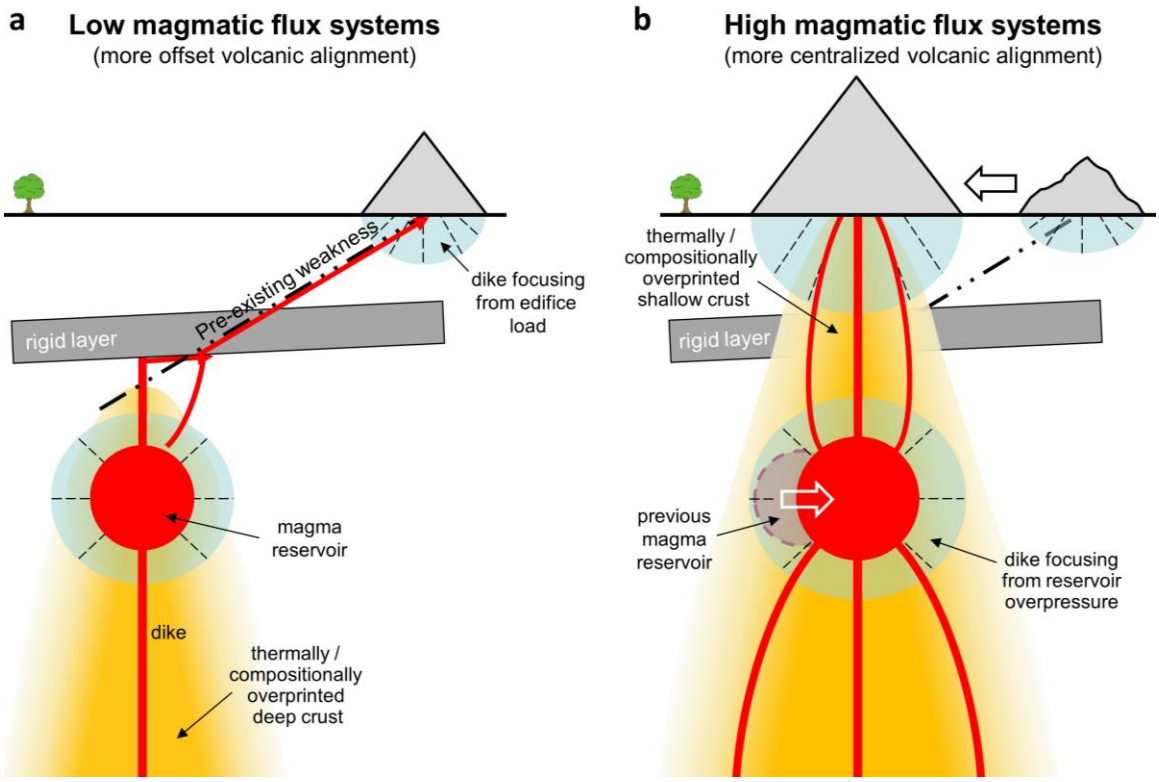

Figure 4. Schematic representation of a magma reservoir and transport system at low- and high-flux volcanoes. *(a)* Small volcanoes may be a consequence of low magnitude or short-lived magmatic flux. In low-flux systems, much of the upper crust retains heterogeneities that may cause increased lateral transport of magma along zones of weakness (e.g., rheologically competent strata blocking or diverting dike propagation to along faults or between lithologic contacts). *(b)* Large volcanoes reflect more long-lived or high-flux magmatic systems, which can overprint crustal heterogeneities leading to more focused vertical dike ascent. Magma reservoir locations may similarly migrate (white arrow) in response to changing edifice locations (large black arrow). These self-reinforcing processes can contribute to progressively more aligned volcanic systems through time.

3.4 Relevance for monitoring active volcanoes

With a simple determination of edifice shape from a DEM (radius, relief, centroid), we can estimate the lateral extent in which underlying shallow crustal reservoirs are likely to occur (Figures 2b and 3). This estimation can be further refined by

quantifying edifice size, since large volcanoes are more likely to have centralized magmatic reservoirs compared with smaller volcanoes.

For example, Mt. Hood in Oregon (USA) is a high-threat andesitic stratovolcano (Ewert et al., 2018), but there are no constraints on the location of its magma reservoir(s). Based on the calculated edifice topography of Mt. Hood (2350 m relief, 6.5 km mean radius, 89 km^3 volume), and assuming a reservoir depth of 6 ± 2 km from geobarometry (Cooper & Kent, 2014), the relation presented in Figure 3b (with 80% prediction intervals; Figure A17) suggests that the magma reservoir centroid is likely to be within 6 km of the edifice centroid (where the edifice centroid is ~1 km SE of the summit [Data Sets S1, S2]). In contrast, Mt. Bachelor (also in Oregon) is a smaller Holocene basaltic stratovolcano (900 m relief, 2.7 km mean radius, 8 km^3 volume) and may host a magma reservoir offset by up to 9 km from its edifice centroid, assuming a reservoir depth equal to the mean depth for basaltic reservoirs in the dataset (6.8 ± 2.4 km).

The relatively common occurrence of offset reservoirs warrants reassessing the design of monitoring networks at arc volcanoes. Focusing monitoring instruments exclusively on an edifice (or a particular eruptive vent) might miss early signs of unrest at offset systems (Ebmeier et al., 2018). Ground-based monitoring networks or satellite survey footprints may thus be planned more strategically based on simple characterization of the edifice topography. Barring *a priori* knowledge of subsurface magma reservoir geometry, monitoring coverage should be expanded at smaller volcanoes given their increased likelihood of being associated with more offset reservoirs. Additionally, as edifice centroids tend to be more aligned with magma reservoirs than recent eruptive vents or summits, focusing monitoring networks around edifice centroids rather than vent or summit locations might enable better detections of unrest.

Finally, laterally offset magma reservoirs require horizontal or inclined pathways of magma ascent to the surface (Aizawa et al., 2014; Aoki et al., 2013; Wicks et al., 2011). Non-vertical transport pathways are not commonly included in models for dike propagation and could alter interpretations of geophysical monitoring signals (Rivalta et al., 2015; White & McCausland, 2016). Inclined dikes may also facilitate fluid phase

separation during transport, with implications for magmatic degassing and modeling of conduit dynamics (Massol et al., 2001; Vandemeulebrouck et al., 2014).

4. Conclusions and future research

By combining geophysical and volcanic landform topography datasets we have identified new constraints on the subsurface geometry of shallow arc magma transport. In particular, we find that magma reservoirs are commonly offset from the presumed volcanic edifices they source. We observe that laterally offset magma reservoirs are more prevalent at small volume volcanoes than at large volcanoes, and consequently propose that the magnitude and duration of magmatic flux influences the degree of vertical alignment between edifices and reservoirs. This hypothesis implies that shallow magma storage zones and volcanic edifice positions evolve through time to become large systems with well-developed, centrally aligned magma transport. The characterization of volcanic edifice topography thus informs the subsurface geometry of shallow magma storage, which may help guide the spatial design of volcano monitoring networks.

An improved ability to consistently constrain geometries and volumes of magma reservoirs would significantly build upon our analysis. For example, dikes may initiate from the edges of magmatic storage zones so that transport pathways could be located away from the centroids of large reservoirs. Further efforts to combine geophysical and topographic datasets from other arc and non-arc volcanoes, along with studies that constrain volcanic histories, will be required to validate the hypothesis that edifice growth corresponds to the centralization of magma transport. Integrating edifice topography and magma reservoir locations with local tectonic features, substrate lithologies, durations of magmatism, and edifice growth and collapse histories has great potential for improving our understanding of the co-evolution of volcanic edifices and underlying magma storage and transport systems.

We hope the compilation and observations presented here motivate further efforts to *a)* expand and refine similar geophysical and topographic datasets at volcanoes worldwide, *b)* assess thermomechanical interactions between edifices and reservoirs to understand the origin and impacts of offset reservoirs, c*)* more routinely publish the centroids of major tomographic anomalies and pressure sources (with uncertainties) in

future geophysical studies, and *d)* reconsider what criteria are used to define volcano locations (e.g., vents or edifice centroids), edifice boundaries, and volcano structures.

5. Bridge

In Chapter II, I compiled a comprehensive database of geophysically detected magma reservoirs at arc volcanoes and quantified their locations relative to surface volcanic features. This compilation has produced provocative findings: while the majority of arc volcanic systems are "centralized", with magma reservoirs not far removed from the volcanic surface landform, about 20% of systems have magma reservoirs laterally offset > 4 km from the center of associated volcanic edifices. This distribution of magma reservoirs appears related to specific volcano characteristics, such as size and structural type (e.g., stratovolcanoes vs. calderas). Recognizing the prevalence of laterally offset magmatic plumbing systems may change paradigms of volcano modeling and monitoring. For example, laterally offset volcanic plumbing systems may have inclined, rather than vertical, conduits that may facilitate gas separation, a phenomenon that would substantially change models of conduit behavior and may facilitate gas emissions.

Interpreting volcanic behavior is challenging because the phenomena controlling volcano eruptibility occur at substantial depths (3 – 15+ km). However, volcanic gases, which are released from rising or cooling magma and percolate upwards through fractures, are a measurable surface expression of subterranean magmatic processes. Consequently, tracking changes in rates and types of gas emissions is a principle method of monitoring volcanic unrest. The depth of magma reservoirs largely controls the solubilities of magmatic gases. Petrologic and geophysical means to estimate magma reservoir depths, such as compiled in Chapter II, are thereby critically important observations in constraining degassing behavior.

Sulfur dioxide (SO_2) is the most routinely monitored volcanic gas because sulfur is relatively abundant in magmas, and emitted SO_2 can be readily detected by ultraviolet spectroscopy. In additional to magma storage pressure, the oxidation state of magma is an important factor in controlling sulfur solubility. Chapter III introduces techniques to improve measurements of a microbeam X-ray fluorescent technique that is used to

identify the speciation of iron and sulfur in magmas. These measurements provide information on the redox state of magma, which is another important parameter that aids in understanding the behavior of sulfur and magmatic degassing. Chapters IV and V combine geophysical information of magma storage depths with redox state measurements and other petrologic information to inform the behavior of sulfur degassing at Kīlauea, Augustine, and Mount St. Helens volcanoes.

CHAPTER III

CORRECTING Fe- AND S-XANES BEAM DAMAGE IN SILICATE GLASSES AND RECOGNIZING RAPID REDOX EQUILIBRATION OF OLIVINE-HOSTED MELT INCLUSIONS

This chapter is in preparation for *American Mineralogist* and contains material coauthored with Michelle Muth and Paul Wallace. I am lead author on the paper, which involved project conception, sample preparation, analysis, data synthesis, and writing the manuscript. Michelle Muth (University of Oregon) contributed to project conception, sample preparation, analysis, and manuscript writing. Paul Wallace (University of Oregon) served as my main advisor, aiding in project conception, data interpretation, and manuscript editing. Antonio Lanzirotti and Matthew Newville (Center for Advanced Radiation Sources, University of Chicago) aided in data analysis and interpretation. Glenn Gaetani (Woods Hole Oceanographic Institution) aided in redox re-equilibration modeling. Proteek Chowdhury and Rajdeep Dasgupta (Rice University) aided in sample preparation.

Overview

The redox state of silicate melts influences crystallization, element partitioning, and degassing behavior. Synchrotron-based μXANES has emerged as a powerful tool to determine redox conditions through the direct measurement of multivalent elements, such as Fe and S. The small beam size afforded by synchrotron XANES makes it one of the few techniques for determining redox conditions within melt inclusions, which may provide insights into pre-eruptive melt conditions. However, the small size of melt inclusions and the high penetrative depth of high energy X-rays can result in mixed spectroscopic signals due to analysis of inclusions or host minerals at depth. Additionally, there is a possibility that some of these elements may undergo beam-induced changes in valence state during XANES analysis.

This study presents observations of the rates of change in Fe and S valence during XANES analysis of olivine-hosted melt inclusions from the southern Cascade arc and

from Kilauea Volcano as a function of incident flux density and approaches developed to potentially minimize the impact of such effects, primarily by use of repeated, short duration XANES scans. We show that rapid scanning (~82 s) coupled with the application of a time-dependent correction to Fe-XANES pre-edge centroid positions allows for more accurate estimates of the initial, undamaged $Fe^{3+}/\Sigma Fe$ speciation even in damage-susceptible glasses. A similar application of this repeated rapid scanning (150 to 300 s) to recognize S-XANES beam damage (S^{6+} photo-reduction to S^{4+}) is also described, coupled with a new proposed peak fitting method to estimate initial $S^{6+}/\Sigma S$ speciation. In melt inclusions from Kilauea, we observe that beam-induced changes in S speciation can occur rapidly even in low-H_2O basaltic glasses when valence state changes in Fe are not observed. Using these approaches, we can more confidently constrain the likely speciation Fe- and S-speciation even in beam damage-susceptible melt inclusions.

However, properly interpreting the redox conditions calculated using XANES oxybarometry methods also requires considerations of a variety of geochemical processes that can occur within melt inclusions to change valence states post-entrapment. Careful evaluation of measured XANES spectra can provide an indication that such processes occurred even when they are not apparent using other imaging or chemical analysis techniques. We show that the presence of Fe-oxide nanolites can be inferred with Fe-XANES measurements even when these crystallites are not optically visible in melt inclusions. Most importantly, we observe rapid oxidation (up to +2 log units) of olivine-hosted melt inclusions in surface flows from the 2018 eruption of Kilauea Volcano. This oxidation is presumably due to atmospheric interaction with the lava during an hours to days long subaerial transit from eruption site to ocean entry quenching. Melt inclusions re-equilibrated to the oxidation state of external oxidized melt over these same short timescales, which is consistent with modeled timescales of metal vacancy diffusion through olivine. We therefore conclude that olivine-hosted melt inclusions are susceptible to rapid redox re-equilibration, as also shown by Bucholz et al. (2013) and Hartley et al. (2017). Depending on the timescales of magma ascent and quenching, measured redox state in melt inclusions may reflect conduit or emplacement conditions rather than melt conditions at the time of inclusion entrapment. While we have developed ways to

accurately measure redox conditions in melt inclusions by XANES, petrologic interpretation of such redox measurements requires additional careful consideration.

1. Introduction

Synchrotron-based micro X-ray absorption near edge structure (μXANES) spectroscopy has become a valuable petrologic tool for in-situ determination of speciation of redox-sensitive elements in magmatic minerals and glasses (see review by Sutton et al., 2020). In particular, Fe- and S-XANES have been applied to quenched matrix glasses and melt inclusions to advance our understanding of magma oxygen fugacity (fO_2) and melt species complexing at mid-ocean ridges, hotspots, and volcanic arcs (Berry et al., 2008; Kelley and Cottrell, 2009; Cottrell and Kelley, 2011; Brounce et al., 2014, 2017; Dyar et al., 2016; Lanzirotti et al., 2019; Sutton et al., 2020), as well as in igneous material from lunar and martian samples (Righter et al., 2013; McCanta et al., 2017, 2019). The fO_2 of magmas exerts a major control on mineral stability and thereby the differentiation paths of magmas (Osborn, 1959; Kelley and Cottrell, 2012), including the behavior of ore-forming species (e.g. Cr, Cu, Fe, Ti; Papike et al., 2016; Lanzirotti et al., 2019; Sutton et al., 2020). Additionally, fO_2 can significantly affect the solubility and degassing of multivalent volatiles (S, C) (Jugo, 2009; Jugo et al., 2010; de Moor et al., 2013; Moussallam et al., 2014, 2016; Helz et al., 2017; Head et al., 2018).

Iron occurs as Fe^{2+} and Fe^{3+} in most terrestrial melts, and as Fe^0 in strongly reduced melts below the IW buffer (generally extraterrestrial) (Schreiber et al., 1987). Many existing calibrations relate measured Fe-XANES spectral centroid position for the pre-edge peaks to $Fe^{2+}/\Sigma Fe$ in silicate glasses based on Mössbauer measured in standard glasses (Galoisy et al., 2001; Wilke et al., 2004, 2007; Cottrell et al., 2009; Dauphas et al., 2014; Zhang et al., 2016, 2018; Fiege et al., 2017) and thereby melt fO_2 (e.g., Kress and Carmichael, 1991; Borisov et al., 2018; O'Neill et al., 2018). Some more recent calibrations have used multivariate analysis of the entire Fe XANES spectrum to relate to Fe-valence in standard glasses measured by Mössbauer (Shorttle et al., 2015; Dyar et al., 2016). Sulfur in silicate melts dominantly occurs as S^{2-} or S^{6+}, with the valence transition between these states occurring over a relatively narrow fO_2 range near the Ni-NO buffer (Carroll and Rutherford, 1988; Jugo et al., 2010), although there is evidence that this

transition is dependent on pressure, temperature, and composition (Baker and Moretti, 2011; Klimm et al., 2012a; Fiege et al., 2014b; Masotta and Keppler, 2015; Matjuschkin et al., 2016; Nash et al., 2019). S-XANES has been used to quantify the $S^{6+}/\Sigma S$ ratios in glasses (Fleet et al., 2005; Jugo et al., 2010) by fitting the relative strength of absorption peaks for sulfate vs. sulfide species, which are generally distinct, although sulfide complexes can display varied lower energy spectroscopic features based on melt composition and cooling history (Fleet et al., 2005; Head et al., 2018).

Fe- and S-XANES are powerful techniques for investigating redox conditions of melt inclusions (MI), which are small parcels of quenched glass from melt entrapped within growing crystals. Melt inclusions are useful because they can preserve information on volatile concentrations and melt diversity that is otherwise lost during magma mixing, ascent, and eruption (Kent, 2008; Métrich and Wallace, 2008). The small size of MI leaves μXANES (hereafter XANES) as one of the few techniques suitable for *in-situ* measurements of element valence states and molecular complexing within MI. However, the large penetrative depths of high-energy X-rays and inclined beam incident beam trajectories require careful sample preparation and analytical strategies to avoid signal contamination during Fe- and S-XANES measurements of MI and matrix glasses (Figure 1). It has also been recognized that many glass compositions are susceptible to X-ray beam induced changes in Fe and S speciation during analysis (Wilke et al., 2008; Métrich et al., 2009; Moussallam et al., 2014; Cottrell et al., 2018). Although Fe-XANES measurements of dry basaltic and rhyolitic glasses are observed to generally reproducible over a broad range of incident X-ray fluxes (Cottrell et al., 2009), hydrous glasses, particularly basaltic compositions, have been observed to undergo rapid oxidation of Fe^{2+} to Fe^{3+} with increasing flux (Cottrell et al., 2018). The mechanisms of Fe photo-oxidation are incompletely known, but involve redox exchange within the glass presumably related to O-H volatilization or migration (Cottrell et al., 2018).

S-XANES measurements have also been observed to undergo beam-induced modifications in speciation in silicate glasses, typically with S^{6+} being reduced to S^{4+} during progressive analysis (Wilke et al., 2008; Métrich et al., 2009). Strategies to mitigate beam damage during Fe- and S-XANES measurements include reducing X-ray dose (photon flux / analytical area) by using defocused beams, continually moving the

sample during analysis, and/or decreasing incident photon flux (Wilke et al., 2008; Métrich et al., 2009; Klimm et al., 2012a; Brounce et al., 2017; Cottrell et al., 2018; Moussallam et al., 2019). Spatially-resolved XANES beamlines are available at a number of synchrotron light sources worldwide with incident X-ray intensities ranging from 10^8 – 10^{12} photons/s (Sutton et al., 2020), where higher X-ray fluxes shorten analysis time but amplify beam damage.

Many of these approaches to lessen beam damage are challenging to apply to MI owing to the small size of the inclusions being analyzed. Melt inclusions in many systems of petrologic interest have spherical diameters of 10s to 100 μm. Small MI and require more focused beam diameters to avoid contamination by the host-phase but are thereby subject to higher photon doses and thus possible beam damage (e.g., Tassara et al., 2020). Melt inclusions are often targeted for petrological investigation *specifically because* they can retain magmatic volatiles, which are otherwise lost from the magma during ascent and degassing (Kent, 2008; Métrich and Wallace, 2008). However, silicate glasses with high H_2O content have been observed to undergo larger changes in Fe and potentially S valence during irradiation that what is observed in anhydrous silicate glasses (Cottrell et al., 2018). These observations make it more challenging to apply XANES oxybarometry methods to the analysis of MI from volcanic arc environments, which tend to be small and relatively hydrous.

For these more challenging inclusions, it is beneficial to develop XANES approaches that both minimize changes in elemental valance and seek to correct for changes that do occur. This can be challenging given that glass composition and differences in natural diffusive H^+ loss within samples (due to MI size and position relative to host grain margins) can lead to different MI susceptibilities to beam-induced changes in speciation.

Beyond measurement reliability, the geologic significance of the measured redox signatures of magmatic glasses needs to be accurately interpreted. Generally, valence state measurements in MI are used to infer pre-eruptive redox states (e.g., Moussallam et al., 2014, 2016; Helz et al., 2017; Head et al., 2018; Tassara et al., 2020), which requires that MI remain closed to redox equilibration from the time of entrapment until quenching. However, if MI behave as closed-systems with respect to redox behavior, processes of

post-entrapment crystallization during cooling can affect the redox state of glasses, leaving measured conditions unrepresentative of magmatic conditions at the time of MI entrapment (Danyushevsky et al., 2000). Open-system processes may also affect MI redox conditions, such as hypothesized melt oxidation due to H^+ diffusion from MI (Mackwell and Kohlstedt, 1990; Danyushevsky et al., 2002; Demouchy and Mackwell, 2006) or through independent MI fO_2 equilibration via proton and metal vacancy diffusion through the mineral host (Gaetani et al., 2012). Reheating experiments by Gaetani et al. (2012) and Bucholz et al. (2013) indicate that redox re-equilibration in olivine-hosted MI occurs rapidly at magmatic temperatures, and Hartley et al. (2017) found that natural olivine-hosted MI from Iceland's 1783 Laki eruption equilibrated to more reduced external melt environments during lava flow transport. Uncertainty in understanding what petrologic conditions are actually represented by redox measured in MI is therefore a critical impediment in using XANES measurements to address petrologic questions.

In this work, we present techniques that can aid in recognizing beam-induced changes in Fe and S valence in silicate glasses that result from XANES analysis of natural MI. We also propose new time-dependent corrections for these. For S-XANES, we present a new spectral fitting approach that may better account for reductions of S^{6+} to S^{4+} that occur during analysis. methods enable reliable quantification of Fe and S speciation, and thereby melt redox state, from small and/or beam damage susceptible glasses and MI. We then apply these techniques to a suite of olivine-hosted MI from the 2018 eruption of Kīlauea volcano, which show substantial atmospheric oxidation during lava flow transport over a time period of hours to days. Our results confirm previous findings that olivine-hosted MI re-equilibrate rapidly (a few days or less) to external redox conditions at magmatic temperatures (Gaetani et al., 2012; Bucholz et al., 2013; Hartley et al., 2017), and therefore measured redox conditions in MI should not necessarily be viewed as representative of originally entrapped melt conditions.

2. Methods

At the Fe X-ray K-edge the characteristic 1/e X-ray absorption depth in basaltic glass is ≈ 40 μm (Elam et al., 2002) and 120 μm ($1/e^3$) thick glass is required for 95% absorption of X-rays during Fe-XANES measurements. The fluorescence from Fe-bearing inclusions or crystalline host phases that may be present within the analytical path will be mixed with signal from the targeted glass, proportional to the elemental mass and accounting for relative absorption effects. This is a particular problem for analyzing MI, as they are often much thinner than the full Fe-XANES X-ray absorption depth. Consequently, most MI must be doubly intersected for Fe-XANES analysis to avoid signal contamination from the host mineral. A further complication in XANES measurements of MI, particularly for highly penetrative Fe-XANES analyses, is that many μXANES beamline configurations utilize a ~45° slant geometry of incoming X-ray beam in fluorescence operating modes. The inclined incidence angle means that as wafer thickness increases in the beam direction, progressively wider doubly intersected MI areas are needed to keep the analytical path free of mineral contamination (Figure 1). A large analytical spot size amplifies this effect. Throughout the X-ray penetration volume, the minimum required doubly intersected MI dimensions for a host-free glass measurement need to be equal to MI thickness plus the beam diameter size. This requires MI to be either wide or ground very thin for clean glass analyses using high energy X-rays (e.g., Fe-XANES, V-XANES, Cu-XANES). Thus, small MI in olivine and other Fe-bearing phases can be challenging to measure for Fe-XANES. Even for analyses of MI in phases that have low, but non-zero, Fe-concentrations (e.g., feldspars), the high penetrative depth of Fe-XANES can excite a large volume of the host phase, so that the host contribution to the Fe-XANES signal may be significant. This issue is of particular concern for small MI and for compositions with relatively low Fe-contents, such as dacites and rhyolites. At the lower energy S K-edge (~2500 eV), X-rays are more strongly attenuated, with the 1/e X-ray absorption depth in basaltic glass only ~5 μm. Consequently, 95% of the S-XANES X-ray absorption occurs within the upper 15 μm and most of these geometric concerns are accordingly lessened (Figure 1A).

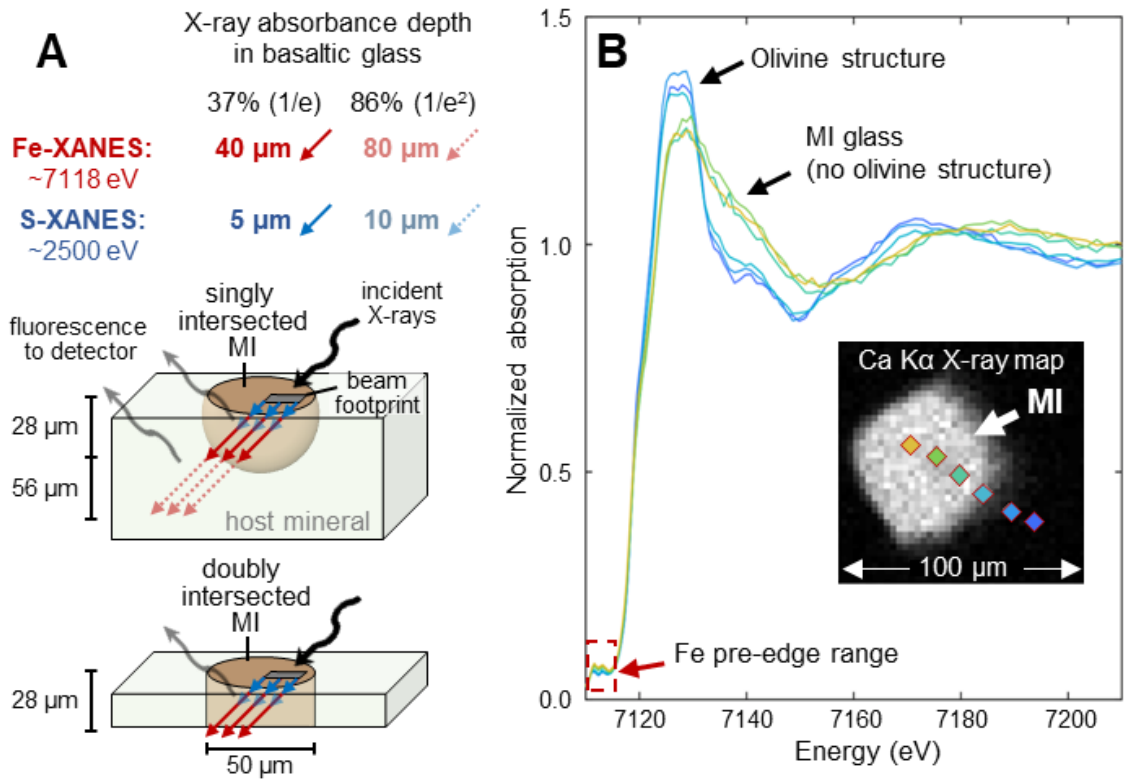

Figure 1. *(A)* Schematic analysis geometry of XANES analyses of a 50 µm diameter melt inclusion (MI) (brown) being analyzed with a 20 µm wide X-ray beam. For XANES fluorescence measurements, the X-ray beam (black arrow) is ~45° incident to the sample surface and the sample fluorescent energy (gray arrows) is measured at 45° in the opposite direction. Depending on the penetration depth of the X-ray energy being used, the beam may interact with substantial host mineral both laterally and at depth, leading to mineral-contaminated spectra. For Fe-XANES (red arrows), 37% and 86% of the X-ray signal is absorbed in 40 and 80 µm hypotenuse paths through basaltic glass (28 and 56 µm vertical thicknesses), requiring the MI be both doubly intersected and sufficiently wide to avoid host mineral contamination. S-XANES X-ray energies are much less penetrating (blue arrows), so MI geometries and thicknesses are not as large concerns. *(B)* A series of Fe-XANES measurements of a doubly-intersected olivine-hosted MI from the southern Cascades (BORG-1_37, Table 1) showing a traverse from within the MI into the olivine-host and illustrating the difference in absorption edge shape between analyses of glass and of olivine. Measurement locations are shown atop a Ca Kα X-ray map (inset), with symbol colors matching the shown spectra.

Fe- and S-XANES measurements were conducted on a variety of volcanic and synthetic silicate glasses at GSECARS beamline 13-ID-E at Argonne National Laboratory's (Illinois, USA) Advanced Photon Source (APS), a third generation synchrotron light source (Sutton et al., 2017). Details of the 13-ID-E beamline configuration are described in Head et al. (2018) and are consistent with measurements

conducted here, except for differences in photon flux and analytical times described below.

The X-ray beamline is stable over the course of standard two to three-day measurement periods and no within-session drift corrections were applied during either Fe- or S-XANES measurements. To account for differences in monochromator calibrations between synchrotron facilities (Cottrell et al., 2009; Jugo et al., 2010), a set of standards (minerals, foils, glasses) were measured at the onset of each analytical session to determine the appropriate energy offset to apply to Fe- and S-XANES measurements relative to reference energy fitting ranges (details below). Prior to each XANES analysis, an X-ray map was made by rapidly rastering across the sample to identify areas in MI and matrix glass targets that were free of host mineral in the beam path. The X-ray beam was then turned off and any further beam interaction with MI was avoided until XANES measurements began to prevent any unnecessary beam damage.

Analyzed samples included doubly intersected MI and matrix glasses mounted on Fe-free glass rounds and thin sections. Samples were embedded in CrystalBond®, EpoThin® epoxy, or thin section resin. All bonding material and glass substrates were analyzed to confirm that they contained only trace Fe and had negligible contribution to Fe-XANES signals. The bonding materials did contain substantial S, but the low energy X-rays for S-XANES measurements are fully absorbed within a ~20 μm path within basaltic glasses (15 μm vertical path with 45º incident beam angle, Figure 1A). All analyzed MI and matrix glass areas are substantially thicker than this so the bonding materials contributed no appreciable signal to S-XANES measurements. We also analyzed singly intersected experimental glass charges, where glass thicknesses of multiple mm fully absorbed X-rays at Fe and S Kα energies so that contamination from the capsule material was insignificant. Care was taken to analyze only crystal-poor experimental glass areas and to avoid measurements near capsule edges.

Table 1. (footnote, next page).
* Fe-XANES beam damage susceptibility index (Cottrell et al., 2018): $XH_2O*2XFeO/XFe_2O_3$; calculated using molar fractions and Fe^{2+}/Fe^{3+} ratios from time-zero interpolated Fe-XANES measurements.
** $Fe^{3+}/\Sigma Fe$ and $S^{6+}/\Sigma S$ ranges for beam damage corrected Fe- and S-XANES analyses, as percentages.
***Incident photon flux was ~3 – 5x10^9 photons/s for Fe-XANES, and ~1 – 40x10^9 photons/s for S-XANES. Analysis footprint sizes ranged from 2x2, 5x5, 10x10, 20x20, and 50x50 μm. Qualitative beam damage observations were based on 2 – 4 repeated scans, with total scan times of 8 – 12 minutes and 10 – 15 minutes per location for Fe- and S-XANES measurements, respectively.

Table 1. Experimental and natural glasses analyzed by Fe- and S-XANES in this study.

Sample, composition	H_2O (wt%)	Fe XANES beam damage susceptibility index (Φ)*	XANES measurement type	$Fe^{3+}/\Sigma Fe$ $S^{6+}/\Sigma S$ ranges**	Photon dose (photons/s/μm^2); observed beam damage***
CAB-47: experimental basaltic glass. 1250 °C, 1.3 GPA, minor phenocrysts (Weaver et al., 2011; this study)	5.5	1.7	Fe-XANES (+ Fe^{3+} ingrowth tests)	13% Fe^{3+}	Fe-XANES: $1 – 1.5x10^8$: high $2 – 4x10^7$: high $6 – 9x10^6$: mod
CAB-33: experimental basaltic glass. 1225 °C, 1.7 GPA, phenocryst-free, but Fe-oxide nanolite spectral signature (Weaver et al., 2011; this study)	7.2	1.8	Fe-XANES (+ Fe^{3+} ingrowth tests)	15% Fe^{3+} (Fe-nanolites present)	Fe-XANES: $2 – 4x10^7$: severe $6 – 9x10^6$: high
P2-F: Mono Craters obsidian pyroclast with <<0.1% microlites (Barnes et al., 2014; Watkins et al., 2017; this study)	2.0 – 2.3	-	Fe^{3+} ingrowth tests	-	Fe-XANES: $1 – 1.5x10^8$: mod $2 – 4x10^7$: slight
G466: experimental basalt glass. 1300 °C, 2 GPA, minor cpx + anh (Chowdhury and Dasgupta, 2019; this study)	6.5	-	S-XANES	100% S^{6+}	S-XANES: $5x10^9$: severe $2x10^8$: high $5x10^7$: mod $8x10^6$: slight
VG-2: MORB glass from Juan de Fuca ridge (NMNH 111240-52) (Jarosewich et al., 1980; this study)	<0.1	0.01	S-XANES	4 – 8% S^{6+}	S-XANES: $1x10^{10}$: severe $4.5x10^8$: high $1x10^8$: slight $6.5x10^6$: none
KE62-2932S: Kīlauea 2018 basaltic pumice MI and matrix glass (**Chapter IV**; this study)	0.1 – 0.3	0.1	Fe-XANES S-XANES	13 – 18% Fe^{3+} 3 – 25% S^{6+}	Fe-XANES: $2 – 4x10^7$: none S-XANES: $2x10^8$: mod $5x10^7$: slight $8x10^6$: none
KE62-3115F: Kīlauea 2018 littoral bomb MI and matrix glass **Chapter IV**; this study)	0.1 – 0.2	0.03	Fe-XANES S-XANES	20 – 34% Fe^{3+} 68 – 96% S^{6+}	Fe-XANES: $2 – 4x10^7$: none S-XANES: $5x10^7$: high $8x10^6$: slight
KE62-3116F: Kīlauea 2018 quenched lava flow MI and matrix glass **Chapter IV**; this study)	0.1 – 0.3	0.1	Fe-XANES S-XANES	12 – 17% Fe^{3+} 1 – 9% S^{6+}	Fe-XANES: $2 – 4x10^7$: none S-XANES: $2x10^6$: none $3.5x10^5$: none
Augustine 2006: **AUG_308** – low silica andesite tephra; **AUG_HSA2** – high silica andesite tephra (**Chapter V**; this study)	1 – 4	0.2	Fe-XANES	26 – 53% / 27 – 49% Fe^{3+} (with / without Fe-nanolites present)	Fe-XANES: $1 – 1.5x10^8$: slight to none
Lassen (southern Cascades): olivine-hosted MI **BRM, BBL, BORG** (Muth et al., in prep; this study)	0.3 – 3.7	0.1 – 0.7	Fe-XANES S-XANES	14 – 31% Fe^{3+} 20 – 98% S^{6+}	Fe-XANES: $2 – 4x10^7$: mod S-XANES: $5x10^7$: mod $8x10^6$: slight
Cerro Negro: olivine-hosted MI (Gaetani et al., 2012; this study)	3 – 4	0.5	Fe-XANES	20 – 33% Fe^{3+} (Fe-nanolites present)	Fe-XANES: not tracked with repeat scans

2.1 Fe-XANES

1) Fe-XANES measurements were made in fluorescence mode at APS sessions from Dec 7–9, 2018 and June 14-17, 2019. APS 13-ID-E can deliver a focused, unattenuated X-ray beam to the sample at the Fe K-edge energy (~7112 eV) with a photon flux exceeding $1x10^{12}$ photons/s. Fully focused beams of ~1x2 μm are achievable, providing focus flux densities up to $5x10^{11}$ photons/sec/μm^2. Cottrell et al. (2018) show that beam damage during Fe-XANES analysis scales with delivered photon dose over the time required to collect the XANES spectrum. Therefore, for the analyses presented here analysis time was minimized during Fe-XANES analyses as follows:
2) Photon flux was attenuated with an aluminum foil filter in the beam path (6 Al-foil sheets, totaling 222 μm thick), which decreased the incident photon flux to ~3 – $5x10^9$ photons/s, consistent with an approach used in previous studies (Brounce et al., 2017; Moussallam et al., 2019; Tassara et al., 2020).
3) Increased beam size so that photon doses were 1 – $1.5x10^8$, 2 – $4x10^7$, and 6 – $9x10^6$ photons/s/μm^2 with 5x5, 10x10, and 20x20 μm beam footprints, respectively.
4) Increased scan speed and decreased the energy region scanned to reduce beam exposure.

We followed the Fe-XANES measurement methodology outlined in Head et al. (2018), but with modified scan times and energy ranges to further identify and correct for beam damage. We used two different analytical setups: rapid pre-edge scans and slower full energy scans. For rapid scans, the incident beam was scanned from 7092 – 7107 eV in 2.5 eV steps, from 7107 – 7119 eV in 0.1 eV steps, and from 7113.355 – 7144 eV in 0.1 – 1 eV steps. Each scan step was 0.5 seconds (s) and the total scan time was 82 s, with ~10 s delay prior to the next analysis for beamline adjustment and computational processing. This rapid pre-edge scan was designed to minimize beam exposure to the extent possible while still collecting spectra with high enough resolution to fit in the pre-edge region. The 82 s scan is much faster than typical Fe-XANES scan durations reported in the literature, which usually range from 270 to >700 s (4.5 to >10 minutes) (e.g., Cottrell et al., 2009, 2018; Moussallam et al., 2016; Head et al., 2018). For our slower, full energy range scans, the incident beam was scanned from 7012 – 7102 eV in 2.5 eV

steps, from 7102 – 7120 eV in 0.1 eV steps, and from 7113.449 – 7355.1 eV in 0.1-3 eV steps. Each scan step time was either 0.5 or 1 s and total scan durations were 176 or 352 s. This full energy range scan served as a higher-resolution scan of both the pre- and post-absorption edge regions.

Raw spectra (fluorescent intensity / incident flux [I0]) were fit using XAS viewer within the LARCH software package (Newville, 2013). As in previous applications of Fe-XANES to silicate glasses (e.g. Cottrell 2009, Berry et al. 2003, Wilke et al. 2005), we use the pre-edge doublet, which is produced by the 1s → 3d electron transition, to determine glass $Fe^{3+}/\Sigma Fe$ proportions. Based on the Fe pre-edge centroid position of reference glass LW-0 (Cottrell et al. [2009] centroid of 7112.30 eV), energies measured at APS 13-ID-E were -0.27 to -0.32 eV lower than measurements at Brookhaven National Laboratory's National Synchrotron Light Source. All Fe-XANES spectra shown here are presented as-measured at APS, but all centroid positions shown and used in calculations have had session-specific energy shifts applied to match the LW-0 centroid energy of Cottrell et al. (2009). Pre-edge peak fitting ranges were similarly adjusted from Cottrell et al. (2009) to span an energy range of 7108.7 – 7116.7 eV, consistent with the methodology discussed in Zhang et al. (2018). Within this fit window, the absorption baseline of the main Fe Kα absorption edge was fit using a linear and a Lorentzian function, and the pre-edge doublet was fit using two Gaussian functions (Cottrell et al., 2009). The centroid value of these two peaks was used to calculate $Fe^{3+}/\Sigma Fe$ using the Mössbauer calibration of Zhang et al. (2018) for basaltic glasses. Iron speciation in rhyolitic glasses was calculated from a parameterization of Fiege et al. (2017) for felsic glasses. To account for energy offsets between our measurements and those of Fiege et al. (2017), our measured centroid positions were shifted by -0.165 eV to match the absorption edge inflection point of measured Fe-foil. We note that compositional differences between the calibration datasets and our natural samples introduces increased uncertainty in the rhyolite Fe speciation calculations.

2.1.1 Fe-XANES beam damage identification and correction

Fe-XANES analysis of hydrous silicate glasses with a high intensity X-ray beam can cause rapid photo-oxidation of Fe^{2+} to Fe^{3+} within the glass, creating large inaccuracies in calculated $Fe^{3+}/\Sigma Fe$ values (Cottrell et al., 2018) (Figure 2). The extent of this oxidation varies depending on glass composition and photon dose. Beam-induced oxidation is not recognizable in either the pre-edge or the main absorption edge regions of the affected spectra. Consequently, users must either analyze samples under extremely conservative analytical conditions, ensuring no possibility of significant beam damage, or must use a method that can both identify and correct for beam damage in each individual analysis spot. In this work we take the latter approach, presenting a method that allows us to reliably analyze small, hydrous glass inclusions with a relatively high-intensity beam.

To identify and correct for beam damage within each analysis spot, we conducted multiple rapid scans of the Fe Kα pre-edge region to create a time series of progressive oxidation (Figure 2). This time series allows us to assess whether beam damage has occurred during analysis and enables us to calculate sample specific corrections, if needed. For each analysis spot, we conducted 3 – 6 rapid pre-edge scans (82 s) followed by one full scan (176 or 352 s) across the entire Fe Kα absorption edge energy range. If the pre-edge centroids calculated from rapid scans did not show progressive oxidation over time, the spectra were merged together to form a single high-resolution pre-edge spectrum. If changes were observed, we use the time series of centroid positions to extrapolate the centroid back to t = 0 s. We take this extrapolated value as the initial, 'correct' centroid position prior to beam exposure.

X-ray induced photo-oxidation during Fe-XANES analysis can be difficult to observe because a large part of the damage occurs rapidly in the first minutes of analysis (Cottrell et al., 2018). To ensure that our rapid-scan time series adequately capture changes to centroid positions during the earliest stages of photo-oxidation, we measured changes to the intensity of the 2nd pre-edge doublet (at ~7113.4 eV at APS) in one single spot over the course of 6 – 16 minutes.

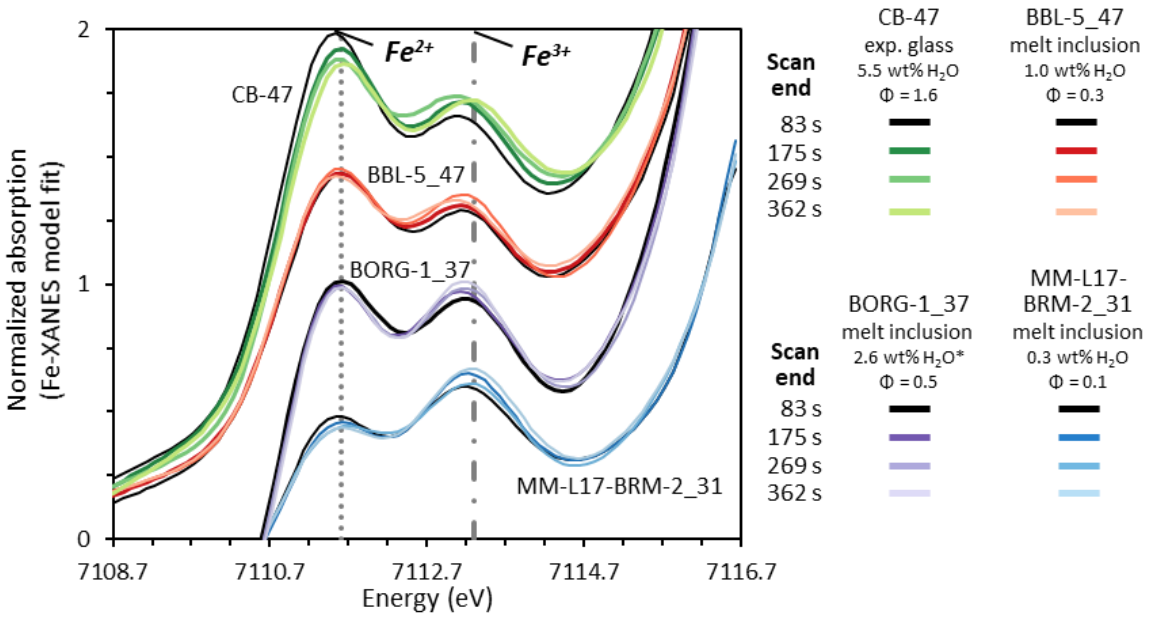

Figure 2. Model fits to Fe-XANES pre-edge spectra for repeated rapid scans of experimental basaltic glass CB-47 and of melt inclusions (MI) from the southern Cascades (CA, USA). Spectra have been vertically shifted for clarity. Progressive oxidation occurs during repeated rapid scans, as shown with lighter colored lines. Samples have different initial $Fe^{3+}/\Sigma Fe$ ratios and H_2O contents, which lead to varying degrees of beam-induced photo-oxidation. Measurements were made with a 10x10 µm beam and photon doses each analysis spot ranged from 2 – $4x10^7$ photons/s/um^2. The lines labeled Fe^{2+} and Fe^{3+} refer to the approximate positions of the first and second pre-edge doublet. *H_2O in BORG-1_37 was not specifically measured and is estimated to be the median H_2O of other MI from that sample.

Such dwell tests measure the ingrowth of Fe^{3+} in the analyzed glass at a much finer resolution than a pre-edge scan allows (Shorttle et al., 2015; Cottrell et al., 2018). We conducted this test on an experimental basaltic glass (CB-47, Weaver et al. [2011]) (Figure 3A, B) with a high H_2O content (5.5 wt%) and a high proportion of Fe^{2+} (~13% $Fe^{3+}/\Sigma Fe$; Fe- and S- valence proportions are reported as percentages throughout). The combined high H_2O and Fe^{2+} contents of CB-47 make it more susceptible to beam damage than most natural glasses and MI (Cottrell et al. 2018). For example, the calculated beam damage susceptibility index (Φ, where $\Phi = XHO_{0.5} * XFeO/FeO_{1.5}$), as described in Cottrell et al. (2018), is 1.7 for CB-47 compared to 0.1 – 0.7 for natural MI investigated here (Figure 5, Table 1). Analyses of CB-47 therefore provide a "worst-case

scenario" benchmark for timescales of Fe-XANES beam damage ingrowth. If beam damage can be observed and corrected for in this highly susceptible glass, then our time-dependent correction approach will be accurate for most natural samples.

To test whether our rapid-pre-edge scans are fast enough to capture rapid photo-oxidation in CB-47, we compared the time series of the 2nd pre-edge doublet dwell test to repeated rapid pre-edge scans of the same glass (Figure 3). The intensity of the 2nd pre-edge doublet is proportional to the pre-edge centroid value, and thus the rate of change of the 2nd pre-edge doublet can be compared to the change in centroid value during time series analyses. During measurements of CB-47 with a 5x5 μm spot, photo-oxidation occurs too quickly in the first minute of analysis to be adequately captured with our rapid pre-edge scans (Figure 3A, C). However, during measurements with a 10x10 μm spot photo-oxidation is progresses slowly enough that changes to both the 2nd pre-edge doublet intensity and centroid values can be adequately described with a linear function (Figure 3B, D).

To substantiate the results of these tests and explore the effect of glass composition, we performed the same dwell tests on another experimental glass similar to CB-47 (CB-33, $\Phi = 1.8$; Weaver et al., 2011) and on a moderately hydrous obsidian pyroclast from Mono-Inyo Craters (CA, USA) (P2-F; Barnes et al., 2014; Watkins et al., 2017) (Figure B1, Table 1). With the same photon flux and spot size as the CB-47 tests, changes to the 2nd doublet intensity during these additional dwell tests were similar to the time series observed in CB-47. This suggests that this correction approach can be used for a range of glass compositions. To improve scan resolution in more silicic, Fe-poor glasses, longer pre-edge scan times than presented here for Fe-rich basaltic glasses may be necessary. Longer scan times should be balanced by increasing analysis spot size as much as possible to keep beam damage to a minimum.

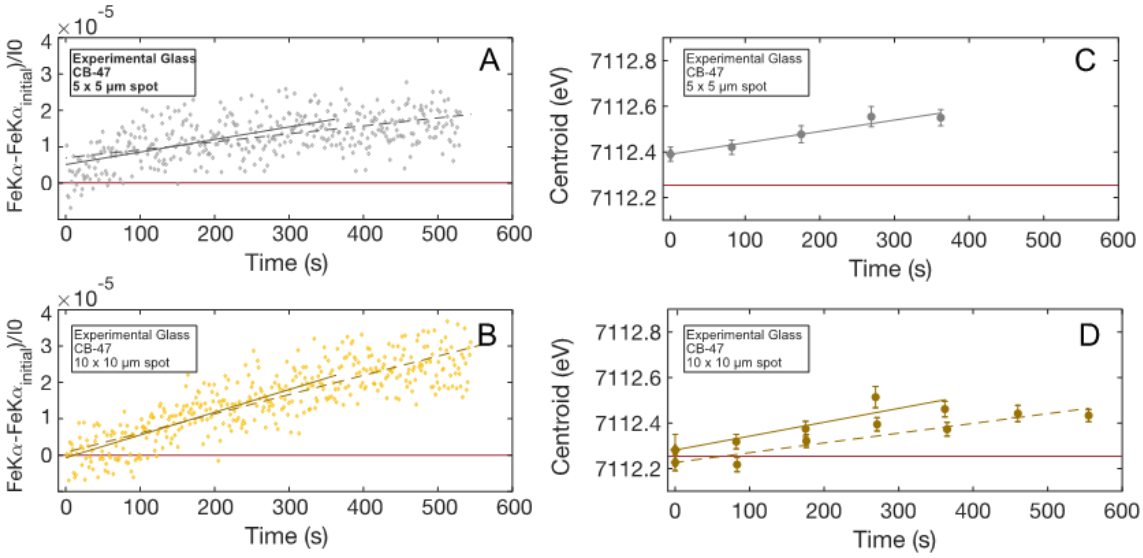

Figure 3. *(A, B)* Intensities of the 2nd pre-edge doublet as a function of time measured with either 5x5 µm or 10x10 µm spots on experimental glass CB-47. Gray and yellow lines are linear regressions through data from 0 to 362 s (solid) or 0 to 537 s (dashed). Fe Kα/I0 initial intensity (red horizontal line) is taken as the average of the first 5 analyses. *(C, D)* Pre-edge centroid positions calculated from repeated rapid scans (see Figure 2) for experimental glass CB-47 collected with either a 5x5 µm or 10x10 µm spots. Each circle is a centroid value calculated with one pre-edge scan. Error bars represent 1 standard error of peak fits to each scan. Diamonds at t=0 s are the intercept of each linear regression, taken to be the beam damage corrected centroid value. Error bars on the t=0 centroid positions represent 1 standard error of the time series linear regression. The estimated initial centroid value (red line) in panels *C* and *D* is the average corrected centroid values for the two 10x10 µm analysis time series (panel *D*). Gray and yellow lines are linear regressions through centroid values from 82 to 362 s (solid) or 82 to 537 s (dashed).

Because glass CB-47 is more susceptible to beam damage than most MI and matrix glasses, changes to pre-edge centroids in most natural samples analyzed under the same conditions (~3.0x10^7 photons/s/um^2) can also be described with a linear function (Figure 6). Hydrous basaltic MI from the southern Cascades arc ($\Phi = 0.1 - 0.7$) show consistent increases in centroid values over the course of several repeated rapid scans, indicating Fe^{3+} ingrowth (Figure 4, Table 1). In basaltic MI from Kīlauea Volcano (HI, USA) ($\Phi \leq 0.1$), we observe no substantial time-dependent change to centroids, as expected based on their low H_2O contents (Figure 4, Table 1). For most samples, linear regressions using 4 pre-edge scans are adequate to correct to initial centroid positions. However, using up to 6 scans provides a more consistent fit between samples, as

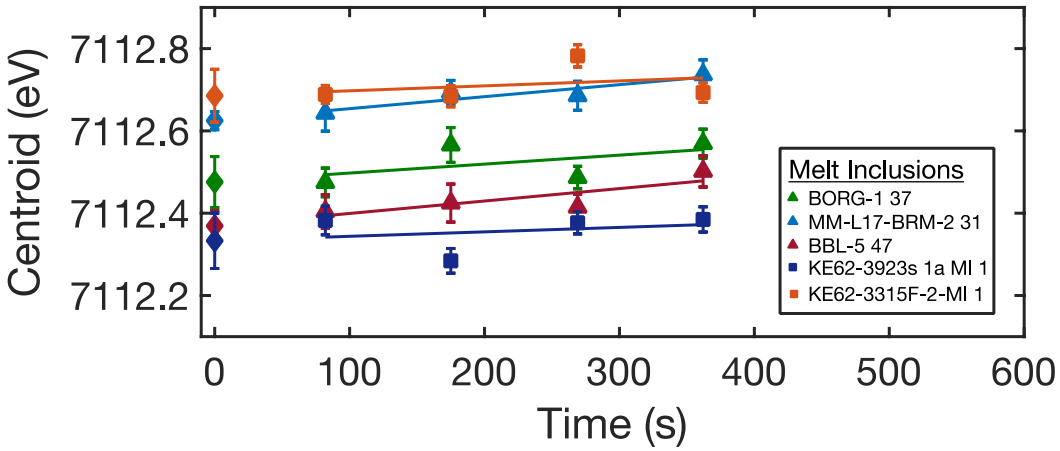

Figure 4. Fe Kα pre-edge centroid positions calculated from repeated rapid scans of MI from the southern Cascades (triangles) and MI from Kīlauea Volcano (squares). Symbol are the centroid values calculated from one pre-edge scan. Error bars represent 1 standard error for individual centroid fits. Lines are linear regressions through centroid values from 82 to 362 s. Diamonds at t=0 s are the intercept of each regression, taken to be the beam damage corrected centroid position. Error bars on diamonds represent 1 standard error of linear regression.

increased scans minimize the leverage of anomalously noisy scans in the regression (Figure 3D). Although polynomial functions may allow for beam damage corrections in unusually susceptible glasses or in glasses analyzed with high photon doses, we find that this often results in significant misfit because the polynomial form is poorly defined for the initial 10s of seconds of analysis, when beam damage occurs rapidly.

The rate of change of calculated centroid values is proportional to the rate of Fe^{3+} ingrowth. Therefore, the slope of linear regressions of centroid value time series is effectively the rate of photo-oxidation. The slopes of these linear regressions are inversely correlated with calculated initial $Fe^{3+}/\Sigma Fe$ and positively correlated with H_2O contents of each glass (Figure 5, Figure B2). This is consistent with observations by Cottrell et al. (2018) that beam damage occurs more readily in reduced and/or hydrous glasses.

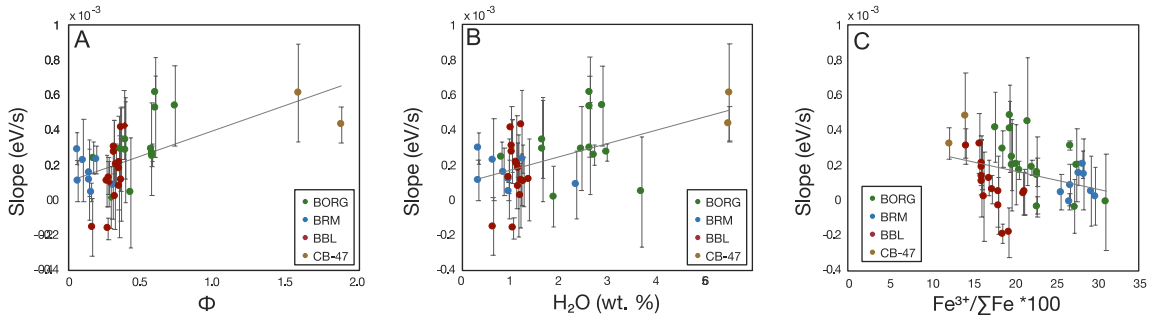

Figure 5. Slopes of linear regressions through centroid value time series for individual analysis spots plotted as a function of *(A)* beam damage susceptibility index ($\Phi = XHO_{0.5} * XFeO/FeO_{1.5}$) as defined in Cottrell et al. (2018), *(B)* H_2O content, and *(C)* initial $Fe^{3+}/\Sigma Fe$ content of each glass. Inclusions from southern Cascades cinder cones (BORG, BRM, BBL) and experimental glasses (CB-47) are grouped by color. Gray lines are linear regression through analysis spots from all samples.

For hydrous basaltic MI from the southern Cascades, the average 1 standard error of regression for corrected centroid values is 0.04 eV, or 1.8 % $Fe^{3+}/\Sigma Fe$ when propagated through the calibration of Zhang et al. (2018). This error is only slightly larger than the average standard error of centroid value fits of our higher resolution full length scans (0.03 eV, 1.4 % $Fe^{3+}/\Sigma Fe$), and is much smaller than the ~15 % variation in $Fe^{3+}/\Sigma Fe$ measured in basaltic arc MI globally (Kelley and Cottrell, 2009; Brounce et al., 2014; Muth et al., in prep). Regressions on replicate analyses within the same MI yield corrected centroid positions that are within error of each other (Figure B3), indicating that our correction approach is reasonably precise. However, this approach is limited by the resolution of each rapid pre-edge scan, which necessarily have shorter count times than slower Fe-XANES scans.

Although this beam damage correction approach introduces some imprecision, it importantly ensures that data sets are not systematically biased to higher calculated $Fe^{3+}/\Sigma Fe$ values due to uncorrected photo-oxidation. In analyses of southern Cascades basaltic MI (0.3 – 3.7 wt% H_2O, 0.1 – 0.7 Φ) the difference between corrected and uncorrected centroid positions is large (Figure 6). Using linear regressions for each of these inclusions, we calculate the difference between centroids interpolated to 362 s, the length of a full length Fe-XANES scan, and centroids extrapolated back to t=0 s. On average, centroid values at 362 s are 0.09 eV higher than those at 0 s. This means that despite measures taken to lower the photon flux, had we analyzed these hydrous MI with

normal 6 minute scans our analyses would have overestimated melt $Fe^{3+}/\Sigma Fe$ by ~3.6%, or 0.5 log units fO_2 (calculated for basalt at 1150 °C, 400 MPa using Kress and Carmichael [1991]).

In summary, photo-oxidation during Fe-XANES measurements can cause large systematic biases toward higher calculated $Fe^{3+}/\Sigma Fe$ in beam-sensitive glasses, which can significantly affect geologic interpretation of redox conditions. Taking measures to mitigate beam damage through reduced X-ray dose (where possible), and/or by applying analysis-specific time-dependent corrections described here, is critical for accurate interpretation of Fe-XANES measurements in beam-sensitive glasses, such as hydrous arc basalts.

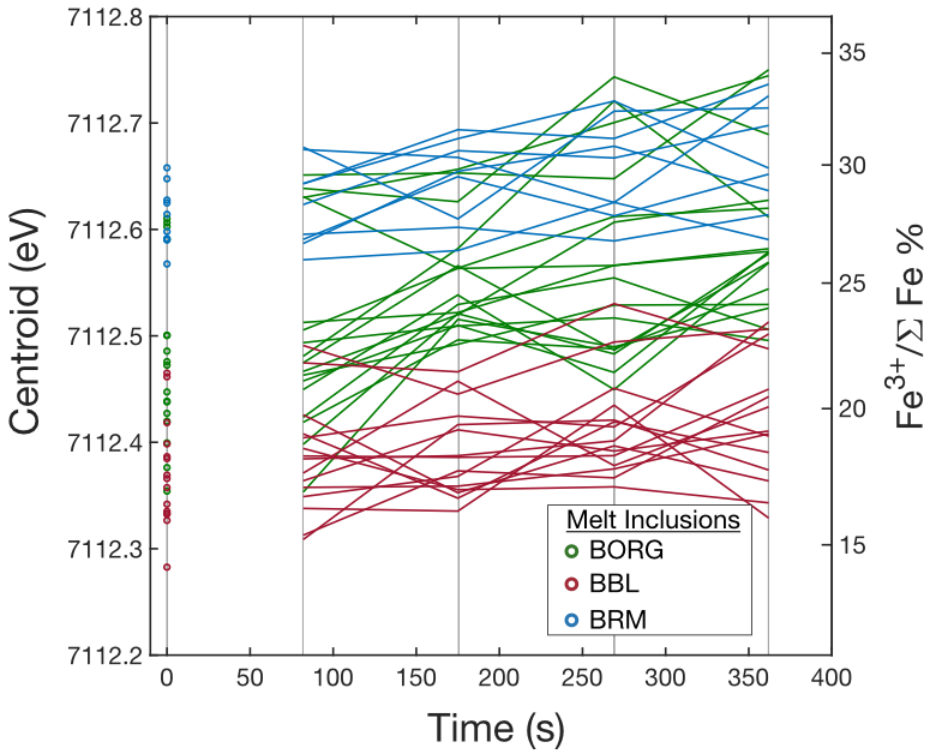

Figure 6. Fe Kα pre-edge centroid positions through time calculated from repeated pre-edge scans for individual southern Cascades MI. Solid lines connect centroids calculated from four consecutive scans of the same analysis spot, and open circles at t=0 s are the corrected initial centroids. Vertical gray lines show the end times of each scan. Right vertical axis is the calculated $Fe^{3+}/\Sigma Fe$ from centroid values using the calibration of Zhang et al. (2018).

2.2 S-XANES

Melt inclusion preparation requirements are somewhat more relaxed for S-XANES measurements than for Fe-XANES because the 1/e absorption depth for X-rays at the S K-edge energy is only 5 μm, so 95% of X-ray energy is effectively absorbed within ~15 μm thick glass (Figure 1A). Most analyzed MI are thicker than 15 μm so that doubly intersecting MI is generally not necessary for S-XANES analyses. Additionally, most host minerals contain little S compared to MI (Callegaro et al., 2020), so beam overlap of the host mineral is less of a concern than in Fe-XANES analyses, where Fe signal contribution from the host phase can be significant. Consequently, larger X-ray analysis footprints can generally be used for S-XANES, which reduces X-ray dose and thereby some of the beam damage susceptibility. However, when analyzing S-poor MI (< ~400 ppm S), even slight contributions from the host phase might be significant relative to the low-S glass signal and beam overlap of the host phase should be avoided. Additionally, cracks and surface contaminants (e.g., oils) may be present on prepared surfaces, both of which can contain undesired S-bearing material (Brounce et al., 2019). Consequently, smaller beam footprints for S-XANES remain more versatile (particularly for low-S samples) in being able to avoid contamination from host minerals or from surface aberrations.

S-XANES beam damage manifests differently from Fe-XANES damage. Sulfur in silicate melts occurs as S^{2-} or S^{6+} but does not naturally occur as S^{4+} (Wilke et al., 2008). In Fe-bearing natural glasses, S-XANES beam damage typically manifests as photo-reduction of S^{6+} to S^{4+} (Wilke et al., 2008). Sulfite has two absorption peaks, which occur at 2477.5 and 2482 eV (Fleet et al., 2005; Wilke et al., 2008; Métrich et al., 2009). The sulfite 2482 eV absorption peak overlaps that of S^{6+}, but the 2477.5 eV sulfite peak is a unique spectral signal that can be used to identify measurements that have undergone beam damage (Wilke et al., 2008). Beam damage is therefore more easily detected in S-XANES than in Fe-XANES, and time-dependent corrections to t=0 s are not necessary because all observed S^{4+} is attributable to beam damage. Photo-oxidation of S^{2-} to S^{4+} or to S^{6+} has been documented during electron microprobe (EPMA) wave scan analyses (Wallace and Carmichael, 1994; Rowe et al., 2007) and during extremely long duration XANES measurements (20 – 80 minutes) of highly alkalic glasses from Mt.

Erebus (Antarctica) (Moussallam et al., 2014). However, S photo-oxidation is not observed in natural glasses during most XANES analyses, suggesting different mechanisms of S beam damage may occur under electron bombardment compared to X-ray irradiation, and during X-ray irradiation of alkali-rich glasses.

The redox mechanism of S-XANES beam damage (S^{6+} to S^{4+}) is imprecisely known. In contrast to Fe-XANES beam damage (Cottrell et al., 2018), H_2O content does not appear a critical control on S beam damage (see below), and the compositional dependence of S beam damage susceptibility has not been thoroughly examined. It is consequently difficult to predict whether any particular sample will be susceptible to S-XANES beam damage. Therefore, as with Fe beam damage, it is important to be able to account for beam damage within each individual measurement rather than applying blanket corrections to an entire sample suite.

Our approach in managing and correcting S-XANES beam damage is similar to that for reducing Fe-XANES beam damage, namely minimizing pre-analysis X-ray irradiation, decreasing photon dose as much as possible while maintaining sufficient signal, and using repeat rapid scans to observe beam damage ingrowth. Where S-XANES beam damage has occurred, we correct for this by calculating the peak area of the damage-induced S^{4+} signal and restoring this to original S^{6+} intensity via a calibrated conversion factor (details below).

2.2.1 S-XANES analysis conditions

S-XANES measurements at APS GSECARS beamline 13-ID-E were conducted in fluorescence mode and within a He-environment to minimize atmospheric absorption of the X-ray fluorescent signal. Incident beam flux ranged from ~1 – 40x10^9 photons/s for S-XANES analyses, which was purposely lowered from the maximum possible flux to reduce rates of beam damage ingrowth. Repeat measurements of sulfate-bearing Scotch® tape during four analytical sessions between 2016 and 2019 indicate a consistent S^{6+} peak position of 2481.8 eV. The sulfate peak position measured by Jugo et al. (2010) at European Synchrotron Radiation Facility beamline ID21 is +1 eV relative to measurements at APS beamline 13-ID-E, likely due to monochromator calibration (Head

et al., 2018). All subsequently presented Jugo et al. (2010) values have been shifted by -1 eV to be consistent with our measurements.

As with our Fe-XANES beam damage correction approach, we conduct repeat rapid scans to identify S-XANES beam damage and, if necessary, apply sample-specific corrections. We followed the S-XANES measurement methodology outlined in Head et al. (2018), collecting S K-edge spectra by scanning the incident beam from 2437 – 2467 eV in 2.5 eV steps, from 2467 – 2487 eV in 0.1 eV steps, and from 2487 – 2622 eV in 1.5 eV steps. However, we used analysis times of either 0.5 or 1.0 s per step bin (continuous steps rather than discrete) for variably rapid scans with total durations of 154 or 308 s, respectively. These scan times are 2.5x to 5x faster than in Head et al. (2018), which results in noisier spectra but allows us to better observe and avoid beam damage (Fiege et al., 2014a; Konecke et al., 2017). We typically conducted three repeat scans of each analysis spot, with cumulative measurement times of ~8 – 15 minutes per location. If S^{4+} peak growth is present during successive scans, we use only the first scan for our analyses, which will have undergone the least S^{6+} to S^{4+} photo-reduction. If no S^{4+} ingrowth is observed, then repeat scans were merged to improve signal quality.

For beam-damaged samples, the S^{6+} to S^{4+} photo-reduction can theoretically be corrected by restoring the S^{4+} 2477.5 eV peak intensity back to S^{6+} signal. However, this correction requires knowing an appropriate signal intensity scaling factor to restore a S^{4+} signal to the original S^{6+} intensity. Konecke et al. (2017) and Nash et al. (2019) apply S-XANES beam damage corrections by assuming a 1:1 intensity scaling between S^{4+} and S^{6+} peaks. However, we caution against assuming this 1:1 scaling relationship of fluorescent energy outputs in absence of direct evidence. To determine how the loss of S^{6+} intensity relates to the growth of S^{4+}, and therefore how to calculate an appropriate signal intensity scaling factor between these peak intensities, we conducted a series of measurements on a hydrous, sulfate-dominated, S-rich synthetic basaltic glass from Chowdury and Gasgupta (2019) (50 wt% SiO_2, 9000 ppm S, ~6.5 wt% H_2O, 1325 °C, 2 GPa). The large area of this experimental glass allowed analyses with a range of spot sizes (2x2, 10x10, 20x20, and 50x50 μm) to observe varying degrees of beam damage, and the sulfate-only initial composition made identification of S^{4+} ingrowth obvious. With repeat measurements, we are able to track the ingrowth of the S^{4+} 2477.5 eV peak

(hereafter "S^{4+} peak") at the expense of the S^{6+} 2481.3 – 2482 eV peak. We can thereby quantify how the S^{4+} peak intensity relates to the loss of S^{6+} intensity, and how consistent the S^{4+} to S^{6+} intensity scaling relationship is with increasing degrees of beam damage.

2.2.2 Quantifying S-XANES spectra via peak fitting

Determining the relationship between S^{4+} signal growth and S^{6+} signal loss during beam damage requires a consistent peak fitting method to quantify the change in signal intensities. Peak fitting approaches to S-XANES spectra have also been employed by other researchers (Manceau and Nagy, 2012; Konecke et al., 2017; Nash et al., 2019), but have not been described or calibrated in silicate glasses at a level of detail to be fully reproducible. We therefore establish a new peak fitting calibration based on the data used by Jugo et al. (2010) to originally define a calibration relating S-XANES signal intensities to S speciation. The S-XANES spectra of silicate glasses consists of fluorescence bands produced by X-ray absorption by S^{2-}, S^{4+}, and S^{6+}, and by S^{1-} and S^{2-} sulfide complexes (Paris et al., 2001; Fleet et al., 2005; Métrich et al., 2009). Jugo et al. (2010) empirically determined a relationship of S^{2-} and S^{6+} XANES intensities to S speciation using a set of experimental glasses by integrating all signal within energy ranges roughly relating to S^{2-} and S^{6+} peaks (2474.7 – 2479 eV and 2480.5 – 2483 eV, respectively; Jugo et al. [2010] ranges have been shifted by -1 eV). However, the S^{4+} absorption peak (2476.8 – 2477.6 eV) occurs within the broad S^{2-} energy range so that the Jugo et al. (2010) approach would inappropriately include photo-reduction induced S^{4+} signal intensity as S^{2-} intensity. Our peak fitting approach differentiates S^{2-}, S^{4+}, and S^{6+} absorption intensities, enabling us to quantify beam damage by isolating S^{4+} from the S^{2-} peak. We can then restore the S^{4+} photo-reduction signal to an original S^{6+} intensity to calculate the undamaged S speciation of the glass.

Our S-XANES peak fitting method again uses the spectral fitting program XAS viewer (Newville, 2013) to correct for instrument deadtime and to fit the S-XANES data. Measured spectra were first scaled by the Si Kα signal intensity, to avoid aberrations in incident beam intensity over the analysis energy range. Following the approach of Jugo et al. (2010) and Anzures et al. (2020), we then normalize each spectrum so that the energy range containing pre-edge features begins at zero intensity (~2467 eV), and the post-edge

signal intensity is 1 (> 2510 eV). This is done by defining a linear relation in the low energy range (~2441 – 2467), and flattening the high energy range (~2525 – 2611 eV) to scale the spectra to between 0 – 1 (Ravel and Newville, 2005; Anzures et al., 2020). These ranges are guidelines that should be modified as necessary for anomalous spectra. However, sulfide X-ray absorption begin at energies just above 2467, so the pre-edge normalization range should be kept below this energy. The normalized post-edge spectrum is fit using an error function and a broad Gaussian, which together define the background. The center point of the error function is fixed and the width of the high-energy Gaussian is constrained to maintain a consistent background fitting approach for all spectra (Table 2).

Assessing spectra of numerous reduced and oxidized glasses across a compositional range from basaltic to rhyolitic, we identify the energy ranges of five peaks within the S Kα absorption region. We distinguish absorption peaks of sulfide complexes and S^{2-}, S^{4+}, and S^{6+} that have been previously recognized (Wilke et al., 2008; Métrich et al., 2009; Jugo et al., 2010; Head et al., 2018). We additionally identify a peak at slightly higher energy than the main S^{6+} peak, whose intensity seems at least partially correlated to S^{6+} intensity, but is also present in some S^{2-} dominated samples. This higher energy peak was similarly identified by Konecke et al. (2017), who refer to it as the S "ionization peak", a term we adopt here. After normalizing the spectra, we simultaneously fit the background error function and Gaussian, and five separate Gaussian functions for each of these S absorption features (Figure 7, Figure B5). Table 2 provides the energy ranges and peak width tolerances for fitting each spectral feature. These fitting ranges have been established to provide flexibility in fitting slight differences in peak energies occurring across a range of compositions and oxidation states, while maintaining peak positions that accurately correspond to the specific S features (important for overlapping features such as the S^{2-} and S^{4+} peaks, and the S^{6+} and ionization peaks).

Table 2. Peak definitions and fit parameters used for quantification of normalized S-XANES spectra using the XAS Viewer spectral fitting program (Newville, 2013).

S-XANES feature	function type / name	peak center bounds (eV)	peak sigma bounds (width)	Peak amplitude bounds
overall fit ranges				
peak fit range	-	2455 – 2550	-	-
pre-edge fit range	-	2466 – 2487	-	-
background fitting				
baseline error function	error1	2485 (fixed)	8 (fixed)	0 – 1.1
baseline Gaussian	gauss1	2493 – 2500	0 – 10	0 – 15
S speciation peaks				
sulfide complexes	gauss2	2465 – 2470	0 – 1	0 – ∞
S^{2-}	gauss3	2475.3 – 2477	2 – 4	0 – ∞
S^{4+}	gauss4	2476.8 – 2477.7	0.1 – 1	0 – ∞
S^{6+}	gauss5	2480 – 2482.3	0.1 – 3	0 – ∞
ionization peak	gauss6	2483.5 – 2486	0 – 4	0 – ∞

To relate the relative fitted peak areas to S speciation, we calibrate our peak fitting method to synthetic hydrous basaltic glasses presented in Jugo et al. (2010). Following the same approach as Jugo et al. (2010), we use their completely S^{2-} and completely S^{6+} bearing synthetic glasses as reduced and oxidized end-members, and apply linear combination fitting of these end-members to produce representative mixed speciation spectra (Figure B4). Complete details are provided in **Appendix B**.

Jugo et al. (2010) focus their calibration on only S^{2-} and S^{6+} peak intensities, and do not include signals from lower energy sulfide-complexes and higher energy features beyond the S^{6+} peak. We follow this approach, and although we fit all spectral features in the calibration glasses, we use only the S^{2-} and S^{6+} peak areas to quantify the S speciation (Figure 7, Figure B5). Jugo et al. (2010) describe an exponential function to relate S-XANES S^{2-} and S^{6+} peak intensities to S speciation, however we find that the following polynomial relationship is more appropriate for our peak fitting method (Figure B6):

$$S^{6+}/\Sigma S = 0.1733 * (IS^{6+}/\Sigma IS^{T})^2 + 0.8343*(IS^{6+}/\Sigma IS^{T}) \text{ , [eq. 1]}$$

where $S^{6+}/\Sigma S$ is the fraction of S^{6+} speciation out of total S, and $IS^{6+}/\Sigma IS^{T}$ is the XANES measured S^{6+} intensity (peak area) out of the total S^{6+} and S^{2-} peak intensities (S^{T}). This

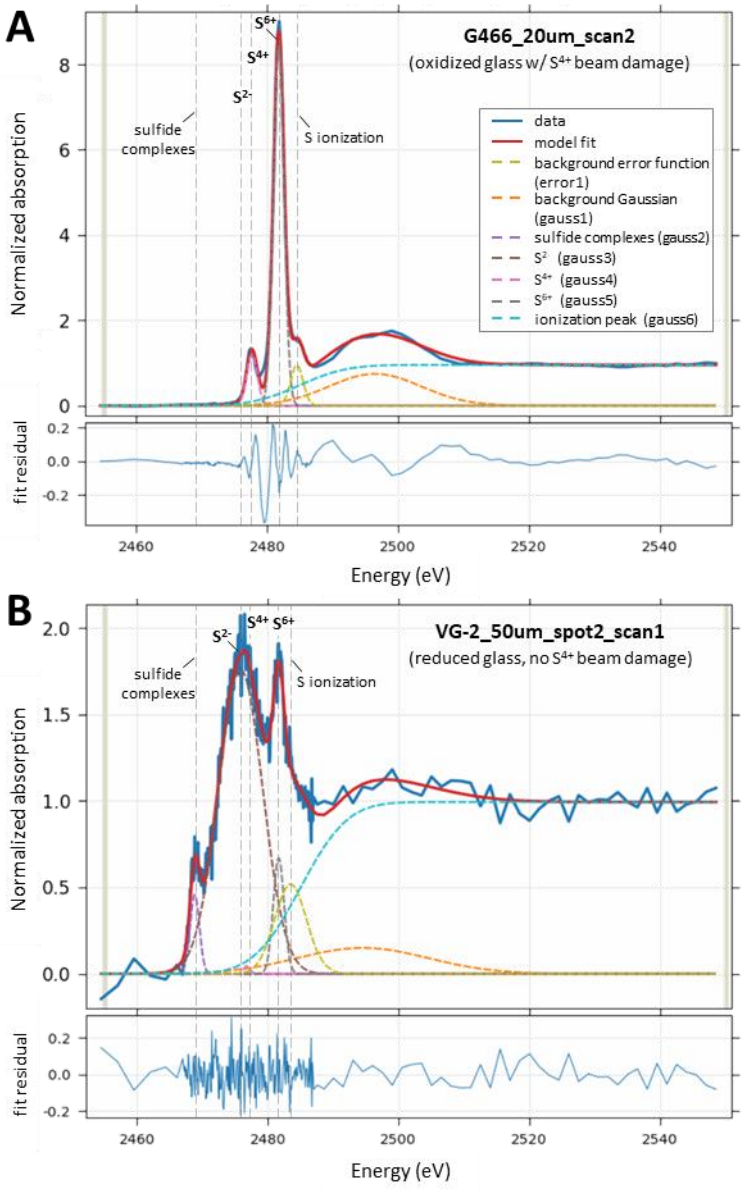

Figure 7. *(A)* Example S-XANES peak fitting to oxidized experimental glass G466. This spectrum is the 2nd of 3 repeat scans with a 20x20 μm beam, and shows a dominant S^{6+} peak (2480 – 2482.3 eV) and a substantial beam damage induced S^{4+} peak (2476.8 – 2477.7 eV). No S^{2-} is observed. The fit residual shows slight remaining unfit structure. *(B)* Example S-XANES peak fitting of reduced VG-2 MORB glass analyzed using a 50x50 μm beam. The noisier spectrum is due to lower S content than G466 and a difference in vertical scale. A main glassy S^{2-} peak (2475.3 – 2477 eV) is present, as well as lesser S^{6+} peak and minor sulfide peak (2465 – 2470 eV). Minimal S^{4+} beam damage ingrowth is observed with this diffuse beam analysis (compare to Figure 9). A S ionization peak is present in S-XANES spectra of the both oxidized and reduced glasses. See Table 2 for identification of peaks and fit parameters. Reference peak position lines are approximate and can vary slightly between samples.

peak fitting approach accurately reproduces observations from additional glasses synthesized by Jugo et al. (2010) across a range of fO_2 and S speciation (Figure B7). We therefore conclude that our peak fitting approach is comparable to the calibration and thermodynamic data originally developed and described by Jugo et al. (2010). However, our method is subject to the same limitations as the Jugo et al. (2010) approach, namely the uncertainty that the linear end-member mixing approach to calibrate mixed S speciation melts is valid, and that the dataset was calibrated to only hydrous basalts, so that the quantification may not be directly applicable to other compositions. Additional uncertainty arises from inconsistencies with normalizing the S-XANES spectra, which can be challenging in S-poor glasses. We note that raw S-XANES spectra are seldom published so that consistency in normalization approaches between studies can never be tested (Rose-Koga and et al., submitted). Based on replicate analyses within the same MI, we estimate the precision of our S-XANES peak fitting method to be ±2% $S^{6+}/\Sigma S$ (1 standard error, n=7). When considering further uncertainties in the peak fitting calibration and from the non-uniqueness of spectra normalization, we consider the total accuracy of this method to be ±5% $S^{6+}/\Sigma S$.

2.2.3 S-XANES beam damage identification and correction

Since we include the S^{4+} peak in our fitting methodology, we can quantitatively separate the beam damage-induced S^{4+} signal from the overlapping broad S^{2-} peak in S-XANES spectra. This was not possible with the Jugo et al. (2010) method because all signal intensity over this region was considered as S^{2-}, which would lead to spurious results in beam-damaged spectra (Figures 8, 9). During repeat measurements of hydrous, S-rich, oxidized basaltic glass G466, we observe that progressive irradiation leads to increasing S^{4+} intensity and concomitant decreasing S^{6+} intensity (Figure 8) (Wilke et al., 2008; Métrich et al., 2009; Konecke et al., 2017). The highly oxidized experimental glass G466 (Chowdhury and Dasgupta, 2019) contains no S^{2-} signal to overlap with the S^{4+} peak, making observation of the S^{4+} signal in this sample straightforward. As expected, increased photon doses with more focused beams cause more rapid S^{6+} to S^{4+} photo-reduction. Comparing the intensity ratio of S^{4+} peak ingrowth and S^{6+} peak loss during progressive beam damage from repeat measurements using 2x2, 10x10, 20x20 and 50x50

μm spot sizes, we find that S^{4+} peak ingrowth relates to S^{6+} intensity decrease by a factor of 1.2 +/- 0.09 (1 SE; n=7). We apply this scaling factor to observed S^{4+} peak intensities in beam damaged samples to restore original S^{6+} peak intensities via:

$$\Sigma IS^{6+} = (IS^{4+} * F_S^{4+/6+}) + IS^{6+} \quad , [eq.\ 2]$$

where IS^{4+} and IS^{6+} are the measured Gaussian peak areas from S-XANES intensities, $F_S^{4+/6+}$ is the S^{4+} to S^{6+} intensity scaling factor (1.2), and ΣIS^{6+} is the restored total S^{6+} S-XANES intensity. The ratio of S^{6+} signal intensity to total S intensity is then:

$$IS^{6+} / \Sigma IS^{T} = \Sigma IS^{6+} / (IS^{2-} + \Sigma IS^{6+}) \quad , [eq.\ 3]$$

where IS^{2-} is the Gaussian area of the broad S^{2-} peak from S-XANES. Inputting this value into our peak fitting calibration based on the Jugo et al. (2010) glass suite (eq. 1) calculates the beam damage restored S speciation.

In addition to the obvious S^{4+} peak growth during beam damage of G466, we observe the ingrowth of a very small peak between 2471.6 – 2472.0 eV (Figure 8 inset), which is in the energy absorption range of S^0 (Fleet et al., 2005; Métrich et al., 2009) or of H_2S (Klimm et al., 2012a). This peak is recognized during successive analyses using 20x20, 10x20, and 2x2 μm spots, but is a trivial feature compared to the S^{4+} and S^{6+} signals. We also observe a slight absorption increase in the broad energy range between 2470 – 2475 eV, which overlaps the S^{2-} glassy absorption range. These subtle features are not included in our beam damage correction approach, as peak-fitting such low-intensity features was inconsistent and sensitive to slight variations in the spectra normalization routine. However, these additional features of S-XANES beam damage invite future investigation.

In addition to S^{6+} to S^{4+} photo-reduction occurring rapidly in the G466 hydrous oxidized basaltic glass, we also observe rapid photo-reduction during analyses of dry tholeiitic basalts. Repeated rapid S-XANES scans of the mid-ocean ridge basalt (MORB) glass standard VG-2 (NMNH 111240-52; Juan de Fuca ridge) again show a marked decrease in S^{6+} and ingrowth of S^{4+} during successive analyses (Figure 9). S-XANES measurements of VG-2 have been presented elsewhere (e.g., Head et al., 2018), but have typically been analyzed with a more focused beam and longer measurement times than used here, which we observe to cause a near complete conversion of S^{6+} to S^{4+}. VG-2 glass is relatively reduced so that the original S^{6+} is low.

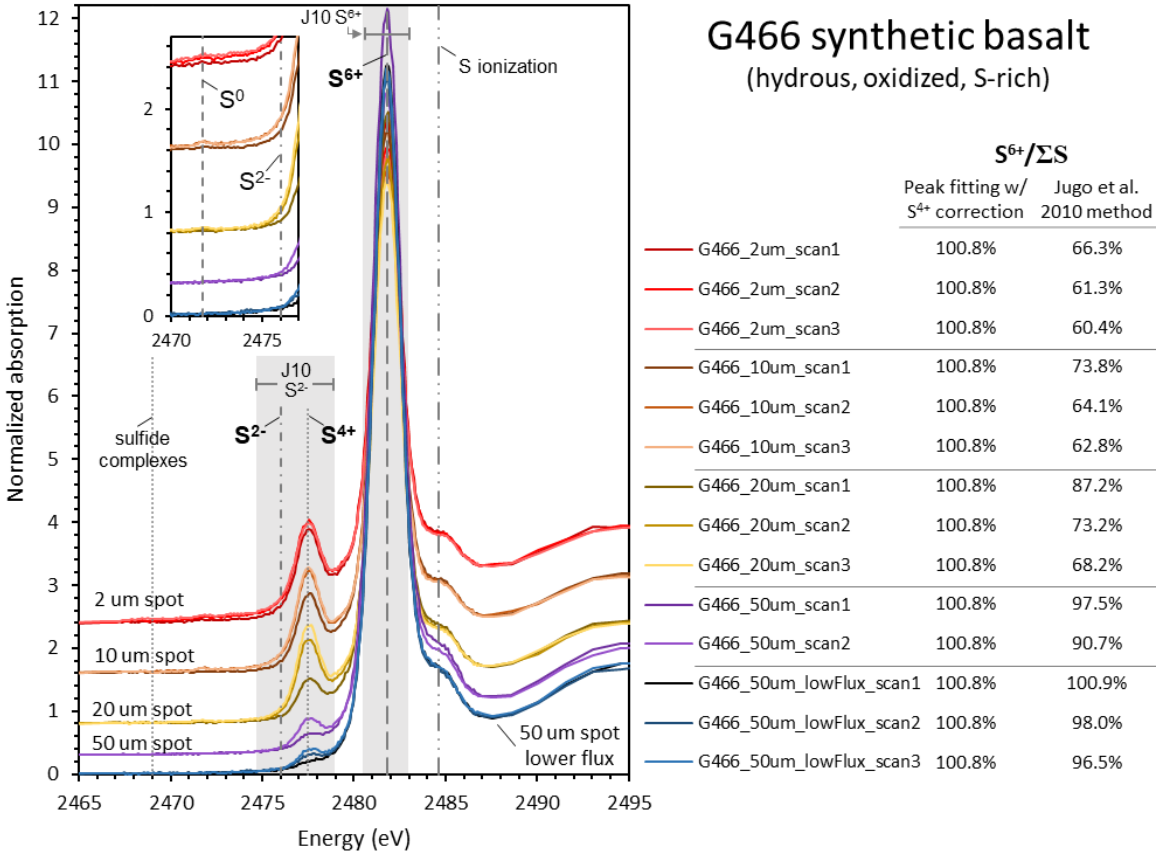

	S6+/ΣS	
	Peak fitting w/ S4+ correction	Jugo et al. 2010 method
G466_2um_scan1	100.8%	66.3%
G466_2um_scan2	100.8%	61.3%
G466_2um_scan3	100.8%	60.4%
G466_10um_scan1	100.8%	73.8%
G466_10um_scan2	100.8%	64.1%
G466_10um_scan3	100.8%	62.8%
G466_20um_scan1	100.8%	87.2%
G466_20um_scan2	100.8%	73.2%
G466_20um_scan3	100.8%	68.2%
G466_50um_scan1	100.8%	97.5%
G466_50um_scan2	100.8%	90.7%
G466_50um_lowFlux_scan1	100.8%	100.9%
G466_50um_lowFlux_scan2	100.8%	98.0%
G466_50um_lowFlux_scan3	100.8%	96.5%

Figure 8. Normalized spectra of oxidized experimental glass G466 with repeat measurements in different locations using progressively more focused spot sizes (50x50, 20x20, 10x10, and 2x2 µm). Spectra have been vertically shifted for clarity. The ingrowth of S^{4+} (2476.8 – 2477.7 eV) at the expense of S^{6+} (2480 – 2482.3 eV) is seen in repeat measurements at all spot sizes, and is increasingly pronounced with more focused beams. S^{4+} ingrowth stops after reaching a maximum intensity during the first focused 2x2 µm spot analysis, with no further ingrowth with subsequent analyses. *(inset)* Detailed view of the 2470 – 2476 eV region showing an ingrowth of a small peak at ~2471.7 eV and a slight absorption increase across 2470 – 2475 eV in analyses with focused beams. Photon doses were $1.1x10^7$, $3.2x10^7$, $7.0x10^7$, $2.8x10^8$, $7.0x10^9$ photons/s/um^2 for the 50µm_lowFlux, 50µm, 20µm, 10µm, and 2µm scans, respectively. Each individual scan length was 5 minutes, except for G466_50um_scans that were each 10 minutes. $S^{6+}/\Sigma S$ calculations using the peak fitting approach and correcting for S^{4+} photo-reduction are compared with $S^{6+}/\Sigma S$ calculated using the Jugo et al. (2010) method ("J10" gray S^{2-} and S^{6+} regions [energy shifted as discussed]), where the S^{4+} photo-reduction peak would be counted as part of the S^{2-} signal. Reference peak position lines are approximate and can vary slightly between samples.

The S^{4+} peak resulting from photo-oxidation of this minor S^{6+} is correspondingly small and difficult to discern from the dominant S^{2-} peak, which potentially explains why beam damage in VG-2 glass has not been previously recognized. A North Pacific MORB glass analyzed via S-XANES with a defocused beam by Métrich et al. (2009) also had a recognizable small S^{6+} peak, consistent with our observations of VG-2. Applying our peak fitting and S^{4+} to S^{6+} correction approach to the least beam-damaged VG-2 analyses (50x50 μm spot size; $1.1x10^7$ photons/s/um^2 dose), we estimate that VG-2 MORB glass has 7.9 ± 0.3% $S^{6+}/\Sigma S$ (1 SE, n=4) (Figure 9). This measured $S^{6+}/\Sigma S$ in VG-2 is similar to the upper end of the 3 – 7% $S^{6+}/\Sigma S$ range measured in MORB glasses via EPMA S Kα wavelength shift by Wallace and Carmichael (1994). However, these measurements are elevated compared to the 0 – 2% $S^{6+}/\Sigma S$ measured in four MORB glass samples by Jugo et al. 2010, although it is unknown if those samples suffered from S^{6+} photo-reduction. Based on global MORB average fO_2 estimates of QFM -0.17 ± 0.15 ($Fe^{3+}/\Sigma Fe$ = 14 ± 1%) by Cottrell et al. (in press) or QFM +0.1 by Berry et al. (2018), the Jugo et al. (2010) relationship of S^{6+} to fO_2 predicts that MORB glasses should be almost completely sulfide-dominated (≤ 1% $S^{6+}/\Sigma S$). However, we note that the Jugo et al. (2010) calibration was established for hydrous basalts rather than anhydrous MORB. We therefore suggest that the MORB glasses are not universally sulfate-free and, at least locally, have low but resolvable S^{6+} (up to 8%).

We also observe irradiation induced S^{6+} to S^{4+} photo-reduction in low-H_2O basaltic MI samples from the 2018 lower East Rift Zone (LERZ) fissure eruption of Kīlauea Volcano, HI (<0.3 wt% H_2O [**Chapter IV**]). Depending on the degree of atmospheric interaction, the Kīlauea MI range from reduced to highly oxidized (QFM -0.7 to +2.4; see discussion section). S-XANES beam damage is observed in Kīlauea MI throughout this wide range of oxidation states (Figure 10). The occurrence of S-XANES photo-reduction in Kīlauea MI and in VG-2 glass is particularly interesting because these low-H_2O OIB and MORB glasses are stable during Fe-XANES measurements (Cottrell et al., 2009; Cottrell and Kelley, 2011) (Figure 10), having Φ values ≤ 0.1 (Table 1). By extension, we initially assumed such glasses would not be susceptible to beam damage during S-XANES measurements.

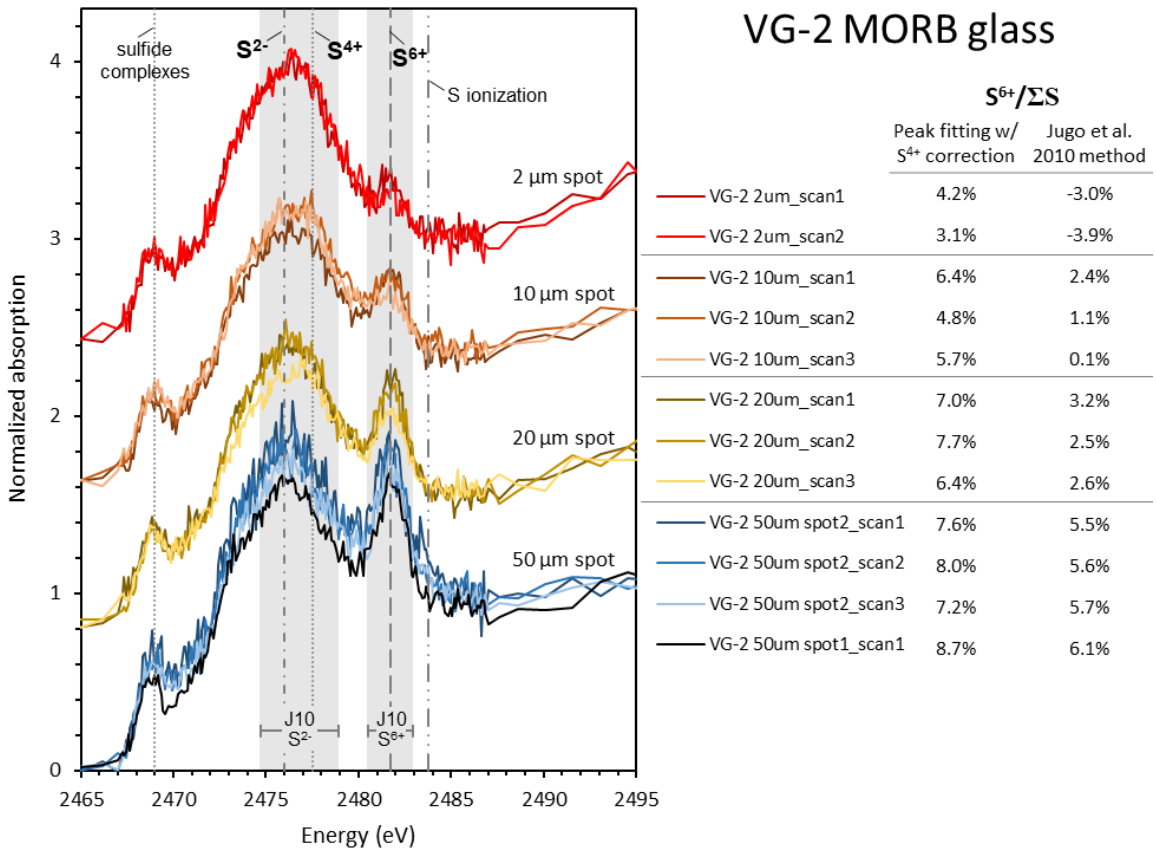

	S6+/ΣS Peak fitting w/ S4+ correction	S6+/ΣS Jugo et al. 2010 method
VG-2 2um_scan1	4.2%	-3.0%
VG-2 2um_scan2	3.1%	-3.9%
VG-2 10um_scan1	6.4%	2.4%
VG-2 10um_scan2	4.8%	1.1%
VG-2 10um_scan3	5.7%	0.1%
VG-2 20um_scan1	7.0%	3.2%
VG-2 20um_scan2	7.7%	2.5%
VG-2 20um_scan3	6.4%	2.6%
VG-2 50um spot2_scan1	7.6%	5.5%
VG-2 50um spot2_scan2	8.0%	5.6%
VG-2 50um spot2_scan3	7.2%	5.7%
VG-2 50um spot1_scan1	8.7%	6.1%

Figure 9. Normalized Fe-XANES spectra of MORB glass standard VG-2 with repeat measurements in different locations using progressively more focused spot sizes (50x50, 20x20, 10x10, 2x2 µm). Spectra have been vertically shifted for clarity. The ingrowth of S^{4+} (2476 – 2477.7 eV) and loss of S^{6+} (2480.5 – 2483.3 eV) is increasingly apparent with more focused beams. Measurements with a fully focused 2x2 µm beam cause the S^{6+} signal to be almost completely lost. Note the difficulty of recognizing the S^{4+} peak against the dominant S^{2-} broad peak (2472 – 2480 eV), giving the illusion of a beam damage-free spectra. Photon doses were $6.4x10^6$, $1.1x10^8$, $4.3x10^8$, $1.1x10^{10}$ photons/s/um^2 for the 50µm, 20µm, 10µm, and 2µm scans, respectively. Each individual scan length was 5 minutes. $S^{6+}/\Sigma S$ calculations using the peak fitting approach and correcting for S^{4+} photo-reduction are compared with $S^{6+}/\Sigma S$ calculated using the Jugo et al. (2010) method ("J10" gray S^{2-} and S^{6+} regions [energy shifted as discussed]), where the S^{4+} photo-reduction peak would be counted as part of the S^{2-} signal. Reference peak position lines are approximate and can vary slightly between samples.

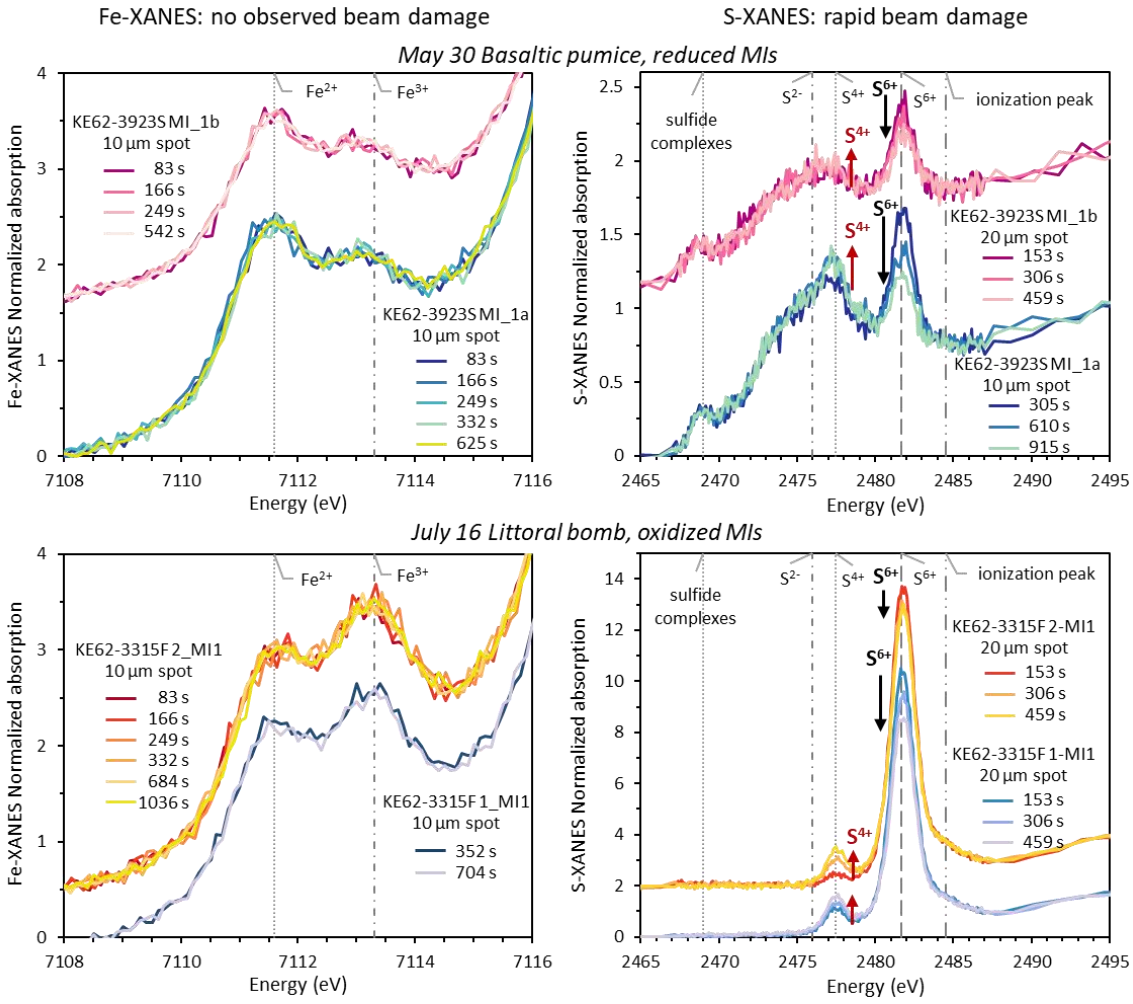

Figure 10. The same MI from the Kīlauea 2018 LERZ eruption were analyzed by both Fe- and S-XANES, and have differing susceptibilities to beam damage. Fe-XANES *(left)* and S-XANES *(right)* analyses were conducted in different locations in the same MI. Repeated rapid analyses were conducted for each technique, as described in the text, and the cumulative ending time in seconds (s) for successive scans are shown. Melt inclusions in both reduced, rapidly quenched basaltic pumice (KE62-3923S, *top*) in the oxidized littoral blast sample (KE62-3315F, *bottom*) exhibit no Fe photo-oxidation during repeat measurements, but the same MI underwent rapid photo-reduction during S-XANES analyses. All MI contain < 0.3 wt% H_2O and have $\Phi < 0.1$. Photon dose ranged from 2 – $4x10^7$ and 2 – $40x10^7$ photons/s/um^2 for Fe- and S-XANES measurements, respectively. Reference peak position lines are approximate and can vary slightly between samples. *(left)* Vertical lines labeled Fe^{2+} and Fe^{3+} refer to the approximate peak positions of the first and second pre-edge doublet.

We note that both the S-XANES peak fitting calibration and the determination of the S^{4+} to S^{6+} intensity scaling factor could be improved with calibrations across different compositions beyond the hydrous synthetic basalts from Jugo et al. (2010) and Chowdhury and Dasgupta (2019) that were tested here. In particular, the concentrations of Ca and Fe^{2+} may exert substantial control on S speciation at given fO_2 conditions and potentially on beam damage susceptibility in glasses (Graz et al., 2007; Klimm et al., 2012a, 2012b). Water content may also play a role in beam damage susceptibility (Wilke et al., 2008) as it does in Fe-XANES photo-oxidation (Cottrell et al., 2018). As an example, calculations of S speciation in VG-2 MORB glass using the S^{4+} to S^{6+} scaling factor of 1.2 to account S photo-reduction result in systematically lower $S^{6+}/\Sigma S$ for progressively more beam damaged analyses (from 8% to 3% $S^{6+}/\Sigma S$) (Figure 9). This indicates that the S^{4+} to S^{6+} scaling factor is likely larger for this anhydrous, reduced basalt than what we have determined for the hydrous, oxidized experimental basaltic glass. A S^{4+} to S^{6+} scaling factor of >3 is required to equate the $S^{6+}/\Sigma S$ of highly beam damaged VG-2 analyses with the undamaged measurements made using a diffuse spot size. However, we note that fitting the S^{4+} peak is challenging in more reduced samples due to the overlap of the dominant S^{2-} peak with the relatively minor S^{4+} peak, and we might be under-fitting the S^{4+} peak in VG-2 spectra. Additionally, in mixed S speciation samples, the slight beam damage-induced energy increase in the 2470 – 2475 eV range (Figure 8 inset) would be completely masked by, and included within, the broad S^{2-} peak area. Further characterizing the complete spectral range of beam damage ingrowth will be important for improving correction procedures. These uncertainties in the S^{4+} correction underscore that the foremost approach during S-XANES measurements should be to minimize beam damage as best as possible, so that the overall uncertainty stemming from any S^{4+} correction is small.

In summary, S-XANES beam damage can be recognized through repeat rapid scans by the presence and growth of a S^{4+} peak. If beam damage is found to occur, we suggest focusing on the least damaged spectra for each measurement, and then applying the S^{4+} to S^{6+} scaling factor to restore S^{4+} signal to the original S^{6+} intensity. In high-S samples, where signal intensity is sufficient even with rapid scans, this is the ideal approach as beam damage is first limited and then restored to a good approximation of

original S^{6+} intensity. Low-S samples may require merging multiple rapid scans to obtain quantifiable spectra, despite the longer cumulative analysis time inducing more photo-reduction. Ingrown S^{4+} can still be restored to S^{6+} in long duration or merged scans, and although this introduces greater uncertainty, it is still a better approach than not applying any correction. In highly oxidized samples lacking S^{2-}, accounting for S^{4+} is less important as it can simply be assumed that all S was originally present as S^{6+}. However, in samples with mixed S speciation, separating any S^{4+} photo-reduction signal from the overlapping S^{2-} peak, and restoring the S^{4+} to original S^{6+} is important in accurately determining the S speciation of the glass.

2.2.4 Mechanism of S photo-reduction beam damage

Through repeated rapid S- and Fe-XANES scans, we observed rapid S photo-reduction and Fe photo-oxidation in hydrous basalts (G-466 synthetic glass, southern Cascades basaltic MI [Muth et al., in prep]), consistent with observations of the susceptibility of hydrous basalts to beam damage (Cottrell et al., 2018). However, we also observed that VG-2 MORB glass and both reduced and oxidized Kīlauea LERZ MI underwent substantial S-XANES beam damage, but no Fe-XANES beam damage (Figure 10). Kīlauea MI (analyzed in this study) and MORB glasses are low-H_2O basalts containing $\leq$ 0.3 wt% H_2O, indicating that S photo-reduction can occur in H_2O-poor glasses where no Fe photo-oxidation is observed. However, because S is a relatively minor element in most silicate melts (~100 – 5000 ppm [Métrich and Wallace, 2008]), we suspect that S might only require another relatively low abundance element(s) to act as the redox couple for the observed S photo-reduction. It is possible that Fe^{2+} to Fe^{3+} photo-oxidation is the counterpart redox couple to S^{6+} to S^{4+} photo-reduction (Métrich et al., 2009), but the Fe oxidation does not have an observable effect on total Fe speciation relative to the large amount of Fe in basaltic glasses (e.g., 5 – 12 wt% FeO^T vs 500 – 1600 ppm S in Kīlauea MI [**Chapter IV**]). Additionally, we note that the Kīlauea MI and VG-2 submarine glasses contain more H_2O (dissolved as OH^- in the glass [Dixon et al., 1988]) than S on a molecular basis, and thus water-dependent beam damage may still be an important mechanism in S photo-reduction.

Finally, as discussed by Métrich et al. (2009), we observe that S^{4+} ingrowth levels off after a certain degree of beam damage (Figure 8), which may indicate the exhaustion of a redox-couple and thereby hint at the mechanism of S^{6+} reduction during beam damage. A similar cessation of beam damage after rapid initial ingrowth is also observed during Fe-XANES photo-oxidation (Cottrell et al., 2018) (Figure B1). However, an alternative possibility is that the cessation of S^{4+} ingrowth indicates that all S^{6+} has been converted to S^{4+}. Measurements of sodium sulfite ($Na_2S^{4+}O_3$) indicate that S^{4+} has absorption peaks at both 2477.5 eV and 2482 eV (Fleet et al., 2005; Jugo et al., 2010), with the 2482 eV peak being in the same position as the S^{6+} absorption peak (Wilke et al., 2008; Métrich et al., 2009). Consequently, if all S^{6+} was converted to S^{4+} during beam-damage, the XANES spectra may still retain a 2482 eV peak, giving an illusion of S^{6+} being present. However, after the complete conversion of S^{6+} to S^{4+}, both the 2477.5 and 2482 eV peaks should remain static under further beam irradiation.

The subtle peak ingrowths during beam damage at 2471.7 eV and in the broad 2470 – 2475 eV range indicate that S^{6+} photo-reduction may be a more complex process than simply converting S^{6+} to S^{4+}, although this latter process is still dominant. More detailed studies will be needed to determine the full mechanism of S photo-reduction, which will be useful for estimating the susceptibility of different glass compositions to beam damage during S-XANES analyses and further improving beam damage correction approaches.

3. Interpreting XANES measurements in melt inclusions

As with any analytical petrologic technique, making accurate XANES measurements are only the first steps in understanding what those quantifications mean geologically. Measurements of MI can be particularly challenging to interpret because they are subject to a number of closed- and open-system modifications occurring with different timescales between entrapment and quenching. Slow cooling during magma mixing, pluton formation, lava extrusion, and ignimbrite emplacement can lead to post-entrapment crystallization (PEC) of the host phase on MI walls (Danyushevsky et al., 2000) and/or the formation of separate daughter crystals. Olivine-hosted MI can rapidly lose (or gain) water via diffusion through the host crystal in response to changing water

concentration in the external melt, such as during ascent and degassing (Sobolev and Danyushevsky, 1994; Hauri, 2002; Portnyagin et al., 2008; Chen et al., 2011; Gaetani et al., 2012; Lloyd et al., 2013; Hartley et al., 2015; Ferriss et al., 2018; Barth et al., 2019). Electron-exchange during glass quenching has also been hypothesized to affect Fe and S speciation, although the extent of this effect remains debated (Métrich et al., 2009; Nash et al., 2019; M. Brounce, personal communication). Here, we discuss some of these processes and their implications for interpreting redox measurements in MI by XANES or other microbeam techniques (e.g., Raman, EPMA peak shifts).

3.1 Effect of nanolite crystals

Under certain conditions, the crystallization of quench minerals in MI can occur in the cryptic form of nanolites - minerals in the sub-micron range that are typically undecipherable with optical microscopes or even with electron microscopes. In some settings, these dispersed crystals become large enough to appear as a fine "dust" within MI (Danyushevsky et al., 2002; Wallace et al., 2003). It has been suggested that Fe-oxides and sulfides may form in MI during cooling and/or diffusive water loss (Danyushevsky et al., 2002; Rowe et al., 2007; Di Genova et al., 2017, 2018; Head et al., 2018). Di Genova et al. (2017, 2018) observe that Fe-oxide nanolites preferentially occur in water-rich glasses across a range of compositions, suggesting that high H_2O promotes nanolite formation during quenching. This might occur, for example, because increased H_2O lowers the glass transition temperature, resulting in a larger cooling interval in the liquid state for H_2O-rich melts. The presence of nanolites complicates XANES, Raman, and EPMA redox measurements in glasses because the bonding coordination in nanolite minerals may lead to different relationships between ion abundances and signal intensities compared to calibrated relationships in glasses.

Fortunately, the short-range ordering of Fe and S in mineral phases can be readily detected via XANES and Raman spectral techniques (Di Genova et al., 2017, 2018; Head et al., 2018). Fe-oxide nanolites have been spectrally identified by Raman measurements in MI from basalts, dacites, and trachytes containing > 4.5 wt% FeO^T and > 3.0 wt% H_2O (Di Genova et al., 2017, 2018). Fe-oxide nanolite abundance correlates with calculated EPMA redox states of MI (Hughes et al., 2018; E. Hughes personal communication),

although it is unclear if nanolites result from redox changes in MI or rather that the presence of nanolites affects the redox quantification. Head et al. (2018) identify spinel and sulfide nanolites via V- and S-XANES in MI in basaltic tephra from Nyamuragira volcano (D.R. Congo), which substantially complicated their interpretation of calculated redox states.

We identify Fe-oxide nanolites in Fe-XANES measurements of doubly-intersected dacitic-rhyolitic MI from the 2006 eruption of Augustine Volcano (AK, USA) (**Chapter V**) and in basaltic MI from Cerro Negro (Nicaragua). Rather than displaying the normally smooth absorption edge profile distinctive of crystal-free glass (Figure 1b), spectra in nanolite-bearing MI have a sharp absorption peak at ~7129.5 eV (Figure 11). This peak is similar to the absorption edge feature observed in magnetite phenocrysts from both Augustine and oxidized Kīlauea samples. A similar magnetite-like peak was observed in optically glassy quartz-hosted MI from Central Andean volcanic centers by Grocke et al. (2016), who also considered this feature to indicate nanolite interference. Melt inclusions in Augustine feldspar and pyroxene that contain Fe-oxide nanolites are consistently a brown color, although no distinct crystals are observable with either optical or electron microscopes (Figures 11, 12). Optically colorless MI are also present in the same samples from Augustine, and have smooth glassy Fe-XANES absorption edge spectra with no Fe-oxide signatures (Figures 11, 12). Colorless and brown colored MI have been long recognized, often occurring within the same rock sample, and the cause and importance of MI coloration has been much debated. Although some studies have observed that colorless MI have lower H_2O and higher CO_2 than co-occurring brown MI, others find negligible differences in volatiles or major element compositions between different colored MI (Wallace et al., 1999; Myers et al., 2016; Myers, 2017; Muth et al., in prep). In Augustine MI, color consistently reflects the presence or absence of Fe-oxide nanolites. Calculated $Fe^{3+}/\Sigma Fe$ proportions are highly variable in the Fe-nanolite bearing Augustine MI, but are generally more Fe^{3+}-rich compared to colorless, nanolite-free MI from the same tephra sample (**Chapter V**). However, it is again unclear whether this observation reflects an increased oxidation state within the nanolite-bearing MI, or if it is a consequence of greater Fe^{3+} signal from the crystalline nanolite phases. We note that many brown colored MI in more basaltic compositions have perfectly glassy XANES

spectra with no evidence of nanolites (e.g., Kīlauea and southern Cascades olivine-hosted MI studied here), so MI color alone does not always indicate the presence of Fe-

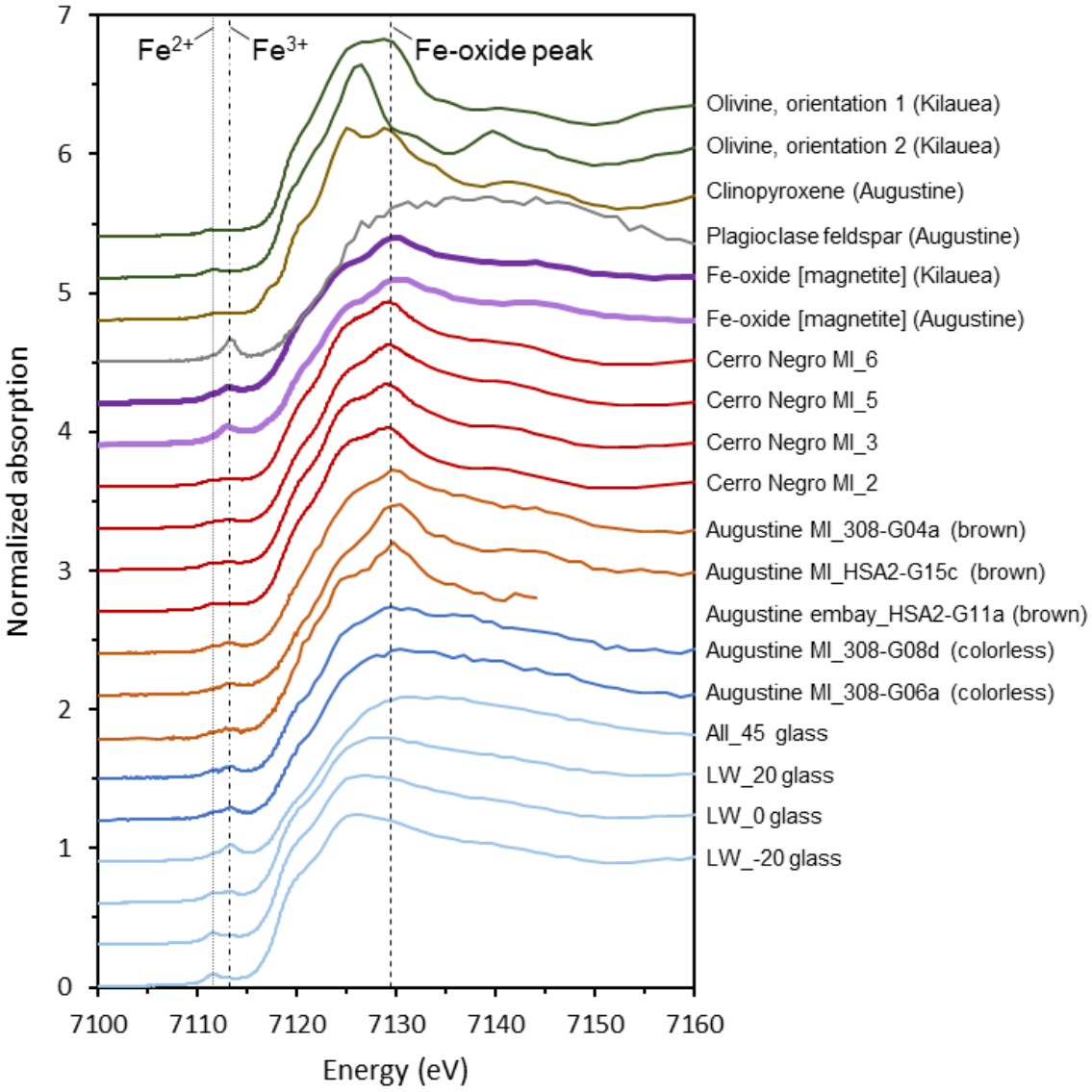

Figure 11. Normalized Fe-XANES spectra of mineral spectra (olivine, clinopyroxene, feldspar, Fe-oxide), reference glasses (LW series, AII_45 [Cottrell et al., 2009]), and doubly-intersected MI or melt embayment glasses from Augustine 2006 (samples shown in Figure 12) and Cerro Negro. Brown colored dacitic-rhyolitic glasses from Augustine (orange lines) have a prominent peak at ~7129.5 eV that closely resembles the Fe-oxide mineral (thick purple lines), indicating the presence of Fe-oxide nanolites. Cerro Negro olivine-hosted basaltic MI (red lines) also have a 7129.5 eV signature of Fe-oxide nanolites. Colorless MI from Augustine (blue lines) have glassy spectra, similar to oxidized reference glasses LW_20 and AII_45 (QFM +2 and +4.5, respectively). Spectra have been vertically shifted for clarity. The lines labeled Fe^{2+} and Fe^{3+} refer to the approximate peak positions of the first and second pre-edge doublet.

nanolites. Future efforts to characterize compositional, temperature, and water variations between co-occurring brown and colorless MI in the same units will better clarify the processes that govern nanolite formation and MI coloration.

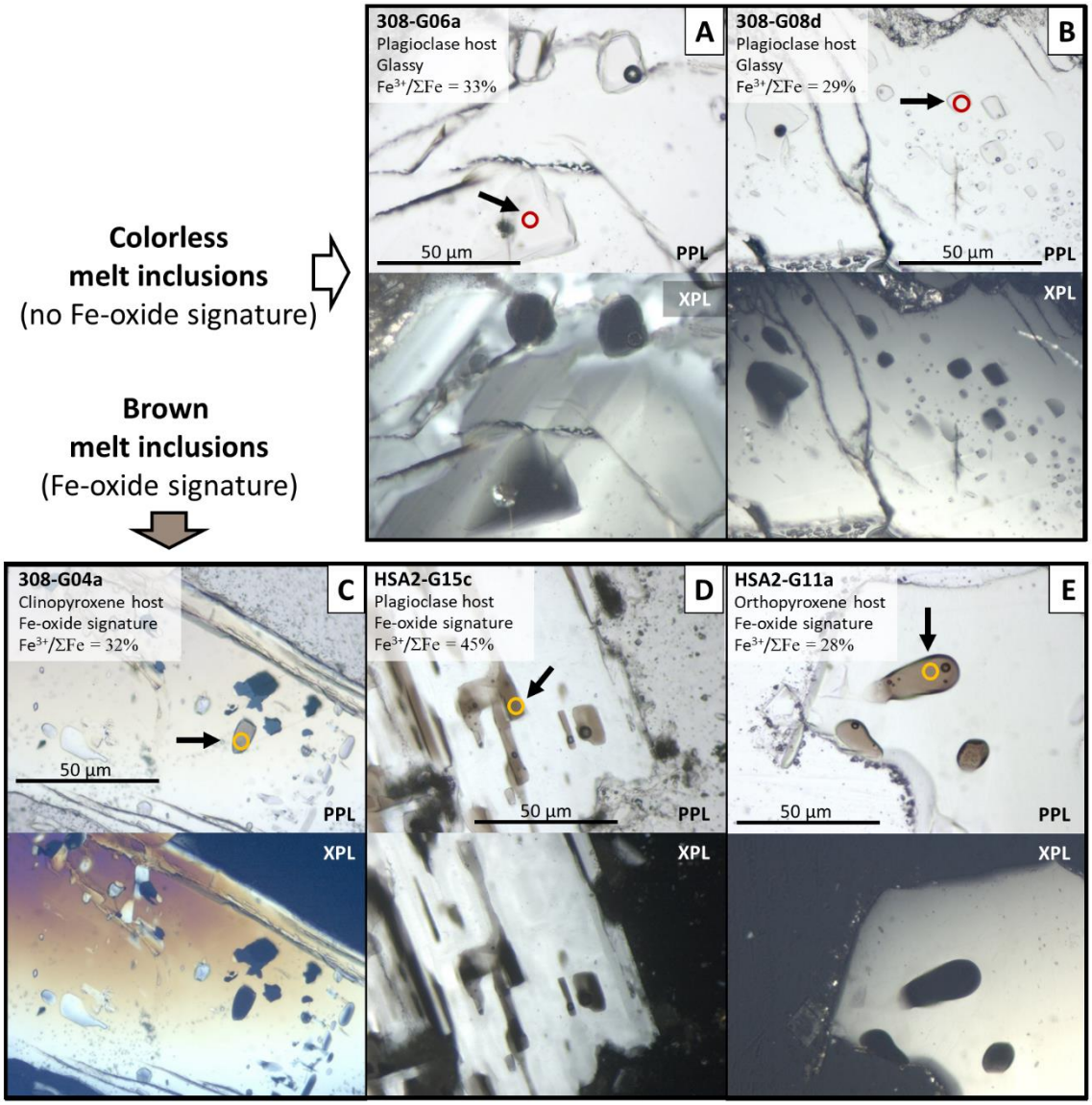

Figure 12: Doubly intersected dacitic-rhyolitic MI (A, B, C, D) and melt embayments (E) erupted from Augustine Volcano in 2006. *(top)* Colorless (A, B) and *(bottom)* brown (C, D, E) glasses are present in inclusions and embayments within plagioclase (A, B, D, E) and pyroxene (C). Each two-pane panel shows images with plane polarized light (PPL) and through crossed polarizers (XPL), with full glass extinction in XPL showing where MI are doubly intersected for host-free Fe-XANES analysis. Fe-XANES analyses were conducted with a 5x5 µm spot size. $Fe^{3+}/\Sigma Fe$ was calculated from the felsic glass calibration of Fiege et al. (2017).

3.2 Post-entrapment crystallization and potential Fe^{3+} enrichment

Melt inclusions occur in almost all igneous minerals, but olivine-hosted MI are perhaps the most commonly studied because olivine is typically the earliest crystallizing phase. With fewer complications from magma mixing, fractionation, crustal assimilation, and degassing, primitive olivine-hosted MI may retain valuable information about mantle sources (Kent, 2008; Métrich and Wallace, 2008). However, olivine-hosted MI are susceptible to PEC during magma residence, ascent, and emplacement. Melt inclusions that are entrapped at temperatures similar to the eruption temperature may experience little to no PEC. However, high Fo-olivine (where Fo is olivine 100*Mg/[Mg + Fe] in mol fractions) that become entrained in lower temperature melts can experience high degrees of PEC due to undercooling, with the crystallized olivine rinds reaching 10 – 25% or more of the original MI mass (Danyushevsky et al., 2000; **Chapter IV**). Olivine preferentially incorporates Fe^{2+} over Fe^{3+}, so if olivine-hosted MI act as closed systems with respect to oxygen or electron transfer during PEC, then $Fe^{3+}/\Sigma Fe$ should increase with degree of PEC and the MI would become highly oxidized (Danyushevsky et al., 2000). The commonly used PEC correction program Petrolog3 (Danyushevsky and Plechov, 2011) includes options for either open or closed system treatment of MI redox state during PEC, which produce substantially different PEC-correction results. The degree to which Fe^{3+} and other redox-sensitive elements are enriched or remain in equilibrium with the crystal host and external melt during PEC is a major question that researchers must consider in reconstructing and interpreting olivine-hosted MI compositions. In the following sections, we present observations from natural and experimental MI that inform this discussion.

3.3 Evidence for redox re-equilibration in natural MI from Kīlauea 2018 eruption

The 2018 LERZ eruption of Kīlauea Volcano, on the Big Island of Hawai'i (USA) was well monitored and sampled, and provides a rare opportunity to examine the effect of PEC and other post-entrapment process affecting natural MI. The 2018 LERZ eruption lasted from May until September, and a range of magma compositions and pyroclast types were erupted (Gansecki et al., 2019; Neal et al., 2019). By late May, the composition of the erupting lava stabilized, becoming similar to Kīlauea summit magmas

erupted in previous decades (Gansecki et al., 2019). Eruptive activity focused at the fissure 8 vent, and high lava fountaining events in late May through early-June produced rapidly quenched, highly vesicular basaltic pumice. From mid-June until early August, high rates of lava effusion fed a fast-flowing lava channel that eventually traveled over 13 km from the fissure 8 vent to the ocean. Most of the lava channel never crusted over into a lava tube, remaining open to the air until the lava flow widened and slowed in the final few km near the coast (Patrick et al., 2019c). Diligent sampling of the proximal lava channel by Hawaiian Volcano Observatory (HVO) personnel throughout the eruption produced a well-documented sample set of rapidly quenched samples (Gansecki et al., 2019), many of which contain glassy olivine-hosted MI. During a period in mid-July, littoral blasts were occurring intermittently at the coastal ocean entry due to interaction between lava flows and wave action and/or bench collapses (Neal and Anderson, 2020). One littoral blast on July 16 showered an unfortunate tour boat with incandescent material, injuring a number of passengers. Samples from aboard this tour boat were given to HVO personnel, and provide an example of material that transited a ~13.4 km long lava flow and then was rapidly quenched by ocean interaction and fragmentation. This sample has increased groundmass crystallization but retains fully glassy olivine-hosted MI and areas of crystal-free matrix glass.

We compare proximally and distally quenched samples from the LERZ eruption to assess whether variation in MI oxidation state occurred with different durations of subaerial lava transport. Samples include rapidly air-quenched basaltic pumice tephra erupted on May 30 (KE62-3293S), material from the littoral blast on July 16 that transited the full subaerial lava channel (KE62-3315F), and a sample erupted just a few days later (July 20) that was extracted from the lava channel ~7 km downstream of the fissure 8 eruption site (KE62-3316F) (Figure 13, Table 3). The duration that latter two samples spent in the surface lava flows (from extrusion at fissure 8 until quenching) are estimated from average flow velocities along the lava channel that were determined from videos by unoccupied aircraft systems (UAS; H. Dietterich, personal communication).

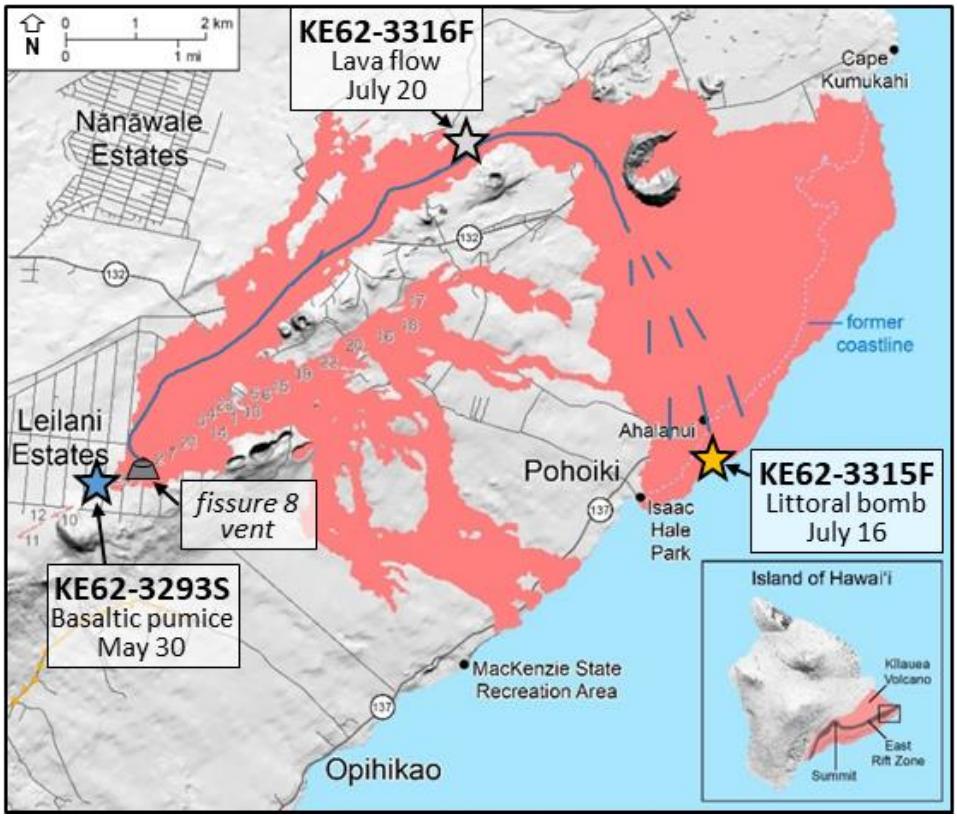

Figure 13. Map of the 2018 Kīlauea LERZ lava flows (red) showing the main fissure 8 vent and locations and dates where samples presented in this study were quenched (stars). A total of 22 eruptive fissures opened during the eruption (gray numbers), but all samples presented in this work were sourced from the dominant lava flow from fissure 8. The path of the main open lava channel in mid-July is shown in blue, with dashed lines indicating the area of slower, more diffuse lava flow that became partially crusted over near the ocean entry. *(inset)* The Big Island of Hawai'i, with the subaerial extent of Kīlauea Volcano highlighted in red. Figure modified from Kern et al. (2020).

Table 3. Samples from 2018 Kīlauea LERZ eruption investigated in this study.

Sample name	Sample type	Eruption date	Distance traveled in lava channel	Time in lava channel before quenching
KE62-3293S	Basaltic pumice	5/30/18	0 km (air-quenched at source)	Seconds
KE62-3315F	Littoral blast quenched fragments	7/16/18 (quenched), erupted hours to days earlier	~13.4 (~9.5 in subaerial channel)	7 hours to 2 – 3 days (?)
KE62-3316F	Bucket-quenched lava flow	7/20/18	7.0 km (in subaerial channel)	~3 – 5 hours

Matrix glass and doubly-intersected olivine-hosted MI from a variety of olivine compositions were measured by both Fe- and S-XANES following the analytical and peak fitting methods described above to detect and correct for beam damage. As discussed, Fe speciation in Kīlauea MI was stable during Fe-XANES analysis but S-XANES photo-reduction occurred rapidly many of the same MI (Figures 4, 10). Where S-XANES beam damage occurred, we use only the first, least damaged, rapid analysis. Beam damage was corrected using a S^{4+} to S^{6+} peak intensity conversion factor of 1.2, where the "restored" S^{4+} signal amounted to an average increase of 0.9 ± 1.5% $S^{6+}/\Sigma S$ (range 0 – 9%; n=54).

Matrix glasses and MI from more proximally quenched lava erupted in both late May and mid-July have 1 – 25% $S^{6+}/\Sigma S$ and 12 – 18% $Fe^{3+}/\Sigma Fe$ (QFM -0.7 to +0.4 from the composition-specific 1-atm relation of Kress and Carmichael [1991]) (Table 1). These measurements are consistent with prior EPMA S Kα wavescan (Wallace and Carmichael, 1992, 1994) and S- and Fe-XANES studies of matrix glasses and MI from Kīlauea (Jugo et al., 2010; Moussallam et al., 2016; Helz et al., 2017) and submarine glasses from *Lō'ihi* volcano (Jugo et al., 2010). However, both matrix glass and MI from the littoral blast sample are dramatically more oxidized (68 – 96% $S^{6+}/\Sigma S$; 21 – 34% $Fe^{3+}/\Sigma Fe$; QFM +0.5 to +2.4) than the more proximally quenched samples (Figure 14A).

Our suite of Kīlauea MI and matrix glasses have higher measured S^{6+} at given $Fe^{3+}/\Sigma Fe$ conditions than would be expected from the Jugo et al. (2010) relationship. These observations differ from measurements by Brounce et al. (2017) in glasses from the neighboring Mauna Kea volcano, who report lower S^{6+} proportions than expected from the Jugo et al. (2010) model. However, if the Brounce et al. (2017) dataset is re-calculated using pre-edge centroid positions and the updated Fe-XANES calibration of Zhang et al. (2018), their S^{6+} and fO_2 relationships are more consistent with our findings (Figure B8).

Deviations from the Jugo et al. (2010) relationship of S speciation and fO_2 have recently been attributed to a possible "quench effect" (Nash et al., 2019). Nash et al. (2019) propose that at a given fO_2, a strong temperature dependence on Fe and S equilibrium causes $S^{6+}/\Sigma S$ to increase at high temperatures and to decrease with cooling. This model predicts that the hotter temperatures of the Kīlauea melts (>1100 ºC, see

thermometry discussion below) should increase S^{6+} proportions at a given fO_2 compared to the Jugo et al. (2010) relationship, which was calibrated at 1050 ºC. Our measured S- and Fe- speciation in Kīlauea matrix glasses and MI are generally consistent with Nash et al. (2019) predictions at sample-specific melt temperatures determined by Mg-thermometry (Figure B8). However, we find no evidence of a quench effect reducing S^{6+} in MI, even though MI would be expected to cool somewhat slower than matrix glass and should therefore be more subject to the proposed electron-exchange during cooling.

Some deviation of MI and matrix glasses from Nash et al. (2019) model predictions suggests that in addition to temperature, further compositional and pressure parameters also affect S speciation in natural glasses (Baker and Moretti, 2011; Klimm et al., 2012a; Fiege et al., 2014a; Masotta and Keppler, 2015; Matjuschkin et al., 2016). Kīlauea MI experienced highly variable degrees of PEC and Fe-loss, which result in MI and matrix glasses having FeO^T concentrations ranging from 5 – 12 wt% (**Chapter IV**). Some low-FeO^T MI have notably higher S^{6+} than predicted by the Nash et al. (2019) model, whereas high-FeO^T matrix glasses (11 – 12 wt%) have lower than predicted S^{6+}. These observations suggest that the concentration of Fe in melts may affect S speciation in glasses, perhaps by stabilizing S^{2-} (Klimm et al., 2012a). The continued uncertainties in pressure, temperature, and compositional dependence on S speciation in silicate glasses underscores the importance of directly measuring both S and Fe speciation.

The difference in redox states of the reduced and oxidized MI from the Kīlauea LERZ samples is dramatic, with the reduced samples having redox states similar to MORB and other OIB glasses (Cottrell and Kelley, 2011; Brounce et al., 2017; Hartley et al., 2017) and the oxidized MI having redox states similar to the upper range of subduction zone glasses (Cottrell et al., in press; Kelley and Cottrell, 2009). Changes in melt composition were relatively minor during the-late May to mid-July time period when these samples were erupted (Gansecki et al., 2019; Lee et al., 2019; **Chapter IV**). Furthermore, sample KE62-3316F, which erupted just four days after the oxidized sample was quenched, has MI with similar redox states as MI in the late May basaltic pumice (QFM -0.7 to 0 and -0.4 to +0.4, respectively) (Figure 14). We therefore conclude that the oxidation of the littoral blast MI was due to post-entrapment processes rather than a short lived, extreme change in magma composition.

During ascent, eruption, and subsequent transport in the fissure 8 lava channel, the littoral blast melt would have undergone degassing of H_2O and S (~0.3 to 0.1 wt% H_2O and ~1100 to 50 ppm S) and cooling, leading to groundmass crystallization and substantial PEC in MI (10 – 35% via Petrolog3 restorations) (**Chapter IV**). More proximally quenched samples KE62-3923S and KE62-3316F contain MI that are hosted within a wide range of olivine compositions (Fo_{78-89}). During pre-eruptive mixing with cooler magma (equilibrium Fo_{77-80} composition), MI in these compositionally diverse host minerals underwent 0 – 35% PEC (**Chapter IV**). Melt inclusions in Mg-rich olivine grains from KE62-3923S and KE62-3316F experienced the same high degrees of PEC as MI in the littoral blast sample, but did not undergo any appreciable Fe^{3+} enrichment (Figure 14B). If highly PEC-affected MI in the more proximally quenched samples are treated as closed-systems for fO_2 during PEC (no redox re-equilibration during Fe^{2+} incorporation by olivine), Petrolog3 corrections restore the initial Fe speciation in MI from high-Mg olivine hosts to as low as 5% $Fe^{3+}/\Sigma Fe$ (QFM -3.0), which is unrealistic for Kīlauea magmas (Anderson and Wright, 1972; Gerlach et al., 2004; Moussallam et al., 2016; Helz et al., 2017). Because MI in these samples underwent highly variable degrees of PEC but still have relatively constant $Fe^{3+}/\Sigma Fe$, we conclude that even extensive PEC did not cause Fe^{3+} enrichment. By extension, the oxidation of the littoral blast MI cannot be attributed to Fe^{3+} enrichment from PEC. To balance Fe^{3+} enrichment during PEC, olivine-hosted MI must behave as open redox systems, exchanging O or electrons with the olivine host and external melt over relatively short timescales.

The matrix glass in the littoral blast sample is also oxidized up to two log units fO_2 compared to more proximally quenched matrix glasses, and contains abundant groundmass magnetite (identified via EPMA measurements). During ascent and S-degassing, Kīlauea melts undergo reduction due to the conversion of S^{2-} in the melt to SO_2 gas (S as S^{4+}) (Kelley and Cottrell, 2012; Moussallam et al., 2016; Helz et al., 2017). This reduction during S degassing is observed in proximally quenched LERZ material (**Chapter IV**) (Figure 14C). Therefore, magmatic degassing cannot explain the severe oxidation observed in the littoral blast lava samples, as degassing causes reduction of the melt.

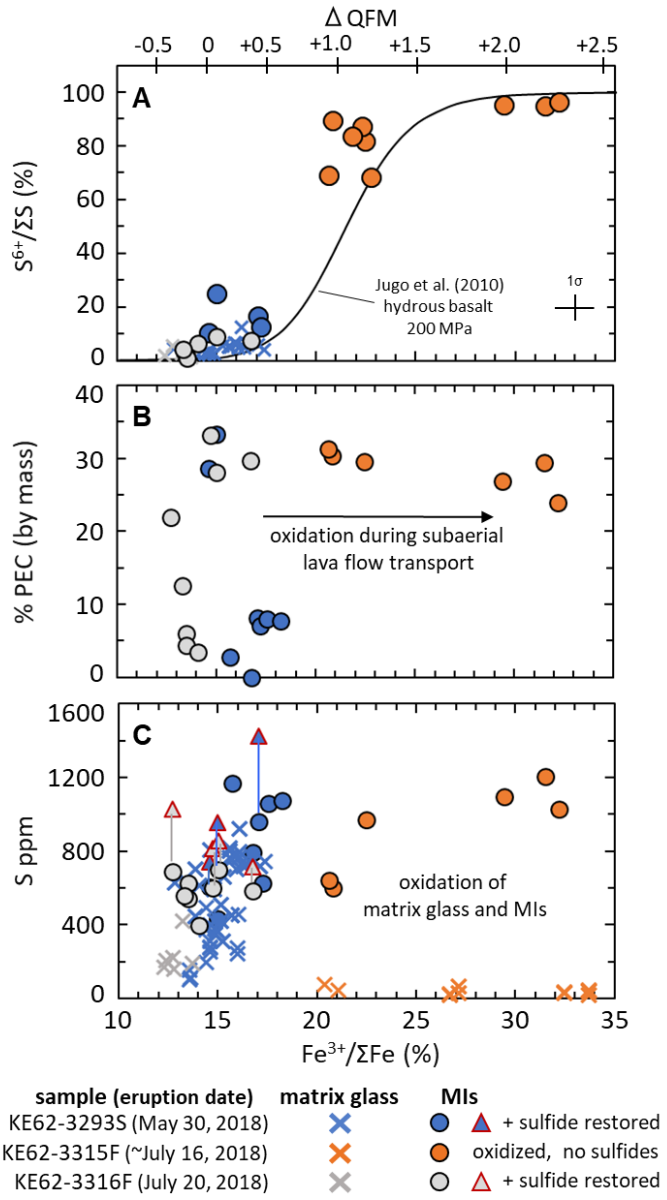

Figure 14. *(A)* Fe and S speciation from XANES measurements, *(B)* Fe speciation relative to the degree of post entrapment crystallization (PEC), and *(C)* Fe speciation relative to PEC-corrected S concentrations in olivine-hosted MI and matrix glasses for rapidly quenched Kīlauea tephra (KE62-3293S), an oxidized lava-flow littoral bomb (KE62-3315F), and a bucket-quenched lava flow sample (KE62-3316F). PEC extents in MI were calculated using Petrolog3 (Danyushevsky and Plechov, 2011). Triangular symbols in *(C)* indicate MI with total S calculated by adding S from precipitated sulfide blebs to PEC-corrected glass S contents. Sulfur concentrations in KE62-3315F littoral bomb matrix glasses were too low to conduct S-XANES measurements. Note: The relation between $Fe^{3+}/\Sigma Fe$ and QFM varies with temperature and melt composition (Kress and Carmichael, 1991), but the upper x-axis scale here assumes an average matrix glass composition and eruption temperature from sample KE62-3293S (**Chapter IV**). Uncertainties in $S^{6+}/\Sigma S$ model fits and calibration are estimated at ±2 – 5% absolute, and uncertainties in $Fe^{3+}/\Sigma Fe$ from centroid fits are < ±1% absolute.

Instead, we propose that the magma involved in the littoral blast became oxidized during subaerial lava flow transport, and that olivine-hosted MI rapidly re-equilibrated with the oxidizing external melt environment. The vast redox differential between atmospheric oxygen ($fO_{2\_air} = 0.2$) and reduced melts ($fO_{2\_melt} = 10^{-8}$) creates a potent driver for oxygenation of subaerial melts. As an extreme example of atmospheric oxidation, Helz et al. (2017) observe that glassy rims of air-cooled scoria clasts from the Kīlauea Iki 1959 eruption are visibly red and contain up to 63% $Fe^{3+}/\Sigma Fe$, compared to 12 – 15% $Fe^{3+}/\Sigma Fe$ in glass from the clast interiors. Atmospheric oxygenation would preferentially affect the upper portions of a lava channel, while underlying melt may be completely insulated from such contamination. The fissure 8 lava channel was ≥ 7 m deep (Patrick et al., 2019c) and it is impossible to know exactly what flow path any particular melt parcel traveled, as changing location in the lava channel and stalling in lava flow eddies were possible during transit. Therefore, while the possibility of oxidation increases with time and distance traveled in the lava flow, these metrics are not necessarily proportional to the degree of atmospheric interaction experienced by any particular sample of magma.

However, any significant atmospheric interaction would cause cooling of the melt. A decrease in MgO content of matrix glass provides an indicator of the degree of cooling and induced crystallization of Mg-rich phases (olivine, pyroxene) plus lesser feldspar (Guilbaud et al., 2007), and thereby may serve as a proxy for atmospheric interaction. Matrix glasses in the rapidly quenched basaltic pumice (KE62-3293S, May 30) erupted from fissure 8 contain 6.3 ± 0.2 wt% MgO, and the July 20 lava flow sample (KE62-3316F) that quenched after traveling ~7 km in the subaerial lava channel has matrix glasses containing 6.2 ± 0.2 wt% MgO. This similarity of MgO contents indicates that the July 20 lava flow sample experienced minimal cooling and crystallization despite a long lava channel transport (**Chapter IV**). In fact, the July 20 lava flow sample is up to 0.3 log units more reduced than the basaltic pumice (likely due to S degassing), indicating no atmospheric oxidation during lava channel transport (Figure 14). In contrast, the July 16 littoral bomb sample (KE62-3315F) underwent substantial crystallization and the residual matrix glass contains 4.9 ± 0.1 wt% MgO (**Chapter IV**). Applying the Helz and Thornber (1987) MgO-thermometer developed for Kīlauea melts,

the Mg-content of the littoral blast matrix glass indicates a cooling from eruption temperatures of 1140 ºC down to ~1115 ºC (**Chapter IV**). A number of other LERZ fissures erupted fractionated magmas that had evolved during prolonged subsurface storage (Gansecki et al., 2019; Lee et al., 2019), and have similar or lower MgO contents (2 – 5 wt% MgO, 1050 – 1100 ºC) than the littoral bomb sample, but are not highly oxidized (**Chapter IV**). Therefore, Fe^{3+} enrichment during cooling and fractionation of Kīlauea magmas is insufficient to explain the high degree of oxidation observed in the littoral bomb sample. We thus conclude that the littoral bomb sample underwent both cooling and substantial oxidation due to atmospheric interaction during transport from fissure 8 to quenching at the ocean entry.

Importantly, olivine-hosted MI in the littoral blast sample have redox conditions similar to the oxidized matrix glass, indicating MI redox re-equilibration with the external melt during the ~13.4 km lava channel transport. The wide range of 21 – 34% $Fe^{3+}/\Sigma Fe$ measured in matrix glass and MI from the littoral blast sample may be a function of heterogeneous melt oxygenation during transport.

The variable oxidation states in our suite of Kīlauea MI lead to interesting consequences for sulfide stability. Sulfide blebs are present in many rapidly quenched tephra MI that experienced high degree of PEC, due to cooling and Fe-loss during PEC (**Chapter IV**). However, none of the oxidized littoral blast MI with comparable degrees of PEC and Fe-loss contain sulfides. This is presumably because the oxidation of the littoral blast MI caused any sulfides to destabilize and re-dissolve into the melt (Jugo et al., 2010; Hartley et al., 2017). In rapidly quenched MI, the combined S from the glass and from the mass of S in co-occurring sulfides results in cumulative S concentrations that are similar to the S measured in the oxidized, sulfide-free littoral blast MI (Figure 14 C). This indicates that MI in these different samples contained similar initial S concentrations and that sulfur behaved as a closed system within the MI, partitioning between the melt and a sulfide phase as PEC and changing redox conditions affected sulfide saturation.

3.4 Timescales of redox re-equilibration

The proximally and distally quenched Kīlauea LERZ samples allow the timescale of redox re-equilibration of MI to be constrained. Videos of the proximal lava channel indicate maximum channel velocities of ≥ 10 m/s (Patrick et al., 2019c), however this velocity slowed dramatically as the lava channel broadened near the coastal ocean entry (H. Dietterich, personal communication). Given this uncertainty in distal lava flow velocity, plus unknown effects of magma slowing along flow margins or in eddies, it is unclear how long the littoral blast lava spent in the lava flow prior to quenching during ocean interaction. Our best estimate is that the littoral blast lava spent between 7 hours and 2 – 3 days in the lava flow based on UAS-derived lava channel speeds and assuming further distal velocity decrease.

Alternatively, we can use calculated timescales of H_2O diffusive loss from olivine-hosted MI to estimate the duration of the littoral blast sample in the lava flow (Hauri, 2002; Portnyagin et al., 2008; Chen et al., 2011; Bucholz et al., 2013). Water measured by FTIR ranges from 0.15 – 0.30 wt% H_2O in proximally quenched MI and matrix glasses. In the littoral blast sample, matrix glass contains 0.07 – 0.11 wt% H_2O, consistent with the melt having equilibrated to 1-atm conditions during transport to the coast (Dixon et al., 1995), and MI have 0.08 – 0.17 wt% H_2O (**Chapter IV**). Assuming that all olivine-hosted MI from the LERZ eruption initially contained ~0.3 wt% H_2O, we calculate the timescale of diffusive water loss from littoral blast MI following the method of Bucholz et al. (2013). With LERZ lava flow temperatures of 1120 – 1150 °C (Gansecki et al., 2019; **Chapter IV)** and assuming that H_2O loss to 0.1 wt% in the melt occurred rapidly during extrusion at fissure 8, constraints from H_2O diffusive loss in littoral blast MI indicates the littoral blast MI resided in the lava flow for 1 – 3 days prior to explosive quenching at the ocean entry (Bucholz et al., 2013).

Redox re-equilibration of olivine-hosted MI has been shown to occur on timescales similar to H_2O equilibration, although redox equilibration is thought to be coupled to metal vacancy diffusion and is thus independent of diffusive H-loss (Gaetani et al., 2012; Bucholz et al., 2013). Initial LERZ lava flow redox conditions are constrained by proximally quenched un-degassed matrix glass and MI (QFM ~+0.3) and final redox conditions are constrained by the most oxidized matrix glass in the littoral

blast sample (QFM +2.4). At melt temperatures of 1120 ºC, metal vacancy diffusion timescales indicate that the littoral blast olivine-hosted MI would have completely equilibrated with external melt redox conditions in < 1 day (Bucholz et al., 2013). Such rapid redox re-equilibration timescales are consistent with 1-atm heating studies of olivine grains in the open atmosphere, where substantial oxidation of the olivine crystal itself occurred within hours at temperatures of 900 – 1200 °C (Kohlstedt et al., 1976; Knafelc et al., 2019; Kądziołka-Gaweł et al., 2019).

Bucholz et al. (2013) note that redox re-equilibration must occur on a timescale comparable to H_2O loss, otherwise they would have observed large Fe^{3+} increases in their experimentally dehydrated MI, as proposed by Danyushevsky et al. (2002). However, the Fe-XANES measurement of Gaetani et al. (2012) and Bucholz et al. (2013) were made in MI from hydrous arc basalts from Cerro Negro (Nicaragua) prior to the recognition of Fe-XANES beam damage. Consequently, their original measurements on these hydrous, beam damage-susceptible MI (Φ = ~0.5, Table 1) were conducted with a focused beam and a high photon dose (G. Gaetani, personal communication). The samples accordingly suffered extensive beam damage-induced photo-oxidation, with originally measured $Fe^{3+}/\Sigma Fe$ as high as 57% (QFM ~+4.3). We re-measured these same Cerro Negro MI at a lower photon dose ($2 – 6 \times 10^7$ photons/s/um^2), although with 14 minute scan durations, which are slower than we now recommend to best track beam damage (see above sections). Under these measurement conditions, Cerro Negro MI have calculated $Fe^{3+}/\Sigma Fe$ values of ~20 to 33% (QFM +0.9 to +2.4, from the composition-specific 1-atm relation of Kress and Carmichael [1991]), which is more consistent with fO_2 estimates for arc basalts (Cottrell et al., in press; Kelley and Cottrell, 2009). However, we note that these MI are brown colored and Fe-XANES spectra display Fe-oxide nanolite signatures (Figure 11). Owing to the presence of nanolites, we do not view these measurements as necessarily representative of the true MI fO_2 conditions, as discussed above.

Gaetani et al. (2012) and Bucholz et al. (2013) also conducted Fe-XANES measurement on a set of experimentally dehydrated Cerro Negro MI, whose water contents decreased from ~4 wt% to 0.1 wt% H_2O. The dehydrated MI are much less susceptible to Fe-XANES beam damage (Φ = ~0.02), and even though the dehydrated MI were also analyzed with long scan durations and high photon doses, they likely

experienced minimal photo-oxidation. Consequently, the 22 – 23% $Fe^{3+}/\Sigma Fe$ originally measured by Gaetani et al. (2012) is likely representative of the Fe speciation in the dehydrated MI. Despite the limitations due to the presence of nanolites in the natural Cerro Negro MI, comparing our re-analyzed measurements of hydrous Cerro Negro MI with the dehydrated MI suggests minor, if any, redox changes occurred during MI dehydration. Importantly, the samples do not exhibit the severe oxidation that the model of Danyushevsky et al. (2002) predicts. With ~11.5 wt% FeO^T and 4 wt% initial H_2O (Gaetani et al., 2012), Cerro Negro MI contain more water than Fe on a molecular basis, and the loss of 4 wt% H_2O would have completely oxidized all the initial Fe^{2+} to Fe^{3+}. This oxidation is decidedly not observed in the dehydrated MI. Therefore, the original conclusions of Gaetani et al. (2012) remain valid: H_2O loss does not result in MI oxidation, perhaps because olivine-hosted MI rapidly adjust to external redox conditions.

3.5 Implications of rapid redox re-equilibration of olivine-hosted MI

Rapid timescales of redox re-equilibration of olivine-hosted MI have also been inferred by Hartley et al. (2017), who observed MI reduction during transport in lava flow samples from the 1783 Laki eruption in Iceland. This reductive re-equilibration of Laki MI in lava flows differs from the oxidation within lava flows experienced by olivine-hosted MI from Kīlauea LERZ samples. We attribute these differences in MI reductive or oxidative re-equilibration to different emplacement styles of Kīlauea and Laki lava flows. Kīlauea LERZ lava transport occurred in an open sub-aerial channel (Neal et al., 2019; Patrick et al., 2019c), whereas the Laki lava flows were transported as insulated flow lobes (Guilbaud et al., 2007). The insulated transport of the Laki lavas would have largely prevented atmospheric oxygenation, as was observed for lava-tube fed flows from Kīlauea's Mauna Ulu eruption (Swanson and Fabbi, 1973). Because S^{2-}-dominated basaltic melts become slightly reduced during shallow SO_2 degassing (Moussallam et al., 2016; Helz et al., 2017; **Chapter IV**), insulated lava flows will re-equilibrate to these more reduced external melt conditions, as observed by Hartley et al. (2017). The same reduction during SO_2 degassing occurred in Kīlauea LERZ lava flows (see proximal matrix glass in Figure 14 C [**Chapter IV**]), however this slight melt reduction was overwhelmed by atmospheric oxygenation during the long open channel

transport experienced by the littoral bomb sample. We additionally note that for well-developed lava flows lasting weeks to months, such as the 2018 Kīlauea LERZ lava channel and the large Laki flows, it is unlikely that burning vegetation would contribute any reductive capacity to all but the initial lava flows.

The rapid timescale of redox re-equilibration of olivine-hosted MI has important implications for interpreting pre-eruptive melt conditions (Hartley et al., 2017). In Kīlauea 2018 LERZ magmas, diffusion modeling of primitive Fo_{88-90} olivine grains show that they mixed with more evolved magma either in the summit region or along the East Rift Zone days to months before being erupted (Mourey et al., 2019). Given their rapid redox re-equilibration, MI in those primitive olivine grains would have completely re-equilibrated with the more evolved carrier liquid prior to eruption, and will not retain redox conditions of the primitive melt. As the redox conditions of Kīlauea magma are unlikely to change dramatically until shallow degassing (Moussallam et al., 2016; Helz et al., 2017) or extreme fractionation (**Chapter IV**), MI re-equilibration is perhaps not a critical problem for interpreting the general redox conditions of Kīlauea magmas. However, in more complex systems where the mixing of substantially different magma types and/or where deep redox-sensitive degassing may occur (e.g., arc stratovolcanoes, bimodal hotspot systems), the redox permeability of olivine-hosted MI may obscure the redox conditions of primitive magmas and mantle sources.

A further implication of rapid redox re-equilibration in olivine-hosted MI is that PEC of olivine rinds during MI cooling does not lead to an enrichment in Fe^{3+}. As Fe^{2+} in the MI is incorporated into the crystallizing olivine rind, $Fe^{3+}/\Sigma Fe$ in the MI is buffered by continued redox exchange with the external melt. Consequently, PEC corrections to olivine-hosted MI can be applied assuming that MI are open systems to redox changes. Similarly, any Fe^{3+} enrichment caused by diffusive water loss should be eliminated by redox re-equilibration with the external melt (Bucholz et al., 2013). However, large-scale degassing can change the redox state of the external melt during decompression or crystallization (Cottrell et al., in press; Métrich et al., 2009; Moussallam et al., 2014, 2016, 2019; Burgisser et al., 2015; Helz et al., 2017), which olivine-hosted MI would re-equilibrate with. Therefore, the degree of degassing-induced redox changes and the relative rates of magma ascent and MI redox re-equilibration will determine what

petrologic conditions redox measurements of olivine-hosted MI reflect (i.e., storage conditions vs conduit conditions vs emplacement conditions).

4. Conclusions

Using repeat, rapid Fe- and S-XANES measurements and implementing a new peak-fitting calibration for S-XANES, we have developed time-dependent corrections to identify and correct for beam damage during Fe- and S-XANES analysis of silicate glasses. Beam damage corrections for Fe photo-oxidation and S photo-reduction are determined for each individual analysis rather than applying blanket corrections. This allows versatility to account for composition differences and the effects of variable water loss from MI (size and proximity to grain edges), which can influence beam damage susceptibility. Testing these XANES analysis conditions and beam damage corrections on hydrous experimental basalts, we show that Fe- and S-XANES measurements can be reliably made on beam damage-susceptible glasses. Additional detailed studies of the mechanism and compositional dependence of S-XANES beam damage could further improve the photo-reduction correction method we have introduced here.

However, it is critical to understand what geologic processes are represented by elemental valence states measured in quenched samples. Melt inclusions containing nanolite phases may invalidate Fe- and S-XANES calibrations for elemental speciation in glasses, and should be interpreted cautiously. In glasses from Kīlauea Volcano's 2018 LERZ eruption that were measured by both Fe- and S-XANES, we do not observe S speciation that is entirely consistent with temperature-sensitive electron transfer. We suggest that composition or pressure may be important parameters in governing S speciation of glasses at a given fO_2. but until these relationships are further constrained, Fe- and S speciation should be determined directly.

Based on observations of rapidly oxidized MI from Kīlauea 2018 LERZ subaerial lava flows, we conclude that olivine-hosted MI rapidly re-equilibrate with their external environment within ~1 day at basaltic temperatures (~1120 C). Oxidative re-equilibration of Kīlauea samples was likely due to atmospheric oxygenation during open channel lava flow. Critically, the same rapid timescales of redox re-equilibration of olivine-hosted MI will be relevant during common magmatic processes, such as ascent and degassing, or

assimilation and hybridization with other magmas. Therefore, we view measurements of redox state in olivine-hosted MI much as the community now views measurements of water contents in olivine-hosted MI: as subject to rapid re-equilibration. Whenever olivine-hosted MI are in an environment with a redox differential for any appreciable amount of time at magmatic temperatures, MI will equilibrate to the external redox conditions (Gaetani et al., 2012; Bucholz et al., 2013; Hartley et al., 2017). Depending on a magma parcel's ascent rate, redox conditions measured in olivine-hosted MI will reflect either the last storage environment those samples equilibrated within, or will reflect conduit conditions (perhaps in a disequilibrium state due to rapidly changing conditions during ascent). Finally, any redox effects from PEC or diffusive water loss in olivine-hosted MI should be rapidly overprinted through redox re-equilibration with the external melt.

Caution should be taken when attempting to link measured MI redox states to primitive magma conditions in all cases except for material that ascended very rapidly to the surface. Further studies are warranted to determine whether other host phases may be less redox-permeable than olivine, and therefore may contain MI that preserve properties more representative of melt redox conditions at time of entrapment.

5. Bridge

In Chapter III, I introduced new techniques to improve Fe- and S-XANES measurements of silicate glasses by identifying and correcting for X-ray induced beam damage. I then applied these techniques to melt inclusions from Kīlauea Volcano's 2018 LERZ eruption. Lavas from this eruption were subaerially transported long distances, during which, some magma parcels underwent atmospheric oxidation. Olivine-hosted melt inclusions in these oxidized magma parcels have re-equilibrated with the external melt over relatively short timescales (hours to days) of lava channel flow. This rapid redox re-equilibration cautions against assuming that olivine-hosted melt inclusions record melt redox conditions at the time of melt inclusion entrapment. The implications and concerns of rapid redox re-equilibration apply to redox studies of olivine-hosted melt inclusions in all high temperature volcanic systems.

In Chapter IV, I utilize the XANES techniques introduced in Chapter II to expand the melt inclusion redox study of Kīlauea's 2018 LERZ eruption. I integrate the redox observations within a larger petrologic dataset of samples from the LERZ eruption to model the behavior of sulfur and other volatiles in Kīlauea magmas. These observations are compared to record-setting gas emissions from the LERZ eruption to better understand the volatile budget of this historic eruption.

CHAPTER IV

THE PETROLOGIC AND DEGASSING BEHAVIOR OF SULFUR AND OTHER MAGMATIC VOLATILES FROM THE 2018 ERUPTION OF KĪLAUEA, HAWAI'I: MELT CONCENTRATIONS, MAGMA STORAGE DEPTHS, AND REDOX VARIATIONS

This chapter is in preparation for a special topical issue of *Bulletin of Volcanology* on the 2018 fissure eruption of Kīlauea Volcano. I am lead author on the paper, which involved project conception, sample preparation, analysis, data synthesis, and writing the manuscript. Paul Wallace (University of Oregon) served as my main advisor, aiding in project conception, data interpretation, and manuscript editing. Thomas Shea and Adrien Mourey (University of Hawai'i – Mānoa) aided in sample preparation, data analysis, and interpretation. Peter Kelly, Patricia Nadeau, Tamar Elias, Christoph Kern, Laura Clor, Lopaka Lee, and Cynthia Werner (U.S. Geological Survey), Cheryl Gansecki (University of Hawai'i – Hilo), and Lowell Moore (Virginia Tech) aided in sample collection and data analysis.

Overview

The 2018 eruption of Kīlauea Volcano's Lower East Rift Zone (LERZ) produced exceptionally high lava extrusion rates and record setting SO_2 emissions exceeding 100 kt/day. The eruption involved a diverse range of magmas, erupting highly primitive basalts ($Fo_{86–90}$ olivine) sourced from Kīlauea's summit reservoirs as well as fractionated basalts and andesite that had evolved during extended LERZ storage. Detailed geologic sampling and gas monitoring throughout the eruption provide exceptional datasets to address the behavior of volatiles in the Kīlauea plumbing system and during degassing. We apply a diverse set of analyses to matrix glasses, melt inclusions, and host minerals from a range of LERZ erupted material to identify magma sources and determine whether a petrologically determined volatile budget is consistent with the extreme gas emissions measured during the eruption.

Magma mixing in the summit reservoirs and in transport along the rift zone, as well as degassing and atmospheric interaction, cause melt inclusions to re-equilibrate to a range of changing melt conditions. Rapidly quenched LERZ glasses have redox states of QFM 0 to +0.4, similar to observations from in past Kīlauea eruptions. Shallow and surficial processes modify the redox state of melts, with shallow SO_2 degassing (from depths ≤ 100 m) causing reduction of the melt by up to -0.5 log units, and atmospheric interaction causing substantial oxidation of +1 to +2 log units in lavas that traveled ≥ 13 km in a subaerial lava channel. Olivine-hosted melt inclusions rapidly equilibrate to the oxidation state of the external melt, becoming either reduced or oxidized to match the oxidation state of their carrier liquids.

We find that LERZ glasses span nearly the entire previously recognized compositional range at Kīlauea. Melt inclusions in high-Fo olivine grains erupted from fissure 8 underwent more than 150 °C of cooling within colder LERZ carrier melts, which caused extensive post-entrapment crystallization and sulfide precipitation in melt inclusions. However, even when accounting for sulfide masses in melt inclusions, many inclusions in high-Fo olivine grains have relatively low S contents (400 – 900 ppm). CO_2 – H_2O vapor saturation pressures indicate that many of these high-Fo melt inclusions were entrapped at depths of ≤ 5 km, consistent with formation within Kīlauea's South Caldera or Halema'uma'u reservoirs. A number of melt inclusions in high-Fo olivine have very low entrapment pressures (< 1 km) and also have low S concentrations (400 – 600 ppm) and degassed S-isotopic signatures (-1.5 to -0.5‰ compared to ~1‰ in S-rich inclusions) that suggest that these primitive melts must have undergone near-surface degassing prior to inclusion formation. We propose that Kīlauea's long history of lava lake activity and episodes of lava drain-back during eruptions (such as 1959 Kīlauea Iki eruption) have caused the recycling of substantial volumes of magma, including highly primitive magmas, within the shallow Kīlauea system.

From melt inclusions that are likely co-genetic with the bulk LERZ fissure 8 melt, we estimate pre-eruptive S concentrations of ~1110 ppm and that fissure 8 melts sulfide were under-saturated. Scaling this melt S concentration with the estimated lava effusion rates can largely account for the extreme levels of SO_2 degassing measured during the eruption. We conclude that the LERZ melts were not particularly volatile rich and it was

the eruption's high lava effusion rates that caused the record-setting SO_2 emissions. We suggest that a decade of degassing and magma recycling within the Halema'uma'u lava lake contributed to the 2018 LERZ melts being more volatile depleted than past Kīlauea eruptions. We also propose that magma recycling from the Halema'uma'u lava lake played a role in the pressurization and rupture beneath Pu'u 'Ō'ō, which initiated the LERZ eruption.

1. Introduction

Kīlauea Volcano on the Big Island of Hawai'i (USA), is among the best monitored and studied volcanoes on Earth. However, each new volcanic event provides additional data that challenge prior conceptions about fundamental aspects of Kīlauea's magma reservoir system, such as its geometry and longevity, and extent and consequences of magma mixing and volatile degassing. The 2018 fissure eruption of Kīlauea's Lower East Rift Zone (LERZ) provides a dramatic example of how multidisciplinary eruption monitoring coupled with detailed geochemistry can be interpreted in the context of a long observational history to provide new insights into volcanic processes at Kīlauea.

The 2018 LERZ eruption was Kīlauea's largest eruption in > 200 years, and was well monitored and sampled by dedicated volcanologists at the U.S. Geological Survey's Hawaiian Volcano Observatory (USGS-HVO) (Anderson et al., 2019; Gansecki et al., 2019; Kern et al., 2020; Neal et al., 2019; Patrick et al., 2019c). Between May and August, fissures in the LERZ extruded > 1 km^3 (DRE) of magma and was accompanied by a summit caldera collapse (Anderson et al., 2019) and record-setting SO_2 gas emissions (Kern et al., 2020). More detailed accounts of the eruption chronology are presented elsewhere (Gansecki et al., 2019; Neal et al., 2019; Patrick et al., 2020), and we provide only a short summary here. Prior to the LERZ eruption, a remarkable dual-sourced eruption had been occurring at Kīlauea since 2008. Magma ascending at the volcano's summit would circulate and degas in a lava lake hosted within the Halema'uma'u summit crater. This magma would then enter the East Rift Zone (ERZ), travel ~20 km down-rift while partially hybridizing with stored magmas, and erupt to the surface at Pu'u 'Ō'ō (Elias & Sutton, 2012; Orr et al., 2015; Patrick et al., 2019b;

Thornber et al., 2015). In early 2018, both Pu‘u ‘Ō‘ō and Kīlauea’s summit began pressurizing, and on April 30 a dike propagated from beneath Pu‘u ‘Ō‘ō towards the LERZ. Pu‘u ‘Ō‘ō partially collapsed in the process, ending an eruption from that area that had been largely ongoing since 1983 (Orr et al., 2015; Wolfe et al., 1987).

On May 3, the first of 24 fissures erupted within the LERZ. Early erupted lavas were evolved basalts, and a small amount of andesite was also explosively erupted from fissure 17 (Gansecki et al., 2019). In late May, hotter more “summit-like” magma began erupting in the LERZ and lava extrusion rates increased rapidly (Gansecki et al., 2019; Neal et al., 2019). Lava ocean entries first occurred to the south in late May. Starting May 28, activity began focusing at fissure 8 (F8), producing lava fountains up to heights of 80 m (Neal et al., 2019). Fissure 8 was the dominant lava extrusion source for the remainder of the eruption, and from June to August, fed a fast-flowing lava channel that traveled > 10 km to reach the ocean (Neal et al., 2019; Patrick et al., 2019c). High lava effusion rates were accompanying by a piston-like collapse of the summit caldera, as magma was drained from the shallow reservoir systems (Anderson et al., 2019). During caldera collapse, the Halema’uma’u lava lake drained and its conduit became filled with collapse debris. By June, SO_2 degassing rates at the summit had decreased from a steady decade-long average of ~4.5 kt/d to ~1 kt/d, and degassing continued to decline to near instrument detection limits (Kern et al., 2020). On August 4 – 5, the LERZ eruption and summit collapse abruptly ended. The last visible surface lava was seen on September 5, marking the official end of the eruption. Over 1 km^3 DRE magma was erupted from LERZ fissures within just three months (early May to early August) (Dietterich et al., in prep; Kern et al., 2020), which is ≥ 10 years’ worth of Kīlauea’s average magma supply (Anderson & Poland, 2017; Poland et al., 2014). This large scale eruption dramatically reshaped southeastern Hawai’i and Kīlauea’s summit magma reservoirs.

The LERZ eruption occurred within the community of Pāhoa, and hazardous lava flows and prodigious gas emissions profoundly impacted the area. Sustained SO_2 emission rates of > 100 kt/day amounted to a ~20-fold increase in SO_2 emissions from the Kīlauea, compared to the already significant degassing that had been occurring from Pu‘u ‘Ō‘ō (1983 – 2018) and the Halema’uma’u lava lake (2008 – 2018) (Elias & Sutton, 2012; Kern et al., 2020). In addition to presenting severe local hazards, the high levels of

SO_2 degassing resulted in large vog plumes that affected the entire island. Understanding the factors that contributed to this remarkable SO_2 output is important for constraining the eruption's lava and S budget, and for improving our ability to anticipate and interpret future degassing activity and associated hazards.

Much of the LERZ lava deposition occurred offshore. Consequently, despite the eruption being extremely well monitored, large uncertainties remain in the fundament question: how much magma was erupted? The summit caldera collapse was in direct hydraulic connection with the LERZ erupting melt, as evidenced by pressure waves, or "surges", of increased lava extrusion that were observed with hours following incremental collapses of the summit (Patrick et al., 2019c). However, the summit caldera collapse volume of 0.8 km^3 (Anderson et al., 2019; Lundgren et al., 2019; Neal et al., 2019) is substantially lower than cumulative eruption volume estimates from lava effusion rates or SO_2 emissions (Dietterich et al., in prep; Kern et al., 2020). An improved understanding of the melt S concentrations and degassing behavior will improve lava extrusion estimates derived from SO_2 emissions.

However, the behavior of S can be complicated due to sulfide saturation, degassing, and mixing. Sulfide saturation and S degassing are both pressure-, composition-, and temperature-dependent processes. Sulfur is a multivalent element that occurs in silicate melts as S^{2-} or S^{6+} complexes depending on melt redox state, temperature, and composition (Carroll & Rutherford, 1988; Jugo et al., 2010; Klimm et al., 2012; Métrich et al., 2009; Nash et al., 2019; Wallace & Carmichael, 1992; Wilke et al., 2008). The solubility of S^{6+} in melts is nearly an order of magnitude greater than for S^{2-} (Carroll & Rutherford, 1988; Jugo, 2009; Jugo et al., 2010). Consequently, melt properties that control S speciation, such as redox state, play a large role in governing the behavior of S in the melt and during degassing. Comprehensively understanding S behavior in the Kīlauea magmatic system and LERZ eruption therefore requires constraining a range of melt properties.

Here, we combine compositional, redox, isotopic, and volatile measurements of matrix glasses, melt inclusions (MI), and their mineral hosts from Kīlauea's 2018 LERZ eruption to provide insights into a variety of processes occurring in the subsurface and during volatile degassing and lava emplacement. The diversity of magma compositions

(basaltic to andesitic), the range of types of erupted material (quenched scoria, basaltic pumice, subaerial lava flows, littoral bombs), and the dedicated chronological sampling throughout the eruption make this a particularly rich dataset for improving our understanding of the 2018 eruption and more general magmatic and degassing processes at Kīlauea. In particular, we recognize that S concentrations in LERZ materials are highly variable and do not conform to a simple down-temperature sulfide-saturated melt evolution. We highlight the complicating effects of extreme post-entrapment crystallization and of rapid diffusive redox re-equilibration of olivine-hosted MI, which strongly affect sulfide saturation conditions within MI (Gaetani et al. 2012; Bucholz et al. 2013; Hartley et al. 2017; **Chapter III**). With an updated C-H-S degassing model based on the work of Gerlach (1986), we can better interpret degassing depths, efficiency of gas release during ascent, and the effects of SO_2 degassing on redox state and S-isotope fractionation. Through these considerations, we are able to identify undegassed MI and re-entrant melt channels, which provide improved estimates of the pre-eruptive S contents of ~1110 ppm for melts feeding fissure 8 lavas. Using this melt S concentration, we petrologically estimate a cumulative eruption volume of ~1.9 km^3, which slightly larger than that estimated by Kern et al. (2020) and is over twice the volume of the summit caldera collapse.

Finally, we use H_2O-CO_2 vapor saturation pressures to constrain MI entrapment depths and find that primitive magmas were likely sourced from shallow depths that are consistent with Kīlauea's inferred South Caldera and Halema'uma'u reservoirs (Poland et al., 2014), rather than being derived from more deeply ascending magmas. Relatively shallow origins for primitive magma sourcing the LERZ eruption are similar to observations for shallow source depths for past Kīlauea summit and rift zone eruptions (Anderson & Brown, 1993; Tuohy et al., 2016). Finally, we find evidence for abundant shallow recycling of magma within the Kīlauea system (Dixon et al., 1991), which we suspect has implications for the volatile loads of the LERZ melts and for the initiation of the LERZ eruption.

2. Methods

2.1 Samples

USGS-HVO teams collected molten or recently cooled samples throughout the May – August LERZ eruptive period (Gansecki et al., 2019; Lee et al., 2019). We focus on a subset of samples that were rapidly cooled: water-quenched molten samples from the active lava channel or overflows, naturally-quenched spatter and basaltic pumice from fissures, and naturally-quenched tephra from explosive ocean entry littoral blasts (Figure 1, Table 1, Figure C1). All these samples contain glassy MI and matrix glass. One more slowly cooled sample from the final lava channel overflow of fissure 8 (F8) was also investigated (LF8, erupted ~Aug 4, 2018). This sample has a mostly crystallized groundmass and most large MI are partially devitrified. However, smaller MI in this sample remained glassy and were analyzed.

Tephra and lava samples were gently crushed and sieved to 250 μm. Phenocrysts of olivine (ol), and lesser numbers of clinopyroxene (cpx), orthopyroxene (opx), and plagioclase (pl) phenocrysts (if present), were picked. Phenocrysts have a variety of textures (e.g., single well-faceted grains, aggregated grains, grains with skeletal growth) reflecting diverse origins and cooling histories (Figure C2). Phenocryst grains were mounted in CrystalBond® and singly or doubly polished to expose targeted MI and re-entrant melt channels (RE). Prior to intersecting targeted MI, the volume of the inclusion was determined by using a calibrated microscope reticle, with the depth dimension taken to be an average of the maximum length and width MI dimensions. If present, the volumes of vapor bubbles, sulfide blebs, and daughter minerals (typically spinel) within MI were similarly quantified, assuming spherical and rectangular dimensions, respectively. Matrix glasses, RE, and interstitial melts (melt pockets bounded between crystals) were also analyzed.

Polished thin sections and randomly intersected grain mounts were produced from a subset of samples. Some of these grains contain MI or RE, however these serendipitously exposed features lack the full petrologic context to determine MI or RE sizes and the presence of any vapor bubbles, sulfide blebs, or other daughter minerals. Additionally, it is uncertain whether apparent MI in thin section were indeed fully sealed within mineral hosts, or are sectioned RE that retained connectivity to the external melt at

quenching. We include analysis of MI and RE from thin sections and randomly sectioned grain mounts in this work, but given the aforementioned concerns, we generally focus our analysis on MI from individually prepared grain mounts. We report data only from fully glassy MI, which are inferred to have quenched rapidly, either during tephra production, or by rapid water-quenching during lava channel sampling by HVO geologists.

We conducted reheating experiments on a subset of devitrified MI from the slowly cooled LF8 sample using a 1 bar, oxygen fugacity (fO_2)-controlled Vernadsky heating stage (Sobolev et al., 1980) to rehomogenize some of the larger devitrified MI. Olivine grains were brought up to 1200 or 1300 °C in ~100 °C/minute steps and held at maximum temperature for 5 minutes. Reheated MI became completely glassy, but the vapor bubble did not dissolve back into the melt.

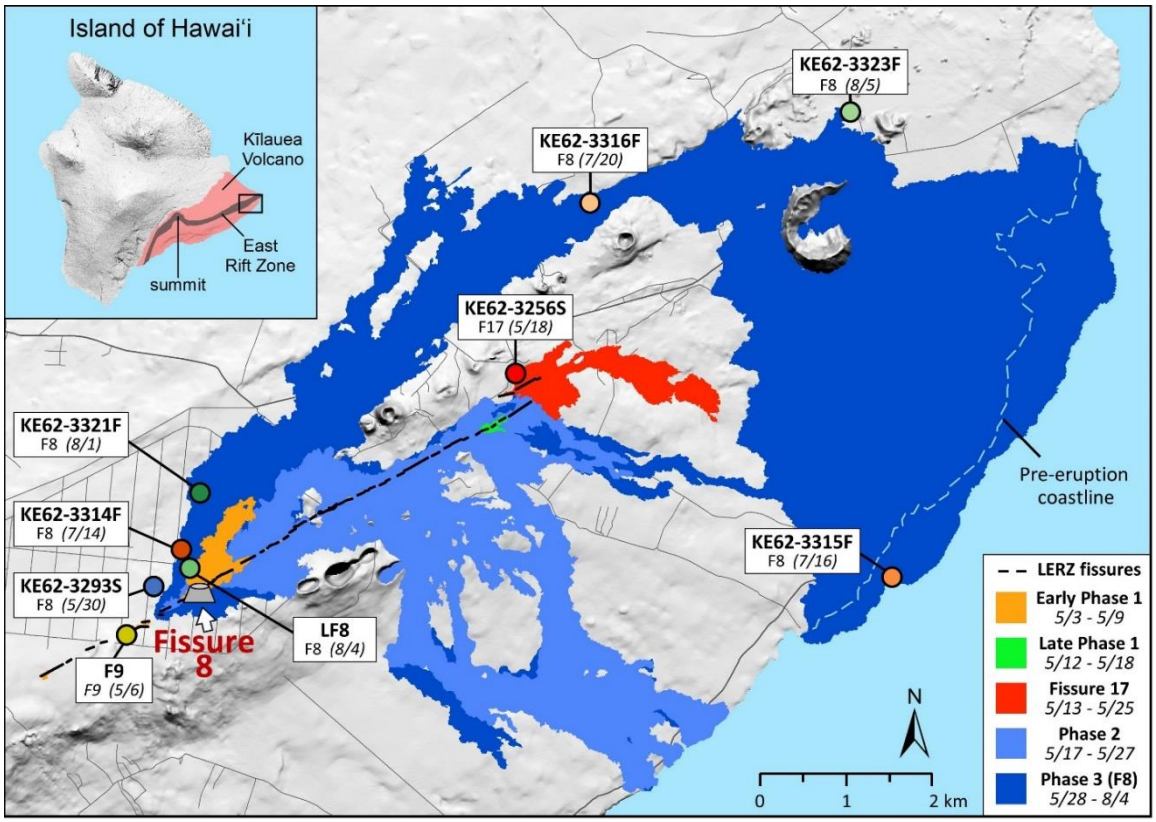

Figure 1. Lava flow map of the 2018 LERZ eruption of Kīlauea, marked with the locations and eruption dates of samples presented in this study. Symbol coloration is maintained throughout all figures. Lava flows are colored by eruption phase (Gansecki et al., 2019) but do not include the substantial amount of offshore deposits. A total of 24 eruptive fissures opened during the eruption, including the en-échelon fissure 17 (F17). The main fissure 8 vent (F8) is marked by a cinder cone. *(inset)* The Big Island of Hawai'i, with the subaerial extent of Kīlauea Volcano highlighted in red. Figure modified from Gansecki et al. (2019), with updated flow extents from Zoeller et al. (2020).

Table 1 – Eruption dates and locations from material sampled in this study, as well as major chronological events of the 2018 LERZ eruption.

Sample name (fissure source)	**Eruption Date**	**Location**	**Description**
First LERZ eruptive fissures	*May 3, 2018*		*Neal et al., 2019*
F9 (fissure 9)	May 5 – 6, 2018	19.457° N 154.917° W	Rapidly cooled spatter
KE62-3256S (fissure 17)	May 18, 2018	19.485° N 154.874° W	Rapidly cooled spatter
Extrusion of hotter summit / Pu'u 'Ō'ō -like lavas	*May 18, 2018*		*Neal et al., 2019; Gansecki et al., 2019*
First ocean entries	*May 19, 2018*		*Neal et al., 2019; Gansecki et al., 2019*
Lava extrusion focuses at re-activated fissure 8	*May 27, 2018*		*Neal et al., 2019; Gansecki et al., 2019*
KE62-3293S (fissure 8)	May 28 – 30, 2018	19.462° N 154.914° W	Naturally air-quenched, freshly fallen basaltic pumice
KE62-3314F (fissure 8)	July 14, 2018	19.466° N 154.911° W	Water-quenched sample from lava channel
KE62-3315F (fissure 8)	~July 15 – 16, 2018	19.464° N 154.832° W	Naturally air/water quenched tephra debris from tour boat struck by littoral blast bomb(s) offshore of ocean entry
KE62-3316F (fissure 8)	July 20, 2018	19.503° N 154.866° W	Water-quenched sample from lava channel
KE62-3321F (fissure F)	Aug 1, 2018	19.472° N 154.909° W	Water-quenched sample from lava channel
LF8 (fissure 8)	~Aug 4, 2018	19.464° N 154.910° W	Slowly cooled vesicular lava with glassy rind from the last lava channel overflow, collected next to channel rim
KE62-3323F (fissure 8)	~Aug 4 – 5, 2018	19.513° N 154.837° W	Water-quenched sample from `a`a flow front
End of major lava effusion	*Aug 5, 2018*		*Neal et al., 2019; Gansecki et al., 2019*
End of eruption (last visible surface lava)	*Sep 5, 2018*		*Neal et al., 2019*

2.2 Electron microprobe

Geochemical analyses were conducted on individually polished grains mounted in epoxy or indium and on randomly sectioned grain mounts and thin sections. Samples were carbon-coated and glass and minerals were analyzed for major element compositions with a Cameca SX100 electron probe microanalyzer (EPMA) at the University of Oregon. Minerals were analyzed at 15 kV with a 3 μm spot size. Glasses

were analyzed at 15 kV with a 10 μm spot size. During glass analyzes, Na, K, Si, Al, and Fe were measured first, and their concentrations were calculated with a linear time-dependent intensity correction (TDI) using the Probe for Windows software package (Donovan et al., 2007) to account for alkali mobility in glasses during electron beam excitement (Kuehn et al., 2011). TDI corrections were minimal for all elements. We report 1 SE relative uncertainties from repeated analyses of glass and mineral standards throughout the paper. Full analytical conditions for EPMA are described in **Appendix C**.

2.3 Post-entrapment crystallization corrections

Melt inclusions in Kīlauea LERZ olivine grains experienced a wide range of post-entrapment crystallization (PEC) during magma mixing, with 0 – 50% of the MI mass crystallizing into olivine rinds during cooling. The extent of PEC is highly correlated with olivine Fo (Fo is the Mg# of olivine: 100*Mg/[Mg + Fe] in mole fractions) and reflects the large degree of cooling experienced by primitive olivine grains during melt hybridization and emplacement (Figure C3). Melt inclusion compositions were corrected for PEC following the methods of Danyushevsky et al. (2000):

1) Uncorrected FeO^T and MgO concentrations in olivine-hosted MI were compared to whole rock and matrix glass compositions from 2018 LERZ, 1983 – 2018 Pu‘u ‘Ō‘ō, and 2008 – 2018 summit samples. Primitive Kīlauea samples have relatively invariant FeO^T concentrations of ~11.5 wt% over a range of 6 – 10 wt% MgO, prior to FeO^T increasing with further fractionation (2.5 – 6 wt% MgO). All 2018 LERZ olivine-hosted MI that experienced PEC contain > 6 wt% MgO and were PEC-corrected to 11.5 wt% FeO^T initial contents, to account for Fe-loss from diffusion into the host olivine during cooling and re-equilibration.
2) PEC was corrected with the Petrolog3 program (Danyushevsky & Plechov, 2011) using the olivine-melt partitioning model of Beattie (1993) and the melt density model of Lange and Carmichael (1987). We maintained fO_2 fixed at QFM +0.25 (using the $Fe^{3+}/\Sigma Fe$ ratio of Kress and Carmichael [1988]), as MI diffusive redox re-equilibration through olivine has been shown to occur very rapidly (Gaetani et al. 2012; Bucholz et al. 2013; Hartley et al. 2017; **Chapter III**). Minor elements were partitioned according to MORB concentrations.

3) Sulfur, Cl, and CO_2 are not included in Petrolog3 and were manually PEC-corrected. These species were considered to follow perfectly incompatible closed-system behavior during PEC (Callegaro et al., 2020) and the as-measured concentrations of these elements were diluted by the PEC correction factor to restore their concentrations at time of MI entrapment. Diffusive equilibration of H_2O in olivine-hosted MI occurs rapidly (Barth et al., 2019; Chen et al., 2011; Ferriss et al., 2018; Gaetani et al., 2012; Hartley et al., 2015; Hauri, 2002; Lloyd et al., 2013; Portnyagin et al., 2008; Sobolev & Danyushevsky, 1994), and we assume that the timescale of H_2O diffusion is faster than that of PEC. Consequently, we do not adjust measured H_2O contents for PEC.
4) We assessed the need for PEC corrections of MI in non-olivine phases (plagioclase, clinopyroxene, orthopyroxene) by comparing FeO^T, MgO, CaO, and Al_2O_3 measured in MI to the whole rock and matrix glass suites (listed above). Most plagioclase-, clinopyroxene-, and orthopyroxene-hosted MI overlap with co-erupted matrix glass compositions, without the expected Al_2O_3 + CaO depletion and FeO^T + MgO enrichment due to respective host-phase PEC. Plagioclase- and pyroxene-hosted MI thus seem to be relatively unaffected by PEC, and no corrections were applied. The lack of appreciable PEC is consistent the formation of these MI, and their mineral hosts, in approximate equilibrium with the carrier melt. This differs from olivine-hosted MI, where primitive olivine grains crystallized at much hotter temperatures than the hybridized LERZ erupted melt, leading to substantial PEC. We note that two plagioclase-hosted MI in from fissure 17 (F17) might have undergone PEC as they do have anomalously low Al_2O_3 and CaO, as well as elevated plagioclase-incompatible element concentrations. However, no PEC-corrections were applied to these MI due to a limited context of major element arrays at this evolved Kīlauea composition, and because there is substantial evidence of magma mixing in the F17 magma (Gansecki et al., 2019).

2.4 Sulfide restorations

Sulfides blebs are present in a number of MI and, despite their small size, can account for a substantial mass of S. To calculate total S in the MI that contain sulfide

blebs, we determine the mass of S in the sulfide and add this to the total S mass from the MI glass. Melt inclusions exposed in thin sections and bulk grain mounts have lost their full petrologic contexts, and in many cases it is unknown whether these intersected MI contained sulfides. In thin sections and bulk grain mounts, if MI are hosted in high-Fo olivine grain (Fo_{86-90}) and no sulfides are observed, we infer whether the MI likely contained a sulfide based on whether sulfides are observed in neighboring MI in the same grain. If sulfides are present in neighbor MI, we assume that the MI in question would have similarly contained a sulfide that accounted for the same percentage of total S as in the neighboring inclusion. However, there are still a number of MI in high-Fo olivine grains that lack sufficient petrologic context for sulfide-restorations, and thus the measured S in MI glass is a minimum for the total S in the MI. See **Appendix C** for further details.

2.5 FTIR and Raman: H_2O, CO_2, and vapor saturation pressure calculations

2.5.1 Vapor bubble CO_2 by Raman

Raman measurements were conducted at Virginia Tech using a JY Horiba LabRam HR (800 mm) spectrometer system following the methods of Moore et al. (2015) and Aster et al. (2016). A synthetic fluid inclusion containing a low-density CO_2 vapor bubble was analyzed multiple times during each session to ensure instrument reproducibility. Samples were polished to within ~10 μm of vapor bubbles within MI, leaving bubbles non-intersected for analysis. Spherical bubble and MI volumes were measured with a calibrated microscope reticle (±1 μm measurement uncertainty) where the z-dimension of MI was taken to be the average of X and Y dimensions. CO_2 bubble densities and bubble volumes determined the total CO_2 bubble masses. CO_2 concentrations in MI were then calculated from the ratios of the CO_2 bubble masses to the masses of MI glass (Steele-Macinnis et al., 2011), where the glass masses are calculated as: *(MI volume – daughter mineral inclusion volumes) * glass density*. Glass densities were calculated from non-PEC corrected MI compositions at 25 °C and 1 bar via the DensityX tool (Iacovino & Till, 2019). To calculate CO_2 contents of MI at time of entrapment, CO_2 concentrations were diluted by the Petrolog3-determined PEC-correction factor for each MI.

2.5.2 H_2O and CO_2 by FTIR

Water and CO_2 concentrations in MI and matrix glasses were measured at the University of Oregon using a Thermo Nicolet Nexus 670 Fourier transform infrared (FTIR) spectrometer interfaced with a Continuum IR microscope. Volatile concentrations were calculated using the Beer-Lambert law following the method of Stolper (1982). Wafer thicknesses were measured by micrometer (±2 μm) or by reflectance interference fringes (Wysoczanski & Tani, 2006). The CO_2 detection limit is estimated to be ~50 ppm for our analytical conditions and wafer thicknesses. H_2O contents in MI are not diluted via PEC-corrections, as we assume H_2O re-equilibration occurs on a similar or more rapid timescale than PEC. Measured CO_2 contents are diluted via PEC-correction factors to determine CO_2 content at time of entrapment, which assumes no diffusive C-exchange from the MI. See **Appendix C** for further analytical details.

2.5.3 Calculation of vapor saturation pressures

H_2O-CO_2 vapor saturation pressures are calculated using the compositionally-dependent basaltic calibration of Iacono-Marziano et al. (2012). Vapor saturation pressures based on H_2O and total CO_2 contents (PEC-corrected FTIR + Raman) and PEC-corrected melt compositions and entrapment temperatures from Petrolog3 were applied to determine saturation pressure using the equilibrium pressure web tool of Iacono-Marziano et al. (2012). Equilibrium pressures were also calculated for FTIR H_2O + CO_2 glass concentrations or Raman-derived CO_2 contents of MI where total volatile concentrations were unavailable. Where glass composition was not measured by EPMA, an average matrix glass or PEC-corrected composition for MI of that sample was assumed. We estimate uncertainties by calculating the saturation pressure of MI H_2O-CO_2 concentrations plus 1 SE propagated uncertainties from Raman-derived CO_2 bubble densities. We assume the uncertainty is symmetrical. Many CO_2 measurements by Raman have large uncertainties due to low CO_2 contents (low signal) and small MIs and vapor bubbles, so that uncertainties in quantifying vapor bubble and MI volumes manifest as large propagated uncertainties.

2.6 Fe- and S-XANES

Synchrotron-based X-ray absorption near edge structure (XANES) spectroscopy measurements to determine Fe and S elemental speciation of matrix glass and MI were conducted at GSECARS beamline 13-ID-E at Argonne National Laboratory's (Illinois, USA) Advanced Photon Source (APS), a third generation synchrotron light source (Sutton et al., 2017) during multiple analytical sessions between 2016 – 2019. Analyses were conducted in reflectance mode, with the incident X-ray beam and the fluorescence detector each at 45° from the sample surface. Details of the 13-ID-E beamline configuration are described in Head et al. (2018) and are consistent with measurements conducted here.

To minimize Fe photo-oxidation and S photo-reduction beam damage during XANES analyses (Cottrell et al., 2018; Wilke et al., 2008), we reduced photon dose on the sample area by utilizing larger beam spot sizes (10 – 50 μm diameters) and decreased photon flux through instrument tuning. We placing Al-foil sheets in the beam path to further reduce flux during Fe-XANES measurements. These methods ameliorated, but did not completely prevent beam damage from occurring. We therefore employed additional techniques to characterize and correct for beam damage through using repeat, rapid Fe- and S-XANES scans and implemented a peak-fitting calibration for S-XANES, as described in detail in **Chapter III**. Spectral fitting was done with the LARCH program's XAS viewer (Newville, 2013) to correct for detector dead time, and normalize and fit the Fe- and S-XANES data. All Fe-XANES spectra were carefully screened to exclude spectra with mineral host or microlite signatures from interaction with the beam at depth, so that only clean glassy spectra are presented here. See **Chapter III** and **Appendices B and C** for further analytical details. Throughout this paper, we report the proportions of Fe and S valence species as percentages, for ease of discussion.

2.7 δ^{34}S analyses by Secondary Ion Mass Spectrometry

Sulfur isotope (δ^{34}S) measurements of MI and matrix glasses were determined using the Cameca IMS 1280 SIMS at the Northeast National Ion Microprobe Facility (NENIMF) at Woods Hole Oceanographic Institute (Woods Hole, MA). We removed prior carbon-coats and pressed samples into indium mounts, which were then gold

coated. We followed the analytical methods of Fiege et al. (2014) and Mandeville et al. (2008) using a 10 μm Cs^+ primary beam, 10 kV accelerating voltage and 1 – 2 nA beam current. Samples were pre-sputtered for 180 s using a 30x30 μm raster area to remove surface contaminants, and then analyzed using a smaller 20x20 μm raster area to minimize extraneous surface contamination. Secondary ions of ^{34}S and ^{32}S were discriminated with a mass resolution power of 4000 – 5500 and counted using an electron multiplier. See **Appendix C** for further analytical details.

3. Results

3.1 Petrography and compositions of minerals and matrix glasses

3.1.1 Early erupted samples

A diverse of mineral and melt compositions and textures were erupted from Kīlauea LERZ fissures (Figure C1). Early fissures (early phase 1; Gansecki et al. 2019) produced ropy scoria clasts during spattering, which have elongate fluidal to partially spindle shapes, and had naturally cooled quickly. Sample F9 is an early phase 1 eruptive that consists of spatter ribbons collected within 20 m of the SW extent of fissure 9 on May 5, 2018. Material from multiple spatter clasts were mixed together for a more representative sample. Phenocrysts in F9 spatter dominantly consist of plagioclase (An_{55-73} n=14; An is (100*Ca/[Ca+Na+K] in mole fractions) laths up to 300 – 800 μm long, as well as clinopyroxene (Mg_{72-84}, n=8) and lesser orthopyroxene (Mg_{72-75}, n=2) grains. These three phases commonly occur in glomerocrystic clusters. Olivine phenocrysts are less common and have zoned profiles, with one measured phenocryst having a Fo_{78} core and Fo_{68} rim. Olivine micro-phenocrysts are present in the groundmass, with Fo_{67} (n=1) compositions that are that is similar to the rim compositions of larger olivine phenocrysts. Abundant matrix glass is present, containing dispersed plagioclase, clinopyroxene, orthopyroxene, and Fe-Ti oxide microlites. Groundmass microlites have lower An and Mg numbers than phenocrystic or glomerocrystic grains. Spherical vesicles are abundant. Matrix glasses contain 120 – 510 ppm S (n=13), whereas RE in plagioclase phenocrysts contain up to 780 ppm S. Small sulfides are present within the cores of some RE. The RE in plagioclase grains are up to 150 μm long and have irregular shapes, suggesting that they are dissolution features. Melt inclusions that are large enough to analyze are very

rare in all observed F9 phenocryst phases. However, some pl-cpx glomerocrystic crystal clots contain pockets of interstitial melt that were partially prevented from degassing during ascent and eruption. These interstitial melts are vesicle-free and retain high S-concentrations of 520 – 1680 ppm S (n=10). Chlorine contents in matrix glasses are between 250 – 350 ppm, whereas RE and interstitial melts contain up to 450 ppm Cl. Matrix and interstitial glasses have similar major element compositions, and all are Fe-rich (13 – 16 wt% FeO^T) and relatively Mg-poor (3.5 – 4.7 wt% MgO) compared to later erupted LERZ F8 melts. Using the Mg-thermometry formulation of Helz and Thornber (1987), we estimate F9 eruption temperatures of 1080 – 1110 °C. We did not analyze additional early phase 1 samples from other fissures. However, given the similarity in eruption style, lava flow viscosities, and hand-sample textures, we assume that our observations in sample F9 are likely to be fairly representative of magmas erupted at other early basaltic fissures.

Fissure 17 was active from May 13 – 25, 2018 and produced the most evolved lavas ever observed to erupt on Kīlauea (Gansecki et al., 2019) (note that in 2005, a dacitic magma was intersected during geothermal drilling in the LERZ [PGV dacite, Figure C5] but this magma never erupted [Teplow et al. 2009]). We analyzed a thin section of a scoria clast erupted from F17 on May 18, 2018 (KE62-3256S). We measured only a small number of minerals and glasses in this sample, but our observations are consistent with descriptions of F17 andesite by Gansecki et al. (2019) except that we additionally observe rare olivine phenocrysts with low-Fo and/or orthopyroxene rims. Plagioclase is the dominant phenocryst (groundmass An_{47-55}; n=2). Lesser clinopyroxene, orthopyroxene, and olivine (Fo_{69}, n=1) are present as phenocrysts and crystal clots. Additionally, Fe-Ti oxides are relatively abundant, and groundmass sulfides and rare elongate apatite are also present (Figure 2b). Interstitial melts and RE channels are variably evolved andesitic to dacitic compositions (Figure C5) that contain 59 – 65 wt% SiO_2, 7.5 – 9.3 wt% FeO^T, and 1.2 – 2.1 wt% MgO (n=7). These glasses are rich in Cl, containing 900 – 1000 ppm Cl, whereas S concentrations are 220 – 590 ppm. Two MI analyzed in more calcic feldspars ($An_{66,72}$) have more primitive, basaltic compositions that are similar to other LERZ basalts. These MI contain ~51 wt% SiO2, ~14 wt% FeO^T, and ~7.4 wt% MgO. However, the MI have low Al_2O_3, suggesting that they might have

undergone PEC of a plagioclase rind that we did not account for. Compared to the matrix glass, these MI are Cl-poor (~170 ppm) but very S-rich (1120 – 1170 ppm), with S concentrations that are similar to high-S basaltic MI from other fissures. Mg-thermometry of the matrix glasses give estimated eruption temperatures of 1040 – 1060 °C. More extensive analyses by Gansecki et al. (2019) indicate complicated magma mixing and temporal changes in magma diversity erupted from F17, and further exploration of the mineral and MI diversity of this unusual andesite will undoubtedly reveal addition insights about magma mixing and storage processes.

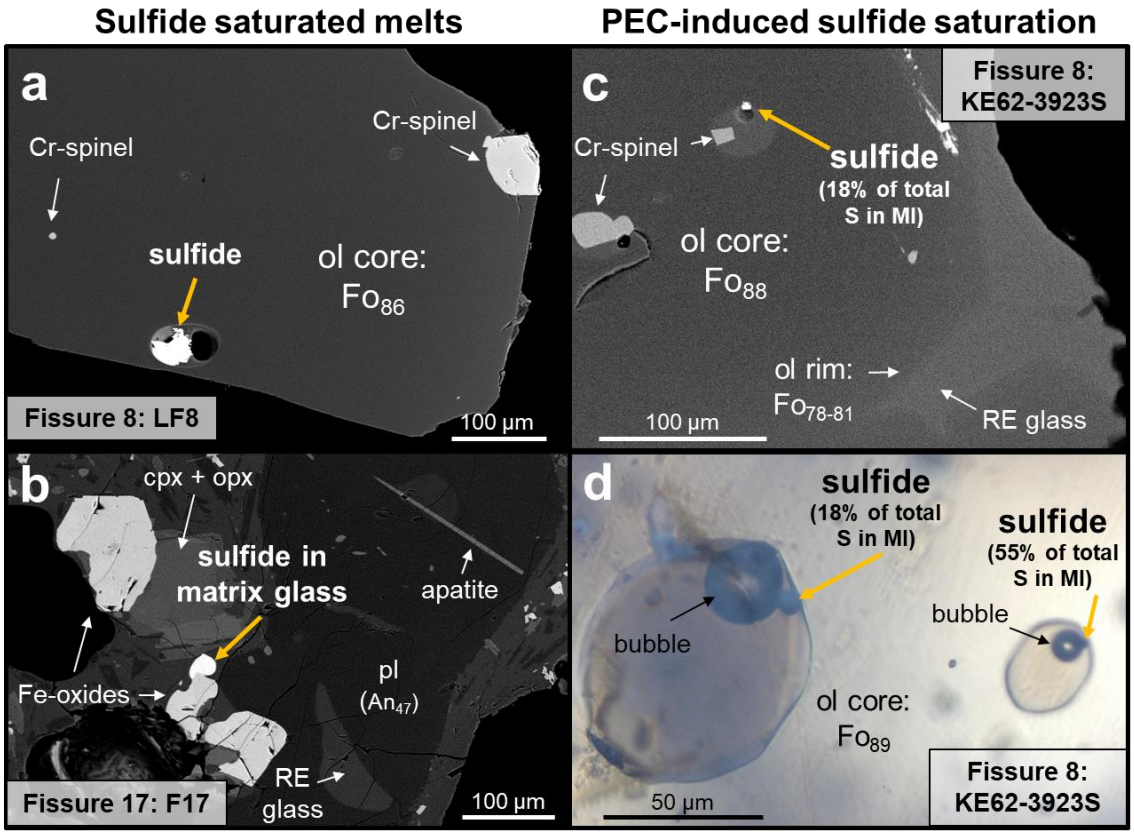

Figure 2. Examples of different sulfide occurrences in LERZ samples. *(a)* A Fo_{86} olivine from F8 sample LF8, with a large sulfide and vapor bubble inclusion, along with a small amount of melt. The large sulfide mass relative to the melt indicates the sulfide was entrapped as a separate phase in a high temperature sulfide-saturate melt. *(b)* A phenocryst and groundmass assemblage from F17, highlighting the diverse phases present including plagioclase, pyroxenes, apatite, Fe-oxides, and a sulfide. The sulfide is in contact with the groundmass glass, indicating a low temperature sulfide-saturated melt. *(c, d)* Fo_{88} and Fo_{89} olivine phenocrysts from F8 basaltic pumice containing sulfide-bearing MI. The sulfides likely formed during cooling, PEC, and Fe-loss, and can make up substantial fractions of total S in the MI. *(a), (b),* and *(c)* are backscattered electron images, and *(d)* is a microphotograph in plane-polarized light.

3.1.2 Main eruption samples from fissure 8

Our study principally focuses on erupted material from the dominant F8 vent, which produced 92 – 96 % of the eruption volume (Gansecki et al., 2019). From May 28 through August 5 (phase 3), F8 fed a fast moving open channel lava flow. The bulk magma composition become only slightly more Mg-rich through the course of the eruption (Gansecki et al., 2019), with Mg-thermometry of proximally quenched samples increasing from ~1140 °C in late May to ~1150 °C in August. Equilibrium olivine compositions correspondingly increased from Fo_{78} to Fo_{80} over the duration of the F8 phase 3 activity (Figure 3). Phenocryst mineralogy also varied during the months of F8 activity, with magma containing less plagioclase and more high-Fo olivine over time (Gansecki et al., 2019). For ease of discussion, we group samples collected within 1-week periods throughout this timespan into "early-" (May 30), "mid-" (July 14 – 20), and "late-" (August 1 – 4) phase 3.

Notable mineralogical and compositional variability in F8 samples results from the different degrees of surficial cooling particular samples experienced prior to quenching. Fissure 8 samples include rapidly quenched basaltic pumice (> 90% vesicularity) from early fountaining, water-quenched samples extracted from the near-vent lava channel and from the distal lava channel, and a lava channel overflow sample that cooled slowly (Table 1). The diverse cooling histories of samples that were sourced from a relatively constant bulk magma allows us to compare the effects of cooling during surface flow on mineralogy, MI post-entrapment processes, and redox state.

Rapidly quenched basaltic pumice erupted during early F8 high-fountaining (50 – 80 m; Neal et al. 2019) was collected on May 28 – 30 downwind of the growing cinder cone (sample KE62-3923S). Many of these highly vesicular samples have glassy rinds, likely from re-melting in the lava fountain (Figure C1). Tephra clasts were either collected directly from the air or once freshly fallen. Freshly fallen samples were cool to the touch, but many produced a crackling noise for a few minutes, likely as delicate bubble walls ruptured during further thermal contraction. A number of vesicles remain fully enclosed by thin glass rinds, so that most of the pumice clasts floated in water. The tephra is fairly crystal rich, although this is not obvious in hand sample because all phenocrysts are coated in a layer of glass. The crystal cargo is diverse, containing olivine

(Fo_{76-90}, n=43), plagioclase (An_{66-76}, n=4), clinopyroxene (Mg_{81}, n=1), and lesser orthopyroxene (Mg_{80}, n=2). Plagioclase, clinopyroxene, and orthopyroxene commonly occur as crystal clots, although individual grains of plagioclase and clinopyroxene are also relatively abundant. Chrome-spinel is present in the groundmass and is common in olivine, being particularly abundant in high-Fo olivine grains.

Matrix glasses in the basaltic pumice are relatively homogeneous, containing 11.3 – 12.5 wt% FeO^T and 5.8 – 6.5 wt% MgO (n=45). Depending on proximity to vesicles, matrix glasses are variably degassed in S (100 – 810 ppm) but have less variable Cl (100 – 170 ppm). Interstitial melt and RE channels contain higher S (360 – 920 ppm) than matrix glasses, but have the same range of Cl. In RE, S concentrations decreased towards the mouth of the melt channel. S/Cl mass ratios in matrix glasses and RE range from 0.8 – 10, depending on the degree of S degassing. Fluorine was measured for some glasses, but concentrations were close to instrument detection limits, thus we can only constrain samples to have relatively low abundances < 300 ppm. Glass temperature estimates from Mg-thermometry are 1130 – 1145 °C and equilibrium olivine compositions are Fo_{75-79}, which are consistent with measured compositions of groundmass olivine and low-Mg rims on high-Fo olivine phenocrysts (Figure 3).

Olivine compositions in F8 magmas are highly diverse (Gansecki et al., 2019; Mourey et al., submitted). In KE62-3923S basaltic pumice, olivine core compositions range from Fo_{76} to Fo_{90}. Low-Fo olivine phenocryst core compositions (Fo_{76-80}) match groundmass olivine and calculated matrix glass equilibrium-olivine compositions, indicating these phenocrysts likely formed within the carrier liquid. These low-Fo olivine grains generally occur as individual euhedral crystals and contain fewer Cr-spinel inclusions. High-Fo olivine crystals are lighter-colored (chartreuse to almost colorless in hand sample), contain abundant Cr-spinel inclusions, and commonly occur as aggregate grains that share one crystallographic orientation (Wieser et al., 2020a). High-Fo olivine grains have 5 – 20 μm thick lower Mg-rims (Fo_{76-81}) (Gansecki et al., 2019). Timescales of high-Fo olivine residence within the lower-temperature carrier liquid derived from Mg-Fe diffusion modeling of these rims is explored by Mourey et al. (2019), and give rough timescales of weeks to months of disequilibrium residence.

The proportion of high-Fo olivine increases in later erupted samples and the lowest-Fo olivine core compositions increase from ~Fo_{77} to Fo_{80} by mid-July (Gansecki et al., 2019; Mourey et al., submitted) (Figure 3). Our analyses of later erupted samples focus on primarily high-Fo olivine grains, however olivine Fo_{80-83} core compositions are present throughout all F8 samples erupted in mid- to late-phase 3. Mourey et al. (submitted) provide more a more detailed analysis of olivine compositions during the 2018 LERZ eruption. Similarly rigorous future investigations of changing plagioclase and pyroxene componentry throughout the eruption are warranted.

For all F8 samples, the S content of matrix glasses strongly depends on how proximal to the vent the melt was sampled. Compared to the basaltic pumice, which was air-quenched within seconds of extrusion and contains up to 800 – 900 ppm S in matrix glass and RE, the highest S concentration measured in F8 lava flow samples was ~600 ppm S. The littoral blast sample (KE62-3315F), which traveled > 13 km in the open lava channel, cooled to ~1115 °C (n=10) and underwent more extensive groundmass crystallization of plagioclase, clinopyroxene, and Fe-oxides (Figure C6). During the long lava channel transport, the melt extensively degassed S and littoral blast matrix glasses contain only 10 – 80 ppm S (at, or close to, analytical detection limits). Chlorine contents in residual glass of the littoral blast sample are 160 – 230 ppm Cl, which are slightly elevated compared to rapidly quenched glasses due to enrichment during groundmass crystallization with less degassing. S/Cl ratios of the S-poor littoral blast matrix glasses range from < 0.1 – 0.4. We do not observe groundmass sulfides in any F8 samples, including the rapidly quenched basaltic pumice.

3.2 Melt inclusion textures

Melt inclusions are common in high-Fo olivine (Fo_{86-90}), low-Fo olivine (Fo_{77-85}), plagioclase, and pyroxene phases throughout all F8 and F17 samples, but are rare in F9 phenocrysts. In F8 samples, we analyzed primarily olivine-hosted MI, but also measured plagioclase-, clinopyroxene-, and orthopyroxene-hosted MI. Olivine-hosted MI are usually present as isolated inclusions, however some MI occur as hourglass inclusion-pairs. The incipient formation of hourglass-inclusions was observed in a few olivine grains exhibiting rapid growth (Mourey & Shea, 2019) (Figure C2). Melt inclusions in olivine grains are generally ellipsoidal, with long-axis diameters of 40 to ≥ 100 μm.

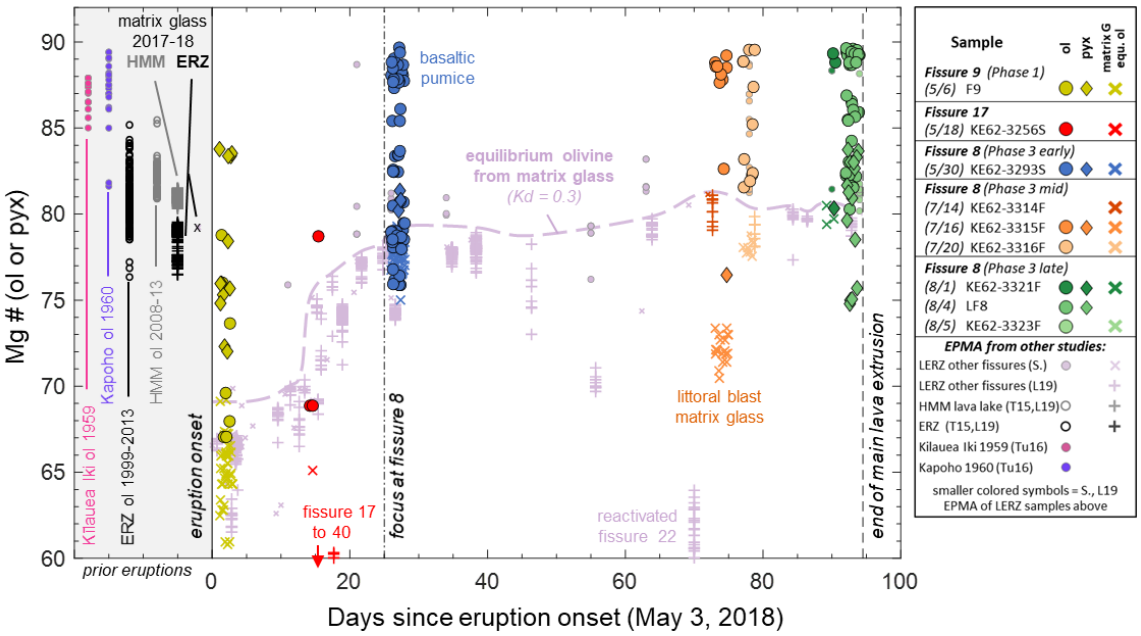

Figure 3. Time series of olivine and pyroxene phenocryst Mg# during the course of the 2018 Kīlauea LERZ eruption. Equilibrium olivine Fo was calculated from matrix glasses using a Kd of 0.3 (Roeder & Emslie, 1970). This Kd value was calibrated at pressures and temperatures relevant to Kīlauea conditions and has been shown to be appropriate for recent Kīlauea eruptions (Thornber et al., 2015). The Kd calculations assume 18% $Fe^{3+}/\Sigma Fe$ (measured by XANES) as representative of pre-eruptive F8 melt compositions, and 30% $Fe^{3+}/\Sigma Fe$ to be appropriate for the oxidized littoral blast sample. The eruption dates of samples analyzed in this study have been shifted by ±1 day for clarity. Left hand side of diagram shows the ranges of olivine phenocryst compositions and matrix glass equilibrium olivine Fo from past summit and LERZ eruptions of Kīlauea (Lee et al., 2019; Thornber et al., 2015; Tuohy et al., 2016). East Rift Zone (ERZ) samples are from Pu‘u ‘Ō‘ō and associated fissures. Halema’uma’u (HMM) samples are from the summit lava lake.

Most MI have smooth walls, but some MI, particularly in high-Fo olivine grains, have faceted morphologies. Inclusions are light brown in color and the majority contain a single vapor bubble. In more slowly cooled samples (KE62-3315F and LF8), larger MI are variably devitrified but smaller MI (less than ~40 μm diameters) remain glassy. Relative vapor bubble volumes are larger in slower cooled and higher-Fo olivine grains, constituting 1 – 8% total MI volume in Fo_{88-90} olivine grains (n=19) and 0 – 4% total MI volume Fo_{80-83} olivine grains (n=5). In the rapidly quenched basaltic pumice, some low-Fo MI in olivine grains that are in approximate equilibrium with the carrier liquid lack any vapor bubble. It is possible that some vapor bubbles were entrapped during MI formation, however it is more likely that the majority of these vapor bubbles are post-

entrapment features due to differential cooling and diffusive H^+-loss (Moore et al., 2015; Riker, 2005; Tuohy et al., 2016).

Cr-spinel are commonly included within olivine-hosted MI (Gansecki et al., 2019; Tassara et al., 2020; Thornber et al., 2015; Wieser et al., 2020b), which suggests a relationship between Cr-spinel presence and MI formation. Rapid olivine growth may create a boundary layer enrichment that promotes Cr-spinel formation, and both rapid growth and the presence of a nucleated Cr-spinel can contribute to MI formation due to the disruption of olivine crystal growth (Maaløe & Hansen, 1982). The majority of MI in high-Fo olivine grains contain small spherical sulfide blebs (2 – 10 μm diameters), which account for 0.01 – 0.1% of the MI volume (Figures 2c, d).

3.3 Melt inclusion compositions

Olivine-hosted MI from F8 magmas were analyzed in a wide range of high- and low-Fo hosts. The F8 carrier liquid had pre-eruptive temperatures of 1140 – 1150 °C and was in equilibrium with Fo_{78-80} olivine. Entrapment temperatures from Mg-thermometry (Helz & Thornber, 1987) of PEC-corrected MI in Fo_{86-90} olivine are 1220 – 1310 °C. Consequently, during residence in the colder carrier liquid, MI in high-Fo olivine grains experienced 70 – 170 °C of pre-eruptive cooling. As a result, MI underwent extensive PEC and Fe-loss and have much lower MgO and FeO^T concentrations than in equilibrium with their host crystals (Figure 4). Melt inclusions in high-Fo olivine grains from slowly cooled samples experienced even greater cooling; in the naturally cooled lava overflow sample LF8, non-PEC corrected Mg-thermometry in MI indicates temperatures of 1060 – 1120 °C, so that MI in high-Fo olivine grains experienced nearly 250 °C of cooling. In contrast, MI in low-Fo olivine grains have undergone little to no cooling and PEC. Measured MI compositions clearly follow Trend 1 described in Danyuschevsy et al. (2000), where MI in the most primitive olivine grains experienced the greatest PEC and Fe-loss (Figure 5, Figure C10). The most severely affected MI experienced 30 – 50% PEC by mass (Figure 6). Fe-contents in PEC-affected MI were restored to 11.5 wt% FeO^T based on the Kīlauea whole rock and glass FeO^T array (Figure 7b).

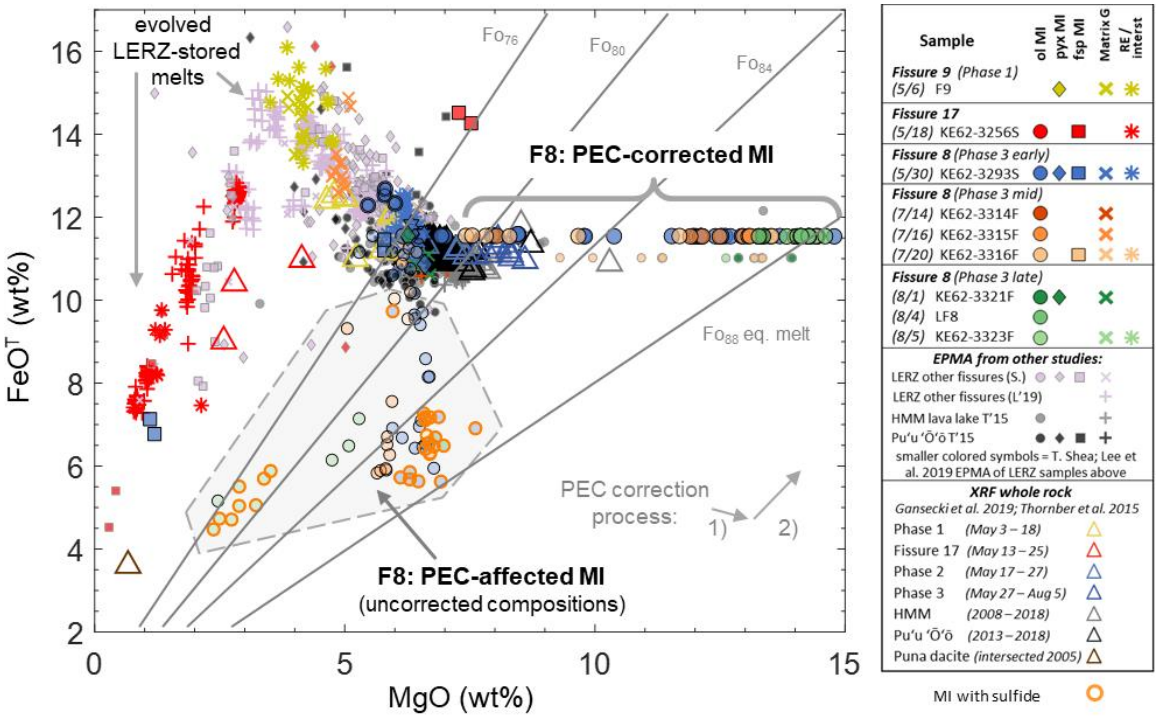

Figure 4. FeO^T and MgO in MI, matrix glasses, and whole rocks from the LERZ eruption and other Kīlauea samples. Large circles are LERZ F8 MI that have been PEC-corrected. Intermediate sized circles at lower FeO^T are PEC-uncorrected LERZ F8 MI compositions, demonstrating the extent of Fe-loss from MI. The PEC-correction process of Petrolog3 (Danyushevsky & Plechov, 2011) is schematically shown in gray arrows: *1)* FeO^T is first removed until in the MI composition is in equilibrium with the host olivine, *2)* MI compositions are then restored to the estimated initial FeO^T by adding FeO^T and MgO in proportions that maintain equilibrium with the host olivine. Circles with orange outlines are MI that contain precipitated sulfides, likely due to extensive Fe-loss. Other data sources are Thornber et al. (2015), Gansecki et al. (2019), Lee et al. (2019), and T. Shea (unpublished).

Some MI were analyzed for H_2O and CO_2 (Raman and FTIR), but not for major elements because of attrition during sample preparation. We assumed these MI experienced a degree of PEC equal to the median PEC extent as all MI in the same sample. This median PEC mass correction factor was then applied to "dilute" CO_2 contents in the MI. As discussed, S and Cl were diluted by the measured PEC correction factors, but measured H_2O contents were not because we assumed that H_2O re-equilibrates in olivine-hosted MI on timescales faster than PEC. Similarly, no PEC corrections were applied to measured $Fe^{3+}/\Sigma Fe$ or $S^{6+}/\Sigma S$ in MI, as it has been shown that redox re-equilibration also occurs rapidly in olivine-hosted MI (Gaetani et al. 2012; Bucholz et al. 2013; Hartley et al. 2017; **Chapter III)**.

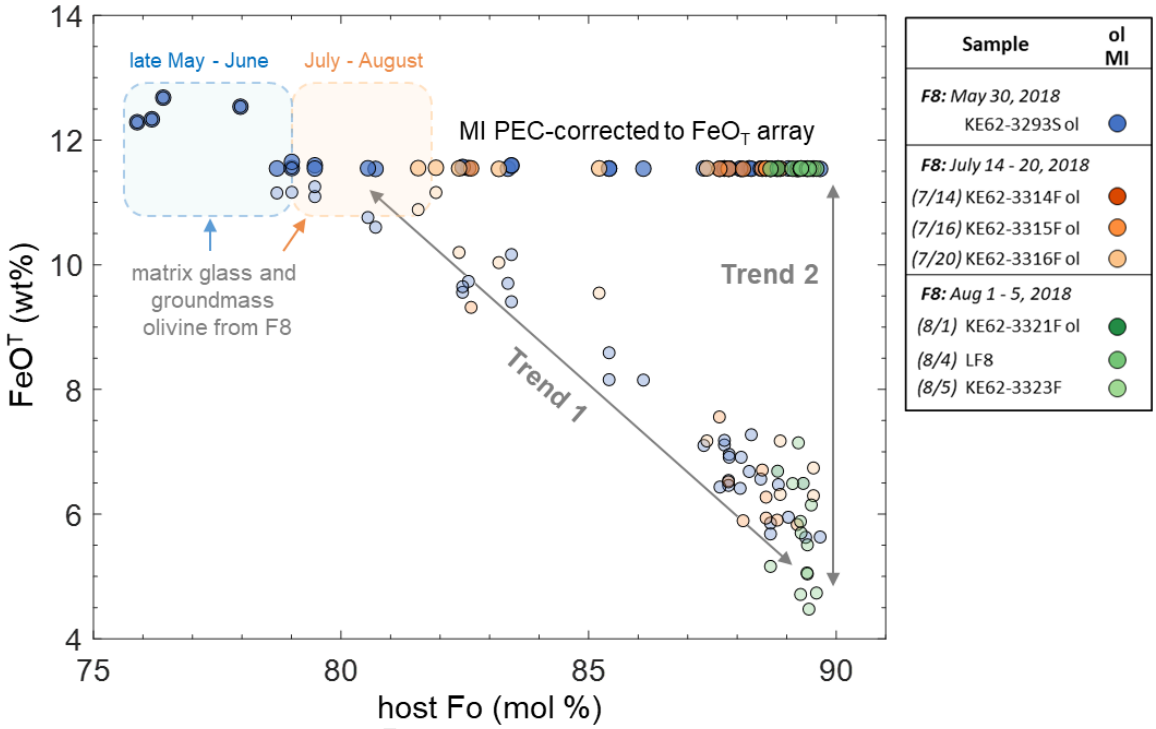

Figure 5. Melt inclusion FeO^T and host olivine Fo in LERZ F8 samples. Smaller lighter colored symbols are PEC-uncorrected FeO^T concentrations, and larger darker symbols are MI compositions that have been PEC-corrected to the Kīlauea FeO^T array (Figure 7b). Fe-loss in MI increases in higher-Fo olivine grains, consistent with the Trend 1 relation of Danyushevsky et al. (2000). Lesser variability in MI FeO^T concentrations at given host Fo-compositions (Trend 2) indicates fairly complete equilibration of MI with their hosts during PEC.

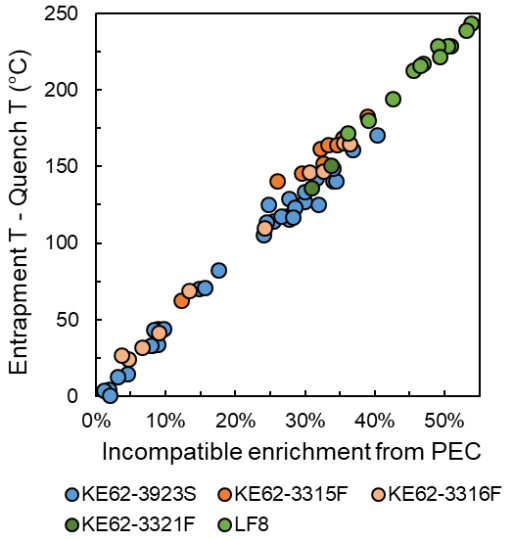

Figure 6. Relation between the degree of MI cooling (difference between entrapment temperatures [1120 – 1310°C; Figure S6] and quench temperatures [1060 – 1150°C]) and the extent of PEC in olivine-hosted MI from F8 samples. Calculations use Petrolog3 (Danyushevsky & Plechov, 2011). Entrapment temperatures are calculated from the Mg-thermometer of Helz and Thornber (1987) using PEC-corrected MgO concentrations.

PEC-corrected MI compositions from LERZ samples fall along the whole rock and matrix glass liquid line of decent for Kīlauea (Figure 7a). Melt inclusions in Fo_{84-90} olivine hosts contain up to 14.5 wt% MgO and MI in Fo_{76-83} hosts contain 5.5 – 8.5 wt% MgO. Two MI in a rare low-Ca plagioclase phenocrysts (An_{54}) from the basaltic pumice have andesitic to trachy-andesitic compositions, similar to F17 glasses, and contain 1.1 – 1.2 wt% MgO. Collectively, LERZ MI (n= 72) span an extensive compositional range that encompass nearly the full major element variability of Kīlauea subaerial and submarine glasses.

PEC-corrected Cl concentrations have relatively minor variability within all LERZ MI, ranging from 100 – 250 ppm. In contrast, S concentrations in LERZ MI are highly variable even within single samples. The highest S concentrations in LERZ MI glasses, measured in an An_{76} plagioclase-hosted inclusion and in Fo_{78} and Fo_{81} olivine-hosted inclusions from the basaltic pumice are 1320 and 1250 ppm S, respectively. Many MI have much lower S concentrations, down to 350 ppm. Most MI in high-Fo olivine grains have low S concentrations, averaging 521 ± 145 ppm S (±1 standard deviation here and throughout unless otherwise stated) with a range of 310 – 780 ppm S (n=37). The two andesitic MI in the low-Ca plagioclase (An_{54}) mentioned above contain 230 – 350 ppm S and 440 – 630 ppm Cl.

However, a critical observation for considering the range of S values is that MI hosted in high-Fo olivine grains underwent extensive PEC and Fe-loss, and many MI contain small sulfide blebs (Figures 2c, 2d, 8, 9). Similar sulfides within MI have been observed by Edmonds et al. (2013) in some olivine grains from the Halema'uma'u lava lake. Given the high S concentration of sulfides, even small sulfide inclusions can account for a substantial fraction of the total S in MI (Hartley et al., 2017). With careful sample preparation and petrography (see Methods), we documented the presence and size of the sulfide blebs in most MI in high-Fo hosts. Sulfides account for 11 – 53% of the total S in MI (average 29% ± 14%), and the average sulfide-restored S contents of MI in high-Fo olivine grains is 680 ± 237 ppm S (414 – 1204 ppm range, n=16). Notably, these sulfide-restored S concentrations in MI within high-Fo olivine grains are still lower than S concentrations of many MI in low-Fo olivine and plagioclase hosts.

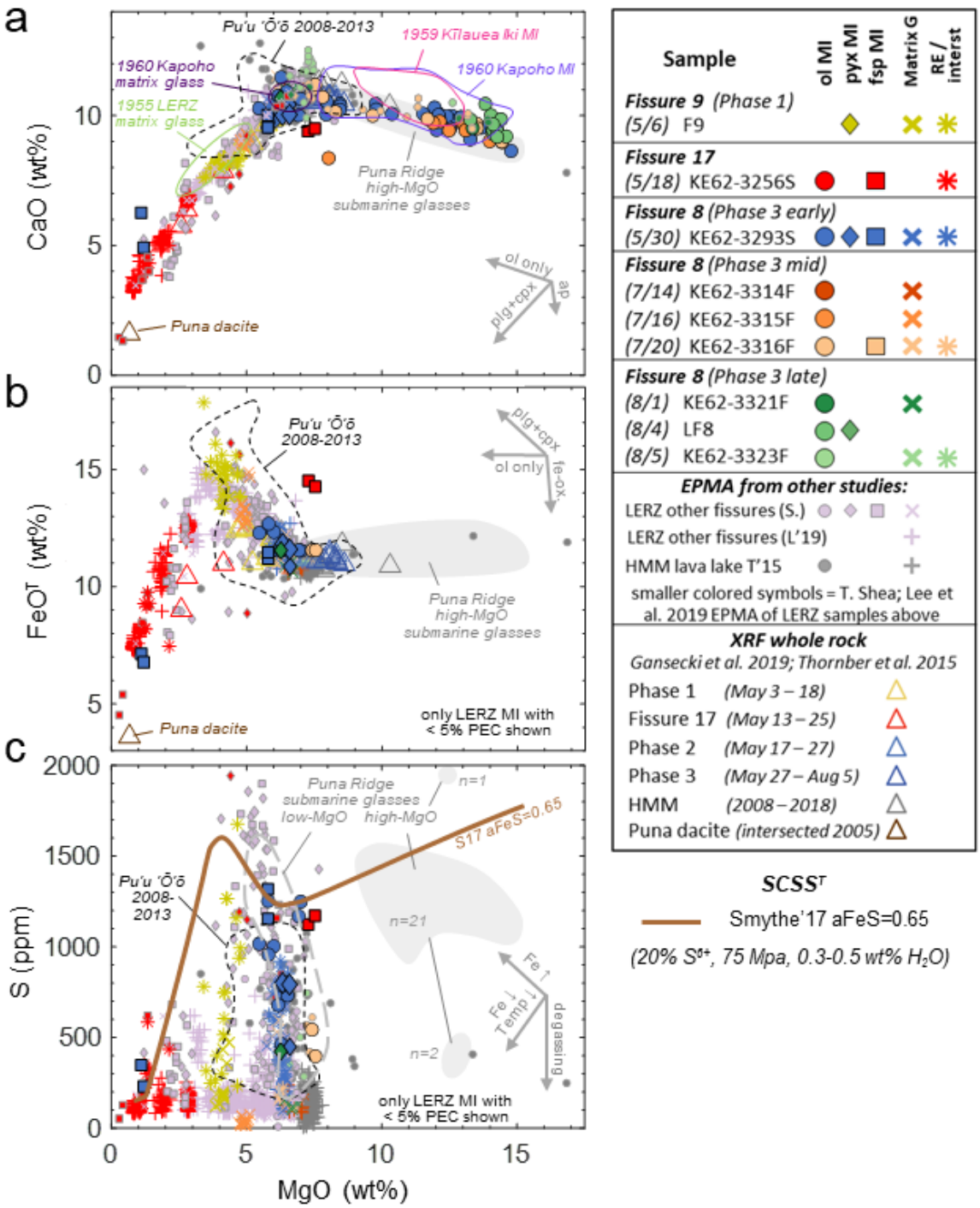

Figure 7. *(a)* MgO vs CaO, *(b)* MgO vs FeO^T, and *(c)* MgO vs S for MI, matrix glasses, and whole rocks from the LERZ eruption and other Kīlauea samples. All PEC-corrected MI compositions are shown in *(a)*, but only MI with < 5% PEC are shown in *(b)* and *(c)*. High-Mg MI have compositions similar to high-Mg submarine glasses from the Puna Ridge (Clague et al., 1995). Crystallization and degassing paths are schematically shown with gray arrows. Down-temperature $SCSS^T$ values in *(c)* are calculated from Smythe et al. (2017) (see text for details). Other data sources are Thornber et al. (2015), Tuohy et al. (2016), Gansecki et al. (2019), Lee et al. (2019), and T. Shea (unpublished).

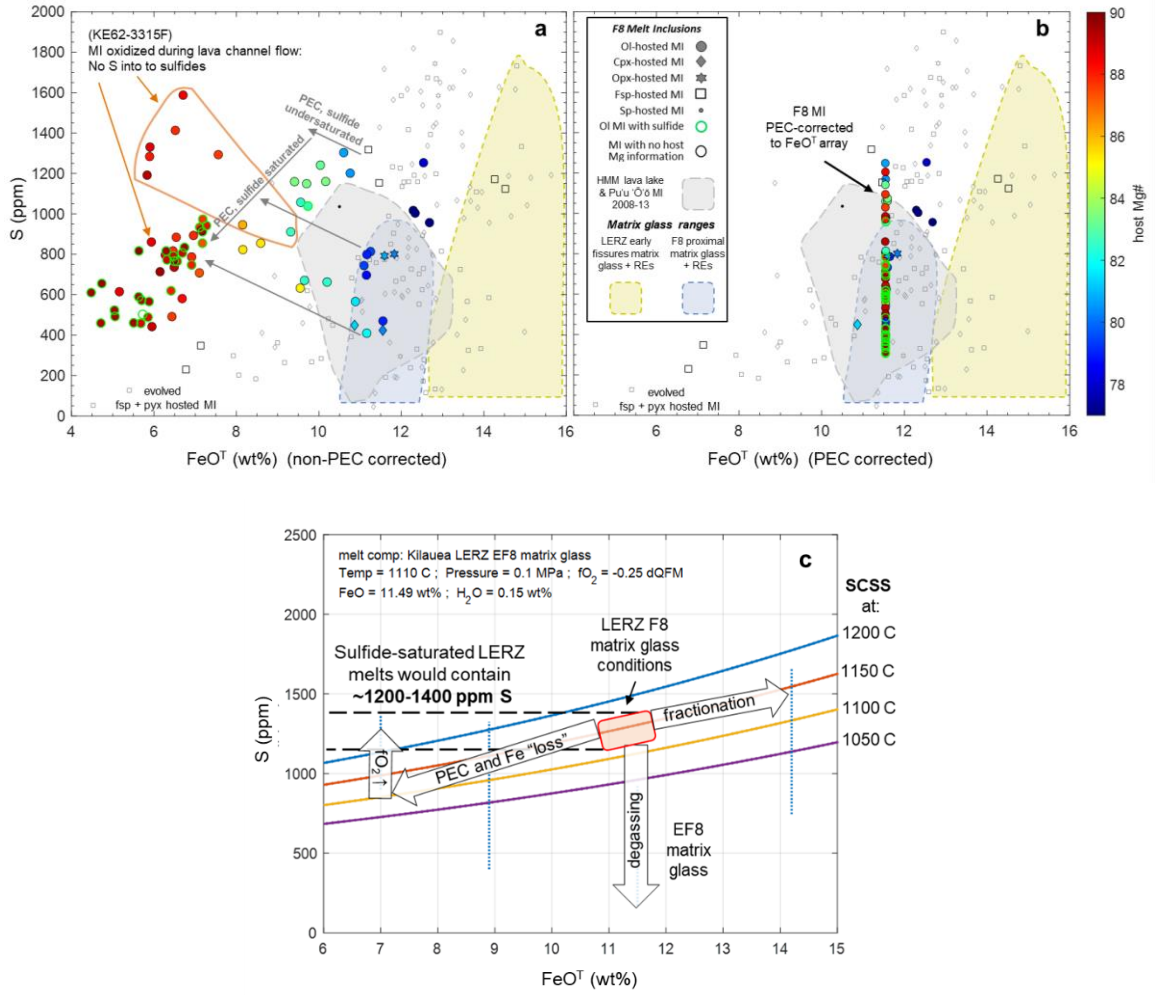

Figure 8. *(a)* Non-PEC corrected and *(b)* PEC-corrected FeO^T and S concentrations of olivine-hosted MI from LERZ phase 3 magmas erupted from F8. Symbols are colored by host Mg mole percent (for olivine and pyroxenes). Symbols with green outlines are LERZ F8 MI that contain sulfides. Compositional ranges of olivine-hosted MI and matrix glasses from Halema'uma'u and Pu'u 'Ō'ō (2008 – 2013, Thornber et al. 2015) and from phase 1 and 2 LERZ fissures are shown as colored fields. Plagioclase- and pyroxene-hosted MI from LERZ F8 phase 1 – 3 magmas (T. Shea, unpublished data) are shown as small unfilled rectangles and diamonds, respectively. *(c)* $SCSS^T$ variations with melt FeO^T and temperature, calculated using the model of Fortin et al. (2015) for Kīlauea LERZ early F8 (EF8; May 30 basaltic pumice) conditions. Processes that can affect sulfide saturation in MI are schematically illustrated.

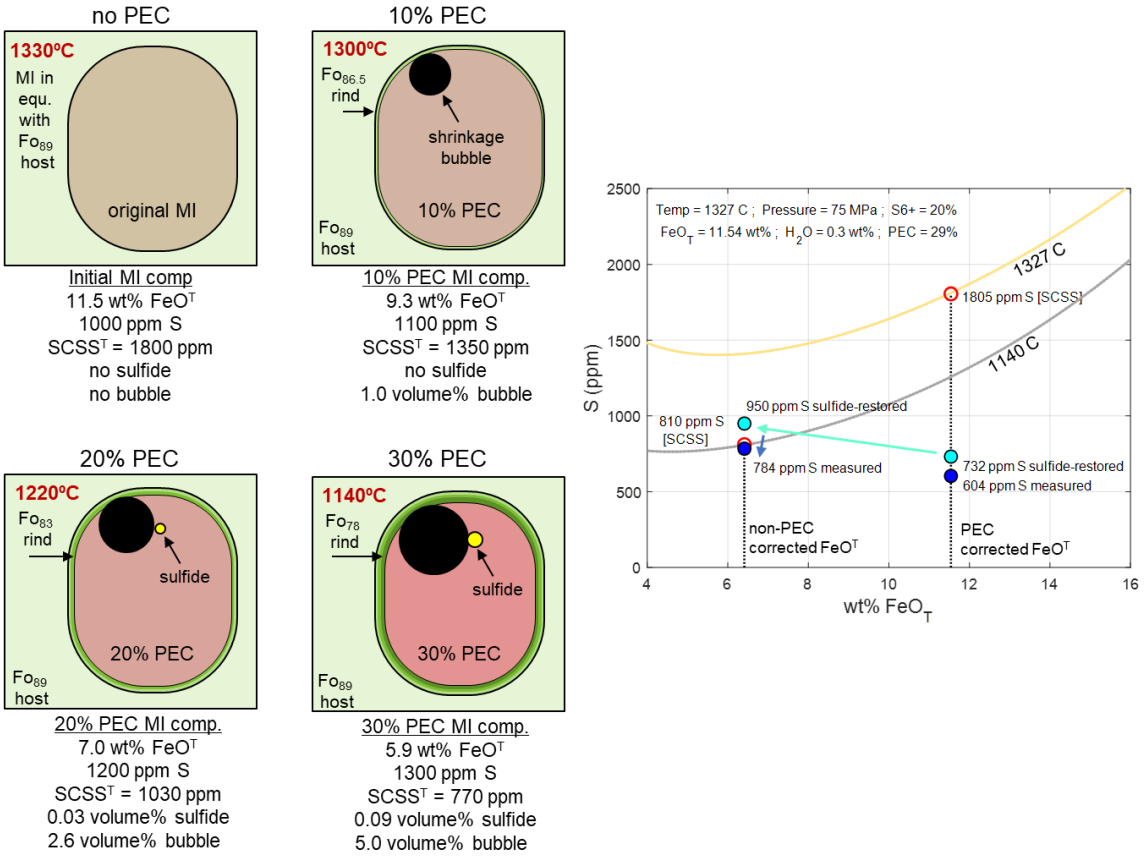

Figure 9. *(left)* Schematic progression of PEC during MI cooling, with increasing vapor bubble size and the formation of an immiscible sulfide during cooling and melt Fe-loss and S enrichment. $SCSS^T$ values at 20% $S^{6+}/\Sigma S$ from the Smythe et al. (2017) model are calculated for the changing temperature and FeO^T content of the MI during progressive PEC. *(right)* Comparison of PEC corrected and non-PEC corrected S and FeO^T concentrations in a basaltic pumice MI (Fo_{88} olivine, 29% PEC) relative to calculated $SCSS^T$ at entrapment and quenching temperatures (red open circles). Dark blue symbols are MI S concentrations as measured in the glass and light blue symbols are sulfide-restored S concentrations. During cooling, Fe-loss, and PEC-enrichment of S, the initially sulfide undersaturated MI will precipitate a sulfide.

A small subset of MI from LF8 were reheated to rehomogenize the glass, and after heating these MI did not contain sulfides. The S concentrations in glass from reheated MI in $Fo_{87\text{-}88}$ olivine grains are 160 – 630 ppm (average 430 ± 250, n=3) compared to 410 – 520 ppm (average 470 ± 37, n=7) in unheated sulfide-restored MI from the same LF8 sample. The similarity between the S concentrations in reheated and sulfide-restored MI suggests that the sulfide mass-balance corrections accurately account

for total MI S contents. Hereafter, we report sulfide-restored S concentrations of MI, unless otherwise indicated.

Sulfides are less common in MI hosted in lower-Fo olivine grains, although one MI in a Fo_{83} olivine from the basaltic pumice sample contains a sulfide that accounts for 32% of the total S in the MI. The sulfide-restored total S concentration of this MI is 1390 ppm, which is the highest observed S content among all naturally quenched MI. One lower-Fo (Fo_{83-84}) olivine from LF8 was reheated to homogenize sulfides, and contains MI with up to 1440 ppm S (600 – 1440 range, average 880 ± 480, n=3). Throughout our dataset, MI in Fo_{83-84} olivine grains have the highest measured S concentrations, although a much larger sample size will be required to confirm this relation. No sulfides were observed in plagioclase- or pyroxene-hosted MI. Finally, no sulfides are present in MI hosted in Fo_{88-89} olivine grains from the littoral blast sample (KE62-3315F) because it is more oxidized (discussed below), and these MI contain 925 ± 210 ppm S (600 – 1210 ppm range, n=8).

3.4 H_2O and CO_2 contents of LERZ glasses and melt inclusions

H_2O was measured in matrix glasses and MI from three F8 samples: basaltic pumice from early F8 fountaining (KE62-3923S), the littoral blast sample from mid-July (KE62-3315F), and the natural lava overflow sample from early August (LF8) (Figure C7). Although these samples represent a temporal record of F8 magma, H_2O contents in these matrix glasses and MI are highly affected by the different cooling rates that these sample experienced during emplacement, and diffusive H^+ loss likely overprints any temporal record of variations in pre-eruptive melt H_2O content. Melt inclusions in the basaltic pumice were rapidly quenched and therefore less affected by diffusive H^+ loss. Olivine- and orthopyroxene-hosted MI in this sample contain 0.20 – 0.31 wt% H_2O (avg. 0.27 ± 0.03, n=9) and thus represent the best estimate of pre-eruptive H_2O content of LERZ melts, at least during high fountaining events on May 28 – 30. H_2O contents in basaltic pumice matrix glasses range from 0.05 – 0.33 wt% (n=12) (Figure 10a). As with S concentrations in matrix glasses, the extent of H_2O degassing varies spatially depends on the glass proximity to vesicles, with interstitial melt and glass farther from vesicles having higher H_2O (and S) contents.

The littoral blast sample has H_2O contents of 0.07 – 0.11 wt% in matrix glass (n=3), consistent with the melt having equilibrated to 1-atm conditions during subaerial lava-channel transport to the coast (Dixon et al., 1995; Iacono-Marziano et al., 2012). Olivine-hosted MI contain 0.08 – 0.17 wt% H_2O (avg. 0.13 ± 0.03, n=7), indicating degrees of diffusive H^+ loss to equilibrate with the degassed external melt. No analyzable matrix glass remains in the more slowly cooled LF8 lava overflow sample, however olivine-hosted MI in this sample contain 0.10 – 0.27 wt% H_2O (avg. 0.21 ± 0.07, n=4). Given the slow cooling rate of this sample, these lower H_2O contents similarly suggest that the LF8 MI experienced partial diffusive H^+ loss during cooling. Consequently, the H_2O contents of MI from the littoral blast and LF8 samples only provide minimum constrains on the pre-eruptive H_2O contents of the mid- and late-phase 3 melts.

H_2O was not measured in F9 or F17 matrix glasses or MI, and it remains to be seen whether H_2O was enriched in these samples during fractionation. However, two andesitic MI in a low-Ca feldspar from the basaltic pumice have major element compositions similar to F17 melts, perhaps indicating entrainment of F17-like material. Compared to basaltic MI, these evolved MI have elevated H_2O contents of 0.31 and 0.55 wt% and also have enriched Cl of 400 – 600 ppm. If these evolved, H_2O-rich MI accurately represent F17 melt compositions, then it is possible that H_2O-enrichment, together with the increased viscosity of F17 andesitic magma, may have contributed to the more explosive character of this magma.

CO_2 concentrations were below instrument detection limit (~50 ppm) in all matrix glasses apart from one analysis of interstitial melt in a basaltic pumice sample. This glass contained 0.25 wt% H_2O and 224 ppm CO_2, which provides a minimum estimate for pre-eruptive CO_2 content in F8 melts in late May. CO_2 in MI glasses was also below detection limit in nearly all MI from F8 samples. Only two MI with detectable CO_2 are in olivine grains from basaltic pumice samples, and the MI do not contain vapor bubbles. These MI contain 0.27 wt% H_2O and 280 ppm CO_2, and 0.29 wt% H_2O and 250 ppm CO_2.

Relations between CO_2 dissolved in MI glass, MI vapor bubble volume, and extent of PEC has been observed and modeled in a number of natural samples, including from Kīlauea (Aster et al., 2016; Sides et al., 2014b; Steele-Macinnis et al., 2011; Tucker et al., 2019; Tuohy et al., 2016). Vapor bubbles form during post-entrapment processes

due to differences in the thermal contraction of olivine and of melt, as well as possible mass reduction from MI during H^+ diffusive loss. Once a bubble is formed, the highly insoluble CO_2 partitions into the vapor phase in accordance with the changing internal MI pressure. Melt inclusions in high-Fo olivine grains from F8 magmas underwent 70 – 240°C of cooling during residence in the cooler carrier liquid and post-eruptive cooling. Consequently, these MI experienced high degrees of PEC and Fe-loss (olivine-incompatible element enrichments of up to 54% in LF8 MI) and the formation of large vapor bubbles (Figure S9) that sequestered the majority of CO_2 within the MI (Figure C12). Most MI that were analyzed for volatiles were in Fo_{88-89} olivine grains, and the combined effects low initial MI entrapment pressures (see below), substantial thermal contraction, and extensive PEC contributed to large pressure decreases in MI that likely explain the below-detection limit CO_2 in MI glass. Indeed, only bubble-free MI in LERZ phenocrysts had resolvable CO_2 in MI glass. Accounting for CO_2 sequestration into a vapor bubble has been accomplished by quantifying thermal contraction and the change in CO_2 solubility from equations of state (Anderson & Brown, 1993; Riker, 2005; Tucker et al., 2019; Tuohy et al., 2016; Wallace et al., 2015), by heating and re-homogenizing MI (although irreversible H^+ loss often leads prevent full bubble re-dissolution) (Tuohy et al., 2016), or by direct measurement of CO_2 in bubbles by Raman spectroscopy (Aster et al., 2016; Moore et al., 2015).

For LERZ MI that contain vapor bubbles, we measured CO_2 densities in vapor bubbles using Raman spectroscopy. From the measured CO_2 density and observed bubble volumes, the masses of CO_2 in bubbles were added to the CO_2 concentrations in MI glasses to calculate total MI CO_2 concentrations. Ideally, both vapor bubbles and MI glass should be measured to determine total volatile content and entrapment pressures. However, in low-H_2O Hawaiian basalts, CO_2 concentrations derived from just the vapor bubble accounts for most of the CO_2 in MI (~50 to 90% of total CO_2) and can be used alone for a minimum estimate of entrapment depth (Moore et al., 2015; Tucker et al., 2019; Wallace et al., 2015). In cases where MI were measured for CO_2 in bubbles by Raman but not for H_2O and CO_2 in the glass by FTIR, we assume the residual melt contains 30 ppm CO_2 (as a conservative minimum) and contains H_2O equal to the average H_2O measured in other MI from that sample. Melt inclusion CO_2 concentrations

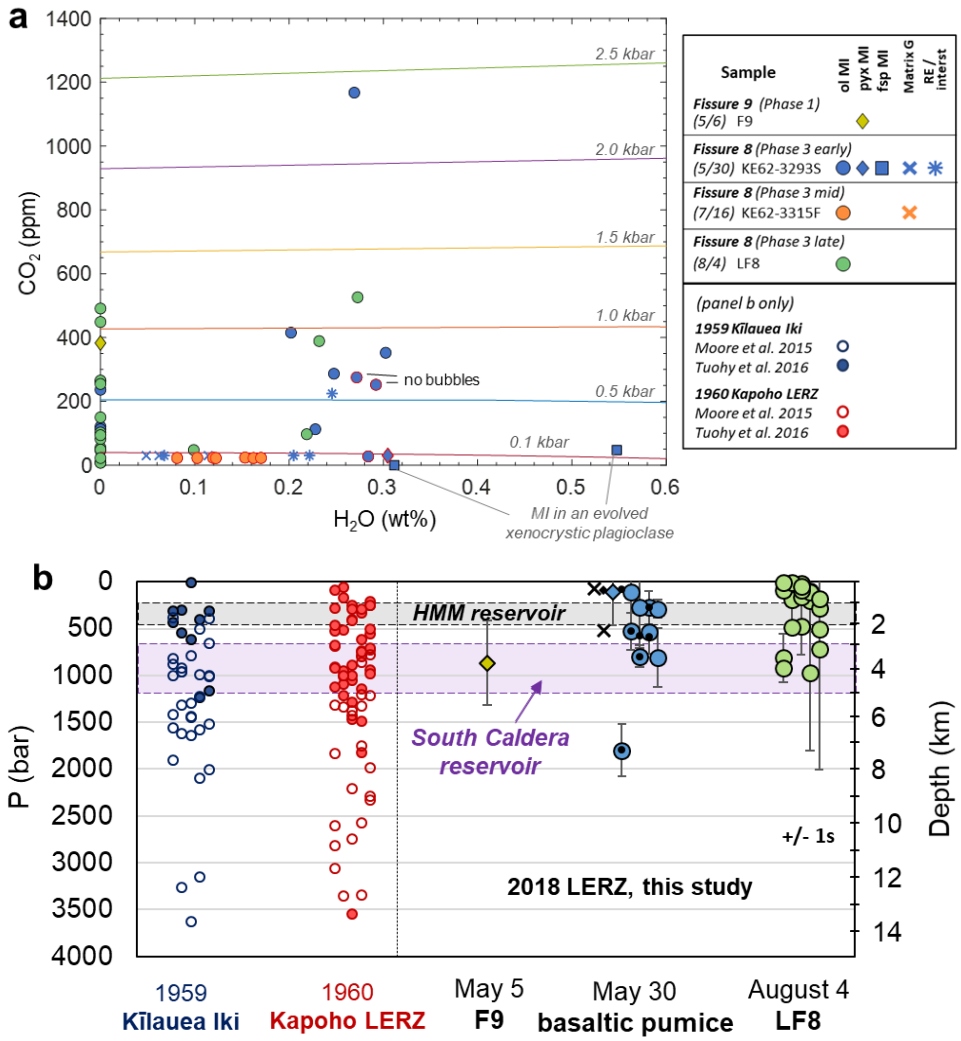

Figure 10. *(a)* H_2O-CO_2 measurements of MI and matrix glasses from LERZ samples. Symbols with black borders and measured H_2O indicate H_2O and CO_2 from Raman and FTIR, and symbols with no H_2O are Raman-only measurements. Symbols with red borders indicate CO_2 and H_2O from FTIR-only, and two bubble-free MI are indicated. Variably degassed matrix glasses analyzed by FTIR are shown as crosses and interstitial melts are shows as asterisks. Where CO_2 in glass was below FTIR detection limits, 30 ppm CO_2 was assumed. Saturation pressure isobars are calculated for the average basaltic pumice matrix glass composition at 1140 °C (Iacono-Marziano et al. 2012). *(b)* Melt inclusion entrapment pressures and corresponding depths below surface (Ryan, 1987) for LERZ samples. Saturation pressures are temperature and composition specific (Iacono-Marziano et al. 2012), causing some differences compared to the isobars in *(a)*. Only matrix glasses with resolvable CO_2, MI with Raman-measured vapor bubbles, and bubble-free MI measured by FTIR are shown. No littoral blast (KE62-3315F) samples appear in *(b)* because MI were not analyzed by Raman. Symbology for LERZ samples is the same as in *(a)* except that dots indicate FTIR measurements. *(b, left side)* Kīlauea Iki and Kapoho MI from Moore et al. (2015) and Tuohy et al. (2016), where CO_2 in bubbles was respectively determined by Raman and by equation of state. Approximate depths of the Halema'uma'u (HMM) and South Caldera reservoirs are from Poland et al. (2014).

were diluted by PEC mass correction factor, but no PEC adjustments were applied to H_2O, because we assume H_2O rapidly re-equilibrates on a timescale faster than PEC.

CO_2 bubble densities were measured in olivine-hosted MI from the basaltic pumice and the lava overflow (LF8) samples. Many vapor bubbles in both samples have very low-CO_2 densities that approached instrument detection limit (~0.02 g/cm^3). The signal to noise on these low-CO_2 measurements is therefore low, resulting in large relative uncertainties of 100% or more. However, with very small calculated CO_2 masses, these large relative uncertainties translate into relatively small absolute uncertainties in CO_2 mass. More CO_2-rich bubbles have CO_2 densities up to 0.03 g/cm^3, and PEC-corrected mass balance results in total calculated CO_2 concentrations in MI (bubble + melt) of < 50 to 530 ppm (n=30). The ranges of CO_2 concentrations in MI from the basaltic pumice and LF8 samples broadly overlap. One outlier MI within a basaltic pumice high-Fo olivine has a vapor bubble CO_2 density of 0.07 g/cm^3 and a total MI CO_2 concentration of 1170 ppm.

Small particles are present on the walls of some MI vapor bubbles. However, broad spectra Raman analysis of these presumed condensate phases did not show evidence of either carbonate or S-bearing phases. It is possible that these are halogen salts, but more complete spectroscopic analysis and mapping is needed to determine this.

3.5 Fe and S speciation and fO_2 conditions

Matrix glasses and doubly-intersected olivine-hosted MI from a variety of olivine compositions were measured by both Fe- and S-XANES following the repeated rapid scan techniques described above to detect and correct for beam damage. We expand on the LERZ Fe- and S-XANES dataset presented in **Chapter III**, which focused on basaltic pumice, littoral bomb, and KE62-3316F lava flow samples from F8. Here, we include an additional 49 Fe-XANES and 17 S-XANES analyses from other F8 samples and from more evolved glasses from F9 and F17. In total, we measured 81 matrix glasses and 43 MI by Fe-XANES and 40 matrix glasses and 31 MI by S-XANES.

As discussed in **Chapter III**, Fe-speciation in Kīlauea MI was observed to be stable during Fe-XANES analysis and no beam damage corrections were applied. However, S-XANES photo-reduction occurred rapidly in many MI. Where S-XANES

beam damage occurred, we use only the first of multiple repeated rapid scans, which had experienced the least beam damage. Beam damage was identified in 53 of 71 S-XANES analyses and was corrected using a S^{4+} to S^{6+} peak intensity conversion factor of 1.2 (**Chapter III**). Because we use only the least beam damaged spectra, the beam damage correction lead to an average increase of only 1% $S^{6+}/\Sigma S$, with two outliers in highly oxidized MI (see below) having beam damage corrections of +5% and +9% $S^{6+}/\Sigma S$.

Proximally quenched F9 and F8 matrix glasses contain 12 – 17% $Fe^{3+}/\Sigma Fe$ (n=69), corresponding to QFM -0.6 to +0.5 at measured compositions and Mg-thermometry melt temperatures using the 1-atm formulation of Kress & Carmichael (1991). LERZ matrix glasses are progressively more reduced with decreasing S content over a range of 100 – 920 ppm S measured here (Figure 11). This positive correlation between fO_2 and S concentration has been previously observed in a number of Kīlauea and Mauna Kea glasses (Brounce et al., 2017; Helz et al., 2017; Moussallam et al., 2016). Melt inclusions in proximally quenched F8 samples contain 13 – 18% $Fe^{3+}/\Sigma Fe$ (n=32), corresponding to QFM -0.7 to +0.4 (calculated with non-PEC corrected MI compositions and eruption temperatures from matrix glasses). In each sample, MI have similar Fe-speciation and calculated fO_2 as their respective carrier liquids (Figure 12).

As discussed in **Chapter III**, matrix glasses in the littoral blast sample are anomalously oxidized (20 – 34% $Fe^{3+}/\Sigma Fe$, QFM +1.0 to +2.4, n=6) compared to the full dataset, including near-contemporaneously erupted proximally quenched samples. Melt inclusions in the littoral blast sample are similarly oxidized (21 – 32% $Fe^{3+}/\Sigma Fe$, QFM +0.5 to +1.9, n=9).

Proximally quenched F9 and F8 samples contain 0 – 14% $S^{6+}/\Sigma S$ in matrix glasses (n=38), and 1 – 33% $S^{6+}/\Sigma S$ in MI (n=17). This range of measurements is broadly consistent with prior EPMA S Kα wavescan (Wallace & Carmichael, 1994) and S- and Fe-XANES studies of matrix glasses and MI from Kīlauea (Helz et al., 2017; Jugo et al., 2010; Moussallam et al., 2016) and of submarine glasses from Mauna Kea (Brounce et al., 2017) and Lō‘ihi volcanoes (Jugo et al., 2010). In contrast, MI in the oxidized littoral blast sample contain 68 – 96% $S^{6+}/\Sigma S$ (n=9). Sulfur concentrations in the degassed littoral blast matrix glass were too low for S-XANES analysis. There is no clear difference in Fe- or S-speciation between proximally quenched MI that contain sulfides

and those that do not. Sulfides are not present in any MI from the oxidized littoral blast sample.

Consistent with the observations presented in **Chapter III**, our larger suite of Kīlauea MI and matrix glasses have higher measured S^{6+} at given $Fe^{3+}/\Sigma Fe$ conditions than would be expected from the Jugo et al. (2010) relationship (Figure 13a). Brounce et al. (2017) present the only other dataset of Hawaiian glasses that have been measured by

both Fe- and S- XANES, and they report that glasses from Mauna Kea have lower S^{6+} proportions than expected from the Jugo et al. (2010) model. However, if the Brounce et al. (2017) dataset is re-calculated using Fe pre-edge centroid positions and the updated Fe-XANES calibration of Zhang et al. (2018) to be consistent with our methodology, their S^{6+} and fO_2 relations are similar to our findings (Figure 13).

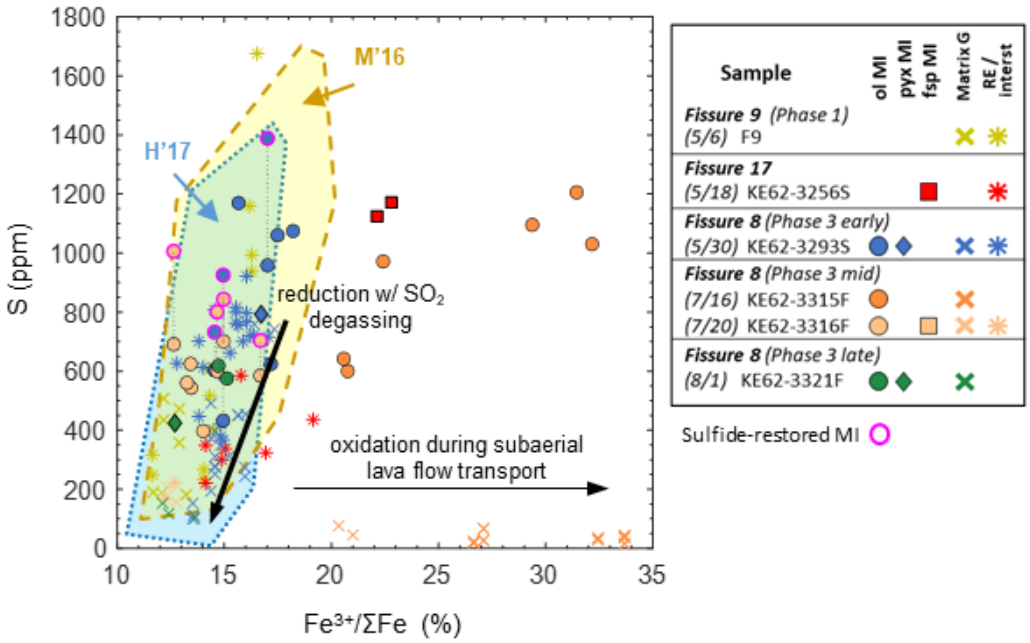

Figure 11. Sulfur concentration in MI and matrix glasses compared to XANES-measured Fe speciation. Reduction during S-loss and oxidation due to subaerial lava transport affect LERZ glasses and MI result in a large $Fe^{3+}/\Sigma Fe$ range in LERZ glasses (corresponding to QFM -1 to + 2). Sulfide-restored MI total S concentrations are indicated with purple symbol borders. Ranges of MI and matrix glass measurements from Moussallam et al. (2016) (M'16) in samples from 2008 and 2010 Halema'uma'u lava lake and 1883 summit eruption, and from Helz et al. (2017) (H'17) for 1959 Kīlauea Iki samples are shown as yellow and blue fields, respectively. Data from oM'16 and H'17 have been reprocessed using the Fe-XANES calibration of Zhang et al. (2018).

As discussed in **Chapter III**, our observed Fe- and S-speciation are in relatively close agreement with the temperature-dependent S speciation model of Nash et al. (2019) for melt quench temperatures determined from glass Mg-thermometry. However, we note that some measurements deviate from this modeled relationship, particularly in MI that have undergone large degrees of PEC and Fe-loss (Figure 13b). We speculate that S-speciation in glasses is affected by the concentrations of H_2O, Fe, and Ca in the melt, with Fe and Ca potentially stabilizing S^{2-} and S^{6+}, respectively (Klimm et al., 2012). The uncertainty in how pressure, temperature, and composition may stabilize S^{6+} in silicate glasses underscores the importance of directly measuring both S and Fe speciation.

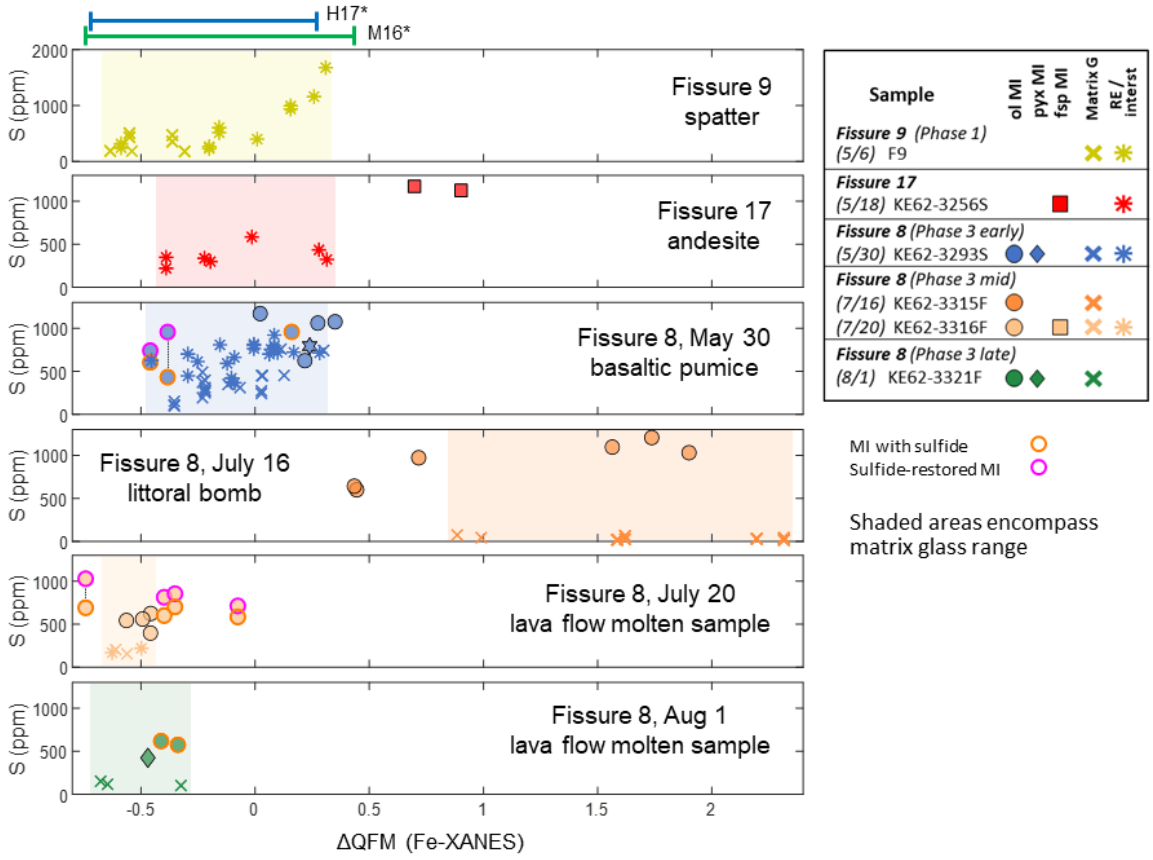

Figure 12. ΔQFM vs S for analyzed LERZ matrix glasses and MI. Within each sample, the fO_2 range of olivine-hosted MI is similar to the fO_2 range of matrix glasses (shaded regions). Lava flow samples are generally more reduced than rapidly quenched basaltic pumices. The July 16 littoral bomb matrix glasses and MI are anomalously oxidized. Sulfide-bearing and sulfide-restored MI are highlighted with orange and magenta symbol outlines. *The ΔQFM ranges of Kīlauea matrix glasses and MI measured by Moussallam et al. (2016) ("M16") and Helz et al. (2017) ("H17") are shown at top, which have been reprocessed using the Fe-XANES calibration of Zhang et al. (2018).

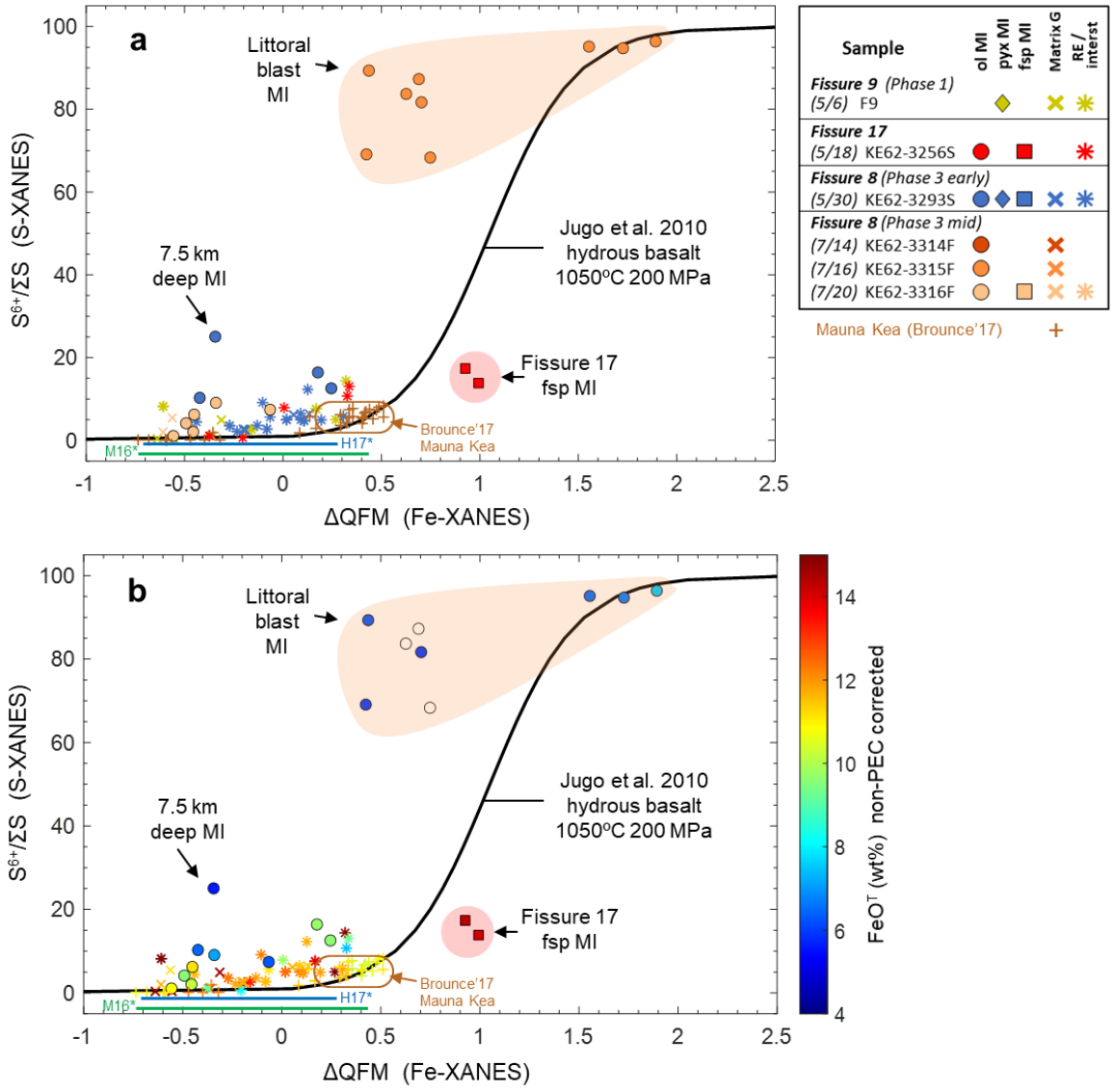

Figure 13. Redox state (Δ QFM) and S-speciation LERZ MI and matrix glasses from Fe- and S-XANES measurements. *(a)* Symbols are colored by sample unit. *(b)* Symbols are colored by non-PEC-corrected FeO^T concentrations. Glasses deviate to higher S^{6+} at a given redox state than predicted from the relationship of Jugo et al. (2010) for hydrous basalts (black curve). Uncertainties in $S^{6+}/\Sigma S$ model fits and calibration are estimated at ±2 – 5% absolute, and uncertainties in Δ QFM from $Fe^{3+}/\Sigma Fe$ centroid fits are < ±0.2 log units. Δ QFM ranges of MI and matrix glass measurements from Fe-XANES studies of Moussallam et al. (2016) (M16*) from Helz et al. (2017) (H17*) are shown in green and blue, respectively. Also shown are S- and Fe-XANES measurements of Mauna Kea submarine glasses by Brounce et al. (2017). Data from other studies have been reprocessed using Fe-XANES pre-edge centroid fits and the calibration of Zhang et al. (2018).

3.6 S-isotopes

$\delta^{34}S$ analyses were analyzed by SIMS on a subset of F8 matrix glasses and olivine- and orthopyroxene-hosted MI from basaltic pumice samples (KE62-3923S), olivine-hosted MI from the littoral blast sample (KE62-3315F), and olivine-hosted MI from the late overflow lava (LF8). Basaltic pumice matrix glasses have $\delta^{34}S$ ranging from -2.8 to +0.3‰ (n=10) across a range of 100 – 800 ppm S. Basaltic pumice MI have $\delta^{34}S$ ranging from -1.3 to +1.5‰ (n=8) across a range of 300 – 1390 ppm total S. Melt inclusions in the littoral blast and LF8 sample have respective $\delta^{34}S$ ranges of -0.7 to +0.9‰ (n=5) and -1.6 to -0.7‰ (n=4), and respective total S contents of 600 – 1100 and 390 – 640 ppm S. Overall, the upper range of $\delta^{34}S$ and S concentrations is similar to that of MORB, although we note that the $\delta^{34}S$ value of MORB is currently being debated (Labidi et al. 2012). The collective F8 suite of glasses exhibits a clear relation with total S content, with both matrix glasses and MI becoming isotopically lighter with decreasing S content. This relationship is consistent with observations at another other basaltic hotspot volcano, El Hierro in the Canary Islands (Beaudry et al., 2018). One andesitic MI in the low-Ca plagioclase from the basaltic pumice was analyzed, and is anomalously $\delta^{34}S$-heavy (+1.1‰) for its relatively low S concentration of 350 ppm.

Many MI hosted in high-Fo olivine grains contain sulfide blebs, which likely formed during PEC and Fe-loss (discussed above). The closed-system formation of sulfides within LERZ MI induces relatively minor $\delta^{34}S$ changes within the residual glass. At LERZ pre-eruptive temperatures of ~1150 ºC, fractionation between S^{2-} in the melt and FeS solid (pyrrhotite is assumed as most analogous to the precipitated sulfide blebs) causes the sulfide to be 0.5‰ heavier (Li & Liu, 2006; Taylor, 1986). At this same temperature, fractionation between S^{6+} in the melt (as SO_4) and sulfides causes the sulfide to be 3.0‰ lighter (Li & Liu, 2006; Miyoshi et al., 1984). Proximally quenched LERZ MI contain 5 – 25% $S^{6+}/\Sigma S$, so the total fractionation during sulfide exsolution would result in sulfides being between 0.3‰ heavier and 0.4‰ lighter than the melt, depending on S speciation. With sulfides accounting for total S fractions of 0.11 to 0.53 in F8 MI, closed-system fractionation would result in the melt becoming a maximum of 0.16‰ lighter or 0.21‰ heavier during sulfide formation. Consequently, the total isotopic fractionation between the relatively reduced F8 MI and precipitated sulfides is relatively

close to 0‰ at magmatic temperatures (Beaudry et al., 2018; Labidi & Cartigny, 2016; Marini et al., 2011). Any effect of sulfide precipitation is less than analytical uncertainties, so we do not apply any isotopic corrections to sulfide-bearing MI.

4. Discussion

4.1 LERZ compositional diversity

The diversity of mineral and glass compositions erupted from the 2018 LERZ fissures span nearly the entire known range of Kīlauea material. Early erupted basalts from phases 1 and 2 are long-stored magmas that had undergone substantial fractionation within the LERZ (Gansecki et al., 2019; Lee et al., 2019). These basalts are mixtures of at least two components: a high-Ti endmember and the more mafic magmas that erupted in phase 3 (Gansecki et al., 2019). The F17 andesite is a result of particularly high degrees of fractionation during prolonged LERZ storage and cooling. The F17 andesite also has evidence of variable mixing with more primitive sources during remobilization and eruption (Gansecki et al., 2019).

Hotter, more primitive lavas began erupting on May 17 – 18 (Gansecki et al., 2019) and by May 28 had focused at F8, beginning the main eruption phase (Neal et al., 2019). Melt inclusions in lavas erupted from F8 are hosted in olivine grains with core compositions ranging from $Fo_{76\text{-}90}$ (Gansecki et al., 2019; Mourey et al., submitted; this study). Melt inclusions in $Fo_{76\text{-}80}$ olivine grains that were in equilibrium with the F8 carrier liquid (1130 – 1140°C) experienced little to no PEC. These MI have compositions consistent with melt temperatures (1135 – 1145 °C) and glass compositions erupted at Puʻu ʻŌʻō since 2012 (Gansecki et al., 2019; Lee et al., 2019; Thornber et al., 2015). In late June, ~30 days after activity focused at F8, the phenocryst assemblage of F8 lavas changed from ol-cpx-pl to mostly ol-cpx only (Gansecki et al., 2019). From this time onward, the lowest Fo olivine core compositions observed were ~Fo_{80} (Gansecki et al., 2019; Mourey et al., submitted), consistent with a slight increase in melt temperature (Figure 3). Melt inclusions in $Fo_{80\text{-}82}$ olivine grains are similar to glass compositions and melt temperatures (1150 – 1160 °C) erupted from the Halemaʻumaʻu summit lava lake since 2012 (Gansecki et al., 2019; Lee et al., 2019; Rowe et al., 2015; Thornber et al., 2015).

High-Mg olivine grains (Fo_{86-90}) first appeared in phase 2 lavas on May 20 and high-Fo grains constituted a progressively increasing proportion of the phenocryst cargo throughout the eruption (Gansecki et al., 2019; Mourey et al., submitted). Melt inclusions in high-Fo olivine grains preserve compositions of more primitive Kīlauea magmas, with entrapment temperatures of 1250 – 1310°C calculated using PEC-corrected MgO concentrations and the Mg-thermometer of Helz and Thornber (1987). The high-Fo olivine grains are in clear disequilibrium with the F8 carrier liquid and MI within these primitive grains experienced 70 – 170°C of cooling during residence in the LERZ melt, causing severe PEC. PEC-corrected MI compositions in high-Fo olivine grains restore to 10 – 15 wt% MgO, which are glass compositions rarely observed in most subaerial Kīlauea magmas (Helz et al., 2015; Thornber et al., 2015). These MI are more Mg-rich than matrix glasses from Kīlauea Iki, but are similar to some MI in high-Fo hosts from that eruption (Helz et al., 2015, 2017; Sides et al., 2014b; Tuohy et al., 2016). Other LERZ eruptions more commonly contain high-Fo olivine grains with primitive MI, such as the 1960 Kapoho eruption (Tuohy et al., 2016). Further along the ERZ, some offshore submarine "turbidite sand" glasses from the Puna Ridge have high-Mg compositions with estimated eruption temperatures up to 1350 °C (Clague et al., 1995), which are comparable to the high-Fo MI analyzed here.

In a detailed study of olivine compositions, Mourey et al. (submitted) show that > Fo_{80} olivine grains likely originated in the Kīlauea summit reservoirs. High-Fo olivine grains from higher-temperature summit reservoirs seem to be preferentially entrained and erupted during LERZ eruptions compared to eruptions at the summit or upper ERZ. As postulated by Epp et al. (1983), eruption sites in the LERZ (and offshore) at low elevations can create a hydraulic potential to drain large amounts of magma from the summit reservoirs.

4.2 Volatile saturation pressures and melt inclusion entrapment depths

An important question is: what are the source depths of summit magmas tapped during LERZ eruptions? Are these magma source depths consistent with seismicity and deformation during the 2018 LERZ eruption, and with the hydraulic driving hypothesis?

Our measurements of H_2O and total CO_2 in MI allow us to address these questions by estimating MI entrapment depths.

H_2O-CO_2 vapor saturation pressures were calculated from the composition- and temperature-dependent solubility models for basalt from Iacono-Marziano et al. (2012). Kīlauea magmas are widely considered to be saturated with a CO_2-rich vapor phase throughout the crust (Anderson & Poland, 2017; Gerlach et al., 2002; Gerlach, 1986; Gerlach & Graeber, 1985), and vapor saturation pressures can therefore be used to calculate the depths of MI entrapment (Anderson & Brown, 1993). Following the approach of Tuohy et al. (2016), we estimate MI entrapment depths from volatile saturation pressures through the depth-rock density model of Ryan (1987), which accounts for changing basalt porosity through Kīlauea's upper crust. We parameterize this depth-pressure relationship for the upper 16 km of crust with a polynomial function and apply this to vapor saturation pressures:

$$D = (4.578\text{x}10^{-2} * P^3) - (0.415 * P^2) + (4.652 * P) \quad \textit{, [eq. 1]}$$

where D is the saturation depth in km, and P is the H_2O-CO_2 vapor saturation pressure in kbar.

The rapid rate of H^+ diffusivity through olivine would have caused all olivine-hosted MI to re-equilibrate with the H_2O content of the bulk LERZ carrier liquid during the ~40 km long dike transport from summit reservoirs to the LERZ. However, for low-H_2O basalts, such as at Kīlauea, vapor saturation pressures are dominantly controlled by CO_2 content, as is evident from sub-horizontal isobars in Figure 10a. Consequently, any diffusive H^+-loss from LERZ MI has little effect on calculated entrapment pressures.

Melt inclusions erupted from F8 in late May (basaltic pumice, KE62-3923S) and in early August (lava overflow, LF8) that contain vapor bubbles have vapor saturation pressures of 0.01 – 1 kbar, which correspond to entrapment depths of < 0.1 – 4.0 km beneath the surface (Figure 10b). The analyzed MI in both samples are mostly hosted in high-Fo olivine grains and the MI in both samples share similar depth distributions. These depths are similar to shallow entrapment depths of ~1 – 5 km determined by Tuohy et al. (2016) for MI in $Fo_{86\text{-}90}$ olivine grains from Kīlauea Iki and Kapoho that were calculated with bubble-restored CO_2. We also measured two MI in lower-Fo olivine grains ($Fo_{80,83}$) that did not contain vapor bubbles. FTIR-derived vapor saturation

pressures from total volatiles in the MI glass are 0.5 – 0.6 kbar, corresponding to entrapment pressures of 2.4 – 2.5 km. These bubble-free MI entrapment depths are similar to those determined for bubble-free MI from Kīlauea Iki (Fo_{86-87}) measured by Anderson and Brown (1993), which ranged from 1 – 3 km. Finally, one outlier MI from a basaltic pumice high-Fo olivine contains a high-CO_2 bubble and has a vapor saturation pressure of 1.8 kbar, corresponding to an entrapment depth of 7.3 km. Tuohy et al. (2016) also observe some MI with deep entrapment depth > 5 km from Kīlauea Iki and Kapoho eruptions, but such MI are rare. Moore et al. (2015), who determine MI CO_2 contents from Raman bubble measurements, find mostly similar entrapment depths of < 6 km for Kīlauea Iki MI, but observe a deeper entrapment range for Kapoho MI, with most entrapment depths > 7 km. Sides et al. (2014a, b) measure H_2O-CO_2 concentrations in MI from a number of summit eruptions, and find entrapment depths of < 6 km (1.5 kbar), with the majority entrapped < 4 km. Moussallam et al. (2016) also measure H_2O-CO_2 in Fo_{78-83} MI from Kīlauea eruptions of 1885 and from the Halemaʻumaʻu lava lake in 2008 – 2010, and determine entrapment depths < 3 km. However, the effect of CO_2 in vapor bubbles in these latter two datasets is unclear, and these entrapment depths are thus minima. Overall, MI in magmas sourcing the 2018 LERZ eruption as well as earlier LERZ and summit eruptions were largely entrapped at shallow depths of 1 – 5 km. These depths are consistent with the geophysically determined extents of the Halema'uma'u (1 – 2 km depths) and South Caldera reservoirs (3 – 5 km depths) (Poland et al., 2014).

4.3 Redox conditions of LERZ melts

4.3.1 Redox conditions of primitive LERZ magmas

Proximally quenched LERZ matrix glasses and MI from F9 and F8 have Fe-XANES determined oxidations states of QFM -0.7 to +0.4. This fO_2 range is similar to the estimates from Fe-XANES studies in glasses from past Kīlauea and Mauna Kea eruptions (Brounce et al., 2017; Helz et al., 2017; Moussallam et al., 2016), when those data are re-processed with the recently updated Fe-XANES calibration of Zhang et al. (2018) (Figures 11, 12, 13). Equilibria of redox-sensitive gas species (SO_2/H_2S, H_2O/H_2, CO_2/CO) measured in 1983 – 1985 from Puʻu ʻŌʻō are consistent with fO_2 conditions of approximately QFM +0.2 at erupted melt temperatures (Gerlach, 1993; Gerlach et al.,

2004). SO_2/H_2S proportions > 26 measured in F8 gases by UAS-based MultiGAS (Kelly et al., in prep) indicate similar redox conditions for F8 melts.

In F9 and F8 matrix glasses, we observe a clear reduction in melt fO_2 with S-loss (Figure 11). This relation has been seen in a number of other XANES studies of Kīlauea (Helz et al., 2017; Moussallam et al., 2016), Mauna Kea (Brounce et al., 2017), and other basaltic volcanic systems (Hartley et al., 2017; Longpré et al., 2017; Moussallam et al., 2019). This relation has been attributed to low-pressure degassing of SO_2 from relatively reduced melt (Anderson & Wright, 1972; Burgisser & Scaillet, 2007; Carmichael & Ghiorso, 1986; Hartley et al., 2017; Helz et al., 2017; Longpré et al., 2017; Moussallam et al., 2014, 2016; Sakai et al., 1982), following the reaction:

$$S^{2-}_{melt} + 3Fe_2^{[3+]}O_{3,melt} = S^{[4+]}O_{2,gas} + 6Fe^{[2+]}O_{melt} + O^{2-}_{melt} \quad . \quad \textit{[eq. 2]}$$

However, from S-XANES measurements we observe that up to 20 – 25% ΣS was present as S^{6+} in pre-eruptive LERZ melts, similar to observations from other Hawaiian glasses (Brounce et al., 2017; Jugo et al., 2010; Wallace & Carmichael, 1994). The degassing of SO_2 from sulfate in the melt results in a slight melt oxidation (Moussallam et al., 2014; Sakai et al., 1982):

$$S^{[6+]}O^{2-}_{4,melt} + 2Fe^{[2+]}O_{melt} = S^{[4+]}O_{2,gas} + Fe_2^{[3+]}O_{3,melt} + O^{2-}_{melt} \quad . \quad \textit{[eq. 3]}$$

Because Kīlauea melts contain mostly S^{2-}, and because the reduction caused by S^{2-} degassing as SO_2 is much greater than the oxidation caused by S^{6+} degassing as SO_2, the overall effect of S degassing from Kīlauea melts is melt reduction, consistent with our Fe-XANES observations. Extensive S degassing of Kīlauea lavas has been proposed to explain the low fO_2 estimates from co-existing Cr-spinel and glass equilibrium in Pu‘u ‘Ō‘ō lava flow samples (approximately QFM -1) compared to measured gases and proximally quenched glasses (Gerlach et al., 2004; Roeder et al., 2003).

Evidence for rapid redox equilibration of olivine-hosted MI is present throughout our dataset. The most extreme MI re-equilibration is present in olivine phenocrysts from the littoral blast sample. As discussed in **Chapter III**, matrix glass and olivine-hosted MI in this sample have redox states of QFM +0.4 to +2.3. These matrix glasses and MI are oxidized to up to +2 log units compared to near-contemporaneously erupted (± 4 days) proximally quenched samples (Figures 11,12). The compositions of F8 melts were relatively stable throughout the entire 3-month eruption, including during the period that

the littoral blast sample formed (Gansecki et al., 2019; Lee et al., 2019). Rather than an extreme, short-lived change in melt composition, we conclude that the littoral blast matrix glasses were oxidized by atmospheric interaction during > 13 km of transport in the F8 lava flow, of which ~9.5 km was in an open lava channel (**Chapter III**). Olivine-hosted MI in this sample rapidly equilibrated with the oxidized external melt over the hours to days long transport in the lava flow (**Chapter III**). H_2O in Kīlauea MI is far too low for H^+-diffusive loss from MI during lava channel transport to account for the scale of oxidation of the littoral blast sample (Danyushevsky et al., 2002) (Figure C7, C8). However, this rapid timescale of redox equilibration in olivine-hosted MI is consistent with metal-vacancy diffusion modeling, which is the presumed mechanism of redox equilibration (Bucholz et al., 2013; Gaetani et al., 2012). Rapid timescales of redox equilibration are also consistent with experimental atmospheric oxidation of olivine crystals, which occurs within hours at temperatures of 900 – 1200 °C (Kądziołka-Gaweł et al., 2019; Knafelc et al., 2019; Kohlstedt et al., 1976).

In other LERZ samples, we find evidence for rapid equilibration of olivine-hosted MI to more reduced conditions. Samples were extracted from the lava channel at different distances down-stream of their extrusion point at F8, and prolonged SO_2 degassing from the lava channel led to different degrees of melt reduction. In all F8 lava flow samples, olivine-hosted MI have fO_2 conditions that overlap their respective ranges of matrix glasses (Figure 12), indicating that MI rapidly equilibrated to the external melt conditions. In comparison to rapidly quenched basaltic pumice, most F8 lava flow samples are more reduced, indicating that the melts were reduced by S degassing rather than oxidized by atmospheric interaction, as in the littoral blast sample. Similarly, Hartley et al. (2017) find that olivine-hosted MI in lava flows from the 1783 Laki eruption in Iceland rapidly equilibrated to reduced external melts following S degassing from insulated lava flows. We therefore take the highest fO_2 conditions of ~QFM +0.3 to +0.4 in MI from the rapidly quenched basaltic pumice to be the most representative of the pre-eruptive LERZ magma.

Rapid redox re-equilibration of olivine-hosted MI means that the preservation of primitive melt redox states will be extremely unlikely unless primitive melts *1)* erupt without mixing with other magmas, *2)* ascend rapidly (minimize redox changes from

prolonged degassing), and *3)* are quenched rapidly (minimize post-eruptive re-equilibration). As with LERZ magmas, most other Kīlauea eruptions containing high-Fo olivine grains have been hybridized with more evolved melts (e.g., Kīlauea Iki, Kapoho; Sides et al. 2014a; Tuohy et al. 2016; Helz et al. 2017; Wieser et al. 2019), and MI in these high-Fo olivine grains would have redox-equilibrated with hybridized carrier liquids and are thus are unlikely to retain redox signatures from the time of MI entrapment. High-temperature carrier liquids, such as the high-Mg submarine glass turbidites analyzed by Clague et al. (1995) hold a potential to contain primitive materials that did not undergo substantial mixing or degassing, and thus may provide the most direct insights into the oxidation state of primitive Kīlauea melts. Additionally, Helz et al. (2017) report early erupted material from Kīlauea Iki with high-Mg matrix glasses (Mg-thermometry temperatures of 1180 – 1220 ºC) and euhedral olivine with rims of Fo_{87-88}, which may represent relatively unmixed high-temperature magmas. Olivine-hosted MI in these samples contain up to 1200 – 1400 ppm S and have Fe-XANES measured fO_2 up to QFM +0.4, which closely matches our estimate of the 2018 LERZ pre-eruptive melt redox state. Additionally, Gerlach (1993) found that both deeply source CO_2-dominated summit gases and shallowly sourced Pu‘u ‘Ō‘ō gases have identical redox states of QFM +0.2, which is very similar to our measurements of LERZ glasses. These similarities suggest that limited redox evolution occurs during the high-temperature evolution of Kīlauea summit magmas.

The rapidity of redox re-equilibration in olivine-hosted MI introduces the question of whether olivine-hosted MI can retain any relationship between composition and fO_2. We observe a clear inverse relationship between fO_2 and S concentrations in F8 matrix glasses, but not in olivine-hosted MI, presumably because MI are closed systems to S but open systems with respect to electrons or oxygen. However, a relation between S and XANES-determined fO_2 has been observed in olivine-hosted MI from past Kīlauea eruptions by Moussallam et al. (2016) and Helz et al. (2017). Given the speed of redox re-equilibration, preserving a relationship in MI between fO_2 and S would require that MI were entrapped from variably S degassed and variably reduced melts and erupted very shortly (< hours) thereafter, so that there was not sufficient time for redox re-equilibration to occur. In 2018 LERZ magma, high-Fo olivine grains were entrained from within the

summit reservoirs (Mourey et al., submitted) and resided in a hybridized melt for the 40 km transport to the LERZ eruption site, providing ample time for redox homogenization of olivine-hosted MI.

4.3.2 Redox conditions of evolved LERZ magmas

Our data also provide information on the down-temperature redox evolution of Kīlauea magmas. Evolved material erupted during phase 1 of the LERZ eruption provides an opportunity to address changes occurring during magmatic differentiation. We did not analyze this material extensively, but present some initial observations here.

During cotectic pl-cpx crystallization, modeling of the closed-system crystallization of Kīlauea melts suggests that $Fe^{3+}/\Sigma Fe$ increases substantially (Wieser et al., 2020b). However, we observe that melts from both F9 and early F8 basaltic pumice, where clinopyroxene and plagioclase were on the liquidus, have similar redox states as more primitive melts from Kīlauea Iki and other summit eruptions (Helz et al., 2017; Moussallam et al., 2016) (Figure 12). Measurements of interstitial glass from F17 andesite have similar $Fe^{3+}/\Sigma Fe$ proportions to that of LERZ basalts. In this case, Fe-oxides are quite abundant in the groundmass, which likely buffers any Fe^{3+} increase during crystallization of olivine and pyroxene. However, two doubly-intersected plagioclase-hosted basaltic MI from F17 are significantly more oxidized (22 – 23% $Fe^{3+}/\Sigma Fe$, QFM +1.1). The large difference in oxidation state between these MI and the F17 groundmass indicates a lack of MI re-equilibration, suggesting that the timescales of redox equilibration in plagioclase-hosted MI are much slower than in olivine-hosted MI. The incorporation of dominantly Fe^{3+} into plagioclase means that unbuffered PEC within plagioclase-hosted MI should cause a decrease in $Fe^{3+}/\Sigma Fe$, whereas we observe the opposite.

The high FeO^T and increased oxidation state of these basaltic plagioclase-hosted MI from F17 causes the SCSS of the MI to increase from the F17 groundmass $SCSS^T$ value of 225 ppm S at QFM +0.2, to > 2750 ppm S in the more oxidized and Fe-enriched (14.5 wt% FeO^T) MI glass, consistent with the MI containing > 1000 ppm S. In contrast to the overall suite of LERZ glasses, these F17 MI have lower $S^{6+}/\Sigma S$ for their fO_2 conditions and F17 temperatures than predicted by either the Jugo et al. (2010) model or

the Nash et al. (2019) thermal model (Figure 13). Further work is warranted on early phase 1 and F17 material to more completely determine the down-temperature redox evolution of Kīlauea magmas, as well as open or closed system processes that may affect redox state within plagioclase-hosted MI.

4.4 Sulfur variability and sulfide saturation LERZ magmas and melt inclusions

4.4.1 Pre-eruptive sulfur concentration of fissure 8 melts

As a consequence of pre-eruptive melt diversity, post-entrapment MI modification, and degassing during ascent and emplacement, LERZ MI and matrix glasses span a wide range of S contents. Constraints on pre-eruptive S content come from MI in equilibrium with matrix glass and from matrix glass regions that have been insulated from degassing (interstitial melts and RE channels). Re-entrant melt channels in the rapidly quenched basaltic pumice have S concentrations that range from 370 – 420 ppm S in areas adjacent to vesicles at RE mouths to 760 – 920 ppm S in RE interiors. Interstitial melts in the basaltic pumice contain 600 – 810 ppm S, compared to matrix glass near vesicles that have degassed to as low as 100 – 200 ppm S. However, it is possible that interstitial melts and even RE interiors had partially degassed during ascent, and RE interiors thereby provide minimum estimates of pre-eruptive S concentrations.

Melt inclusions in minerals that likely formed within the F8 carrier liquid (Fo_{76-80} olivine, plagioclase, clinopyroxene, orthopyroxene) provide upper estimates for S concentrations of the pre-eruptive LERZ melts. In basaltic pumice samples from late May and in a lava flow sample from mid-July, these types of cognate minerals host MI containing 400 – 1390 ppm S (avg. 900 ± 280, n=32). However, a number of these inclusions are in thin sections or bulk grain mounts, and therefore it is uncertain whether these MI were fully sealed inclusions or are sectioned RE channels, which might have partially degassed during eruption. To avoid this uncertainty, we focus on a set of 13 MI in low-Fo olivine and plagioclase hosts, principally from the basaltic pumice sample, which were individually intersected to ensure that they were fully enclosed inclusions. These MI generally do not contain sulfides and have a higher average S concentration of 1110 ± 110 ppm, which we take to be the best approximation of the pre-eruptive F8 melts.

The S/Cl mass ratios of these same MI average 7.0 ± 1.6, which is higher than the average S/Cl ratio of 3.2 ± 1.7 (n=45) in partially degassed basaltic pumice matrix glasses. This indicates that S degasses preferential to Cl during ascent, consistent with past observations of Kīlauea melts (Edmonds et al., 2013; Rowe et al., 2015). If the Cl contents of basaltic pumice matrix glasses are scaled by the average S/Cl ratio from cognate MI, the estimated undegassed S concentrations of these glasses range from 800 – 1200 ppm, consistent with the range of S in RE interiors and high-S MI (Figure C9). In the littoral bomb sample, which traveled ~13 km in the subaerial lava channel, matrix glasses have fully degassed S (0 – 80 ppm S remaining) but have elevated Cl compared to proximally quenched samples (averages of 200 and 140 ppm Cl, respectively), resulting in matrix glass S/Cl of 0.2 ± 0.1 (n=20). Chlorine degassing was observed in gas measurements from F8 fountains and lava flows (T. Nadeau, personal communication), but relatively high Cl-solubility and enrichment by groundmass crystallization during lava flow cooling led to an overall increase in down-flow Cl concentrations.

4.4.2 Sulfide saturation in LERZ melts

The S contents of MI from the 2018 LERZ eruption and from past Kīlauea eruptions are highly variable. As discussed, the melts feeding the bulk of the F8 lava flows are estimated to have contained ~1110 ppm S, whereas MI in high-Fo olivine grains contain 310 – 1200 ppm S in their glasses. Melt inclusions and interstitial glasses in evolved basalts from phase 1 fissures contain up to 2000 ppm S (this study; T. Shea, unpublished data), which is elevated above estimated S concentrations of primary Kīlauea melts (1390 – 1600 ppm; Clague et al. 1995; Sides et al. 2014b; Rowe et al. 2015). Here we discuss the roles of sulfide saturation, fractional crystallization, and degassing in producing the wide range of S observed in Kīlauea samples.

Sulfur content at sulfide saturation (SCSS) is the amount of S that can dissolve in a melt before exsolving an immiscible sulfide phase. SCSS is dependent on melt temperature, pressure, composition (principally FeO^T), oxygen fugacity, sulfur fugacity, and composition of the sulfide phase (Fortin et al., 2015; Jugo et al., 2010; Smythe et al., 2017; Wallace & Carmichael, 1992). We calculate the expected down-temperature variation of SCSS for Kīlauea primary melts based on matrix and submarine glass

compositions and temperatures across the full range of Kīlauea compositions, from dacitic glasses of F17 to high-Mg submarine glasses of the Puna Ridge (0.8 – 15 wt% MgO; 1030 – 1320 °C) (Clague et al. 1995; Lee et al. 2019, this study). Representative glass compositions that align with the overall Kīlauea glass and whole rock MgO and FeO^T arrays (Figure 7b) were chosen for our SCSS calculations. A number of temperature-, pressure-, and compositional-dependent models exist to calculate SCSS (e.g., Wallace and Carmichael 1992; Li and Ripley 2009; Fortin et al. 2015). We used the SCSS formulation of Smythe et al. (2017), which includes a dependence on sulfide composition. Wieser et al. (2020b) demonstrate that high temperature sulfides at Kīlauea contain substantial Cu and Ni, with Fe/(Fe+Cu+Ni) ≈ 0.65 (aFeS = 0.65). We follow their approach and calculate SCSS values assuming this sulfide composition. For simplicity we maintain this sulfide composition for all temperatures, although there is evidence that sulfide composition may change significantly in low temperature Kīlauea melts (Greaney et al., 2017; Stone & Fleet, 1991). H_2O contents of the melt were assumed to be 0.5 wt% H_2O for melt temperatures > 1140 °C and 0.3 wt% H_2O for temperatures ≤ 1140 °C, consistent with measurements of MI from Halema'uma'u and Kīlauea Iki (Edmonds et al., 2013; Sides et al., 2014b), submarine glasses from the Puna Ridge (Clague et al., 1995), and F8 matrix glasses studied here. Pressure was kept constant at 0.75 kbar (75 MPa; ~3.3 km depth) to approximate conditions relevant to LERZ magma storage at the summit and along the ERZ. The SCSS model of Smythe et al. (2017) assumes only S^{2-} in the melt (hereafter referred to as $SCSS^{2-}$), however Jugo et al. (2010) demonstrate that S^{6+} species are an order of magnitude more soluble in silicate melts than S^{2-} species, so that SCSS is exponentially dependent on the $S^{6+}/\Sigma S$ proportion in the melt. We account for this S speciation dependence by scaling the $SCSS^{2-}$ values calculated from the Smythe et al. (2017) model by the exponential relation from Jugo et al. (2010) (Longpré et al., 2017; Wieser et al., 2020b). Following Wieser et al. (2020b), we adopt the terminology of this mixed S^{2-} and S^{6+} sulfur solubility as the total SCSS ($SCSS^T$). As discussed, Kīlauea glasses have higher $S^{6+}/\Sigma S$ proportions at their Fe-XANES determined fO_2 conditions than predicted by the model of Jugo et al. (2010). To account for this discrepancy, we vary the fO_2 condition used in the Jugo et al. (2010) scaling term to match our observed $S^{6+}/\Sigma S$ proportions. We measure ~10 – 30% $S^{6+}/\Sigma S$ in proximally quenched F8 MI and

use assume a constant 20% $S^{6+}/\Sigma S$ for $SCSS^T$ calculations. Modeling $SCSS^T$ with a sulfide composition of aFeS = 0.65 decreases the $SCSS^T$ by 35% compared to aFeS = 1, and the inclusion of 20% $S^{6+}/\Sigma S$ increases the $SCSS^T$ by 25% compared to $SCSS^{2-}$ calculations.

The resulting down-temperature $SCSS^T$ model reproduces the upper ranges of observed S concentrations in Kīlauea melts fairly well (Figure 7c). At high-MgO, $SCSS^T$ gradually decreases with decreasing melt temperature. Melt fractionation is dominated by olivine crystallization until ~7 – 8 wt% MgO (1150 – 1175 °C) (Thornber et al., 2015). At temperatures below this, clinopyroxene and plagioclase join the crystallizing assemblage and the FeO^T content of the melt increases from ~11.5 wt% to 15 wt% over a relatively narrow change of temperature. The strong dependence of S solubility on FeO^T leads to a local maximum in $SCSS^T$ in melt compositions with 3.5 – 5.5 wt% MgO (1080 – 1125 °C). Many phase 1 evolved basalts have this high-FeO^T composition (Gansecki et al., 2019), which is consistent with the elevated S concentrations up to 2000 ppm observed in phase 1 MI and interstitial melts. We note that the composition of sulfides may become variable at these lower temperatures (Greaney et al., 2017; Stone & Fleet, 1991), and the fO_2 of these melts may increase due to the fractionating assemblage prior to the formation of Fe-oxides (see discussion of oxidized F17 basaltic MI, above). With further decreasing temperatures, Fe-oxides begin crystallizing and strongly deplete melt FeO^T. The combination of decreasing melt temperature and FeO^T results in the steep decrease in $SCSS^T$ in melts with < 3 wt% MgO.

S degassing from Kīlauea melts is expected to be minimal at depths greater than a few 100 m (see discussion below). As evidence of the high solubility of S in Kīlauea melts, even during dike ascent to the surface, just one day prior to the onset of the LERZ eruption, no anomalous SO_2 or H_2S was detected in the area (Clor et al., 2018; Kern et al., 2020). Consequently, S should remain largely dissolved in melt during Kīlauea magma storage. During cooling and crystallization, S contents should behave incompatibly, increasing until $SCSS^T$ is reached (Wieser et al., 2020b). Indeed, sulfides are observed as inclusions within silicate minerals and in the groundmass glasses of low-temperature phase 1 basalts (including the F9 sample studied here) and F17 andesite (Gansecki et al., 2019).

Sulfides have also been observed in a number of higher temperature Kīlauea melts (~6 – 14 wt% MgO, ~1130 – 1300 °C), occurring as inclusions in silicate minerals and within groundmass glasses from Kīlauea Iki, Mauna Ulu, the 1955 and 1977 eruptions of Kīlauea, and from some Puna Ridge submarine glasses (Clague et al., 1995; Desborough et al., 1968; Helz et al., 2017; Helz & Wright, 1992; Moore et al., 1980; Wieser et al., 2020b). We observe that some high-Fo olivine grains from F8 contain large sulfide inclusions with co-trapped minor melt and vapor bubbles (Figure 2a). Similar textures have been observed in Mauna Ulu olivine grains (Wieser et al., 2020b). The sulfide mass relative to the small mass of co-trapped melt indicates that these sulfides must have been included as a separate immiscible melt phase (Wieser et al., 2020b). These types of sulfide-bearing inclusions generally occur as stringers of small inclusions throughout the grain, indicating olivine crystallization in the presence of abundant sulfide globules (Figure C1). Olivine grains with these types of inclusion have compositions ≥ Fo_{86} indicating olivine crystallization in sulfide-saturated melts at ≥ 1260 °C. These high temperature melts would have $SCSS^T$ values of > 1500 ppm S (at 20% $S^{6+}/\Sigma S$), which is similar to some estimates of 1390 – 1600 ppm S in primary Kīlauea melts (Clague et al. 1995; Sides et al. 2014b; Rowe et al. 2015). As discussed by Wieser et al. (2020b), given the high S content of primary Kīlauea melts, most magmas derived from closed-system cooling should become sulfide saturated upon reaching ~10 – 14 wt% MgO (~1215 – 1300 °C).

However, despite LERZ F8 melts containing ~6 – 7 wt% MgO and occurring in a local trough of the down-temperature $SCSS^T$ trend (Figure 7c), no sulfides are observed in F8 matrix glasses (Gansecki et al., 2019; P. Wieser, personal communication; this study). The possibility exists that the lack of groundmass sulfides is due to sulfide breakdown during magma ascent and S degassing, as was observed for Mauna Ulu magmas (Wieser et al., 2020b). However, we do not observe sulfide inclusions in silicate phases that are cognate to the carrier liquid, and our estimated pre-eruptive S concentration in F8 melts is ~1110 ppm S, which is below $SCSS^T$ for the melt composition and eruption temperature ($SCSS^T$ ~1220 ppm S at 1140 °C). These observations indicate that S must have previously been lost from F8 source melts, otherwise sulfide saturation should have occurred. Such a conclusion has important

implications for the S budget of the LERZ eruption and for the dynamics of the Kīlauea magmatic system, which we discuss further below.

4.4.3 Post-entrapment effects on sulfide saturation in melt inclusions

As discussed, the mixing of high-Fo olivine grains into much lower temperature LERZ F8 carrier liquids led to substantial undercooling and severe PEC and Fe-loss in MI. Melt inclusions are closed systems with respect to S, and residence of high-Fo grains in a lower temperature melt affect MI sulfide saturation in the following ways: *1)* MI cooling decreases $SCSS^T$, *2)* Fe incorporation into the olivine PEC rind, as well as diffusive Fe-loss into the larger host grain, decreases $SCSS^T$, *3)* the crystallization of the olivine rind and Fe-loss causes a proportional increase in olivine-incompatible elements in the MI, enriching S towards levels of $SCSS^T$, *4)* H_2O and redox diffusive exchange can either increase or decrease $SCSS^T$ in the MI, depending on the external melt conditions (Figures 11, 12). Melt inclusions in high-Fo hosts experienced temperature decreases of 70 – 240 °C during residence in F8 melts and cooling in the lava flow. This cooling led to extensive PEC and Fe-loss that caused S enrichments of 15 – 54% in the residual MI. Melt inclusions that initially contained ~11.5 wt% FeO^T experienced Fe-losses down to 4 – 6 wt% FeO^T remaining. Additionally, MI fO_2 was likely decreasing due to re-equilibration with the external melt that was undergoing reduction via SO_2 degassing. All of these factors contributed to the majority of MI in high-Fo olivine grains reaching sulfide saturation during residence in and emplacement of F8 melts (Figures 2c, 2d, 8, 9). Similar observations have been made in olivine-hosted MI from the Laki eruption of Iceland, which achieved sulfide-saturation with cooling, 8 – 10 wt% FeO^T-loss during PEC, and MI reduction of ~1.2 log units fO_2 due to re-equilibration with a reduced external melt (Hartley et al., 2017). These phenomena underscore the importance of careful petrography during MI identification and preparation, as accurately determining total S in PEC-affected MI requires detailed measurements of the sizes of the MI, sulfide globules, vapor bubbles, and any daughter minerals (e.g. Cr-spinel) within MI. This contextual information is generally lost for MI analyzed in thin sections or in randomly

sectioned bulk grain mounts, and the measured S concentration in the MI glass could be a substantial underestimation of total S if precipitated sulfides were not accounted for.

Interestingly, MI in F8 high-Fo olivine grains have a wide range of sulfide-restored S concentrations, and most are more S-poor than MI in lower-Fo olivine, clinopyroxene, and plagioclase grains (Figure 14). Even when acknowledging the uncertainties in estimating MI and sulfide sizes, the calculated sulfide-restored S concentrations in high-Fo MI indicate that most must have been entrapped in high temperature melts that were substantially sulfide under-saturated.

Finally, it is worth discussing the unique case of MI in the littoral blast sample that underwent atmospheric oxidation during subaerial transport in the lava channel. As introduced in **Chapter III**, olivine-hosted MI in this sample re-equilibrated with the oxidized external melt over a period of hours to days. Melt inclusions in Fo_{88-89} olivine grains from this sample experienced similar high degrees of PEC (20 – 30%) and Fe-loss (from ~11.5 wt% down to 6 – 7 wt% FeO^T) as MI in high-Fo hosts from other F8 samples, however none of the littoral blast MI contain sulfides. This is presumably because oxidation of the littoral blast MI to QFM +0.5 to +1.9 increased $SCSS^T$ and caused any sulfides to destabilize and re-dissolve into the melt (Hartley et al., 2017; Jugo et al., 2010). These oxidized MI therefore do not require accounting for sulfide mass balance and MI glass measurements provide a more direct view of the range of S content of primitive MI hosted within high-Fo olivine grains. These oxidized MI contain 600 – 1200 ppm S (avg. 910 ± 200, n=9), covering a similarly wide range of S as high-Fo MI in other F8 samples where total S was calculated from sulfide restorations (Figure 14).

4.5 Volatile degassing model and S-isotopic fractionation

4.5.1 Kīlauea degassing model

Prodigious SO_2 degassing occurs during subaerial Kīlauea eruptions, and we propose that such S degassing is the reason for the wide range of S contents observed in Kīlauea matrix glasses and MI. Here, we discuss the conditions of S degassing at Kīlauea and the effects of S degassing on the $\delta^{34}S$ signatures of melts.

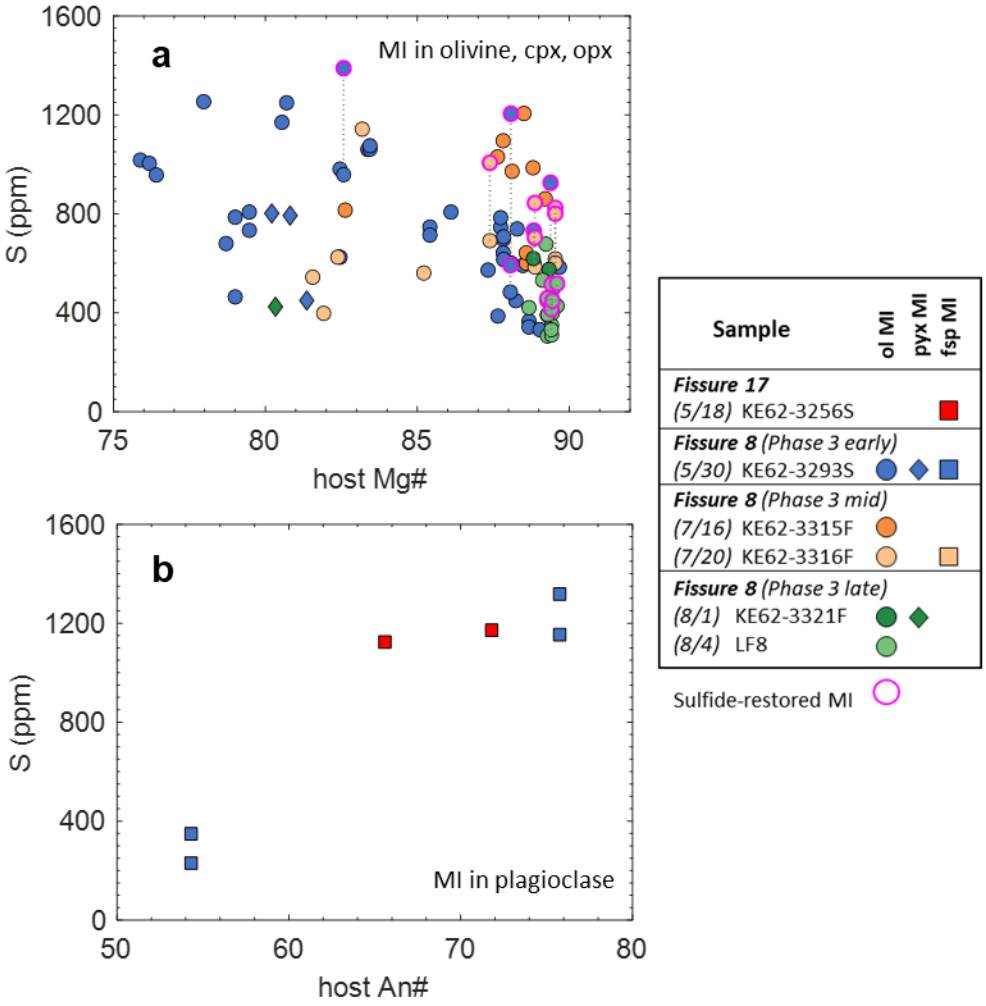

Figure 14. PEC-corrected S concentrations of MI in different host compositions. *(a)* MI S concentrations relative to host Mg# (olivine, clinopyroxene, and orthopyroxene). *(b)* MI S concentrations relative to host An# (plagioclase). Symbols with purple outlines are sulfide-restored MI, with vertical tie-lines connecting sulfide-restored S concentrations to S concentrations as measured in MI glasses.

Sulfur degassing is dependent on pressure, temperature, melt composition and oxidation state (Burgisser & Scaillet, 2007; Jugo et al., 2010). As discussed, SO_2 degassing from S^{2-}-rich melt can induce redox changes in the melt, which can affect subsequent degassing. The multiple dependencies on S degassing make modeling of S degassing challenging. Progress has been made in thermodynamically consistent degassing models that include S (Burgisser et al., 2015; Burgisser & Scaillet, 2007; Moussallam et al., 2016; Witham et al., 2012), however the experimental datasets that

underlie such models and the treatment of sulfide saturation are not always relevant to Kīlauea melt conditions. Instead, we adopt the approach of Gerlach (1986), who derived an empirical relationship for C-H-S-O degassing based on decades of gas measurements at Kīlauea. The Gerlach (1986) model is based on the observation that S gas species consistently constitute ~15% of the molar volume of both CO_2-dominated gases emitted at Kīlauea's summit during quiescence (Type 1 gases) and H_2O-dominated gases emitted during rift zone eruptions (Type 2 gases) (Gerlach, 1986; Gerlach & Graeber, 1985). When coupled with H_2O-CO_2 solubility models, this steady S gas fraction reproduces observations of degassing at Kīlauea remarkably well (Gerlach, 1986). The Gerlach (1986) approach initially used H_2O and CO_2 solubilities of Burnham (1979) and Harris (1981). We update this approach with more recent H_2O-CO_2 solubility models of Dixon et al. (1995) for low-pressure tholeiitic basalts that are directly relevant to Kīlauea melts.

Primary Kīlauea magmas are hypothesized to contain up to 1.0 wt% CO_2 (Anderson & Poland, 2017; Tucker et al., 2019), and the low CO_2 solubility in tholeiitic basalts causes Kīlauea magmas to be saturated in a CO_2-dominated fluid phase throughout nearly the entire crust (Gerlach, 1986). Consequently, melts are already largely depleted in CO_2 by the time they ascend to the shallow levels of the Kīlauea summit reservoirs. Continued low-level CO_2 degassing occurs from the shallow summit reservoirs. With S degassing accounting for 15% mole fraction of this small mass of CO_2-rich vapor loss in the shallow reservoirs, relatively little S is lost from the melt. The low viscosity of Kīlauea basaltic melts would likely cause exsolved vapors to buoyantly separate from the melt and ascend to the surface. This open-system behavior from deeply ascending melts gives rise to the CO_2-dominated (Type 1) degassing continuously observed at Kīlauea's summit, even during periods of eruptive quiescence (Elias & Sutton, 2007; Gerlach et al., 2002; Gerlach, 1986; Gerlach & Graeber, 1985; Greenland et al., 1985).

The low initial H_2O content of Kīlauea melts results in no substantial H_2O degassing occurring until melts ascend to very shallow depths. At these shallow depths, the mass fraction of exsolving H_2O-rich vapor is much larger and S degassing from the melt increases as a result (Type 2 gases). The updated H_2O-CO_2 solubility model of Dixon et al. (1995) predicts the onset of major H_2O and S degassing at ~100 – 200 m

over a range of initial H_2O contents of 0.3 – 0.6 wt%. Figure 15 shows the results of the degassing model for initial volatile concentrations appropriate for the deep Halema‘uma‘u reservoir (Edmonds et al., 2013) and the pre-eruptive LERZ dike based on measurements of MI from basaltic pumice erupted from F8 on May 30 (265 ppm CO_2, 0.3 wt% H_2O, 1110 ppm S).

A two-stage degassing model for South Caldera-sourced magmas feeding the F8 eruption follows: We assume an initial melt at 5 km depth that was CO_2-saturated (~560 ppm CO_2) and contained 1150 ppm S and 0.3 wt% H_2O. This would be considered a type of “reservoir-equilibrated” melt by Gerlach (1986). As this melt ascended (either prior to or during the 2018 activity) from deep South Caldera reservoir to depths consistent with the ~265 CO_2 measured in bubble-free LERZ MI (~2.5 km) it would degas 7.3% of its total volatiles (by mass) in open-system degassing of CO_2-rich gas. During this ascent the melt would have degassed 53% of its CO_2 (260 ppm remaining), but would have lost only 3% of its S (1112 ppm remaining) and essentially no H_2O.

During the LERZ eruption, this CO_2-degassed magma was transported laterally from the shallow summit reservoirs to the LERZ eruption site. Lateral dike transport occurred at 2 – 3 km depths (Neal et al., 2019), and thus there was effectively no pressure change to cause any degassing during transit, which is consistent with no anomalous surface degassing being observed along the dike axis. During magmatic ascent in the LERZ from 2.5 km to 100 m depths, the melts would exsolve an additional 8.5% of its total initial volatiles (by mass), including another 5% of the initial S (1053 ppm remaining) and 3% of the initial H_2O (0.29 wt% remaining). In the final 100 m of ascent to the surface, ~80% of total initial volatiles would be released (assuming 0.1 wt% H_2O remains in the melt at atmospheric pressure Dixon et al. [1995]), and nearly all remaining S would degas (Type 2 gas). Assuming closed system degassing of magma being transported from the base of the Halema’uma’u reservoir to ascent and eruption at F8, this model predicts molar gas proportions of 0.6 C/S and 5.3 H_2O/S at a melt fragmentation depth of ~25 m (where *gas volume/melt volume* ≈ 4 [Gerlach, 1986; Sparks, 1978]). Gas ratios of 0.30 ± 0.01 C/S and 5.4 ± 0.5 H_2O/S (averages and 1 standard error) were measured at F8 in June and July with a UAS-based MultiGAS

(Kelly et al., in prep; Kern et al., 2020). The modeled and measured H_2O/S gas ratios agree very well. However, the lower UAS-measured C/S gas ratio at F8 indicates that *1)* LERZ magmas were sourced by CO_2-saturated melts from shallower depths than the 2.5 km modeled here, *2)* LERZ magmas contained higher initial S and H_2O than modeled here, or *3)* more S- and H_2O-rich gases from shallow open-system degassing were mixed in the UAS-measured F8 gas plumes. We suggest that post-fragmentation open-system degassing of S- and H_2O-rich gases is the most likely explanation for the discrepancy between the closed-system modeled C/S and the observed C/S ratios. Kelly et al. (in prep) further explore the ranges of initial melt volatile concentrations that would be consistent with the gas ratios observed at F8.

Overall, we conclude that S degassing occurred dominantly at very shallow depths during magma ascent feeding the LERZ eruptions. A high proportion of SO_2 relative to H_2S in high temperature gases at low pressures is thermodynamically favored (Burgisser et al., 2015; Burgisser & Scaillet, 2007), consistent with observations of $SO_2/H_2S > 26$ in gas plumes from F8 fountains (Kelly et al., in prep) and of limited H_2S degassing observed in past Kīlauea eruptions (Gerlach, 1986; Gerlach & Graeber, 1985). This same degassing regime is applicable for the shallow ascent of all low-H_2O Kīlauea melts, including 1983 – 2008 degassing from Pu‘u ‘Ō‘ō (Gerlach, 1986; Gerlach & Graeber, 1985; Greenland et al., 1985), and the 2008 – 2018 lava lake degassing from Halema‘uma‘u (Beirle et al., 2014; Edmonds et al., 2013; Elias & Sutton, 2012). The requirement of low pressure needed to cause S and H_2O degassing can also explain the rapid cessation of summit degassing in mid-May, 2018 (Kern et al., 2020). During the early stages of the summit caldera collapse, the degassing conduit of the draining Halema‘uma‘u lava lake became infilled with collapse debris, which was sufficient to re-establish > 100 m of lithostatic pressure and thereby prevent further H_2O and S degassing.

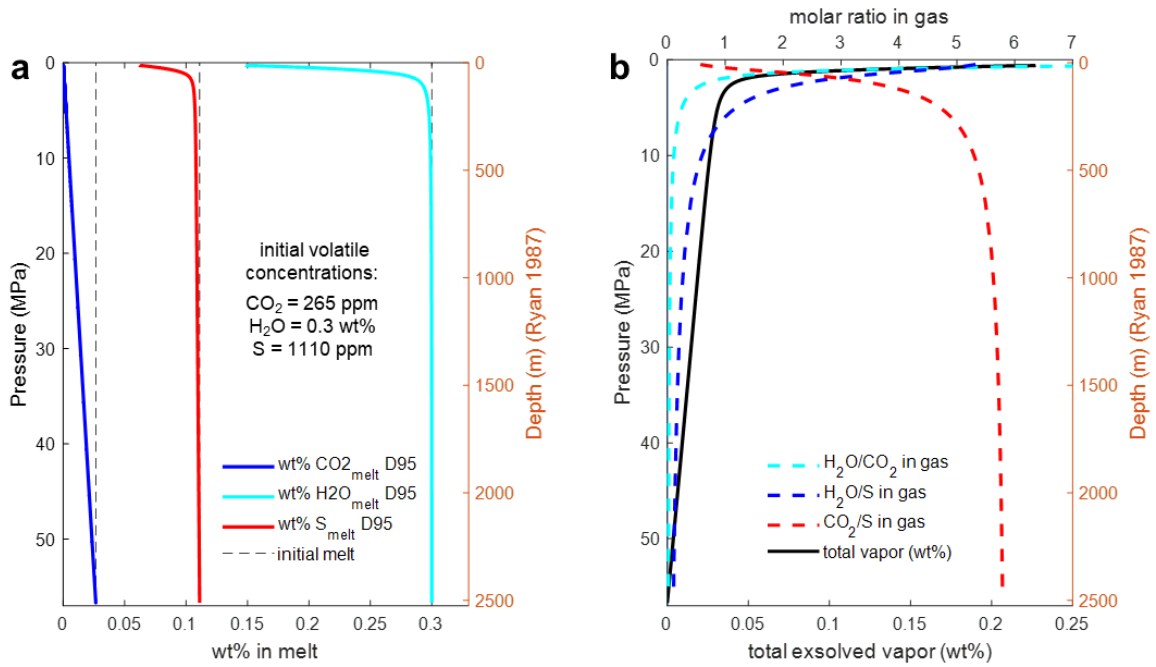

Figure 15. Closed-system C-H-S degassing model for Kīlauea melt ascent, following the formulation of Gerlach (1986), where S is always 15% mole fraction of the total gas. The model has been updated to use H_2O-CO_2 solubilities from Dixon et al. (1995) (D95). Conditions of pre-eruptive F8 melts are simulated here. *(a)* CO_2, H_2O, and S remaining in the melt. Vertical lines indicate the initial volatile concentrations in the melt. Substantial degassing of H_2O and S occurs at < 100 m depths. *(b)* Exsolved vapor mass (wt% of total melt) and gas molar proportions during melt ascent. Depth below the surface is from the depth-density parameterization after Ryan (1987).

4.5.2 The effect of SO_2 degassing on melt redox state and S-isotopic signature

The shallow degassing of SO_2 from reduced, S^{2-} dominated melts is consequential for the redox and isotopic evolution of residual melts. As previously discussed, SO_2 degassing from S^{2-} dominated melts causes a reduction in fO_2 of the melt (Helz et al., 2017; Moussallam et al., 2016). The redox difference between gaseous SO_2 and S^{2-} in the melt imparts a fractionation of S-isotopes during degassing, where SO_2 is the more oxidized phase and is isotopically heavier (Marini et al., 2011; Miyoshi et al., 1984; Richet et al., 1977). At 1150 °C, the fractionation between SO_2 vapor and the melt ranges from 1.5‰ to 2.2‰ depending on the proportion of S^{6+} in the melt (20% and 0% $S^{6+}/\Sigma S$, respectively) (Miyoshi et al., 1984; Richet et al., 1977). We observe this isotopic fractionation during SO_2 degassing in the clear correlation between S concentrations and $\delta^{34}S$ in basaltic pumice matrix glasses and MI (Figure 16a). The most S-rich matrix

glasses contain 650 – 800 ppm S with $\delta^{34}S$ values of -0.2 to +0.3‰, and the most S-rich basaltic pumice MI contain 1170 – 1390 ppm S with $\delta^{34}S$ values of +1.0 to +1.5‰. The $\delta^{34}S$ values of the glasses decrease linearly with S degassing, and the most S degassed matrix glasses retain only 100 ppm S and have $\delta^{34}S$ values of -2.5‰.

With the fractionation factors above, we construct an isotopic degassing model that parameterizes decreasing $S^{6+}/\Sigma S$ with S degassing and progressive reduction of the melt (Figure 16b). We assume an initial melt contains 1100 ppm S and has a $\delta^{34}S$ value of 1.0‰. We then model closed-system degassing of ~75% of the initial S, at which point we assume magma fragmentation and fountaining (Gerlach, 1986; Sparks, 1978) that leads to open system degassing until ~90% of the initial S is degassed. Based on S-XANES measurements of how $S^{6+}/\Sigma S$ decreases with S-loss, we assume 20% initial $S^{6+}/\Sigma S$ in the melt that decreases to 10% S^{6+} after 30% S degassing, 5% S^{6+} after 50% S degassing, and 0% S^{6+} after 70% S degassing. This mixed closed- and open-system degassing model matches our observations well: S-rich matrix glass $\delta^{34}S$ compositions of +0.2‰ are reproduced at ~40% S degassing (660 ppm S remaining in the melt), and S-poor matrix glass compositions of -2.5‰ are reproduced at ~90% total S degassing (110 ppm S remaining in the melt). After 90% S degassing, the cumulative exsolved SO_2 gas will be 3.5‰ heavier than the residual degassed melt. Kinetic effects may also affect isotopic fractionation during S degassing due to different diffusivities of ^{32}S and ^{34}S isotopes, and between S^{2-} and S^{6+} melt complexes. However, these effects are thought to be minimal in 1150 °C basaltic melts (Fiege et al., 2015).

The only other S-isotope measurements of Kīlauea glasses that we know of are those of Sakai et al. (1982), who analyzed a range of sublimates, gasses, and subaerial and submarine bulk lavas. Subaerially erupted bulk lavas are largely S degassed, with bulk concentrations of 30 – 180 ppm S and $\delta^{34}S$ values of -2.2 to +0.4‰ (avg. -0.8 ± 0.8, n=12). Submarine lavas from the Puna Ridge are less degassed, and have bulk S concentrations of 530 – 840 ppm S and higher $\delta^{34}S$ values of -0.6 to +0.8‰ (avg. +0.5 ± 0.6, n=6). Sakai et al. (1982) estimate that degassing SO_2 will have a $\delta^{34}S$ signature that is 1‰ heavier than the residual melt. These findings agree fairly well with the $\delta^{34}S$ ranges we observe in S degassed and undegassed matrix glasses from F8 basaltic pumice, with difference perhaps due to initial S concentrations or $\delta^{34}S$ values of our respective

samples. We therefore conclude that low $\delta^{34}S$ signatures in Kīlauea melts are a robust indicator of S-loss by SO_2 degassing.

The same correlation between S concentration and $\delta^{34}S$ is also present in MI from the F8 littoral blast and late overflow lava (LF8) samples. Many $\delta^{34}S$ analyzed MI in these samples, as well as in basaltic pumice MI, are in high-Fo olivine grains and underwent substantial cooling and PEC. In LF8 and basaltic pumice samples, these post-entrapment processes caused the precipitation of sulfides in MI hosted in high-Fo olivine grains. However, as discussed, the oxidation of the littoral blast sample caused any sulfides to re-dissolve in the MI. Measured $\delta^{34}S$ values and sulfide-restored total S concentrations of the sulfide-bearing MI have the same observed $\delta^{34}S$ -S concentration relationship as the matrix glasses. As discussed, the closed-system isotopic fractionation between the precipitated sulfide and the residual MI melt should be trivial at Kīlauea temperatures and fO_2 conditions (Marini et al., 2011), so that glass measurements are representative of the total MI $\delta^{34}S$ signature (Beaudry et al., 2018). One anomalous sulfide-bearing MI in a high-Fo olivine from the basaltic pumice falls off this $\delta^{34}S$-S concentration trend. This MI also has a very CO_2-rich vapor bubble that translates into an entrapment depth of 7.5 km, which is the deepest observed in our dataset. This MI also has relatively large sulfide for its size and the glass has very high $S^{6+}/\Sigma S$ for a relatively low calculated fO_2. However, apart from this outlier, the relationship between S concentration and $\delta^{34}S$ is robust in matrix glasses and MI. This indicates that *A)* the sulfide mass-balance restorations in MI are largely accurate, and *B)* many of the MI in high-Fo olivine grains have low S contents due to S degassing, suggesting the MI were trapped from variably degassed melts that must have experienced close to near-surface pressures.

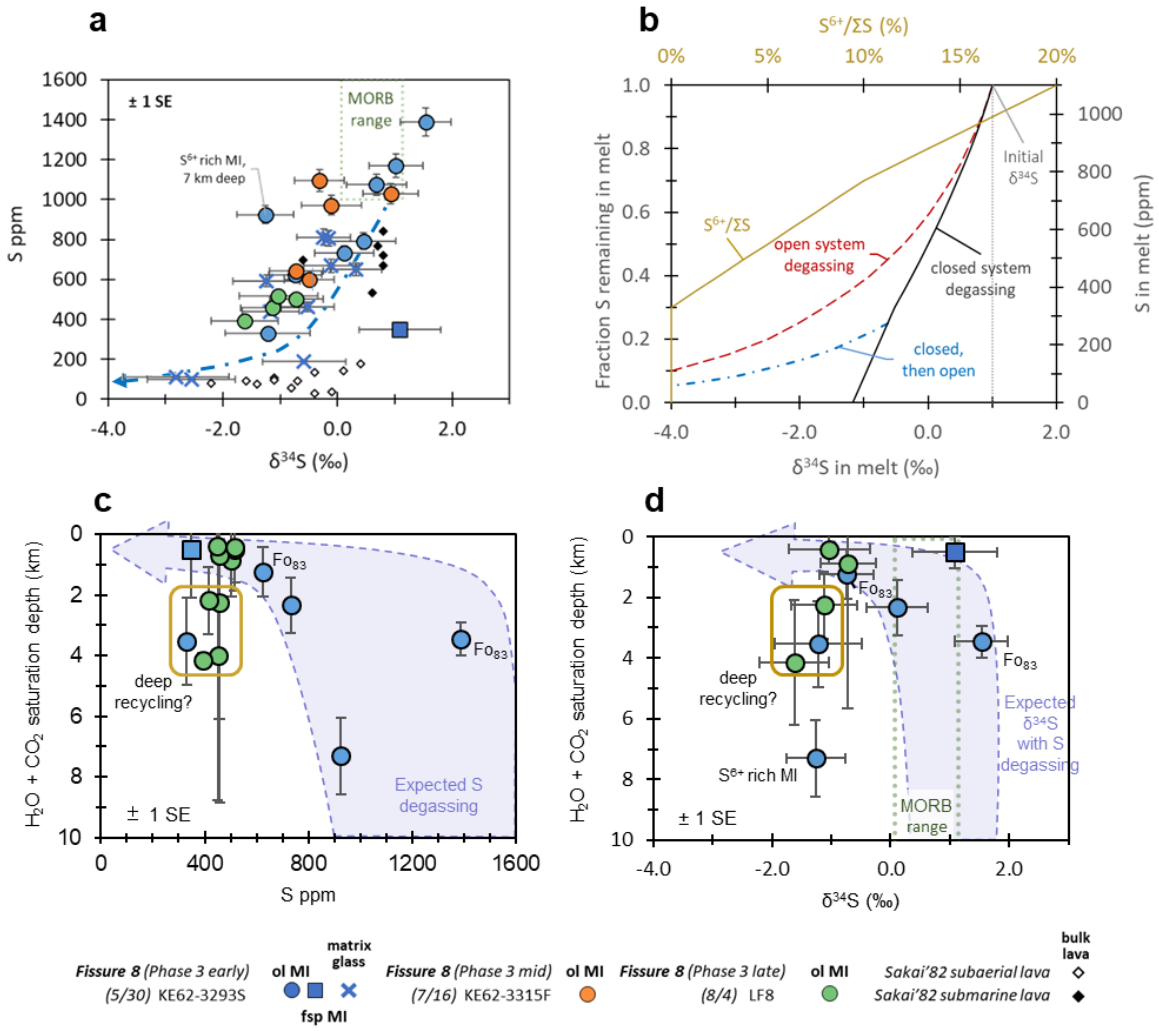

Figure 16. *(a)* $\delta^{34}S$ and S concentrations in matrix glasses and MI from LERZ F8 samples. Blue curve is the mixed closed- and open-system degassing path from panel *b*. Degassed subaerial and S-rich submarine bulk lava analyses of Sakai et al. (1982) are shown as smaller open and closed symbols. The $\delta^{34}S$ and S concentration ranges of MORB is shown for comparison. *(b)* Closed- (black) and open-system (red) degassing models from the assumed F8 pre-eruptive $\delta^{34}S$ values and S concentrations. A mixed closed-open system degassing model (blue) assumes a change from closed to open system behavior at the point of fragmentation (~75% gas exsolution). All models include a decreasing $S^{6+}/\Sigma S$ proportion in the melt during degassing (yellow), based on observations from S-XANES measurements. *(c)* Melt inclusion entrapment depth vs S concentrations in MI. Major S loss from degassing should not occur until near surface pressures (schematically shown). *(d)* Melt inclusion entrapment depth vs $\delta^{34}S$ in LERZ samples. $\delta^{34}S$ fractionation occurs during S degassing at shallow depths (schematically shown). *(c, d)* All MI are hosted in $Fo_{87\text{-}90}$ olivine, except for two in Fo_{83} olivine grains (labeled). Sulfur concentrations in all MI have been sulfide-restored, where applicable.

4.6 Sulfur budget of the LERZ eruption

4.6.1 Petrologically derived gas emissions

With constraints on pre-eruptive S contents of the melt feeding LERZ fissures and a model for S degassing, we can relate lava effusion volumes with measured SO_2 gas emissions (Kern et al., 2020; Sutton et al., 2003). Kern et al. (2020) present a time series of SO_2 emission rates throughout the LERZ eruption measured by vehicle-based ultraviolet DOAS spectroscopy, which we summarize here: Gas emission rates were extremely high during the LERZ eruption and the dense gas and aerosol loads complicated light paths through the eruptive plumes. These conditions required the development of new analytical techniques to more accurately quantify SO_2 emissions. Maximum SO_2 emissions rates reached 600 kt/day and sustained emission rates of ≥ 100 kt/day occurred for most of June and July. For comparison, the average SO_2 emission rate from the Halemaʻumaʻu lava lake during the 2008 – 2018 activity was ~4.5 kt/day (Beirle et al., 2014; Elias et al., 2018a). The cumulative SO_2 emissions for the 3-month long LERZ eruption are estimated to be 10.2 Mt (7.1 – 13.6 Mt at a 68% confidence interval) making it one of the largest SO_2 emitting eruption of the last century, with total SO_2 emissions being comparable to the SO_2 release from Holuhraun, Iceland (2014 – 2015) and about half that of Mijakejima, Japan (2000 – 2002) and Pinatubo, Philippines (1991) (Pfeffer et al. 2018; Shinohara et al. 2003; Kazahaya et al. 2004; Matsushima 2005; Guo et al. 2004). Kern et al. (2020) use the cumulative SO_2 emissions and an estimated melt S content at sulfide saturation for F8 melt conditions (~1250 ppm S) to calculate dense rock equivalent (DRE) erupted lava volumes of ~1.7 km^3 (1.1 – 2.3 km^3 at a 68% confidence interval).

Here, we petrologically calculate SO_2 emission rates through the eruption by combining our measurements of S contents in F8 glasses and MI with estimates of lava extrusion rates calculated from UAS videos of the F8 lava channel (Dietterich et al., in prep). We then compare these to petrologic estimates to measured SO_2 emissions (Kern et al., 2020). Despite observations that Fe-rich basalts erupted at the onset of the LERZ activity were more S-rich than melts erupted from F8, the total erupted mass of the phase 1 magmas is trivial compared to the voluminous outpourings of more primitive, "summit-like" magma during phases 2 and 3 of the eruption (Gansecki et al., 2019; Neal et al.,

2019; Zoeller et al., 2020). The volume of andesitic magma erupted from F17 was very low and this magma was S-poor so that the contribution of this magma to the overall eruption gas budget was also trivial. We therefore make a simplifying assumption in calculating the LERZ sulfur budget that melts from these early fissures have the same S concentrations as F8 melts. This assumption only makes a very small difference in the overall scope of the SO_2 emissions during the eruption because of the small magma volumes erupted from the early fissures.

As shown in our Kīlauea degassing models, efficient S degassing only occurs if magma is brought to depths ≤ 100 m. Although non-erupted magma certainly ascended to relatively shallow depths throughout the LERZ fissure system, we view it unlikely that substantial masses of magma were either stored or convecting at depths < 100 m beneath the surface. If this was the case, more significant degassing would have been observed during field campaigns at non-erupting fissures (Clor et al., 2018). We therefore consider the contribution of SO_2 degassing from non-erupted LERZ magma to be negligible compared to the large SO_2 emissions from high lava effusion rates at active vents. For our calculations, we therefore follow the assumption of Kern et al. (2020) that all degassed magma was erupted.

Our best estimate of pre-eruptive S concentrations of F8 melts is 1110 ppm S, which comes largely from the MI in low-Fo olivine and plagioclase grains within the basaltic pumice erupted in late May (see section 4.4.1). Unfortunately, we lack further constrains on how pre-eruptive S concentrations may have varied temporally during the eruption because our dataset undersamples MI that are hosted in phenocrysts that likely formed in equilibrium with the F8 melt. A dearth of chronologically constrained tephra from F8 fountains in June and July means that we also lack a temporal record of rapidly quenched matrix glasses and RE, which could provide additional constrains on pre-eruptive S content of the LERZ melt over time. However, if we assume that the pre-eruptive S/Cl ratio of later-erupted matrix glasses was the same as the S/Cl ratio of basaltic pumice high-S MI, we can approximate the pre-eruptive S content of variably degassed matrix glasses based on their Cl concentrations because Cl does not change substantially during degassing or until substantial crystallization (Figure C9). With this approach, we estimate that melts feeding F8 contained 900 – 1200 ppm S through mid-

July, and perhaps decreased to 750 – 950 ppm S in early August. We therefore assume that LERZ melts contained 1110 ppm S throughout the eruption, with upper and lower estimates of 900 and 1200 ppm S. Matrix glasses in the littoral bomb sample, which traveled the full length of the > 13 km lava flow, are essentially completely S degassed. We therefore assume that all erupted melts fully degas S during ascent and lava flow transport. The average melt density for proximally quenched matrix glasses at 1 bar and 1140 °C is calculated to be 2700 kg/m^3 (from the DensityX calculator of Iacovino and Till [2019]), which we take as the erupted bubble-free melt density throughout the eruption.

With these conditions, we calculate the expected daily rates of SO_2 mass degassed (M_{SO2}, in Mt per day) based on DRE lava extruded volumes (V, in million m^3 per day):

$$M_{SO2} = V \cdot (1 - f_{xtl}) \cdot \rho \cdot C_S \cdot 2 \qquad [eq.\ 4]$$

where f_{xtl} is the (S-free) crystal fraction in the melt, ρ is the melt density, C_S is the weight fraction of S in the melt, and the factor of 2 accounts for S constituting half the mass of SO_2. For these calculations we assume $f_{xtl} \approx 0.1$ for the bubble-free magma, consistent with modal mineralogy we observe in thin sections of proximally quenched F8 lavas. Applying this calculation to the time series of estimated LERZ lava extrusion from Dietterich et al. (in prep), we obtain petrologically estimated SO_2 emission rates throughout the eruption (Figure 17).

Some complications with our petrologic approach include fairly high uncertainties in the bubble and crystal fractions of erupted lavas, which factor into DRE estimates of lava effusion rates (Dietterich et al., in prep) and into our calculations of melt fraction in *eq. 4*. Additionally, both lava effusion and gas emission rates from F8 fluctuated rapidly over short timescales. Lava effusion rates varied with minutes-long "pulsing" due to conduit processes, and with hours long "surges" following summit collapse events (Patrick et al. 2019c). SO_2 emission rates would vary in accordance with changing lava extrusion rates, but are additionally complicated by turbulent atmospheric dynamics that can lead to plume "puffing" and short-term variability in measurements (Kern et al., 2020). To smooth out these short term variations, our calculations are based on 3-measurement running daily averages of SO_2 emission rates and lava extrusion rates.

Despite these substantial uncertainties, the petrologically constructed time series of SO_2 emissions using constant 1110 ppm S melt concentrations agree fairly well with observed degassing rates. However, petrologic estimates of SO_2 emission rates are notably lower than observed values in late May to mid-June, and higher than observed values in mid- to late July. If we assume that measured SO_2 emission rates and lava extrusion rates are accurate, then the bulk S concentration of LERZ melt would need to be > 2000 ppm to account for the late May to mid-June SO_2 emission rates. This would require a melt S concentration at the $SCSS^T$ value (~1250 ppm S) and would additionally require 0.1 – 0.3 volume % sulfides to have been present in the bubble-free melt and completely broken down to add to the SO_2 emissions. Sulfide breakdown during ascent and degassing has been suggested to have a large role in cumulative S degassing from some Kīlauea eruptions (Edmonds et al., 2018; Wieser et al., 2020b). However, in no F8 sample do we observe residual sulfides in matrix glass or as inclusions in minerals cognate to the F8 melts, including in the carefully studied basaltic pumice that erupted during this time period in question. Consequently, we find the possibility of such a substantial sulfide load to be unlikely in the F8 melts. Rather, we find it more probable that either the lava extrusion rates were underestimated and/or that SO_2 emission rates were overestimated during this time. The possible role of sulfides in F8 melts could be better informed by detailed petrographic surveys and chalcophile trace element measurements throughout the eruption (Wieser et al., 2020b).

In mid- to late July, petrologically-derived SO_2 emission rates are overestimated compared to the observed SO_2 emissions. Assuming that lava extrusion rates are correct, the pre-eruptive LERZ melt would need to have 700 – 900 ppm S at this time to bring the petrologic estimates into accord with the SO_2 emission rates. Matrix glasses erupted in early August have pre-eruptive S concentrations estimated from their Cl contents (see above) of 750 – 950 ppm, although this is based on a small number of analyses. Interestingly, the extruded lavas during this time were slightly higher temperature than earlier in the eruption (Figure 3) and the olivine phenocryst cargo became increasingly more Fo-rich (Gansecki et al., 2019; Mourey et al., submitted). Despite the more primitive character, many MI in these high-Fo olivine grains have low total S concentrations and $\delta^{34}S$ degassed signatures. While these high-Fo grains were not

crystallized from the bulk LERZ carrier liquid, we speculate that previously degassed, primitive melts containing the high-Fo grains became increasingly mixed with the LERZ magma toward the end of the eruption. This could have resulted in the unusual scenario of hotter, more primitive melts erupting that were actually more S-poor than previously erupted, cooler melts. We further explore this scenario in the next section.

Finally, we note that our estimate of 1110 ppm S in the pre-eruptive LERZ magma is lower than the sulfide-saturated estimate of 1250 ppm S used by Kern et al. (2020) to estimate the erupted DRE magma volume. Re-arranging *eq. 4* to calculate lava volumes, our lower S estimate proportionately increases the required erupted DRE lava volume to 1.9 km^3 to account for the cumulative 10.2 Mt of SO_2 emitted. Our minimum and maximum estimates of S content of the pre-eruptive melt (900 – 1200 ppm S) would equate to cumulative eruptive DRE lava volumes of 2.3 – 1.8 km^3. We note that with H_2O degassing and cooling during emplacement, the density of LERZ glasses increases (~2950 kg/m^3 at ambient temperatures) and the continued crystallization of mineral phases would further increase the bubble-free density, so that the DRE volume of the emplaced lavas would be ~10% lower than the high-temperature melt volumes calculated here and by Kern et al. (2020).

From our best estimated melt-only eruption volume (1.7 km^3 DRE melt at magmatic temperature, excluding crystal cargo) and our estimated pre-eruptive H_2O and CO_2 contents in F8 melts (~0.3 wt% H_2O and ~265 ppm CO_2), and assuming complete degassing during ascent and lava flow emplacement, we calculate cumulative emissions of 13.8 Mt H_2O and 1.3 Mt CO_2. These compare to the estimated (68% confidence bounds) cumulative emissions of 11 – 21 Mt H_2O and 1.5 – 2.8 Mt CO_2 determined from Kern et al. (2020) based on cumulative SO_2 emissions and measured H_2O/S and C/S gas ratios (Kelly et al., in prep). The petrologic estimate of H_2O agrees well with the measured gas emissions (0.25 – 0.45 wt% H_2O degassing bracket the confidence bounds) but the petrologic CO_2 estimate is lower than the 330 – 620 ppm CO_2 degassing that would be required to bracket the confidence bounds. As our pre-eruptive CO_2 estimate is constrained by only a few measurements at the onset of F8 activity, it is likely that the CO_2 may be underestimated and/or might change as deeper magma was tapped during the eruption. The C/S ratio of gas emissions suggest higher CO_2 concentrations of LERZ

melts that require storage pressures consistent with the South Caldera reservoir. Higher melt CO_2 might also require higher initial S and H_2O melt contents to account for the observed C/S and H_2O/S gas ratios at F8, as discussed more completely by Kelly et al. (in prep).

The large uncertainties in SO_2 emission rates, lava extrusion rates, and pre-eruptive S concentration of LERZ melts through time makes these cumulative erupted volume estimates very approximate. Still, we share the conclusion of Kern et al. (2020) and Dietterich et al. (in prep) that the LERZ eruption produced substantially more lava than the 0.8 km^3 summit caldera collapse volume would account for.

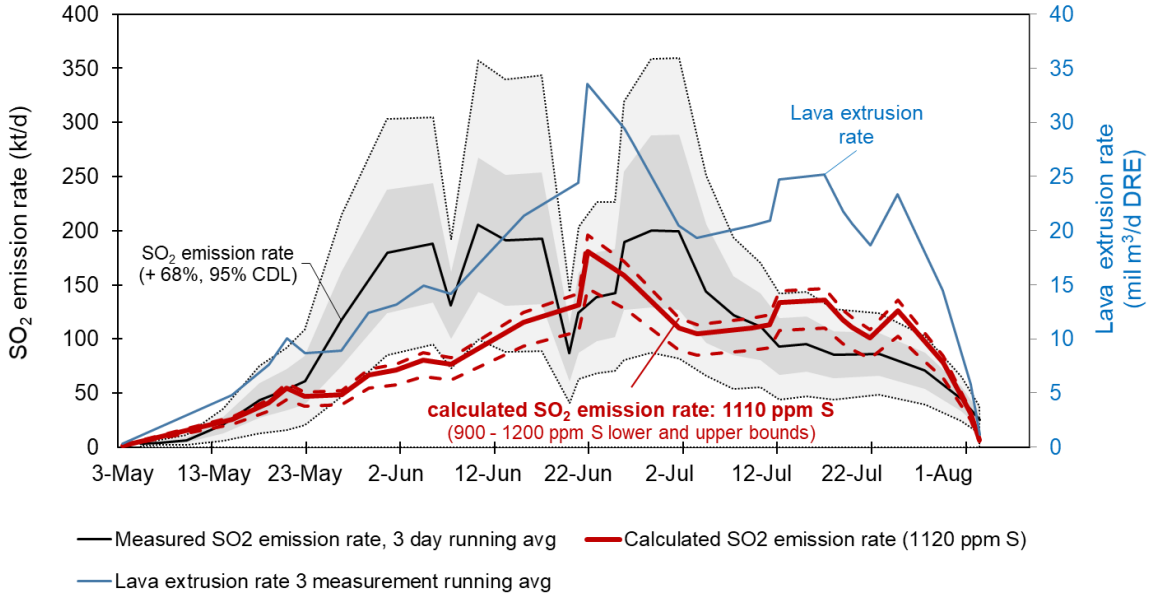

Figure 17. Time series of SO_2 emission rates (black line with shaded bounds for 68 and 95% confidence bounds) (Kern et al., 2020) and lava effusion rates (blue line) (Dietterich et al., in prep) during the 2018 LERZ eruption. SO_2 emission rates and lava effusion rates are 3-measurement running means. Petrologically calculated SO_2 emission rates based on lava extrusion rates and melt S concentrations are shown in red; the solid line assumes a pre-eruptive melt concentration of 1110 ppm S, and the dashed lines assume lower and upper bounds of 900 and 1200 ppm S.

4.6.2 Degassing from fissure vs flow

The prodigious SO_2 degassing during the LERZ eruption was dominantly sourced from F8 for most of the eruption. However, substantial SO_2 was also measured downwind of the lava flow channel. During subaerial eruptions, the exsolution of H_2O and other volatiles should cause most S to enter the vapor and degas (Gerlach, 1986; Wallace & Carmichael, 1992). However, we observe a range of ~150 – 900 ppm S measured in matrix glasses and RE from the rapidly quenched basaltic pumice samples. Sulfur concentrations in matrix glasses and RE have a clear dependence on the proximity of the glass to nearby vesicles, with the caveat that this is a 2-dimensional analysis for a 3-dimensional phenomenon. The elevated S in subaerially erupted glasses is a function of the relatively slow diffusivity of S (Behrens & Stelling, 2011) and of incomplete degassing of H_2O and other species, which limits S partitioning (Wallace & Carmichael, 1992). Unsurprisingly, matrix glasses in samples from more distal locations in the lava channel have lower S contents. Matrix glasses in the littoral blast sample, which traveled the full 13 km lava channel prior to quenching, have S concentrations that are approaching, or below, instrument detection limit (0 – 80 ppm S). Assuming pre-eruptive S concentrations of 1110 ppm S, the observed range of 100 – 500 ppm S remaining in the basaltic pumice matrix glass shows that ~55 – 90% of the magmatic S was degassed during ascent and extrusion at F8, whereas 10 – 45% of S remained in the lava and degassed during surface flow (Figure 18a, b). For comparison, Rowe et al. (2015) estimate ~80% S was degassed from Halemaʻumaʻu lava lake spattering. The petrologic estimates of S degassing during lava effusion at F8 are consistent with measurements of SO_2 emissions during conditions of easterly winds, which allowed the F8 lava fountain gas plume and "channel gas" to be spatially resolvable. The proportion of S degassing from the eruptive fissure will depend on the vigor of fountain activity and fragmentation, in that shorter diffusive paths would be required for S to enter vesicles. Fissure 8 fountain heights peaked at 80 m in late May to early June, and generally diminished over the course of the LERZ eruption (Neal et al., 2019), so we expect that the proportion of S degassing from the lava channel increased over time. Estimates of bulk lava density in the proximal lava channel were as low as 500 – 1300 kg/m^3, requiring that the proximal

lava channel volumetrically contained 50 – 82% vesicles (Patrick et al., 2019c), which is consistent with substantial degassing occurring from the lava channel.

These observations indicate that 1.0 – 4.6 Mt of the total 10.2 Mt SO_2 emissions may have degassed from the lava channel. The thermal buoyancy of the main F8 gas plume caused the emitted fountain gases to be quickly lofted to elevations typically ranging from 0.5 to 1.5 km (Kern et al., 2020), becoming substantially diluted in the process. Eventually, these emissions impacted large portions of Hawai'i in the form of vog (Kern et al., 2020; Neal et al., 2019). However, degassing from the lava channel was more distributed and had less thermal loft, so that gases were more readily blown to ground level by moderate winds. The prevailing northeasterly trade winds caused the regions to the SSW of the main LERZ lava channel to be frequently inundated by hazardous levels of SO_2. The impact of these acidic gases on the downwind vegetation was obvious, causing widespread damage and presenting a locally severe health hazard (Figure 18c).

4.7 Petrologic insights into the Kīlauea plumbing system from LERZ magmas

4.7.1 LERZ magma sources

The broad conclusions from MI entrapment depths (this study; Anderson and Brown 1993; Moore et al. 2015; Tuohy et al. 2016; P. Wallace, unpublished) and from the summit provenance of high-Fo olivine grains (Mourey et al., submitted) follow: Lower-Fo olivine grains (< ~Fo_{83}) crystallize at depths ≤ 3 km, consistent with origins in the geophysically determined Halema'uma'u reservoir (1 – 2 km depth beneath the summit) (Anderson et al., 2019; Poland et al., 2014). Many erupted high-Fo olivine grains also crystallize at relatively shallow depth of ~1 – 5 km beneath Kīlauea's summit, with some exceptions having deeper origins. The common 3 – 5 km range of MI entrapment depths in high-Fo olivine grains is consistent with crystallization in the geophysically inferred South Caldera reservoir (Cervelli & Miklius, 2003; Poland et al., 2014). However, a substantial number of high-Fo olivine grains have shallower MI entrapment depths, indicating that high-temperature primitive Kīlauea magmas ascend to and crystallize at shallow, near-surface depths. The most recent example of this scenario would be the 1959 Kīlauea Iki eruption, which contained groundmass olivine up to

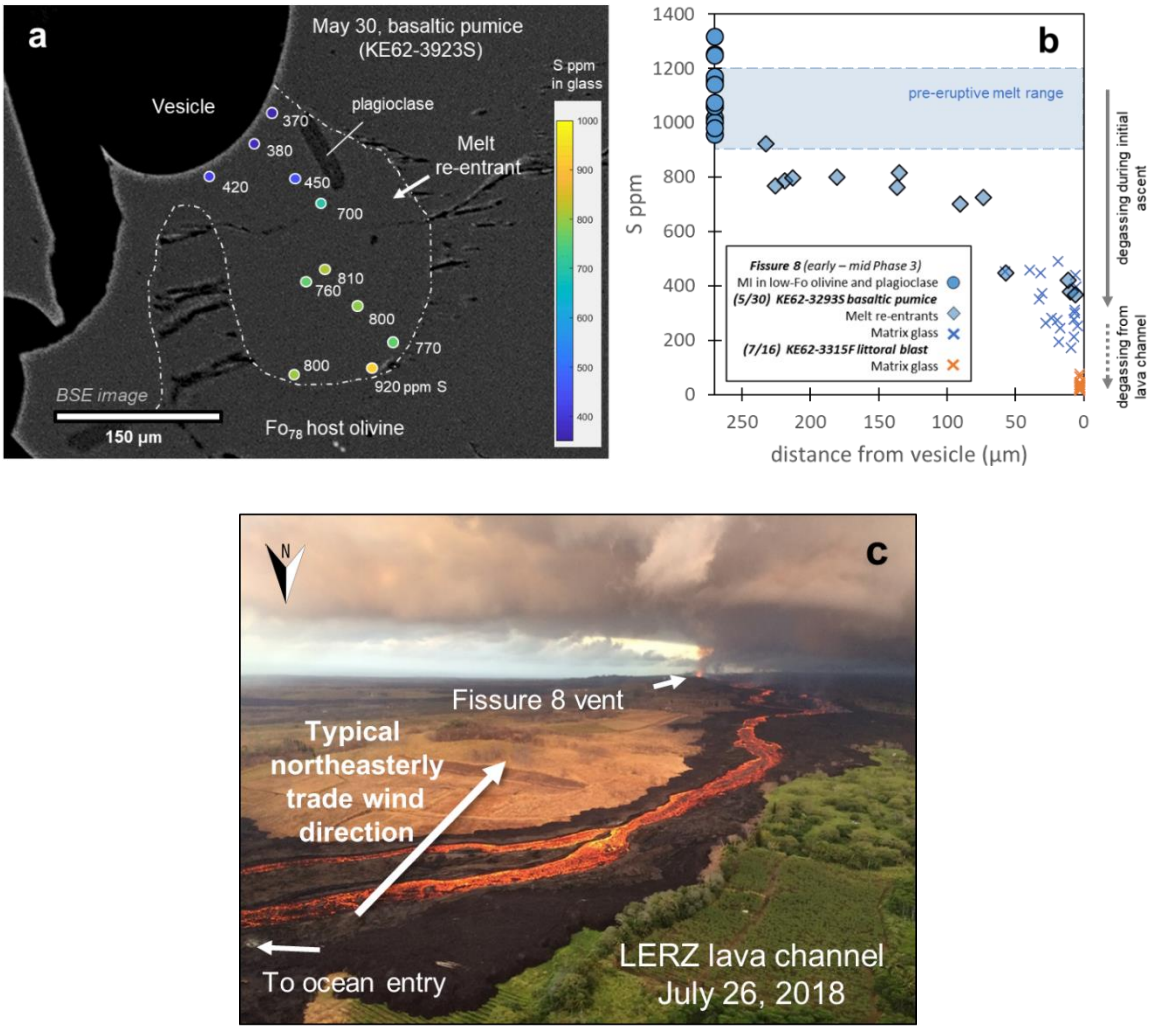

Figure 18. *(a)* Melt re-entrant within an olivine from the basaltic pumice, showing spatial differences in S concentration from the interior to the mouth of the RE channel. *(b)* S concentration measured in matrix glasses (blue Xs) and RE (blue diamonds) from rapidly quenched basaltic pumice compared to the distance from the nearest vesicle. The rapidly quenched matrix glasses have lost ~55 – 90 % of initial S, compared to F8 MI in low-Fo olivine and plagioclase grains (blue circles) that provide the best estimate of pre-eruptive melt S concentrations. Matrix glasses from the littoral blast sample (orange Xs) have completely degassed S during prolonged lava channel transit. *(c)* The effect of continued SO_2 degassing from the lava flow is very apparent in downwind vegetation die-offs. Photo by L. Desmither, USGS.

Fo_{84-88} and had variably hybridized matrix glasses with calculated melt temperatures reaching 1200 °C (Anderson & Brown, 1993; Helz et al., 2017; Sides et al., 2014b; Tuohy et al., 2016).

However, we must question what relevance the entrapment depths of MI in high-Fo olivine grains erupted in F8 lavas have for LERZ magma storage conditions. Although these MI in high-Fo olivine grains provide insights into primitive Kīlauea magmas, they do not represent the bulk erupted F8 melt and are not necessarily consanguineous with recently erupted magma at Kīlauea. Garcia et al. (2003) and Pietruszka et al. (2015, 2018) have demonstrated that the Kīlauea magmas are generated from the melting of a somewhat heterogeneous mantle source, which imparts distinct isotopic and trace-element signatures that vary through time. Similar signatures in MI show that genetically unrelated crystal cargoes are often incorporated from cumulate zones into erupting Kīlauea magmas (Sides et al., 2014b; Tuohy et al., 2016; Wieser et al., 2019). The same considerations likely hold that many of the high-Fo olivine crystals within the 2018 LERZ magmas are antecrystic. This has important implications in whether observations from MI in high-Fo olivine grains are relevant to the bulk LERZ melt.

Melt inclusion vapor saturation pressures for high-Fo olivine grains indicate the depths that those MI became entrapped. Subsequent crystal settling or entrainment in convective currents or ascending magma could cause crystals to be transported to either deeper or shallower levels. Melt inclusion entrapment depths from the Kīlauea Iki and Kapoho eruptions are also mostly < 5 km, although an appreciable number of MI have calculated entrapment depths of 6 to > 10 km (Moore et al., 2015; Tuohy et al., 2016). Deep seismicity was observed some months prior to the LERZ eruption (Mourey et al., submitted), however the shallow entrapment depths that we determined for most MI in high-Fo olivine grains from F8 are inconsistent with origins in deep magmas. We therefore consider the upward transport of high-Fo crystals from deep crystal accumulation storage zones into shallower reservoirs to be of lesser importance in the LERZ eruption compared to the Kīlauea Iki and Kapoho eruptions. Instead, we favor a model where high-Fo olivine grains in LERZ magmas formed within older primitive magmas that had ascended to shallow levels within the summit reservoir, and then underwent density-driven settling (Wieser et al., 2019). High-Fo olivine-bearing magmas

clearly became hybridized with colder melt during transport within the summit and along the ERZ, resulting in the hybridized melts of 1140 – 1150 °C that erupted from F8. High-Fo olivine grains in F8 lavas have relatively thin low-Fo rims, indicating that they became entrained within colder magma not long prior to eruption (Mourey et al., 2019).

More directly relevant information about LERZ magma source conditions come from MI entrapped within lower-Fo olivine grains that are in approximate equilibrium with the carrier liquid. As discussed, we determined vapor saturation pressures for only two MI in low-Fo olivine grains, and both have calculated entrapment depths of ~2.5 km. One solitary analysis of interstitial matrix glass from the rapidly quenched basaltic pumice, which was buffered from degassing due to surrounding crystals, had resolvable CO_2 (~220 ppm) and a calculated vapor saturation depth of 2.2 ± 0.6 km. This provides a rough constraint on the shallowest depth that melts travelling from the summit region to the LERZ could have attained, which is consistent with seismicity and deformation modeling of the down-rift dike propagation from Puʻu ʻŌʻō (Neal et al., 2019). Lastly, measurements of bubble CO_2 in a single clinopyroxene-hosted MI from F9 derive an entrapment depth of 3.8 ± 2 km. This depth is consistent with pre-eruptive seismicity in the LERZ and provides a loose estimate on storage depths of phase 1 evolved magma bodies in the LERZ.

In summary, we have determined rough constraints on pre-eruptive LERZ melt depths (≥ 2.2 km) and pre-eruptive CO_2 contents (≥ 220 – 280 ppm) from volatile measurements in matrix glasses and MI. Melt inclusions from the basaltic pumice tightly constrain the pre-eruptive H_2O contents of F8 melts at ~0.3 wt%, at least at their time of eruption in late May. We have also identified that F8 magmas were likely sourced from depths of 1 – 5 km within the Halemaʻumaʻu and South Caldera reservoirs, or along ERZ. These petrologic observations are in good agreement with seismicity and deformation models for of summit magma extraction and diking depths (Anderson et al., 2019; Neal et al., 2019), and do not require anomalously deep origins for magma feeding the LERZ eruption.

The relatively shallow magma source depths support the hypothesis that hydraulic head influences the style and volumes of eruptions at low elevations in the LERZ and further offshore (Epp et al., 1983; Patrick et al., 2015). A similar hydraulic connection

was noted by Patrick et al. (2019b) between the Halemaʻumaʻu lava lake and Puʻu ʻŌʻō lava levels (2008 – 2018), as the tops of these two magma columns were at roughly the same absolute elevations. The 2018 LERZ eruption occurred at ~200 m above sea level and the dike feeding the LERZ eruption was ~2 – 3 km beneath the surface in the LERZ (1.8 – 2.8 km below sea level [bsl]), and would be at absolute elevation below the Halemaʻumaʻu reservoir (0 – 1 km bsl) and comparable to the upper portions of the South Caldera reservoir (2 – 4 km bsl). Eruptions further offshore would amplify the effect of the hydraulic head. Low-elevation and offshore eruptions sourced from relatively shallow Kīlauea reservoirs can thereby drain large volumes of the summit reservoirs (Epp et al., 1983). Indeed, large lava-draining events in the LERZ have led to summit collapses during dike intrusion (and possible offshore eruption) in 1924, during the 1960 Kapoho eruption (Delaney & McTigue, 1994), and witnessed dramatically during the 2018 LERZ eruption (Anderson et al., 2019; Neal et al., 2019).

4.7.2 Recycling of degassed magmas at Kīlauea

Further insights into subsurface magma diversity at Kīlauea come from the range of S contents and $\delta^{34}S$ signatures of MI from F8 lavas. To understand our observations, we must consider processes occurring within the Kīlauea plumbing system in recent decades. In particular, we propose that the decade of degassing from the Halemaʻumaʻu lava lake may have had a significant impact on LERZ magmas.

Rowe et al. (2015) observed that MI erupted in 2008 from the Halemaʻumaʻu lava lake commonly contained 900 – 1300 ppm S (some anomalous S-rich MI contain 1400 – 1600 ppm S) but MI have S concentrations as low as 200 ppm. The presence of low-S MI was interpreted to indicate formation in S degassed melts. They also measured ~200 ppm S in matrix glasses and concluded that ~80% of initial S was degassed from the melt during ascent and circulation within the lava lake (Edmonds et al., 2013; Rowe et al., 2015). The degassed magma that circulated through the Halemaʻumaʻu lava lake from 2008 – 2018 is thought to have eventually erupted at Puʻu ʻŌʻō. This association is based on observed hydraulic connections between the lava lake and Puʻu ʻŌʻō (Patrick et al., 2015; 2019b), similar K_2O and TiO_2 compositions of magma erupting at both locations (Gansecki et al., 2019; Lee et al., 2019; Thornber et al., 2015), and a drastic decrease in

Pu‘u ‘Ō‘ō SO_2 emissions in the years following the onset of degassing at Halema‘uma‘u (Elias & Sutton, 2012; Elias et al., 2018a; Kern et al., 2020). Based on average SO_2 emission rates of 4.5 kt/d from the Halema‘uma‘u lava lake since 2011 (Beirle et al. 2014; Elias et al. 2018a), the cumulative mass of SO_2 degassed during convection within the lava lake from March 2008 – May 2018 (3710 days of activity) was ~16.7 Mt. Following the methodology of Kern et al. (2020), if we assume that the melt entering the lava lake contained 1100 – 1300 ppm S and degassed 80% of the total S (Rowe et al., 2015), and that the bubble-free melt contained 2% crystals (Thornber et al., 2015) and had a density of 2700 kg/m^3, the cumulative SO_2 emissions would require 3.0 – 3.6 km^3 (DRE) of source melt convecting and degassing over the lifespan of the lava lake.

Over this same approximate timespan (July 2007 to May 2018), ~1.2 km^3 of magma (DRE) was erupted from Pu‘u ‘Ō‘ō (compiled from Neal et al., 2019 and Orr et al., 2015). While comparing these time periods at Halema‘uma‘u and Pu‘u ‘Ō‘ō is not perfect due to a delay between magma circulating in the lava lake and erupting at Pu‘u ‘Ō‘ō (Patrick et al., 2019b; Thornber et al., 2015), the fundamental conclusion is that far more magma underwent extensive degassing in the Halema‘uma‘u lava lake than was erupted at Pu‘u ‘Ō‘ō. Assuming that magma erupting at Pu‘u ‘Ō‘ō was sourced entirely from Halema‘uma‘u degassed magma, ≥ 2 km^3 of magma that was degassed during lava lake circulation was not erupted. If some portion of magmas erupted from Pu‘u ‘Ō‘ō had not cycled through the lava lake, then the amount of degassed but non-erupted magma correspondingly increases. This importance of Halema‘uma‘u lava lake recycling has been discussed (Edmonds et al., 2013; Elias & Sutton, 2012; Patrick et al., 2019a), however the magnitude of non-erupted degassed magma that was recycled in the Kīlauea plumbing system over the last decade has perhaps not been fully appreciated. This large volume of degassed melt likely remains within the summit Halema‘uma‘u and South Caldera reservoir systems in varying states of hybridization with non-degassed magmas.

Sulfur and H_2O largely degas in tandem from Kīlauea melts (Dixon et al., 1991; Edmonds et al., 2013; Gerlach, 1986; Wallace & Anderson, 1998), so degassed Halema‘uma‘u lava lake melts would be depleted in both S and H_2O. Our estimated pre-eruptive melt S content of LERZ F8 magmas (~1110 ppm) is on the low range of S concentrations measured in MI from Halema‘uma‘u (Rowe et al., 2015). We assume the

lower S contents of LERZ melts are a consequence of the magma containing some degree of previously lava lake-degassed melt. This may also explain why the LERZ melts are below $SCSS^T$, in comparison to other eruptions during the 20th century (1959, 1960, 1969-1974, 1977 eruptions were sulfide saturated; Clague et al. 1995; Desborough et al. 1968; Helz and Wright 1992; Helz et al. 2017; Moore et al. 1980; Wieser et al. 2020b). Early phase 3 melts erupted from F8 were also relatively H_2O-poor (0.3 wt%) compared to H_2O measured in Kīlauea Iki MI (0.3 – 0.7 wt%, Anderson and Brown 1993; Wallace and Anderson 1998; Sides et al. 2014b; Tuohy et al. 2016), but were similar to MI from the early Halema'uma'u lava lake (Edmonds et al., 2013). Wallace and Anderson (1998) observe that undegassed Kīlauea melts across a range of compositions have an average H_2O/K_2O ratio of 1.3. Rapidly quenched MI from early phase 3 basaltic pumice dominantly contain 0.3 – 0.5 wt% K_2O and have maximum H_2O contents of 0.3 wt%, with resulting H_2O/K_2O of 0.6 – 1.0. These low H_2O/K_2O ranges are similar to MI from Kīlauea Iki and Pu'u 'Ō'ō, and submarine glasses from the Puna Ridge that Wallace and Anderson (1998) proposed to have experienced H_2O-loss during lava drain-back and recycling. We similarly attribute the low-H_2O in these early F8 LERZ melts to hybridization with previously degassed magmas. Unfortunately, we lack rapidly quenched MI from later in the LERZ eruption to constrain whether melt H_2O varied over time.

Paradoxically, despite the extremely high gas emissions from the LERZ fissures, the erupting melt was actually not particularly volatile rich compared to past Kīlauea eruptions. The relatively low F8 lava fountain heights support this hypothesis. The highest lava fountains at F8 during early phase 3 had maximum heights of ~80 m (Neal et al., 2019), whereas the1959 Kīlauea Iki fountain heights reached 600 m, the 1960 Kapoho fountain heights reached 450 m, the 1969 Mauna Ulu fountains reached 300 – 540 m (Swanson et al., 1979), and the 1983 Pu'u 'Ō'ō fountain heights reached 200 – 400 m (Richter et al., 1970; Wolfe et al., 1987). The total volatile content of the melt strongly controls lava fountain heights (Head & Wilson, 1987), although the conduit geometry and lava ponding with the F8 cinder cone would also modulate fountaining (Wilson et al., 1995). However, we point out that of these eruptions, the 2018 LERZ

activity was the only eruption that was preceded by a decade of sustained lava lake degassing.

Prolonged summit lava lake activity is not uncommon in Kīlauea's history. Persistent lava lakes have been present for much of the 19th and early 20th centuries (1823 [and likely earlier] – 1894 and 1906 – 1924) (Ellis, 1825; Patrick et al., 2019a; Wright & Klein, 2014), and presumably lava lakes would have similarly occurred during pre-historic phases of effusive activity (Holcomb, 1987; Swanson et al., 2014). Any period of sustained lava lake activity requires active melt convection to shallow depths, with concomitant H_2O and S degassing. The degassed melt would be then recycled back into the Kīlauea magma storage system. Furthermore, the drain-back of extruded lava is a relatively common occurrence during summit and rift zone eruptions at Kīlauea. Lava drain-back during the Kīlauea Iki eruption was well documented visually and petrologically (Richter et al., 1970; Wallace & Anderson 1998). Lava drain-back also occurred during early phases of the Pu'u 'Ō'ō eruption (Wolfe et al., 1987) and was documented most recently during the 2011 Kamoamoa eruption, where surface lava flows poured into a nearby ground crack (Orr et al., 2015). As with lava lake convection, lava drain-back events would recycle volatile depleted magma back into the Kīlauea storage systems (Wallace & Anderson 1998). We therefore strongly agree with the notion originally postulated by Dixon et al. (1991), Clague et al. (1995), and Wallace and Anderson (1998) that recycling of degassed magma is a common and important phenomenon at Kīlauea.

The subsequent vertical mixing of degassed magma is an inescapable consequence of increasing melt density with volatile loss and cooling. However, it is unknown to what degree recycled partially degassed magma is re-homogenized within larger magma storage regions, or to what depths degassed magma might sink. If mixing is incomplete, then the possibility exists for multiple heterogeneous magma batches with variable volatile contents to exist within Kīlauea's magma storage network. Observations of S-poor Puna Ridge submarine lava flows that erupted in water depths > 1 km, where hydrostatic pressure would have prevented S degassing, have been cited as strong evidence of the recycling of shallowly degassed magma batches through the Kīlauea system and ERZ (Dixon et al., 1991). In these cases, the signature of shallow degassing

was not completely re-homogenized by mixing, despite the Puna Ridge magmas travelling through the full Kīlauea magma transport system.

Melt inclusions are particularly suited to capturing heterogeneities in magma volatile contents. Melt inclusions preferentially form during periods of rapid crystal growth associated with subaerial degassing and cooling, and thereby trap and preserve evidence of degassing even if the magma is subsequently re-homogenized within the larger reservoir system. Water has been shown to rapidly re-homogenize in olivine-hosted MI (Bucholz et al., 2013; Gaetani et al., 2012) and would re-equilibrate with the bulk melt, but low S and CO_2 contents reflecting shallow degassing would be preserved in MI indefinitely.

In olivine-hosted MI from Pu‘u ‘Ō‘ō (measured from 1994 – 2013) and from the Halema‘uma‘u lava lake (measured from 2008 – 2013), S contents increase in more primitive olivine grains (Fo_{81-83}) and therefore magmatic S was expected to correlate with higher melt temperatures (Rowe et al., 2015; Thornber et al., 2015). However, this correlation between S and melt temperature does not hold for MI in high-Fo (Fo_{86-90}) olivine grains erupted in LERZ F8 magma, as many of these MI are S-poor. Furthermore, H_2O-CO_2 derived entrapment depths some of these S-poor, primitive MI are as shallow as < 1 – 2 km. These S-poor MI also have low $\delta^{34}S$ signatures (Figure 16), consistent with melt becoming isotopically light during SO_2 degassing. As has been shown, significant S degassing of Kīlauea melts only occurs at very low pressures, equivalent to < 100 – 200 m depth. These three independent lines of evidence lead us to conclude that at times in the past, highly primitive Kīlauea magmas (1200 – 1300 °C) reached very shallow depths and underwent substantial degassing. Convective degassing and recycling during 2008 – 2018 Halema‘uma‘u lava lake activity involved more evolved magma (Fo_{81-83}, rarely to Fo_{86}) (Rowe et al., 2015; Thornber et al., 2015) and is not an appropriate scenario to explain our observations of degassed MI in high-Fo olivine grains. A more analogous situation would be 1959 Kīlauea Iki eruption, which involved eruption and drain-back of primitive Fo_{86-90} bearing magma (Helz et al., 2017; Sides et al., 2014b; Tuohy et al., 2016; Wallace & Anderson 1998). Other eruptions of primitive melts have occurred throughout Kīlauea’s history (e.g., the prehistoric Kulanaokuaiki and

Pāhala Ash eruptions; Helz et al. 2015), and perhaps a number of these eruptions similarly involved lava drain-back or convective recycling of surface degassed melt.

One further observation needing attention is the occurrence of MI that are S-poor and δ^{34}S-light but contain fairly high CO_2 (bubble + melt) concentrations consistent with MI entrapment depths of 3 – 5 km. This combination of observations suggests that S degassed magma existed at South Caldera reservoir depths. Any Kīlauea melts undergoing S degassing would also degas substantial H_2O and would have almost completely degassed CO_2 (Gerlach, 1986). To reconcile S-poor melt with high CO_2 concentrations, it seems necessary that some S and CO_2 degassed melts descended to substantial depths and were then fluxed by CO_2-rich but relatively S- and H_2O-poor fluids ascending from greater depths (e.g., Type 1 gas; Gerlach 1986). Melt inclusions forming in this setting would thereby entrap melts that are S- and H_2O-poor but CO_2-rich. H_2O in olivine-hosted MI would quickly re-equilibrate with external melt H_2O concentrations during subsequent mixing (e.g., Barth et al., 2019; Bucholz et al., 2013; Hauri, 2002; Portnyagin et al., 2008), but the originally entrapped S and CO_2 concentrations would be preserved. This scenario requires that certain batches of recycled, shallowly degassed magma do not become extensively re-homogenized during vertical sinking through the Kīlauea magma storage system, but are in communication with ascending C-rich fluids (Figure 19). Pervasive CO_2 degassing occurs throughout the Kīlauea summit caldera during both eruptive and quiescent periods (Gerlach et al., 2002), indicating a steady influx of deep CO_2-staturated magma, so that fluxing of C-rich vapors through portions of the summit reservoirs should be expected.

4.7.3 The role of magma recycling in triggering the LERZ eruption

The underlying causes that led to the LERZ eruption are highly debated. Recently proposed eruption triggers include pressurization due to magma recharge (Mourey et al., submitted) or rain water infiltration (Farquharson & Amelung, 2020). Our interpretations from melt compositions and Kīlauea's degassing history lead us to propose an alternative hypothesis for the underlying cause of the 2018 LERZ eruption:

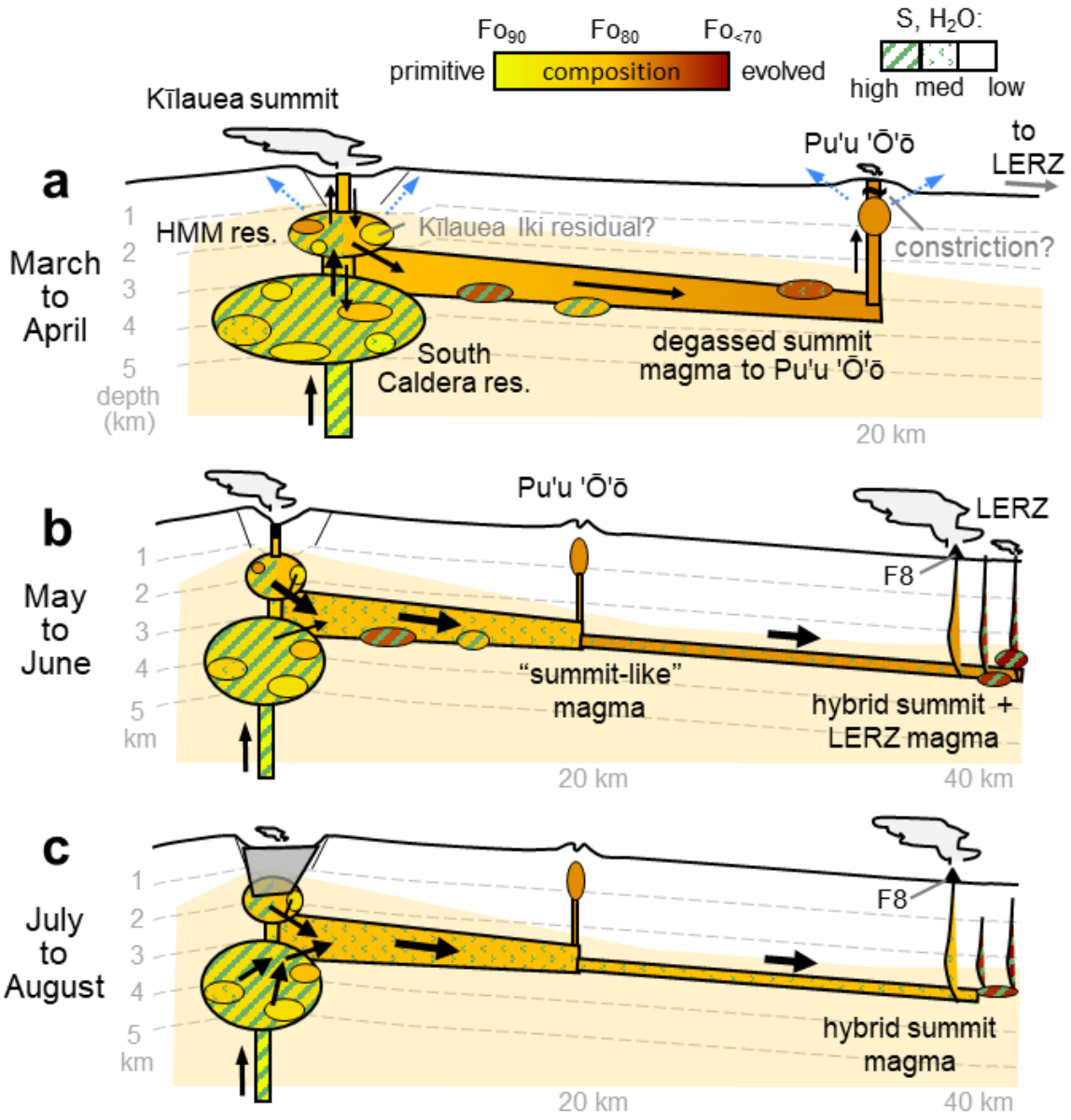

Figure 19. Conceptual model of processes occurring at Kīlauea's summit and East Rift Zone (ERZ) from March to August 2018. *(a)* Volatile-rich melts ascend into Kīlauea's South Caldera and Halema'uma'u (HMM) reservoirs, exsolving CO_2-rich gases. Convecting magma at the summit lava lake degasses S and H_2O and sinks to lower levels in the Halema'uma'u (+/- South Caldera) reservoir, as well as into the ERZ where it feeds the Pu‘u ‘Ō‘ō eruption. In March to April, a constriction within the shallow Pu‘u ‘Ō‘ō system decreases lava and gas extrusion, however continued lava lake degassing and inflow into the ERZ causes pressurization at Pu‘u ‘Ō‘ō and at the summit (blue arrows). *(b)* May to June: A dike propagates from beneath Pu‘u ‘Ō‘ō to feed the LERZ eruption. Magma sourced from the summit reservoir hybridizes with various degassed summit magmas, as well as ERZ and LERZ magmas. *(c)* July to August: The summit collapse broadens and melts sourcing F8 are increasingly hotter and carry more high-Fo olivine grains. Magma is sourced from the deep Halema'uma'u and South Caldera reservoirs, and includes antecrystic phenocrysts from variably degassed and primitive magmas.

Magma circulation and degassing in the Halema'uma'u lava lake causes substantial H_2O loss and likely slight cooling of the melt, both of which have an effect of increasing melt density and viscosity (Lesher & Spera, 2015). During the 10 years of Halema'uma'u lava lake and Pu'u 'Ō'ō connectivity, the magmas feeding Pu'u 'Ō'ō became increasingly comprised of lava lake-degassed magma, as evidenced by the progressive decrease in SO_2 emission rates from Pu'u 'Ō'ō starting within a year of the onset of lava lake degassing (Elias & Sutton, 2012). SO_2 emission rates from Pu'u 'Ō'ō decreased from 2 – 3 kt/d in 2005 – 2008 to < 0.3 kt/d in 2018 (Kern et al., 2020; Elias & Sutton, 2012; Elias et al., 2018a, b) (Figure 20). Meanwhile, degassing from Halema'uma'u remained relatively steady from 2009 – 2018, indicating a fairly constant magma supply into the summit reservoir (Beirle et al., 2014; Elias & Sutton, 2012; Elias et al., 2018a, b). As magmas feeding Pu'u 'Ō'ō became increasingly comprised of lava lake-degassed material, the increased density and viscosity of the magma may have made it less able to easily ascend and erupt at Pu'u 'Ō'ō. In addition, starting in ~2016 more K_2O- and TiO_2-rich magma compositions began erupting from both Halema'uma'u and Pu'u 'Ō'ō, with Pu'u 'Ō'ō magma becoming particularly K_2O-rich starting in 2017 (Gansecki et al., 2019; Lee et al., 2019) (Figure 20).

We propose that some combination of a changing magma source and the long-term decreasing magma volatile content increased magma viscosity to the point that the Pu'u 'Ō'ō conduit started clogging (Orr et al., 2015; Patrick et al., 2019b), which led to the observed decrease in both gas emissions (Kern et al., 2020) and lava effusion rates (Neal et al., 2019) from Pu'u 'Ō'ō in early 2018. The constriction at Pu'u 'Ō'ō led to the system-wide pressurization of Kīlauea in March to April (Neal et al., 2019; Patrick et al., 2019c). The pressurization built to the point that a dike rupture occurred beneath Pu'u 'Ō'ō, thus initiating the dramatic LERZ eruption sequence (Figure 19a, b). We therefore consider the 2018 LERZ eruption to be caused by a top-down process related to decreasing melt volatile contents and increasing magma viscosity. In this scenario, the LERZ eruption "trigger" was a decade in the making, since degassing began at the Halema'uma'u lava lake in 2008. Future efforts to mechanically model the consequences of changing viscosity on lava extrusion and pressurization at Pu'u 'Ō'ō would provide insights into the feasibility of this top-down model for the LERZ eruption trigger.

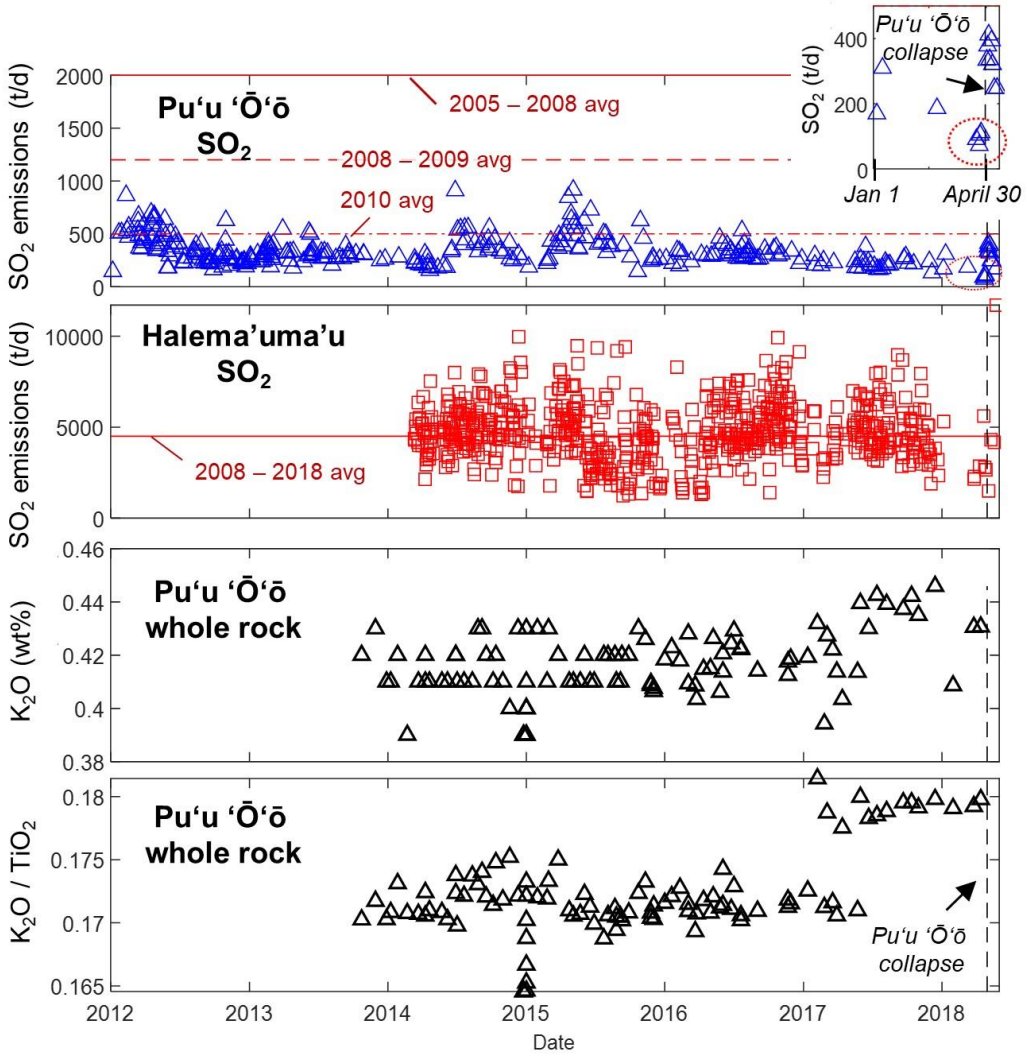

Figure 20. Time series of daily averaged SO_2 emissions from Pu‘u ‘Ō‘ō and Halema’uma’u, and of Pu‘u ‘Ō‘ō whole rock K_2O and K_2O/TiO_2 concentrations from January 2012 – May 2018. SO_2 emission rates at Pu‘u ‘Ō‘ō consistently declined after the onset of degassing from the summit Halema’uma’u lava lake 2008. Horizontal lines show average SO_2 emission rates from prior years. In the two months prior to the collapse of Pu‘u ‘Ō‘ō and onset of the LERZ eruption (vertical dashed line), SO_2 emission rates were among the lowest ever measured at Pu‘u ‘Ō‘ō (see inset at top). SO_2 emission rates from Halema’uma’u remained relatively constant from 2008 until the summit collapse began during the 2018 LERZ eruption. Changes in whole rock chemistry of Pu‘u ‘Ō‘ō lavas since ~2017 suggests that variations in the lava source or mixing proportions occurred in the 1 to 1.5 years prior to the Pu‘u ‘Ō‘ō collapse. Data are from Elias & Sutton (2012), Elias et al. (2018b), Gansecki et al. (2019), and Kern et al. (2020).

5. Conclusions and future work

5.1 Summary of observations and interpretations

We combine compositional, redox, isotopic, and volatile measurements of matrix glasses and MI from Kīlauea's 2018 LERZ eruption to provide insights into a variety of subsurface and lava emplacement processes. The diversity of lavas, phenocrysts, and glasses produced during the different phases of LERZ eruption make this a particularly rich dataset for improving our understanding of the 2018 eruption and the overall Kīlauea magmatic system.

Sulfur contents of matrix glasses and MI are particularly variable in LERZ glasses and MI. Maximum S concentrations in undegassed melts are governed by $SCSS^T$ values, which are dependent on melt temperature, fO_2, and FeO^T content. Rather than long-stored LERZ magmas being cold and degassed, evolved basalts erupted in phase 1 of the LERZ activity are significantly more S and Cl (and possibly H_2O) rich than more primitive Kīlauea melts. This was likely due to fractional crystallization enriching volatiles in the melt and also increasing melt FeO^T (and thereby $SCSS^T$). Melt inclusions from the dominant erupted magma from F8 contain 300 – 1390 ppm S and were generally entrapped at depths < 1 – 5 km. Sulfur concentrations in MI do not correlate with magma composition or entrapment depth, indicating complex degassing and recycling histories prior to entrapment. We estimate that melts feeding the bulk of the LERZ lava effusion from F8 had pre-eruptive S contents of ~1110 ppm, H_2O contents of 0.3 wt%, and CO_2 contents of at least 225 – 280 ppm. These estimates are roughly consistent with measured SO_2 emissions and gas ratios (Kelly et al., in prep; Kern et al., 2020), although pre-eruptive H_2O and CO_2 may have been as high as 0.45 wt% and 350 – 600 ppm, respectively. Based on updated degassing models of Gerlach (1986), large scale S and H_2O degassing from Kīlauea melts likely occurs at very shallow depths of ≤ 100 – 200 m below the surface, whereas CO_2 degassing occurs throughout the crust.

The difference between S in MI that are cognate to the F8 melt and in rapidly quenched RE interiors (900 – 1110 ppm S) and matrix glasses (100 – 500 ppm S) shows that ~55 – 90% of the magmatic S was degassed during ascent and extrusion, whereas 10 – 45% of S remained in the lava and degassed during surface flow. These estimates are

consistent with measured SO_2 gas emissions and help explain the substantial lava flow degassing that devastated downwind vegetation and resulted in local health hazards.

Redox conditions from matrix glasses and MI indicate initial magmatic fO_2 conditions of approximately QFM +0.3 to +0.4, and that the melts underwent reduction during SO_2 degassing, consistent with observations of gases and glasses from past Kīlauea eruptions (Gerlach et al., 2004; Helz et al., 2017; Moussallam et al., 2016). Over relatively short timescales (hours to days), we observe that olivine-hosted MI rapidly re-equilibrate to the external melt conditions (**Chapter III**), either becoming reduced (up to -0.5 log units) or highly oxidized (up to +1.5 log units) within the LERZ lava channel depending on the degree of S-loss or atmospheric oxidation that specific magma parcels experienced. Sulfur isotopic fractionation occurs during SO_2 degassing and causes $\delta^{34}S$ in the melt to decrease from initial values of +1.0 to +1.5‰ down to -2.5‰ in S degassed matrix glasses. This range is largely consistent with past $\delta^{34}S$ measurements of degassed subaerial and non-degassed submarine lavas (Sakai et al., 1982) and indicates that $\delta^{34}S$ signatures provide an additional means to identify S degassing from Kīlauea melts.

Melt inclusion volatile concentrations, isotopic degassing signatures, and vapor-bubble restored pressure estimates support the idea first introduced by Dixon et al. (1991) that the recycling of shallowly degassed magma is common at Kīlauea. In particular, many MI in high-Fo olivine grains are S-poor, indicating the ascent of high temperature melts to near-surface conditions followed by degassing, melt densification, and sinking. This scenario is similar to the lava drain-back events observed during the 1959 primitive Kīlauea Iki eruption (Richter et al., 1970; Wallace & Anderson, 1998). Melt inclusion entrapment depths of 1 – 5 km indicate that magma feeding the LERZ F8 eruption was sourced at depths consistent with the geophysically inferred Halemaʻumaʻu and South Caldera reservoirs, and do not require the input of more deeply-derived magmas during the LERZ eruption.

Given the preponderance of magma recycling during lava lake activity and lava drain-back events that have occurred at Kīlauea in historic time, and likely throughout the volcano's subaerial existence, we conclude that deeper and/or hotter melts do not necessitate higher H_2O and S concentrations in Kīlauea melts. The 2018 LERZ eruption was similar to 1960 LERZ eruption of Kapoho, with both eruptions having largely

shallow magma source regions and containing a diverse range of melts and phenocrysts, ranging from evolved to very primitive compositions. However, despite the prodigious gas emissions during the 2018 LERZ activity, erupted melts at F8 were likely somewhat volatile-poor compared to other Kīlauea eruptions, presumably due to the previous decade of melt degassing and recycling within the Halemaʻumaʻu lava lake.

5.2 Future directions

Future work to better constrain the temporal variation of LERZ pre-eruptive volatiles is warranted. Many conclusions presented here are based on rapidly quenched F8 basaltic pumice from late May because these samples experienced minimal degassing. Unfortunately, we lack similar rapidly quenched, chronologically constrained tephra from other periods of the eruption at F8. Most available F8 samples are lava flows that have undergone varying degrees of degassing and shallow re-equilibration. However, interstitial melt and RE in crystals from proximally quenched lava flows may retain relatively undegassed volatile conditions. Future work on these types of material will be important to better determine whether temporal changes in magmatic S, H_2O, and CO_2 accompanied the transition to hotter erupting melts in July and August. However, we note that gas ratios stay very consistent throughout F8 eruption (Kelly et al., in prep), suggesting that the volatile proportions in the melt may have remained constant, or must have changed proportionally.

Although we do not observe evidence of the F8 magma being sulfide saturated, extremely high SO_2 emission rates in late May and June cannot be accounted for petrologically, which raises the possibility that the breakdown of sulfides might play a role. Chalcophile trace element systematics could help inform the possible role of sulfides and sulfides in LERZ melts (Edmonds et al., 2018; Wieser et al., 2020b). Diffusion modeling of volatiles in RE channels could help constrain decompression rates and timescales of magma ascent at F8 (Ferguson et al., 2016; Lloyd et al., 2013) that can be compared to timescales of potential sulfide breakdown. Determining magma ascent rates would also provide constraints on physical models of F8 fountain heights and effusion rates.

At the time of writing (June 2020), the summit of Kīlauea is gradually inflating, indicating new magma recharge into residual shallow Halemaʻumaʻu reservoir (Poland et al., 2019). Additionally, groundwater ingress into Kīlauea's vastly deepened summit caldera is leading to the growth of a water lake (Hawaiian Volcano Observatory, 2019; Hsieh & Ingebritsen, 2019). Low-level S degassing at the summit is present in the form of solfatara fumaroles in the walls of the collapse caldera, as well as in high sulfate levels of the caldera lake waters (S. Hurwitz, personal communication). Our updated Gerlach (1986) degassing model indicates that the exsolution of Type 1 gas (CO_2-rich, with 15 mole % S) during magma ascent from South Caldera depths to the depth of the refilling shallow Halemaʻumaʻu reservoir can result in 5 – 10% of initial S degassing from the melt. We suspect that this type of degassing from the new magma ascending into Halemaʻumaʻu reservoir depths is the source of the observed summit fumaroles and lake sulfate. However, given the high solubility of S in Kīlauea melts until very shallow depths, and the large capacity of groundwater to scrub SO_2 gasses (Symonds et al., 2001), SO_2 emissions from future magma ascent to the near-surface may be challenging to observe. Consequently, measurements of CO_2 emissions and dissolved sulfate levels in the summit caldera lake and groundwater system (Hurwitz & Anderson, 2019), in conjunction with geophysical observations (Poland et al., 2019), may provide earlier indications of magma ascent.

The removal of large masses of recycled, partially degassed magma from the Halemaʻumaʻu and South Caldera reservoirs during the LERZ eruption may lead to newly ascending primitive magma undergoing less hybridization with previously degassed melts. This raises the possibility that future summit eruptions at Kīlauea may involve more volatile rich magmas, akin to the 1959 Kīlauea Iki eruption.

6. Bridge

In Chapter IV, I utilize a diverse petrologic dataset of melt inclusions, matrix glasses, and mineral compositions from Kīlauea Volcano's historic 2018 LERZ. By combining melt major element and volatile compositions, redox states, and sulfur isotopes, I was able to model the behavior of sulfur and other volatiles in Kīlauea melts and to compare these observations with independently measured gas emissions. Sulfur

concentrations and $\delta^{34}S$ signatures proved valuable to identifying degassing and magma recycling processes at Kīlauea.

In Chapter V, I apply a similar suite of petrologic analyses to Augustine and Mount St. Helens volcanoes. These two arc volcanoes share many similarities with one another, but Augustine is a sulfur-rich system whereas Mount St. Helens is relatively S-poor. Using redox measurement techniques introduced in Chapter III, I apply the framework developed in Chapter IV to understand how sulfur degassing affects melt redox and isotopic fractionation at Augustine and Mount St. Helens volcanoes.

CHAPTER V

SULFUR DEGASSING AND MAGMA OXIDATION STATE AT AUGUSTINE (AK) AND MOUNT ST. HELENS (WA) VOLCANOES

This chapter is in preparation for *Bulletin of Volcanology*. I am lead author on the paper, which involved project conception, sample preparation, analysis, data synthesis, and writing the manuscript. Paul Wallace (University of Oregon) served as my main advisor, aiding in project conception, data interpretation, and manuscript editing. Peter Kelly (U.S. Geological Survey) aided in project conception, data interpretation, and manuscript editing. Mary Benage, Michelle Coombs, Charles Mandeville, and Carl Thornber (U.S. Geological Survey) aided in project conception, sample collection, and analysis.

Overview

Sulfur (S) is a highly redox-sensitive element. Redox variations induced by magmatic S degassing can change magma oxygen fugacity (fO_2), which affects phase stability, S solubility, and further degassing. We test whether S degassing and fO_2 are linked in oxidized systems (NNO ~0 to +2) by conducting a combined EPMA, XANES, and S-isotopic study of glasses from recent eruptions of Augustine (AK, USA) and Mount St. Helens (WA, USA) volcanoes.

We analyzed melt inclusions and matrix glasses from the 2006 eruption of Augustine and from the 1980 – 1986 and 2004 – 2008 eruptions of Mount St. Helens. Sulfur in plagioclase-, amphibole-, and pyroxene-hosted melt inclusions ranges from 80 – 2600 ppm in Augustine samples, reflecting progressive S degassing during stages of magma ascent and storage. Historical eruptions at Augustine have been triggered by mafic recharge, and we analyze rare olivine-hosted melt inclusions in the 2006 deposits that provide the first direct measurements of these intruding basaltic melts. The olivine-hosted inclusions have high Al-basaltic compositions (23 wt% Al_2O_3) and are S-rich (3500 ppm) indicating a very volatile-rich source melt.

Augustine melt inclusions record a wide range of S concentrations and S speciation, but S^{6+} is the dominant S species in the melt. Fe-XANES-determined fO_2 in melt inclusions from Augustine's low silica andesitic magmatic composition are in good agreement with reported oxidation states of NNO +1 to +2 from Fe-Ti oxides in the same unit. However, there is textural evidence of redox disequilibrium within Augustine samples, possibly due to melt oxidation during S degassing. Sulfur isotopes ($\delta^{34}S$) in Augustine melt inclusions range from +4 to +9‰ in low-S melt inclusions and narrowly range from +5.9 to +6.2‰ in the high-S olivine-hosted inclusions. Some of the isotopic variation can be explained with open system degassing of SO_2 of H_2S from the high-S basaltic melt composition. However, melt inclusions with light $\delta^{34}S$ values cannot be derived from the basaltic parent melt through S degassing, which suggests temporal variations in source magmas at Augustine.

In contrast, melt inclusions in Mount St. Helens samples have low S (40 – 340 ppm). Mount St. Helens melt inclusions generally have lower proportions of S^{6+} speciation compared to Augustine glasses, which are in agreement with more reduced fO_2 estimates from Fe-Ti oxides (NNO 0 to +1). Mount St. Helens is a S-poor system overall and does not show strong relations between S and fO_2 changes. In summary, we find that magmatic oxidation and S-isotope fractionation can be linked to S degassing. Integrating these datasets can provide constraints on the extent and style of S degassing at relatively oxidized arc volcanoes.

1. Introduction

Interpreting the behavior of active volcanic systems is challenging because the magmatic phenomena controlling volcano eruptibility occur at depths 3 – 15+ km below the surface. However, volcanic gases provide a direct link to the subterranean magma that can be measured at the surface. SO_2 is the most routinely monitored volcanic gas because sulfur is relatively abundant in magmas and is readily detected in volcanic plumes by ultraviolet spectroscopy (Carn et al., 2017; Galle et al., 2003; Stoiber et al., 1983). However, to fully utilize SO_2 measurements as a monitoring tool, it is imperative to understand what volcanic phenomena are controlling the S being emitted. For example, whether S is primarily sourced from a stagnant shallow silicic body or from an ascending

deep mafic intrusion has substantial implications for assessing the state of volcanic unrest. However, interpreting S degassing signals is complicated because in addition to pressure, temperature, and melt composition, S solubility also strongly depends on the oxidation state of the melt (oxygen fugacity; hereafter fO_2) (e.g., Jugo et al., 2010).

Sulfur has widely ranging valence states, from S^{2-} to S^{6+}, leading to complex geochemical behaviors. In reduced silicate melts (< NNO +0), S occurs dominantly as S^{2-}, whereas S occurs as S^{6+} in more oxidized melt (Jugo et al., 2010). Sulfur dominantly degasses from melts as either H_2S (S as S^{2-}) or SO_2 (S as S^{4+}), depending on the melt fO_2, H_2O content, and depth of degassing (Burgisser & Scaillet, 2007; Carroll & Rutherford, 1988). Consequently, the exsolution of S can involve substantial S redox changes between the melt and gas (e.g., $SO_4^{2-}{}_{melt} = SO_{2\ vapor} + 0.5\ O_{2\ vapor} + O^{2-}{}_{melt}$).

These redox-changing gas exsolution phenomena produce relatively large equilibrium S-isotopic fractionations between the melt and gas (Fiege et al., 2015; Ohmoto & Rye, 1979). Oxidized S species are typically enriched in ^{34}S over ^{32}S (represented with $\delta^{34}S$ notation), with significant melt-gas isotopic fractionation during S degassing from oxidized melts ($SO_4^{2-}{}_{melt} \rightarrow SO_{2_{gas}}$ or $SO_4^{2-}{}_{melt} \rightarrow H_2S_{gas}$), and during SO_2 degassing from reduced melts ($S^{2-}{}_{melt} \rightarrow SO_{2_{gas}}$). Importantly, redox reactions during gas exsolution can result in significant changes in magmatic fO_2, with concomitant effects on mineral stability and further volatile solubility (Burgisser and Scaillet, 2007; Moussallam et al. 2016). Consequently, constraining magmatic fO_2 and S speciation is necessary for understanding S gas emissions and broader magmatic evolution. Melt inclusions in phenocrysts are uniquely suited to answer these questions because they can preserve records of magmatic evolution during different stages of degassing and crystallization.

Our study focuses on recent dacitic to andesitic eruptions at Augustine (AK, USA) and Mount St. Helens (WA, USA) volcanoes (Figure 1). Both volcanoes have rich petrologic histories and are sites of multidisciplinary monitoring. Augustine is an evolved/hybridized, highly oxidized system (NNO +1 to +2.5) where eruptions have been repeatedly triggered by mafic recharge events over the past 50 years (Power et al., 2010). Mount St. Helens is also an evolved, moderately oxidized system (NNO +0 to +1), with deep-sourced eruptions in 1980 and more shallowly-source eruptions in 2004 – 2008 from a more degassed melt (Sherrod et al., 2008).

1.1 Overview of Mt St. Helens and Augustine Volcanoes

Augustine has been frequently active through the past century, most recently with VEI 3 – 4 eruptions in 1976, 1986, and 2006. Each of these eruptions followed a similar pattern of a basaltic magma intruding a shallow silicic dike network, triggering an explosive phase, which eventually dwindles to dome-building activity (Larsen et al., 2010; Power et al., 2010). The eruptions include variably mixed magmas from basaltic andesite to high-silica andesite, with temperatures of 830 – 1020 °C and fO_2 of NNO +1.0 to +2.5 (Benage et al., submitted; Larsen et al., 2010; Webster et al., 2010). During the 1986 and 2006 eruption sequences, SO_2 emissions became elevated days to weeks prior to eruptive activity, peaked strongly during explosive phases (24 and 8 kt/day during 1986 and 2006 eruptions, respectively), and decreased to near detection limits (< 0.05 kt/d) within months after the eruptions ceased (McGee et al., 2010; Rose et al., 1988). Direct gas samples from Augustine's summit in 1987 indicate that Augustine is a very Cl- and S-rich, and H_2O-poor system (Symonds et al., 1990). Deformation during the 2006 eruption suggests a shallow, siliceous source at 2 – 4 km depths, and a deeper, presumably basaltic source at 7 – 12 km (Lee et al., 2010). Petrologic estimates and experimental phase equilibria indicate the siliceous source located between 4 – 6 km deep (De Angelis et al., 2020; Webster et al., 2010),

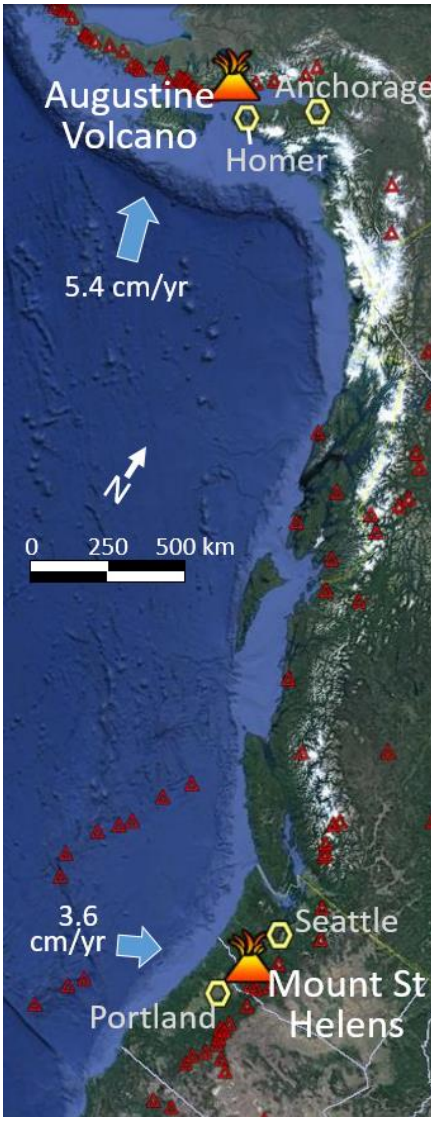

Figure 1. Locations of Augustine and Mount St. Helens volcanoes. Small red triangles are additional volcano locations from the Global Volcanism Program (http://volcano.si.edu/). Relative subduction velocity vectors from Ide (2013) for Alaska and McCrory et al. (2004) for Cascadia. Base map from Google Earth.

somewhat deeper than the shallow geodetic source. Paradoxically, despite high pre- and syn-eruptive SO_2 emissions, petrologic investigations of Augustine glasses find dominantly rhyolitic melts with low S concentration (Webster et al., 2010).

Mount St. Helens is the most active volcano in the Cascade arc. Recent activity includes the iconic VEI 5 eruption on May 18, 1980, which was followed by intermittently explosive activity through 1982 and then dome forming activity until 1986. The volcano re-awoke with phreatic eruptions followed by a gentle dome forming eruption from 2004 – 2008 (Sherrod et al., 2008). All eruptions were dacitic, with petrology and seismicity showing that the 1980s explosive eruptions were sourced from a range of depths, extending to 12 – 15 km, and the 2004 – 2008 activity was more shallowly sourced, from ~4 to 7 km (Lisowski et al., 2008; Pallister et al., 2008; Rutherford et al., 1985) (Figure 2). These depth estimates are consistent with recent seismic tomographic imaging of a presumed magma body between ~4 and 12 km depths (Kiser et al., 2016), although this tomographically inferred reservoir is laterally offset multiple km from the geodetically inferred magma source (**Chapter II**). The shallow magma reservoir depths sourcing the 2004 – 2008 Mount St. Helens eruption are similar to the inferred storage depths of Augustine's siliceous magmas (Figure 2).

Magma temperatures and fO_2 for the 2004 – 2008 Mount St. Helens eruption are estimated between 850 – 950 °C and NNO +0 to +1 (Pallister et al., 2008). SO_2 emission rates were lower during this eruption (< 0.24 kt/day) than during activity from the early 1980s (frequently > 1.0 kt/day; McGee and Casadevall 1994; Gerlach et al. 2008). The 1980s activity from Mount St. Helens was caused by the ascent of magma from substantial crustal depths, whereas the 2004 – 2008 activity was a reactivation of residual magma from the 1980s (Gerlach et al., 2008; Pallister et al., 2008). Slight changes in C isotopes in hydrothermal fluids provide a subtle indication that recharging magma was involved in the 2004 – 2008 eruptive activity (Bergfeld et al., 2017).

Both Augustine and Mount St. Helens remain active today, with numerous gas fumaroles and frequent earthquakes that are linked to the underlying magmatic system. These two systems share similar compositional, thermal, and storage properties, but have different styles of eruptive activity. At Augustine, the effects of mafic recharge are likely to play a large role, whereas deep recharge is not as obviously important for recent

Recent eruptions:
1976, 1986, 2006

Composition: Basaltic-Andesite to Dacitic

Eruption Trigger:
basaltic intrusions for
1976, 1986, 2006 eruptions

Temperatures: 830 - 950˚ C

ΔNNO = +1.5 to +2.5 (via oxide pairs)

Eruptive SO_2 degassing:
~20,000 t/d (1986)
~8,000 t/d (2006)

Current S emissions:
~ 99% S as SO_2
<< 10 t/d SO_2

from: *Rose et al. (1988); Larsen et al. (2010); McGee et al. (2010); Webster et al. (2010); USGS active monitoring*

Augustine Volcano, AK
2006

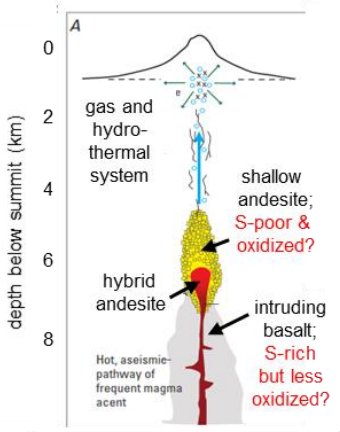

Modified from *Larsen et al. (2010)*, based on observations in this study

Recent eruptions:
1980-1986, 2004-2008

Composition: Dacitic

Eruption Trigger:
ascending silicic magma
1980 – deep source ; 2004-08 – shallow

Temperatures: 850 – 950 ˚ C

ΔNNO = 0 to +1 (via oxide pairs)

Eruptive SO_2 degassing:
> 1,000 t/d (1980s)
< 240 t/d (2004-08)

Current S emissions:
~ 99% S as SO_2
<< 10 t/d SO_2

from: *McGee and Casadevall (1994); Blundy et al. (2008); Gerlach et al. (2008); Pallister et al. (2008); USGS active monitoring*

Mount St. Helens, WA
1980s, 2000s

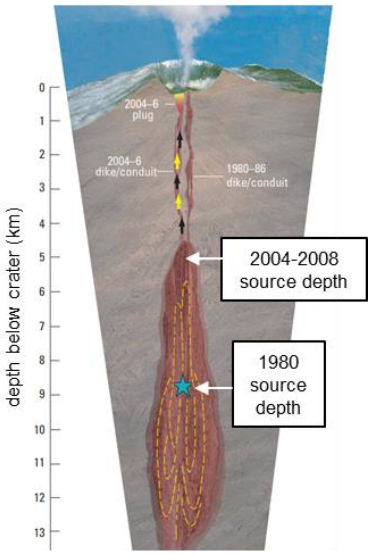

Modified from *Pallister et al. (2008)*

Figure 2. Summary characteristics of recent activity at Augustine (AUG) and Mount St. Helens (MSH) volcanoes, along with schematic models for the sources of their most recent eruptions. *(top)* The triggering of the 2006 eruption of AUG was due to a basaltic magma intruding into a 4 – 6 km andesitic-dacitic magma body. *(bottom)* The 1980s activity at MSH was sourced from deeply ascending magma, whereas the 2000s activity is thought to be sourced from the stagnant shallow remnants of that earlier material. Modified from Pallister et al. (2008) and Larsen et al. (2010).

eruptive activity at Mount St. Helens. Here, we use major element compositions, Fe and S speciation, and S-isotope analyses of melt inclusions from recent eruptions of Augustine and Mount St. Helens to explore the associations between melt chemistry, fO_2, and S degassing these relatively oxidized arc systems (NNO +0 to +2). The main questions we address are: *1)* whether S was primarily sourced from a resident shallow magma reservoir or from more primitive ascending magmas, and *2)* whether S degassing affected the oxidation state of the melts.

2. Methods

2.1 Samples

Tephra samples from Augustine (AUG) and Mount St. Helens (MSH) were obtained from archives at the U.S. Geological Survey's Alaska and Cascades Volcano Observatories. Augustine samples consist of lapilli-sized tephra (1.6 – 3.2 cm diameter) of low silica andesite (LSA) and high silica andesite (HSA) whole rock compositions. The hand-sample classification of the sample types followed the mineralogy and clast density identification criteria of Wallace et al. (2010) and Vallance et al. (2010). The LSA scoria samples are from a tephra fall deposit erupted during events 3 to 8 on January 13 – 14, 2006 (full sample name: 10AUMLC308; hereafter "LSA308"). The pumiceous HSA tephra are from a pyroclastic flow deposit erupted during events 10 – 12 (January 27 – 28), or possibly earlier (full sample name: 10AUMLC307_HSA2; hereafter "HSA2") (Coombs et al., 2010; Wallace et al., 2010). Mount St. Helens samples consist of pumice from the May 18, 1980 climactic eruption (2015Sel-MSH12; hereafter "MSH12", Seligman et al., 2018), pumice from a June 12, 1980 pyroclastic flow (SH229A), and vesicular dome-forming lava from November 30, 2004 (SH-305-1; hereafter "SH305").

Samples were gently crushed and sieved to 125 μm, and phenocrysts of plagioclase (pl), orthopyroxene (opx), clinopyroxene (cpx), and amphibole (amph) were picked, if present. Of the AUG samples, amphibole was present only in HSA2. In AUG sample LSA308, small unaltered olivine (ol) grains were also present in low abundance (Larsen et al., 2010; Tilman, 2008), and were specifically sought for sampling. We do not observe unaltered olivine grains in any other AUG or MSH samples. Grains were

mounted in CrystalBond® and singly or doubly polished to expose targeted melt inclusions (MI). Adhering matrix glass was present on most mounted grains. All samples were cleaned and polished in isopropyl alcohol, in order to avoid dissolving any water-soluble anhydrite ($CaSO_4$) that might be present. Anhydrite was observed as inclusions within silicate minerals in AUG samples (Larsen et al., 2010), but not within MSH material.

2.2 Electron microprobe

Geochemical analyses were conducted on individually polished grains mounted in epoxy or indium, and from randomly sectioned grain mounts. Samples were carbon-coated and glass and minerals were analyzed for major element compositions with a Cameca SX100 electron probe microanalyzer (EPMA) at the University of Oregon. Minerals were analyzed at 15 kV with a 3 μm spot size. Glasses were analyzed at 15 kV with a 10 μm spot size. During glass analyzes, Na, K, Si, Al, and Fe were measured first, and their concentrations were calculated using a linear time-dependent intensity correction (TDI) using the Probe for Windows software package (Donovan et al., 2007) to account for alkali mobility in glasses during electron beam excitement (Kuehn et al., 2011). TDI corrections were severe for some more primitive AUG MI, suggesting rapid Na^+ mobility likely in the presence of significant H_2O. Similar extensive alkali mobility in AUG glasses has been observed by De Angelis et al. (2020) and Benage et al. (submitted). An exponential or hyper-exponential TDI correction for Na-loss was applied to each individual analysis, depending on the extent of alkali loss. Relative uncertainties (1 SE) of glass analyses from repeated analyses of glass and mineral standards are generally < 0.8% for SiO_2, Al_2O_3, and CaO, < 2% for Na_2O, MgO, and Cl, < 5% for K_2O, FeO^T, and TiO_2, and 5 – 10% for MnO, P_2O_5, and S. Detection limits for all oxides in both mineral and glass analyses are < 0.1 wt% at 99% confidence levels, and are ~40 ppm for both S and Cl in glasses. Further analytical conditions for EPMA measurements are as described in **Appendix C**.

2.3 Post-entrapment crystallization corrections

Post entrapment crystallization (PEC) occurs readily in olivine-hosted MI during magma mixing and pre- or post-eruptive cooling (Danyushevsky et al., 2000). Olivine-hosted MI compositions from AUG LSA308 were corrected for PEC following the methods of Danyushevsky et al. (2000):

1) To account for diffusive FeO^T-loss from the MI into the host olivine, the measured 4 – 6 wt% FeO^T was restored to 7.5 wt% based on the AUG whole-rock MgO-FeO^T array (Larsen et al., 2010).
2) PEC was corrected with the Petrolog3 program (Danyushevsky & Plechov, 2011) with using the olivine-melt partitioning model of Danyushevsky (2001) and Toplis (2005), the melt density model of Lange and Carmichael (1987), while maintaining fO_2 fixed at NNO (using the $Fe^{3+}/\Sigma Fe$ ratio of Kress and Carmichael [1988]). Maintaining a fixed fO_2 condition assumes that MI diffusive redox re-equilibration through olivine hosts occurs fairly rapidly at LSA temperatures of ~1020 °C (Benage et al. submitted; Bucholz et al. 2013; Gaetani et al. 2012; Hartley et al. 2017; **Chapter III**).
3) Sulfur, Cl, and CO_2 are not included in Petrolog3 and were manually PEC-corrected. These species were considered to follow perfectly incompatible closed-system behavior during PEC (Callegaro et al., 2020) and the as-measured concentrations of these elements were diluted by the PEC correction factor to restore their concentrations at time of MI entrapment. Diffusive equilibration of H_2O in olivine-hosted MI occurs rapidly (Barth et al., 2019; Chen et al., 2011; Ferriss et al., 2018; Gaetani et al., 2012; Hartley et al., 2015; Hauri, 2002; Lloyd et al., 2013; Portnyagin et al., 2008; Sobolev & Danyushevsky, 1994), and we assume that the timescale of H_2O diffusion is faster than that of PEC. Consequently, we do not adjust measured H_2O contents for PEC.
4) We did not apply PEC corrections to MI hosted in non-olivine phases. Most of the non-olivine-hosted MI are likely cognate to their host melts and FeO^T, MgO, CaO, and Al_2O_3 measured in MI generally conform to whole rock and matrix glass arrays. Further detailed comparison of MI and matrix glasses may identify some anomalous plagioclase-, pyroxene-, or amphibole-hosted MI that have suffered from PEC.

2.4 H_2O and CO_2 by FTIR

Water and CO_2 concentrations in AUG glasses were measured at the University of Oregon using a Thermo Nicolet Nexus 670 Fourier transform infrared (FTIR) spectrometer interfaced with a Continuum IR microscope. Volatile concentrations were calculated using the Beer-Lambert law following the method of Stolper (1982). Wafer thicknesses were measured by micrometer (±2 μm) or by reflectance interference fringes (Wysoczanski & Tani, 2006). In rhyolitic compositions, the melt density and H_2O and CO_2 molar absorption coefficients depend on total H_2O concentration, which requires an iterative calculation process to converge on appropriate values. The H_2O absorption coefficient for rhyolitic compositions of AUG HSA2 glasses was calculated using the formulation of Leschik et al. (2004). The dacitic and high-Al basaltic H_2O absorption coefficients of Yamashita et al. (1997) were respectively used for AUG LSA308 dacitic MI and basaltic olivine-hosted MI. The CO_2 absorption coefficients of Behrens et al. (2004) were used for all dacitic and rhyolitic MI (CO_2 was unresolvable in olivine-hosted MI). Measurements were generally made in doubly-intersected MI and matrix glasses, with wafers 15 – 40 μm thick. A subset of MI was measured through host olivine or plagioclase crystals, where MI thickness was determined by comparing peak heights of Si-O bands for pure host mineral and for host + MI spectra (Nichols & Wysoczanski, 2007; Roman et al., 2006). We then do a scaled subtraction of the host spectra from the host + MI spectra to calculate the 3570 cm^{-1} H_2O and 1515 / 1430 cm^{-1} carbonate peak heights. For our analytical conditions and wafer thicknesses, the CO_2 detection limit is estimated to be ~50 ppm. However, olivine-hosted MI were only ~10 – 30 μm thick and were measured within thicker olivine sections (80 – 160 μm thick) to keep the sample structurally intact. In these conditions, CO_2 detection limits were > 200 ppm, and CO_2 was not resolvable in any analyzed olivine-hosted MI (n=4). As discussed above, measured H_2O concentrations in olivine-hosted MI were not corrected for PEC, as we assume H_2O re-equilibration at LSA temperatures occurred on a similar or more rapid timescale than PEC. Measured H_2O and CO_2 concentrations have 1 SE uncertainties of < 15%, which include uncertainties in glass thickness, density, and absorbance. Volatile contents in vapor bubbles were not measured, although the low CO_2 abundance and high solubility of H_2O in rhyolitic melts results in most volatiles being retained in the glass.

2.5 Fe- and S-XANES

Synchrotron-based micro X-ray absorption near edge structure (XANES) spectroscopy measurements to determine Fe and S elemental speciation of matrix glass and MI were conducted at GSECARS beamline 13-ID-E at Argonne National Laboratory's (Illinois, USA) Advanced Photon Source (APS). Analytical conditions are as-described in **Chapters III and IV** and **Appendices B and C**.

Spectral fitting was done with the LARCH program's XAS viewer (Newville, 2013) to correct for detector dead time and normalize and fit the Fe- and S-XANES data. All Fe-XANES spectra were carefully screened to exclude any mineral host or microlite signatures from interaction with the beam at depth so that only clean glassy spectra are presented here. A combination of host contamination and Fe-oxide nanolites (**see Chapter III**) caused many Fe-XANES analyses to be discarded. We use the Fe-XANES calibration of Fiege et al. (2017) for felsic glasses, which includes a large set of dacitic and rhyolitic experimental glasses that are relevant to AUG and MSH glasses. However, we note that uncertainty remains in the compositional effects of dacitic and rhyolitic glasses due to a limited compositional range of the calibration datasets (Cottrell et al., 2009; Dauphas et al., 2014). Fe speciation is used to calculate fO_2 through the composition dependent 1-atm formulation of Kress and Carmichael (1991). At the relatively low temperatures and pressures of AUG and MSH melts, the 1-atm fO_2 formulation of Kress and Carmichael (1991) more closely parallels redox buffer curves than does the pressure-dependent fO_2 formulation of Kress and Carmichael (1991).

Due to the lower penetration of X-rays at the S Kα energy and the low S-content of most host minerals (Callegaro et al., 2020) compared to Fe, smaller diameter and singly-intersected MI could be analyzed by S-XANES. Consequently, we have a much larger dataset of S-XANES measurements than Fe-XANES measurements. S-XANES measurements were used to calculate S speciation through the peak fitting calibration presented in **Chapter III**. Throughout this paper, we report the proportions of Fe and S valence species as percentages, for ease of discussion.

2.6 $\delta^{34}S$ analyses by Secondary Ion Mass Spectrometry

Sulfur isotope ($\delta^{34}S$) measurements of MI and matrix glasses were determined using the Cameca IMS 1280 SIMS at the Northeast National Ion Microprobe Facility (NENIMF) at Woods Hole Oceanographic Institute (Woods Hole, MA). We removed prior carbon-coats and pressed samples into indium mounts, which were then gold coated. We followed the analytical methods of Fiege et al. (2014) and Mandeville et al. (2008) using a 10 μm Cs^+ primary beam, 10 kV accelerating voltage and 1 – 2 nA beam current. Samples were pre-sputtered for 180 s using a 30x30 μm raster area to remove surface contaminants, and then analyzed using a smaller 20x20 μm raster area to minimize extraneous surface contamination. Small olivine-hosted MI with high S-concentrations were pre-sputtered for 60 s over a 20x20 μm area and analyzed within a 10x10 μm area. Secondary ions of ^{34}S and ^{32}S were discriminated with a mass resolution power of 4000 – 5500 and counted using an electron multiplier.

^{32}S ion yields ranged from $4x10^4$ to $1x10^6$ depending on S concentration of the AUG glasses (200 – 3500 ppm S). $\delta^{34}S$ analyses of AUG glasses have propagated 1 SE uncertainties of ±0.4 – 1.1‰, with one MI having a larger uncertainty of ±2.2‰. See **Appendix C** for further analytical details.

3. Results

3.1 Mineralogy and melt inclusion textures and major element compositions

Mineral textures and compositions are diverse in both AUG and MSH samples, and have been described in detail elsewhere (e.g., Pallister et al. 2008; Streck et al. 2008; Thornber et al. 2008; Tilman 2008; Larsen et al. 2010). Here, we focus on describing specific textural features that have important implications for interpreting MI compositions and redox variations within the magmatic systems.

3.1.1 Augustine

Plagioclase grains in both AUG LSA308 and HSA2 samples are highly zoned (An_{49-90}, where An is 100*Ca/[Ca+Na+K] in mole fractions) and are commonly sieve-textured. Abundant MI and re-entrant (RE) melt channels occur within discrete growth zones within plagioclase phenocrysts. Plagioclase grains contain sulfide and anhydrite

mineral inclusions, and we have observed both types of S-rich phases occurring within different growth zones in a single phenocryst. Pyroxenes, particularly clinopyroxene, contain abundant Fe-Ti oxide inclusions, but also contain sulfides and rare anhydrite (Figure D1). Apatite inclusions are relatively common within plagioclase, pyroxene, and amphibole phenocrysts. Amphibole is abundant in HSA2 but is totally absent in LSA308 tephra. Fe-Ti oxides are common and a number of oxides in both LSA308 and HSA2 contain sulfides. Where in contact with the matrix glass, sulfide-bearing portions of Fe-Ti oxide clusters are visibly breaking down. Sulfides in contact with matrix glasses have a mottled appearance and the surrounding matrix glass is stained red-orange due to sulfide break-down. Fluid inclusions are also present in plagioclase and pyroxene grains.

Melt inclusions occur in all phases and are generally small (< 50 μm diameters) (Figure D1). Melt inclusions have both clear and brown colorations. Small (<< 1 μm) dark inclusions are present within some of the brown MI, similar to the "dust" described by Danyushevsky et al. (2002). However, other brown MI have no daughter minerals visible either optically or with electron microscopy. Most plagioclase- and pyroxene-hosted MI are rhyolitic, although some rare MI in LSA308 plagioclase and clinopyroxene hosts have dacitic and andesitic compositions (Figure 3). Melt inclusions in HSA2 phenocrysts are S-poor, with plagioclase- and amphibole- hosted MI containing ≤ 200 ppm S, and some pyroxene-hosted MI containing up to 350 ppm S (Figure 4). Melt inclusions within sieve zones in high-Ca (An_{80-90}) plagioclase grains in HSA2 are not compositionally different than MI in $An_{40–60}$ plagioclase grains, indicating that the sieve zones in high-An plagioclase grains formed during mineral dissolution in more evolved magmatic conditions and may have been open to the exterior melt at the time of eruption (Figure 5).

LSA308 MI in plagioclase and pyroxene phases are mostly dacitic and generally contain 200 – 400 ppm S. The few LSA308 MI with more primitive dacitic to andesitic compositions are notably more S-rich, containing 600 – 2600 ppm S (n=3). One orthopyroxene-hosted MI contains a large sulfide, which was likely co-trapped during MI formation. This sulfide-bearing MI contains 600 ppm S, ~4 wt% FeO^T, and ~50% $S^{6+}/\Sigma S$, providing an example of the S concentrations at sulfide saturation (SCSS) at these conditions. Two clinopyroxene-hosted MI with higher S (1100, 2700 ppm) contain more

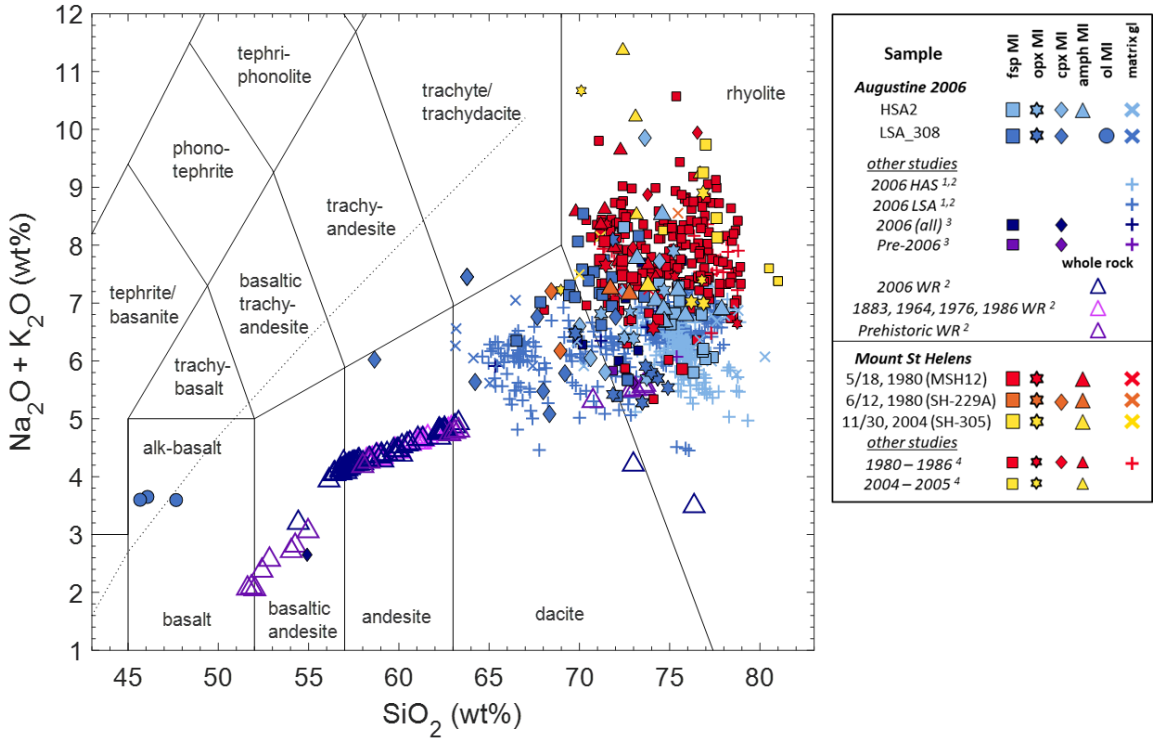

Figure 3. Total alkalis versus silica diagram for MI, matrix glasses, and whole rocks from AUG 2006 (and older samples), and MI and matrix glasses for MSH 1980s and 2000s eruptions. Data from other sources are slightly smaller symbols. Other data sources are: [1]Benage et al. (submitted), [2]Larsen et al. (2010), [3]Webster et al. (2010), and [4]Blundy et al. (2008). See Figures D2, D4 for data of each individual volcano.

FeO^T (5 – 6 wt%) and increased $S^{6+}/\Sigma S$ proportions (60 – 90% S^{6+}), both of which increase SCSS values (Jugo et al., 2010; Smythe et al., 2017) and allowed these MI to remain sulfide-undersaturated even with higher S concentrations. LSA308 MI are generally more Cl-rich than HSA2 MI, containing 0.3 – 0.4 wt% Cl compared to HSA2 MI that contain 0.2 – 0.3 wt% Cl. However, two HSA2 plagioclase-hosted MI are extremely Cl-rich, containing 0.7 – 0.8 wt% Cl. Webster et al. (2010) also measured HSA MI with up to 0.8 wt% Cl. It is unclear if these Cl-rich compositions represent a unique magmatic/pegmatitic/hydrothermal environment, although these MI have otherwise unremarkable major element compositions. These high Cl concentrations indicate that some portions of the HSA magmas were likely saturated at low pressures with a H_2O-poor, Cl-rich saline brine (Webster et al., 2010, 2015; Webster & De Vivo, 2002).

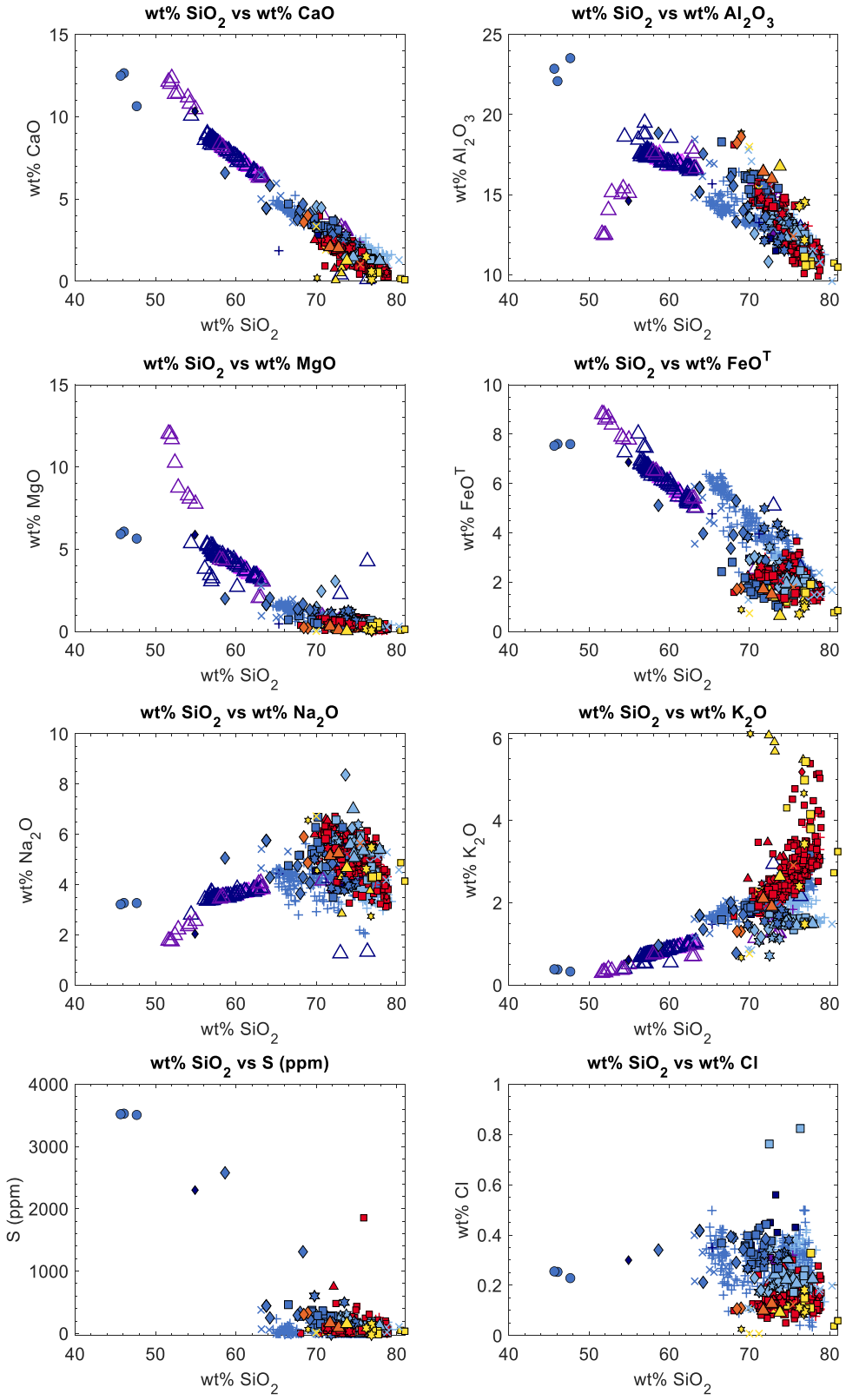

Figure 4. Major element Harker diagrams of MI, matrix glasses, and whole rock composition from AUG and MSH samples. Symbology is as in Figure 3. See Figures D3, D5 for data of each individual volcano.

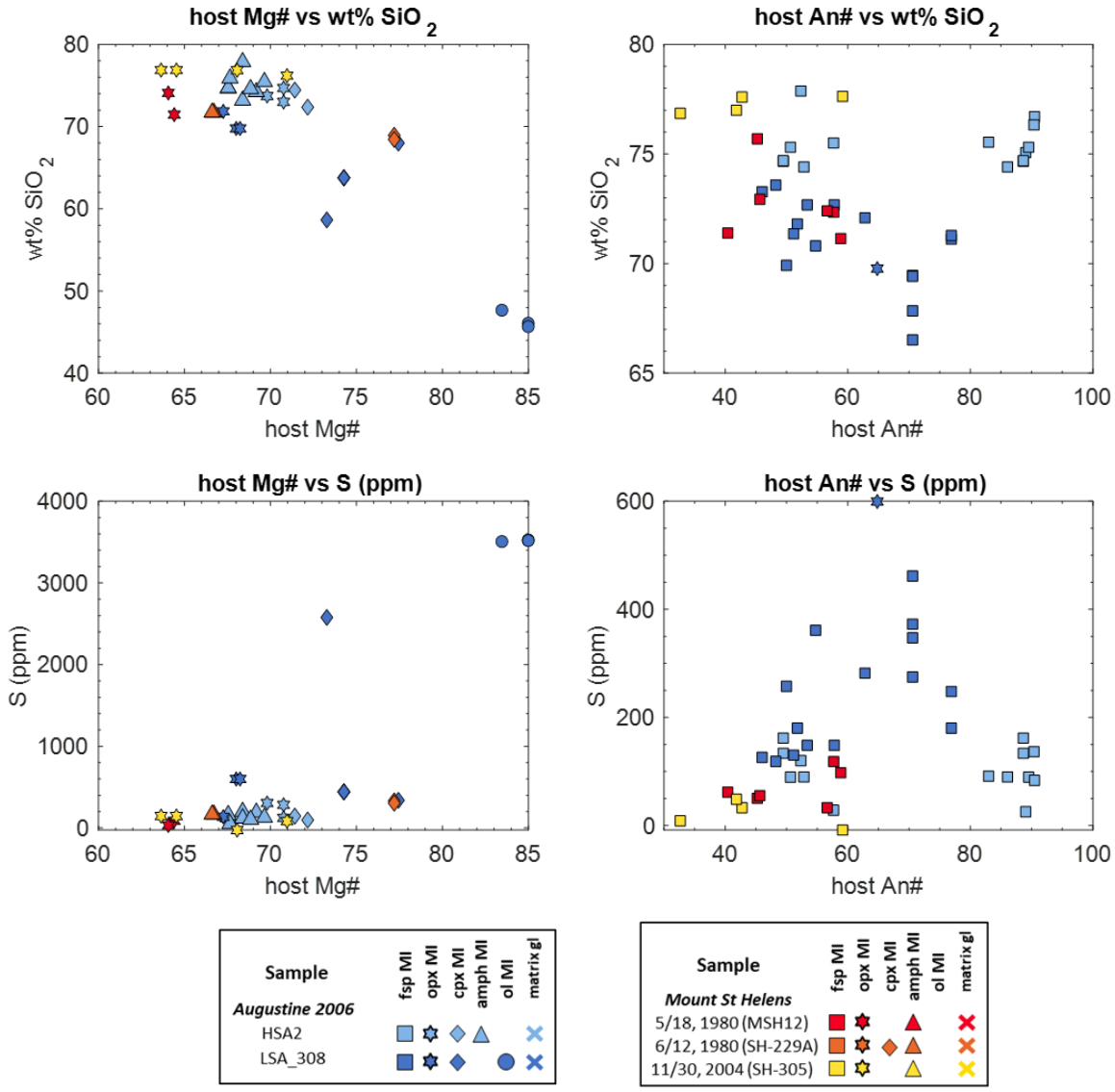

Figure 5. Variations in SiO_2 and S concentrations of AUG and MSH MI with mineral-host compositions. *(left)* Mg# is 100*Mg/(Mg+Fe) in mole fractions for orthopyroxene, clinopyroxene, and is equal to the forsterite (Fo) content of olivine. *(right)* An# is 100*Ca/(Ca+Na+K) in mole fractions for plagioclase. The single hexagram symbol on the *(right)* plots is a MI within an orthopyroxene grain that has a co-trapped plagioclase grain, where the An# of plagioclase is plotted. Note the bimodal plagioclase compositions in the AUG HSA2 sample.

Matrix glasses in HSA tephra are exclusively rhyolitic, whereas matrix glasses in LSA308 tephra range from rhyolitic to dacitic. Many LSA308 matrix glasses are more mafic than the majority of LSA308 MI, which has been interpreted as evidence of hybridization with the intruding basaltic magma (Larsen et al., 2010). Matrix glasses in both LSA308 and HSA2 samples are degassed, containing < 100 ppm S (n=16). However, RE channels contain higher S, with RE channels in HSA2 orthopyroxene phenocrysts containing 180 – 250 ppm S (n=2) and a RE channel in a euhedral olivine phenocryst in LSA308 containing 380 ppm S.

Olivine grains in erupted products of the AUG 2006 eruption have been described by Larsen et al. (2010) as constituting 0 – 2% modal abundance of the mineral cargo across LSA, HSA, and intermediate clast types. They describe a number of olivine textures, including euhedral, hopper, pyroxene-rimmed, and symplectite-rimmed phenocrysts. We observe both euhedral olivine and symplectic-rimmed olivine grains in LSA308 samples.

Euhedral olivine phenocrysts are small (< 300 μm diameters), chartreuse colored, and contain abundant Cr-spinel inclusions (Figure 6). We analyzed a small number of euhedral olivine phenocrysts and find core compositions of Fo_{83-85} (where Fo is forsterite content: 100*Mg/[Mg+Fe] in mole fractions). Larsen et al. (2010) measured core compositions of Fo_{83-86} in euhedral olivine phenocrysts in a number of AUG 2006 samples, indicating this was the main olivine population in an intruding basaltic magma that became widely dispersed in variably hybridized magmas. These euhedral olivine phenocrysts have 5 – 10 μm rims of lower-Mg compositions to Fo_{77}, and some have thin orthopyroxene reaction rims (Larsen et al., 2010) (Figure 7).

A number of the euhedral olivine phenocrysts contain MI that have partially crystallized to various degrees (Figure 6). However, we found rare, small oval MI (<30 μm long axes dimensions) that remained largely glassy. We were able to analyze three of these glassy olivine-hosted MI by EPMA, S-XANES, and SIMS. Post-entrapment crystallization corrections of 11 – 13% olivine (by mass) were applied to the MI, and measured 4 – 6 wt% FeO^T was restored to 7.5 wt% based on the AUG whole-rock MgO-FeO^T array (Larsen et al., 2010). These PEC-corrected olivine-hosted MI have basaltic to alkali-basaltic compositions, which are the most primitive glasses that have been

measured from historical eruptions of AUG. The PEC-corrected olivine-hosted MI have very high CaO and Al_2O_3 (10 – 13 wt%, and 22 – 24 wt%, respectively), and are also very S-rich, containing a consistent 3500 ± 10 ppm S. The olivine-hosted MI have 0.25 ± 0.01 wt% Cl, which is comparable to Cl contents of LSA308 MI and matrix glasses. The average S/Cl molar ratio of the olivine-hosted MI is ~1.6, which is > 10x that of dacitic and rhyolitic MI in LSA308 and HSA2.

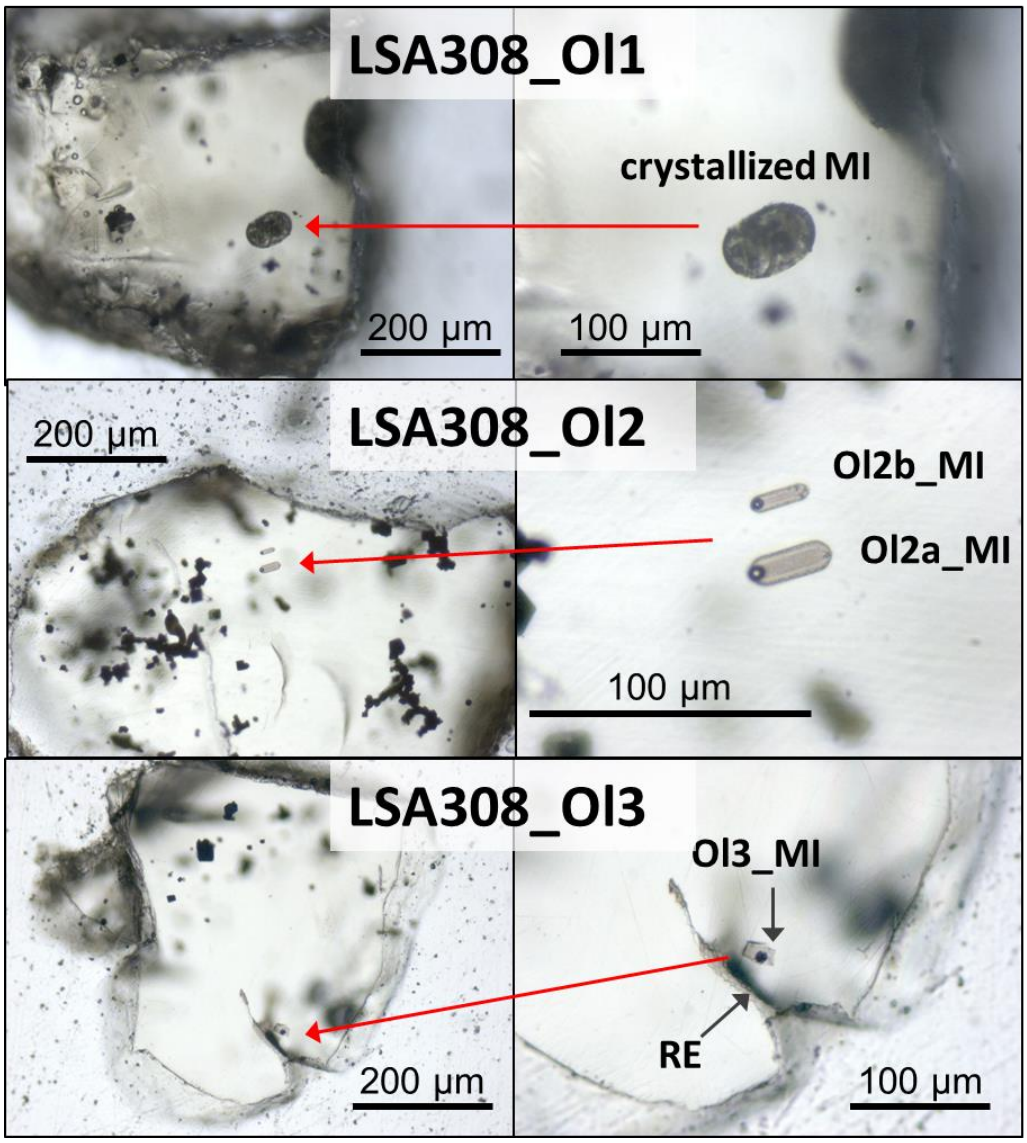

Figure 6. Euhedral olivine phenocrysts in AUG LSA308 that contain crystallized *(top)* and glassy *(middle, bottom)* MI. Cr-spinel inclusions (black rectangular habits) are abundant in most olivine phenocrysts. Melt inclusions in the middle and lower panels are the three olivine-hosted MI analyzed in this study. A re-entrant (RE) channel within the olivine in the bottom panel was also analyzed.

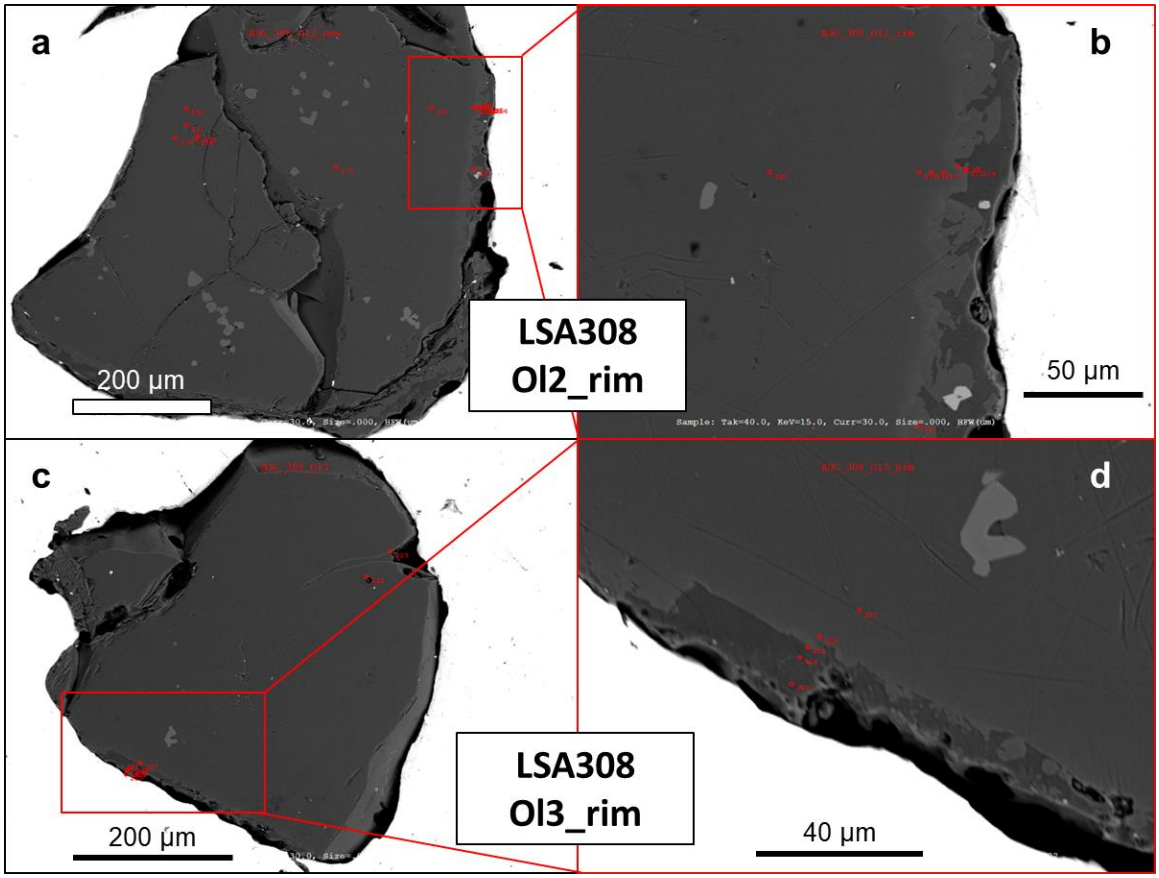

Figure 7. *(a, c)* Backscattered electron images (BDE) of two euhedral olivine phenocrysts in AUG LSA308 (see previous figure) with *(b,d)* magnification of grain edges showing thin low-Mg rims +/- orthopyroxene growth. Red circles on figure are locations of EPMA analyses. The low-Mg olivine rims appear lighter in BSE due to the increased abundance Fe compared to the high-Mg cores.

We analyzed only one LSA308 olivine with a symplectite texture (Figure 8). This olivine was dark green in color and was chemically unzoned, with a core-to-rim composition of $Fo_{75\text{-}77}$, consistent with observations of symplectite olivine by Tilman (2008) and Larsen et al. (2010). Symplectite textures are formed by the decomposition of olivine to orthopyroxene and magnetite in the presence of changing melt redox conditions (Johnston & Stout, 1984; Tilman, 2008). The particular symplectite olivine grain we analyzed did not contain any MI. Symplectite rims render the olivine grains opaque, so it is unknown whether MI are present in other symplectite-rimmed olivine grains. Further investigation of MI in symplectite olivine which would be valuable to compare to MI in the euhedral olivine described above.

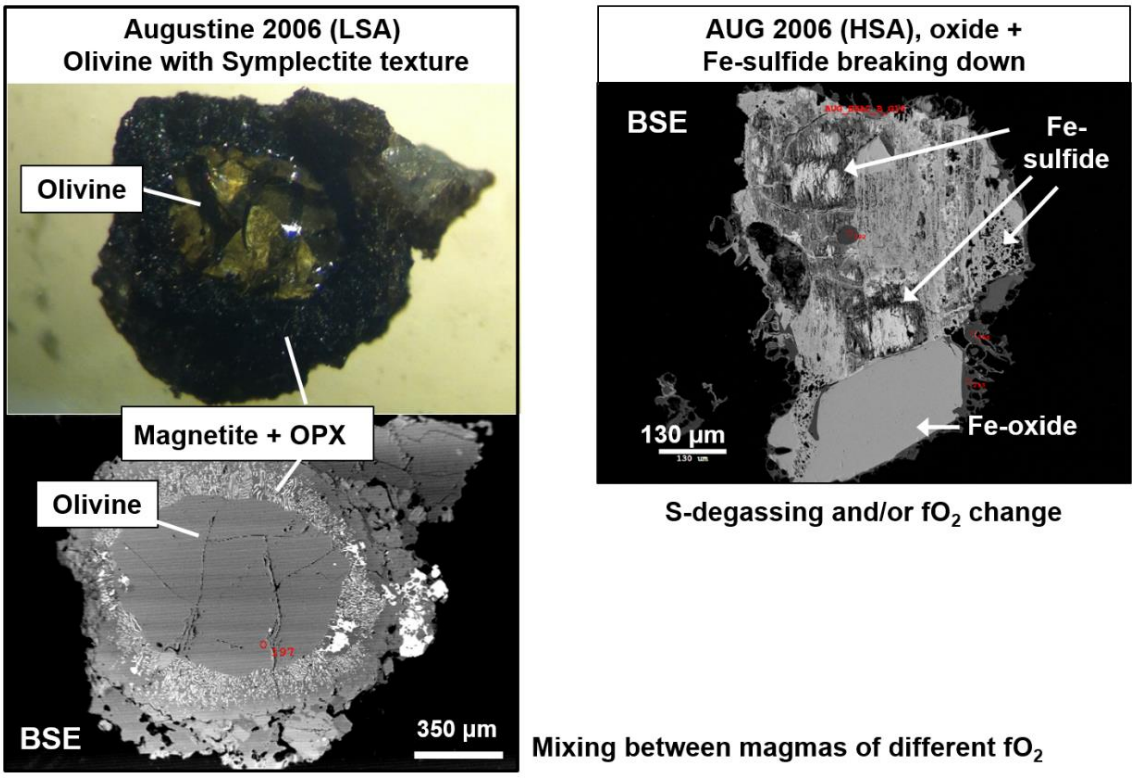

Figure 8. Mineral textures show evidence for significant fO_2 and/or sulfur fugacity (fS_2) variations within the AUG 2006 magmatic system. *(left)* Olivine in LSA308 with symplectite texture (microphotograph and back-scattered electron image). *(right)* Sulfide in HSA2 with mottled texture during decomposition.

3.1.2 Mount St. Helens

For the purposes of this study, the most notable observation regarding MSH minerals and MI is that they have much less compositional diversity than AUG material. Melt inclusions are present in all phases (plagioclase, clinopyroxene, orthopyroxene, and amphibole), but are generally small (< 50 µm diameters) (Figure D1). Almost all MSH MI and matrix glasses are rhyolitic, with the four most primitive MI having high-Si dacitic compositions (Figures 3 – 5). Some MI in MSH 1980 and 2004 samples contain very high K_2O, up to 4 – 6 wt%. Fluid inclusions are common in plagioclase, with a number of plagioclase phenocrysts having sieve textures that include both fluid and melt inclusions. Sulfides are rarely present within amphibole and plagioclase grains. Apatite is a common inclusion in larger phenocrysts of all phases.

Almost all MI contain 0.1 – 0.2 wt% Cl and < 200 ppm S. Two higher-S exceptions are clinopyroxene-hosted MI with dacitic compositions from the June 12, 1980 sub-plinian sample (SH229A), which contain 300 – 330 ppm S (n=2). Clinopyroxene phenocrysts are rare in the MSH samples and these were the only two clinopyroxene-hosted MI that we analyzed. Some higher S concentrations of 400 – 800 ppm have been measured in plagioclase- and amphibole-hosted MI from May to July 1980 pumice samples by Blundy et al. (2008, 2010). These authors also report one high-SiO_2 plagioclase-hosted MI from an October 1980 dome fragment that contains 1850 ppm S, however it is unlikely that this anomalous measurement is representative of the overall magmatic system. Collectively, these MI with 300 – 800 ppm S are the highest-S glasses measured in historically erupted MSH material.

3.2 H_2O-CO_2 measurements

Only a small number of AUG MI and matrix glasses were analyzed for H_2O and CO_2 by FTIR. No samples from MSH were analyzed in this study, although we present H_2O measurements of MSH glasses from the 1980s by Blundy et al. (2010) for comparison to AUG samples. H_2O measured in AUG HSA2 and LSA308 MI ranges from < 0.5 to 3.6 wt%, and CO_2 ranges from below detection limits (~50 ppm) to 140 ppm (Figure 9). H_2O is widely variable at given CO_2 concentrations. Given the relatively slow ascent rate prior to the 2006 eruption (Benage et al., submitted), we interpret this range of H_2O to be due to diffusive H_2O loss during ascent (Myers et al., 2016; Severs et al., 2007). Olivine-hosted MI from AUG have particularly low H_2O (0.3 – 1.0 wt%), which is likely a function of the small size of these MI and of the rapid diffusivity of H_2O through olivine (Gaetani et al., 2012) at the relatively high LSA temperatures of ~1020 °C (Benage et al., submitted). At MSH, H_2O contents measured by Blundy et al. (2010) are also widely variable (< 0.5 – 7 wt%) and have been interpreted as a consequence of CO_2 fluxing. However, this range of H_2O but may also reflect variable ascent rates and diffusive dehydration, given that evidence exists for prolonged magma ascent during the 1980 – 1986 MSH eruptive period (Cashman & McConnell, 2005; Riker et al., 2015; Rutherford & Hill, 1993).

The most H_2O-rich MI from AUG measured in this study are consistent with measurements of AUG 2006 MI by Webster et al. (2010). The H_2O-CO_2 vapor saturation pressures calculated for these H_2O-rich rhyolitic melts using VolatileCalc 2.0 (Newman & Lowenstern, 2002) at 960 °C (the average temperature of LSA and HSA melts) are 1 to 1.5 kbar. Recent phase equilibria experiments by De Angelis et al. (2020) reproduce HSA mineralogy and compositions at pressures of 1.2 – 1.7 kbar, which is in agreement with the calculated MI vapor saturation pressures. With a starting composition of 4.5 wt% H_2O and 150 ppm CO_2 (1.6 kbar saturation pressure), closed system degassing with between 0 – 3 wt% initial vapor can explain a range of the higher H_2O MI in evolved AUG samples (Webster et al., 2010) (Figure 9a). We note that olivine-hosted MI in AUG Pleistocene basalts contain up to 7 wt% H_2O and have estimated storage pressures of 4 kbar (Zimmer, 2009; Zimmer et al., 2010), and clearly did not experience shallow magmatic storage of modern LSA and HSA magmas. Melt inclusions from MSH eruptions between 1980 and 1986 also have higher maximum H_2O and CO_2 contents than modern AUG MI (Blundy et al., 2010), consistent with deeper storage conditions of MSH 1980s magmas compared to recent AUG magmas (Figure 9b).

3.3 Fe and S speciation and fO_2 conditions

Due to X-ray interferences with Fe-bearing host minerals and groundmass phenocrysts at depth, and because of the presence of Fe-oxide nanolites in many MI, only a small number of MI and matrix glasses were successfully measured by Fe-XANES in AUG samples. Only one HSA2 MI was measured by Fe-XANES, and it has the highest calculated redox state of the entire AUG data set (NNO +3.2) (Figure 10). More MI were successfully measured by Fe-XANES in LSA308 samples. LSA308 MI have calculated redox states ranging from NNO +0.5 to +2.0, with the majority of MI (8 of 13) having a narrower fO_2 range of NNO +1.0 and +1.5. This fO_2 range agrees very well with fO_2 estimates from Fe-Ti oxides measured in LSA samples by Benage et al. (submitted). We note that the fO_2 calculations of Benage et al. (submitted) use the oxythermometer of Ghiorso and Evans (2008) and are 0.5 to 1.0 log units more reduced than fO_2 estimates of Larsen et al. (2010) and Webster et al. (2010) who use the QUILF oxythermometer (Andersen et al., 1993). The lone HSA2 MI analyzed by Fe-XANES is > 2 log units more

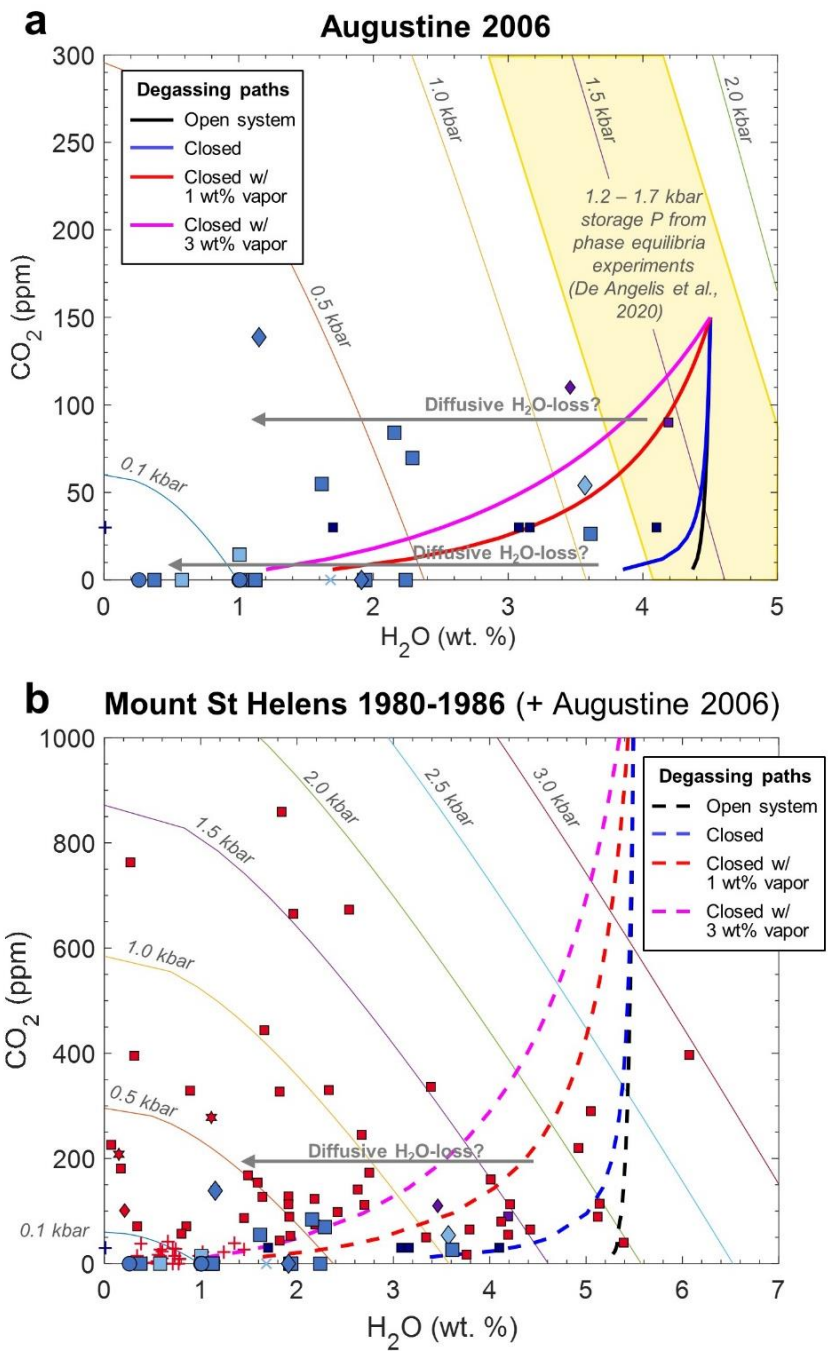

Figure 9. *(a)* H_2O and CO_2 concentrations in AUG MI and matrix glasses. A wide range of H_2O in MI likely reflects varying degrees of diffusive H^+-loss during slow ascent. Note the particularly low H_2O measured in olivine-hosted MI (circles). Smaller symbols are AUG 2006 MI from Webster et al. (2010). *(b)* AUG data overlain with H_2O-CO_2 measurements of 1980 – 1986 MSH MI from Blundy et al. (2010) (red symbols). H_2O-CO_2 vapor saturation isobars and open and closed system degassing trends with varying initial vapor fractions are for rhyolitic melts at 960 °C (VolatileCalc 2.0, Newman and Lowenstern 2002). Initial H_2O and CO_2 values for degassing trends are after Webster et al. (2010) and Blundy et al. (2010) for evolved AUG and MSH melts, respectively. Note change in axes scales between top and bottom panels. Symbology as in Figure 3.

oxidized than Fe-Ti oxides in HSA samples measured by Benage et al. (submitted). Interestingly, both matrix glasses in both LSA308 and HSA2 are ~1.5 log units more reduced than the MI measurements from their same units. However, the small number of matrix glasses and of HSA2 MI analyses limits interpretations about this relation. Sulfur speciation via S-XANES was measured in a greater number of AUG MI. Melt inclusions within both HSA2 (n=18) and LSA308 (n=38) are largely S^{6+}-rich, but S speciation ranges to lower $S^{6+}/\Sigma S$ proportions in both samples (Figure 10).

No successful Fe-XANES measurements were made on MSH samples due to phenocryst interference. However, S speciation from S-XANES was measured in MI from samples MSH12 and SH305 (Figure 10). Most MI in MSH12 contain 25 – 50% $S^{6+}/\Sigma S$ (n=7), with a subset of MI containing 60 – 70% S^{6+} (n=2). Melt inclusions in SH305 have more variable S speciation, ranging from 10 – 90 % S^{6+} (n=10). As an ensemble, $S^{6+}/\Sigma S$ in MSH MI is variable but is generally lower than in AUG samples. This is consistent with fO_2 estimates of MSH magma from Fe-Ti oxides (NNO +0 to +1; Blundy et al., 2008), which are 0.5 to 1 log units lower than fO_2 calculations for most AUG glasses and Fe-Ti oxides (Benage et al. submitted; this study). Still, we caution that the factors that govern the relation between S speciation and fO_2 are currently poorly known. S speciation is likely dependent on both temperature and pressure (Matjuschkin et al., 2016; Nash et al., 2019). The concentrations of CaO, FeO^T and H_2O in melts has also been proposed to stabilize S^{6+} or S^{2-} species in the melt (Klimm et al., 2012; Masotta & Keppler, 2015; **Chapter III**). Within our dataset, S^{6+} speciation tends to increase with increasing CaO, but is less related to FeO^T melt contents (Figure 11). As both CaO and FeO^T decrease with fractionation, the ratio of CaO/FeO^T may better isolate the particular effect of Ca in stabilizing S^{6+}, and indeed a weak positive correlation exists between CaO/FeO^T and S^{6+} speciation (Figure 11). We have insufficient Fe-XANES analyzes to more thoroughly assess the multi-parameter dependencies between melt composition and S and Fe speciation. Until the relation between S speciation and fO_2 is better constrained, these parameters should be measured independently.

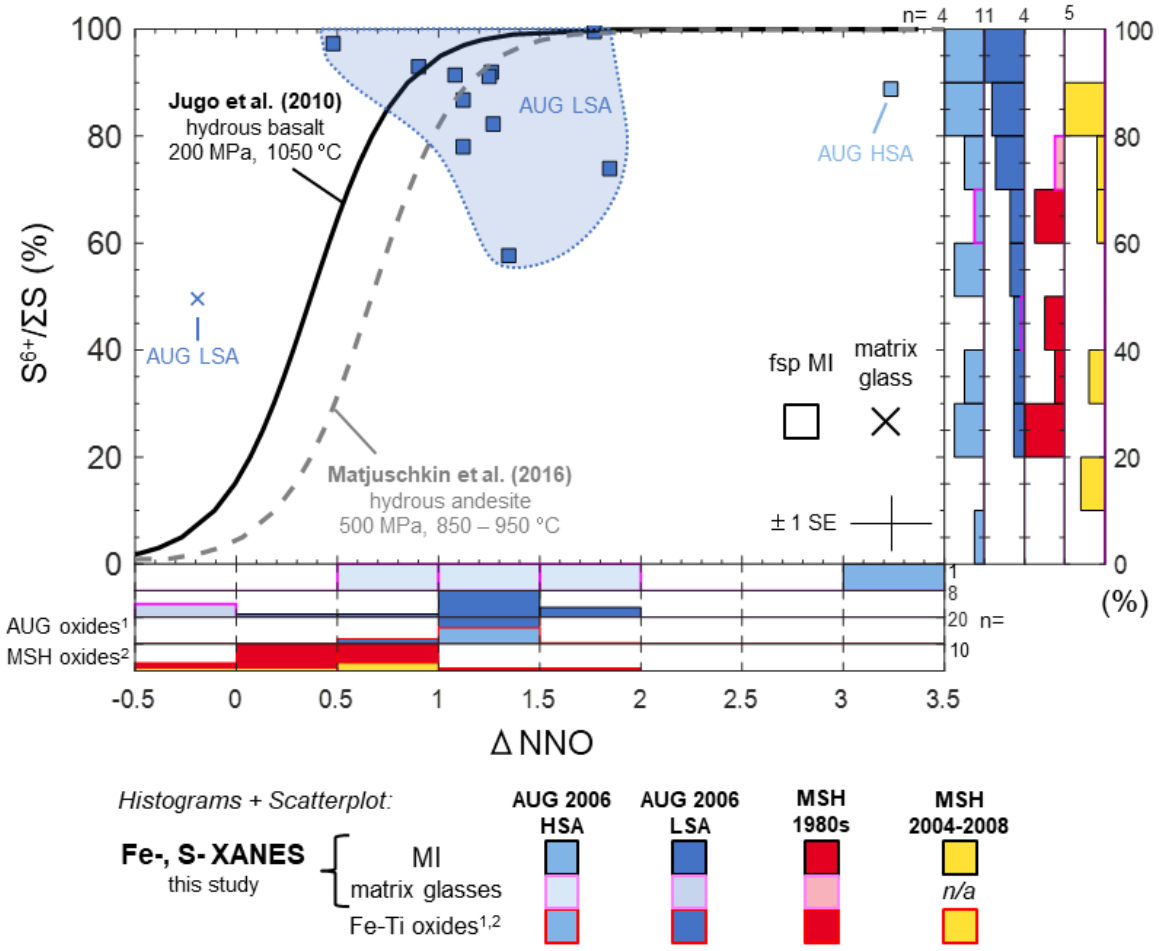

Figure 10. Redox state (ΔNNO) and S speciation of AUG and MSH MI and matrix glasses from Fe- and S-XANES measurements. For the subset of glasses measured by both XANES techniques, the relation between S speciation and redox state is similar to the formulations of Jugo et al. (2010) for hydrous basalts (black curve) and Matjuschkin et al. (2016) for hydrous andesites (gray dashed curve). The broader datasets of fO_2 from Fe-XANES and of S speciation from S-XANES are shown as histograms on the bottom and right axes. Matrix glass measurements in the histograms are outlined in pink. Uncertainties in $S^{6+}/\Sigma S$ model fits and calibration are estimated at ±5% absolute, and uncertainties in ΔNNO from $Fe^{3+}/\Sigma Fe$ centroid fits are ±0.2 log units. Redox state estimated from Fe-Ti oxides at AUG and MSH are also shown from: [1]Benage et al. (submitted) – AUG 2006 HSA and LSA calculated using Ghiorso and Evans (2008); [2]Blundy et al. (2008) – MSH 1980s and 2000s samples calculated using Spencer and Lindsley (1981) and Andersen and Lindsley (1988). Note: S concentrations in matrix glasses were too low for S-XANES measurements.

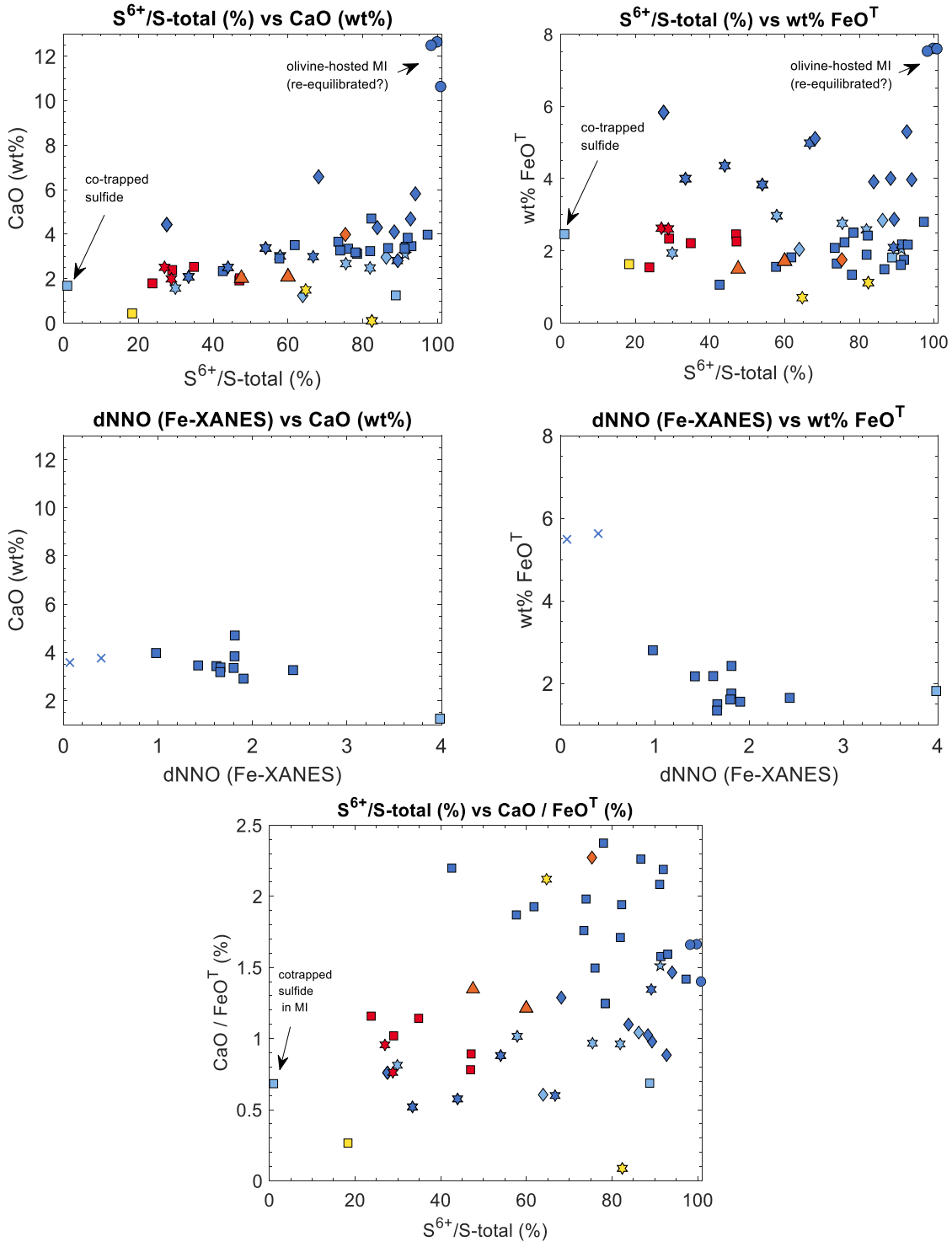

Figure 11. *(top, middle)* The relation between CaO and FeO^T with S speciation and redox state in AUG and MSH MI and matrix glasses. *(bottom)* Sulfur speciation is weakly related to CaO/FeO^T across both AUG and MSH MI. Note: S concentrations in matrix glasses were too low for S-XANES measurements. Symbology as in Figure 3.

3.4 S-isotopes

$\delta^{34}S$ was analyzed by SIMS in a subset of plagioclase-, clinopyroxene-, and olivine-hosted MI in AUG LSA308, and in plagioclase-hosted MI and one higher-S RE channel glass in HSA2 (Figures 12, 13). LSA308 dacitic and rhyolitic MI have $\delta^{34}S$ ranging from +3.7 to +9.2‰ (n=11) across a range of 130 – 460 ppm S. HSA2 rhyolitic glasses in MI and RE channels have $\delta^{34}S$ ranging from +5.9 to +8.3‰ (n=4) across a narrow range of 100 – 190 ppm S. Olivine-hosted basaltic MI in LSA308 have consistent $\delta^{34}S$ values of +6.1 ± 0.2‰ (n=3) and S concentrations of 3520 ± 10 ppm. Overall, the range of $\delta^{34}S$ is consistent with measurements of glasses, whole rocks, and gases from arc volcanoes (Mandeville et al., 2009; Oppenheimer et al., 2014), with elevated $\delta^{34}S$ presumably related to the recycling of isotopically heavy seawater sulfate (Alt et al., 1993). The high-S olivine-hosted MI have $\delta^{34}S$ compositions in the middle of the isotopic range of more evolved lower-S glasses, and overall there is no clear relation between $\delta^{34}S$ and S content of the glasses. No MSH glasses were analyzed for $\delta^{34}S$.

4. Discussion

4.1 Magma mixing at Augustine and Mount St. Helens

There is abundant evidence that basaltic intrusions triggered the 2006 eruption of AUG, including seismic and geodetic signals of a deep intrusion (Cervelli et al., 2010; Power et al., 2010), and the range of mineral and melt compositions, juxtaposed magma types, and mineral zonation (Larsen et al., 2010). Similar seismic and petrologic features were observed during the 1976 and 1986 AUG eruptions, leading to the conclusion that historical eruptions follow a similar eruptive cycle that is initiated by basaltic recharge (Larsen et al., 2010; Power et al., 2010; Roman et al., 2006). Linear whole rock and matrix glass mixing trends indicate a basaltic source composition of the intruding magma, and olivine phenocrysts and more mafic enclaves have been analyzed in samples from the 2006 and 1986 eruptions. However even the more mafic samples are highly hybridized and contain abundant silicic phenocrysts, so that no direct evidence of recent mafic recharge has been identified (Harris, 1994; Larsen et al., 2010; Roman et al., 2006). The only exposed basalts on AUG are from the late Pleistocene, and these basalts have

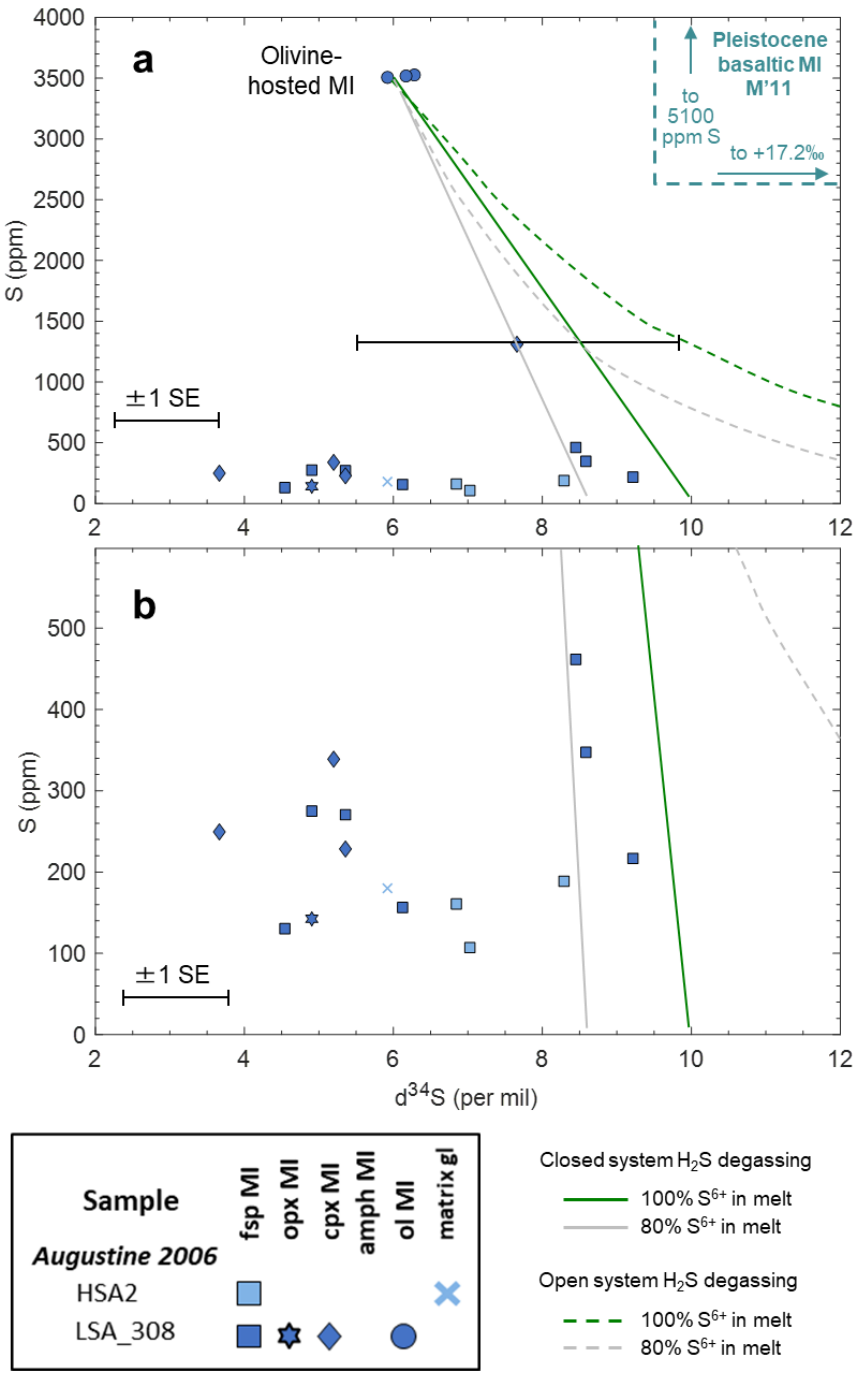

Figure 12. $\delta^{34}S$ measured in MI and matrix glasses from AUG LSA308 and HSA2 samples. *(a)* Full S-range, including olivine-hosted MI. *(b)* Zoomed in view of low-S dacitic and rhyolitic glasses. The shown 1SE uncertainty of ±0.7‰ is representative for all analyses except for one S-rich clinopyroxene-hosted MI with anomalously high uncertainty. The range of S-rich and $\delta^{34}S$-heavy MI from AUG Pleistocene basalts measured by Mandeville et al. (2011) ("M'11") are shown, and fall largely off-scale. Open- (green) and closed- (gray) system degassing trends for H_2S degassing of the high-S olivine-hosted MI are shown. $S^{6+}/\Sigma S$ in the melt is taken to be either 100% (solid lines) or 80% (dashed lines) for the degassing models. See text for details.

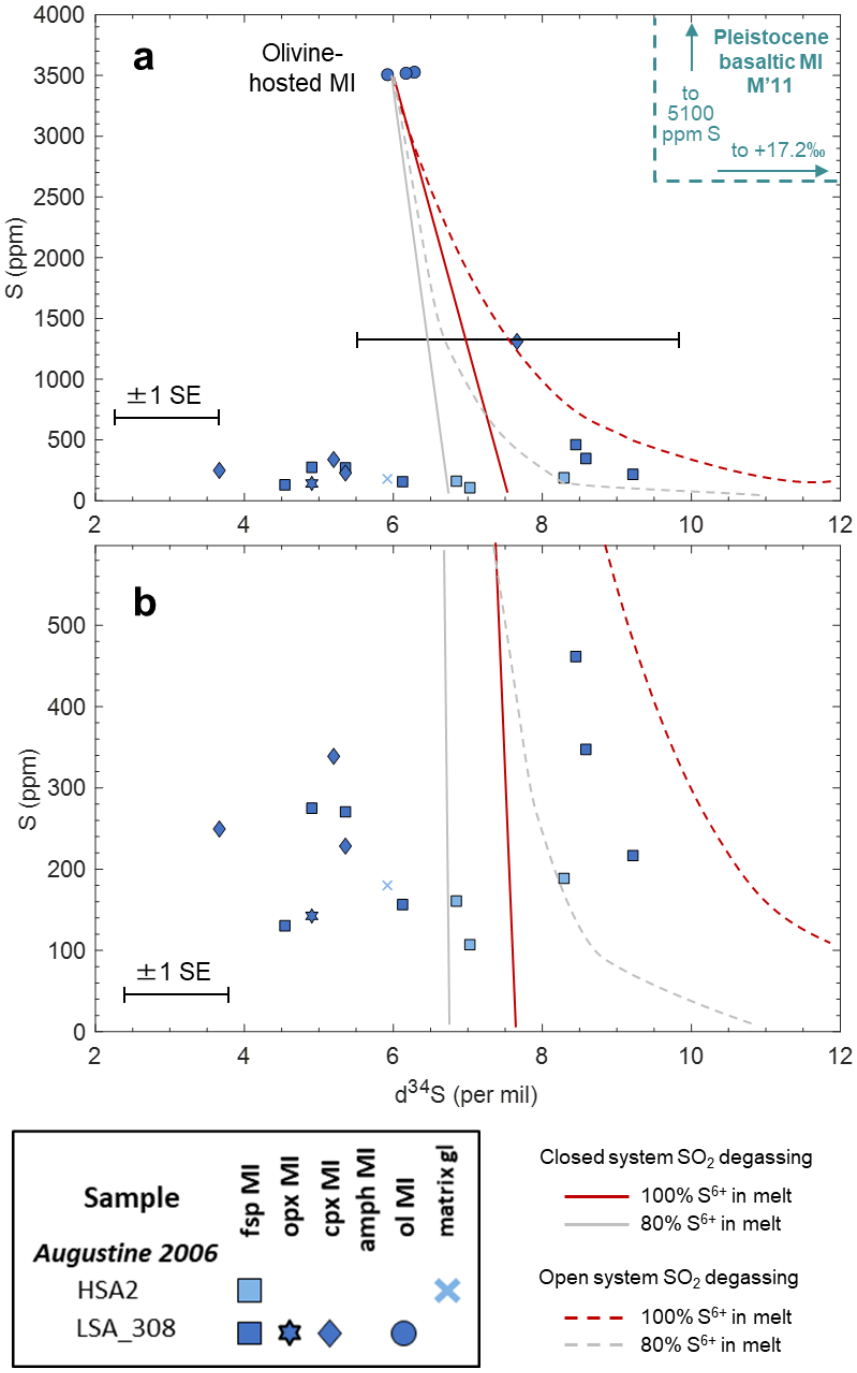

Figure 13. Same as Figure 12, except with open- (red) and closed- (gray) system trends for the degassing of SO_2 rather than H_2S. See text for details.

major and trace element abundances that are inconsistent with the observed mixing arrays of historical eruptions (Larsen et al., 2010; Webster et al., 2010) (Figures 3, 4). Indeed, Larsen et al. (2010) lament that "no good candidates for the pure mafic mixing end member exist in the geologic record at Augustine".

Our measurements of olivine-hosted MI provide the first direct constrains on the melt composition of the intruding basalt that triggered the AUG 2006 eruption. Olivine-hosted MI are high-Al and high-Ca for relatively low FeO^T and MgO contents, suggesting that plagioclase crystallization was strongly inhibited during early fractionation (Gust & Perfit, 1987; Panjasawatwong et al., 1995; Parman et al., 2011). The suppression of plagioclase crystallization indicates that substantial H_2O was present in the primitive melt (Panjasawatwong et al., 1995; Parman et al., 2011). Based on the high-Al_2O_3 concentrations in these MI, we infer that the primitive AUG melts must have contained substantial H_2O in order to produce the high-Al basaltic melt. According to the relation between maximum Al_2O_3 and H_2O content of the melt developed by Parman et al. (2011) for volcanoes of the Marianas arc ($wt\%\ H_2O_{plag\text{-}in} = 1.34 * wt\%\ Al_2O_3^{max} - 21.05$), the 22 – 24 wt% Al_2O_3 contents of the olivine-hosted MI predict > 8 wt% H_2O melt concentrations. Significant uncertainties arise from compositional differences and extrapolating the higher AUG Al_2O_3 values beyond the range that the Parman et al. (2011) relation was derived from. However, high H_2O contents of 4 – 7 wt% have been measured by Zimmer et al. (2010) in olivine-hosted MI from AUG Pleistocene basalts, and the high Al_2O_3 in olivine-hosted MI from the AUG 2006 eruption suggest the melt had similarly high H_2O concentrations. Low-H_2O FTIR measurements of the AUG 2006 olivine-hosted MI (0.3 – 1.0 wt% H_2O) are likely the result of substantial diffusive H^+-loss from the small MI during magma mixing and slow ascent.

Of particular importance for understanding S emissions and redox evolution of the AUG magmatic system, we find that olivine-hosted MI contain very high S concentrations of 3500 ± 10 ppm (n=3). The intruding basaltic melt was therefore ≥ 10 as S-rich as HSA and most LSA melts. Taking into account the high crystallinity of HSA and LSA magmas (> 50% crystal fractions; Larsen et al. 2010), the total S concentration of the silicic erupted magma is further reduced. However, high pre- and syn-eruption SO_2 emissions from AUG (6 – 8 kt/d in 2006, up to 24 kt/d in 1986) require substantial S

degassing sources (McGee et al., 2010; Rose et al., 1988), which is hard to reconcile with the relatively small mass of low-S siliceous magma erupted. Consequently, we propose that intruding S-rich basalts sourced the high SO_2 emissions during Augustine's 2006 eruption and other historic AUG eruptions. The S and Cl contents of the AUG 2006 olivine-hosted MI are similar to concentrations of 800 – 5100 ppm S and 0.27 – 0.60 wt% Cl measured in MI from AUG Pleistocene basalts (Johnston, 1978; Mandeville et al., 2011; Zimmer et al., 2010). Therefore, although differences in major and trace elements, and S-isotopes (discussed below) exist between the Pleistocene basalts and the modern basalts, the similarity of high S and Cl, as likely also high H_2O contents, suggests a persistent volatile-rich source for AUG basalts (Zimmer et al., 2010).

One additional possible S source at AUG is the decomposition of sulfides during magmatic ascent and extrusion. Upon hybridization, cooling, and fractionation (decreasing FeO^T and CaO with crystallization) within the shallow silicic AUG magma reservoirs, the high S-content of the intruding basalt likely resulted in the formation of substantial sulfides and anhydrite, depending on the redox conditions. However, more than 0.9 wt% of sulfides would crystallization would be necessary sequester enough S to decrease the 3500 ppm S in the basaltic melt to the ~200 ppm S observed in the HSA glasses. Although sulfides are present in varying stages of decomposition within matrix glasses, groundmass sulfides are rare in 2006 and other historical AUG samples (Johnston, 1978) and do not approach the abundance required account for the S budget. Consequently, we share the conclusion of Webster et al. (2010) that S partitioning into degassing fluids is the most likely means for S-loss from intruding S-rich melts. The high S content of primitive melts likely gives controls both the S degassing and sulfide/anhydrite crystallization behavior at AUG. The important consequences of the high initial S concentration of the intruding AUG 2006 basalt underscores the importance of identifying MI in most primitive materials to holistically understand the behavior of volatiles in magmatic systems (Kent, 2008; Métrich & Wallace, 2008; Myers et al., 2014).

In comparison, gas measurements and thermodynamic modeling at MSH by Gerlach et al. (2008) indicate that observed degassing during the 2004 – 2005 renewed eruptive activity at MSH was incompatible with the delivery of gas-rich magma into the

system prior to unrest. They favor a model where previously volatile depleted magma from activity in the 1980s fed the dome forming eruptions in 2004 – 2008. During the 1980 – 1986 eruptive activity, SO_2 emission rates during non-explosive events were 0.2 – 3 kt/d, and SO_2 emission rates during 2004 – 2005 activity were even lower (< 0.3 kt/d) (Gerlach et al., 2008; McGee & Casadevall, 1994). During periods where groundwater scrubbing was unlikely to play a large role in removing SO_2, the measured molar ratio of CO_2/SO_2 in gas emissions during the 2004 – 2005 eruption was ~9 (Gerlach et al., 2008). This compares with a CO_2/SO_2 ratio of ~1.1 during the 2006 eruption of AUG (McGee et al., 2010). Thus, gas emissions from AUG and MSH are consistent with our petrologic observations that the S-rich basaltic intrusion at AUG caused the system to be much more S-rich than the MSH magmatic system. In contrast to AUG, there is no convincing evidence at MSH that ascending S-rich melts contributed substantially to recent eruptions, and the modern MSH system appears to be overall S-poor. We speculate that the anomalous position of MSH relative to the subducting slab (Bedrosian et al., 2018; Kiser et al., 2016, 2018) might give rise to limited slab-derived S in the source melt, and possible non-vertical ascent pathways of mafic magmas (Lerner et al., 2020; **Chapter II**) could be causing off-axis H_2O-S degassing during deep magmatic ascent.

4.2 Constraints on redox and S-isotope variations during S degassing at Augustine

By combining our Fe- and S-XANES measurements with fO_2 estimates from Fe-Ti oxides and observations of redox-sensitive mineral textures we can roughly constrain redox changes through the AUG 2006 compositional array.

4.2.1 Redox conditions of Augustine's 2006 basaltic recharge magma

Olivine-hosted MI from AUG 2006 are completely sulfate dominated (100% $S^{6+}/\Sigma S$). However, these S speciation measurements cannot be used to derive melt fO_2 conditions of the intruding basaltic magma for the following reasons:

1) Redox re-equilibration occurs rapidly in olivine-hosted MI due to metal vacancy diffusion (Gaetani et al. 2012; Bucholz et al. 2013; Hartley et al. 2017; **Chapter III**). The low H_2O content of the olivine-hosted MI, and the < 10 μm thick lower-Fo rims on the olivine phenocrysts indicate that the olivine grains likely spent 10s of days

within the hybridized LSA magma (~1020 °C) prior to eruption (Bucholz et al., 2013; Coombs & Gardner, 2004; Lerner et al., 2018). Within this timeframe, it is likely that olivine-hosted MI would have fully redox re-equilibrated with the external melt.

2) As discussed, the relation between S speciation and melt fO_2 is currently unclear. Olivine-hosted MI have high CaO relative to the FeO^T concentrations, with PEC uncorrected CaO/FeO^T mass ratios of 2.2 ± 0.8 wt% and molar ratios 2.8 ± 1.0. We suspect the high CaO/FeO^T ratio of these MI preferentially stabilizes sulfate melt species (i.e., $CaSO_4$) compared to sulfide species (i.e., FeS) at a given fO_2. This perhaps explains why the olivine-hosted MI contain ~100% $S^{6+}/\Sigma S$ whereas LSA308 MI contain dominantly > 80% $S^{6+}/\Sigma S$ but range to as low as 20% $S^{6+}/\Sigma S$ (Figure 10).

However, the high S concentrations in the olivine-hosted MI can constrain the minimum $S^{6+}/\Sigma S$ required to for the melts to have been sulfide undersaturated at the time of MI entrapment. We calculate the sulfur content at sulfide saturation (SCSS) using the model of Smythe et al. (2017) and adding an exponential relation of S solubility with S^{6+} proportions (Jugo et al., 2010). At 1020 °C and 150 MPa, the average PEC-corrected olivine-hosted MI composition, with an estimated 3 wt% H_2O, the melt requires ≥ 80% $S^{6+}/\Sigma S$ to be sulfide undersaturated at 3500 ppm S. Varying the Fe-Cu-Ni composition of the precipitating sulfide (e.g., FeS activities of 0.65 to 1.0) with the Smythe et al. (2017) model does not appreciably change this S speciation requirement. The relations of Jugo et al. (2010) and Matjuschkin et al. (2016) predict that hydrous basaltic and andesitic melts will contain 80% S^{6+} between NNO +0.5 to +1. However, it is uncertain how appropriate these relations between S speciation and fO_2 are for the specific compositions of AUG olivine-hosted MI. As discussed above, we caution against over-interpreting the significance of this calculated redox state based on expected S^{6+} proportions.

Fe-XANES MI measurements and Fe-Ti oxide oxythermometry estimate the redox state of LSA melts to be NNO +1 to +1.5. However, Fe-XANES analyses of LSA308 matrix glasses calculate lower fO_2 of NNO -0.5 to +0. LSA308 matrix glasses are generally more mafic than LSA308 MI, presumable due to hybridization with the intruding basalt. Consequently, it is possible that the intruding basaltic magma was more reduced than the dacitic melt preserved within LSA308 MI, which caused the hybridized LSA308 matrix glasses to be more reduced. However, as discussed above, the basaltic

melt would have required high $S^{6+}/\Sigma S$ to explain the high S concentrations of the olivine-hosted MI. High $S^{6+}/\Sigma S$ at fO_2 less than NNO +0 could be a result of high CaO and H_2O in the basaltic melt (Klimm et al., 2012; Masotta & Keppler, 2015).

The presence of $Fo_{<80}$ olivine grains with symplectite textures in LSA and HSA (Larsen et al., 2010) (Figure 8) indicates significant redox disequilibrium between those particular olivine grains and the host melt, with the basaltic-sourced olivine being introduced into a more oxidizing melt environment (Johnston & Stout, 1984). Substantial time is required for symplectite rims to form and for olivine compositions to re-homogenize to lower Fo compositions. Consequently, these symplectite-rimmed olivine grains are likely from an older period of basaltic input (Larsen et al., 2010; Tilman, 2008). However, given the repeated evidence for basaltic intrusions at AUG, it can be reasonably assumed that the basaltic intrusion prior to the 2006 eruption would have had similar reduced redox states as prior basaltic intrusions. It is probable that the euhedral Fo_{83-86} olivine phenocrysts introduced with the 2006 basaltic injection are destined to become symplectite-rimmed olivine after prolonged residence in the more oxidized silicic AUG magmas.

4.2.2 Redox and isotopic changes with S loss

Olivine-hosted MI from the 2006 intruding basalt contain ~3500 ppm S. LSA308 matrix glasses and MI generally contain < 500 ppm S, indicating that the basaltic melt would have degassed 3000 ppm S (~85% of its initial S) to produce conditions of LSA melts. Depending on the relative speciation of S in the melt and S in the exsolving phase, the basaltic melt could experience a range of redox changes during S-loss (Burgisser & Scaillet, 2007; Moussallam et al., 2014; Sakai et al., 1982).

If S speciation in the basaltic melt consisted of 80% S^{6+} and 20% S^{2-}, and S degassed as H_2S (S as S^{2-}), each molecule of degassing S would cause 6.4 electrons to be transferred from the melt into the vapor phase. Presumably this electron transfer would occur via the oxidation of Fe^{2+} to Fe^{3+} in the melt, as Fe is the most abundant multivalent element in the melt. Assuming that S is the only major redox-sensitive degassing species, if 3000 ppm S degassed as H_2S, the net result would be the oxidation of 1.9 wt% of FeO. For an estimated initial FeO^T concentration of 7.3 wt% in the basalt, this would translate

into an increase in +26% $Fe^{3+}/\Sigma Fe$, or an fO_2 increase of ~+2.5 log units. This is a large effect that would require the basalt to have initially had a redox state of NNO -1. The large redox changes that H_2S degassing from a S^{6+}-rich melt could explain some of the redox disequilibrium textures observed in AUG material, including symplectite rims on olivine grains. Additionally, as the exsolved H_2S-bearing fluid percolates through other magma bodies, it may react with surrounding magmas to induce localized reduction, perhaps explaining the presence of sulfides in the overall oxidized anhydrite-bearing LSA and HAS melts. If instead S-loss from the basalt occurred by SO_2 degassing (S as S^{4+}), the loss of 3000 ppm S from a basalt with 80% S^{6+} and 20% S^{2-} would result in the net oxidation of only 0.12 wt% FeO. This translates into a much smaller increase of +1.6% $Fe^{3+}/\Sigma Fe$, or an fO_2 increase of ~+0.2 log units.

Redox-sensitive S degassing also results in isotopic differences during progressive S-loss. The large redox exchange involved in H_2S degassing from a S^{6+} dominated melt induces a substantial $\delta^{34}S$ isotopic fractionation between the melt and vapor phase. At 1020 °C, this fractionation leaves the SO_4 melt species 3.9‰ heavier than the H_2S vapor (Miyoshi et al., 1984). Open-system H_2S degassing of 85% of the initial S from the basalt results in the melt becoming 5.8% to 7.4‰ heavier, depending on whether the melt contained 80% or 100% $S^{6+}/\Sigma S$, respectively. In contrast, the degassing of SO_2 from a S^{6+} dominated melt involves a more minor redox exchange and a smaller $\delta^{34}S$ isotopic fractionation, where the SO_4 melt species is 1.6‰ heavier than the SO_2 vapor (Miyoshi et al., 1984; Richet et al., 1977; Taylor, 1986). Open-system SO_2 degassing of 85% of the initial S from the basalt results in the melt becoming 1.3% to 3.0‰ heavier if the melt contained 80% or 100% $S^{6+}/\Sigma S$, respectively.

The olivine-hosted MI have an average $\delta^{34}S$ value of +6.1 ± 0.2‰. LSA308 and HSA2 MI have a wide range of $\delta^{34}S$ values at low S concentrations, including MI that are both isotopically heavier (+7.0 to +9.5‰) and lighter (+3.5 to +6.0‰) than the olivine-hosted MI. Figures 12 and 13 show open- and closed-system degassing and $\delta^{34}S$ fractionation for a parent melt containing constant $S^{6+}/\Sigma S$ proportions of 80% or 100% and degassing S as either H_2S or SO_2. The average S and $\delta^{34}S$ compositions of the olivine-hosted MI are used as initial melt values. The subset of low-S, $\delta^{34}S$-heavy MI compositions can be produced by 80 – 90% closed-system H_2S degassing of a melt

containing 80 – 100% $S^{6+}/\Sigma S$ (Figure 12). Alternatively, the low-S, $\delta^{34}S$-heavy MI can be produced with 80 – 90% open-system degassing of SO_2 from a parent melt containing 80 – 100% $S^{6+}/\Sigma S$ (Figure 13). Closed-system SO_2 degassing results in less isotopic fractionation, and some HAS2 MI compositions could be reproduced with ~90% closed-system SO_2 degassing.

We therefore consider the following scenarios for recent eruption cycles at AUG: Moderately oxidized, sulfate-rich basaltic melts ascend to depths of 4 – 6 km (~1.5 kbar) where they mix with more evolved magmas that remain from prior eruptive cycles (Cervelli et al., 2010; Larsen et al., 2010; Webster et al., 2010). During ascent, hybridization, and cooling, the basaltic magma degasses substantial H_2O and 80 – 90% of its initial S. If S is degassed as SO_2, only slight oxidation of the melt would occur and the residual melt would be slightly enriched in ^{34}S. If S is degassed as H_2S, substantial melt oxidation would occur and would be accompanied by large S-isotopic fractionations. To reproduce the $\delta^{34}S$ signatures of low-S MI, H_2S degassing would have to occur as closed-system degassing. Some amount of basalt-hybridized magma (LSA compositions) further ascend into highly evolved shallow silicic reservoirs or dike complexes (HAS compositions), causing addition mixing and S degassing. Eventually, variably hybridized LSA and HSA magmas erupt, producing the compositional range observed in the AUG historical eruptions.

4.2.3 Magmatic source variation through time at Augustine

There remains a subset of low-S, $\delta^{34}S$-light MI in LSA308 and HSA2 samples cannot be explained by degassing scenario that assume a sulfate-rich parental source melt with the $\delta^{34}S$ composition of the olivine-hosted MI (Figures 12, 13). The only degassing scenario that causes residual melts to become isotopically lighter during S-loss would be for the initial melt to contain dominantly S^{2-} and degas S as SO_2. However, as implied from the SCSS considerations of the olivine-hosted MI, this scenario is unlikely because a S^{2-}-dominated basaltic melt would become sulfide saturated at S concentrations lower than what is observed in the olivine-hosted MI. Consequently, we conclude that the S-poor, isotopically light LSA308 and HSA2 MI could not be derived from a parental melt represented by the olivine-hosted MI. We suspect that the isotopic source character of

AUG melts has evolved over time, and these low-S, δ^{34}S-light MI are derived from a substantially different parental melt. The most striking example of a changing isotopic source of parental melts is the late Pleistocene AUG basalt, which is highly enriched in volatiles and has very heavy δ^{34}S values (+9 to +17‰; Mandeville et al. 2011). These Pleistocene basalts have different major and trace element whole rock characteristics compared to historical AUG eruptives, suggesting different magma sources (Larsen et al., 2010; Mandeville et al., 2011; Zimmer, 2009; Zimmer et al., 2010). The isotopically heavy δ^{34}S values of this basalt indicates a sulfate-rich source melt (Mandeville et al., 2011). However, the Pleistocene basaltic melts were also S^{6+} rich (Mandeville et al., 2011; Zimmer, 2009) and therefore cannot explain the isotopically light, low-S LSA308 and HSA2 MI. Consequently, source melts at Augustine must be more variable than the two basaltic examples discussed here. Differences in magmatic K_2O over time have been proposed (Benage et al. submitted; Larsen et al. 2010), providing further evidence for temporally varying magmatic sources that may give rise to the isotopic and compositional diversity observed at AUG.

An additional mechanism that may contribute to the low-S, δ^{34}S-light LSA308 and HSA2 MI is the fluxing of isotopically light S vapors (particularly H_2S vapors) from degassing basaltic melts at depth. However, this effect may be localized to along degassing pathways.

4.3 Implications of sulfur degassing on redox state at Augustine, Mount St. Helens, and other systems

Edifice deformation at AUG began about two months prior to the January 11, 2006 eruption (Cervelli et al., 2010). In those months before the eruption, H_2S odors were reported in neighboring communities and yellow-green colored plumes were observed, which were interpreted to be the result of the reaction of H_2S and SO_2 to form native sulfur (McGee et al., 2010). These observations of H_2S degassing were inferred to represent SO_2 scrubbing by hydrolysis in groundwater and subsequent boiling and degassing of H_2S from the hydrothermal system (McGee et al., 2010; Symonds et al., 2001). By early January, about a week prior to the eruption, significant SO_2 was being

emitted from Augustine's summit, which was taken to indicate the heating and drying of degassing pathways due to prolonged degassing and magma ascent (McGee et al., 2010).

However, due to homogenous equilibration in the gas phase during vapor ascent and depressurization, emitted gas species do not necessarily reflect the degassing species at depth (Burgisser et al., 2015; Burgisser & Scaillet, 2007; Oppenheimer et al., 2018). Sulfur species equilibrium can be described by the reaction:

$SO_2 + H_2O = H_2S + 1.5O_2$.

For conditions relevant to the 2004 – 2005 MSH dacitic magma, Gerlach et al. (2008) show that H_2S vapor is strongly thermodynamically favored at depths greater than 0.5 km. Similar conclusions were reached by Burgisser and Scaillet (2007) and Burgisser et al. (2015), that H_2S degassing would be favorable in H_2O-rich melts at pressures > 0.5 kbar (~2 km depth) for magmas that are more reduced than NNO +1.5. The redox state of AUG melts straddles this NNO +1.5 value, suggesting that deep H_2S degassing may likely occur. However, open-system degassing of H_2S during S-loss from the intruding basalt at AUG is not fully consistent with our considerations of redox conditions and S-isotopes. Reconciling the thermodynamic degassing calculations with petrologic observations and field measurements of active degassing remains an important topic for future investigation.

In erupted material from MSH in the 1980s, Blundy et al. (2008) observe slight magmatic reduction over time, based on Fe-Ti oxides. They propose that SO_2 degassing might be the cause of this reducing trend. Fe-Ti oxide oxythermometry indicate that the redox states of MSH magmas range between NNO +0 to +1 (Blundy et al., 2008; Pallister et al., 2008), which is somewhat more reduced than AUG magmas. This more reduced redox state of MSH is makes it more likely for S to occur as mixed S^{6+} and S^{2-} species in the melt rather than being S^{6+}-dominated (Jugo et al., 2010; Matjuschkin et al., 2016). This is consistent with our S-XANES measurements, where MSH MI have variable S speciation but are generally more S^{2-}-rich compared to S^{6+}-dominant AUG MI (Figure 10). Considering electron exchange reactions during S degassing (discussed above), SO_2 degassing from a melt with < 75% S^{6+} will undergo reduction during S-loss, whereas SO_2 degassing from a melt with > 75% S^{6+} will cause oxidation (Figure 14). In S^{6+}-dominated AUG melts, SO_2 degassing will cause slight melt oxidation. In comparison, melt

reduction due to SO_2 degassing has been widely observed at more reduced basaltic systems, such as at Kīlauea volcano (Moussallam et al. 2016; Helz et al. 2017; **Chapter IV**). Mount St. Helens melts are in a intermediate redox regime where the melts are fairly oxidized but sufficient S^{2-} is likely present to cause reduction during SO_2 degassing, as suggested by Blundy et al. (2008). The magnitude of redox change that occurs during any S degassing scenario depends on the proportion of S species present in the melt and the extent of S loss. At MSH, the overall system is S-poor and the extent of reduction due to SO_2 degassing should therefore be relatively limited.

	Low-H_2O magmas (e.g., MOR, hotspots)				**High-H_2O magmas** (e.g., arcs)			
	⊢ Kilauea ⊣				⊢ MSH ⊣	⊢ AUG ⊣		
Net melt ΔfO_2 w/ ascent:	reduction	reduction	oxidation	oxidation	reduction	depends	oxidation	oxidation
Shallow ascent:	SO_2 degassing	SO_2 degassing		SO_2 degassing	SO_2 degassing	SO_2 degassing		SO_2 degassing
ΔfO_2 in melt:	↓ ↓	↓ if <75% S^{6+}	↑ if >75% S^{6+}	↑	↓	↓ if <75% S^{6+}	↑ if >75% S^{6+}	↑
Deep ascent:	minimal S degassing	minimal S degassing		minimal S degassing	H_2S degassing	H_2S or SO_2 degassing		H_2S or SO_2 degassing
ΔfO_2 in melt:	no change	no change		no change	no change	↑ if H_2S; ↑ or ↓ if SO_2		↑ ↑ if H_2S, ↑ if SO_2
Initial H_2O:	Low H_2O	Low H_2O		Low H_2O	High H_2O	High H_2O		High H_2O
Initial $S^{6+}/\Sigma S$:	0% S^{6+}	mixed S^{6+}		100% S^{6+}	0% S^{6+}	mixed S^{6+}		100% S^{6+}

Figure 14. A summary of redox changes that can occur during magmatic ascent and S degassing, depending on the initial S speciation of the melt and the type of S vapor exsolving. The direction of redox change is governed by the following reactions: $S^{2-}_{melt} \rightarrow H_2S_{vapor}$ = no S redox changes; $S^{6+}_{melt} \rightarrow H_2S_{vapor} = 8e^-$ lost from the melt (melt oxidation); $S^{2-}_{melt} \rightarrow SO_{2\,vapor} = 6e^-$ added to the melt (melt reduction); $S^{6+}_{melt} \rightarrow SO_{2\,vapor} = 2e^-$ lost from the melt (melt oxidation). Assuming that S^{2-} and S^{6+} melt species degas with equal efficiency, SO_2 degassing of melts with < 75% $S^{6+}/\Sigma S$ will cause melt reduction but SO_2 degassing of melts with > 75% $S^{6+}/\Sigma S$ will cause oxidation. The direction and magnitude of redox changes depends on the S speciation of the melt, the degassing S-species, and the extent of S-loss. The conditions relevant to H_2O-rich AUG and MSH melts, and H_2O-poor Kīlauea melts (**Chapter IV**) are shown.

5. Conclusions

The diverse valence states of S in melt and vapor can lead to notable changes in melt redox state, degassing behavior, and mineral stability during magma ascent and vapor loss. We compare Augustine and Mount St. Helens volcanoes, which have similar bulk compositions, temperatures, and redox states, but have different eruption mechanisms.

Historical eruptions at Augustine are due to mafic recharge, whereas eruptions at Mount St. Helens do not contain a major mafic component. We measured MI hosted in euhedral olivine phenocrysts that were sourced from the mafic recharge magma that initiated Augustine's 2006 eruption. These are the first direct representations of the basaltic melt that hybridized within the Augustine system. The olivine-hosted MI contain ~3500 ppm S, which is > 10x the S content of the more abundant dacitic and rhyolitic MI and glasses from Augustine, and is the likely source of the high SO_2 emissions observed during the 2006 eruption. Sulfur degassing of the basaltic melt to reproduce low-S concentrations of dacitic and rhyolitic Augustine melts would be accompanied by redox and $\delta^{34}S$ variations. Deep degassing of H_2S from the ascending basalt is thermodynamically favored and would result in the residual melt becoming oxidized and very $\delta^{34}S$-heavy. Textural evidence of oxidation of the basalt exists in the form of symplectite-rimmed olivine, but large magnitude of ^{34}S-enrichment during open system H_2S degassing is not fully consistent with our measurements of low-S MI. Widespread SO_2 degassing during basaltic intrusion and magma hybridization would cause more limited oxidation and ^{34}S-enrichment of the residual melts. Further work is required to reconcile thermodynamic considerations of S degassing with the observed ranges of redox and $\delta^{34}S$ in Augustine samples.

Mount St. Helens represents a S-poor arc system. Melts at Mount St. Helens are slightly reduced than at Augustine, so that a substantial fraction S^{2-} melt species are present. Low-level SO_2 degassing from a mixed S species melt possibly caused a slight reduction of the Mount St. Helens melt during eruptive activity in the 1980s. Difference in initial S speciation, redox changes during S degassing, and the total extent of S loss during magmatic ascent and eruption lead to a number of difference scenarios that affect melt redox state and $\delta^{34}S$ fractionation.

If future activity at Augustine and Mount St. Helens follow similar behavior as over the last 50 years, basaltic recharge events at Augustine will source high pre- and syn-eruptive S emissions (in the absence of extreme groundwater scrubbing), whereas S emissions are likely to remain low at Mount St. Helens even during unrest. These considerations are important when anticipating how precursory signals of unrest will manifest at these different systems.

CHAPTER VI

DISSERTATION SUMMARY

Volcanology is an inherently multidisciplinary field that couples fundamental questions about crustal architecture and geochemical cycling, with the societal importance of addressing numerous natural hazards. My dissertation research reflects this intellectual diversity and combines geophysical and geochemical approaches to improve our understanding of the location of magma reservoirs, and how magma depth, redox state, and chemical composition affect the behavior of sulfur and other volcanic gases.

By assembling a compilation of geophysically imaged magma reservoirs (Chapter II), I expand our understanding of magma reservoir depths and lateral positioning. Magma reservoir depths are of first-order importance for determining the pressure conditions of volatile solubilities and magma degassing. The lateral positioning of magma reservoirs relative to associated volcanic edifices determine whether magma travels through vertical or inclined ascent pathways, which may affect the ease of magmatic degassing (i.e., open- or closed-system degassing) and whether off-axis degassing may be important in during magmatic ascent.

In addition to magma depths, the redox state of magmas is a critical parameter that affects volatiles solubility. Sulfur is particularly redox-sensitive, being a multivalent element that can occur as a variety of melt and vapor species. I introduce techniques for more accurately measuring S and Fe valence states in glasses by XANES, which focuses on identifying and correcting X-ray induced beam damage (Chapter III). Improved measurements of melt redox states provide important input parameters for modeling sulfur solubility, constraining degassing species, and understanding mineral stability during magmatic evolution.

These analytical techniques are combined with broader suites of petrologic analyses of melt inclusions, matrix glasses, and mineral compositions to characterize and interpret the behavior of sulfur and other magmatic volatiles at Kīlauea, Augustine, and Mount St. Helens volcanoes (Chapters IV and V). The ultimate goal of this dissertation was to use physical and geochemical data to create degassing frameworks at these high-threat volcanoes to better interpret and utilize sulfur and other gas emission data in

volcano monitoring. Degassing frameworks and geochemical interpretations are assessed in the context of geophysical models of magma reservoir locations and transport pathways. Only by combining petrologic approaches, gas and geochemical monitoring, and geophysical constraints can holistic views of volcanic systems be accurately developed.

APPENDICES

APPENDIX A
CHAPTER II SUPPLEMENTARY INFORMATION AND FIGURES

Here we provide an extended methods discussion of data sources and analysis, assessment of uncertainty, and supporting figures relevant to discussion in the main text. Additional datasets include Excel data tables, and PDF containing a maps with volcanic edifice bounds and centroid locations, and a Google Earth (.kmz) database volcanic edifice bounds and geophysically imaged magma reservoir locations.

Text A1. Determination of magma reservoir centroids at arc volcanoes

From an extensive literature survey, we compiled 54 different geophysical studies of arc volcanoes fitting the following criteria:

1) Only arc volcanoes (continental and oceanic), in order to reduce tectonic variability. Most studies are from continental arcs, due to data coverage. We do not subdivide our dataset in terms of open or closed system behavior because this metric is poorly defined for most systems and recently observed behavior is likely a transient state over timescales relevant to volcanic lifespans (10s to 100s kyr).

2) Studies published between 2000-2018, to acknowledge rapid increases in geophysical monitoring capabilities. Where multiple studies exist for an individual volcano, we generally include the most recent study of high confidence, which implicitly assumes that subsequent research continues to build upon previous efforts and becomes more refined. However, we acknowledge that volcanic systems can be highly dynamic, and magma reservoirs and deformation sources vary over time, leading to some credible yet different reservoir identifications at the same volcano. Magma reservoirs were inferred by both tomographic and geodetic means at 11 volcanoes, and we include results of both types of studies in the database as separate reservoirs. At 8 volcanoes, authors using a single technique describe multiple distinct magmatic reservoirs at one volcano, and we include multiple reservoirs locations for these systems.

3) Authors explicitly infer a magma body located 2.5 – 15 km depth beneath the surface. The shallow depth threshold is an attempt to filter out hydrothermal and transient sources from our analysis, as volcanic hydrothermal features are dominantly located in the shallowest upper crust (Fournier, 1999), as well as shallow, more ephemeral dikes and sills. This differs from the recent InSAR compilation of volcanic deformation by Ebmeier et al. (2018), which included signals described by shallow geodetic sources attributed to both magmatic and hydrothermal processes. As imaging resolution decreases with increased depth, we impose a lower depth threshold of 15 km to exclude deeper crustal features.

Overall, our compilation includes 47 geodetically inferred magma reservoirs (30 via InSAR, 8 via ground-based GPS, 1 via a leveling survey, 8 via combined geodetic means), and 30 tomographically inferred magma reservoirs (24 via seismic tomography, 4 via MT tomography, 1 via seismic reflection, 1 via seismic receiver functions). Collectively, these studies identified 77 distinct magmatic bodies at 56 volcanic systems, where 18 volcanoes have multiple inferred magma reservoirs (Tables S1, S2, Figure A1). We note that over 100 geophysical studies at 70 additional arc volcanoes were investigated but ultimately excluded from our database for failure to meet our required inclusion criteria.

As discussed in the main text, tomographic and geodetic studies are sensitive to the presence of magma storage regions in different ways and potentially over different timescales. In contrast to geodetic studies, which require active volume changes in the crust, seismic and MT tomography can identify crustal anomalies related to static magma reservoirs, including those with relatively low melt fractions (although melt fraction is challenging to uniquely constrain). Tomographic studies, however, often have relatively lower spatial resolution compared to geodetic surveys, so that smaller magmatic zones may be recognized preferentially by InSAR or GPS. The substantial disagreement between geodetic and tomographic techniques seen in recognizing magmatic features at single volcanoes (Figure A7) is likely due to co-occurring subsurface magmatic features that express in different ways depending on measurement technique.

Given the wide range of data analysis techniques, model variability, and instrumentation, it is challenging to normalize published studies. Therefore, we have

limited our analysis to include only magma reservoirs that are explicitly claimed in refereed publications. We exclude studies that are equivocal in identifying subsurface features as being hydrothermal or fracture zones rather than magmatic bodies. We do not attempt to include any constraints on size of the inferred magma reservoirs as this would require an arbitrary cutoff threshold in what anomaly values defined the "edges" of a magmatic body. Rather, we focus our analysis on the centers of deformation sources and tomographic anomalies to represent magma reservoirs. Where information is provided, we use author-defined latitude, longitude, and depth of the centers of deformation or tomographic features identified by the authors. The hypocenter (latitude, longitude, depth) of magma body centroids are typically defined in geodetic pressure source models, but are rarely explicitly defined in tomographic studies; in these cases, we pick magma body centroids from published figures and descriptions in the text. Seismic features interpreted as magmatic bodies in our database typically have V_p anomalies of -10 to -15%, V_s anomalies of -15 to -30%, and V_p/V_s anomalies of +10 to +30% (Jaxybulatov et al., 2011; Kiser et al., 2018; Tamura & Okada, 2016). Magnetotelluric features interpreted as magmatic bodies typically have resistivity anomalies of 1 - 10 Ωm, which is generally -95 to -99% of the regional background resistivity (Comeau et al., 2015; Hill et al., 2015). Geodetic inflation and deflation sources are usually modeled as inflating spheres in an elastic half space (McTigue, 1987; Mogi, 1958), where lateral position is generally better constrained than source depth or volume change. A number of studies recognize vertically extensive zones suggestive of dike complexes, which makes the definition of a single magma body centroid effectively meaningless, and we exclude such cases from our database.

How accurate are subsurface locations of magma reservoirs?

In this study, we assume published magma reservoir locations have been sufficiently scrutinized and faithfully represented free from confirmation-biases. Compiling such diverse data sources, with each study having varying degrees of reported error analysis and uncertainties, precludes defining a rigorous and consistent uncertainty in inferred magma reservoir locations. We also note a lack of consistency in what reference datum magma body depths are reported in the literature (e.g., relative to sea

level, surface elevation, or to the geoid). When unstated in published studies, we attempt to determine the reference datum from text and figures. Most tomographic studies present results using vertical cross sections and horizontal depth slices, which provide very limited views of three-dimensional models. Consequently, defining the true centroids of tomographic anomalies from figures is imprecise. However, the overall uncertainty in our tomographic magma reservoir centroid determinations is usually small compared to their often substantial lateral offset and depth locations. We also consider that errors in our centroid determinations would be non-systematical so that the overall interpretations derived from this database should not be biased. To aid in future compilations, we suggest that tomographic and geodetic studies publish centroid details (latitude, longitude, depth, and uncertainty) for major anomalies referenced in the text, and also explicitly define the reference datum for depth.

How robust are the links between inferred subsurface magma reservoirs and particular volcanic edifices?

In most cases, magma reservoirs have been associated with the closest most recently active volcanic edifice. However, subsurface features may not necessarily be part of the plumbing system of the nearest recently active edifice – magma reservoirs could be linked to less active volcanic edifices, or may not be related to singular surface volcanic expressions at all, such as in monogenetic fields. The connection between a subsurface magmatic feature and any particular surface landform is robust only if an eruption occurs and a connection can be clearly mapped between magma body and eruption site.

In order to quantify uncertainties associated with reservoir centroid locations, we developed a confidence quality factor based on author interpretations, the quality of data coverage (e.g., number of stations, ray path coverage, duration of measurement or number of InSAR acquisitions, goodness of model fits, and author-stated accuracy and precision), and independent corroborative evidence (e.g., petrologic geobarometry studies or earthquake locations around magma reservoirs). We perform a similar assessment to evaluate the confidence that each magma reservoir is reasonably associated to the nearby volcanic edifice. In this case, we follow the approach of Ebmeier et al. (2018) and

highlight the subset of magma reservoirs (n=15) that are linked explicitly to eruptions from their associated edifice (Figures A10, A11). These co-eruptive links are identified either through tracking earthquakes between the magma body and the erupting edifice, or via precursory or syn-eruptive geodetic or tomographic changes (e.g., Nevado del Ruiz, Columbia; Tungurahua, Ecuador; Kirishima, Japan; Asama, Japan; Sakurajima, Japan; Unzen, Japan).

Magma reservoirs with co-eruptive links to the associated edifice are slightly more centrally located than the full dataset (27% vs 34% of reservoirs are laterally offset > 4 km, respectively) (Table S3). However, nine of 13 magma reservoirs with co-eruptive links occur at large volcanoes (volume > 43 km^3), which overall have less offset reservoirs (24% of reservoirs at large volcanoes are laterally offset > 4 km). Therefore, reservoirs with co-eruptive links have very similar degrees of offset as the full set of reservoirs at comparably sized volcanoes.

Magma reservoirs with lower confidence in either subsurface locations or in their connectivity to nearby edifices are more laterally offset (10 reservoirs; 80% offset > 4 km) than the full database. The low confidence classification of these studies are partially influenced by the distance of the inferred reservoir from the edifice, which we acknowledge leads to some degree of circular reasoning. However, when excluding the lower quality studies from the database, the overall distribution of magma reservoirs relative to volcanic edifices is not dramatically different from considering the full database (27% vs 34% of reservoirs are laterally offset > 4 km, respectively).

An additional way to assess connectivity between edifices and active magma reservoirs at depth is the occurrence of active magmatic degassing. We incorporate a compilation of volcanoes passively degassing sulfur dioxide (SO_2) recognized by the Ozone Mapping Instrument (OMI) satellite (Carn et al., 2017), in order to identify which volcanoes in our dataset had a clear hydraulic connection to magma at depth. Of the 56 volcanoes in our dataset, 20 volcanoes (hosting 30 inferred magma reservoirs) had OMI-detected passive SO_2 degassing between 2005 - 2015. We note that there are numerous reasons that magma reservoirs at depth may not result in observable SO_2 degassing (magma is too deep or too S-poor to reach volatile saturation, the reservoir is small so SO_2 emissions are low, SO_2 can by scrubbed by groundwater, OMI satellite resolution

may be poor for certain latitudes and altitudes). Still, we observe that SO_2 degassing and non-degassing volcanoes have similar proportions of centralized and offset inferred reservoirs locations (33% of magma reservoirs are laterally offset > 4 km at SO_2 degassing volcanoes) (Figures A12, A13). This recognition, in addition to co-eruptive evidence of some offset reservoirs, lends further support that laterally offset reservoirs may indeed be connected to edifices.

Text A2. Topographic characterization of volcanic edifices

Defining what constitutes a volcanic edifice is not always straightforward, particularly in complex terrain and where numerous volcanic vents are closely located (e.g., volcanic complexes). To map the topography of volcanic edifices, we first define which landforms are likely related to a given volcanic system. We classify volcanoes into four types: stratovolcanoes (25 volcanoes; 34 magma reservoirs), volcanic complexes (16 volcanoes; 22 reservoirs), calderas (including stratovolcanoes with summit calderas) (9 volcanoes; 10 reservoirs), and calderas with ring-fracture vents that formed post-collapse (6 volcanoes; 11 reservoirs) (Tables S1, S2). The classifications for volcanoes in the database are generally taken from the Global Volcanism Project's (GVP) databases of Holocene and Pleistocene volcanism (Smithsonian Institution, 2013). However, for a number of volcanoes, we modified the GVP classifications based on edifice structural and petrologic relationships to other features (e.g., calderas and ring fracture vents, volcanic complexes). As an example, at the Sisters volcanic cluster (Oregon, USA) a number of composite volcanoes are located in close proximity. However petrologic evidence indicates that North, Middle, and South Sister volcanoes tap notably different magmas from presumably different crustal depths (Calvert et al., 2018; Hildreth, 2007), and we thereby classify these as separate edifices (where a geodetically modeled magma body is associated with the nearest edifice, South Sister). Based on such considerations, where information is available, we reclassified certain GVP-defined stratovolcanoes as "volcanic complexes" and *vice versa*. If a summit caldera > 5 km diameter is present, we reclassify stratovolcanoes as "calderas". GVP-defined stratovolcanoes and calderas with clearly related post-caldera vents along ring fractures are reclassified as "caldera ring fracture vents" to avoid considering the post-caldera features as independent edifices.

To make the topographic characterization of volcanic edifices systematic and repeatable, we utilize the Modified Basal Outlining Algorithm (MBOA) (Bohnenstiehl et al., 2012) for defining the outset bounds of features. The MBOA algorithm expands upon the typical closed contour basal analysis method for defining volcanic features, while also accounting for background slope and the presence of other nearby topographic features. We use a global 30 m digital elevation dataset collected in February 2000 from NASA's SRTM-1 global topography mission (NASA JPL, 2013), and include bathymetric datasets from the ETOPO1 mission (Amante & Eakins, 2009) for offshore edifices, where available. Data Set S1 and the Google Earth database (Data Set S2) include figures and shape files showing all quantified edifice boundaries for volcanoes in this database.

Topography within the volcanic edifice basal contour is used to determine the topographic moments via:

$$M_{i,j} = \int \int x^i \, y^j \, Z(x,y) \, dy \, dx, \tag{1}$$

where *(i,j)* define moment order, *(x,y)* are spatial coordinates in latitude and longitude, and *Z(x,y)* is topography. $M_{0,0}$ is total edifice volume and $M_{1,0}$ and $M_{0,1}$ are the first-order moments in the x and y directions, respectively (Flusser et al., 2016). The center of topography in the x and y directions are calculated as

$$\frac{M_{1,0}}{M_{0,0}} \text{ and } \frac{M_{0,1}}{M_{0,0}}, \tag{2}$$

which together define the edifice centroid.

Mean edifice radius was calculated from the distance between the edifice centroid and edifice bounds measured in 1 azimuthal degree increments. We note that our calculated edifice volumes are generally conservative and may not necessarily reflect total eruptive volumes, given distal outfall volumes and the effects of erosion, collapses, and other non-volcanic processes on volcano edifices (e.g., South Sister edifice calculated at 11 km^3 and MSH at 43 km^3 compared to estimates by Hildreth [2007] of 20 km^3 and 40-50 km^3 for total erupted volume for each respective volcano, which includes distal fallout deposits). Additionally, we do not attempt to account for past erosion and flank collapses that may affect our edifice centroid and volume calculations. However, in comparing the recent example of topographic changes at Mount St. Helens from before

and after the 1980 eruption, where the debris avalanche and eruption removed ~2.5 km^3 of material from the summit and north flank, we observe only a very minor shift in edifice centroid position of 190 m to the SSW (Figure A18). Although the 1980 events caused dramatic changes to the volcano topography, our calculations of edifice volume and centroid are largely determined by the broad basal distribution of volume, so that the remobilized volume at Mount St. Helens was a small component of the overall volcano size. Extending this observation more generally, edifice volume and centroid location are unlikely to change drastically over short timescales, barring very major caldera collapses or flank collapses that remove huge portions of the edifice. In summary, our approach provides a reproducible, globally applicable, and objective means to characterize edifice sizes and centroid positions.

Edifice topographies for 9 volcanoes with 13 inferred magma reservoirs were undefined due to highly complex topography or because of low-lying or negative volcanic landforms. These volcanic systems are typically subaqueous or partially submerged calderas where sufficiently resolved bathymetry is unavailable (e.g., Rabaul Caldera, Papua New Guinea), broad volcanic fields lacking prominent topography (e.g., Laguna del Maule, Chile), or in complex terrain where edifices cannot be easily isolated from non-volcanic structures (e.g., Santorini, Greece; Spurr, USA). In these cases, a rough mean radius was determined by fitting an ellipse to the planform view of the volcano, and the ellipse center was approximated as the edifice center. Edifice volumes and relief were unquantifiable for these volcanoes, and thus are excluded from analyses involving these topographic parameters.

Importantly, we note that by focusing on edifice centroids, we define our volcanic edifice locations differently than volcano locations given in the GVP database, which focuses on locations of recent eruptive vents or volcano summits (which are important for hazard assessment, but are a geologically transient features). Comparing the locations of edifice centroids to the location of the most recently active vents (which we define via historical observations, visible evidence of eruption such as vent craters, or otherwise taken to be the volcano summit), we observe that although edifice centroids and vents are generally roughly co-located, in many cases edifice centroids are multiple kilometers from vent locations. The differences between recent vent locations and edifice centroids

are greatest for volcanic complexes and calderas with ring fracture vents (Figure A8). Differences between vent and edifice centroid locations translate into appreciable differences in magma reservoir offset distances from recent vents or from edifice centroids (Figure A9).

Text A3. Depth datum

The lithostatic pressure affecting a subsurface magma body is a function of the overlying crustal rock column averaged over a surface area roughly equal to the reservoir depth (McTigue & Segall, 1988). Given this, and because depths are inconsistently reported in published studies, we recalculate magma reservoir centroids as depth from the mean local surface elevation. The average local surface elevation for each magma reservoir is determined from a circular area around the reservoir centroid epicenter, where the circle's diameter is equal to the depth of the reservoir centroid beneath the surface (Tables S1, S2). Thus, the mean surface elevation is calculated over a smaller surface region for shallower reservoirs than for deeper reservoirs. Given that a substantial number of reservoir centroids are significantly offset from volcano summits, these recalculated depths can be notably different from the more conventional view of assuming depth beneath a volcanic summit. For 6 cases where magma reservoir centroids are subaqueous, we use depth beneath the sea floor as the diameter to average local bathymetry elevation. We then add the 1/3 of the mean water column height to the reservoir depth to account for the pressure that the water column exerts (where water density is ~1/3 that of non-porous crustal rock).

Text A4. Auxiliary Data: Volcanic compositions, Crustal stress regimes, Visualization with Google Earth database

Volcanic compositions: Many volcanic systems exhibit compositional diversity in erupted products in time and space. However, given the scope of our analyses, we consolidate this complexity and classify volcano types as simply "basaltic", "andesitic", "dacitic", or "rhyolitic" based on their dominant rock type, either reported in the GVP database or in recent publications (Tables S1, S2). For bimodal systems, we consider the volcano composition as that of most recent eruption, hereby assuming that inferred

magma reservoirs are likely related to the recent activity. Our “basaltic” classification includes GVP dominant compositions of “Basalt/Picro-basalt” and “Trachybasalt/Tephrite Basanite”. Our “andesitic” classification includes GVP dominant compositions of “Andesite/Basaltic”, “Andesite/Basaltic andesite”, and “Phono-tephrite/Tephri-phonolite”. Our “dacitic” and “rhyolitic” classifications include GVP dominant compositions of “Dacite” and “Rhyolite”, respectively.

Crustal stress regimes: Characteristics of arc stress regime for each volcanic center are from the compilation of Heuret and Lallemand (2005) where stress state is classified on a -3 to +3 scale from highly compressional to highly extensional (Tables S1, S2, Figures A1, A2). This compilation specifically calculates stress state in the back-arc, however these stress states should generally apply to the main volcanic arc as well. The Heuret and Lallemand (2005) compilation does not include arcs in the Mediterranean, so Italian and Hellenic arc volcanoes are excluded from this metric. Some stress regimes are under-represented in our database, so relationships of magma reservoir depth distributions in different stress regimes remain inconclusively resolved.

Visualization with Google Earth database: Volcanic edifice bounds and the locations of edifice centroids, vents, summits, and magma reservoir centroids (with depth information in metadata) have been compiled into a Google Earth database. Image overlays from key publication figures are also included, which were in some cases used to determine the reservoir centroid, or in other cases simply as illustrative examples. This Google Earth database is available as Data Set S2.

Supplementary Figures

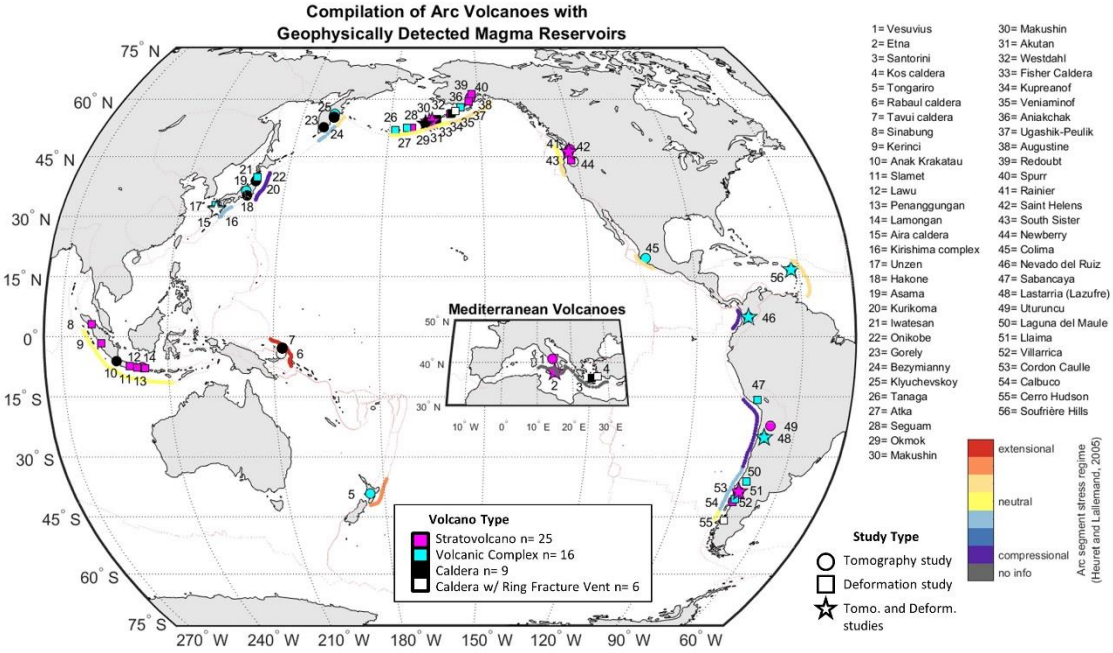

Chapter II, Figure A1. Global distribution of arc volcanoes with geophysically inferred magma reservoirs used in this study. Symbol colors indicate volcanic edifice type and symbol shape indicates the types of geophysical study at each volcano. Subduction zone segments are colored according to back-arc stress regime. Volcanoes are identified by numbers 1 - 56 (see Tables S1, S2).

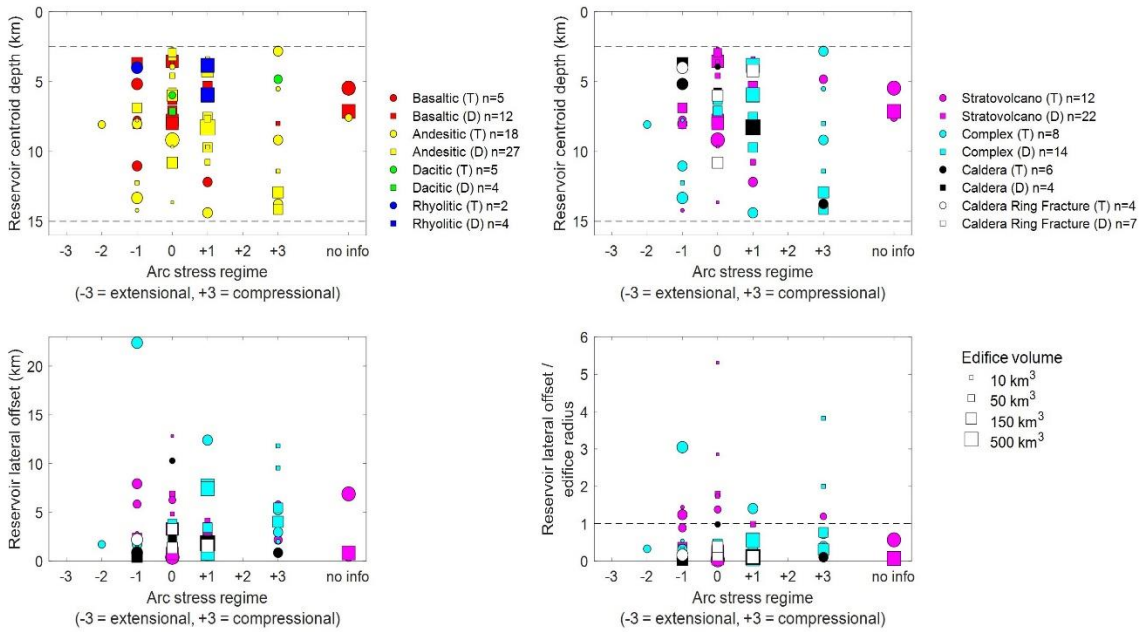

Chapter II, Figure A2. *(top)* Magma reservoir centroid depths and *(bottom)* absolute and scaled lateral offsets from edifice centroids for volcanoes in different arc stress regimes. Arc stress regimes are taken from back-arc stresses defined by Heuret and Lallemand (2005). No stress state was defined for Mediterranean subduction zones, and are listed here as "no info". Symbols sizes are scaled to edifice volumes. *(T)* and *(D)* indicate tomography and deformation studies, respectively. 13 magma reservoirs at volcanoes with unquantified volumes are not shown. Dashed horizontal lines are the shallowest and deepest depths considered in this study.

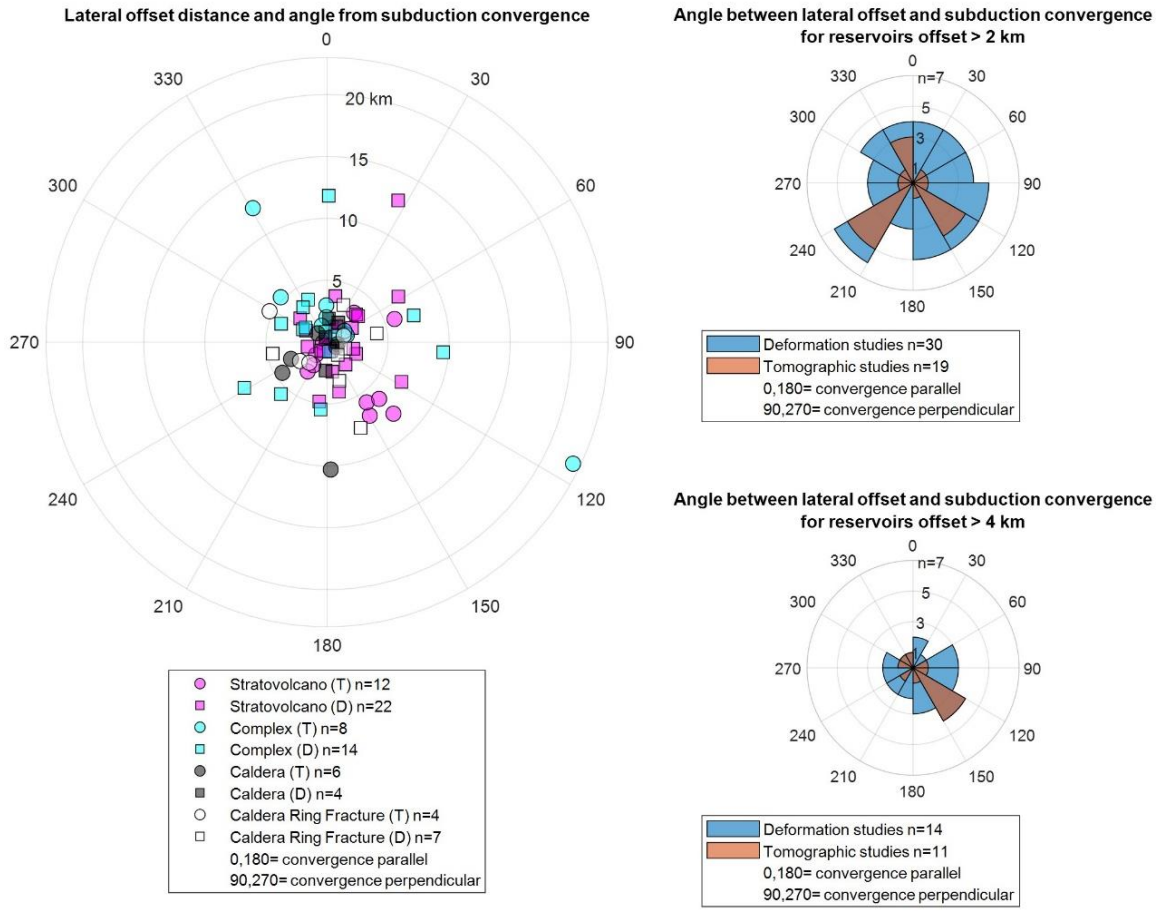

Chapter II, Figure A3. (*left)* Planform view of the lateral offset distance between edifice and magma reservoir centroids, and angle between edifice-reservoir offset direction and the direction of local subducting plate convergence. Directions of 0° and 180° indicate that reservoirs are offset parallel to local subduction plate convergence direction, in directions distal (0°) and proximal (180°) to the trench. Directions of 90° and 270° indicated reservoirs offset perpendicular to plate convergence, along strike of the subduction. (*right*) Polar histograms of magma reservoir offset from edifice centroid relative to convergence direction for reservoirs offset > 2 km *(top)* and > 4 km *(bottom)* from the edifice centroid. Histogram counts are cumulative (not overlapping). Direction of plate convergence in the vicinity of each volcano location is taken from the NNR-MORVEL no net rotation model (Argus et al., 2011).

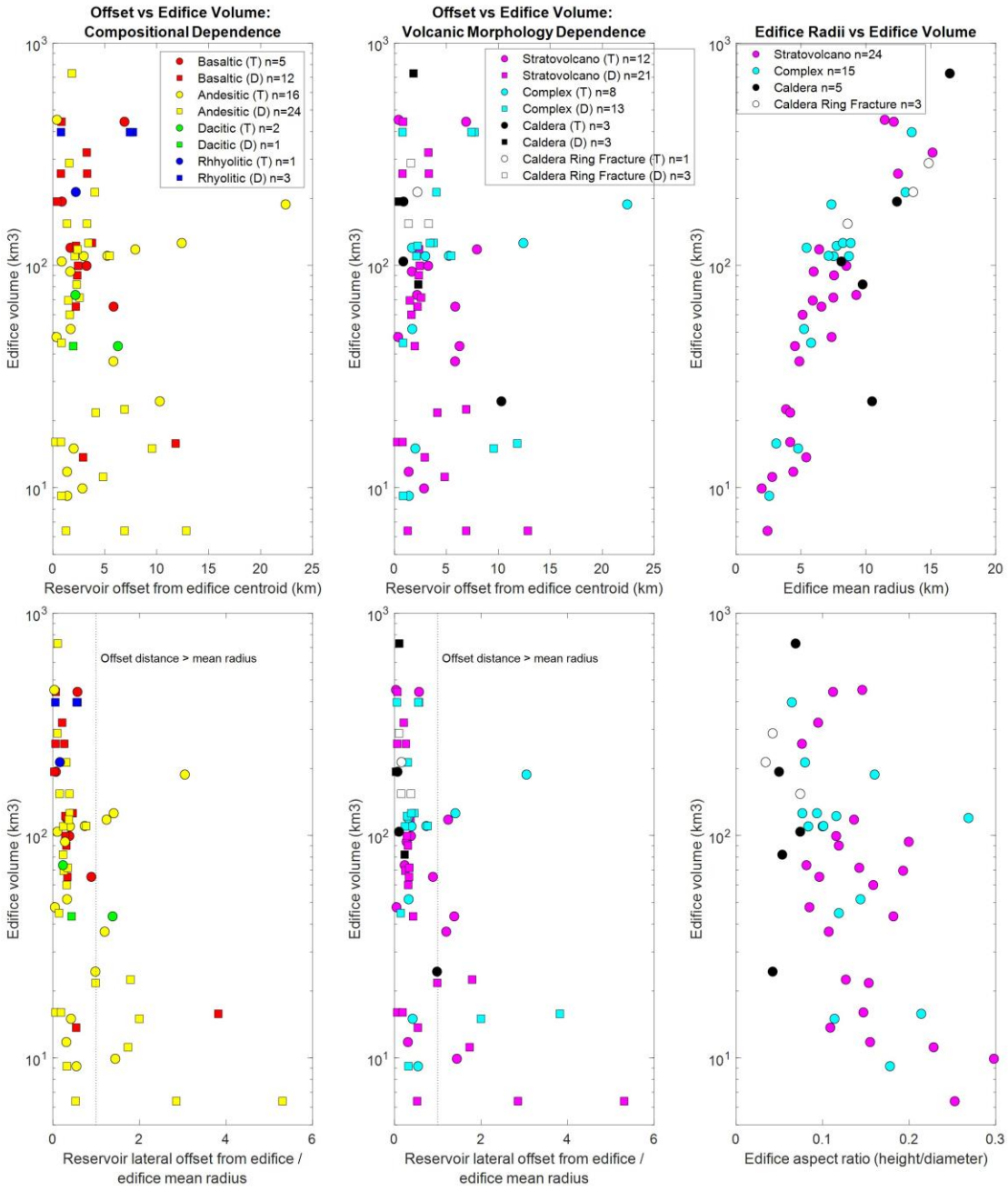

Chapter II, Figure A4. Edifice volume compared to magma reservoir lateral offset and edifice radius and aspect ratios, in absolute *(top)* and scaled *(bottom)* offsets. *(T)* and *(D)* indicate tomography and deformation studies, respectively. 13 magma reservoirs at volcanoes with unquantified volumes are not shown. Legend is the same for sets of upper and lower panels.

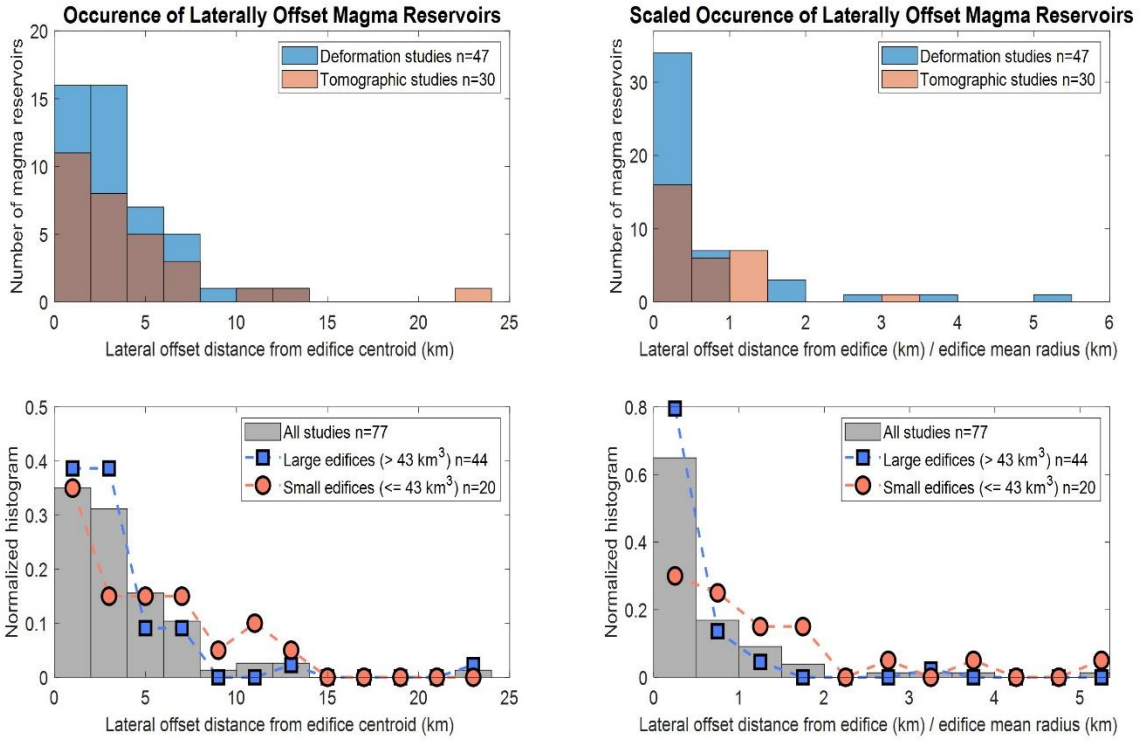

Chapter II, Figure A5. *Upper panels:* Histograms of absolute lateral offset *(top left)* and scaled offset *(top right)* for deformation and tomographic studies. A greater number of geodetically inferred magma reservoirs are included in our database than tomographically located reservoirs, but a similar proportion of reservoirs offset > 4 km are recognized by both techniques (32% vs. 37%, respectively). Histogram counts are overlapping (not cumulative). *Lower panels:* Deformation and tomography studies are combined and the full dataset is separated into large and small edifice volumes for magma reservoir absolute offsets *(bottom left)* and scaled offsets *(bottom right)*. Setting a threshold volume of ≤ 43 km^3, smaller edifices are notably more offset than larger edifices ($p = 0.25$; Chapter II, Figure A15). 13 magma reservoirs at volcanoes with unquantified volumes are not shown in lower panel.

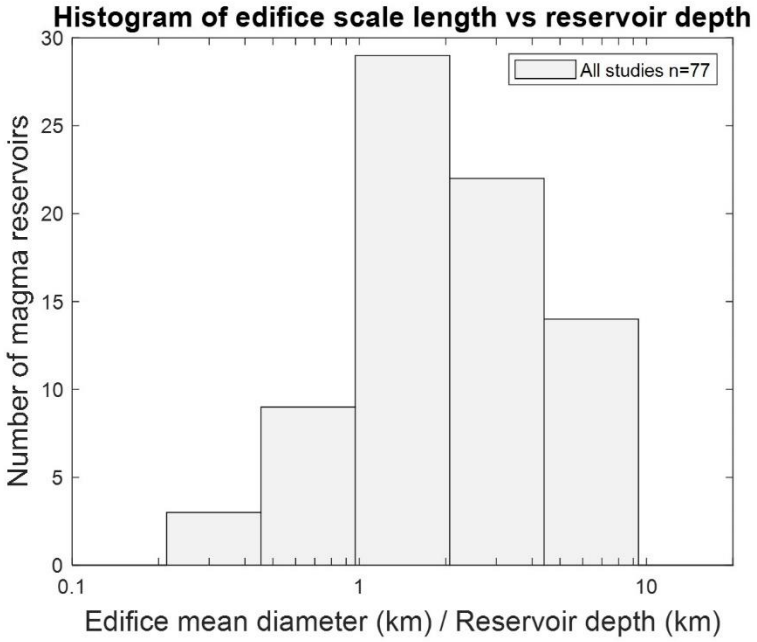

Chapter II, Figure A6. Histogram of edifice mean diameter scaled by reservoir depth. All magma reservoir depths are within an order of magnitude of associated edifice diameters, implying that stresses and deformation from each structure are in phase (McTigue & Segall, 1988) and that sub-volcanic magma reservoirs and their edifices are likely mechanically coupled.

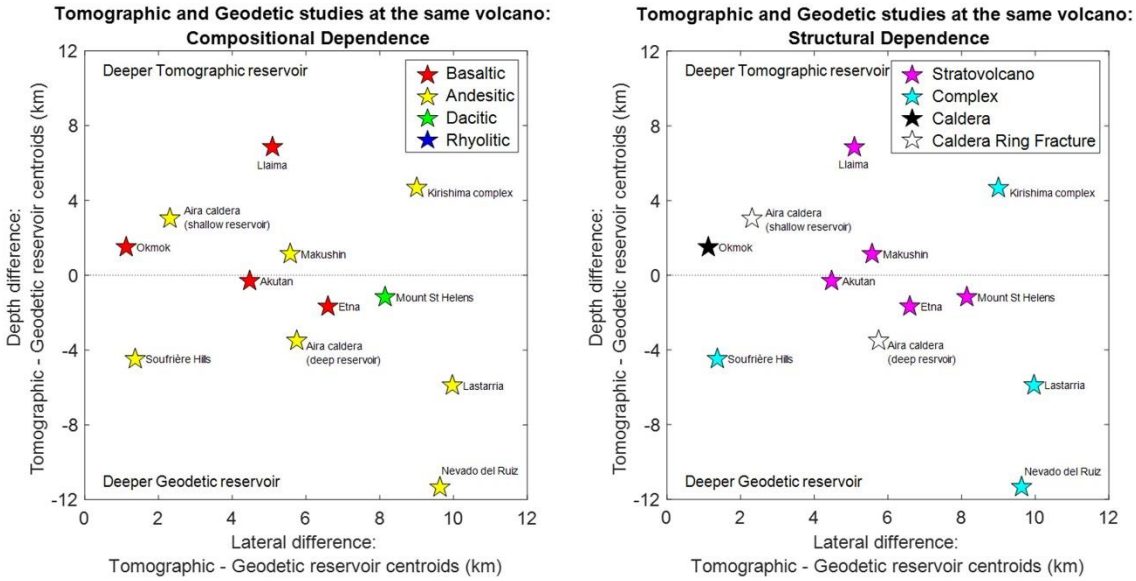

Chapter II, Figure A7. The lateral distance and depth differences between tomographically and geodetically inferred magma reservoir centroids at the same volcano. Volcanoes are categorized by *(left)* dominant composition and *(right)* structural type. Major differences in both depth and lateral position of inferred magma reservoirs exist between the different techniques.

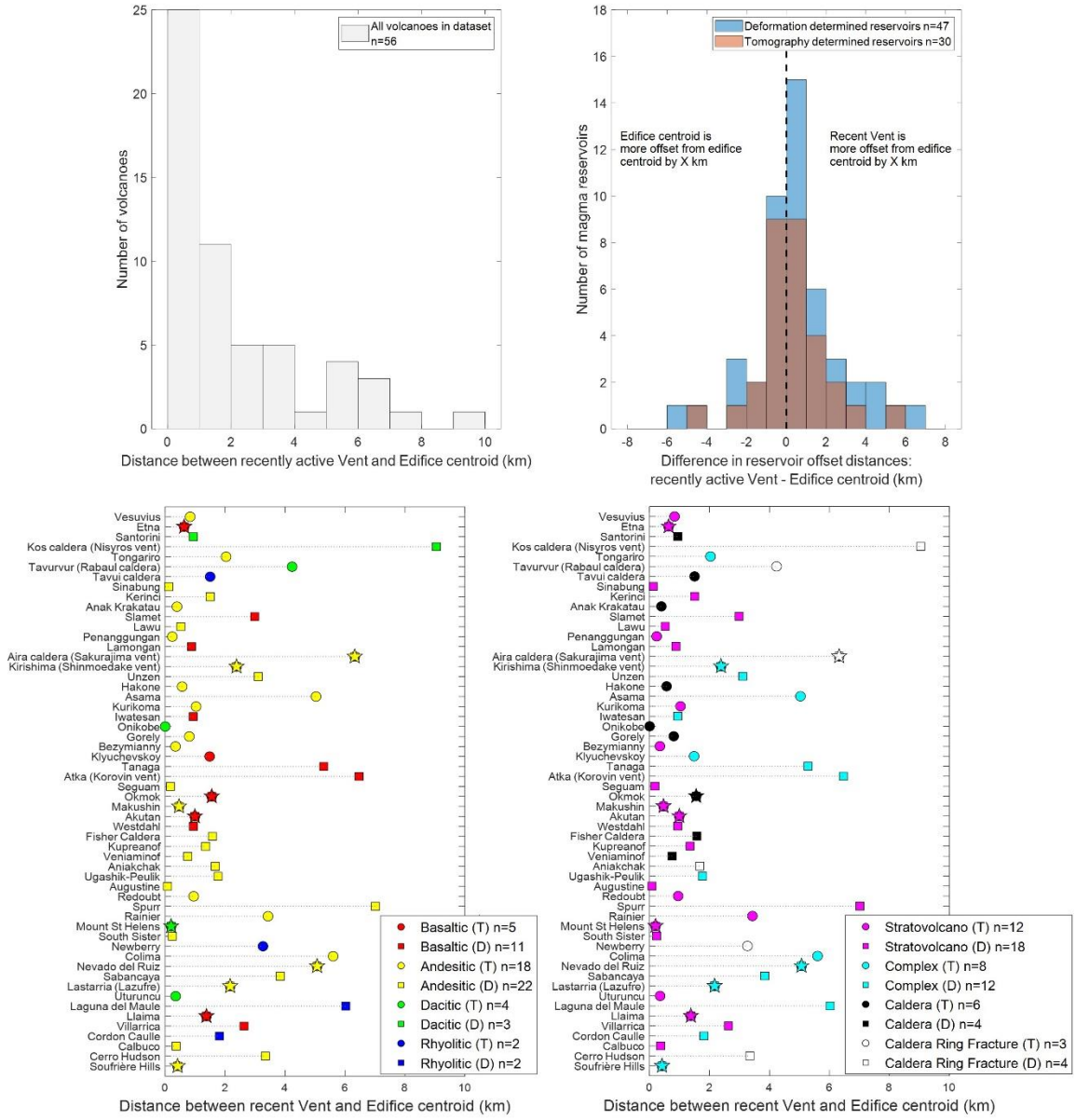

Chapter II, Figure A8. *(top left)* Comparison of edifice centroids and recently active vents (or summits where no vent was identified). Edifice centroids can be substantially removed from vent/summit locations, leading to notable differences in offset distances of magma reservoirs if considering distance from magma reservoir to edifice centroid or to vent location *(top right)*. Histogram counts are overlapping (not cumulative). *(bottom panels)* Distances between edifice centroids and recent vent or volcanic summits for each volcano in this database, with volcanoes classified by composition *(bottom left)* or structural type *(bottom right)*. *(T)* and *(D)* indicate tomography and deformation studies, respectively. Star symbols are volcanoes with magma reservoirs inferred from both tomography and deformation studies.

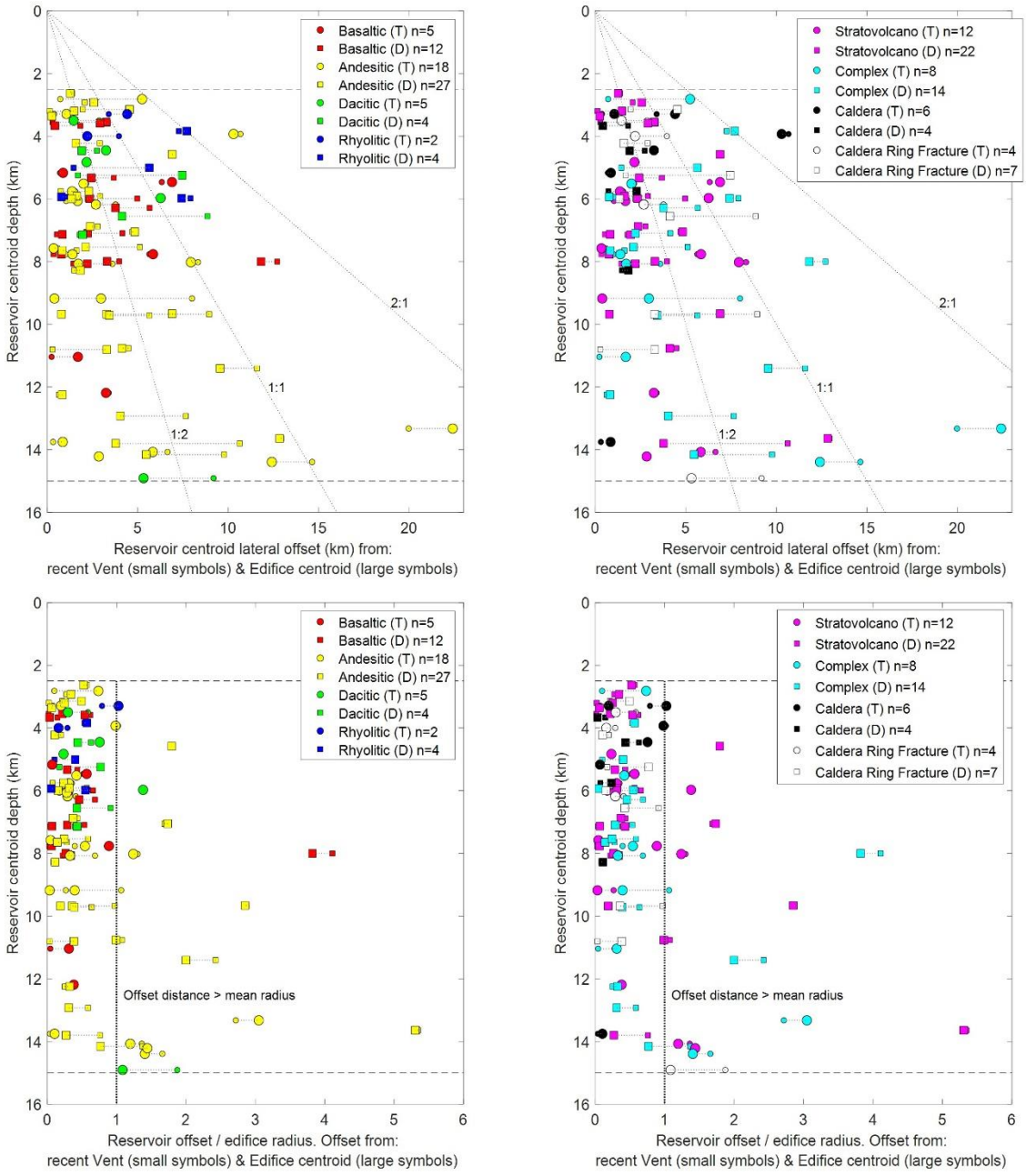

Chapter II, Figure A9. Magma reservoir centroid depths and absolute lateral offsets *(top)* and scaled lateral offsets *(bottom)* from edifice centroids (large symbols) and recent vents (small symbols). Volcanoes are classified by composition *(left)* or structural type *(right)*. *(T)* and *(D)* indicate tomography and deformation studies, respectively. Dashed horizontal lines are the shallowest and deepest depths considered in this study.

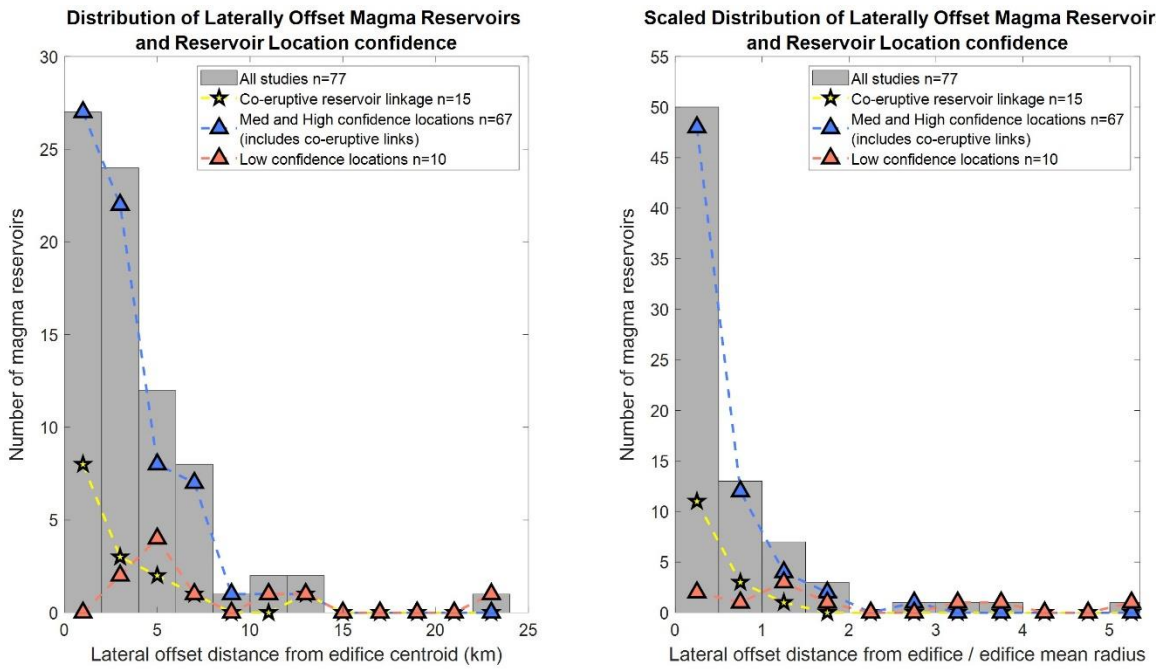

Chapter II, Figure A10. Histograms of absolute *(left)* and scaled *(right)* magma reservoir offsets from edifice centroids for different confidence levels in reservoir location and link to the edifice. Co-eruptive links are identified either through tracking earthquakes between the magma body and the erupting edifice, or via precursory or syn-eruptive geodetic or tomographic changes.

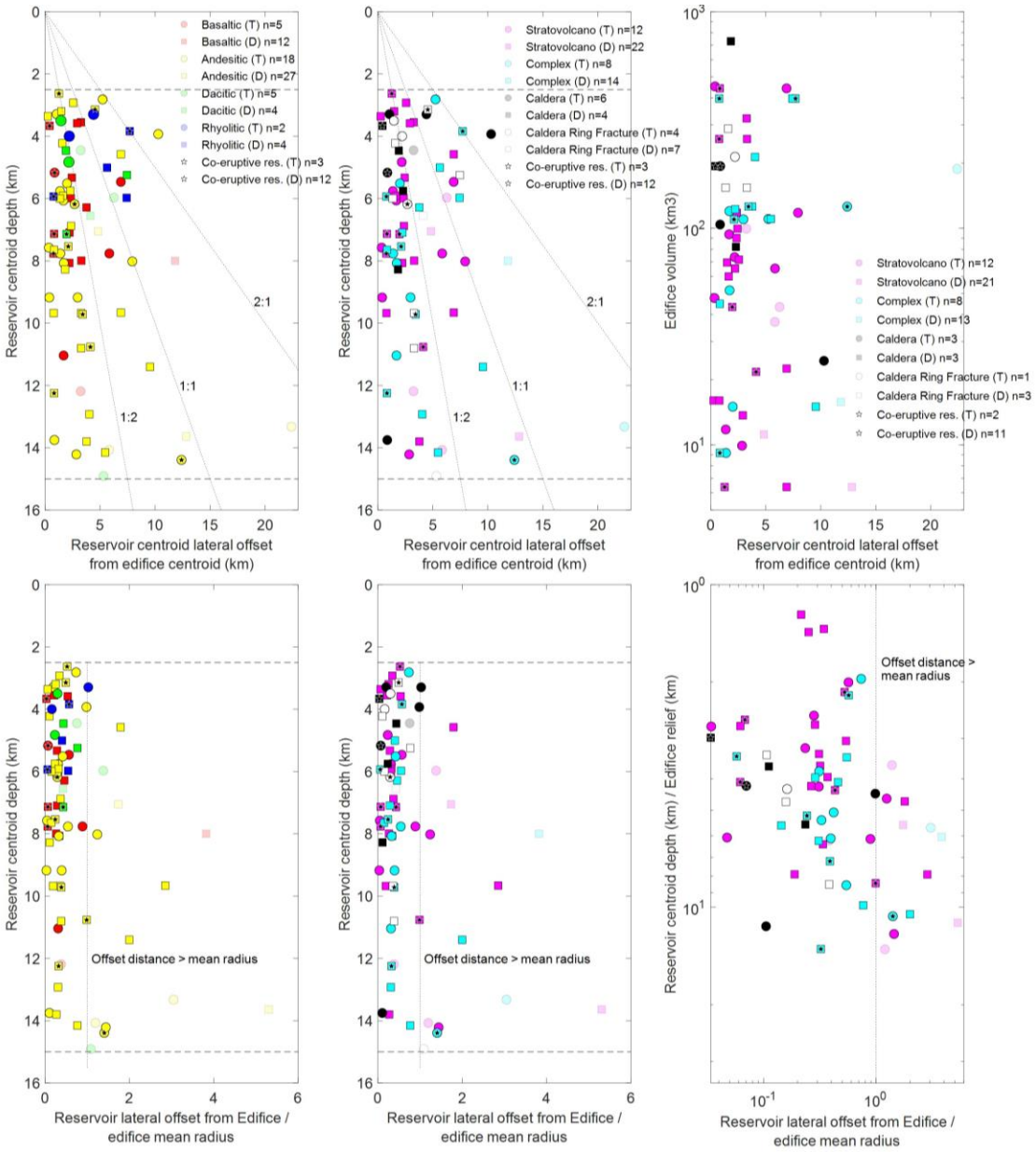

Chapter II, Figure A11. Absolute *(top)* and scaled *(lower)* magma reservoir centroid offset from edifice centroid relative to reservoir depth and edifice volume or height. Magma reservoir locations with low imaging quality or low confidence in connection to the edifice are shown in transparency (n=10). A subset of magma reservoirs with co-eruptive evidence of occurrence and linkage to the edifice are highlighted with central stars (n=15). Symbols in all left and middle figures are not scaled by edifice volume, so that the 13 reservoirs at volcanoes with unquantified edifice volumes are included in this figure, as opposed to Figures 2 and 3 in the main text. Dashed horizontal lines are the shallowest and deepest depths considered in this study. *(T)* and *(D)* indicate tomography and deformation studies, respectively. Legend is the same for sets of upper and lower panels.

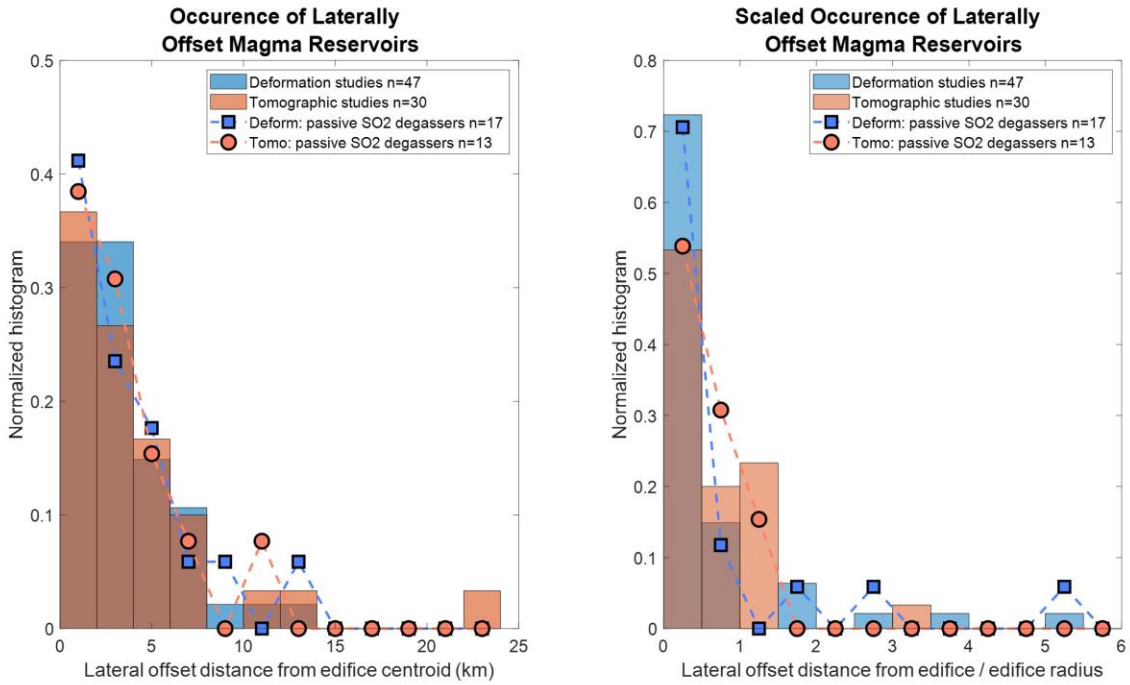

Chapter II, Figure A12. Histogram of magma reservoir absolute offset from edifice centroid *(left)* and offset scaled to edifice radius *(right)* for the full dataset (bars) and for volcanoes with passive SO_2 degassing (lines; 20 volcanoes hosting 30 magma reservoirs) detected between 2005 - 2015 via OMI satellite (Carn et al., 2017). The distribution of reservoir lateral offsets is very similar between volcanoes with passive SO_2 degassing compared to the full database. Histogram bar counts are overlapping (not cumulative).

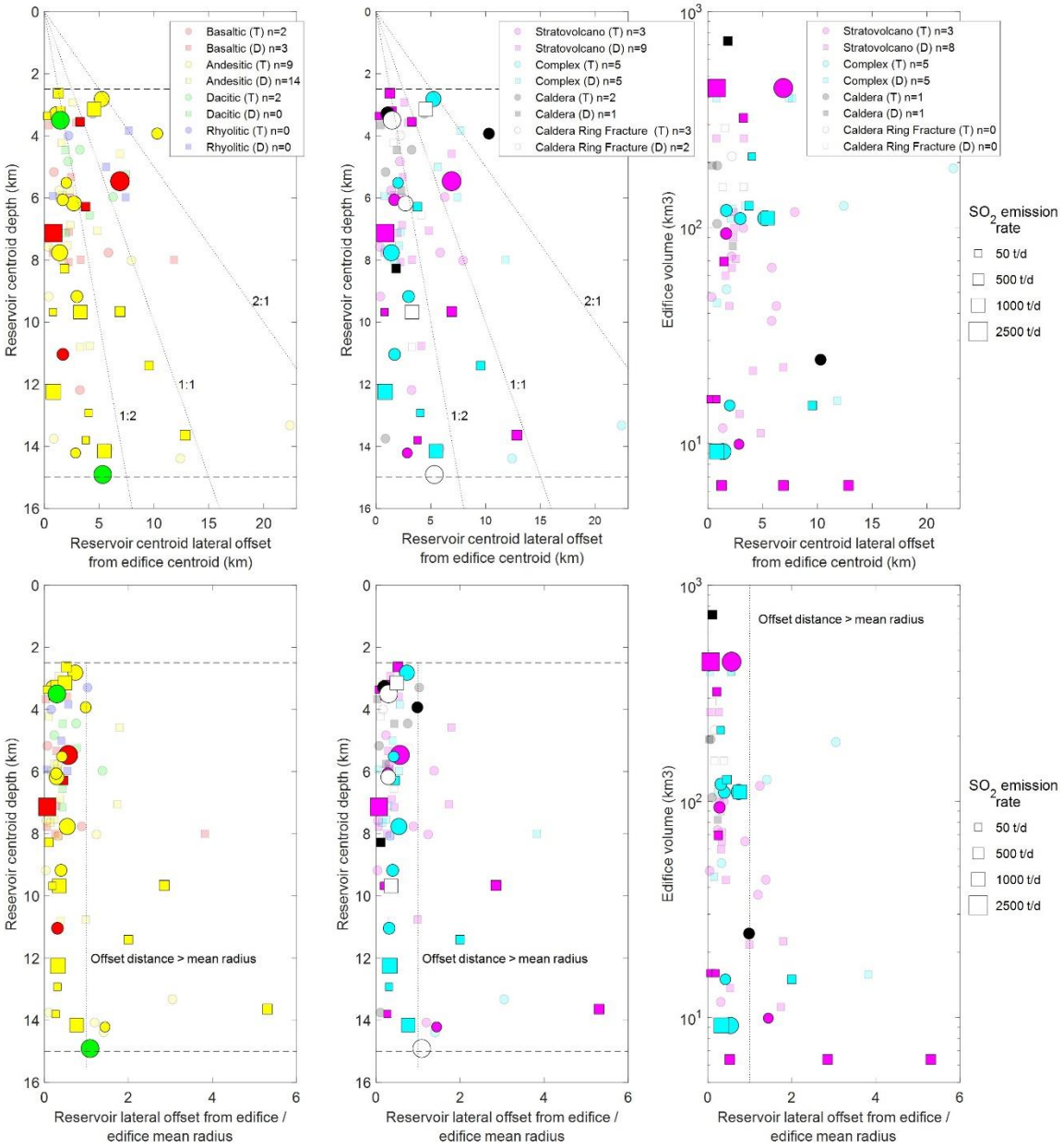

Chapter II, Figure A13. Absolute *(upper panels)* and scaled *(lower panels)* magma reservoir centroid offset from edifice centroid relative to reservoir depth and edifice volume. Volcanoes with passive SO_2 degassing detected between 2005 - 2015 via OMI satellite (Carn et al., 2017) are highlighted (20 volcanoes hosting 30 magma reservoirs), with symbol sizes scaled to average SO_2 degassing rate during the detection time interval. Volcanoes without detected passive SO_2 degassing are shown in transparency (36 volcanoes hosting 47 magma reservoirs). *(T)* and *(D)* indicate tomography and deformation studies, respectively. Legend is the same for sets of upper and lower panels.

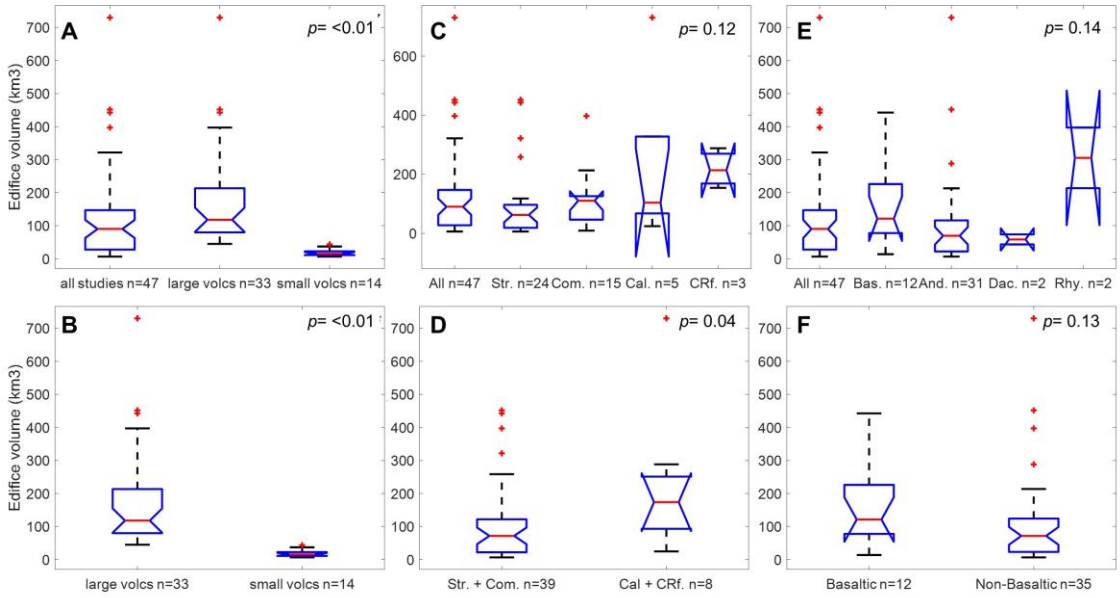

Chapter II, Figure A14. Notched box and whisker plots comparing edifice volumes for volcanoes of different size classifications *(A, B)*, structural types *(C, D)*, and compositions *(E, F)*. The red horizontal line is the median value and the notched area defines the 95% confidence range for the median. *P*-values from Kruskal-Wallis ANOVA tests (non-parametric data) show the probability that all groups are from a single distribution. Volcanoes with edifice volumes ≤ 43 km^3 are considered "small". Str. = stratovolcano; Com. = volcanic complex; Cal. = calderas; CRf. = calderas with ring fracture vents; Bas = basaltic; And = andesitic; Dac = dacitic; Rhy = rhyolitic.

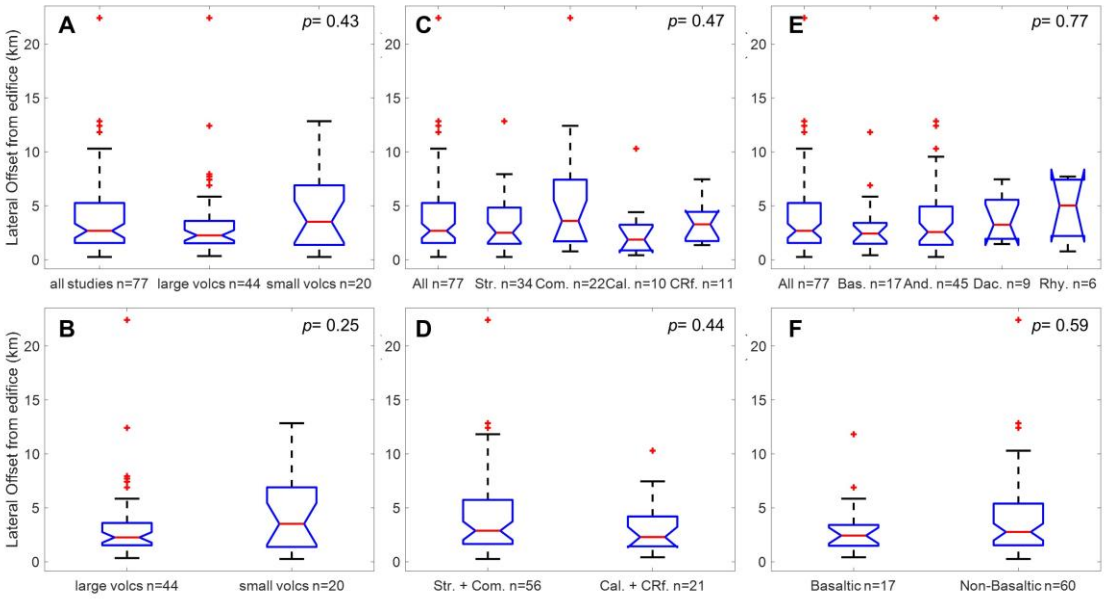

Chapter II, Figure A15. Notched box and whisker plots comparing magma reservoir lateral offsets from edifice centroids for volcanoes of different size classifications *(A, B)*, structural types *(C, D)*, and compositions *(E, F)*. The red horizontal line is the median value and the notched area defines the 95% confidence range for the median. *P*-values from Kruskal-Wallis ANOVA tests (non-parametric data) show the probability that all groups are from a single distribution. Volcanoes with edifice volumes ≤ 43 km^3 are considered "small". Str. = stratovolcano; Com. = volcanic complex; Cal. = calderas; CRf. = calderas with ring fracture vents; Bas = basaltic; And = andesitic; Dac = dacitic; Rhy = rhyolitic.

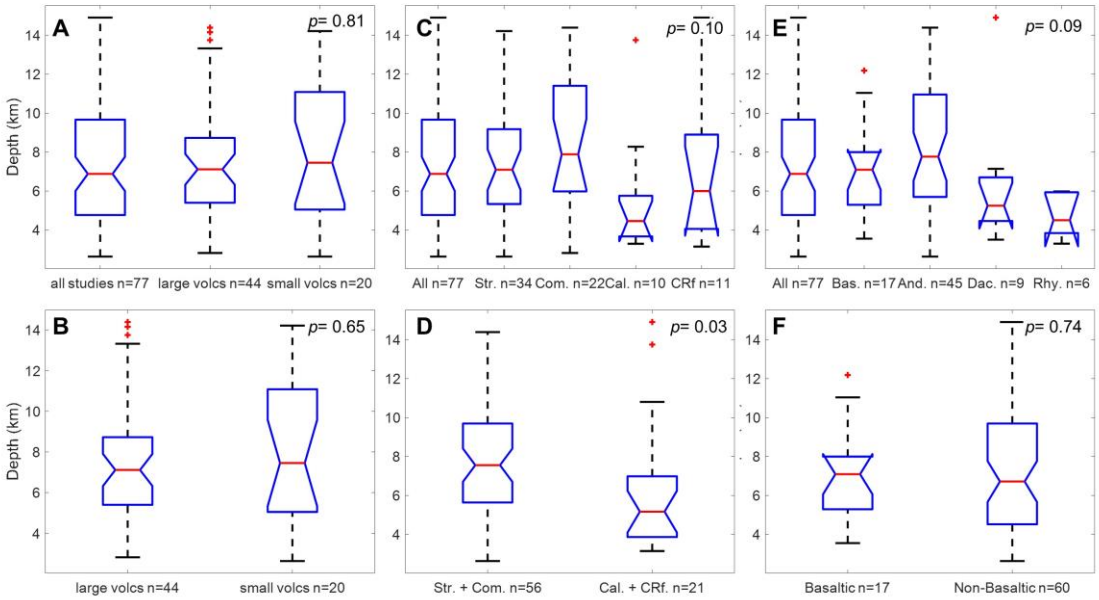

Chapter II, Figure A16. Notched box and whisker plots comparing magma reservoir depths for volcanoes of different size classifications *(A, B)*, structural types *(C, D)*, and compositions *(E, F)*. The red horizontal line is the median value and the notched area defines the 95% confidence range for the median. *P*-values from Kruskal-Wallis ANOVA tests (non-parametric data) show the probability that all groups are from a single distribution. Volcanoes with edifice volumes ≤ 43 km^3 are considered "small". Str. = stratovolcano; Com. = volcanic complex; Cal. = calderas; CRf. = calderas with ring fracture vents; Bas = basaltic; And = andesitic; Dac = dacitic; Rhy = rhyolitic.

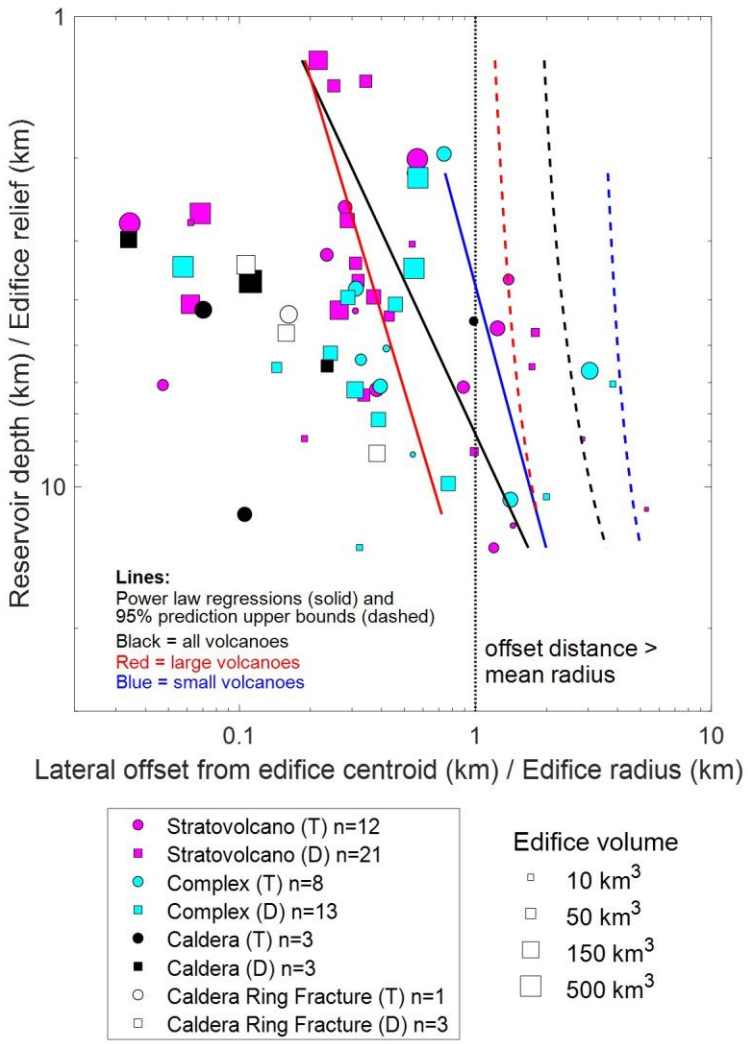

Chapter II, Figure A17. Non-dimensional view of reservoir offset relative to depth (same as Figure 3b in main text). Power law regressions and 80% upper prediction bounds are shown for the full database (black), large volcanoes (red), and small volcanoes (blue). Volcanoes with edifice volumes ≤ 43 km^3 are considered "small". The scaled reservoir lateral offset (x-axis) is taken as the dependent variable. Power laws fits are of the form: $x = b \cdot y^m$, where x is the magma reservoir scaled lateral offset and y is the scaled reservoir depth. Fit coefficients are: All volcanoes: $x = 0.1510 * y^{0.9249}$, $R^2 = 0.15$; Large volcanoes: $x = 0.1667 * y^{0.6006}$, $R^2 = 0.05$; Small volcanoes: $x = 0.4925 * y^{0.5374}$, $R^2 = 0.10$. *(T)* and *(D)* indicate tomography and deformation studies, respectively. 13 magma reservoirs at volcanoes with unquantified volumes are not included in the figure or in regression fitting.

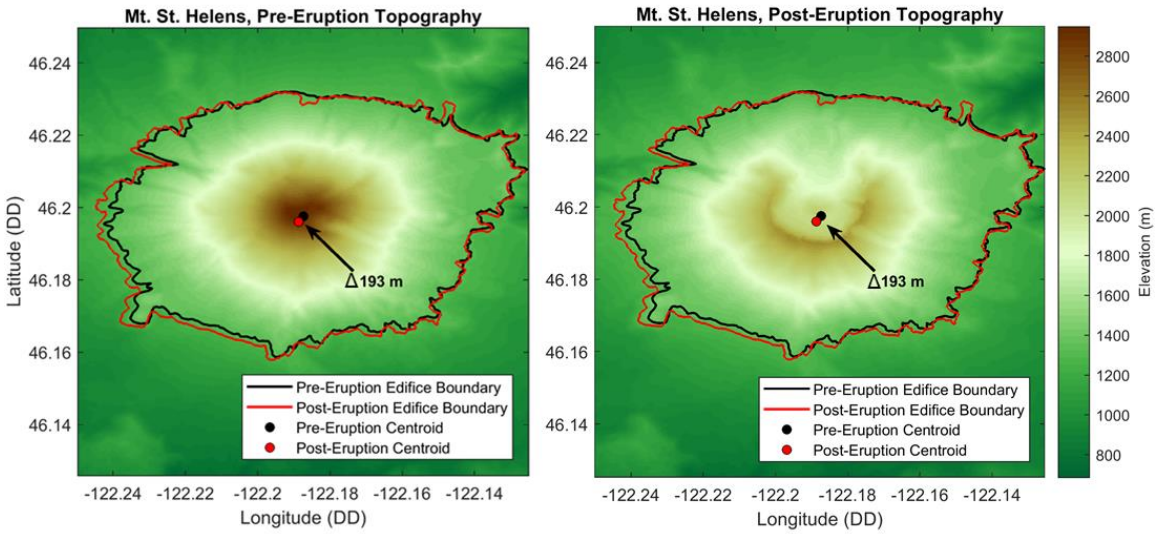

Chapter II, Figure A18. Surface topography of Mount St. Helens volcano (WA, USA) *(left)* before and *(right)* after the 1980 eruption and flank collapse/lateral blast, where ~2.5 km^3 of the 43 km^3 edifice was mobilized. Pre- and post-eruption edifice bounds and calculated edifice centroids are shown on each panel for comparison. The pre-eruption edifice centroid was nearly co-located with the pre-eruption summit, and the post-eruption edifice centroid is shifted only 193 m to the SSW. This minor centroid change is a consequence of only a relatively small part of the overall edifice volume being mobilized during the 1980 events. Elevation and lateral scales are equal for both panels. Pre-eruptive topography was accessed from http://gis.ess.washington.edu/data/raster/thirtymeter/mtsthelens/. Post-eruptive topography is from February 2000 SRTM (NASA JPL, 2013).

Additional Supporting Information

Files available at: https://doi.org/10.7910/DVN/LHD1HY (Lerner, 2020)

Supplementary Tables and Data Sets

Table S1. List of volcanoes and key edifice morphology and magma reservoir parameters in this study ("Table S1_simplified database" sheet; Microsoft Excel 2016 file).

Table S2. List of volcanoes and full edifice morphology and magma reservoir parameters in this study ("Table S2_full database" sheet; Microsoft Excel 2016 file).

Table S3. Summary statistics of geophysically inferred magma reservoirs at different volcano types, compositions, and edifice sizes ("Table S3_summary statistics" sheet; Microsoft Excel 2016 file).

Data Set S1. A collection of maps (as a PDF) showing edifice bounds and centroids overlain on topographic maps of each volcano in the database.

Data Set S2. Google Earth database of volcanic edifice bounds and geophysically imaged magma reservoirs. This is a Google Earth .kmz file with all volcano edifice bounds and locations of edifice centroids, vents, summits, and magma reservoirs, as well as supporting figure overlays from the literature that were used for mapping magma reservoir locations.

APPENDIX B

CHAPTER III SUPPLEMENTARY INFORMATION AND FIGURES

B1. Fe-XANES beam damage assessment and corrections

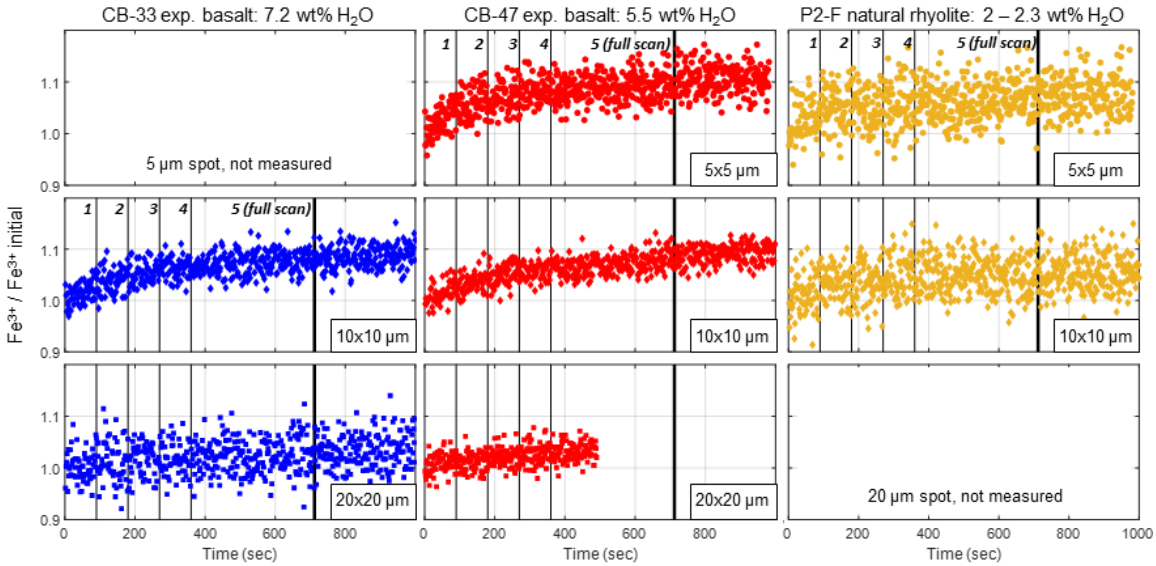

Chapter III, Figure B1. Time-dependence of the relative increase of 2nd pre-edge doublet (Fe Kα/IO / Fe Kα/$IO_{initial}$ at 7113.4 eV, referred to here as Fe^{3+}/Fe^{3+} initial) during irradiation with X-ray beams of 5x5 µm *(upper)*, 10x10 µm *(middle)*, and 20x20 µm *(lower)* footprint sizes. Fe^{3+} initial is the average of the first 10 measurements (13 – 15 s of analysis). Thin vertical lines (labeled 1 – 4) indicate analysis end times for repeat pre-edge Fe-XANES analyses (0.5 s/point), as described in the text. Thick vertical line (5) is the end time after the final full energy scan. Beam damage occurs rapidly in analyses with a focused 5x5 µm beam. However, linear time-dependent functions can be regressed through the rapid scanning sequence in the first 4.5 – 6 minutes of analyses with 10x10 and 20x20 µm beams to correct beam-damaged induce oxidation to the initial (t=0 s) conditions. Photon doses for analyses with 5x5, 10x10, and 20x20 µm beams were 1 – 1.5x10^8, 2.5 – 4.2x10^7, and 2.6 – 8.9x10^6 photons/s/um^2, respectively. We note that synthetic glass CB-33 has a spectra signature consistent with the presence of Fe-oxide nanolites (see discussion in text).

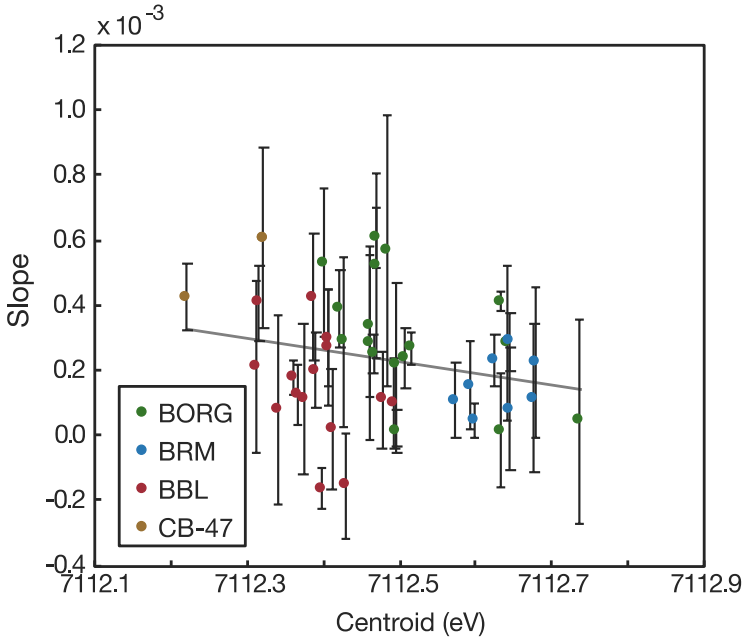

Chapter III, Figure B2. Slopes of linear regressions through Fe Kα pre-edge centroid time series as a function of the centroid position of the first rapid scan (least affected by beam damage) for individual samples. Melt inclusions from three cinder cones in the southern Cascade arc (BORG, BRM, BBL) and experimental glasses (CB-47) are grouped by color. Gray line represents linear fit through all data. See text for discussion.

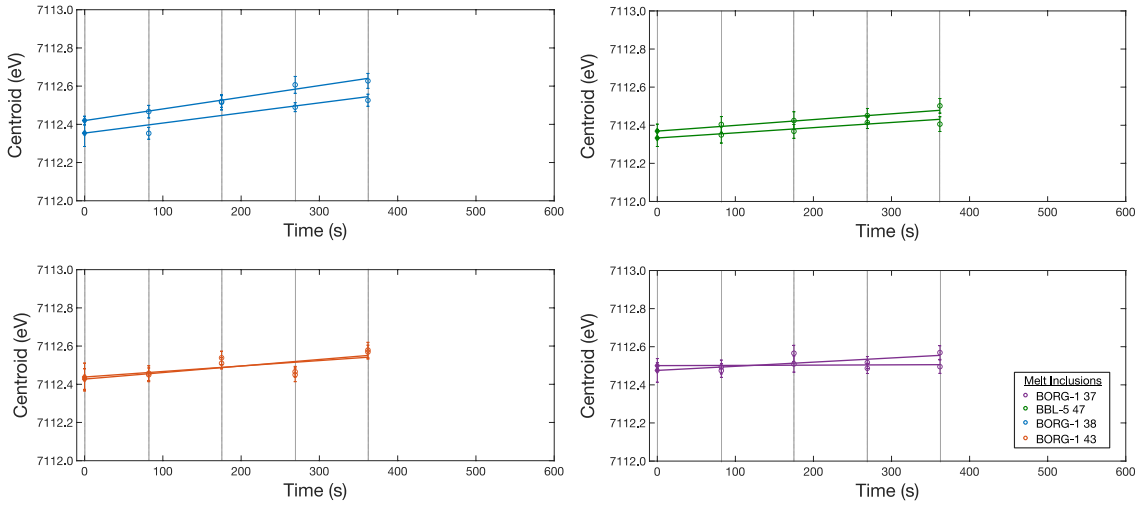

Chapter III, Figure B3. Centroid positions calculated from replicate sets of rapid pre-edge Fe-XANES scans within single MI from the southern Cascades, analyzed with a 10x10 μm beam. Each sequence represents repeated measurements in one analyzed spot. Open circles are centroids calculated for each pre-edge scan. Error bars represent 1 standard error of centroid fits to individual scans. Filled diamonds at t=0 s are the intercept of each linear regression used as the corrected centroid. Error bars on the t=0 centroid represent 1 standard error of linear regression. Vertical lines indicate analysis end times for repeat pre-edge Fe-XANES analyses.

B2. S-XANES peak fitting

We calibrate our peak fitting approach to the suite of experimental hydrous basaltic glasses (45 – 48 wt% SiO_2, 8 – 10 wt% FeO^T, 8 – 10 wt% CaO) presented in Jugo et al. (2010). These glasses were synthesized at different oxidation states and were used by Jugo et al. (2010) to develop an empirical fit relationship of S^{2-} and S^{6+} S-XANES intensities to S speciation. Their calibration was based on the assumption that their most reduced and oxidized end-member glasses occurred S entirely as either S^{2-} or S^{6+}, and that linear combination fitting of the end-members produces representative spectra for glasses with mixed S speciation. Using these end-members and linear combination mixed spectra, Jugo et al. (2010) construct a calibration of S-XANES intensity to S speciation across a range of mixed S states (Figure B4). We note that the presumed linear combination relationship between end-member S-intensities and S speciation has not been shown independently to be true, but in absence of confirmation from Mössbauer or wet chemistry measurements, it is currently a reasonable assumption, and the results agree well with thermodynamic calculations (Jugo et al., 2010).

We use S-XANES spectra presented in Jugo et al. (2010) for these end-member reduced and oxidized glasses to construct linear mixtures of the two and create a S-XANES intensity to S speciation calibration for our peak fitting method (see main text for details). The main difference between our peak fitting method and the Jugo method is that we isolate the S^{6+} peak from the ionization peak at slightly higher energy. By including the ionization peak in our fit procedure, we end up with no S^{6+} intensity in S^{6+}-free glasses, whereas the Jugo fit either convolutes the S^{6+} peak with the ionization peak or fits the step-function background differently than we do, which results in ~30% $S^{6+}/\Sigma S$ XANES intensity in S^{6+}-free glasses. Applying our peak fitting to the full set of synthetic glasses presented in Jugo et al. (2010), we find good agreement between S speciation calculated from our method with that of Jugo et al. (2010) (Figure B7).

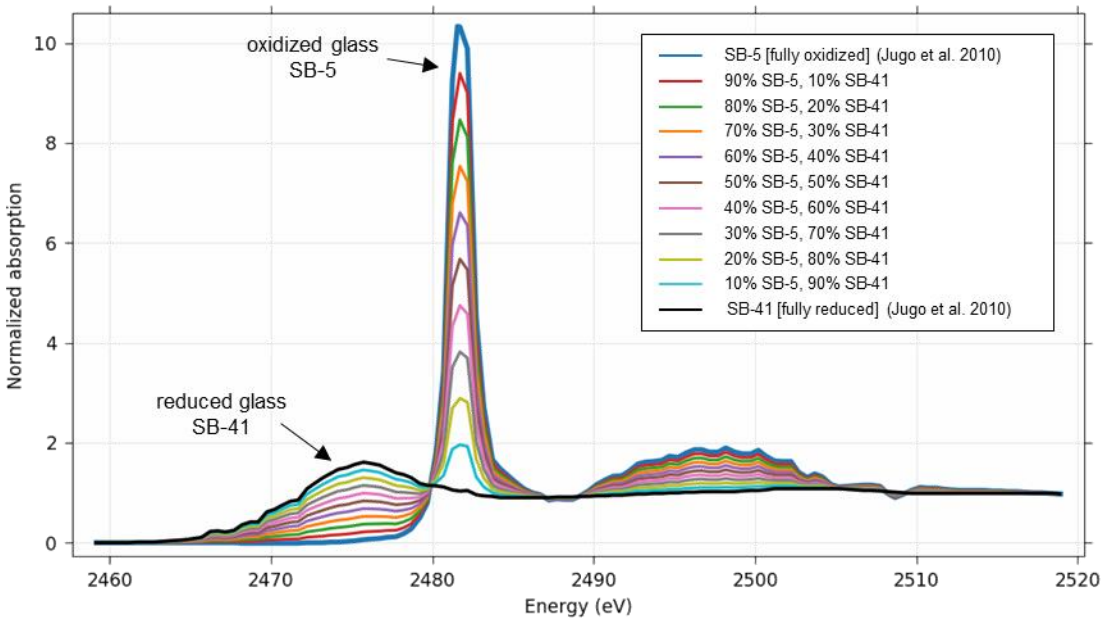

Chapter III, Figure B4. Normalized spectra of completely oxidized (SB-5; $S^{6+}/S\Sigma$ = 100%; blue curve) and completely reduced (SB-41; $S^{6+}/S\Sigma$ = 0%, black curve) synthetic glasses reproduced from Jugo et al. (2010). Linear two-component mixing of these endmember glasses provides a simulated set of spectra to calibrate S-XANES intensities to S speciation in glasses in both Jugo et al. (2010) and in the peak-fitting method presented here. An energy shift of -1 eV has been applied to all the Jugo et al. (2010) data, as discussed in the main text.

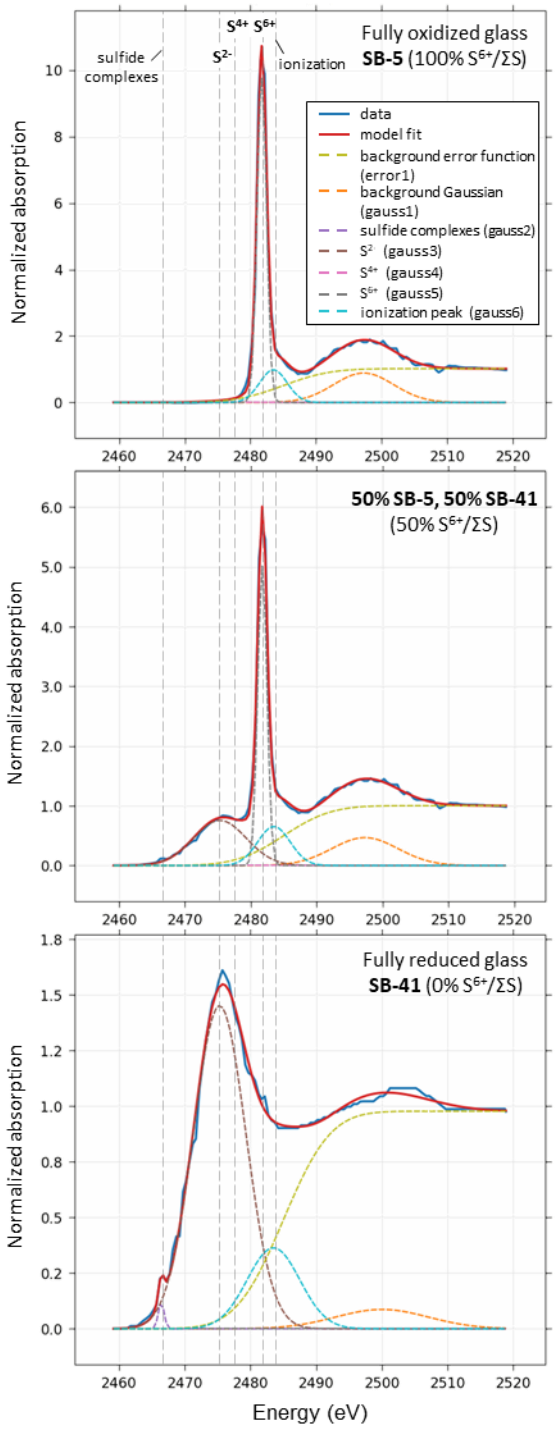

Chapter III, Figure B5. Example peak fits to the normalized end-member oxidized *(upper)* and reduced *(lower)* synthetic glasses reproduced from Jugo et al. (2010), as well as a 50% linear mixture of the two endmembers *(middle)*. Parameters of the fit functions are identified in Table 2. Reference peak position lines are approximate and can vary slightly between samples. An energy shift of -1 eV has been applied to all the Jugo et al. (2010) data (see text).

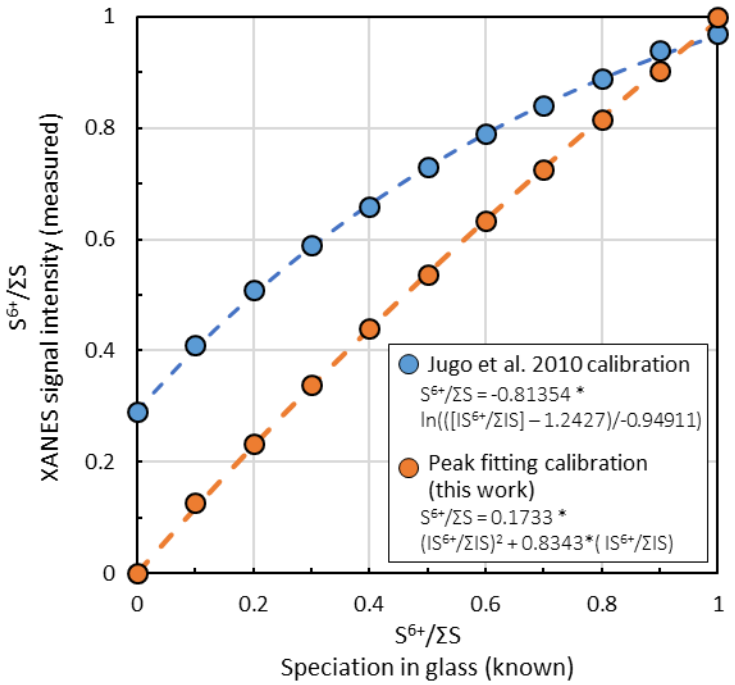

Chapter III, Figure B6. Fit relationships between S-XANES $S^{6+}/\Sigma S$ signal intensity and $S^{6+}/\Sigma S$ speciation in synthetic end-member glasses and linear component mixtures for the Jugo et al. (2010) calibration (blue) and the peak fitting calibration (orange). Uncertainties in S-intensity calculations via peak fitting are estimated to be ~±2 – 5% $S^{6+}/\Sigma S$ based on the reproducibility of spectra normalization and fitting.

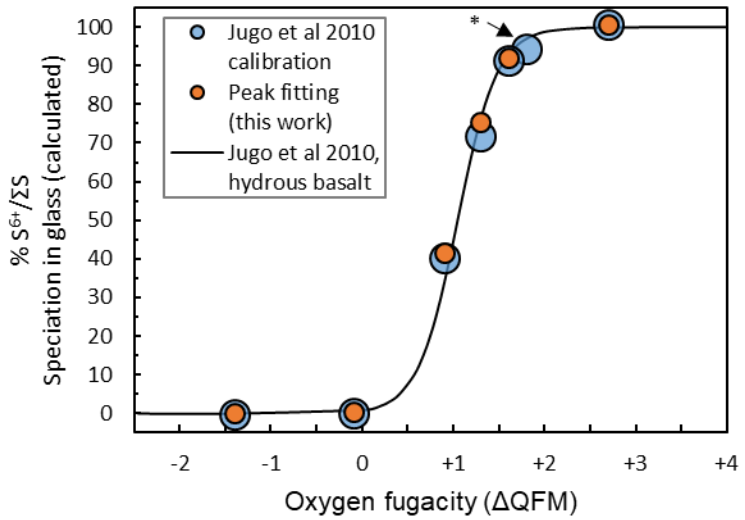

Chapter III, Figure B7. Calculated S speciation vs fO_2 experimental conditions of the set of synthesized glasses from Jugo et al. (2010), with XANES spectral fits from our peak fitting method (orange) compared to the Jugo et al. (2010) approach (blue). Only the most oxidized and reduced glasses, and linear mixtures of the two, were used to calibrate the peak fitting method. Uncertainty in S speciation via peak fitting is estimated to be ~±2 – 5% $S^{6+}/\Sigma S$ based on the reproducibility of spectra normalization and fitting. *Indicates that the normalized XANES spectra for this glass was not presented in Jugo et al. (2010), precluding inclusion in our comparison.

B3. Comparison of measured Fe and S speciation with the model of Nash et al. (2019)

We observe generally good agreement between the calculated melt temperatures and the Nash et al. (2019) model predictions for those temperatures (Figure B8). There is no clear evidence of a quench effect reducing S^{6+} in MI, even though MI would be expected to cool somewhat slower than matrix glass and should therefore be more subject to the proposed electron-exchange during cooling. The substantial deviation of a number of MI and matrix glasses from the Nash et al. (2019) predictions suggests that additional parameters are likely also important in controlling S speciation in natural glasses. Some low-FeO^T MI, which had experienced significant Fe-loss during PEC, have notably higher S^{6+} than predicted, whereas high-FeO^T matrix glasses deviate to lower than predicted S^{6+}, suggesting that Fe concentration may affect S speciation in glasses. The Nash et al. (2019) model was fit through an experimental dataset with a wide range of FeO^T (see Figure 5 of Nash et al. 2019), which might be masking more nuanced compositional effects of Fe on S speciation.

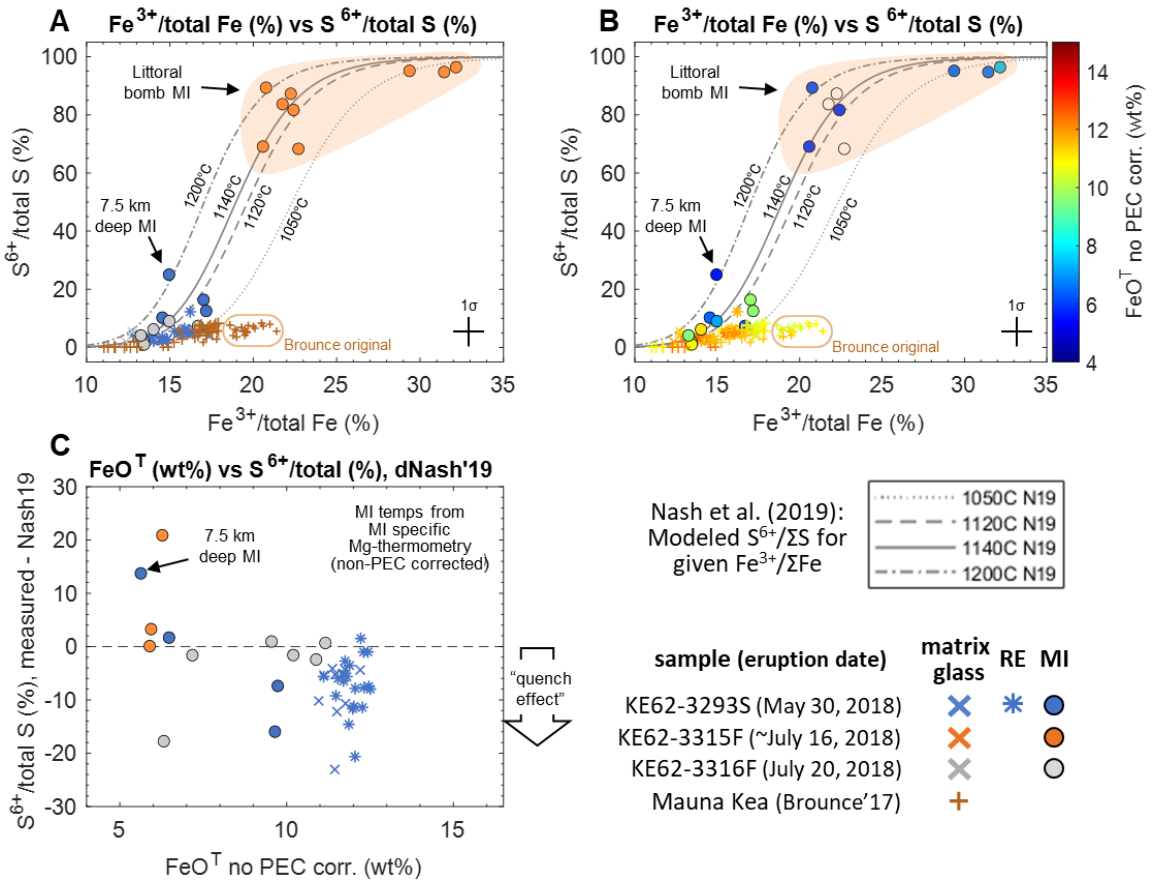

Chapter III, Figure B8. Fe and S speciation from XANES measurements compared to predicted S speciation for a given $Fe^{3+}/\Sigma Fe$ from Nash et al. (2019) modeled relationships at a range of temperatures relevant to Kīlauea samples. Mg-thermometry calculations of matrix glasses indicate temperatures of 1140 °C for proximally quenched samples (KE62-3293S, KE62-3316F) and 1110 – 1120 °C for the littoral blast sample (KE62-3315F). *(A)* Kīlauea 2018 matrix glasses and MI colored by sample type, and *(B)* colored by wt% FeO^T (non-PEC corrected). Fe and S speciation measured in submarine glasses from Mauna Kea by Brounce et al. (2017) are also shown as "+" symbols; small "+" symbols are the originally published data, and large symbols are those data reprocessed using Fe-XANES pre-edge centroid positions and the calibration of Zhang et al. (2018), which shifts the dataset to lower $Fe^{3+}/\Sigma Fe$ proportions. *(C)* The difference in $S^{6+}/\Sigma S$ (absolute) in Kīlauea glasses measured by S-XANES and predicted by the Nash et al. (2019) model at temperatures, compared to FeO^T concentrations (non-PEC corrected). Temperatures for Nash et al. (2019) model predictions for each MI and matrix glass analyses were calculated using the Helz and Thornber (1987) Mg-thermometer for Kīlauea glasses. Positive values indicate higher measured $S^{6+}/\Sigma S$ compared to modeled. Only glasses with mixed S^{6+} and S^{2-} speciation (~13 – 28% $Fe^{3+}/\Sigma Fe$) are shown in *(C)* to compare with the Nash et al. (2019) model. $S^{6+}/\Sigma S$ model fits and calibration are estimated at ±2 – 5% absolute, and uncertainties in $Fe^{3+}/\Sigma Fe$ from centroid fits are < ±1% absolute. Symbology is the same as Figure 14, with a reclassification of some matrix glasses as melt re-entrants (RE).

APPENDIX C
CHAPTER IV SUPPLEMENTARY INFORMATION AND FIGURES

7.1 Extended methods

7.1.1 Electron microprobe

EPMA measurements of major-element compositions of glass and minerals were conducted at the University of Oregon's CAMCOR Laboratories with a Cameca SX100 electron microprobe. Minerals were analyzed with a focused 3 μm beam operating at 15 kV with a current of 30 nA for all elements. Count times were 20 – 40 seconds for Na, Si, Al, Fe, K, which were analyzed first, and 45 – 90 seconds for Mg, Ca, Mn, and Ni, which were analyzed second. Ti and Cr were measured in minerals in a subset of analytical sessions, where count times were 60 and 80 seconds, respectively. Based on repeated analyses of mineral and oxide standards, relative 1-standard error (SE) uncertainties of mineral analyses are < 0.3% for SiO_2, Al_2O_3, FeO^T, Cr_2O_3, MgO, CaO, and TiO_2, < 0.5% for Na_2O, and < 1 % for K_2O.

Melt inclusions and matrix glasses were measured with a diffuse 10 μm beam operating at 15 KeV with a current of 10 nA for Na, Si, K, Al, and Fe, and 50 nA for Mg, Ca, Mn, P, Ti, S, and Cl. Count times were 30 – 40 seconds for Na, Si, K, Al, and Fe, 40 – 90 seconds for Mg, Ca, and Mn, 200 seconds for P and Ti, and 100 – 160 seconds for S and Cl. Na, K, Si, Al, and Fe were measured first, and their concentrations were calculated using a time-dependent intensity correction (TDI) using the Probe for Windows software package (Donovan et al., 2007) to account for alkali mobility in glasses during electron beam excitement (Kuehn et al., 2011). The S Kα peak position in silicate glass is sensitive to S redox state (Rowe et al., 2007; Wallace & Carmichael, 1994), and we optimized the S peak position locations by repeat measurements within single reduced and oxidized Kīlauea MI at different spectrometer peak positions. Sulfur Kα was calibrated on pyrite (S^{1-}) and measured at the pyrite peak for reduced glasses, but measured at -26 spectrometer units (toward the anhydrite peak) from the pyrite peak for oxidized glasses. Measuring at the optimal peak positions for reduced and oxidized glasses increased total calculated S concentrations by 5 – 15% compared to measuring all

glasses at the S^{2-} peak (+4 spectrometer units from the pyrite peak). Relative uncertainties (1 SE) of glass analyses from repeated analyses of glass and mineral standards are generally < 0.4% for MgO and CaO, 0.5 – 1.0% for SiO_2 and Al_2O_3, < 2% for Na_2O, FeO^T, and TiO_2, < 5% for K_2O, MnO, P_2O_5, and S, and 5 – 15% for Cl. Detection limits for all oxides in both mineral and glass analyses are < 0.1 wt% at 99% confidence levels, and are 40 – 70 ppm for S and Cl in glasses. Glass and mineral analyses included in our datasets have oxide totals of 96 – 101 wt% and are presented normalized to anhydrous 100% totals.

7.1.2 Sulfide restorations

Melt inclusion and sulfide dimensions were measured either by optical reticle, or during EPMA imaging. Sulfides are assumed to be spherical and MI are assumed to be ellipsoidal, with the unmeasured depth dimension taken as average of width and height dimensions. Bubble volume and presence of other daughter minerals (typically co-trapped spinel) are removed from MI melt volume during these mass balance calculations. Melt density in MI were calculated from non-PEC corrected compositions at 25 °C and 1 bar via the DensityX tool (Iacovino & Till, 2019), and ranged from 2.8 – 3.0 g/cm^3 depending on H_2O content (0.1 – 0.3 wt%) and the extent of Fe-loss the MI experienced (4 – 11.5 wt% FeO^T). High-T sulfides at Kīlauea contain an appreciable fraction of Cu, having a composition of $Fe_{0.65}(Cu,Ni)_{0.35}S$ (Wieser et al., 2020b). With qualitative EDS measurements, we also observe the presence of some amounts of Cu and Ni in sulfide blebs. We therefore assume a mixed sulfide composition of $Fe_{0.65}Cu_{0.18}Ni_{0.17}S$, which contains 35.7% S by mass, and a sulfide density of 4.5 g/cm^3 (Mungall & Su, 2005). For comparison, pure FeS contains 36.5% S by mass, and thus our assumption of sulfide composition makes little difference in the S mass balance calculations.

Sulfur masses from sulfide blebs are added to the PEC-uncorrected MI glass S concentrations, and the initial MI S concentrations are calculated by scaling these values by the MI PEC-correction factors. Depending on relative sulfide sizes and remaining melt S contents, mass-balance restorations of S in sulfides increases the total S content of MI by 10% to 100% compared to the as-measured S contents of MI glasses. Precipitated

sulfides should play a similarly large role on chalcophile elements like Cu and Ni, but these elements were not measured in MI. The effect of restoring Fe in sulfide blebs to MI glass FeO^T concentrations is very minor (increases of ≤ 0.1 wt% FeO^T) due to the small sulfide sizes and substantial abundance of Fe in the melt. These trivial increases in FeO^T from sulfide mass balance were ignored in further MI PEC-corrections.

7.1.3 H_2O and CO_2 by FTIR

Melt inclusion glass densities were calculated at 25 °C and 1 bar from non-PEC corrected compositions using the DensityX tool (Iacovino & Till, 2019), with iterative calculations to converge on H_2O. Total H_2O and CO_2 concentrations were calculated using the Beer–Lambert law with absorption coefficients of 62.8 L mol^{-1} cm^{-1} for ε_{3550} (total H_2O) (Mercier et al., 2010) and the compositionally-dependent (non-PEC corrected glass compositions) absorption coefficients from Mandeville et al. (2002) for ε_{1430} and ε_{1515} (the carbonate doublet), which ranged from 344 – 350 L mol^{-1} cm^{-1}. Measurements were generally made in doubly-intersected MI and matrix glasses, with wafers 20 – 50 μm thick. A subset of MI was measured through host olivine or plagioclase, where MI thickness was determined by comparing peak heights of Si-O bands for the pure host mineral and for the mineral + MI spectra (Nichols & Wysoczanski, 2007; Roman et al., 2006). We then did a scaled subtraction of the host mineral spectra from the mineral + MI spectra to calculate the 3570 cm^{-1} H_2O and 1515 / 1430 cm^{-1} carbonate peak heights. Measured H_2O and CO_2 concentrations have 1 SE uncertainties of < 15%, which include uncertainties in glass thickness, density, and absorbance.

7.1.4 Fe- and S-XANES

At the onset of each Fe-XANES session, the instrument energy offset relative to the Cottrell et al. (2009) measurements was determined based on the Fe pre-edge centroid position of reference glass LW-0. Energy adjustments ranging from +0.27 to +0.32 eV were applied to the measurements at 13-ID-E across five analytical sessions (Cottrell et al., 2009; Zhang et al., 2018). S-XANES measurements were conducted in a He-environment to minimize atmospheric absorption of the X-ray fluorescent signal. At the onset of each S-XANES analytical session, the instrument energy calibration was

conducted using SO_4-bearing tape to determine the position of the S^{6+} peak, which showed analyses of Jugo et al. 2010 are consistently are -1 eV relative to our measurements at APS beamline 13-ID-E.

To minimize Fe photo-oxidation and S photo-reduction beam damage during XANES analyses (Cottrell et al., 2018; Wilke et al., 2008), we reduce photon dose on the sample area by utilize larger beam spot sizes (10 – 50 μm diameters) and decreased photon flux through instrument tuning and applying Al-foil sheets to further reduce flux during Fe-XANES measurements. The methods ameliorated, but did not completely prevent beam damage from occurring. We therefore employed additional techniques to characterize and correct for beam damage through using repeat, rapid Fe- and S-XANES scans and implemented a peak-fitting calibration for S-XANES, as described in detail in **Chapter III**. Spectral fitting was done with the LARCH program's XAS viewer (Newville, 2013) to correct for detector dead time, and normalize and fit the Fe- and S-XANES data.

To summarize our beam-damage correction approaches: The Fe-XANES beam damage correction is done by determining the Fe Kα pre-edge centroid following the methods of Cottrell et al., (2009) and Zhang et al. (2018) during three to four repeated 90 second scans through the pre-edge region, following by one full-length scan to cover the full pre and post-edge energy range. If a progressive change in Fe pre-edge centroid position due to Fe oxidation is observed, a linear fit through the centroid positions is applied to determine the original, un-modified centroid position at time = 0. We use the basaltic calibration from Cottrell et al., (2009) and updated by Zhang et al. (2018) to determine $Fe^{3+}/\Sigma Fe$ molar proportions. The andesitic calibration of (Zhang et al., 2018) is used for measurements in andesitic interstitial glasses erupted from F17. Fe-speciation is related to fO_2 through the 1-atm relation of Kress and Carmichael (1991) using matrix glass temperatures from Mg-thermometry (Helz & Thornber, 1987), where MI temperatures are taken as the average matrix glass temperature for each sample. Melt inclusions were dominantly entrapped at relatively low pressures (see discussion), so the 1-atm formulation of Kress and Carmichael (1991) remains appropriate for these MI due to the limited pressure dependence of the QFM buffer. We note that many MI in high-Fo olivine grains have undergone extensive PEC and Fe-loss. Olivine-hosted MI have been

shown undergo rapid redox re-equilibration (Gaetani et al. 2012; Bucholz et al. 2013; Hartley et al. 2017; **Chapter III**), so we use measured compositions of matrix glasses and non-PEC corrected MI compositions in the Kress and Carmichael (1991) relation. If PEC-corrected MI compositions were instead used to calculate fO_2, some MI redox states would be oxidized up to +0.5 log units for a given $Fe^{3+}/\Sigma Fe$ measured value due to the compositional dependence on fO_2 calculations (Figure C11).

Sulfur beam damage during X-ray excitation manifests as the photo-reduction of S^{6+} to form S^{4+}, which normally does not exist in natural silicate glasses (Wilke et al., 2008). A peak fitting method was calibrated in **Chapter III** based on experimental samples of Jugo et al., (2010), which fits normalized and flattened spectra with background functions and Gaussian peaks corresponding to sulfides, S^{2-}, S^{4+}, S^{6+}, and S-ionization (Jugo et al., 2010; Konecke et al., 2017; Wilke et al., 2008). The S^{4+} beam-damage induced peak was restored to the original S^{6+} peak intensity through a scaling factor of 1.2, as determined in **Chapter III** from an experimental hydrous basaltic glass. The validity of applying this scaling factor to glasses of different compositions is uncertain, so scans were kept relatively short (154 to 308 seconds) to minimize S^{4+} beam damage overall, and thus reduce the effect of uncertainty in the S^{4+} to S^{6+} scaling conversion. Reproducibility in the **Chapter III** peak fitting approach is estimated to be ±2% $S^{6+}/\Sigma S$ (1 SE). Including potential issues arising from the peak fitting calibration and from non-uniqueness in spectra normalization for low-S samples, a conservative estimate of accuracy is ±5% $S^{6+}/\Sigma S$ (1 SE).

Collectively, rapid scans with diffusive beams combined with time-dependent corrections for Fe-XANES and S^{4+} to S^{6+} peak restorations for S-XANES allowed us to identify and correct for beam damage during glass analyses. Importantly, these methods account for beam damage within each specific MI analysis, which are more useful than applying blanket corrections because MI compositional differences and different water contents (either original H_2O variability or due to different degrees of diffusive H^+ loss) can lead to different MI susceptibilities to beam damage, even within the same sample.

Analyzed samples included uncoated doubly intersected MI and matrix glasses on Fe-free glass rounds and thin section slides. Samples were embedded in CrystalBond®, EpoThin® epoxy, or thin section resin. All bonding material and glass substrates were

analyzed to confirm that they contained only trace Fe and had negligible contribution to Fe-XANES signals. The bonding materials did contain substantial S, but the low energy X-rays for S-XANES measurements are fully absorbed within a ~20 μm path within basaltic glasses (**Chapter III**). All analyzed MI and matrix glass areas are substantially thicker than this so the bonding materials contributed no appreciable signal to S-XANES measurements. X-rays at the Fe Kα energy range are highly penetrative (only 37% of X-ray energy absorbed within a 40 μm beam path) and the 45° incident beam geometry require that either a large vertical and lateral path area of glass must be present for a clean Fe-XANES analysis, or that a thin doubly intersected sample be prepared. All Fe-XANES spectra were carefully screened to exclude any mineral host or microlite signatures from interaction with the beam at depth, so that only clean glassy spectra are presented here.

7.1.5 $\delta^{34}S$ analyses by Secondary Ion Mass Spectrometry

Each SIMS analysis consisted of 40 measurement cycles totaling 15 minutes, with each cycle consisting of ^{32}S measured for 4 seconds and ^{34}S measured for 10 seconds. Measurements were dead-time corrected and time-aligned to account for mono-collector time differences for ^{32}S and ^{34}S collection times. Instrument mass fractionation and beam stability was monitored by repeat measurements of VG-2 MORB glass secondary standards (2 analyses of VG-2 per 5 unknown analyses). The $\delta^{34}S$ value of VG-2 was determined to be 0.7 ± 0.5‰ from 15 measurements of multiple VG-2 glass chips amidst a wide suite of glasses (basalts to high-Si compositions, both reduced and oxidized) with independently known $\delta^{34}S$ ranging from -5 to +18‰. We note that some of the isotopic standards used in our calibration we determined via the Kiba solution S-extraction method, which has been recently called into some question owing to unknowns whether this approach results in total S-extraction (Labidi et al., 2012). However, until this debate is better resolved, we maintain the as-published $\delta^{34}S$ values of standards derived by Kiba extraction methods. Further appraisal of the accurate value of these standard glasses would shift the absolute $\delta^{34}S$ values of our dataset, but not the relative isotopic differences.

Background S was monitored through measurements of S-free Suprasil quartz glass and host-minerals, and background S counts amounted to < 10 ppm S (~1% of low-S concentrations MIs and 0.1% of higher-S concentration MI). The background $\delta^{34}S$ signature was generally lighter than that of measured MI, however no correction was applied to remove background signals, as the uncertainty in the background measurement corrections overwhelmed any systematic background correction to the analyses. Reported uncertainty is propagated from 1 SE analytical precision on each measurement and from 1 standard deviation of the mass fractionation factor based on repeat measurements of VG-2 secondary standard. ^{32}S ion yields ranged from $3\text{-}80 \times 10^4$ depending on S concentration of the glasses. Analyses of LERZ glasses had $\delta^{34}S$ 1 SE uncertainties of ±0.4 – 0.6‰ in glasses with S concentrations 400 – 1200 ppm, and 1 SE uncertainties of ±0.7 – 0.9‰ in glasses with S concentrations 100 – 400 ppm. Some partially devitrified MI in the slower cooled sample LF8 had higher uncertainties of ±1.0 – 2.0‰ (310 – 530 ppm S), and are generally ignored in subsequent analyses.

7.2 Supplemental figures

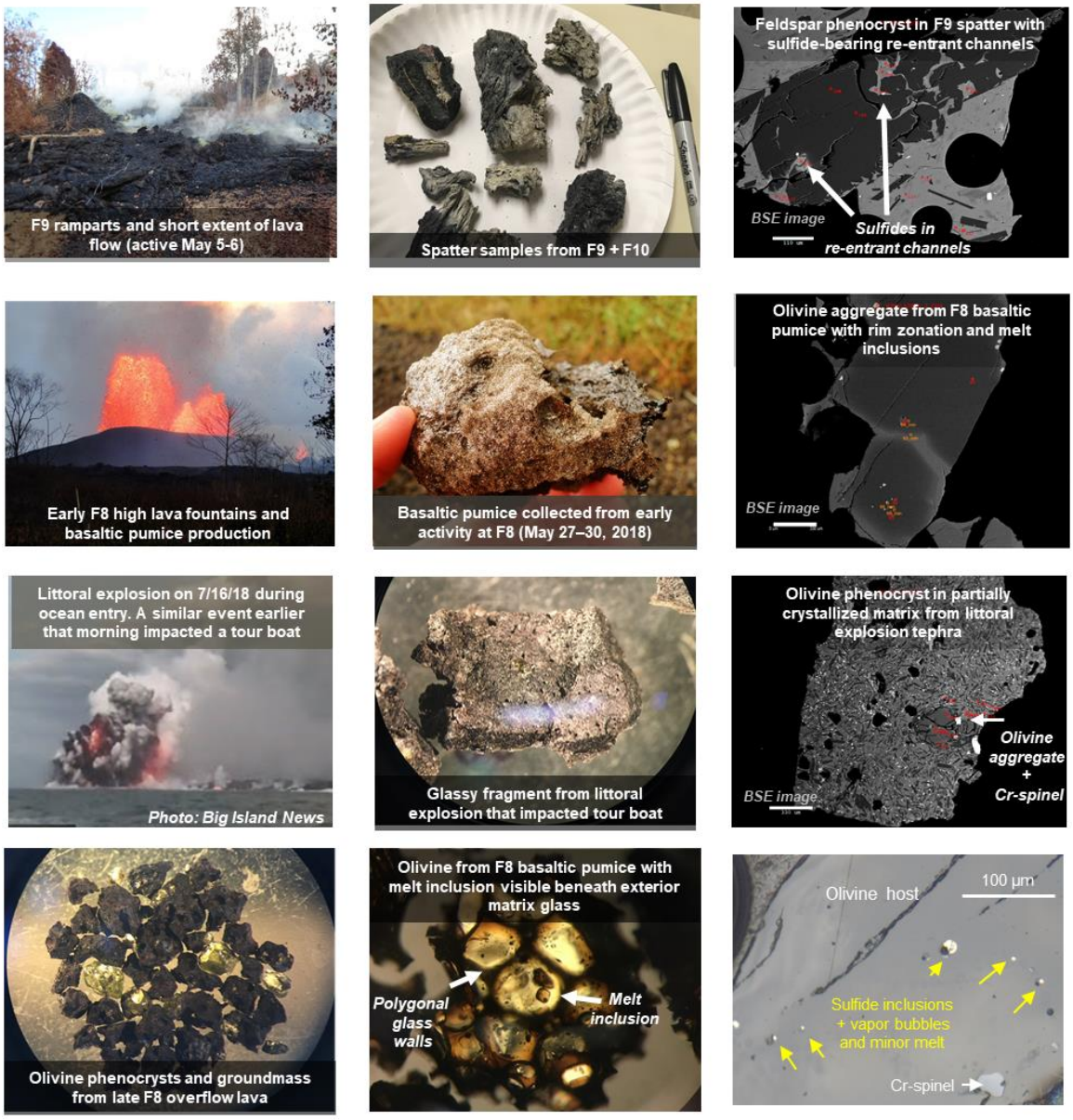

Chapter IV, Figure C1. A range of eruption activity, eruptive products, and melt and mineral compositions were produced during the 2018 LERZ eruption. See individual captions within each panel. Grayscale panels are backscattered electron images.

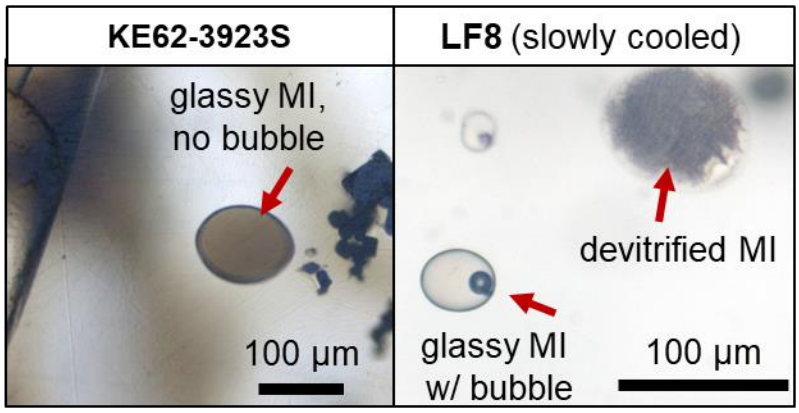

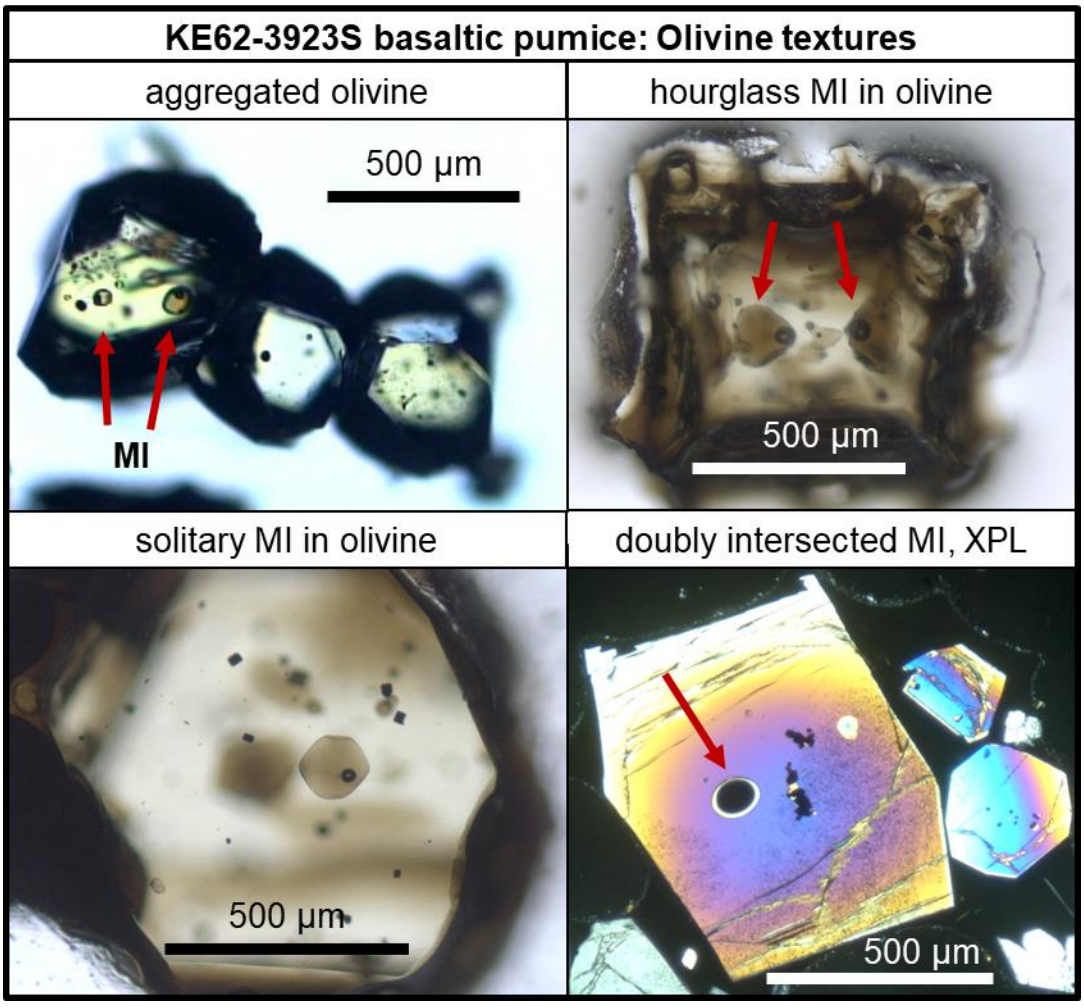

Chapter IV, Figure C2. Examples of some types of olivine phenocrysts and MI textures from LERZ material.

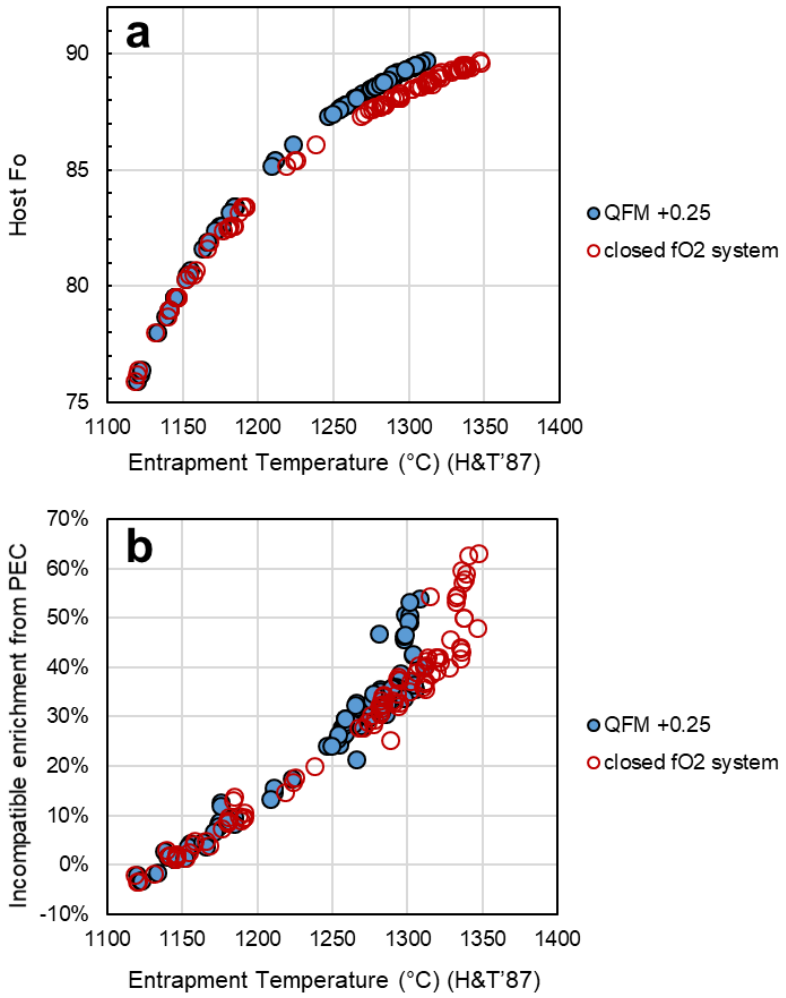

Chapter IV, Figure C3. Results of post-entrapment crystallization (PEC) corrections of olivine-hosted MI from LERZ samples using Petrolog3 (Danyushevsky & Plechov, 2011), with fO_2 fixed at QFM +0.25 or evolving as a closed-system. *(a)* PEC-corrected MI entrapment temperatures calculated from the MgO thermometer of Helz and Thornber (1987) range from 1140 – 1150 °C in Fo_{76-80} olivine grains to 1310 °C in Fo_{89-90} olivine grains. *(b)* The difference between MI entrapment temperatures and eruption temperatures up to 240 °C led to severe degrees of PEC and Fe-loss, resulting in up to 54% enrichment of olivine-incompatible elements when assuming a constant fO_2 of QFM +0.25 (the conditions used in this study). Even higher post-entrapment enrichments of olivine-incompatible elements up to 63% are calculated if MI were assumed to be closed systems to fO_2 during PEC.

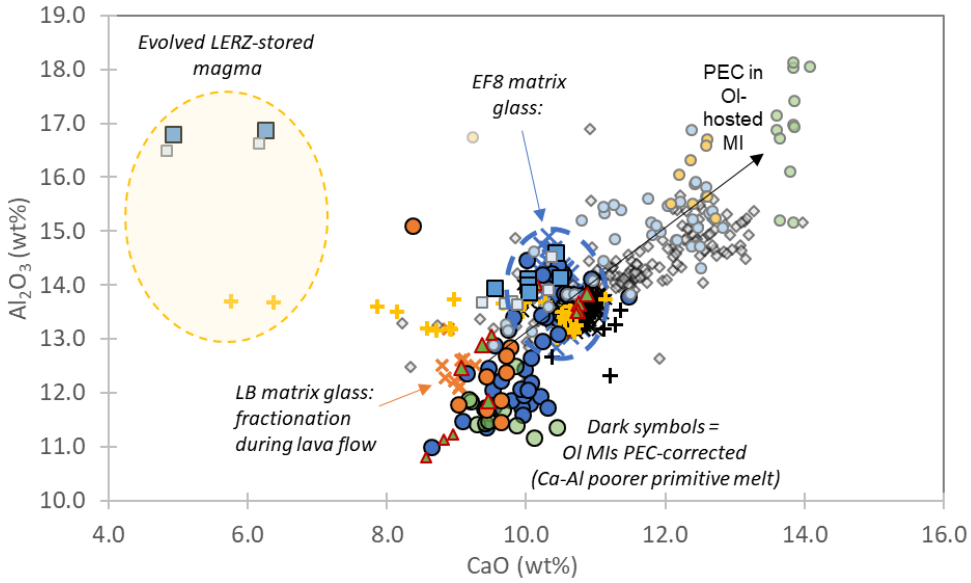

Chapter IV, Figure C4. CaO versus Al_2O_3 variation for analyzed MI and matrix glasses. We assessed the possibility of post entrapment crystallization (PEC) of plagioclase-hosted MI by comparing measured concentrations to the array of non-plagioclase-hosted MI and matrix glasses. Plagioclase-hosted MI generally conform to the overall compositional array, so we did not any apply PEC corrections. The two plagioclase-hosted MI stray far from the overall CaO-Al_2O_3 array are highly evolved compositions in a xenocrystic crystal that was likely entrained from a long-stored LERZ magma body. Symbology as in main text figures.

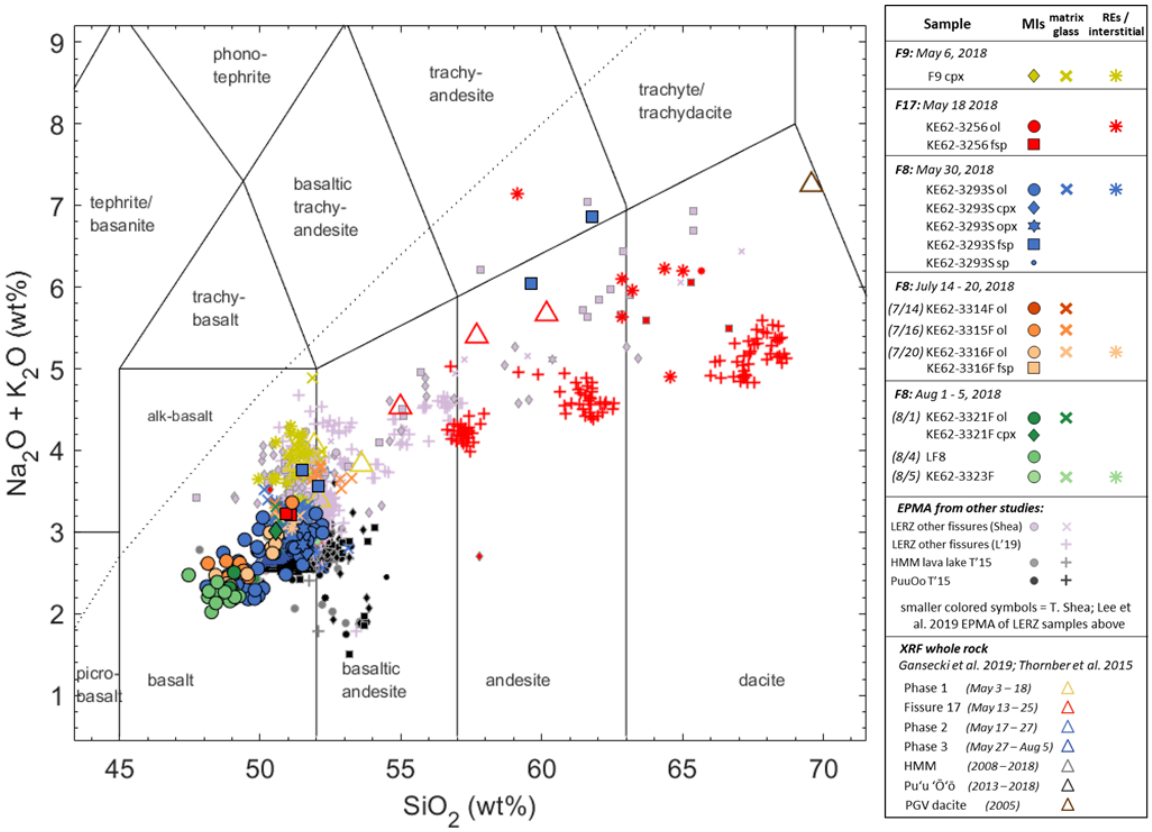

Chapter IV, Figure C5. Total alkalis versus silica diagram, showing the wide range of MI (PEC-corrected), matrix glasses, and whole rock compositions erupted during the 2018 LERZ activity. Gray and black symbols are samples from Halema'uma'u lava lake and Pu'u 'Ō'ō, respectively.

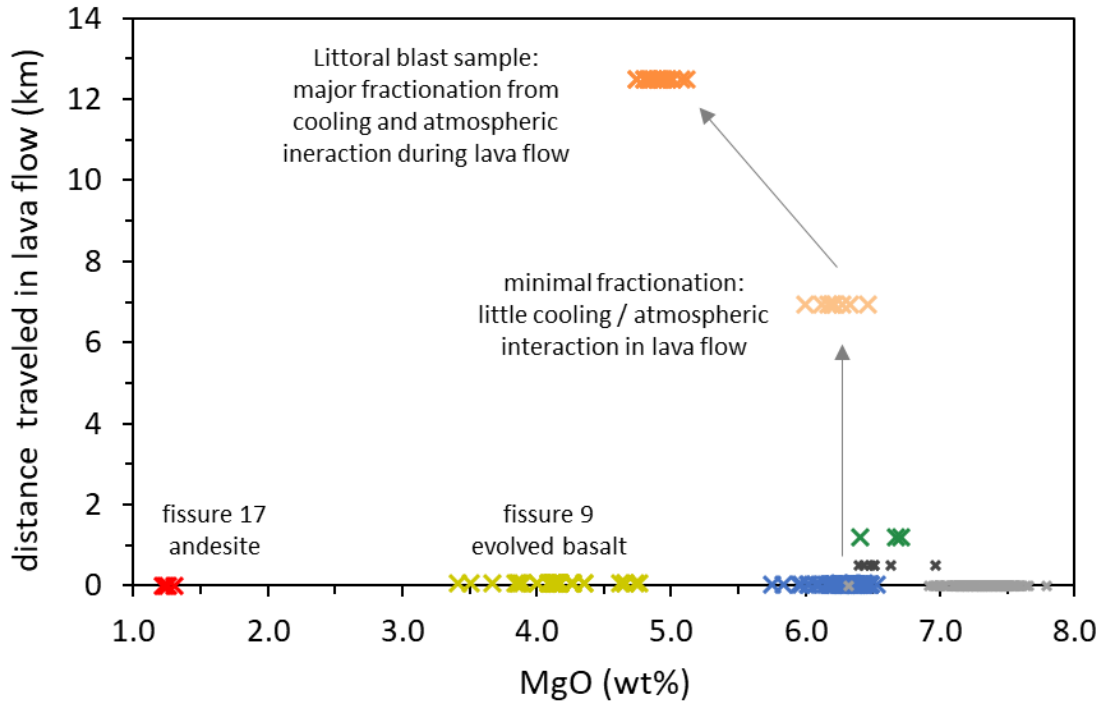

	sample (eruption date)	matrix glass	sample (eruption date)	matrix glass
Fissure 8 samples	KE62-3293S (May 30, 2018)	×	KE62-3315F (July 16, 2018)	×
	KE62-3316F (July 20, 2018)	×	KE62-3321F (August 1, 2018)	×
other samples	F9 (May 5, 2018)	×	F17 KE62-3256S (May 18, 2018)	×
	Pu'u 'Ō'ō (2001 – 2013) *(Thornber et al. 2015)*	×	Halema'uma'u (2008 - 2013) *(Thornber et al. 2015)*	×

Chapter IV, Figure C6. MgO contents of matrix glasses compared to the distance the lava traveled before quenching. Sample KE62-3923S is the basaltic pumice that quenched immediately from F8 lava fountaining. Samples that traveled up to 6 km in the open F8 lava channel did not undergo appreciable cooling and crystallization, and retain high MgO contents (KE62-3316F, KE62-3321F). Sample KE62-3315F is the littoral blast sample that traveled 13 km in the lava channel and was quenched during ocean entry; this sample has lower matrix glass MgO, indicating cooling and crystallization during atmospheric interaction. Evolved basaltic fissure 9 (F9) and andesitic fissure 17 (F17, KE62-3256S) scoria glasses where rapidly quenched at their eruption sites. Small gray and black symbols are matrix glasses from the Halema'uma'u lava lake and from Pu'u 'Ō'ō, respectively.

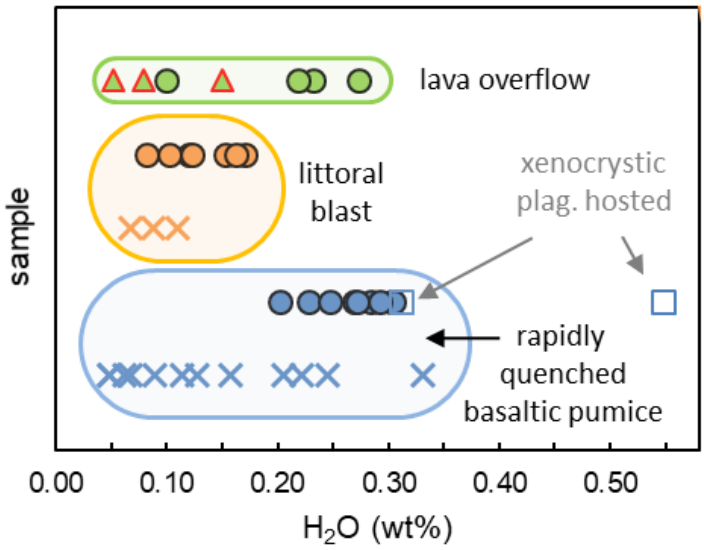

Chapter IV, Figure C7. FTIR-measured H_2O contents of different LERZ MI (circles, squares) and matrix glasses (Xs). Blue symbols are rapidly quenched basaltic pumice samples. Orange symbols are littoral blast material that degassed during 13 km of transport in a subaerial lava channel. Green symbols are late fissure 8 (LF8) lava overflow that had slowly cooled; this sample has no glassy matrix and MI have experienced variable degrees of H_2O-loss. Red triangles are experimentally reheated MI in LF8, which have lost further H_2O during heating. The highest H_2O in rapidly quenched basaltic pumice MI and matrix glasses cluster around 0.3 wt%, which we take to be the best estimate of pre-eruptive melt H_2O contents of melts sourcing F8. Blue squares are two MI with evolved compositions in a xenocrystic plagioclase from the basaltic pumice, which contain higher H_2O contents of 0.30 – 0.55 wt%.

Effect of H_2O diffusive loss on melt inclusion redox state

The diffusive loss of hydrogen from MI has been theorized to cause oxidation of MI through the reaction:

$$2FeO_{melt} + H_2O_{melt} = Fe_2O_{3,melt} + 2H^+_{olivine} \ ,$$

so that the degree of MI oxidation would be limited by the water content of the inclusion (Danyushevsky et al., 2002). Olivine-hosted MI from the Kīlauea LERZ littoral blast samples are relatively anhydrous and underwent only ~0.2 wt% H_2O loss (0.01 mole H_2O), which would have the potential to oxidize 0.79 wt% FeO to Fe_2O_3 via the reaction above. With FeO^T contents of ~11.5 wt% FeO^T (0.16 mole FeO^T) in the LERZ lavas, oxidation by H^+-loss could account for a maximum 7% increase in $Fe^{3+}/\Sigma Fe$. The littoral blast MI, however, have $Fe^{3+}/\Sigma Fe$ increased 7 – 25% compared to the proximally quenched LERZ MI (Figure C8). Consequently, this scale of oxidation of Kīlauea olivine-hosted MI by the theoretical mechanism of hydrogen loss would be impossible.

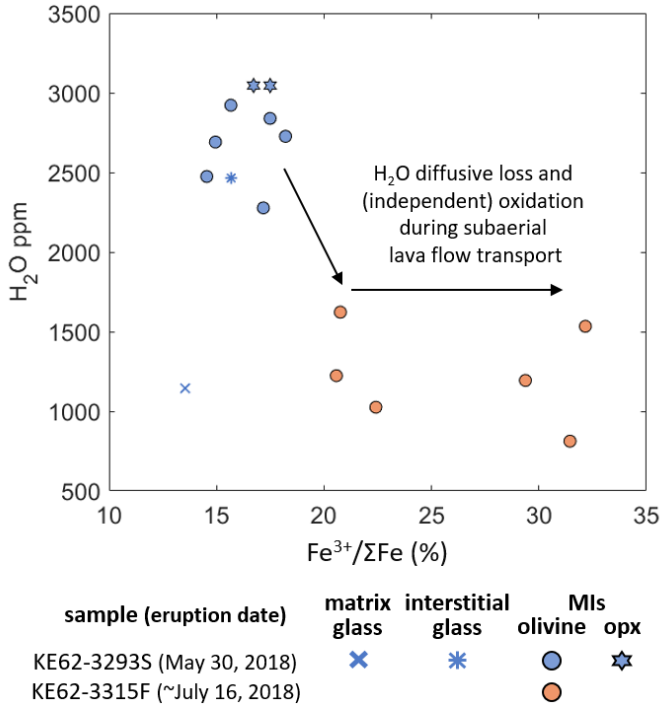

Chapter IV, Figure C8. H_2O content vs $Fe^{3+}/\Sigma Fe$ for matrix and interstitial glass, and olivine- and orthopyroxene- (opx) hosted MI from LERZ rapidly quenched basaltic pumice (KE62-3923S) and lava-channel transported littoral bomb (KE62-3315F). Both diffusive H_2O loss and atmospheric oxidation occur during subaerial lava flow transport, although the relatively minor H_2O loss cannot explain the magnitude of Fe-oxidation (see text).

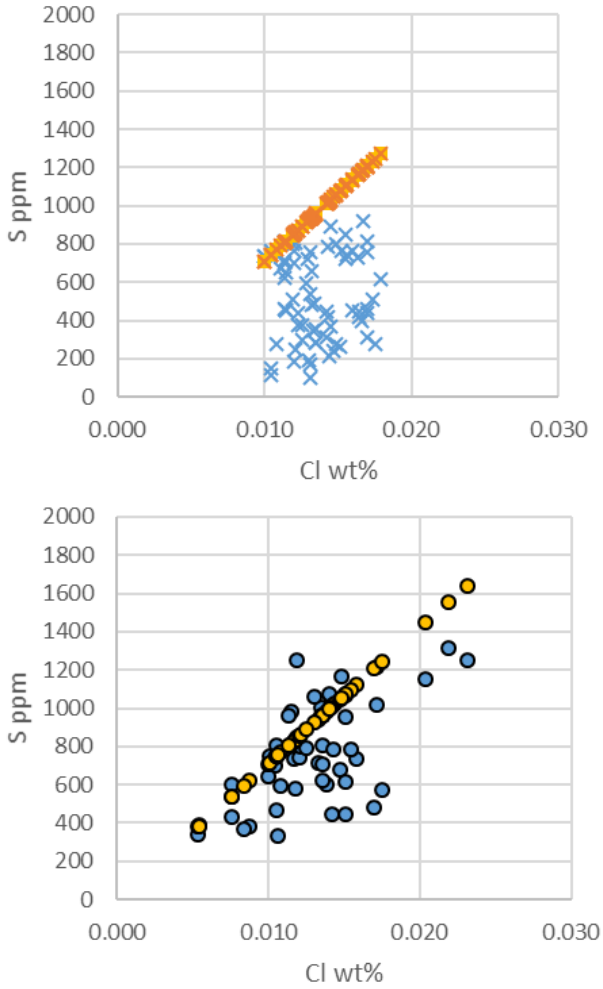

Chapter IV, Figure C9. Relation between S and Cl in rapidly quenched basaltic pumice matrix glasses *(top)* and MI *(bottom)*. Blue symbols are measured glass compositions. To account for S degassing, S concentrations in matrix glasses and MI can be "restored" to undegassed concentrations by scaling measured concentrations of Cl (which does not degas as readily) by an average S/Cl mass ratio of 7.0, which was determined for undegassed MI that were in equilibrium with the erupting F8 melt. Orange and yellow symbols are "restored" S concentrations based on this S/Cl ratio of 7. Restored matrix glass S concentrations range from 800 – 1200 ppm S, while MI are more variable, likely reflecting different initial S/Cl ratios.

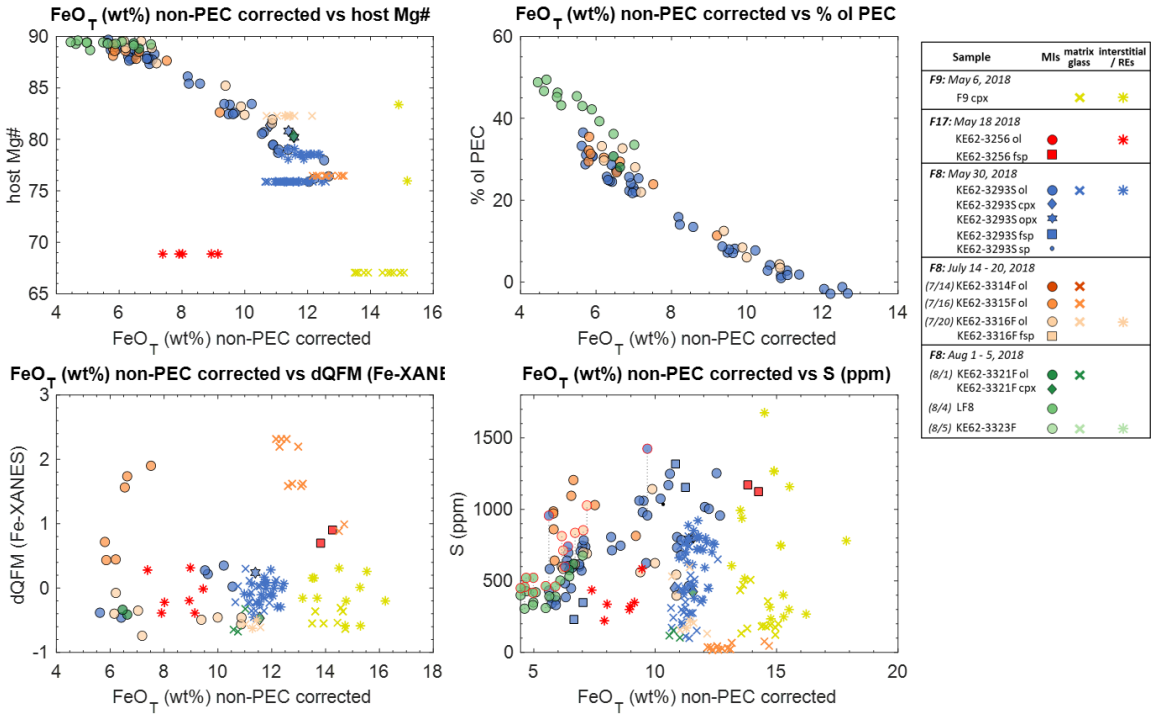

Chapter IV, Figure C10. Variation of non-PEC FeO^T contents of LERZ MI (and matrix glasses) with host Mg number, percent of PEC correction, measured redox state, and S concentrations.

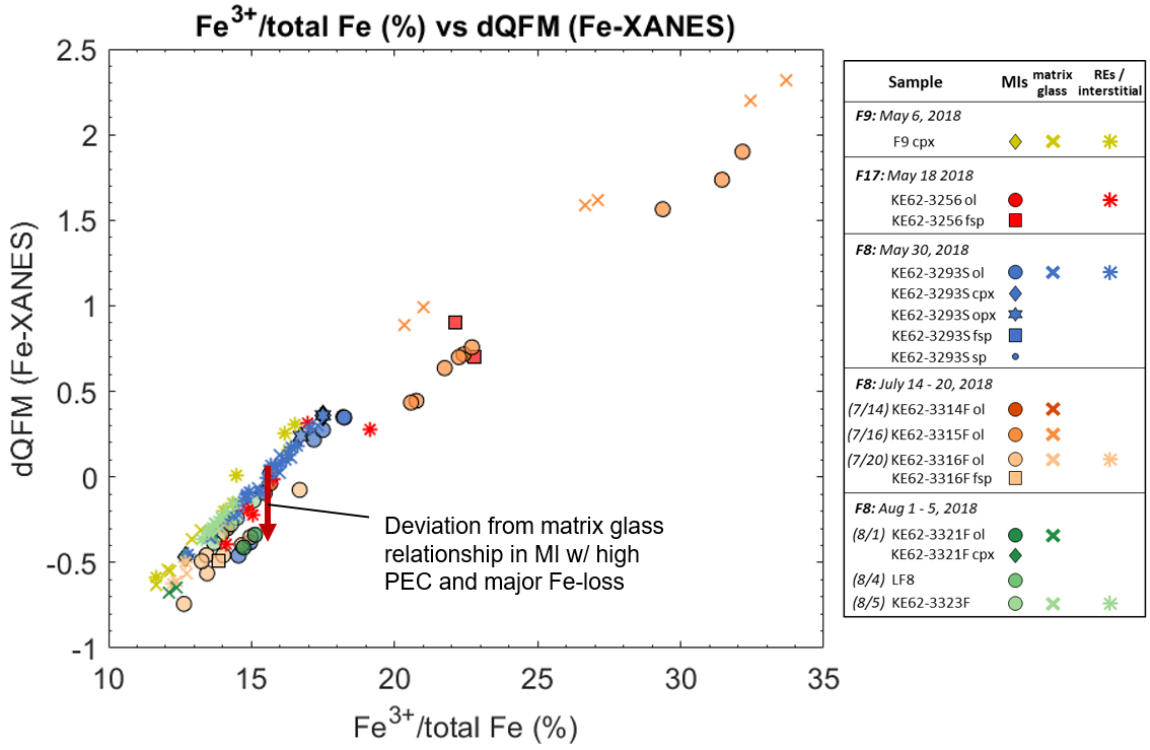

Chapter IV, Figure C11. A comparison of Fe-XANES measured Fe speciation and calculated glass redox state (dQFM) from the 1-atm relation of Kress and Carmichael (1991). dQFM was calculated for melt temperatures and using non-PEC-corrected MI compositions. The compositional effect is apparent in the different dQFM values calculated for given $Fe^{3+}/\Sigma Fe$ proportions (red arrow).

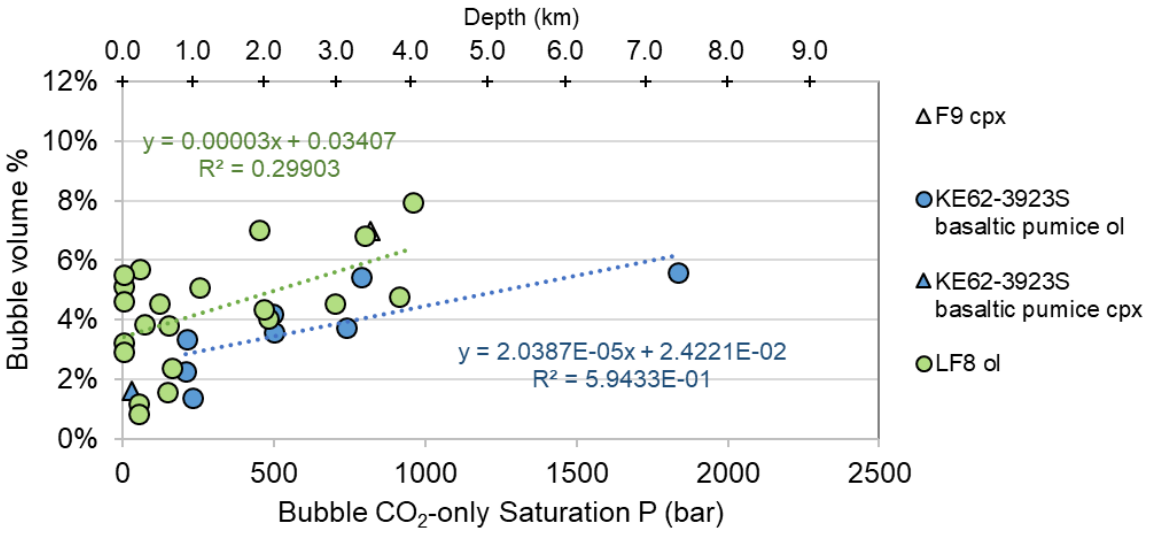

Chapter IV, Figure C12. Relation between bubble volume (% relative to total MI volume) and saturation pressure calculated from Raman-only measurements of CO_2 vapor bubble density. Melt inclusions in olivine (ol) grains from the slowly cooled LF8 sample experienced more PEC (35 – 50% by mass) and have larger bubbles relative to calculated CO_2 vapor pressures than olivine-hosted MI in the rapidly quenched basaltic pumice, which experienced less PEC (10 – 30% by mass). Depth below the surface is from the depth-density parameterization after Ryan (1987).

Supplementary Table 1C. Kīlauea 2018 LERZ glass descriptions, major element and volatile concentrations (wt%, ppm, normalized PEC-corrected), S-isotopic signatures, and Fe and S speciation.

Analysis Name	Fissure #	Sample Name	Eruption Date	Distance traveled before quench (km)	Glass Type	Host mineral	Sulfide present?
Fissure 9 spatter, May 3 2018							
F9_mins_g01_matrixG_01_112	9	F9	5/3/18	0.05	matrix glass	-	-
F9_mins_g01_matrixG_01_113	9	F9	5/3/18	0.05	matrix glass	-	-
F9_mins_g01_matrixG_01_114	9	F9	5/3/18	0.05	matrix glass	-	-
F9_mins_g01_matrixG_01_115	9	F9	5/3/18	0.05	matrix glass	-	-
F9_mins_g03_matrixG_01_124	9	F9	5/3/18	0.05	matrix glass	-	-
F9_mins_g03_matrixG_01_125	9	F9	5/3/18	0.05	matrix glass	-	-
F9_mins_g03_matrixG_01_126	9	F9	5/3/18	0.05	matrix glass	-	-
F9_mins_g03_matrixG_01_127	9	F9	5/3/18	0.05	matrix glass	-	-
F9_mins_g03_matrixG_01_128	9	F9	5/3/18	0.05	matrix glass	-	-
F9_mins_g04_matrixG_01_134	9	F9	5/3/18	0.05	matrix glass	-	-
F9_mins_g04_matrixG_01_135	9	F9	5/3/18	0.05	matrix glass	-	-
F9_mins_g04_matrixG_01_136	9	F9	5/3/18	0.05	matrix glass	-	-
F9_mins_g01_matrixG_01_112	9	F9	5/3/18	0.05	matrix glass	-	-
F9_mins_g01_matrixG_01_113	9	F9	5/3/18	0.05	matrix glass	-	-
F9_mins_g01_matrixG_01_114	9	F9	5/3/18	0.05	matrix glass	-	-
F9_mins_g01_matrixG_01_115	9	F9	5/3/18	0.05	matrix glass	-	-
F9_mins_g03_matrixG_01_124	9	F9	5/3/18	0.05	matrix glass	-	-
F9_mins_g03_matrixG_01_125	9	F9	5/3/18	0.05	matrix glass	-	-
F9_mins_g03_matrixG_01_126	9	F9	5/3/18	0.05	matrix glass	-	-
F9_mins_g03_matrixG_01_127	9	F9	5/3/18	0.05	matrix glass	-	-
F9_mins_g03_matrixG_01_128	9	F9	5/3/18	0.05	matrix glass	-	-
F9_mins_g04_matrixG_01_134	9	F9	5/3/18	0.05	matrix glass	-	-
F9_mins_g04_matrixG_01_135	9	F9	5/3/18	0.05	matrix glass	-	-
F9_mins_g04_matrixG_01_136	9	F9	5/3/18	0.05	matrix glass	-	-
F9_mins_g09_matrixG_145	9	F9	5/3/18	0.05	matrix glass	-	-
F9_mins_g01_fsp_RE_01_105	9	F9	5/3/18	0.05	re-entrant	Plag_RE	-
F9_mins_g01_fsp_RE_01_106	9	F9	5/3/18	0.05	re-entrant	Plag_RE	-
F9_mins_g01_fsp_RE_01_107	9	F9	5/3/18	0.05	re-entrant	Plag_RE	-
F9_mins_g01_fsp_RE_01_108	9	F9	5/3/18	0.05	re-entrant	Plag_RE	-
F9_mins_g01_fsp_RE_01_109	9	F9	5/3/18	0.05	re-entrant	Plag_RE	-
F9_mins_g01_fsp_RE_01_110	9	F9	5/3/18	0.05	re-entrant	Plag_RE	-
F9_mins_g01_fsp_RE_01_111	9	F9	5/3/18	0.05	re-entrant	Plag_RE	-
F9_mins_g03_REs_01_122	9	F9	5/3/18	0.05	interstitial melt	Pl + Cpx_glom	-
F9_mins_g03_REs_01_122	9	F9	5/3/18	0.05	interstitial melt	Pl + Cpx_glom	-
F9_mins_g03_REs_01_123	9	F9	5/3/18	0.05	interstitial melt	Pl + Cpx_glom	-
F9_mins_g05_REs_01_137	9	F9	5/3/18	0.05	interstitial melt	Pl + Cpx_glom	-
F9_mins_g05_REs_01_138	9	F9	5/3/18	0.05	interstitial melt	Pl + Cpx_glom	-
F9_mins_g05_REs_01_139	9	F9	5/3/18	0.05	interstitial melt	Pl + Cpx_glom	-

Supplementary Table 1C (continued).

Analysis Name	Fissure #	Sample Name	Na2O wt%	SiO2 wt%	CaO wt%	K2O wt%	Al2O3 wt%	FeOT wt%	MgO wt%	TiO2 wt%	MnO wt%
Fissure 9 spatter, May 3 2018											
F9_mins_g01_matrixG_01_112	9	F9	2.69	51.52	8.17	1.12	12.66	14.43	4.14	4.46	0.19
F9_mins_g01_matrixG_01_113	9	F9	2.81	51.00	8.10	1.15	12.62	14.97	4.13	4.39	0.21
F9_mins_g01_matrixG_01_114	9	F9	2.97	51.24	8.17	1.10	12.33	14.73	4.13	4.50	0.19
F9_mins_g01_matrixG_01_115	9	F9	2.84	51.43	8.18	1.12	12.35	14.58	4.11	4.56	0.19
F9_mins_g03_matrixG_01_124	9	F9	2.84	52.20	8.19	1.15	12.67	13.53	4.12	4.48	0.19
F9_mins_g03_matrixG_01_125	9	F9	3.00	51.48	8.23	1.13	12.63	14.03	4.18	4.47	0.20
F9_mins_g03_matrixG_01_126	9	F9	2.84	51.17	8.22	1.04	12.46	14.65	4.26	4.51	0.20
F9_mins_g03_matrixG_01_127	9	F9	2.93	51.56	8.44	1.01	12.34	13.83	4.35	4.64	0.21
F9_mins_g03_matrixG_01_128	9	F9	3.74	51.88	7.99	1.15	12.45	13.50	4.01	4.47	0.18
F9_mins_g04_matrixG_01_134	9	F9	2.87	52.14	8.32	1.02	12.24	13.86	4.15	4.56	0.20
F9_mins_g04_matrixG_01_135	9	F9	2.81	51.36	8.17	1.13	12.32	14.82	4.09	4.45	0.20
F9_mins_g04_matrixG_01_136	9	F9	2.60	51.66	8.10	1.07	12.47	14.91	3.86	4.48	0.20
F9_mins_g01_matrixG_01_112	9	F9	2.69	51.52	8.17	1.12	12.66	14.43	4.14	4.46	0.19
F9_mins_g01_matrixG_01_113	9	F9	2.81	51.00	8.10	1.15	12.62	14.97	4.13	4.39	0.21
F9_mins_g01_matrixG_01_114	9	F9	2.97	51.24	8.17	1.10	12.33	14.73	4.13	4.50	0.19
F9_mins_g01_matrixG_01_115	9	F9	2.84	51.43	8.18	1.12	12.35	14.58	4.11	4.56	0.19
F9_mins_g03_matrixG_01_124	9	F9	2.84	52.20	8.19	1.15	12.67	13.53	4.12	4.48	0.19
F9_mins_g03_matrixG_01_125	9	F9	3.00	51.48	8.23	1.13	12.63	14.03	4.18	4.47	0.20
F9_mins_g03_matrixG_01_126	9	F9	2.84	51.17	8.22	1.04	12.46	14.65	4.26	4.51	0.20
F9_mins_g03_matrixG_01_127	9	F9	2.93	51.56	8.44	1.01	12.34	13.83	4.35	4.64	0.21
F9_mins_g03_matrixG_01_128	9	F9	3.74	51.88	7.99	1.15	12.45	13.50	4.01	4.47	0.18
F9_mins_g04_matrixG_01_134	9	F9	2.87	52.14	8.32	1.02	12.24	13.86	4.15	4.56	0.20
F9_mins_g04_matrixG_01_135	9	F9	2.81	51.36	8.17	1.13	12.32	14.82	4.09	4.45	0.20
F9_mins_g04_matrixG_01_136	9	F9	2.60	51.66	8.10	1.07	12.47	14.91	3.86	4.48	0.20
F9_mins_g09_matrixG_145	9	F9	2.89	51.28	8.18	1.16	12.66	14.64	3.88	4.39	0.22
F9_mins_g01_fsp_RE_01_105	9	F9	2.38	51.50	8.19	0.99	11.90	15.29	3.90	4.89	0.23
F9_mins_g01_fsp_RE_01_106	9	F9	2.72	51.35	8.07	1.47	10.90	14.74	4.66	5.15	0.19
F9_mins_g01_fsp_RE_01_107	9	F9	2.39	50.96	8.16	1.22	11.57	16.09	3.85	4.80	0.24
F9_mins_g01_fsp_RE_01_108	9	F9	2.43	51.49	8.09	1.31	11.42	15.61	4.08	4.66	0.22
F9_mins_g01_fsp_RE_01_109	9	F9	2.41	50.46	7.59	1.26	11.20	17.85	3.41	4.83	0.25
F9_mins_g01_fsp_RE_01_110	9	F9	2.93	51.42	7.64	1.13	12.57	14.77	3.51	5.06	0.21
F9_mins_g01_fsp_RE_01_111	9	F9	2.79	51.04	7.99	1.15	12.39	15.33	3.67	4.73	0.21
F9_mins_g03_REs_01_122	9	F9	2.61	50.54	8.29	1.05	12.36	15.14	4.18	4.92	0.22
F9_mins_g03_REs_01_122	9	F9	2.61	50.54	8.29	1.05	12.36	15.14	4.18	4.92	0.22
F9_mins_g03_REs_01_123	9	F9	2.59	49.94	8.50	1.05	12.18	15.57	4.62	4.60	0.21
F9_mins_g05_REs_01_137	9	F9	2.52	51.20	8.24	1.17	12.21	14.82	4.66	4.26	0.22
F9_mins_g05_REs_01_138	9	F9	3.04	51.49	8.43	1.16	12.43	13.80	4.73	4.15	0.20
F9_mins_g05_REs_01_139	9	F9	3.21	51.09	8.44	1.09	12.70	13.84	4.76	4.10	0.21

Supplementary Table 1C (continued).

Analysis Name	Fissure #	Sample Name	P2O5 wt%	Cl ppm	S ppm	un-normalized total	S/Cl (mass ratio)	non-sulfide corrected S ppm	non-PEC corrected FeOT	melt Mg#	Host Mg#	Host An#
Fissure 9 spatter, May 3 2018												
F9_mins_g01_matrixG_01_112	9	F9	0.57	290	182	99.67	0.6	182	14.43	33.9	-	-
F9_mins_g01_matrixG_01_113	9	F9	0.57	279	200	100.66	0.7	200	14.97	33.0	-	-
F9_mins_g01_matrixG_01_114	9	F9	0.60	281	190	100.05	0.7	190	14.73	33.3	-	-
F9_mins_g01_matrixG_01_115	9	F9	0.59	284	182	99.86	0.6	182	14.58	33.5	-	-
F9_mins_g03_matrixG_01_124	9	F9	0.55	315	435	99.77	1.4	435	13.53	35.2	-	-
F9_mins_g03_matrixG_01_125	9	F9	0.56	315	507	99.26	1.6	507	14.03	34.7	-	-
F9_mins_g03_matrixG_01_126	9	F9	0.58	280	358	99.94	1.3	358	14.65	34.2	-	-
F9_mins_g03_matrixG_01_127	9	F9	0.61	284	473	98.45	1.7	473	13.83	35.9	-	-
F9_mins_g03_matrixG_01_128	9	F9	0.59	262	133	100.31	0.5	133	13.50	34.6	-	-
F9_mins_g04_matrixG_01_134	9	F9	0.60	271	167	99.50	0.6	167	13.86	34.8	-	-
F9_mins_g04_matrixG_01_135	9	F9	0.59	304	174	100.85	0.6	174	14.82	33.0	-	-
F9_mins_g04_matrixG_01_136	9	F9	0.60	345	123	100.22	0.4	123	14.91	31.6	-	-
F9_mins_g01_matrixG_01_112	9	F9	0.57	290	182	99.67	0.6	182	14.43	33.9	-	-
F9_mins_g01_matrixG_01_113	9	F9	0.57	279	200	100.66	0.7	200	14.97	33.0	-	-
F9_mins_g01_matrixG_01_114	9	F9	0.60	281	190	100.05	0.7	190	14.73	33.3	-	-
F9_mins_g01_matrixG_01_115	9	F9	0.59	284	182	99.86	0.6	182	14.58	33.5	-	-
F9_mins_g03_matrixG_01_124	9	F9	0.55	315	435	99.77	1.4	435	13.53	35.2	-	-
F9_mins_g03_matrixG_01_125	9	F9	0.56	315	507	99.26	1.6	507	14.03	34.7	-	-
F9_mins_g03_matrixG_01_126	9	F9	0.58	280	358	99.94	1.3	358	14.65	34.2	-	-
F9_mins_g03_matrixG_01_127	9	F9	0.61	284	473	98.45	1.7	473	13.83	35.9	-	-
F9_mins_g03_matrixG_01_128	9	F9	0.59	262	133	100.31	0.5	133	13.50	34.6	-	-
F9_mins_g04_matrixG_01_134	9	F9	0.60	271	167	99.50	0.6	167	13.86	34.8	-	-
F9_mins_g04_matrixG_01_135	9	F9	0.59	304	174	100.85	0.6	174	14.82	33.0	-	-
F9_mins_g04_matrixG_01_136	9	F9	0.60	345	123	100.22	0.4	123	14.91	31.6	-	-
F9_mins_g09_matrixG_145	9	F9	0.66	238	188	98.65	0.8	188	14.64	32.1	-	-
F9_mins_g01_fsp_RE_01_105	9	F9	0.65	337	401	99.93	1.2	401	15.29	31.3	-	-
F9_mins_g01_fsp_RE_01_106	9	F9	0.70	276	234	100.14	0.8	234	14.74	36.0	-	-
F9_mins_g01_fsp_RE_01_107	9	F9	0.66	349	267	100.80	0.8	267	16.09	29.9	-	-
F9_mins_g01_fsp_RE_01_108	9	F9	0.61	329	300	99.38	0.9	300	15.61	31.8	-	-
F9_mins_g01_fsp_RE_01_109	9	F9	0.63	345	780	100.15	2.3	780	17.85	25.4	-	-
F9_mins_g01_fsp_RE_01_110	9	F9	0.68	475	316	99.68	0.7	316	14.77	29.8	-	-
F9_mins_g01_fsp_RE_01_111	9	F9	0.62	446	248	99.75	0.6	248	15.33	29.9	-	-
F9_mins_g03_REs_01_122	9	F9	0.60	305	748	100.23	2.5	748	15.14	33.0	-	-
F9_mins_g03_REs_01_122	9	F9	0.60	305	748	100.23	2.5	748	15.14	33.0	-	-
F9_mins_g03_REs_01_123	9	F9	0.58	317	1159	99.74	3.7	1159	15.57	34.6	-	-
F9_mins_g05_REs_01_137	9	F9	0.49	455	1676	97.83	3.7	1676	14.82	35.9	-	-
F9_mins_g05_REs_01_138	9	F9	0.44	250	938	98.36	3.8	938	13.80	37.9	-	-
F9_mins_g05_REs_01_139	9	F9	0.44	281	993	97.60	3.5	993	13.84	38.0	-	-

Supplementary Table 1C (continued).

Analysis Name	Fissure #	Sample Name	% PEC (olivine mass)	PEC correction coefficient	Temperature of matrix glass quenching or MI entrapment (°C)	H2O in melt (wt%) (FTIR)	CO2 in melt (ppm) (FTIR)	CO2 in melt + bubble (ppm) (FTIR + Raman)	vapor bubble volume (%)
Fissure 9 spatter, May 3 2018									
F9_mins_g01_matrixG_01_112	9	F9	-	-	1097	-	-	-	-
F9_mins_g01_matrixG_01_113	9	F9	-	-	1097	-	-	-	-
F9_mins_g01_matrixG_01_114	9	F9	-	-	1097	-	-	-	-
F9_mins_g01_matrixG_01_115	9	F9	-	-	1097	-	-	-	-
F9_mins_g03_matrixG_01_124	9	F9	-	-	1097	-	-	-	-
F9_mins_g03_matrixG_01_125	9	F9	-	-	1098	-	-	-	-
F9_mins_g03_matrixG_01_126	9	F9	-	-	1100	-	-	-	-
F9_mins_g03_matrixG_01_127	9	F9	-	-	1102	-	-	-	-
F9_mins_g03_matrixG_01_128	9	F9	-	-	1095	-	-	-	-
F9_mins_g04_matrixG_01_134	9	F9	-	-	1097	-	-	-	-
F9_mins_g04_matrixG_01_135	9	F9	-	-	1096	-	-	-	-
F9_mins_g04_matrixG_01_136	9	F9	-	-	1092	-	-	-	-
F9_mins_g01_matrixG_01_112	9	F9	-	-	1097	-	-	-	-
F9_mins_g01_matrixG_01_113	9	F9	-	-	1097	-	-	-	-
F9_mins_g01_matrixG_01_114	9	F9	-	-	1097	-	-	-	-
F9_mins_g01_matrixG_01_115	9	F9	-	-	1097	-	-	-	-
F9_mins_g03_matrixG_01_124	9	F9	-	-	1097	-	-	-	-
F9_mins_g03_matrixG_01_125	9	F9	-	-	1098	-	-	-	-
F9_mins_g03_matrixG_01_126	9	F9	-	-	1100	-	-	-	-
F9_mins_g03_matrixG_01_127	9	F9	-	-	1102	-	-	-	-
F9_mins_g03_matrixG_01_128	9	F9	-	-	1095	-	-	-	-
F9_mins_g04_matrixG_01_134	9	F9	-	-	1097	-	-	-	-
F9_mins_g04_matrixG_01_135	9	F9	-	-	1096	-	-	-	-
F9_mins_g04_matrixG_01_136	9	F9	-	-	1092	-	-	-	-
F9_mins_g09_matrixG_145	9	F9	-	-	1092	-	-	-	-
F9_mins_g01_fsp_RE_01_105	9	F9	-	-	1092	-	-	-	-
F9_mins_g01_fsp_RE_01_106	9	F9	-	-	1108	-	-	-	-
F9_mins_g01_fsp_RE_01_107	9	F9	-	-	1091	-	-	-	-
F9_mins_g01_fsp_RE_01_108	9	F9	-	-	1096	-	-	-	-
F9_mins_g01_fsp_RE_01_109	9	F9	-	-	1083	-	-	-	-
F9_mins_g01_fsp_RE_01_110	9	F9	-	-	1085	-	-	-	-
F9_mins_g01_fsp_RE_01_111	9	F9	-	-	1088	-	-	-	-
F9_mins_g03_REs_01_122	9	F9	-	-	1098	-	-	-	-
F9_mins_g03_REs_01_122	9	F9	-	-	1098	-	-	-	-
F9_mins_g03_REs_01_123	9	F9	-	-	1107	-	-	-	-
F9_mins_g05_REs_01_137	9	F9	-	-	1108	-	-	-	-
F9_mins_g05_REs_01_138	9	F9	-	-	1109	-	-	-	-
F9_mins_g05_REs_01_139	9	F9	-	-	1110	-	-	-	-

Supplementary Table 1C (continued).

Analysis Name	Fissure #	Sample Name	Saturation pressure (bar) (Iacono-Marziano 2012)	Saturation depth (km) (Ryan 1987)	Saturation depth 1σ uncertainy (km)	δ34S (‰)	δ34S 1σ uncertainy (‰)	Fe3+/ΣFe % [Fe-XANES]	ΔQFM [Fe-XANES]	S6+/ΣS % [S-XANES]
Fissure 9 spatter, May 3 2018										
F9_mins_g01_matrixG_01_112	9	F9	-	-	-	-	-	-	-	-
F9_mins_g01_matrixG_01_113	9	F9	-	-	-	-	-	-	-	-
F9_mins_g01_matrixG_01_114	9	F9	-	-	-	-	-	11.7	-0.48	0.4
F9_mins_g01_matrixG_01_115	9	F9	-	-	-	-	-	13.2	-0.15	4.9
F9_mins_g03_matrixG_01_124	9	F9	-	-	-	-	-	12.2	-0.40	0.4
F9_mins_g03_matrixG_01_125	9	F9	-	-	-	-	-	12.2	-0.40	0.4
F9_mins_g03_matrixG_01_126	9	F9	-	-	-	-	-	12.9	-0.21	1.1
F9_mins_g03_matrixG_01_127	9	F9	-	-	-	-	-	12.9	-0.21	1.1
F9_mins_g03_matrixG_01_128	9	F9	-	-	-	-	-	-	-	-
F9_mins_g04_matrixG_01_134	9	F9	-	-	-	-	-	-	-	-
F9_mins_g04_matrixG_01_135	9	F9	-	-	-	-	-	-	-	-
F9_mins_g04_matrixG_01_136	9	F9	-	-	-	-	-	-	-	-
F9_mins_g01_matrixG_01_112	9	F9	-	-	-	-	-	-	-	-
F9_mins_g01_matrixG_01_113	9	F9	-	-	-	-	-	-	-	-
F9_mins_g01_matrixG_01_114	9	F9	-	-	-	-	-	11.7	-0.48	0.4
F9_mins_g01_matrixG_01_115	9	F9	-	-	-	-	-	13.2	-0.15	4.9
F9_mins_g03_matrixG_01_124	9	F9	-	-	-	-	-	12.2	-0.40	0.4
F9_mins_g03_matrixG_01_125	9	F9	-	-	-	-	-	12.2	-0.40	0.4
F9_mins_g03_matrixG_01_126	9	F9	-	-	-	-	-	12.9	-0.21	1.1
F9_mins_g03_matrixG_01_127	9	F9	-	-	-	-	-	12.9	-0.21	1.1
F9_mins_g03_matrixG_01_128	9	F9	-	-	-	-	-	-	-	-
F9_mins_g04_matrixG_01_134	9	F9	-	-	-	-	-	-	-	-
F9_mins_g04_matrixG_01_135	9	F9	-	-	-	-	-	-	-	-
F9_mins_g04_matrixG_01_136	9	F9	-	-	-	-	-	-	-	-
F9_mins_g09_matrixG_145	9	F9	-	-	-	-	-	12.1	-0.39	-
F9_mins_g01_fsp_RE_01_105	9	F9	-	-	-	-	-	14.5	+0.16	-
F9_mins_g01_fsp_RE_01_106	9	F9	-	-	-	-	-	14.0	-0.04	2.3
F9_mins_g01_fsp_RE_01_107	9	F9	-	-	-	-	-	14.0	-0.04	2.3
F9_mins_g01_fsp_RE_01_108	9	F9	-	-	-	-	-	-	-	-
F9_mins_g01_fsp_RE_01_109	9	F9	-	-	-	-	-	-	-	-
F9_mins_g01_fsp_RE_01_110	9	F9	-	-	-	-	-	11.6	-0.43	8.2
F9_mins_g01_fsp_RE_01_111	9	F9	-	-	-	-	-	11.6	-0.43	8.2
F9_mins_g03_REs_01_122	9	F9	-	-	-	-	-	-	-	-
F9_mins_g03_REs_01_122	9	F9	-	-	-	-	-	-	-	-
F9_mins_g03_REs_01_123	9	F9	-	-	-	-	-	16.2	+0.41	5.0
F9_mins_g05_REs_01_137	9	F9	-	-	-	-	-	16.5	+0.47	14.4
F9_mins_g05_REs_01_138	9	F9	-	-	-	-	-	16.3	+0.31	7.6
F9_mins_g05_REs_01_139	9	F9	-	-	-	-	-	16.3	+0.31	7.6

Supplementary Table 1C (continued).

Analysis Name	Fissure #	Sample Name	Eruption Date	Distance traveled before quench (km)	Glass Type	Host mineral	Sulfide present?
F9_mins_g05_REs_01_140	9	F9	5/3/18	0.05	interstitial melt	Pl + Cpx_glom	-
F9_mins_g05_REs_01_140	9	F9	5/3/18	0.05	interstitial melt	Pl + Cpx_glom	-
F9_mins_g05_MI_3_146	9	F9	5/3/18	0.05	interstitial melt	Pl + Cpx_glom	-
F9_mins_g05_MI_3_147	9	F9	5/3/18	0.05	interstitial melt	Pl + Cpx_glom	-
F9_1	9	F9	5/3/18	0.05	MI	Cpx_MI	-
Fissure 17 andesite, May 18 2018							
KE62-3256s_8_interstitialG_190	17	KE62-3256S	5/18/18	0.0	interstitial melt	-	-
KE62-3256s_11_interstitialG_193	17	KE62-3256S	5/18/18	0.0	interstitial melt	-	-
KE62-3256s_11_interstitialG_194	17	KE62-3256S	5/18/18	0.0	interstitial melt	-	-
KE62-3256s_12_interstitialG_195	17	KE62-3256S	5/18/18	0.0	interstitial melt	-	-
KE62-3256s_2_MI_183	17	KE62-3256S	5/18/18	0.0	re-entrant	Plag_RE	-
KE62-3256s_8_MI_187	17	KE62-3256S	5/18/18	0.0	re-entrant	Olivine_RE	-
KE62-3256s_11_MI_191	17	KE62-3256S	5/18/18	0.0	re-entrant	Plag_RE	-
KE62-3256s_1_MI_181	17	KE62-3256S	5/18/18	0.0	MI	Plag_MI	-
KE62-3256s_5ish_MI_185	17	KE62-3256S	5/18/18	0.0	MI	Plag_MI	-
Fissure 8 basaltic pumice, May 30 2018							
KE62-3293S_1_G01_MatrixGlass_51	8	KE62-3923S	5/30/18	0.02	matrix glass	-	-
KE62-3293S_1_G01_MatrixGlass_52	8	KE62-3923S	5/30/18	0.02	matrix glass	-	-
KE62-3293S_1_G03_MatrixGlass_64	8	KE62-3923S	5/30/18	0.02	matrix glass	-	-
KE62-3293S_1_G03_MatrixGlass_65	8	KE62-3923S	5/30/18	0.02	matrix glass	-	-
KE62-3293S_1_G06_MatrixGlass_76	8	KE62-3923S	5/30/18	0.02	matrix glass	-	-
KE62-3293S_1_G06_MatrixGlass_77	8	KE62-3923S	5/30/18	0.02	matrix glass	-	-
KE62-3293S_1_G07_MatrixGlass_78	8	KE62-3923S	5/30/18	0.02	matrix glass	-	-
KE62-3293S_1_G07_MatrixGlass_78	8	KE62-3923S	5/30/18	0.02	matrix glass	-	-
KE62-3293S_1_G07_MatrixGlass_79	8	KE62-3923S	5/30/18	0.02	matrix glass	-	-
KE62-3293S_1_G07_MatrixGlass_79	8	KE62-3923S	5/30/18	0.02	matrix glass	-	-
KE62-3293S_1_G08_MatrixGlass_82	8	KE62-3923S	5/30/18	0.02	matrix glass	-	-
KE62-3293S_glass_1_220	8	KE62-3923S	5/30/18	0.02	matrix glass	-	-
KE62-3293S_glass_1_221	8	KE62-3923S	5/30/18	0.02	matrix glass	-	-
KE62-3293S_glass_1_222	8	KE62-3923S	5/30/18	0.02	matrix glass	-	-
KE62-3293S_glass_1_223	8	KE62-3923S	5/30/18	0.02	matrix glass	-	-
KE62-3293S_glass_1_224	8	KE62-3923S	5/30/18	0.02	matrix glass	-	-
KE62-3293S_glass_2_225	8	KE62-3923S	5/30/18	0.02	matrix glass	-	-
KE62-3293S_glass_2_226	8	KE62-3923S	5/30/18	0.02	matrix glass	-	-
KE62-3293S_glass_2_227	8	KE62-3923S	5/30/18	0.02	matrix glass	-	-
KE62-3293S_glass_2_228	8	KE62-3923S	5/30/18	0.02	matrix glass	-	-
KE62-3293S_glass_2_229	8	KE62-3923S	5/30/18	0.02	matrix glass	-	-

Supplementary Table 1C (continued).

Analysis Name	Fissure #	Sample Name	Na2O wt%	SiO2 wt%	CaO wt%	K2O wt%	Al2O3 wt%	FeOT wt%	MgO wt%	TiO2 wt%	MnO wt%
F9_mins_g05_REs_01_140	9	F9	2.98	50.54	8.16	1.11	12.38	15.05	4.27	4.62	0.20
F9_mins_g05_REs_01_140	9	F9	2.98	50.54	8.16	1.11	12.38	15.05	4.27	4.62	0.20
F9_mins_g05_MI_3_146	9	F9	3.04	51.09	8.38	1.17	13.00	13.93	4.15	4.36	0.21
F9_mins_g05_MI_3_147	9	F9	2.88	51.76	8.38	1.10	13.14	13.31	4.17	4.36	0.21
F9_1	9	F9	-	-	-	-	-	-	-	-	-
Fissure 17 andesite, May 18 2018											
KE62-3256s_8_interstitialG_190	17	KE62-3256S	3.73	65.02	4.07	2.47	12.83	8.19	1.26	1.59	0.15
KE62-3256s_11_interstitialG_193	17	KE62-3256S	3.78	64.36	4.30	2.45	13.36	8.22	1.24	1.49	0.16
KE62-3256s_11_interstitialG_194	17	KE62-3256S	3.54	63.20	4.22	2.42	13.81	9.28	1.22	1.49	0.17
KE62-3256s_12_interstitialG_195	17	KE62-3256S	3.73	62.85	4.32	2.38	13.85	9.16	1.30	1.48	0.16
KE62-3256s_2_MI_183	17	KE62-3256S	3.27	62.87	4.64	2.36	12.86	9.76	1.34	1.80	0.19
KE62-3256s_8_MI_187	17	KE62-3256S	4.81	59.15	4.99	2.34	15.96	7.46	2.13	1.90	0.14
KE62-3256s_11_MI_191	17	KE62-3256S	2.39	64.55	4.31	2.52	13.58	9.29	1.41	1.38	0.16
KE62-3256s_1_MI_181	17	KE62-3256S	2.58	51.08	9.40	0.64	10.31	14.52	7.28	3.47	0.23
KE62-3256s_5ish_MI_185	17	KE62-3256S	2.57	50.94	9.50	0.65	10.25	14.26	7.53	3.54	0.23
Fissure 8 basaltic pumice, May 30 2018											
KE62-3293S_1_G01_MatrixGlass_51	8	KE62-3923S	2.53	51.44	10.64	0.58	13.89	11.52	6.08	2.79	0.20
KE62-3293S_1_G01_MatrixGlass_52	8	KE62-3923S	2.29	51.84	10.56	0.57	13.97	11.45	5.95	2.79	0.18
KE62-3293S_1_G03_MatrixGlass_64	8	KE62-3923S	3.03	50.14	10.64	0.50	14.23	11.77	6.44	2.71	0.21
KE62-3293S_1_G03_MatrixGlass_65	8	KE62-3923S	2.65	50.92	10.49	0.57	13.91	11.84	6.33	2.82	0.16
KE62-3293S_1_G06_MatrixGlass_76	8	KE62-3923S	2.31	53.12	10.43	0.50	12.83	11.66	5.97	2.68	0.16
KE62-3293S_1_G06_MatrixGlass_77	8	KE62-3923S	2.73	51.94	10.41	0.53	13.29	11.59	6.27	2.67	0.16
KE62-3293S_1_G07_MatrixGlass_78	8	KE62-3923S	2.74	50.81	10.56	0.49	14.31	11.55	6.31	2.71	0.18
KE62-3293S_1_G07_MatrixGlass_78	8	KE62-3923S	2.74	50.81	10.56	0.49	14.31	11.55	6.31	2.71	0.18
KE62-3293S_1_G07_MatrixGlass_79	8	KE62-3923S	2.41	51.59	10.46	0.56	13.92	11.56	6.37	2.69	0.18
KE62-3293S_1_G07_MatrixGlass_79	8	KE62-3923S	2.41	51.59	10.46	0.56	13.92	11.56	6.37	2.69	0.18
KE62-3293S_1_G08_MatrixGlass_82	8	KE62-3923S	2.02	52.21	10.64	0.55	13.04	12.51	5.75	2.73	0.17
KE62-3293S_glass_1_220	8	KE62-3923S	2.61	50.86	10.65	0.55	13.36	12.21	6.48	2.75	0.18
KE62-3293S_glass_1_221	8	KE62-3923S	2.54	51.83	10.64	0.51	13.83	10.96	6.36	2.80	0.18
KE62-3293S_glass_1_222	8	KE62-3923S	2.63	51.34	10.71	0.52	13.61	11.45	6.42	2.78	0.18
KE62-3293S_glass_1_223	8	KE62-3923S	2.81	51.68	10.66	0.51	13.36	11.37	6.37	2.73	0.18
KE62-3293S_glass_1_224	8	KE62-3923S	2.71	51.75	10.81	0.56	13.19	11.12	6.47	2.85	0.18
KE62-3293S_glass_2_225	8	KE62-3923S	2.66	51.15	10.69	0.56	13.72	11.55	6.37	2.77	0.17
KE62-3293S_glass_2_226	8	KE62-3923S	2.73	51.02	10.83	0.54	13.28	11.79	6.48	2.78	0.17
KE62-3293S_glass_2_227	8	KE62-3923S	2.72	50.98	10.52	0.59	14.24	11.31	6.37	2.76	0.17
KE62-3293S_glass_2_228	8	KE62-3923S	2.80	51.44	10.67	0.54	13.88	10.99	6.44	2.73	0.17
KE62-3293S_glass_2_229	8	KE62-3923S	2.52	51.05	10.77	0.50	13.95	11.50	6.36	2.79	0.19

Supplementary Table 1C (continued).

Analysis Name	Fissure #	Sample Name	P2O5 wt%	Cl ppm	S ppm	un-normalized total	S/Cl (mass ratio)	non-sulfide corrected S ppm	non-PEC corrected FeOT	melt Mg#	Host Mg#	Host An#
F9_mins_g05_REs_01_140	9	F9	0.53	283	1267	98.99	4.5	1267	15.05	33.6	-	-
F9_mins_g05_REs_01_140	9	F9	0.53	283	1267	98.99	4.5	1267	15.05	33.6	-	-
F9_mins_g05_MI_3_146	9	F9	0.60	287	516	98.29	1.8	516	13.93	34.7	-	-
F9_mins_g05_MI_3_147	9	F9	0.61	250	606	98.80	2.4	606	13.31	35.8	-	-
F9_1	9	F9	-	-	-	-	-	-	-	-	-	-
Fissure 17 andesite, May 18 2018												
KE62-3256s_8_interstitialG_190	17	KE62-3256S	0.57	981	337	97.94	0.3	337	8.19	21.5	-	-
KE62-3256s_11_interstitialG_193	17	KE62-3256S	0.54	886	222	96.21	0.3	222	8.22	21.2	-	-
KE62-3256s_11_interstitialG_194	17	KE62-3256S	0.53	909	349	98.50	0.4	349	9.28	18.9	-	-
KE62-3256s_12_interstitialG_195	17	KE62-3256S	0.65	933	300	97.59	0.3	300	9.16	20.2	-	-
KE62-3256s_2_MI_183	17	KE62-3256S	0.75	1054	585	96.90	0.6	585	9.76	19.7	-	-
KE62-3256s_8_MI_187	17	KE62-3256S	0.96	1017	436	98.97	0.4	436	7.46	33.7	-	-
KE62-3256s_11_MI_191	17	KE62-3256S	0.30	910	324	96.68	0.4	324	9.29	21.3	-	-
KE62-3256s_1_MI_181	17	KE62-3256S	0.37	178	1124	98.20	6.3	1124	14.52	47.2	-	65.6
KE62-3256s_5ish_MI_185	17	KE62-3256S	0.39	160	1172	96.87	7.3	1172	14.26	48.5	-	71.8
Fissure 8 basaltic pumice, May 30 2018												
KE62-3293S_1_G01_MatrixGlass_51	8	KE62-3923S	0.33	170	759	97.02	4.5	759	11.51	48.5	-	-
KE62-3293S_1_G01_MatrixGlass_52	8	KE62-3923S	0.34	156	742	96.30	4.7	742	11.44	48.1	-	-
KE62-3293S_1_G03_MatrixGlass_64	8	KE62-3923S	0.31	135	352	95.54	2.6	352	11.77	49.4	-	-
KE62-3293S_1_G03_MatrixGlass_65	8	KE62-3923S	0.28	170	459	96.65	2.7	459	11.84	48.8	-	-
KE62-3293S_1_G06_MatrixGlass_76	8	KE62-3923S	0.31	174	509	99.67	2.9	509	11.66	47.7	-	-
KE62-3293S_1_G06_MatrixGlass_77	8	KE62-3923S	0.35	132	479	100.08	3.6	479	11.59	49.1	-	-
KE62-3293S_1_G07_MatrixGlass_78	8	KE62-3923S	0.31	134	281	96.69	2.1	281	11.55	49.3	-	-
KE62-3293S_1_G07_MatrixGlass_78	8	KE62-3923S	0.31	134	281	96.69	2.1	281	11.55	49.3	-	-
KE62-3293S_1_G07_MatrixGlass_79	8	KE62-3923S	0.26	100	739	98.58	7.4	739	11.55	49.6	-	-
KE62-3293S_1_G07_MatrixGlass_79	8	KE62-3923S	0.26	100	739	98.58	7.4	739	11.55	49.6	-	-
KE62-3293S_1_G08_MatrixGlass_82	8	KE62-3923S	0.34	160	454	97.24	2.8	454	12.50	45.0	-	-
KE62-3293S_glass_1_220	8	KE62-3923S	0.30	123	373	97.58	3.0	373	12.21	48.6	-	-
KE62-3293S_glass_1_221	8	KE62-3923S	0.32	147	243	98.03	1.7	243	10.96	50.8	-	-
KE62-3293S_glass_1_222	8	KE62-3923S	0.32	166	398	97.71	2.4	398	11.45	50.0	-	-
KE62-3293S_glass_1_223	8	KE62-3923S	0.30	130	194	97.80	1.5	194	11.37	50.0	-	-
KE62-3293S_glass_1_224	8	KE62-3923S	0.31	170	311	95.76	1.8	311	11.12	50.9	-	-
KE62-3293S_glass_2_225	8	KE62-3923S	0.30	142	447	97.48	3.1	447	11.55	49.6	-	-
KE62-3293S_glass_2_226	8	KE62-3923S	0.33	151	264	95.82	1.7	264	11.79	49.5	-	-
KE62-3293S_glass_2_227	8	KE62-3923S	0.31	144	212	98.07	1.5	212	11.31	50.1	-	-
KE62-3293S_glass_2_228	8	KE62-3923S	0.32	131	173	97.19	1.3	173	10.99	51.1	-	-
KE62-3293S_glass_2_229	8	KE62-3923S	0.33	125	300	96.41	2.4	300	11.50	49.6	-	-

Supplementary Table 1C (continued).

Analysis Name	Fissure #	Sample Name	% PEC (olivine mass)	PEC correction coefficient	Temperature of matrix glass quenching or MI entrapment (°C)	H2O in melt (wt%) (FTIR)	CO2 in melt (ppm) (FTIR)	CO2 in melt + bubble (ppm) (FTIR + Raman)	vapor bubble volume (%)
F9_mins_g05_REs_01_140	9	F9	-	-	1100	-	-	-	-
F9_mins_g05_REs_01_140	9	F9	-	-	1100	-	-	-	-
F9_mins_g05_MI_3_146	9	F9	-	-	1097	-	-	-	-
F9_mins_g05_MI_3_147	9	F9	-	-	1098	-	-	-	-
F9_1	9	F9	-	-	-	-	-	383	7%
Fissure 17 andesite, May 18 2018									
KE62-3256s_8_interstitialG_190	17	KE62-3256S	-	-	1039	-	-	-	-
KE62-3256s_11_interstitialG_193	17	KE62-3256S	-	-	1039	-	-	-	-
KE62-3256s_11_interstitialG_194	17	KE62-3256S	-	-	1038	-	-	-	-
KE62-3256s_12_interstitialG_195	17	KE62-3256S	-	-	1040	-	-	-	-
KE62-3256s_2_MI_183	17	KE62-3256S	-	-	1041	-	-	-	-
KE62-3256s_8_MI_187	17	KE62-3256S	-	-	1057	-	-	-	-
KE62-3256s_11_MI_191	17	KE62-3256S	-	-	1042	-	-	-	-
KE62-3256s_1_MI_181	17	KE62-3256S	-	-	-	-	-	-	-
KE62-3256s_5ish_MI_185	17	KE62-3256S	-	-	-	-	-	-	-
Fissure 8 basaltic pumice, May 30 2018									
KE62-3293S_1_G01_MatrixGlass_51	8	KE62-3923S	-	-	1136	-	-	-	-
KE62-3293S_1_G01_MatrixGlass_52	8	KE62-3923S	-	-	1134	-	-	-	-
KE62-3293S_1_G03_MatrixGlass_64	8	KE62-3923S	-	-	1143	-	-	-	-
KE62-3293S_1_G03_MatrixGlass_65	8	KE62-3923S	-	-	1141	-	-	-	-
KE62-3293S_1_G06_MatrixGlass_76	8	KE62-3923S	-	-	1134	-	-	-	-
KE62-3293S_1_G06_MatrixGlass_77	8	KE62-3923S	-	-	1140	-	-	-	-
KE62-3293S_1_G07_MatrixGlass_78	8	KE62-3923S	-	-	1141	-	-	-	-
KE62-3293S_1_G07_MatrixGlass_78	8	KE62-3923S	-	-	1141	-	-	-	-
KE62-3293S_1_G07_MatrixGlass_79	8	KE62-3923S	-	-	1142	-	-	-	-
KE62-3293S_1_G07_MatrixGlass_79	8	KE62-3923S	-	-	1142	-	-	-	-
KE62-3293S_1_G08_MatrixGlass_82	8	KE62-3923S	-	-	1130	-	-	-	-
KE62-3293S_glass_1_220	8	KE62-3923S	-	-	1144	-	-	-	-
KE62-3293S_glass_1_221	8	KE62-3923S	-	-	1142	-	-	-	-
KE62-3293S_glass_1_222	8	KE62-3923S	-	-	1143	-	-	-	-
KE62-3293S_glass_1_223	8	KE62-3923S	-	-	1142	-	-	-	-
KE62-3293S_glass_1_224	8	KE62-3923S	-	-	1144	-	-	-	-
KE62-3293S_glass_2_225	8	KE62-3923S	-	-	1142	-	-	-	-
KE62-3293S_glass_2_226	8	KE62-3923S	-	-	1144	-	-	-	-
KE62-3293S_glass_2_227	8	KE62-3923S	-	-	1142	-	-	-	-
KE62-3293S_glass_2_228	8	KE62-3923S	-	-	1143	-	-	-	-
KE62-3293S_glass_2_229	8	KE62-3923S	-	-	1142	-	-	-	-

Supplementary Table 1C (continued).

Analysis Name	Fissure #	Sample Name	Saturation pressure (bar) (Iacono-Marziano 2012)	Saturation depth (km) (Ryan 1987)	Saturation depth 1σ uncertainy (km)	δ34S (‰)	δ34S 1σ uncertainy (‰)	Fe3+/ΣFe % [Fe-XANES]	ΔQFM [Fe-XANES]	S6+/ΣS % [S-XANES]
F9_mins_g05_REs_01_140	9	F9	-	-	-	-	-	-	-	-
F9_mins_g05_REs_01_140	9	F9	-	-	-	-	-	-	-	-
F9_mins_g05_MI_3_146	9	F9	-	-	-	-	-	14.3	-0.00	2.7
F9_mins_g05_MI_3_147	9	F9	-	-	-	-	-	14.3	-0.00	2.7
F9_1	9	F9	867	3.8	2.0	-	-	-	-	-
Fissure 17 andesite, May 18 2018										
KE62-3256s_8_interstitialG_190	17	KE62-3256S	-	-	-	-	-	15.0	+0.03	0.6
KE62-3256s_11_interstitialG_193	17	KE62-3256S	-	-	-	-	-	14.1	-0.13	1.1
KE62-3256s_11_interstitialG_194	17	KE62-3256S	-	-	-	-	-	14.1	-0.13	1.1
KE62-3256s_12_interstitialG_195	17	KE62-3256S	-	-	-	-	-	14.9	+0.06	-
KE62-3256s_2_MI_183	17	KE62-3256S	-	-	-	-	-	15.8	+0.24	7.9
KE62-3256s_8_MI_187	17	KE62-3256S	-	-	-	-	-	19.1	+0.54	10.7
KE62-3256s_11_MI_191	17	KE62-3256S	-	-	-	-	-	16.9	+0.57	13.1
KE62-3256s_1_MI_181	17	KE62-3256S	-	-	-	-	-	22.1	+1.08	17.4
KE62-3256s_5ish_MI_185	17	KE62-3256S	-	-	-	-	-	22.8	+1.14	13.8
Fissure 8 basaltic pumice, May 30 2018										
KE62-3293S_1_G01_MatrixGlass_51	8	KE62-3923S	-	-	-	-	-	16.4	+0.25	6.4
KE62-3293S_1_G01_MatrixGlass_52	8	KE62-3923S	-	-	-	-	-	17.3	+0.44	4.1
KE62-3293S_1_G03_MatrixGlass_64	8	KE62-3923S	-	-	-	-	-	-	-	-
KE62-3293S_1_G03_MatrixGlass_65	8	KE62-3923S	-	-	-	-	-	-	-	-
KE62-3293S_1_G06_MatrixGlass_76	8	KE62-3923S	-	-	-	-	-	-	-	-
KE62-3293S_1_G06_MatrixGlass_77	8	KE62-3923S	-	-	-	-	-	-	-	-
KE62-3293S_1_G07_MatrixGlass_78	8	KE62-3923S	-	-	-	-	-	-	-	-
KE62-3293S_1_G07_MatrixGlass_78	8	KE62-3923S	-	-	-	-	-	-	-	-
KE62-3293S_1_G07_MatrixGlass_79	8	KE62-3923S	-	-	-	-	-	-	-	-
KE62-3293S_1_G07_MatrixGlass_79	8	KE62-3923S	-	-	-	-	-	-	-	-
KE62-3293S_1_G08_MatrixGlass_82	8	KE62-3923S	-	-	-	-	-	16.0	+0.26	-
KE62-3293S_glass_1_220	8	KE62-3923S	-	-	-	-	-	14.4	-0.09	2.7
KE62-3293S_glass_1_221	8	KE62-3923S	-	-	-	-	-	16.0	+0.16	6.2
KE62-3293S_glass_1_222	8	KE62-3923S	-	-	-	-	-	14.6	-0.08	2.5
KE62-3293S_glass_1_223	8	KE62-3923S	-	-	-	-	-	14.4	-0.09	2.7
KE62-3293S_glass_1_224	8	KE62-3923S	-	-	-	-	-	14.6	-0.08	2.5
KE62-3293S_glass_2_225	8	KE62-3923S	-	-	-	-	-	-	-	-
KE62-3293S_glass_2_226	8	KE62-3923S	-	-	-	-	-	-	-	-
KE62-3293S_glass_2_227	8	KE62-3923S	-	-	-	-	-	-	-	-
KE62-3293S_glass_2_228	8	KE62-3923S	-	-	-	-	-	-	-	-
KE62-3293S_glass_2_229	8	KE62-3923S	-	-	-	-	-	-	-	-

Supplementary Table 1C (continued).

Analysis Name	Fissure #	Sample Name	Eruption Date	Distance traveled before quench (km)	Glass Type	Host mineral	Sulfide present?
KE62-3293S_glass_2_230	8	KE62-3923S	5/30/18	0.02	matrix glass	-	-
KE62-3293S_glass_1b_303	8	KE62-3923S	5/30/18	0.02	matrix glass	-	-
KE62-3293S_glass_1b_304	8	KE62-3923S	5/30/18	0.02	matrix glass	-	-
KE62-3293S_glass_1b_305	8	KE62-3923S	5/30/18	0.02	matrix glass	-	-
KE62-3293S_glass_1c_481	8	KE62-3923S	5/30/18	0.02	matrix glass	-	-
KE62-3293S_glass_1c_482	8	KE62-3923S	5/30/18	0.02	matrix glass	-	-
KE62-3923s_9_matrixG_279	8	KE62-3923S	5/30/18	0.02	matrix glass	-	-
KE62-3923s_9_matrixG_280	8	KE62-3923S	5/30/18	0.02	matrix glass	-	-
KE62-3923s_9_matrixG_281	8	KE62-3923S	5/30/18	0.02	matrix glass	-	-
EF8_bubble_free_matrixG1_262	8	KE62-3923S	5/30/18	0.02	matrix glass	-	-
EF8_bubble-free_matrixG2_87	8	KE62-3923S	5/30/18	0.02	matrix glass	-	-
EF8_bubble-free_matrixG2_88	8	KE62-3923S	5/30/18	0.02	matrix glass	-	-
KE62-3923s_11_matrixG_102	8	KE62-3923S	5/30/18	0.02	matrix glass	-	-
KE62-3923s_12_matrixG_104	8	KE62-3923S	5/30/18	0.02	matrix glass	-	-
KE62-3923s_1a_matrixG_90	8	KE62-3923S	5/30/18	0.02	matrix glass	-	-
KE62-3923s_1a_matrixG_91	8	KE62-3923S	5/30/18	0.02	matrix glass	-	-
KE62-3923s_9_matrixG2_107	8	KE62-3923S	5/30/18	0.02	matrix glass	-	-
KE62-3923s_9_matrixG2_108	8	KE62-3923S	5/30/18	0.02	matrix glass	-	-
KE62-3923s_glass1_163	8	KE62-3923S	5/30/18	0.02	matrix glass	-	-
KE62-3923s_glass1_162	8	KE62-3923S	5/30/18	0.02	matrix glass	-	-
KE62-3923s_glass1_163	8	KE62-3923S	5/30/18	0.02	matrix glass	-	-
KE62-3923s_glass1_164	8	KE62-3923S	5/30/18	0.02	matrix glass	-	-
KE62-3923s_mins_g01_matrixG_148	8	KE62-3923S	5/30/18	0.02	matrix glass	-	-
KE62-3923s_mins_g01_matrixG_154	8	KE62-3923S	5/30/18	0.02	matrix glass	-	-
KE62-3923s_mount1_G02_matrixG_156	8	KE62-3923S	5/30/18	0.02	interstitial melt	Pl + Cpx_glom	-
KE62-3923s_1a_matrixG_92	8	KE62-3923S	5/30/18	0.02	interstitial melt	Olivine aggregate	-
KE62-3923s_1a_matrixG_93	8	KE62-3923S	5/30/18	0.02	interstitial melt	Olivine aggregate	-
KE62-3923s_4matrixG_97	8	KE62-3923S	5/30/18	0.02	interstitial melt	Olivine aggregate	-
KE62-3923s_4matrixG_96	8	KE62-3923S	5/30/18	0.02	interstitial melt	Olivine aggregate	-
KE62-3923s_mins_g08_RE_149	8	KE62-3923S	5/30/18	0.02	interstitial melt	Olivine aggregate	-
KE62-3923s_mins_g08_RE_150	8	KE62-3923S	5/30/18	0.02	interstitial melt	Olivine aggregate	-
KE62-3923s_mins_g08_RE_151	8	KE62-3923S	5/30/18	0.02	interstitial melt	Olivine aggregate	-
KE62-3923s_mins_g08_RE_152	8	KE62-3923S	5/30/18	0.02	interstitial melt	Olivine aggregate	-
KE62-3923s_mins_g08_RE_153	8	KE62-3923S	5/30/18	0.02	interstitial melt	Olivine aggregate	-
FeXANES_fullrange_1s_KE62-3923s_14_matrixG_1merge	8	KE62-3923S	5/30/18	0.02	interstitial melt	Pl + Cpx_glom	-
FeXANES_fullrange_1s_KE62-3923s_14_matrixG_2merge	8	KE62-3923S	5/30/18	0.02	interstitial melt	Pl + Cpx_glom	-

Supplementary Table 1C (continued).

Analysis Name	Fissure #	Sample Name	Na2O wt%	SiO2 wt%	CaO wt%	K2O wt%	Al2O3 wt%	FeOT wt%	MgO wt%	TiO2 wt%	MnO wt%
KE62-3293S_glass_2_230	8	KE62-3923S	2.80	50.80	10.79	0.49	13.86	11.50	6.44	2.76	0.19
KE62-3293S_glass_1b_303	8	KE62-3923S	2.59	51.10	10.60	0.51	13.78	11.71	6.39	2.76	0.18
KE62-3293S_glass_1b_304	8	KE62-3923S	2.47	51.25	10.59	0.52	13.86	11.66	6.36	2.75	0.18
KE62-3293S_glass_1b_305	8	KE62-3923S	2.58	51.00	10.64	0.56	13.76	11.74	6.40	2.76	0.18
KE62-3293S_glass_1c_481	8	KE62-3923S	2.73	51.42	10.46	0.61	13.36	11.74	6.42	2.73	0.18
KE62-3293S_glass_1c_482	8	KE62-3923S	2.53	51.17	10.56	0.57	13.62	11.76	6.46	2.80	0.17
KE62-3923s_9_matrixG_279	8	KE62-3923S	2.40	50.89	10.32	0.56	14.66	11.42	6.41	2.77	0.18
KE62-3923s_9_matrixG_280	8	KE62-3923S	2.57	51.09	10.40	0.48	14.25	11.54	6.40	2.70	0.17
KE62-3923s_9_matrixG_281	8	KE62-3923S	2.57	50.74	10.41	0.55	14.46	11.42	6.48	2.76	0.20
EF8_bubble_free_matrixG1_262	8	KE62-3923S	2.53	51.40	10.34	0.58	14.26	11.27	6.43	2.72	0.17
EF8_bubble-free_matrixG2_87	8	KE62-3923S	2.62	50.93	10.39	0.55	14.30	11.81	6.26	2.68	0.18
EF8_bubble-free_matrixG2_88	8	KE62-3923S	2.67	50.79	10.54	0.54	14.25	11.64	6.35	2.73	0.18
KE62-3923s_11_matrixG_102	8	KE62-3923S	2.56	51.35	10.23	0.55	14.75	11.16	6.19	2.74	0.17
KE62-3923s_12_matrixG_104	8	KE62-3923S	2.85	50.27	10.21	0.55	14.24	12.56	6.26	2.59	0.18
KE62-3923s_1a_matrixG_90	8	KE62-3923S	2.65	51.49	10.55	0.51	14.00	11.32	6.24	2.77	0.18
KE62-3923s_1a_matrixG_91	8	KE62-3923S	2.47	51.33	10.57	0.55	14.28	11.38	6.15	2.78	0.19
KE62-3923s_9_matrixG2_107	8	KE62-3923S	2.70	50.84	10.56	0.51	14.26	11.53	6.40	2.72	0.19
KE62-3923s_9_matrixG2_108	8	KE62-3923S	2.65	51.25	10.42	0.57	14.13	11.55	6.26	2.69	0.18
KE62-3923s_glass1_163	8	KE62-3923S	2.65	50.61	10.38	0.53	14.63	11.74	6.28	2.69	0.18
KE62-3923s_glass1_162	8	KE62-3923S	2.67	51.21	10.40	0.47	14.27	11.41	6.31	2.75	0.18
KE62-3923s_glass1_163	8	KE62-3923S	2.65	50.61	10.38	0.53	14.63	11.74	6.28	2.69	0.18
KE62-3923s_glass1_164	8	KE62-3923S	2.67	50.75	10.33	0.57	14.22	11.96	6.27	2.75	0.17
KE62-3923s_mins_g01_matrixG_148	8	KE62-3923S	2.46	51.80	10.52	0.56	14.35	10.75	6.35	2.73	0.18
KE62-3923s_mins_g01_matrixG_154	8	KE62-3923S	2.61	51.18	10.34	0.53	14.51	11.52	6.21	2.62	0.18
KE62-3923s_mount1_G02_matrixG_156	8	KE62-3923S	2.40	51.20	10.34	0.55	14.91	11.61	5.84	2.68	0.18
KE62-3923s_1a_matrixG_92	8	KE62-3923S	2.59	50.81	10.33	0.56	14.42	11.90	6.22	2.70	0.18
KE62-3923s_1a_matrixG_93	8	KE62-3923S	2.57	50.47	10.23	0.58	14.38	12.52	6.10	2.68	0.18
KE62-3923s_4matrixG_97	8	KE62-3923S	2.68	50.76	10.30	0.58	14.18	12.23	6.02	2.75	0.19
KE62-3923s_4matrixG_96	8	KE62-3923S	2.49	51.44	10.37	0.54	14.05	11.76	6.03	2.82	0.18
KE62-3923s_mins_g08_RE_149	8	KE62-3923S	2.55	50.35	10.40	0.52	14.66	12.06	6.29	2.70	0.18
KE62-3923s_mins_g08_RE_150	8	KE62-3923S	2.42	51.04	10.44	0.52	14.28	11.87	6.29	2.67	0.18
KE62-3923s_mins_g08_RE_151	8	KE62-3923S	2.76	51.53	10.47	0.52	14.15	11.12	6.32	2.66	0.18
KE62-3923s_mins_g08_RE_152	8	KE62-3923S	2.41	51.55	10.53	0.50	14.01	11.49	6.39	2.65	0.19
KE62-3923s_mins_g08_RE_153	8	KE62-3923S	2.74	51.18	10.32	0.53	14.02	11.71	6.40	2.62	0.19
FeXANES_fullrange_1s_KE62-3923s_14_matrixG_1merge	8	KE62-3923S	-	-	-	-	-	-	-	-	-
FeXANES_fullrange_1s_KE62-3923s_14_matrixG_2merge	8	KE62-3923S	-	-	-	-	-	-	-	-	-

Supplementary Table 1C (continued).

Analysis Name	Fissure #	Sample Name	P2O5 wt%	Cl ppm	S ppm	un-normalized total	S/Cl (mass ratio)	non-sulfide corrected S ppm	non-PEC corrected FeOT	melt Mg#	Host Mg#	Host An#
KE62-3293S_glass_2_230	8	KE62-3923S	0.31	170	438	96.67	2.6	438	11.50	50.0	-	-
KE62-3293S_glass_1b_303	8	KE62-3923S	0.33	121	251	97.37	2.1	251	11.71	49.3	-	-
KE62-3293S_glass_1b_304	8	KE62-3923S	0.31	175	277	97.77	1.6	277	11.66	49.3	-	-
KE62-3293S_glass_1b_305	8	KE62-3923S	0.33	134	491	97.45	3.7	491	11.74	49.3	-	-
KE62-3293S_glass_1c_481	8	KE62-3923S	0.31	149	275	98.36	1.8	275	11.74	49.4	-	-
KE62-3293S_glass_1c_482	8	KE62-3923S	0.32	108	274	97.54	2.5	274	11.76	49.5	-	-
KE62-3923s_9_matrixG_279	8	KE62-3923S	0.30	153	765	99.06	5.0	765	11.42	50.0	-	-
KE62-3923s_9_matrixG_280	8	KE62-3923S	0.31	113	812	98.51	7.2	812	11.54	49.7	-	-
KE62-3923s_9_matrixG_281	8	KE62-3923S	0.32	120	762	98.17	6.3	762	11.42	50.3	-	-
EF8_bubble_free_matrixG1_262	8	KE62-3923S	0.29	104	112	99.86	1.1	112	11.27	50.5	-	-
EF8_bubble-free_matrixG2_87	8	KE62-3923S	0.26	105	152	99.18	1.5	152	11.81	48.6	-	-
EF8_bubble-free_matrixG2_88	8	KE62-3923S	0.28	132	99	97.97	0.8	99	11.64	49.3	-	-
KE62-3923s_11_matrixG_102	8	KE62-3923S	0.29	120	188	99.55	1.6	188	11.16	49.7	-	-
KE62-3923s_12_matrixG_104	8	KE62-3923S	0.28	114	651	100.13	5.7	651	12.55	47.0	-	-
KE62-3923s_1a_matrixG_90	8	KE62-3923S	0.29	114	463	96.77	4.1	463	11.31	49.6	-	-
KE62-3923s_1a_matrixG_91	8	KE62-3923S	0.30	123	441	96.99	3.6	441	11.38	49.1	-	-
KE62-3923s_9_matrixG2_107	8	KE62-3923S	0.28	111	669	97.37	6.0	669	11.53	49.7	-	-
KE62-3923s_9_matrixG2_108	8	KE62-3923S	0.27	131	539	99.17	4.1	539	11.55	49.1	-	-
KE62-3923s_glass1_163	8	KE62-3923S	0.31	115	451	98.44	3.9	451	11.74	48.8	-	-
KE62-3923s_glass1_162	8	KE62-3923S	0.30	142	312	98.47	2.2	312	11.41	49.6	-	-
KE62-3923s_glass1_163	8	KE62-3923S	0.31	115	451	98.44	3.9	451	11.74	48.8	-	-
KE62-3923s_glass1_164	8	KE62-3923S	0.30	133	349	99.25	2.6	349	11.96	48.3	-	-
KE62-3923s_mins_g01_matrixG_148	8	KE62-3923S	0.29	164	419	97.43	2.5	419	10.74	51.3	-	-
KE62-3923s_mins_g01_matrixG_154	8	KE62-3923S	0.29	119	507	99.73	4.3	507	11.51	49.0	-	-
KE62-3923s_mount1_G02_matrixG_156	8	KE62-3923S	0.29	114	626	97.54	5.5	626	11.60	47.3	-	-
KE62-3923s_1a_matrixG_92	8	KE62-3923S	0.29	121	807	98.40	6.7	807	11.89	48.2	-	-
KE62-3923s_1a_matrixG_93	8	KE62-3923S	0.27	132	756	99.43	5.7	756	12.51	46.5	-	-
KE62-3923s_4matrixG_97	8	KE62-3923S	0.30	128	592	98.47	4.6	592	12.22	46.7	-	-
KE62-3923s_4matrixG_96	8	KE62-3923S	0.31	179	613	98.14	3.4	613	11.75	47.7	-	-
KE62-3923s_mins_g08_RE_149	8	KE62-3923S	0.27	114	716	99.25	6.3	716	12.05	48.2	-	-
KE62-3923s_mins_g08_RE_150	8	KE62-3923S	0.27	129	721	98.69	5.6	721	11.87	48.6	-	-
KE62-3923s_mins_g08_RE_151	8	KE62-3923S	0.28	132	661	98.75	5.0	661	11.11	50.3	-	-
KE62-3923s_mins_g08_RE_152	8	KE62-3923S	0.28	114	701	98.02	6.2	701	11.48	49.8	-	-
KE62-3923s_mins_g08_RE_153	8	KE62-3923S	0.28	156	719	100.11	4.6	719	11.71	49.4	-	-
FeXANES_fullrange_1s_KE62-3923s_14_matrixG_1merge	8	KE62-3923S	-	-	-	-	-	-	-	-	-	-
FeXANES_fullrange_1s_KE62-3923s_14_matrixG_2merge	8	KE62-3923S	-	-	-	-	-	-	-	-	-	-

Supplementary Table 1C (continued).

Analysis Name	Fissure #	Sample Name	% PEC (olivine mass)	PEC correction coefficient	Temperature of matrix glass quenching or MI entrapment (°C)	H2O in melt (wt%) (FTIR)	CO2 in melt (ppm) (FTIR)	CO2 in melt + bubble (ppm) (FTIR + Raman)	vapor bubble volume (%)
KE62-3293S_glass_2_230	8	KE62-3923S	-	-	1143	-	-	-	-
KE62-3293S_glass_1b_303	8	KE62-3923S	-	-	1142	-	-	-	-
KE62-3293S_glass_1b_304	8	KE62-3923S	-	-	1142	-	-	-	-
KE62-3293S_glass_1b_305	8	KE62-3923S	-	-	1143	-	-	-	-
KE62-3293S_glass_1c_481	8	KE62-3923S	-	-	1143	-	-	-	-
KE62-3293S_glass_1c_482	8	KE62-3923S	-	-	1144	-	-	-	-
KE62-3923s_9_matrixG_279	8	KE62-3923S	-	-	1143	-	-	-	-
KE62-3923s_9_matrixG_280	8	KE62-3923S	-	-	1143	-	-	-	-
KE62-3923s_9_matrixG_281	8	KE62-3923S	-	-	1144	-	-	-	-
EF8_bubble_free_matrixG1_262	8	KE62-3923S	-	-	1143	-	-	-	-
EF8_bubble-free_matrixG2_87	8	KE62-3923S	-	-	1140	-	-	-	-
EF8_bubble-free_matrixG2_88	8	KE62-3923S	-	-	1142	0.11	30	-	-
KE62-3923s_11_matrixG_102	8	KE62-3923S	-	-	1138	0.05	30	-	-
KE62-3923s_12_matrixG_104	8	KE62-3923S	-	-	1140	0.06	30	-	-
KE62-3923s_1a_matrixG_90	8	KE62-3923S	-	-	1139	-	-	-	-
KE62-3923s_1a_matrixG_91	8	KE62-3923S	-	-	1138	-	-	-	-
KE62-3923s_9_matrixG2_107	8	KE62-3923S	-	-	1143	-	-	-	-
KE62-3923s_9_matrixG2_108	8	KE62-3923S	-	-	1140	-	-	-	-
KE62-3923s_glass1_163	8	KE62-3923S	-	-	1140	-	-	-	-
KE62-3923s_glass1_162	8	KE62-3923S	-	-	1141	-	-	-	-
KE62-3923s_glass1_163	8	KE62-3923S	-	-	1140	-	-	-	-
KE62-3923s_glass1_164	8	KE62-3923S	-	-	1140	-	-	-	-
KE62-3923s_mins_g01_matrixG_148	8	KE62-3923S	-	-	1142	-	-	-	-
KE62-3923s_mins_g01_matrixG_154	8	KE62-3923S	-	-	1139	-	-	-	-
KE62-3923s_mount1_G02_matrixG_156	8	KE62-3923S	-	-	1131	-	-	-	-
KE62-3923s_1a_matrixG_92	8	KE62-3923S	-	-	1139	0.20	30	-	-
KE62-3923s_1a_matrixG_93	8	KE62-3923S	-	-	1137	0.25	224	-	-
KE62-3923s_4matrixG_97	8	KE62-3923S	-	-	1135	0.07	30	-	-
KE62-3923s_4matrixG_96	8	KE62-3923S	-	-	1135	0.22	30	-	-
KE62-3923s_mins_g08_RE_149	8	KE62-3923S	-	-	1140	-	-	-	-
KE62-3923s_mins_g08_RE_150	8	KE62-3923S	-	-	1140	-	-	-	-
KE62-3923s_mins_g08_RE_151	8	KE62-3923S	-	-	1141	-	-	-	-
KE62-3923s_mins_g08_RE_152	8	KE62-3923S	-	-	1142	-	-	-	-
KE62-3923s_mins_g08_RE_153	8	KE62-3923S	-	-	1143	-	-	-	-
FeXANES_fullrange_1s_KE62-3923s_14_matrixG_1merge	8	KE62-3923S	-	-	-	-	-	-	-
FeXANES_fullrange_1s_KE62-3923s_14_matrixG_2merge	8	KE62-3923S	-	-	-	-	-	-	-

Supplementary Table 1C (continued).

Analysis Name	Fissure #	Sample Name	Saturation pressure (bar) (Iacono-Marziano 2012)	Saturation depth (km) (Ryan 1987)	Saturation depth 1σ uncertainy (km)	δ34S (‰)	δ34S 1σ uncertainy (‰)	Fe3+/ΣFe % [Fe-XANES]	ΔQFM [Fe-XANES]	S6+/ΣS % [S-XANES]
KE62-3293S_glass_2_230	8	KE62-3923S	-	-	-	-	-	-	-	-
KE62-3293S_glass_1b_303	8	KE62-3923S	-	-	-	-	-	14.6	-0.08	2.5
KE62-3293S_glass_1b_304	8	KE62-3923S	-	-	-	-	-	14.6	-0.08	2.5
KE62-3293S_glass_1b_305	8	KE62-3923S	-	-	-	-	-	14.4	-0.09	2.7
KE62-3293S_glass_1c_481	8	KE62-3923S	-	-	-	-	-	14.6	-0.08	2.5
KE62-3293S_glass_1c_482	8	KE62-3923S	-	-	-	-	-	16.0	+0.16	6.2
KE62-3923s_9_matrixG_279	8	KE62-3923S	-	-	-	-	-	-	-	-
KE62-3923s_9_matrixG_280	8	KE62-3923S	-	-	-	-0.2	0.5	-	-	-
KE62-3923s_9_matrixG_281	8	KE62-3923S	-	-	-	-	-	-	-	-
EF8_bubble_free_matrixG1_262	8	KE62-3923S	-	-	-	-2.8	0.9	13.6	-0.22	-
EF8_bubble-free_matrixG2_87	8	KE62-3923S	-	-	-	-	-	13.5	-0.22	-
EF8_bubble-free_matrixG2_88	8	KE62-3923S	-	-	-	-2.5	0.8	13.5	-0.22	-
KE62-3923s_11_matrixG_102	8	KE62-3923S	-	-	-	-0.6	0.7	-	-	-
KE62-3923s_12_matrixG_104	8	KE62-3923S	-	-	-	0.3	0.5	-	-	-
KE62-3923s_1a_matrixG_90	8	KE62-3923S	-	-	-	-0.5	0.5	-	-	-
KE62-3923s_1a_matrixG_91	8	KE62-3923S	-	-	-	-1.2	0.5	-	-	-
KE62-3923s_9_matrixG2_107	8	KE62-3923S	-	-	-	-0.1	0.5	-	-	-
KE62-3923s_9_matrixG2_108	8	KE62-3923S	-	-	-	-	-	-	-	-
KE62-3923s_glass1_163	8	KE62-3923S	-	-	-	-	-	15.6	+0.16	-
KE62-3923s_glass1_162	8	KE62-3923S	-	-	-	-	-	15.2	+0.07	-
KE62-3923s_glass1_163	8	KE62-3923S	-	-	-	-	-	15.7	+0.17	-
KE62-3923s_glass1_164	8	KE62-3923S	-	-	-	-	-	14.8	+0.02	-
KE62-3923s_mins_g01_matrixG_148	8	KE62-3923S	-	-	-	-	-	15.1	+0.04	-
KE62-3923s_mins_g01_matrixG_154	8	KE62-3923S	-	-	-	-	-	15.1	+0.04	-
KE62-3923s_mount1_G02_matrixG_156	8	KE62-3923S	-	-	-	-	-	12.8	-0.32	4.4
KE62-3923s_1a_matrixG_92	8	KE62-3923S	-	-	-	-0.2	0.5	14.5	-0.02	3.6
KE62-3923s_1a_matrixG_93	8	KE62-3923S	521	2.2	0.6	-	-	15.7	+0.21	5.0
KE62-3923s_4matrixG_97	8	KE62-3923S	-	-	-	-1.2	0.6	14.8	+0.01	9.2
KE62-3923s_4matrixG_96	8	KE62-3923S	-	-	-	-1.2	0.6	14.0	-0.12	2.1
KE62-3923s_mins_g08_RE_149	8	KE62-3923S	-	-	-	-	-	17.1	+0.42	5.8
KE62-3923s_mins_g08_RE_150	8	KE62-3923S	-	-	-	-	-	16.4	+0.31	4.9
KE62-3923s_mins_g08_RE_151	8	KE62-3923S	-	-	-	-	-	15.3	+0.05	5.6
KE62-3923s_mins_g08_RE_152	8	KE62-3923S	-	-	-	-	-	15.9	+0.20	6.5
KE62-3923s_mins_g08_RE_153	8	KE62-3923S	-	-	-	-	-	16.2	+0.24	12.3
FeXANES_fullrange_1s_KE62-3923s_14_matrixG_1merge	8	KE62-3923S	-	-	-	-	-	16.3	+0.26	-
FeXANES_fullrange_1s_KE62-3923s_14_matrixG_2merge	8	KE62-3923S	-	-	-	-	-	16.6	+0.32	-

Supplementary Table 1C (continued).

Analysis Name	Fissure #	Sample Name	Eruption Date	Distance traveled before quench (km)	Glass Type	Host mineral	Sulfide present?
KE62-3293S_1_G04_66	8	KE62-3923S	5/30/18	0.02	re-entrant	Olivine_RE	-
KE62-3293S_1_G04_67	8	KE62-3923S	5/30/18	0.02	re-entrant	Olivine_RE	-
KE62-3293S_1_G04_69	8	KE62-3923S	5/30/18	0.02	re-entrant	Olivine_RE	-
KE62-3293S_1_G04_70	8	KE62-3923S	5/30/18	0.02	re-entrant	Olivine_RE	-
KE62-3923S_mins_g11_RE_2_486	8	KE62-3923S	5/30/18	0.02	re-entrant	Olivine_RE	-
KE62-3923S_mins_g11_RE_2_487	8	KE62-3923S	5/30/18	0.02	re-entrant	Olivine_RE	-
KE62-3923S_mins_g11_RE_2_488	8	KE62-3923S	5/30/18	0.02	re-entrant	Olivine_RE	-
KE62-3923S_mins_g11_RE_2_489	8	KE62-3923S	5/30/18	0.02	re-entrant	Olivine_RE	-
KE62-3923S_mins_g11_RE_2_490	8	KE62-3923S	5/30/18	0.02	re-entrant	Olivine_RE	-
KE62-3923S_mins_g11_RE_2_491	8	KE62-3923S	5/30/18	0.02	re-entrant	Olivine_RE	-
KE62-3923S_mins_g11_RE_2_492	8	KE62-3923S	5/30/18	0.02	re-entrant	Olivine_RE	-
KE62-3923S_mins_g11_RE_2_493	8	KE62-3923S	5/30/18	0.02	re-entrant	Olivine_RE	-
KE62-3923S_mins_g11_RE_2_494	8	KE62-3923S	5/30/18	0.02	re-entrant	Olivine_RE	-
KE62-3923S_mins_g11_RE_2_495	8	KE62-3923S	5/30/18	0.02	re-entrant	Olivine_RE	-
KE62-3923S_mins_g11_RE_2_496	8	KE62-3923S	5/30/18	0.02	re-entrant	Olivine_RE	-
KE62-3293S_1_G01_53, 54 avg	8	KE62-3923S	5/30/18	0.02	MI	Olivine_MI	-
KE62-3293S_1_G01_55, 56 avg	8	KE62-3923S	5/30/18	0.02	MI	Olivine_MI	-
KE62-3293S_1_G02_57, 58 avg	8	KE62-3923S	5/30/18	0.02	MI	Olivine_MI	-
KE62-3293S_1_G02_59	8	KE62-3923S	5/30/18	0.02	MI	Olivine_MI	-
KE62-3293S_1_G03_61	8	KE62-3923S	5/30/18	0.02	MI	Olivine_MI	-
KE62-3293S_1_G03_62, 63 avg	8	KE62-3923S	5/30/18	0.02	MI	Olivine_MI	Yes
KE62-3293S_1_G04_68	8	KE62-3923S	5/30/18	0.02	MI	Olivine_MI	-
KE62-3293S_1_G05_71	8	KE62-3923S	5/30/18	0.02	MI	Olivine_MI	-
KE62-3293S_1_G05_72	8	KE62-3923S	5/30/18	0.02	MI	Olivine_MI	-
KE62-3293S_1_G06_73	8	KE62-3923S	5/30/18	0.02	MI	Olivine_MI	-
KE62-3293S_1_G06_74	8	KE62-3923S	5/30/18	0.02	MI	Olivine_MI	-
KE62-3293S_1_G06_75	8	KE62-3923S	5/30/18	0.02	MI	Olivine_MI	-
KE62-3293S_1_G08_80	8	KE62-3923S	5/30/18	0.02	MI	Plag_MI	-
KE62-3293S_1_G08_81	8	KE62-3923S	5/30/18	0.02	MI	Plag_MI	-
KE62-3293S_1_G09_83	8	KE62-3923S	5/30/18	0.02	MI	Olivine_MI	-
KE62-3293S_1_G09_85	8	KE62-3923S	5/30/18	0.02	MI	Olivine_MI	-
KE62-3293S_1_G11_87	8	KE62-3923S	5/30/18	0.02	MI	Olivine_MI	Inferred, but unquantifiable
KE62-3293S_1_G11_89	8	KE62-3923S	5/30/18	0.02	MI	Olivine_MI	Inferred, but unquantifiable
KE62-3293S_1_G11_90	8	KE62-3923S	5/30/18	0.02	MI	Olivine_MI	Inferred, but unquantifiable
KE62-3293S_1_G11_91	8	KE62-3923S	5/30/18	0.02	MI	Olivine_MI	Inferred, but unquantifiable

Supplementary Table 1C (continued).

Analysis Name	Fissure #	Sample Name	Na2O wt%	SiO2 wt%	CaO wt%	K2O wt%	Al2O3 wt%	FeOT wt%	MgO wt%	TiO2 wt%	MnO wt%
KE62-3293S_1_G04_66	8	KE62-3923S	2.47	52.19	10.31	0.51	13.76	11.49	6.20	2.62	0.17
KE62-3293S_1_G04_67	8	KE62-3923S	2.55	51.10	10.35	0.50	13.78	12.01	6.39	2.81	0.19
KE62-3293S_1_G04_69	8	KE62-3923S	2.25	51.94	10.78	0.50	13.43	11.58	6.27	2.73	0.17
KE62-3293S_1_G04_70	8	KE62-3923S	2.48	51.18	10.59	0.46	13.86	11.63	6.53	2.75	0.18
KE62-3923S_mins_g11_RE_2_486	8	KE62-3923S	2.59	50.96	10.46	0.54	13.65	12.27	6.20	2.74	0.18
KE62-3923S_mins_g11_RE_2_487	8	KE62-3923S	2.71	50.77	10.45	0.49	13.67	12.32	6.23	2.78	0.18
KE62-3923S_mins_g11_RE_2_488	8	KE62-3923S	2.62	50.92	10.50	0.53	13.66	12.05	6.28	2.82	0.18
KE62-3923S_mins_g11_RE_2_489	8	KE62-3923S	2.60	51.01	10.34	0.51	13.46	12.44	6.22	2.85	0.18
KE62-3923S_mins_g11_RE_2_490	8	KE62-3923S	2.79	50.58	10.30	0.57	13.89	12.31	6.22	2.78	0.18
KE62-3923S_mins_g11_RE_2_491	8	KE62-3923S	2.44	51.35	10.40	0.55	13.96	11.81	6.18	2.75	0.19
KE62-3923S_mins_g11_RE_2_492	8	KE62-3923S	2.51	50.77	10.47	0.55	13.83	12.27	6.20	2.82	0.18
KE62-3923S_mins_g11_RE_2_493	8	KE62-3923S	2.44	51.44	10.62	0.58	13.66	11.54	6.30	2.82	0.19
KE62-3923S_mins_g11_RE_2_494	8	KE62-3923S	2.56	50.92	10.34	0.55	13.65	12.47	6.18	2.74	0.18
KE62-3923S_mins_g11_RE_2_495	8	KE62-3923S	2.61	51.60	10.46	0.55	13.23	12.02	6.17	2.77	0.17
KE62-3923S_mins_g11_RE_2_496	8	KE62-3923S	2.68	51.04	10.48	0.58	13.60	11.98	6.25	2.77	0.18
KE62-3293S_1_G01_53, 54 avg	8	KE62-3923S	1.84	49.89	10.05	0.38	11.80	11.54	12.13	1.91	0.12
KE62-3293S_1_G01_55, 56 avg	8	KE62-3923S	2.01	50.11	9.94	0.29	11.72	11.54	12.11	1.80	0.12
KE62-3293S_1_G02_57, 58 avg	8	KE62-3923S	2.05	50.91	10.55	0.43	13.86	11.56	7.94	2.17	0.16
KE62-3293S_1_G02_59	8	KE62-3923S	2.30	51.40	10.65	0.41	13.82	11.54	7.00	2.34	0.16
KE62-3293S_1_G03_61	8	KE62-3923S	2.01	48.55	9.98	0.39	12.45	11.55	12.60	2.04	0.11
KE62-3293S_1_G03_62, 63 avg	8	KE62-3923S	1.89	49.50	9.55	0.40	12.21	11.54	12.51	1.95	0.12
KE62-3293S_1_G04_68	8	KE62-3923S	2.47	52.19	9.54	0.62	12.89	12.54	5.80	3.16	0.18
KE62-3293S_1_G05_71	8	KE62-3923S	2.49	51.91	10.28	0.54	13.40	12.29	5.46	2.97	0.21
KE62-3293S_1_G05_72	8	KE62-3923S	2.43	51.80	9.81	0.56	13.41	12.33	6.00	2.94	0.20
KE62-3293S_1_G06_73	8	KE62-3923S	2.30	49.91	10.07	0.47	12.66	11.54	10.38	2.14	0.17
KE62-3293S_1_G06_74	8	KE62-3923S	2.46	49.45	10.45	0.44	13.09	11.55	9.77	2.27	0.15
KE62-3293S_1_G06_75	8	KE62-3923S	2.31	49.96	10.24	0.46	12.97	11.54	9.80	2.25	0.12
KE62-3293S_1_G08_80	8	KE62-3923S	3.10	51.48	10.02	0.67	14.12	11.20	5.79	3.05	0.18
KE62-3293S_1_G08_81	8	KE62-3923S	2.83	52.08	9.54	0.74	13.94	11.46	5.79	3.09	0.16
KE62-3293S_1_G09_83	8	KE62-3923S	2.42	51.67	10.59	0.48	13.83	11.60	6.51	2.37	0.16
KE62-3293S_1_G09_85	8	KE62-3923S	2.42	51.16	10.93	0.40	14.11	11.54	6.48	2.44	0.19
KE62-3293S_1_G11_87	8	KE62-3923S	2.02	49.20	9.79	0.42	11.86	11.54	12.71	1.97	0.12
KE62-3293S_1_G11_89	8	KE62-3923S	1.82	49.57	8.64	0.36	11.00	11.54	14.78	1.87	0.12
KE62-3293S_1_G11_90	8	KE62-3923S	1.97	49.02	10.20	0.49	11.94	11.55	11.98	2.41	0.12
KE62-3293S_1_G11_91	8	KE62-3923S	2.12	48.43	10.31	0.33	11.73	11.54	11.95	3.07	0.10

Supplementary Table 1C (continued).

Analysis Name	Fissure #	Sample Name	P2O5 wt%	Cl ppm	S ppm	un-normalized total	S/Cl (mass ratio)	non-sulfide corrected S ppm	non-PEC corrected FeOT	melt Mg#	Host Mg#	Host An#
KE62-3293S_1_G04_66	8	KE62-3923S	0.23	143	786	99.06	5.5	786	11.48	49.0	-	-
KE62-3293S_1_G04_67	8	KE62-3923S	0.29	163	725	98.91	4.4	725	12.00	48.7	-	-
KE62-3293S_1_G04_69	8	KE62-3923S	0.32	145	888	98.11	6.1	888	11.57	49.1	-	-
KE62-3293S_1_G04_70	8	KE62-3923S	0.32	155	852	99.63	5.5	852	11.62	50.0	-	-
KE62-3923S_mins_g11_RE_2_486	8	KE62-3923S	0.32	160	767	98.73	4.8	767	12.27	47.4	-	-
KE62-3923S_mins_g11_RE_2_487	8	KE62-3923S	0.31	119	800	98.05	6.7	800	12.32	47.4	-	-
KE62-3923S_mins_g11_RE_2_488	8	KE62-3923S	0.33	170	816	97.77	4.8	816	12.05	48.1	-	-
KE62-3923S_mins_g11_RE_2_489	8	KE62-3923S	0.32	121	701	99.19	5.8	701	12.44	47.1	-	-
KE62-3923S_mins_g11_RE_2_490	8	KE62-3923S	0.31	164	447	99.16	2.7	447	12.31	47.4	-	-
KE62-3923S_mins_g11_RE_2_491	8	KE62-3923S	0.33	125	378	98.29	3.0	378	11.81	48.3	-	-
KE62-3923S_mins_g11_RE_2_492	8	KE62-3923S	0.34	145	367	97.47	2.5	367	12.27	47.4	-	-
KE62-3923S_mins_g11_RE_2_493	8	KE62-3923S	0.35	143	420	96.89	2.9	420	11.54	49.3	-	-
KE62-3923S_mins_g11_RE_2_494	8	KE62-3923S	0.32	105	763	99.35	7.3	763	12.47	46.9	-	-
KE62-3923S_mins_g11_RE_2_495	8	KE62-3923S	0.33	149	797	98.34	5.3	797	12.02	47.8	-	-
KE62-3923S_mins_g11_RE_2_496	8	KE62-3923S	0.32	167	921	98.17	5.5	921	11.98	48.2	-	-
KE62-3293S_1_G01_53, 54 avg	8	KE62-3923S	0.24	105	697	98.13	6.6	697	6.54	65.2	87.8	-
KE62-3293S_1_G01_55, 56 avg	8	KE62-3923S	0.26	100	642	98.44	6.4	642	6.46	65.2	87.8	-
KE62-3293S_1_G02_57, 58 avg	8	KE62-3923S	0.26	115	980	99.09	8.5	980	9.56	55.1	82.5	-
KE62-3293S_1_G02_59	8	KE62-3923S	0.23	119	1249	99.91	10.5	1249	10.60	52.0	80.7	-
KE62-3293S_1_G03_61	8	KE62-3923S	0.24	142	449	97.70	3.1	449	6.68	66.1	88.2	-
KE62-3293S_1_G03_62, 63 avg	8	KE62-3923S	0.21	139	1204	99.45	8.7	601	6.91	65.9	88.1	-
KE62-3293S_1_G04_68	8	KE62-3923S	0.45	231	1253	99.91	5.4	1253	12.54	45.2	78.0	-
KE62-3293S_1_G05_71	8	KE62-3923S	0.31	171	1017	98.00	5.9	1017	12.29	44.2	75.9	-
KE62-3293S_1_G05_72	8	KE62-3923S	0.37	135	1004	99.00	7.4	1004	12.33	46.5	76.2	-
KE62-3293S_1_G06_73	8	KE62-3923S	0.25	136	807	100.30	5.9	807	8.15	61.6	86.1	-
KE62-3293S_1_G06_74	8	KE62-3923S	0.25	101	746	99.73	7.4	746	8.59	60.1	85.4	-
KE62-3293S_1_G06_75	8	KE62-3923S	0.25	133	714	100.67	5.4	714	8.16	60.2	85.4	-
KE62-3293S_1_G08_80	8	KE62-3923S	0.36	219	1318	96.76	6.0	1318	11.19	48.0	-	75.8
KE62-3293S_1_G08_81	8	KE62-3923S	0.34	204	1154	98.13	5.7	1154	11.45	47.4	-	75.8
KE62-3293S_1_G09_83	8	KE62-3923S	0.27	117	733	98.16	6.3	733	11.09	50.0	79.5	-
KE62-3293S_1_G09_85	8	KE62-3923S	0.22	106	807	96.80	7.6	807	11.25	50.0	79.5	-
KE62-3293S_1_G11_87	8	KE62-3923S	0.24	159	739	97.86	4.7	739	7.27	66.2	88.3	-
KE62-3293S_1_G11_89	8	KE62-3923S	0.21	118	583	100.31	5.0	583	5.63	69.5	89.7	-
KE62-3293S_1_G11_90	8	KE62-3923S	0.22	120	745	98.26	6.2	745	7.11	64.9	87.7	-
KE62-3293S_1_G11_91	8	KE62-3923S	0.31	143	784	98.14	5.5	784	7.18	64.9	87.7	-

Supplementary Table 1C (continued).

Analysis Name	Fissure #	Sample Name	% PEC (olivine mass)	PEC correction coefficient	Temperature of matrix glass quenching or MI entrapment (°C)	H2O in melt (wt%) (FTIR)	CO2 in melt (ppm) (FTIR)	CO2 in melt + bubble (ppm) (FTIR + Raman)	vapor bubble volume (%)
KE62-3293S_1_G04_66	8	KE62-3923S	-	-	1139	-	-	-	-
KE62-3293S_1_G04_67	8	KE62-3923S	-	-	1142	-	-	-	-
KE62-3293S_1_G04_69	8	KE62-3923S	-	-	1140	-	-	-	-
KE62-3293S_1_G04_70	8	KE62-3923S	-	-	1145	-	-	-	-
KE62-3923S_mins_g11_RE_2_486	8	KE62-3923S	-	-	1139	-	-	-	-
KE62-3923S_mins_g11_RE_2_487	8	KE62-3923S	-	-	1139	-	-	-	-
KE62-3923S_mins_g11_RE_2_488	8	KE62-3923S	-	-	1140	-	-	-	-
KE62-3923S_mins_g11_RE_2_489	8	KE62-3923S	-	-	1139	-	-	-	-
KE62-3923S_mins_g11_RE_2_490	8	KE62-3923S	-	-	1139	-	-	-	-
KE62-3923S_mins_g11_RE_2_491	8	KE62-3923S	-	-	1138	-	-	-	-
KE62-3923S_mins_g11_RE_2_492	8	KE62-3923S	-	-	1139	-	-	-	-
KE62-3923S_mins_g11_RE_2_493	8	KE62-3923S	-	-	1141	-	-	-	-
KE62-3923S_mins_g11_RE_2_494	8	KE62-3923S	-	-	1138	-	-	-	-
KE62-3923S_mins_g11_RE_2_495	8	KE62-3923S	-	-	1138	-	-	-	-
KE62-3923S_mins_g11_RE_2_496	8	KE62-3923S	-	-	1140	-	-	-	-
KE62-3293S_1_G01_53, 54 avg	8	KE62-3923S	24.5	0.79	1298	-	-	-	-
KE62-3293S_1_G01_55, 56 avg	8	KE62-3923S	24.7	0.78	1299	-	-	-	-
KE62-3293S_1_G02_57, 58 avg	8	KE62-3923S	7.2	0.93	1198	-	-	-	-
KE62-3293S_1_G02_59	8	KE62-3923S	4.1	0.96	1173	-	-	-	-
KE62-3293S_1_G03_61	8	KE62-3923S	27.3	0.77	1310	-	-	-	-
KE62-3293S_1_G03_62, 63 avg	8	KE62-3923S	22.3	0.80	1308	-	-	-	-
KE62-3293S_1_G04_68	8	KE62-3923S	-1.2	1.02	1148	-	-	-	-
KE62-3293S_1_G05_71	8	KE62-3923S	-1.7	1.02	1121	-	-	-	-
KE62-3293S_1_G05_72	8	KE62-3923S	-2.9	1.03	1126	-	-	-	-
KE62-3293S_1_G06_73	8	KE62-3923S	15.9	0.85	1264	-	-	-	-
KE62-3293S_1_G06_74	8	KE62-3923S	13.5	0.87	1249	-	-	-	-
KE62-3293S_1_G06_75	8	KE62-3923S	14.0	0.87	1249	-	-	-	-
KE62-3293S_1_G08_80	8	KE62-3923S	-	-	-	-	-	-	-
KE62-3293S_1_G08_81	8	KE62-3923S	-	-	-	-	-	-	-
KE62-3293S_1_G09_83	8	KE62-3923S	1.6	0.98	1161	-	-	-	-
KE62-3293S_1_G09_85	8	KE62-3923S	1.0	0.99	1157	-	-	-	-
KE62-3293S_1_G11_87	8	KE62-3923S	25.4	0.78	1313	-	-	-	-
KE62-3293S_1_G11_89	8	KE62-3923S	36.5	0.71	1354	-	-	-	-
KE62-3293S_1_G11_90	8	KE62-3923S	23.1	0.80	1295	-	-	-	-
KE62-3293S_1_G11_91	8	KE62-3923S	22.1	0.80	1293	-	-	-	-

Supplementary Table 1C (continued).

Analysis Name	Fissure #	Sample Name	Saturation pressure (bar) (Iacono-Marziano 2012)	Saturation depth (km) (Ryan 1987)	Saturation depth 1σ uncertainy (km)	δ34S (‰)	δ34S 1σ uncertainy (‰)	Fe3+/ΣFe % [Fe-XANES]	ΔQFM [Fe-XANES]	S6+/ΣS % [S-XANES]
KE62-3293S_1_G04_66	8	KE62-3923S	-	-	-	-	-	-	-	-
KE62-3293S_1_G04_67	8	KE62-3923S	-	-	-	-	-	-	-	-
KE62-3293S_1_G04_69	8	KE62-3923S	-	-	-	-	-	-	-	-
KE62-3293S_1_G04_70	8	KE62-3923S	-	-	-	-	-	-	-	-
KE62-3923S_mins_g11_RE_2_486	8	KE62-3923S	-	-	-	-	-	16.0	+0.22	4.8
KE62-3923S_mins_g11_RE_2_487	8	KE62-3923S	-	-	-	-	-	15.6	+0.13	5.0
KE62-3923S_mins_g11_RE_2_488	8	KE62-3923S	-	-	-	-	-	15.6	+0.13	5.0
KE62-3923S_mins_g11_RE_2_489	8	KE62-3923S	-	-	-	-	-	13.8	-0.16	3.5
KE62-3923S_mins_g11_RE_2_490	8	KE62-3923S	-	-	-	-	-	13.8	-0.16	3.5
KE62-3923S_mins_g11_RE_2_491	8	KE62-3923S	-	-	-	-	-	14.8	+0.03	2.7
KE62-3923S_mins_g11_RE_2_492	8	KE62-3923S	-	-	-	-	-	14.9	+0.05	-
KE62-3923S_mins_g11_RE_2_493	8	KE62-3923S	-	-	-	-	-	14.8	+0.03	2.7
KE62-3923S_mins_g11_RE_2_494	8	KE62-3923S	-	-	-	-	-	15.6	+0.13	5.0
KE62-3923S_mins_g11_RE_2_495	8	KE62-3923S	-	-	-	-	-	16.0	+0.22	4.8
KE62-3923S_mins_g11_RE_2_496	8	KE62-3923S	-	-	-	-	-	16.0	+0.22	4.8
KE62-3293S_1_G01_53, 54 avg	8	KE62-3923S	-	-	-	-	-	-	-	-
KE62-3293S_1_G01_55, 56 avg	8	KE62-3923S	-	-	-	-	-	-	-	32.6
KE62-3293S_1_G02_57, 58 avg	8	KE62-3923S	-	-	-	-	-	-	-	17.0
KE62-3293S_1_G02_59	8	KE62-3923S	-	-	-	-	-	-	-	-
KE62-3293S_1_G03_61	8	KE62-3923S	-	-	-	-	-	-	-	-
KE62-3293S_1_G03_62, 63 avg	8	KE62-3923S	-	-	-	-	-	-	-	-
KE62-3293S_1_G04_68	8	KE62-3923S	-	-	-	-	-	-	-	-
KE62-3293S_1_G05_71	8	KE62-3923S	-	-	-	-	-	-	-	-
KE62-3293S_1_G05_72	8	KE62-3923S	-	-	-	-	-	-	-	-
KE62-3293S_1_G06_73	8	KE62-3923S	-	-	-	-	-	-	-	-
KE62-3293S_1_G06_74	8	KE62-3923S	-	-	-	-	-	-	-	-
KE62-3293S_1_G06_75	8	KE62-3923S	-	-	-	-	-	-	-	-
KE62-3293S_1_G08_80	8	KE62-3923S	-	-	-	-	-	-	-	17.4
KE62-3293S_1_G08_81	8	KE62-3923S	-	-	-	-	-	-	-	-
KE62-3293S_1_G09_83	8	KE62-3923S	-	-	-	-	-	-	-	-
KE62-3293S_1_G09_85	8	KE62-3923S	-	-	-	-	-	-	-	-
KE62-3293S_1_G11_87	8	KE62-3923S	-	-	-	-	-	-	-	-
KE62-3293S_1_G11_89	8	KE62-3923S	-	-	-	-	-	-	-	-
KE62-3293S_1_G11_90	8	KE62-3923S	-	-	-	-	-	-	-	-
KE62-3293S_1_G11_91	8	KE62-3923S	-	-	-	-	-	-	-	-

Supplementary Table 1C (continued).

Analysis Name	Fissure #	Sample Name	Eruption Date	Distance traveled before quench (km)	Glass Type	Host mineral	Sulfide present?
KE62-3293S_2_G04_92	8	KE62-3923S	5/30/18	0.02	MI	Olivine_MI	Yes
KE62-3293S_2_G04_93	8	KE62-3923S	5/30/18	0.02	MI	Olivine_MI	Inferred, but unquantifiable
KE62-3293S_2_G04_94	8	KE62-3923S	5/30/18	0.02	MI	Olivine_MI	Inferred, but unquantifiable
KE62-3293S_2_G04_95	8	KE62-3923S	5/30/18	0.02	MI	Olivine_MI	Inferred, but unquantifiable
KE62-3293S_2_G04_96	8	KE62-3923S	5/30/18	0.02	MI	Spinel_MI	-
KE62-3293S_2_G05_97	8	KE62-3923S	5/30/18	0.02	MI	Olivine_MI	-
KE62-3293S_2_G05_98	8	KE62-3923S	5/30/18	0.02	MI	Olivine_MI	-
KE62-3293S_2_G10_99	8	KE62-3923S	5/30/18	0.02	MI	Cpx_MI	-
KE62-3293S_2_G11_101	8	KE62-3923S	5/30/18	0.02	MI	Olivine_MI	-
KE62-3293S_2_G13_102	8	KE62-3923S	5/30/18	0.02	MI	Olivine_MI	-
KE62-3293S_2_G18_103	8	KE62-3923S	5/30/18	0.02	MI	Olivine_MI	-
KE62-3293S_2_G18_104	8	KE62-3923S	5/30/18	0.02	MI	Olivine_MI	-
KE62-3293S_2_G23_107	8	KE62-3923S	5/30/18	0.02	MI	Olivine_MI	-
KE62-3293S_2_G23_108	8	KE62-3923S	5/30/18	0.02	MI	Olivine_MI	-
KE62-3293S_2_G02_109	8	KE62-3923S	5/30/18	0.02	MI	Olivine_MI	Inferred, but unquantifiable
KE62-3923s_8_MI_256, 257 avg	8	KE62-3923S	5/30/18	0.02	MI	Olivine_MI	-
KE62-3923s_1a_MI_263	8	KE62-3923S	5/30/18	0.02	MI	Olivine_MI	Yes
KE62-3923s_1b_MI_264	8	KE62-3923S	5/30/18	0.02	MI	Olivine_MI	-
KE62-3923s_4a_MI_266, 267 avg	8	KE62-3923S	5/30/18	0.02	MI	Olivine_MI	Yes
KE62-3923s_4b_MI_268	8	KE62-3923S	5/30/18	0.02	MI	Olivine_MI	Yes
KE62-3923s_10_MI run2_287	8	KE62-3923S	5/30/18	0.02	MI	Olivine_MI	-
KE62-3923s_11_MIs_271	8	KE62-3923S	5/30/18	0.02	MI	Opx_MI	-
KE62-3923s_11_MIs_272	8	KE62-3923S	5/30/18	0.02	MI	Opx_MI	-
KE62-3923s_12_MIs_273	8	KE62-3923S	5/30/18	0.02	MI	Olivine_MI	-
KE62-3923s_12_MIs_274	8	KE62-3923S	5/30/18	0.02	MI	Olivine_MI	-
KE62-3923s_14_MI_275, 276 avg	8	KE62-3923S	5/30/18	0.02	MI	Olivine_MI	-
KE62-3923s_9a_MI_277	8	KE62-3923S	5/30/18	0.02	MI	Plag_MI	-
KE62-3923s_9b_MI_278	8	KE62-3923S	5/30/18	0.02	MI	Plag_MI	-
EF8_3	8	KE62-3923S	5/30/18	0.02	MI	Olivine_MI	-
EF8_5	8	KE62-3923S	5/30/18	0.02	MI	Olivine_MI	-
EF8_6	8	KE62-3923S	5/30/18	0.02	MI	Olivine_MI	-
FeXANES_fullrange_1s_KE62_3923s_11_MI_1merge	8	KE62-3923S	5/30/18	0.02	MI	Opx_MI	-
FeXANES_fullrange_1s_KE62_3923s_11_MI_1merge	8	KE62-3923S	5/30/18	0.02	MI	Cpx_MI	-

Supplementary Table 1C (continued).

Analysis Name	Fissure #	Sample Name	Na2O wt%	SiO2 wt%	CaO wt%	K2O wt%	Al2O3 wt%	FeOT wt%	MgO wt%	TiO2 wt%	MnO wt%
KE62-3293S_2_G04_92	8	KE62-3923S	2.26	48.69	9.97	0.48	11.96	11.54	12.41	2.21	0.13
KE62-3293S_2_G04_93	8	KE62-3923S	1.95	49.93	9.51	0.27	12.06	11.55	12.53	1.83	0.13
KE62-3293S_2_G04_94	8	KE62-3923S	1.87	49.80	9.43	0.31	11.36	11.54	13.27	2.01	0.12
KE62-3293S_2_G04_95	8	KE62-3923S	2.05	49.82	9.09	0.24	11.47	11.54	13.27	2.02	0.11
KE62-3293S_2_G04_96	8	KE62-3923S	1.93	54.49	10.48	0.51	14.14	10.50	5.89	1.60	0.16
KE62-3293S_2_G05_97	8	KE62-3923S	2.17	49.23	10.07	0.48	12.20	11.55	11.53	2.32	0.11
KE62-3293S_2_G05_98	8	KE62-3923S	2.20	49.48	9.45	0.34	12.45	11.54	12.03	2.10	0.11
KE62-3293S_2_G10_99	8	KE62-3923S	2.34	51.64	10.42	0.42	14.60	10.86	6.60	2.65	0.18
KE62-3293S_2_G11_101	8	KE62-3923S	2.53	51.55	10.75	0.44	13.80	11.55	6.16	2.60	0.22
KE62-3293S_2_G13_102	8	KE62-3923S	2.41	52.22	9.74	0.59	13.17	12.68	5.81	2.78	0.18
KE62-3293S_2_G18_103	8	KE62-3923S	2.18	51.51	11.47	0.42	13.79	11.55	6.28	2.26	0.13
KE62-3293S_2_G18_104	8	KE62-3923S	2.76	51.98	10.21	0.46	13.44	11.65	6.33	2.59	0.17
KE62-3293S_2_G23_107	8	KE62-3923S	1.92	49.18	9.91	0.44	12.08	11.54	12.13	2.34	0.11
KE62-3293S_2_G23_108	8	KE62-3923S	2.03	49.09	10.03	0.46	12.06	11.54	12.10	2.32	0.10
KE62-3293S_2_G02_109	8	KE62-3923S	2.10	48.86	9.95	0.37	11.59	11.54	12.93	2.20	0.11
KE62-3923s_8_MI_256, 257 avg	8	KE62-3923S	1.85	49.03	9.54	0.33	11.75	11.55	13.69	1.93	0.11
KE62-3923s_1a_MI_263	8	KE62-3923S	2.35	50.50	10.53	0.40	14.22	11.55	7.97	1.99	0.17
KE62-3923s_1b_MI_264	8	KE62-3923S	2.47	51.24	10.05	0.33	14.12	11.57	7.94	1.82	0.15
KE62-3923s_4a_MI_266, 267 avg	8	KE62-3923S	2.05	48.60	9.63	0.37	12.22	11.55	13.39	1.82	0.13
KE62-3923s_4b_MI_268	8	KE62-3923S	2.02	48.10	9.14	0.31	12.36	11.54	14.31	1.87	0.11
KE62-3923s_10_MI run2_287	8	KE62-3923S	2.16	49.92	10.45	0.40	14.37	11.54	8.46	2.14	0.16
KE62-3923s_11_MIs_271	8	KE62-3923S	2.31	51.52	10.02	0.54	14.01	11.83	6.33	2.88	0.19
KE62-3923s_11_MIs_272	8	KE62-3923S	2.57	51.54	10.04	0.47	13.87	11.59	6.59	2.75	0.19
KE62-3923s_12_MIs_273	8	KE62-3923S	2.39	49.90	10.37	0.43	14.22	11.59	8.47	2.13	0.18
KE62-3923s_12_MIs_274	8	KE62-3923S	2.56	49.96	10.23	0.47	14.19	11.59	8.45	2.05	0.16
KE62-3923s_14_MI_275, 276 avg	8	KE62-3923S	2.50	50.10	10.01	0.68	14.47	11.55	6.93	3.07	0.18
KE62-3923s_9a_MI_277	8	KE62-3923S	4.37	59.62	6.26	1.67	16.87	7.13	1.11	1.03	0.13
KE62-3923s_9b_MI_278	8	KE62-3923S	5.10	61.77	4.92	1.76	16.79	6.77	1.20	1.09	0.15
EF8_3	8	KE62-3923S	-	-	-	-	-	-	-	-	-
EF8_5	8	KE62-3923S	-	-	-	-	-	-	-	-	-
EF8_6	8	KE62-3923S	-	-	-	-	-	-	-	-	-
FeXANES_fullrange_1s_KE62_3923s_11_MI_1merge	8	KE62-3923S	-	-	-	-	-	-	-	-	-
FeXANES_fullrange_1s_KE62_3923s_11_MI_1merge	8	KE62-3923S	-	-	-	-	-	-	-	-	-

Supplementary Table 1C (continued).

Analysis Name	Fissure #	Sample Name	P2O5 wt%	Cl ppm	S ppm	un-normalized total	S/Cl (mass ratio)	non-sulfide corrected S ppm	non-PEC corrected FeOT	melt Mg#	Host Mg#	Host An#
KE62-3293S_2_G04_92	8	KE62-3923S	0.23	170	592	97.92	3.5	483	6.41	65.7	88.1	-
KE62-3293S_2_G04_93	8	KE62-3923S	0.20	87	382	99.78	4.4	382	5.73	65.9	-	-
KE62-3293S_2_G04_94	8	KE62-3923S	0.22	84	366	100.76	4.4	366	5.86	67.2	88.7	-
KE62-3293S_2_G04_95	8	KE62-3923S	0.31	54	342	100.87	6.4	342	5.68	67.2	88.7	-
KE62-3293S_2_G04_96	8	KE62-3923S	0.23	144	1036	98.37	7.2	1036	10.49	50.0	-	-
KE62-3293S_2_G05_97	8	KE62-3923S	0.26	175	572	98.00	3.3	572	7.10	64.0	87.3	-
KE62-3293S_2_G05_98	8	KE62-3923S	0.23	54	386	98.11	7.1	386	6.43	65.0	87.7	-
KE62-3293S_2_G10_99	8	KE62-3923S	0.25	151	449	99.41	3.0	449	10.86	52.0	81.4	-
KE62-3293S_2_G11_101	8	KE62-3923S	0.29	147	679	99.08	4.6	679	11.15	48.8	78.7	-
KE62-3293S_2_G13_102	8	KE62-3923S	0.29	151	957	99.90	6.3	957	12.68	44.9	76.4	-
KE62-3293S_2_G18_103	8	KE62-3923S	0.31	105	464	98.47	4.4	464	11.55	49.2	79.0	-
KE62-3293S_2_G18_104	8	KE62-3923S	0.29	155	786	99.13	5.1	786	11.16	49.2	79.0	-
KE62-3293S_2_G23_107	8	KE62-3923S	0.24	136	707	99.41	5.2	707	6.96	65.2	87.8	-
KE62-3293S_2_G23_108	8	KE62-3923S	0.17	151	615	99.37	4.1	615	6.91	65.1	87.8	-
KE62-3293S_2_G02_109	8	KE62-3923S	0.25	108	591	99.96	5.5	591	6.56	66.6	88.5	-
KE62-3923s_8_MI_256, 257 avg	8	KE62-3923S	0.18	106	331	99.31	3.1	331	5.95	67.9	89.0	-
KE62-3923s_1a_MI_263	8	KE62-3923S	0.22	114	1388	99.42	12.2	958	9.73	55.2	82.6	-
KE62-3923s_1b_MI_264	8	KE62-3923S	0.23	136	624	99.75	4.6	624	9.65	55.0	82.5	-
KE62-3923s_4a_MI_266, 267 avg	8	KE62-3923S	0.18	76	732	99.01	9.7	604	6.47	67.4	88.8	-
KE62-3923s_4b_MI_268	8	KE62-3923S	0.18	76	925	99.84	12.2	433	5.63	68.8	89.4	-
KE62-3923s_10_MI run2_287	8	KE62-3923S	0.29	130	1060	98.13	8.1	1060	9.70	56.7	83.4	-
KE62-3923s_11_MIs_271	8	KE62-3923S	0.29	122	801	97.80	6.6	801	11.83	48.8	80.2	-
KE62-3923s_11_MIs_272	8	KE62-3923S	0.29	125	792	98.27	6.3	792	11.59	50.3	80.8	-
KE62-3923s_12_MIs_273	8	KE62-3923S	0.21	141	1061	99.34	7.5	1061	9.41	56.6	83.4	-
KE62-3923s_12_MIs_274	8	KE62-3923S	0.22	140	1075	100.54	7.7	1075	10.16	56.5	83.4	-
KE62-3923s_14_MI_275, 276 avg	8	KE62-3923S	0.38	149	1169	98.01	7.9	1169	10.76	51.7	80.5	-
KE62-3923s_9a_MI_277	8	KE62-3923S	1.72	441	349	98.49	0.8	349	7.13	21.7	-	54.3
KE62-3923s_9b_MI_278	8	KE62-3923S	0.37	625	230	98.20	0.4	230	6.77	23.9	-	54.3
EF8_3	8	KE62-3923S	-	-	-	-	-	-	-	-	-	-
EF8_5	8	KE62-3923S	-	-	-	-	-	-	-	-	-	-
EF8_6	8	KE62-3923S	-	-	-	-	-	-	-	-	-	-
FeXANES_fullrange_1s_KE62_3923s_11_MI_1merge	8	KE62-3923S	-	-	-	-	-	-	-	-	-	-
FeXANES_fullrange_1s_KE62_3923s_11_MI_1merge	8	KE62-3923S	-	-	-	-	-	-	-	-	-	-

Supplementary Table 1C (continued).

Analysis Name	Fissure #	Sample Name	% PEC (olivine mass)	PEC correction coefficient	Temperature of matrix glass quenching or MI entrapment (°C)	H2O in melt (wt%) (FTIR)	CO2 in melt (ppm) (FTIR)	CO2 in melt + bubble (ppm) (FTIR + Raman)	vapor bubble volume (%)
KE62-3293S_2_G04_92	8	KE62-3923S	25.7	0.78	1309	-	-	-	-
KE62-3293S_2_G04_93	8	KE62-3923S	28.8	0.76	1307	-	-	-	-
KE62-3293S_2_G04_94	8	KE62-3923S	30.7	0.75	1322	-	-	-	-
KE62-3293S_2_G04_95	8	KE62-3923S	31.1	0.74	1325	-	-	-	-
KE62-3293S_2_G04_96	8	KE62-3923S	-	-	-	-	-	-	-
KE62-3293S_2_G05_97	8	KE62-3923S	21.8	0.81	1288	-	-	-	-
KE62-3293S_2_G05_98	8	KE62-3923S	24.9	0.78	1300	-	-	-	-
KE62-3293S_2_G10_99	8	KE62-3923S	-	-	-	-	-	-	-
KE62-3293S_2_G11_101	8	KE62-3923S	2.8	0.97	1149	-	-	-	-
KE62-3293S_2_G13_102	8	KE62-3923S	-2.8	1.03	1128	-	-	-	-
KE62-3293S_2_G18_103	8	KE62-3923S	1.8	0.98	1147	-	-	-	-
KE62-3293S_2_G18_104	8	KE62-3923S	1.7	0.98	1160	-	-	-	-
KE62-3293S_2_G23_107	8	KE62-3923S	24.1	0.79	1298	-	-	-	-
KE62-3293S_2_G23_108	8	KE62-3923S	25.7	0.78	1298	-	-	-	-
KE62-3293S_2_G02_109	8	KE62-3923S	27.1	0.77	1317	-	-	-	-
KE62-3923s_8_MI_256, 257 avg	8	KE62-3923S	30.7	0.75	1331	0.20	-	415	5%
KE62-3923s_1a_MI_263	8	KE62-3923S	8.2	0.92	1201	0.30	28	352	4%
KE62-3923s_1b_MI_264	8	KE62-3923S	7.1	0.93	1204	0.23	28	113	2%
KE62-3923s_4a_MI_266, 267 avg	8	KE62-3923S	28.7	0.76	1327	0.25	23	287	4%
KE62-3923s_4b_MI_268	8	KE62-3923S	33.3	0.73	1346	0.27	23	1167	6%
KE62-3923s_10_MI run2_287	8	KE62-3923S	8.0	0.92	1213	0.28	28	no bubble	0%
KE62-3923s_11_MIs_271	8	KE62-3923S	-	-	-	-	-	-	-
KE62-3923s_11_MIs_272	8	KE62-3923S	-	-	-	0.30	30	no bubble	0%
KE62-3923s_12_MIs_273	8	KE62-3923S	8.7	0.91	1216	-	-	-	-
KE62-3923s_12_MIs_274	8	KE62-3923S	7.7	0.92	1218	0.27	275	no bubble	0%
KE62-3923s_14_MI_275, 276 avg	8	KE62-3923S	2.8	0.97	1176	0.29	252	no bubble	0%
KE62-3923s_9a_MI_277	8	KE62-3923S	-	-	-	0.55	-	47	2%
KE62-3923s_9b_MI_278	8	KE62-3923S	-	-	-	0.31	-	-	3%
EF8_3	8	KE62-3923S	-	-	-	-	-	121	
EF8_5	8	KE62-3923S	-	-	-	-	-	113	
EF8_6	8	KE62-3923S	-	-	-	-	-	236	
FeXANES_fullrange_1s_KE62_3923s_11_MI_1merge	8	KE62-3923S	-	-	-	0.30	30	no bubble	0%
FeXANES_fullrange_1s_KE62_3923s_11_MI_1merge	8	KE62-3923S	-	-	-	-	-	-	-

Supplementary Table 1C (continued).

Analysis Name	Fissure #	Sample Name	Saturation pressure (bar) (Iacono-Marziano 2012)	Saturation depth (km) (Ryan 1987)	Saturation depth 1σ uncertainy (km)	δ34S (‰)	δ34S 1σ uncertainy (‰)	Fe3+/ΣFe % [Fe-XANES]	ΔQFM [Fe-XANES]	S6+/ΣS % [S-XANES]
KE62-3293S_2_G04_92	8	KE62-3923S	-	-	-	-	-	-	-	-
KE62-3293S_2_G04_93	8	KE62-3923S	-	-	-	-	-	-	-	-
KE62-3293S_2_G04_94	8	KE62-3923S	-	-	-	-	-	-	-	-
KE62-3293S_2_G04_95	8	KE62-3923S	-	-	-	-	-	-	-	-
KE62-3293S_2_G04_96	8	KE62-3923S	-	-	-	-	-	-	-	-
KE62-3293S_2_G05_97	8	KE62-3923S	-	-	-	-	-	-	-	-
KE62-3293S_2_G05_98	8	KE62-3923S	-	-	-	-	-	-	-	-
KE62-3293S_2_G10_99	8	KE62-3923S	-	-	-	-	-	-	-	-
KE62-3293S_2_G11_101	8	KE62-3923S	-	-	-	-	-	-	-	-
KE62-3293S_2_G13_102	8	KE62-3923S	-	-	-	-	-	-	-	-
KE62-3293S_2_G18_103	8	KE62-3923S	-	-	-	-	-	-	-	-
KE62-3293S_2_G18_104	8	KE62-3923S	-	-	-	-	-	-	-	-
KE62-3293S_2_G23_107	8	KE62-3923S	-	-	-	-	-	-	-	-
KE62-3293S_2_G23_108	8	KE62-3923S	-	-	-	-	-	-	-	-
KE62-3293S_2_G02_109	8	KE62-3923S	-	-	-	-	-	-	-	-
KE62-3923s_8_MI_256, 257 avg	8	KE62-3923S	813	3.5	1.4	-1.2	0.7	-	-	-
KE62-3923s_1a_MI_263	8	KE62-3923S	794	3.5	0.5	1.5	0.4	17.0	+0.22	16.4
KE62-3923s_1b_MI_264	8	KE62-3923S	275	1.2	0.8	-0.7	0.5	17.2	+0.28	12.6
KE62-3923s_4a_MI_266, 267 avg	8	KE62-3923S	526	2.3	0.9	0.1	0.5	14.5	-0.40	10.3
KE62-3923s_4b_MI_268	8	KE62-3923S	1801	7.3	1.3	-1.3	0.5	14.9	-0.32	25.1
KE62-3923s_10_MI run2_287	8	KE62-3923S	77	0.3	0.1	-	-	17.5	+0.33	-
KE62-3923s_11_MIs_271	8	KE62-3923S	-	-	-	-	-	-	-	-
KE62-3923s_11_MIs_272	8	KE62-3923S	90	0.4	0.1	0.5	0.6	16.7	+0.30	-
KE62-3923s_12_MIs_273	8	KE62-3923S	-	-	-	-	-	-	-	-
KE62-3923s_12_MIs_274	8	KE62-3923S	578	2.4	0.7	0.7	0.5	18.2	+0.41	-
KE62-3923s_14_MI_275, 276 avg	8	KE62-3923S	584	2.5	0.7	1.0	0.5	15.7	+0.08	-
KE62-3923s_9a_MI_277	8	KE62-3923S	112	0.5	1.6	1.1	0.7	-	-	-
KE62-3923s_9b_MI_278	8	KE62-3923S	-	-	-	3.5	12.7	-	-	-
EF8_3	8	KE62-3923S	288	1.3	0.4	-	-	-	-	-
EF8_5	8	KE62-3923S	270	1.2	2.0	-	-	-	-	-
EF8_6	8	KE62-3923S	540	2.4	1.0	-	-	-	-	-
FeXANES_fullrange_1s_KE62_3923s_11_MI_1merge	8	KE62-3923S	90	0.4	0.1	-	-	17.5	+0.42	-
FeXANES_fullrange_1s_KE62_3923s_11_MI_1merge	8	KE62-3923S	-	-	-	-	-	17.5	+0.42	-

Supplementary Table 1C (continued).

Analysis Name	Fissure #	Sample Name	Eruption Date	Distance traveled before quench (km)	Glass Type	Host mineral	Sulfide present?
FeXANES_fullrange_1s_KE62-3923s_13a_MI_1merge	8	KE62-3923S	5/30/18	0.02	MI	Olivine_MI	-
FeXANES_fullrange_1s_KE62-3923s_14_MI_2merge	8	KE62-3923S	5/30/18	0.02	MI	Olivine_MI	-
Fissure 8 lava flow, July 14 2018							
FeXANES_fullrange_1s_KE62-3314F_MatrixG_1_001merge	8	KE62-3314F	7/14/18	0.5	matrix glass	-	-
FeXANES_fullrange_1s_KE62-3314F_MatrixG_1_002merge	8	KE62-3314F	7/14/18	0.5	matrix glass	-	-
FeXANES_fullrange_1s_KE62-3314F_MatrixG_2_001	8	KE62-3314F	7/14/18	0.5	matrix glass	-	-
FeXANES_fullrange_1s_KE62-3314F_MatrixG_2_002	8	KE62-3314F	7/14/18	0.5	matrix glass	-	-
FeXANES_fullrange_1s_KE62-3314F_MatrixG_2_003	8	KE62-3314F	7/14/18	0.5	matrix glass	-	-
FeXANES_fullrange_1s_KE62-3314F_MatrixG_3_001	8	KE62-3314F	7/14/18	0.5	matrix glass	-	-
KE62-3314f_2a_MI	8	KE62-3314F	7/14/18	0.5	MI	Olivine_MI	-
KE62-3314f_2b_MI	8	KE62-3314F	7/14/18	0.5	MI	Olivine_MI	-
Fissure 8 littoral blast, July 16 2018							
LB_glass_g01_glass_01_232	8	KE62-3315F	7/16/18	12.5	matrix glass	-	-
LB_glass_g01_glass_01_233	8	KE62-3315F	7/16/18	12.5	matrix glass	-	-
LB_glass_g01_glass_01_234	8	KE62-3315F	7/16/18	12.5	matrix glass	-	-
LB_glass_g01_glass_02_483	8	KE62-3315F	7/16/18	12.5	matrix glass	-	-
LB_glass_g02_glass_01_243	8	KE62-3315F	7/16/18	12.5	matrix glass	-	-
LB_glass_g02_glass_01_244	8	KE62-3315F	7/16/18	12.5	matrix glass	-	-
LB_glass_g02_glass_01_246	8	KE62-3315F	7/16/18	12.5	matrix glass	-	-
LB_glass_g02_glass_02_484	8	KE62-3315F	7/16/18	12.5	matrix glass	-	-
LB_glass_g02_glass_02_485	8	KE62-3315F	7/16/18	12.5	matrix glass	-	-
LB_glass_g01_glass_01_232	8	KE62-3315F	7/16/18	12.5	matrix glass	-	-
LB_glass_g01_glass_01_233	8	KE62-3315F	7/16/18	12.5	matrix glass	-	-
LB_glass_g01_glass_01_234	8	KE62-3315F	7/16/18	12.5	matrix glass	-	-
LB_glass_g01_glass_02_483	8	KE62-3315F	7/16/18	12.5	matrix glass	-	-
LB_glass_g02_glass_01_243	8	KE62-3315F	7/16/18	12.5	matrix glass	-	-
LB_glass_g02_glass_01_244	8	KE62-3315F	7/16/18	12.5	matrix glass	-	-
LB_glass_g02_glass_01_246	8	KE62-3315F	7/16/18	12.5	matrix glass	-	-
LB_glass_g02_glass_02_484	8	KE62-3315F	7/16/18	12.5	matrix glass	-	-

Supplementary Table 1C (continued).

Analysis Name	Fissure #	Sample Name	Na2O wt%	SiO2 wt%	CaO wt%	K2O wt%	Al2O3 wt%	FeOT wt%	MgO wt%	TiO2 wt%	MnO wt%
FeXANES_fullrange_1s_KE62-3923s_13a_MI_1merge	8	KE62-3923S	-	-	-	-	-	-	-	-	-
FeXANES_fullrange_1s_KE62-3923s_14_MI_2merge	8	KE62-3923S	-	-	-	-	-	-	-	-	-
Fissure 8 lava flow, July 14 2018											
FeXANES_fullrange_1s_KE62-3314F_MatrixG_1_001merge	8	KE62-3314F	-	-	-	-	-	-	-	-	-
FeXANES_fullrange_1s_KE62-3314F_MatrixG_1_002merge	8	KE62-3314F	-	-	-	-	-	-	-	-	-
FeXANES_fullrange_1s_KE62-3314F_MatrixG_2_001	8	KE62-3314F	-	-	-	-	-	-	-	-	-
FeXANES_fullrange_1s_KE62-3314F_MatrixG_2_002	8	KE62-3314F	-	-	-	-	-	-	-	-	-
FeXANES_fullrange_1s_KE62-3314F_MatrixG_2_003	8	KE62-3314F	-	-	-	-	-	-	-	-	-
FeXANES_fullrange_1s_KE62-3314F_MatrixG_3_001	8	KE62-3314F	-	-	-	-	-	-	-	-	-
KE62-3314f_2a_MI	8	KE62-3314F	-	-	-	-	-	-	-	-	-
KE62-3314f_2b_MI	8	KE62-3314F	-	-	-	-	-	-	-	-	-
Fissure 8 littoral blast, July 16 2018											
LB_glass_g01_glass_01_232	8	KE62-3315F	2.99	52.15	8.97	0.83	12.21	13.52	4.83	3.73	0.20
LB_glass_g01_glass_01_233	8	KE62-3315F	2.85	52.00	8.88	0.88	13.18	12.99	4.75	3.73	0.20
LB_glass_g01_glass_01_234	8	KE62-3315F	2.64	52.89	9.03	0.89	12.09	13.10	4.80	3.76	0.22
LB_glass_g01_glass_02_483	8	KE62-3315F	2.91	52.13	8.80	0.88	12.51	13.29	4.90	3.80	0.20
LB_glass_g02_glass_01_243	8	KE62-3315F	2.82	51.88	9.10	0.84	12.62	12.98	4.94	4.02	0.21
LB_glass_g02_glass_01_244	8	KE62-3315F	2.89	51.55	9.06	0.83	12.61	13.31	4.93	4.02	0.20
LB_glass_g02_glass_01_246	8	KE62-3315F	2.80	52.07	9.27	0.89	12.51	12.70	5.01	3.95	0.21
LB_glass_g02_glass_02_484	8	KE62-3315F	2.86	52.84	9.04	0.79	12.13	12.86	4.97	3.75	0.20
LB_glass_g02_glass_02_485	8	KE62-3315F	2.83	53.23	8.84	0.83	12.28	12.60	4.87	3.76	0.19
LB_glass_g01_glass_01_232	8	KE62-3315F	2.99	52.15	8.97	0.83	12.21	13.52	4.83	3.73	0.20
LB_glass_g01_glass_01_233	8	KE62-3315F	2.85	52.00	8.88	0.88	13.18	12.99	4.75	3.73	0.20
LB_glass_g01_glass_01_234	8	KE62-3315F	2.64	52.89	9.03	0.89	12.09	13.10	4.80	3.76	0.22
LB_glass_g01_glass_02_483	8	KE62-3315F	2.91	52.13	8.80	0.88	12.51	13.29	4.90	3.80	0.20
LB_glass_g02_glass_01_243	8	KE62-3315F	2.82	51.88	9.10	0.84	12.62	12.98	4.94	4.02	0.21
LB_glass_g02_glass_01_244	8	KE62-3315F	2.89	51.55	9.06	0.83	12.61	13.31	4.93	4.02	0.20
LB_glass_g02_glass_01_246	8	KE62-3315F	2.80	52.07	9.27	0.89	12.51	12.70	5.01	3.95	0.21
LB_glass_g02_glass_02_484	8	KE62-3315F	2.86	52.84	9.04	0.79	12.13	12.86	4.97	3.75	0.20

Supplementary Table 1C (continued).

Analysis Name	Fissure #	Sample Name	P2O5 wt%	Cl ppm	S ppm	un-normalized total	S/Cl (mass ratio)	non-sulfide corrected S ppm	non-PEC corrected FeOT	melt Mg#	Host Mg#	Host An#
FeXANES_fullrange_1s_KE62-3923s_13a_MI_1merge	8	KE62-3923S	-	-	-	-	-	-	-	-	-	-
FeXANES_fullrange_1s_KE62-3923s_14_MI_2merge	8	KE62-3923S	-	-	-	-	-	-	-	-	-	-
Fissure 8 lava flow, July 14 2018												
FeXANES_fullrange_1s_KE62-3314F_MatrixG_1_001merge	8	KE62-3314F	-	-	-	-	-	-	-	-	-	-
FeXANES_fullrange_1s_KE62-3314F_MatrixG_1_002merge	8	KE62-3314F	-	-	-	-	-	-	-	-	-	-
FeXANES_fullrange_1s_KE62-3314F_MatrixG_2_001	8	KE62-3314F	-	-	-	-	-	-	-	-	-	-
FeXANES_fullrange_1s_KE62-3314F_MatrixG_2_002	8	KE62-3314F	-	-	-	-	-	-	-	-	-	-
FeXANES_fullrange_1s_KE62-3314F_MatrixG_2_003	8	KE62-3314F	-	-	-	-	-	-	-	-	-	-
FeXANES_fullrange_1s_KE62-3314F_MatrixG_3_001	8	KE62-3314F	-	-	-	-	-	-	-	-	-	-
KE62-3314f_2a_MI	8	KE62-3314F	-	-	-	-	-	-	-	-	-	-
KE62-3314f_2b_MI	8	KE62-3314F	-	-	-	-	-	-	-	-	-	-
Fissure 8 littoral blast, July 16 2018												
LB_glass_g01_glass_01_232	8	KE62-3315F	0.53	201	67	97.25	0.3	67	13.52	38.9	-	-
LB_glass_g01_glass_01_233	8	KE62-3315F	0.53	218	27	98.21	0.1	27	12.99	39.5	-	-
LB_glass_g01_glass_01_234	8	KE62-3315F	0.55	231	18	96.20	0.1	18	13.10	39.5	-	-
LB_glass_g01_glass_02_483	8	KE62-3315F	0.57	209	22	98.50	0.1	22	13.29	39.7	-	-
LB_glass_g02_glass_01_243	8	KE62-3315F	0.58	195	43	96.69	0.2	43	12.98	40.4	-	-
LB_glass_g02_glass_01_244	8	KE62-3315F	0.57	221	29	97.52	0.1	29	13.31	39.8	-	-
LB_glass_g02_glass_01_246	8	KE62-3315F	0.56	167	36	95.74	0.2	36	12.70	41.3	-	-
LB_glass_g02_glass_02_484	8	KE62-3315F	0.54	203	16	96.12	0.1	16	12.86	40.8	-	-
LB_glass_g02_glass_02_485	8	KE62-3315F	0.55	170	35	97.57	0.2	35	12.60	40.8	-	-
LB_glass_g01_glass_01_232	8	KE62-3315F	0.53	201	67	97.25	0.3	67	13.52	38.9	-	-
LB_glass_g01_glass_01_233	8	KE62-3315F	0.53	218	27	98.21	0.1	27	12.99	39.5	-	-
LB_glass_g01_glass_01_234	8	KE62-3315F	0.55	231	18	96.20	0.1	18	13.10	39.5	-	-
LB_glass_g01_glass_02_483	8	KE62-3315F	0.57	209	22	98.50	0.1	22	13.29	39.7	-	-
LB_glass_g02_glass_01_243	8	KE62-3315F	0.58	195	43	96.69	0.2	43	12.98	40.4	-	-
LB_glass_g02_glass_01_244	8	KE62-3315F	0.57	221	29	97.52	0.1	29	13.31	39.8	-	-
LB_glass_g02_glass_01_246	8	KE62-3315F	0.56	167	36	95.74	0.2	36	12.70	41.3	-	-
LB_glass_g02_glass_02_484	8	KE62-3315F	0.54	203	16	96.12	0.1	16	12.86	40.8	-	-

Supplementary Table 1C (continued).

Analysis Name	Fissure #	Sample Name	% PEC (olivine mass)	PEC correction coefficient	Temperature of matrix glass quenching or MI entrapment (°C)	H2O in melt (wt%) (FTIR)	CO2 in melt (ppm) (FTIR)	CO2 in melt + bubble (ppm) (FTIR + Raman)	vapor bubble volume (%)
FeXANES_fullrange_1s_KE62-3923s_13a_MI_1merge	8	KE62-3923S	-	-	-	-	-	-	-
FeXANES_fullrange_1s_KE62-3923s_14_MI_2merge	8	KE62-3923S	-	-	-	-	-	-	-
Fissure 8 lava flow, July 14 2018									
FeXANES_fullrange_1s_KE62-3314F_MatrixG_1_001merge	8	KE62-3314F	-	-	-	-	-	-	-
FeXANES_fullrange_1s_KE62-3314F_MatrixG_1_002merge	8	KE62-3314F	-	-	-	-	-	-	-
FeXANES_fullrange_1s_KE62-3314F_MatrixG_2_001	8	KE62-3314F	-	-	-	-	-	-	-
FeXANES_fullrange_1s_KE62-3314F_MatrixG_2_002	8	KE62-3314F	-	-	-	-	-	-	-
FeXANES_fullrange_1s_KE62-3314F_MatrixG_2_003	8	KE62-3314F	-	-	-	-	-	-	-
FeXANES_fullrange_1s_KE62-3314F_MatrixG_3_001	8	KE62-3314F	-	-	-	-	-	-	-
KE62-3314f_2a_MI	8	KE62-3314F	-	-	-	-	-	-	-
KE62-3314f_2b_MI	8	KE62-3314F	-	-	-	-	-	-	-
Fissure 8 littoral blast, July 16 2018									
LB_glass_g01_glass_01_232	8	KE62-3315F	-	-	1111	-	-	-	-
LB_glass_g01_glass_01_233	8	KE62-3315F	-	-	1109	-	-	-	-
LB_glass_g01_glass_01_234	8	KE62-3315F	-	-	1110	-	-	-	-
LB_glass_g01_glass_02_483	8	KE62-3315F	-	-	1112	-	-	-	-
LB_glass_g02_glass_01_243	8	KE62-3315F	-	-	1113	-	-	-	-
LB_glass_g02_glass_01_244	8	KE62-3315F	-	-	1113	-	-	-	-
LB_glass_g02_glass_01_246	8	KE62-3315F	-	-	1115	-	-	-	-
LB_glass_g02_glass_02_484	8	KE62-3315F	-	-	1114	-	-	-	-
LB_glass_g02_glass_02_485	8	KE62-3315F	-	-	1112	-	-	-	-
LB_glass_g01_glass_01_232	8	KE62-3315F	-	-	1111	-	-	-	-
LB_glass_g01_glass_01_233	8	KE62-3315F	-	-	1109	-	-	-	-
LB_glass_g01_glass_01_234	8	KE62-3315F	-	-	1110	-	-	-	-
LB_glass_g01_glass_02_483	8	KE62-3315F	-	-	1112	-	-	-	-
LB_glass_g02_glass_01_243	8	KE62-3315F	-	-	1113	-	-	-	-
LB_glass_g02_glass_01_244	8	KE62-3315F	-	-	1113	-	-	-	-
LB_glass_g02_glass_01_246	8	KE62-3315F	-	-	1115	-	-	-	-
LB_glass_g02_glass_02_484	8	KE62-3315F	-	-	1114	-	-	-	-

Supplementary Table 1C (continued).

Analysis Name	Fissure #	Sample Name	Saturation pressure (bar) (Iacono-Marziano 2012)	Saturation depth (km) (Ryan 1987)	Saturation depth 1σ uncertainy (km)	δ34S (‰)	δ34S 1σ uncertainy (‰)	Fe3+/ΣFe % [Fe-XANES]	ΔQFM [Fe-XANES]	S6+/ΣS % [S-XANES]
FeXANES_fullrange_1s_KE62-3923s_13a_MI_1merge	8	KE62-3923S	-	-	-	-	-	18.2	+0.41	-
FeXANES_fullrange_1s_KE62-3923s_14_MI_2merge	8	KE62-3923S	-	-	-	-	-	15.5	-0.03	-
Fissure 8 lava flow, July 14 2018										
FeXANES_fullrange_1s_KE62-3314F_MatrixG_1_001merge	8	KE62-3314F	-	-	-	-	-	13.0	-0.35	-
FeXANES_fullrange_1s_KE62-3314F_MatrixG_1_002merge	8	KE62-3314F	-	-	-	-	-	12.9	-0.37	-
FeXANES_fullrange_1s_KE62-3314F_MatrixG_2_001	8	KE62-3314F	-	-	-	-	-	13.0	-0.36	-
FeXANES_fullrange_1s_KE62-3314F_MatrixG_2_002	8	KE62-3314F	-	-	-	-	-	13.6	-0.23	-
FeXANES_fullrange_1s_KE62-3314F_MatrixG_2_003	8	KE62-3314F	-	-	-	-	-	15.1	+0.04	-
FeXANES_fullrange_1s_KE62-3314F_MatrixG_3_001	8	KE62-3314F	-	-	-	-	-	12.4	-0.47	-
KE62-3314f_2a_MI	8	KE62-3314F	-	-	-	-	-	15.7	-0.10	-
KE62-3314f_2b_MI	8	KE62-3314F	-	-	-	-	-	14.1	-0.36	-
Fissure 8 littoral blast, July 16 2018										
LB_glass_g01_glass_01_232	8	KE62-3315F	-	-	-	-	-	27.1	+1.73	-
LB_glass_g01_glass_01_233	8	KE62-3315F	-	-	-	-	-	27.1	+1.73	-
LB_glass_g01_glass_01_234	8	KE62-3315F	-	-	-	-	-	26.6	+1.69	-
LB_glass_g01_glass_02_483	8	KE62-3315F	-	-	-	-	-	26.6	+1.69	-
LB_glass_g02_glass_01_243	8	KE62-3315F	-	-	-	-	-	33.7	+2.42	-
LB_glass_g02_glass_01_244	8	KE62-3315F	-	-	-	-	-	32.4	+2.30	-
LB_glass_g02_glass_01_246	8	KE62-3315F	-	-	-	-	-	33.7	+2.42	-
LB_glass_g02_glass_02_484	8	KE62-3315F	-	-	-	-	-	33.7	+2.42	-
LB_glass_g02_glass_02_485	8	KE62-3315F	-	-	-	-	-	32.4	+2.30	-
LB_glass_g01_glass_01_232	8	KE62-3315F	-	-	-	-	-	27.1	+1.73	-
LB_glass_g01_glass_01_233	8	KE62-3315F	-	-	-	-	-	27.1	+1.73	-
LB_glass_g01_glass_01_234	8	KE62-3315F	-	-	-	-	-	26.6	+1.69	-
LB_glass_g01_glass_02_483	8	KE62-3315F	-	-	-	-	-	26.6	+1.69	-
LB_glass_g02_glass_01_243	8	KE62-3315F	-	-	-	-	-	33.7	+2.42	-
LB_glass_g02_glass_01_244	8	KE62-3315F	-	-	-	-	-	32.4	+2.30	-
LB_glass_g02_glass_01_246	8	KE62-3315F	-	-	-	-	-	33.7	+2.42	-
LB_glass_g02_glass_02_484	8	KE62-3315F	-	-	-	-	-	33.7	+2.42	-

Supplementary Table 1C (continued).

Analysis Name	Fissure #	Sample Name	Eruption Date	Distance traveled before quench (km)	Glass Type	Host mineral	Sulfide present?
LB_glass_g02_glass_02_485	8	KE62-3315F	7/16/18	12.5	matrix glass	-	-
LB_6_matrixG_pyrite-26 S peak_297	8	KE62-3315F	7/16/18	12.5	matrix glass	-	-
LB_6_matrixG_pyrite-26 S peak_298	8	KE62-3315F	7/16/18	12.5	matrix glass	-	-
LB_glass_g02_ol_MI_01_247, 248 avg	8	KE62-3315F	7/16/18	12.5	MI	Olivine_MI	-
LB_mins_g12_MI-01_465, 466 avg	8	KE62-3315F	7/16/18	12.5	MI	Olivine_MI	-
LB_mins_g17_MI-01_471	8	KE62-3315F	7/16/18	12.5	MI	Olivine_MI	-
LB_1_MIs_pyrite -26 S peak_292, 293, 294, 142 avg	8	KE62-3315F	7/16/18	12.5	MI	Olivine_MI	-
LB_1b_pyrite -26 S peak_109	8	KE62-3315F	7/16/18	12.5	MI	Olivine_MI	-
LB_2_MI_pyrite-26 S peak_299, 300 avg	8	KE62-3315F	7/16/18	12.5	MI	Olivine_MI	-
LB_3_MI_pyrite-26 S peak_301, 302 avg	8	KE62-3315F	7/16/18	12.5	MI	Olivine_MI	-
LB_6.2_MI_pyrite-26 S peak_303, 304 avg	8	KE62-3315F	7/16/18	12.5	MI	Olivine_MI	-
LB_6.3_MI_pyrite-26 S peak_305	8	KE62-3315F	7/16/18	12.5	MI	Olivine_MI	-
FeXANES_fullrange_1s_LB_4_MI_1merge	8	KE62-3315F	7/16/18	12.5	MI	Olivine_MI	-
FeXANES_fullrange_1s_LB_5_MI_1merge	8	KE62-3315F	7/16/18	12.5	MI	Olivine_MI	-
FeXANES_fullrange_1s_LB_6_MI_1merge	8	KE62-3315F	7/16/18	12.5	MI	Olivine_MI	-
Fissure 8 lava flow, July 20 2018							
KE62-3316F_6b_matrixG_244	8	KE62-3316F	7/20/18	6.95	matrix glass	-	-
KE62-3316F_14_matrixG_259	8	KE62-3316F	7/20/18	6.95	matrix glass	-	-
KE62-3316F_14_matrixG_260	8	KE62-3316F	7/20/18	6.95	matrix glass	-	-
KE62-3316F_14_matrixG_261	8	KE62-3316F	7/20/18	6.95	matrix glass	-	-
KE62-3316F_14_matrixG_262	8	KE62-3316F	7/20/18	6.95	matrix glass	-	-
FeXANES_fast_fullrange_1s_KE62-3316F_15_MatrixG_001_merge	8	KE62-3316F	7/20/18	6.95	matrix glass	-	-
KE62-3316F_4_interstitialG_245	8	KE62-3316F	7/20/18	6.95	interstitial melt	-	-
KE62-3316F_7_interstitialG_248	8	KE62-3316F	7/20/18	6.95	interstitial melt	-	-
S_XANES_faster_50um_KE62-3316F_6b_interstitialG_merge	8	KE62-3316F	7/20/18	6.95	interstitial melt	-	-
KE62-3316F_1_RE_237	8	KE62-3316F	7/20/18	6.95	re-entrant	Olivine_RE	-
KE62-3316F_6b_RE_243	8	KE62-3316F	7/20/18	6.95	re-entrant	Olivine_RE	-

Supplementary Table 1C (continued).

Analysis Name	Fissure #	Sample Name	Na2O wt%	SiO2 wt%	CaO wt%	K2O wt%	Al2O3 wt%	FeOT wt%	MgO wt%	TiO2 wt%	MnO wt%
LB_glass_g02_glass_02_485	8	KE62-3315F	2.83	53.23	8.84	0.83	12.28	12.60	4.87	3.76	0.19
LB_6_matrixG_pyrite-26 S peak_297	8	KE62-3315F	2.53	50.51	9.13	0.82	12.43	14.67	5.11	4.08	0.20
LB_6_matrixG_pyrite-26 S peak_298	8	KE62-3315F	2.50	50.54	9.11	0.76	12.32	14.87	5.07	4.10	0.20
LB_glass_g02_ol_MI_01_247, 248 avg	8	KE62-3315F	2.87	51.13	8.36	0.49	15.11	11.55	8.03	1.92	0.15
LB_mins_g12_MI-01_465, 466 avg	8	KE62-3315F	2.25	49.27	9.64	0.37	11.46	11.54	13.31	1.74	0.10
LB_mins_g17_MI-01_471	8	KE62-3315F	1.94	49.02	9.02	0.34	11.79	11.54	13.99	1.83	0.10
LB_1_MIs_pyrite -26 S peak_292, 293, 294, 142 avg	8	KE62-3315F	2.02	48.85	9.77	0.42	12.86	11.54	12.15	1.93	0.12
LB_1b_pyrite -26 S peak_109	8	KE62-3315F	2.24	48.14	9.71	0.38	12.70	11.54	12.97	1.86	0.12
LB_2_MI_pyrite-26 S peak_299, 300 avg	8	KE62-3315F	2.10	49.58	9.72	0.35	12.39	11.54	11.91	1.98	0.12
LB_3_MI_pyrite-26 S peak_301, 302 avg	8	KE62-3315F	2.10	49.37	9.43	0.41	12.30	11.54	12.49	1.92	0.11
LB_6.2_MI_pyrite-26 S peak_303, 304 avg	8	KE62-3315F	2.25	48.80	9.63	0.39	11.86	11.54	13.07	2.02	0.11
LB_6.3_MI_pyrite-26 S peak_305	8	KE62-3315F	2.18	49.41	9.43	0.35	11.69	11.55	13.10	1.92	0.10
FeXANES_fullrange_1s_LB_4_MI_1merge	8	KE62-3315F	-	-	-	-	-	-	-	-	-
FeXANES_fullrange_1s_LB_5_MI_1merge	8	KE62-3315F	-	-	-	-	-	-	-	-	-
FeXANES_fullrange_1s_LB_6_MI_1merge	8	KE62-3315F	-	-	-	-	-	-	-	-	-
Fissure 8 lava flow, July 20 2018											
KE62-3316F_6b_matrixG_244	8	KE62-3316F	2.47	50.77	10.63	0.54	13.86	12.22	6.46	2.57	0.18
KE62-3316F_14_matrixG_259	8	KE62-3316F	2.59	51.42	10.95	0.60	13.94	11.21	6.20	2.64	0.17
KE62-3316F_14_matrixG_260	8	KE62-3316F	2.66	50.68	10.91	0.53	14.21	11.72	6.27	2.56	0.17
KE62-3316F_14_matrixG_261	8	KE62-3316F	2.44	50.48	11.53	0.44	15.06	10.96	6.12	2.49	0.18
KE62-3316F_14_matrixG_262	8	KE62-3316F	2.35	50.49	11.29	0.49	14.73	11.54	6.19	2.42	0.18
FeXANES_fast_fullrange_1s_KE62-3316F_15_MatrixG_001_merge	8	KE62-3316F	-	-	-	-	-	-	-	-	-
KE62-3316F_4_interstitialG_245	8	KE62-3316F	2.49	51.14	10.60	0.55	14.26	11.63	6.33	2.53	0.17
KE62-3316F_7_interstitialG_248	8	KE62-3316F	2.59	51.21	10.87	0.54	14.22	11.42	6.22	2.49	0.18
S_XANES_faster_50um_KE62-3316F_6b_interstitialG_merge	8	KE62-3316F	-	-	-	-	-	-	-	-	-
KE62-3316F_1_RE_237	8	KE62-3316F	2.53	51.30	10.91	0.49	15.13	10.58	6.17	2.43	0.17
KE62-3316F_6b_RE_243	8	KE62-3316F	2.58	50.77	10.94	0.45	14.54	11.78	6.00	2.48	0.16

Supplementary Table 1C (continued).

Analysis Name	Fissure #	Sample Name	P2O5 wt%	Cl ppm	S ppm	un-normalized total	S/Cl (mass ratio)	non-sulfide corrected S ppm	non-PEC corrected FeOT	melt Mg#	Host Mg#	Host An#
LB_glass_g02_glass_02_485	8	KE62-3315F	0.55	170	35	97.57	0.2	35	12.60	40.8	-	-
LB_6_matrixG_pyrite-26 S peak_297	8	KE62-3315F	0.48	209	77	98.82	0.4	77	14.67	38.3	-	-
LB_6_matrixG_pyrite-26 S peak_298	8	KE62-3315F	0.50	165	45	98.77	0.3	45	14.87	37.8	-	-
LB_glass_g02_ol_MI_01_247, 248 avg	8	KE62-3315F	0.29	134	815	98.77	6.1	815	9.32	55.4	82.6	-
LB_mins_g12_MI-01_465, 466 avg	8	KE62-3315F	0.21	107	986	98.32	9.2	986	5.90	67.3	88.8	-
LB_mins_g17_MI-01_471	8	KE62-3315F	0.34	136	861	99.72	6.3	861	5.83	68.4	89.2	-
LB_1_MIs_pyrite -26 S peak_292, 293, 294, 142 avg	8	KE62-3315F	0.22	145	1095	100.38	7.6	1095	6.52	65.2	87.8	-
LB_1b_pyrite -26 S peak_109	8	KE62-3315F	0.21	97	1205	98.89	12.5	1205	6.71	66.7	88.5	-
LB_2_MI_pyrite-26 S peak_299, 300 avg	8	KE62-3315F	0.21	118	1030	99.41	8.7	1030	7.56	64.8	87.6	-
LB_3_MI_pyrite-26 S peak_301, 302 avg	8	KE62-3315F	0.22	165	972	98.46	5.9	972	5.89	65.9	88.1	-
LB_6.2_MI_pyrite-26 S peak_303, 304 avg	8	KE62-3315F	0.26	91	600	98.92	6.6	600	6.27	66.9	88.6	-
LB_6.3_MI_pyrite-26 S peak_305	8	KE62-3315F	0.21	110	642	98.62	5.8	642	5.94	66.9	88.6	-
FeXANES_fullrange_1s_LB_4_MI_1merge	8	KE62-3315F	-	-	-	-	-	-	-	-	-	-
FeXANES_fullrange_1s_LB_5_MI_1merge	8	KE62-3315F	-	-	-	-	-	-	-	-	-	-
FeXANES_fullrange_1s_LB_6_MI_1merge	8	KE62-3315F	-	-	-	-	-	-	-	-	-	-
Fissure 8 lava flow, July 20 2018												
KE62-3316F_6b_matrixG_244	8	KE62-3316F	0.27	142	131	99.34	0.9	131	12.22	48.5	-	-
KE62-3316F_14_matrixG_259	8	KE62-3316F	0.25	139	157	98.40	1.1	157	11.21	49.7	-	-
KE62-3316F_14_matrixG_260	8	KE62-3316F	0.26	87	206	98.79	2.4	206	11.72	48.8	-	-
KE62-3316F_14_matrixG_261	8	KE62-3316F	0.25	131	531	97.57	4.1	531	10.96	49.9	-	-
KE62-3316F_14_matrixG_262	8	KE62-3316F	0.23	132	595	98.88	4.5	595	11.54	48.9	-	-
FeXANES_fast_fullrange_1s_KE62-3316F_15_MatrixG_001_merge	8	KE62-3316F	-	-	-	-	-	-	-	-	-	-
KE62-3316F_4_interstitialG_245	8	KE62-3316F	0.25	120	221	98.35	1.8	221	11.63	49.3	-	-
KE62-3316F_7_interstitialG_248	8	KE62-3316F	0.24	159	170	98.84	1.1	170	11.42	49.3	-	-
S_XANES_faster_50um_KE62-3316F_6b_interstitialG_merge	8	KE62-3316F	-	-	-	-	-	-	-	-	-	-
KE62-3316F_1_RE_237	8	KE62-3316F	0.26	136	191	98.92	1.4	191	10.58	51.0	-	-
KE62-3316F_6b_RE_243	8	KE62-3316F	0.26	120	418	100.21	3.5	418	11.78	47.6	-	-

Supplementary Table 1C (continued).

Analysis Name	Fissure #	Sample Name	% PEC (olivine mass)	PEC correction coefficient	Temperature of matrix glass quenching or MI entrapment (°C)	H2O in melt (wt%) (FTIR)	CO2 in melt (ppm) (FTIR)	CO2 in melt + bubble (ppm) (FTIR + Raman)	vapor bubble volume (%)
LB_glass_g02_glass_02_485	8	KE62-3315F	-	-	1112	-	-	-	-
LB_6_matrixG_pyrite-26 S peak_297	8	KE62-3315F	-	-	1117	-	-	-	-
LB_6_matrixG_pyrite-26 S peak_298	8	KE62-3315F	-	-	1116	-	-	-	-
LB_glass_g02_ol_MI_01_247, 248 avg	8	KE62-3315F	11.4	0.89	1219	-	-	-	-
LB_mins_g12_MI-01_465, 466 avg	8	KE62-3315F	32.2	0.74	1329	-	-	-	-
LB_mins_g17_MI-01_471	8	KE62-3315F	35.5	0.72	1340	-	-	-	-
LB_1_MIs_pyrite -26 S peak_292, 293, 294, 142 avg	8	KE62-3315F	26.8	0.77	1301	0.12	23	-	4%
LB_1b_pyrite -26 S peak_109	8	KE62-3315F	29.4	0.76	1321	0.08	23	-	2%
LB_2_MI_pyrite-26 S peak_299, 300 avg	8	KE62-3315F	23.9	0.79	1296	0.15	24	-	4%
LB_3_MI_pyrite-26 S peak_301, 302 avg	8	KE62-3315F	29.5	0.75	1310	0.10	23	-	5%
LB_6.2_MI_pyrite-26 S peak_303, 304 avg	8	KE62-3315F	30.4	0.75	1324	0.16	23	-	4%
LB_6.3_MI_pyrite-26 S peak_305	8	KE62-3315F	31.3	0.74	1323	0.12	22	-	4%
FeXANES_fullrange_1s_LB_4_MI_1merge	8	KE62-3315F	-	-	-	-	-	-	-
FeXANES_fullrange_1s_LB_5_MI_1merge	8	KE62-3315F	-	-	-	-	-	-	-
FeXANES_fullrange_1s_LB_6_MI_1merge	8	KE62-3315F	-	-	-	0.17	23	-	4%
Fissure 8 lava flow, July 20 2018									
KE62-3316F_6b_matrixG_244	8	KE62-3316F	-	-	1144	-	-	-	-
KE62-3316F_14_matrixG_259	8	KE62-3316F	-	-	1139	-	-	-	-
KE62-3316F_14_matrixG_260	8	KE62-3316F	-	-	1140	-	-	-	-
KE62-3316F_14_matrixG_261	8	KE62-3316F	-	-	1137	-	-	-	-
KE62-3316F_14_matrixG_262	8	KE62-3316F	-	-	1138	-	-	-	-
FeXANES_fast_fullrange_1s_KE62-3316F_15_MatrixG_001_merge	8	KE62-3316F	-	-	-	-	-	-	-
KE62-3316F_4_interstitialG_245	8	KE62-3316F	-	-	1141	-	-	-	-
KE62-3316F_7_interstitialG_248	8	KE62-3316F	-	-	1139	-	-	-	-
S_XANES_faster_50um_KE62-3316F_6b_interstitialG_merge	8	KE62-3316F	-	-	-	-	-	-	-
KE62-3316F_1_RE_237	8	KE62-3316F	-	-	1138	-	-	-	-
KE62-3316F_6b_RE_243	8	KE62-3316F	-	-	1135	-	-	-	-

Supplementary Table 1C (continued).

Analysis Name	Fissure #	Sample Name	Saturation pressure (bar) (Iacono-Marziano 2012)	Saturation depth (km) (Ryan 1987)	Saturation depth 1σ uncertainy (km)	δ34S (‰)	δ34S 1σ uncertainy (‰)	Fe3+/ΣFe % [Fe-XANES]	ΔQFM [Fe-XANES]	S6+/ΣS % [S-XANES]
LB_glass_g02_glass_02_485	8	KE62-3315F	-	-	-	-	-	32.4	+2.30	-
LB_6_matrixG_pyrite-26 S peak_297	8	KE62-3315F	-	-	-	-	-	20.3	+0.99	-
LB_6_matrixG_pyrite-26 S peak_298	8	KE62-3315F	-	-	-	-	-	21.0	+1.10	-
LB_glass_g02_ol_MI_01_247, 248 avg	8	KE62-3315F	-	-	-	-	-	-	-	-
LB_mins_g12_MI-01_465, 466 avg	8	KE62-3315F	-	-	-	-	-	-	-	-
LB_mins_g17_MI-01_471	8	KE62-3315F	-	-	-	-	-	-	-	-
LB_1_MIs_pyrite -26 S peak_292, 293, 294, 142 avg	8	KE62-3315F	-	-	-	-0.3	0.4	29.4	+1.59	95.1
LB_1b_pyrite -26 S peak_109	8	KE62-3315F	-	-	-	-	-	31.4	+1.77	94.7
LB_2_MI_pyrite-26 S peak_299, 300 avg	8	KE62-3315F	-	-	-	0.9	0.5	32.2	+1.93	96.4
LB_3_MI_pyrite-26 S peak_301, 302 avg	8	KE62-3315F	-	-	-	-0.1	0.5	22.4	+0.75	81.7
LB_6.2_MI_pyrite-26 S peak_303, 304 avg	8	KE62-3315F	-	-	-	-0.5	0.4	20.8	+0.47	89.3
LB_6.3_MI_pyrite-26 S peak_305	8	KE62-3315F	-	-	-	-0.7	0.5	20.6	+0.46	69.1
FeXANES_fullrange_1s_LB_4_MI_1merge	8	KE62-3315F	-	-	-	-	-	22.7	+0.79	68.3
FeXANES_fullrange_1s_LB_5_MI_1merge	8	KE62-3315F	-	-	-	-	-	22.2	+0.73	87.3
FeXANES_fullrange_1s_LB_6_MI_1merge	8	KE62-3315F	-	-	-	-	-	21.8	+0.66	83.7
Fissure 8 lava flow, July 20 2018										
KE62-3316F_6b_matrixG_244	8	KE62-3316F	-	-	-	-	-	-	-	7.6
KE62-3316F_14_matrixG_259	8	KE62-3316F	-	-	-	-	-	12.7	-0.45	5.4
KE62-3316F_14_matrixG_260	8	KE62-3316F	-	-	-	-	-	12.4	-0.50	2.0
KE62-3316F_14_matrixG_261	8	KE62-3316F	-	-	-	-	-	-	-	4.5
KE62-3316F_14_matrixG_262	8	KE62-3316F	-	-	-	-	-	-	-	3.9
FeXANES_fast_fullrange_1s_KE62-3316F_15_MatrixG_001_merge	8	KE62-3316F	-	-	-	-	-	13.9	-0.20	-
KE62-3316F_4_interstitialG_245	8	KE62-3316F	-	-	-	-	-	12.7	-0.39	-
KE62-3316F_7_interstitialG_248	8	KE62-3316F	-	-	-	-	-	12.3	-0.51	-
S_XANES_faster_50um_KE62-3316F_6b_interstitialG_merge	8	KE62-3316F	-	-	-	-	-	-	-	2.2
KE62-3316F_1_RE_237	8	KE62-3316F	-	-	-	-	-	13.7	-0.23	1.0
KE62-3316F_6b_RE_243	8	KE62-3316F	-	-	-	-	-	13.2	-0.30	2.6

Supplementary Table 1C (continued).

Analysis Name	Fissure #	Sample Name	Eruption Date	Distance traveled before quench (km)	Glass Type	Host mineral	Sulfide present?
KE62-3316F_1_MI_235	8	KE62-3316F	7/20/18	6.95	MI	Olivine_MI	-
KE62-3316F_2a_MI_239	8	KE62-3316F	7/20/18	6.95	MI	Olivine_MI	-
KE62-3316F_6_MI_241	8	KE62-3316F	7/20/18	6.95	MI	Olivine_MI	-
KE62-3316F_7_MI_246	8	KE62-3316F	7/20/18	6.95	MI	Olivine_MI	-
KE62-3316F_9_MI_249	8	KE62-3316F	7/20/18	6.95	MI	Olivine_MI	Inferred
KE62-3316F_9b_MI_250	8	KE62-3316F	7/20/18	6.95	MI	Olivine_MI	Yes
KE62-3316F_11_MI_252	8	KE62-3316F	7/20/18	6.95	MI	Olivine_MI	Yes
KE62-3316F_12_MI_254	8	KE62-3316F	7/20/18	6.95	MI	Olivine_MI	-
KE62-3316F_14a_MI_256	8	KE62-3316F	7/20/18	6.95	MI	Olivine_MI	Inferred
KE62-3316F_14b_MI_257	8	KE62-3316F	7/20/18	6.95	MI	Olivine_MI	Inferred
FeXANES_fast_fullrange_1s_KE62-3316F_15_MI_001_merge	8	KE62-3316F	7/20/18	6.95	MI	Plag_MI	-
Fissure 8 lava flow, August 1 2018							
KE62-3321f_3_matrixG_176	8	KE62-3321F	8/1/18	1.2	matrix glass	-	-
KE62-3321f_3_matrixG_177	8	KE62-3321F	8/1/18	1.2	matrix glass	-	-
KE62-3321f_3_matrixG_178	8	KE62-3321F	8/1/18	1.2	matrix glass	-	-
KE62-3321f_1_MI_172	8	KE62-3321F	8/1/18	1.2	MI	Cpx_MI	-
KE62-3321f_3_MI_174	8	KE62-3321F	8/1/18	1.2	MI	Olivine_MI	Inferred, but not quantifiable
KE62-3321f_4_MI_179	8	KE62-3321F	8/1/18	1.2	MI	Olivine_MI	Inferred, but not quantifiable
Fissure 8 late overflow lava, August 4 2018							
LF8_glass_g01_ol_MI_01_259	8	LF8	8/4/18	0.2	MI	Olivine_MI	-
LF8_mins_g21_MI-01_448	8	LF8	8/4/18	0.2	MI	Olivine_MI	-
LF8_3_MI_	8	LF8	8/4/18	0.2	MI	Olivine_MI	Yes
LF8_3_MI_devitrified_306, 307 avg	8	LF8	8/4/18	0.2	MI	Olivine_MI	-
LF8_4_MI_308, 309 avg	8	LF8	8/4/18	0.2	MI	Olivine_MI	-
LF8_11a_MI_310	8	LF8	8/4/18	0.2	MI	Olivine_MI	Inferred
LF8_11c_MI_311	8	LF8	8/4/18	0.2	MI	Olivine_MI	Inferred
LF8_11b_MI_312	8	LF8	8/4/18	0.2	MI	Olivine_MI	Yes
LF8_12a_MI_313	8	LF8	8/4/18	0.2	MI	Olivine_MI	Yes
LF8_12b_MI_314	8	LF8	8/4/18	0.2	MI	Olivine_MI	Yes
LF8_13a_MI_315	8	LF8	8/4/18	0.2	MI	Olivine_MI	Yes
LF8_13b_MI_316	8	LF8	8/4/18	0.2	MI	Olivine_MI	Yes
LF8_14_MI_317, 318 avg	8	LF8	8/4/18	0.2	MI	Olivine_MI	Inferred
LF8_1	8	LF8	8/4/18	0.2	MI	Olivine_MI	-

Supplementary Table 1C (continued).

Analysis Name	Fissure #	Sample Name	Na2O wt%	SiO2 wt%	CaO wt%	K2O wt%	Al2O3 wt%	FeOT wt%	MgO wt%	TiO2 wt%	MnO wt%
KE62-3316F_1_MI_235	8	KE62-3316F	2.43	50.60	10.72	0.54	13.64	11.55	7.82	2.23	0.18
KE62-3316F_2a_MI_239	8	KE62-3316F	2.41	50.40	10.99	0.40	14.11	11.55	7.42	2.25	0.18
KE62-3316F_6_MI_241	8	KE62-3316F	2.54	50.35	10.14	0.46	13.78	11.54	8.29	2.36	0.17
KE62-3316F_7_MI_246	8	KE62-3316F	2.39	50.55	11.19	0.46	13.57	11.56	7.54	2.29	0.18
KE62-3316F_9_MI_249	8	KE62-3316F	2.00	48.79	8.97	0.33	11.77	11.55	14.45	1.75	0.12
KE62-3316F_9b_MI_250	8	KE62-3316F	2.06	48.81	9.00	0.31	11.73	11.54	14.43	1.75	0.12
KE62-3316F_11_MI_252	8	KE62-3316F	2.14	49.54	9.87	0.35	12.63	11.55	11.69	1.66	0.14
KE62-3316F_12_MI_254	8	KE62-3316F	2.28	50.44	10.00	0.46	13.06	11.55	9.67	2.11	0.17
KE62-3316F_14a_MI_256	8	KE62-3316F	2.05	48.42	9.69	0.42	12.03	11.54	13.50	1.96	0.13
KE62-3316F_14b_MI_257	8	KE62-3316F	1.96	48.95	9.52	0.38	11.87	11.54	13.53	1.87	0.12
FeXANES_fast_fullrange_1s_KE62-3316F_15_MI_001_merge	8	KE62-3316F	-	-	-	-	-	-	-	-	-
Fissure 8 lava flow, August 1 2018											
KE62-3321f_3_matrixG_176	8	KE62-3321F	2.79	50.57	11.00	0.53	14.83	10.61	6.71	2.51	0.18
KE62-3321f_3_matrixG_177	8	KE62-3321F	2.61	50.66	11.05	0.53	14.88	10.85	6.41	2.54	0.18
KE62-3321f_3_matrixG_178	8	KE62-3321F	2.34	50.63	10.99	0.48	14.88	11.09	6.68	2.47	0.18
KE62-3321f_1_MI_172	8	KE62-3321F	2.56	50.54	10.67	0.45	14.95	11.55	6.26	2.54	0.16
KE62-3321f_3_MI_174	8	KE62-3321F	2.22	49.07	9.53	0.28	11.85	11.55	13.36	1.76	0.13
KE62-3321f_4_MI_179	8	KE62-3321F	2.00	48.92	9.43	0.32	11.50	11.54	14.10	1.80	0.12
Fissure 8 late overflow lava, August 4 2018											
LF8_glass_g01_ol_MI_01_259	8	LF8	2.05	47.46	10.45	0.42	11.35	11.54	13.83	2.43	0.13
LF8_mins_g21_MI-01_448	8	LF8	1.83	48.15	9.84	0.38	12.51	11.54	13.28	2.06	0.11
LF8_3_MI_	8	LF8	-	-	-	-	-	-	-	-	-
LF8_3_MI_devitrified_306, 307 avg	8	LF8	1.98	48.46	10.01	0.32	11.17	11.54	14.04	1.99	0.12
LF8_4_MI_308, 309 avg	8	LF8	1.75	48.27	9.85	0.27	11.41	11.54	14.41	1.91	0.12
LF8_11a_MI_310	8	LF8	1.91	49.25	9.29	0.31	11.42	11.54	14.12	1.80	0.10
LF8_11c_MI_311	8	LF8	1.87	48.93	9.42	0.28	11.43	11.54	14.27	1.92	0.11
LF8_11b_MI_312	8	LF8	1.99	48.52	9.42	0.28	11.73	11.55	14.27	1.87	0.10
LF8_12a_MI_313	8	LF8	1.93	49.10	9.46	0.27	11.48	11.54	14.11	1.73	0.12
LF8_12b_MI_314	8	LF8	1.98	48.75	9.39	0.28	11.71	11.54	14.26	1.73	0.11
LF8_13a_MI_315	8	LF8	1.88	48.18	9.20	0.39	11.85	11.54	14.60	1.97	0.10
LF8_13b_MI_316	8	LF8	2.01	48.48	9.18	0.38	11.89	11.54	14.27	1.87	0.10
LF8_14_MI_317, 318 avg	8	LF8	1.84	48.43	9.66	0.29	11.68	11.55	14.12	2.09	0.11
LF8_1	8	LF8	-	-	-	-	-	-	-	-	-

Supplementary Table 1C (continued).

Analysis Name	Fissure #	Sample Name	P2O5 wt%	Cl ppm	S ppm	un-normalized total	S/Cl (mass ratio)	non-sulfide corrected S ppm	non-PEC corrected FeOT	melt Mg#	Host Mg#	Host An#
KE62-3316F_1_MI_235	8	KE62-3316F	0.23	153	625	97.98	4.1	625	10.20	54.7	82.4	-
KE62-3316F_2a_MI_239	8	KE62-3316F	0.22	114	544	99.80	4.8	544	10.88	53.4	81.6	-
KE62-3316F_6_MI_241	8	KE62-3316F	0.25	250	1142	98.42	4.6	1142	10.04	56.2	83.2	-
KE62-3316F_7_MI_246	8	KE62-3316F	0.22	97	397	97.46	4.1	397	11.16	53.8	81.9	-
KE62-3316F_9_MI_249	8	KE62-3316F	0.19	95	823	99.40	8.6	618	6.74	69.1	89.5	-
KE62-3316F_9b_MI_250	8	KE62-3316F	0.17	73	800	97.73	11.0	601	6.30	69.0	89.5	-
KE62-3316F_11_MI_252	8	KE62-3316F	0.36	87	1006	100.19	11.5	691	7.17	64.3	87.4	-
KE62-3316F_12_MI_254	8	KE62-3316F	0.19	83	560	98.31	6.7	560	9.55	59.9	85.2	-
KE62-3316F_14a_MI_256	8	KE62-3316F	0.18	115	844	98.07	7.3	701	7.17	67.6	88.9	-
KE62-3316F_14b_MI_257	8	KE62-3316F	0.19	100	704	98.30	7.0	585	6.32	67.6	88.9	-
FeXANES_fast_fullrange_1s_KE62-3316F_15_MI_001_merge	8	KE62-3316F	-	-	-	-	-	-	-	-	-	-
Fissure 8 lava flow, August 1 2018												
KE62-3321f_3_matrixG_176	8	KE62-3321F	0.26	113	118	99.74	1.0	118	10.61	53.0	-	-
KE62-3321f_3_matrixG_177	8	KE62-3321F	0.26	133	153	99.02	1.1	153	10.85	51.3	-	-
KE62-3321f_3_matrixG_178	8	KE62-3321F	0.25	79	103	99.34	1.3	103	11.09	51.8	-	-
KE62-3321f_1_MI_172	8	KE62-3321F	0.26	99	424	100.02	4.3	424	11.55	49.1	80.3	-
KE62-3321f_3_MI_174	8	KE62-3321F	0.18	83	619	99.18	7.4	619	6.69	67.4	88.8	-
KE62-3321f_4_MI_179	8	KE62-3321F	0.21	71	575	99.52	8.1	575	6.49	68.5	89.3	-
Fissure 8 late overflow lava, August 4 2018												
LF8_glass_g01_ol_MI_01_259	8	LF8	0.25	141	677	98.14	4.8	677	7.14	68.1	89.2	-
LF8_mins_g21_MI-01_448	8	LF8	0.24	312	420	98.34	1.3	420	5.16	67.2	88.7	-
LF8_3_MI_	8	LF8	-	-	-	-	-	-	-	-	89.1	-
LF8_3_MI_devitrified_306, 307 avg	8	LF8	0.30	88	531	99.58	6.1	531	6.49	68.4	89.1	-
LF8_4_MI_308, 309 avg	8	LF8	0.40	80	502	99.05	6.3	502	6.15	69.0	89.5	-
LF8_11a_MI_310	8	LF8	0.22	134	451	98.06	3.4	306	4.71	68.6	89.3	-
LF8_11c_MI_311	8	LF8	0.19	58	514	98.82	8.8	349	5.04	68.8	89.4	-
LF8_11b_MI_312	8	LF8	0.24	86	457	99.70	5.3	310	5.51	68.8	89.4	-
LF8_12a_MI_313	8	LF8	0.21	84	458	100.08	5.5	391	5.88	68.5	89.3	-
LF8_12b_MI_314	8	LF8	0.20	72	414	98.14	5.7	331	5.06	68.8	89.4	-
LF8_13a_MI_315	8	LF8	0.23	134	518	98.97	3.9	428	4.73	69.3	89.6	-
LF8_13b_MI_316	8	LF8	0.23	143	448	99.54	3.1	400	4.48	68.8	89.4	-
LF8_14_MI_317, 318 avg	8	LF8	0.18	112	392	98.93	3.5	392	5.70	68.6	89.3	-
LF8_1	8	LF8	-	-	-	-	-	-	-	-	-	-

Supplementary Table 1C (continued).

Analysis Name	Fissure #	Sample Name	% PEC (olivine mass)	PEC correction coefficient	Temperature of matrix glass quenching or MI entrapment (°C)	H2O in melt (wt%) (FTIR)	CO2 in melt (ppm) (FTIR)	CO2 in melt + bubble (ppm) (FTIR + Raman)	vapor bubble volume (%)
KE62-3316F_1_MI_235	8	KE62-3316F	6.1	0.94	1198	-	-	-	-
KE62-3316F_2a_MI_239	8	KE62-3316F	4.3	0.96	1184	-	-	-	-
KE62-3316F_6_MI_241	8	KE62-3316F	8.5	0.92	1213	-	-	-	-
KE62-3316F_7_MI_246	8	KE62-3316F	3.5	0.97	1188	-	-	-	-
KE62-3316F_9_MI_249	8	KE62-3316F	32.7	0.74	1349	-	-	-	-
KE62-3316F_9b_MI_250	8	KE62-3316F	33.2	0.73	1349	-	-	-	-
KE62-3316F_11_MI_252	8	KE62-3316F	22.0	0.81	1293	-	-	-	-
KE62-3316F_12_MI_254	8	KE62-3316F	12.5	0.88	1246	-	-	-	-
KE62-3316F_14a_MI_256	8	KE62-3316F	28.0	0.77	1330	-	-	-	-
KE62-3316F_14b_MI_257	8	KE62-3316F	29.7	0.75	1329	-	-	-	-
FeXANES_fast_fullrange_1s_KE62-3316F_15_MI_001_merge	8	KE62-3316F	-	-	-	-	-	-	-
Fissure 8 lava flow, August 1 2018									
KE62-3321f_3_matrixG_176	8	KE62-3321F	-	-	1149	-	-	-	-
KE62-3321f_3_matrixG_177	8	KE62-3321F	-	-	1143	-	-	-	-
KE62-3321f_3_matrixG_178	8	KE62-3321F	-	-	1148	-	-	-	-
KE62-3321f_1_MI_172	8	KE62-3321F	-	-	-	-	-	-	-
KE62-3321f_3_MI_174	8	KE62-3321F	28.1	0.76	1328	-	-	-	-
KE62-3321f_4_MI_179	8	KE62-3321F	30.7	0.75	1341	-	-	-	-
Fissure 8 late overflow lava, August 4 2018									
LF8_glass_g01_ol_MI_01_259	8	LF8	33.5	0.74	1334	-	-	-	-
LF8_mins_g21_MI-01_448	8	LF8	43.2	0.68	1322	-	-	-	-
LF8_3_MI_	8	LF8	-	-	-	0.23	-	389	5%
LF8_3_MI_devitrified_306, 307 avg	8	LF8	36.2	0.72	1339	-	-	-	-
LF8_4_MI_308, 309 avg	8	LF8	39.3	0.70	1344	0.22	-	97	4%
LF8_11a_MI_310	8	LF8	46.7	0.66	1341	-	-	491	5%
LF8_11c_MI_311	8	LF8	46.3	0.67	1342	-	-	55	4%
LF8_11b_MI_312	8	LF8	45.4	0.67	1344	-	-	82	5%
LF8_12a_MI_313	8	LF8	42.2	0.69	1340	-	-	263	4%
LF8_12b_MI_314	8	LF8	45.2	0.67	1344	-	-	265	4%
LF8_13a_MI_315	8	LF8	49.4	0.65	1351	0.10	-	48	1%
LF8_13b_MI_316	8	LF8	48.8	0.65	1346	-	-	46	1%
LF8_14_MI_317, 318 avg	8	LF8	43.0	0.68	1339	0.27	-	526	8%
LF8_1	8	LF8	-	-	-	-	-	255	7%

Supplementary Table 1C (continued).

Analysis Name	Fissure #	Sample Name	Saturation pressure (bar) (Iacono-Marziano 2012)	Saturation depth (km) (Ryan 1987)	Saturation depth 1σ uncertainy (km)	δ34S (‰)	δ34S 1σ uncertainy (‰)	Fe3+/ΣFe % [Fe-XANES]	ΔQFM [Fe-XANES]	S6+/ΣS % [S-XANES]
KE62-3316F_1_MI_235	8	KE62-3316F	-	-	-	-	-	13.4	-0.42	2.1
KE62-3316F_2a_MI_239	8	KE62-3316F	-	-	-	-	-	13.4	-0.53	1.1
KE62-3316F_6_MI_241	8	KE62-3316F	-	-	-	-	-	-	-	9.1
KE62-3316F_7_MI_246	8	KE62-3316F	-	-	-	-	-	14.0	-0.42	6.2
KE62-3316F_9_MI_249	8	KE62-3316F	-	-	-	-	-	-	-	-
KE62-3316F_9b_MI_250	8	KE62-3316F	-	-	-	-	-	14.7	-0.36	-
KE62-3316F_11_MI_252	8	KE62-3316F	-	-	-	-	-	12.6	-0.71	-
KE62-3316F_12_MI_254	8	KE62-3316F	-	-	-	-	-	13.3	-0.46	4.1
KE62-3316F_14a_MI_256	8	KE62-3316F	-	-	-	-	-	15.0	-0.32	9.1
KE62-3316F_14b_MI_257	8	KE62-3316F	-	-	-	-	-	16.7	-0.04	7.4
FeXANES_fast_fullrange_1s_KE62-3316F_15_MI_001_merge	8	KE62-3316F	-	-	-	-	-	13.9	-0.45	-
Fissure 8 lava flow, August 1 2018										
KE62-3321f_3_matrixG_176	8	KE62-3321F	-	-	-	-	-	12.4	-0.53	-
KE62-3321f_3_matrixG_177	8	KE62-3321F	-	-	-	-	-	12.1	-0.56	-
KE62-3321f_3_matrixG_178	8	KE62-3321F	-	-	-	-	-	13.6	-0.21	-
KE62-3321f_1_MI_172	8	KE62-3321F	-	-	-	-	-	12.7	-0.43	-
KE62-3321f_3_MI_174	8	KE62-3321F	-	-	-	-	-	14.7	-0.38	-
KE62-3321f_4_MI_179	8	KE62-3321F	-	-	-	-	-	15.1	-0.30	-
Fissure 8 late overflow lava, August 4 2018										
LF8_glass_g01_ol_MI_01_259	8	LF8	-	-	-	-	-	-	-	-
LF8_mins_g21_MI-01_448	8	LF8	-	-	-	-	-	-	-	-
LF8_3_MI_	8	LF8	722	3.2	1.2	-	-	-	-	-
LF8_3_MI_devitrified_306, 307 avg	8	LF8	-	-	-	1.2	1.8	-	-	-
LF8_4_MI_308, 309 avg	8	LF8	191	0.9	4.8	-0.7	0.5	-	-	-
LF8_11a_MI_310	8	LF8	924	4.0	1.4	0.3	1.4	-	-	-
LF8_11c_MI_311	8	LF8	112	0.5	5.4	-	-	-	-	-
LF8_11b_MI_312	8	LF8	156	0.7	6.6	-1.5	1.2	-	-	-
LF8_12a_MI_313	8	LF8	507	2.3	1.1	-1.1	0.6	-	-	-
LF8_12b_MI_314	8	LF8	489	2.2	1.2	-	-	-	-	-
LF8_13a_MI_315	8	LF8	89	0.4	0.5	-1.0	0.7	-	-	-
LF8_13b_MI_316	8	LF8	87	0.4	0.2	-	-	-	-	-
LF8_14_MI_317, 318 avg	8	LF8	967	4.2	2.1	-1.6	0.6	-	-	-
LF8_1	8	LF8	474	2.1	3.2	-	-	-	-	-

Supplementary Table 1C (continued).

Analysis Name	Fissure #	Sample Name	Eruption Date	Distance traveled before quench (km)	Glass Type	Host mineral	Sulfide present?
LF8_2	8	LF8	8/4/18	0.2	MI	Olivine_MI	-
LF8_5	8	LF8	8/4/18	0.2	MI	Olivine_MI	-
LF8_6	8	LF8	8/4/18	0.2	MI	Olivine_MI	-
LF8_7	8	LF8	8/4/18	0.2	MI	Olivine_MI	-
LF8_8	8	LF8	8/4/18	0.2	MI	Olivine_MI	-
LF8_9	8	LF8	8/4/18	0.2	MI	Olivine_MI	-
LF8_15	8	LF8	8/4/18	0.2	MI	Olivine_MI	-
LF8_16c	8	LF8	8/4/18	0.2	MI	Olivine_MI	-
Fissure 8 late overflow lava, August 4 2018 (REHEATED)							
LF8_rh02_matrixG_133	8	LF8 re-heated	8/4/18	0.2	matrix glass, reheated 1200C	-	-
LF8_rh03a_matrixG_141	8	LF8 re-heated	8/4/18	0.2	matrix glass, reheated 1300C	-	-
LF8_rh01_126, 127 avg	8	LF8 re-heated	8/4/18	0.2	MI reheated 1200C	Olivine_MI	-
LF8_rh02a_129	8	LF8 re-heated	8/4/18	0.2	MI reheated 1200C	Olivine_MI	-
LF8_rh02b_130	8	LF8 re-heated	8/4/18	0.2	MI reheated 1200C	Olivine_MI	-
LF8_rh03a1_134	8	LF8 re-heated	8/4/18	0.2	MI reheated 1300C	Olivine_MI	-
LF8_rh03a2_135	8	LF8 re-heated	8/4/18	0.2	MI reheated 1300C	Olivine_MI	-
LF8_rh03a3_136	8	LF8 re-heated	8/4/18	0.2	MI reheated 1300C	Olivine_MI	-
Fissure 8 lava flow, August 5 2018							
FeXANES_fast_fullrange_1s_KE62-3323F_MatrixG1_001_merge	8	KE62-3323F	8/5/18	10.45	matrix glass	-	-
FeXANES_fast_fullrange_1s_KE62-3323F_MatrixG1_002_merge	8	KE62-3323F	8/5/18	10.45	matrix glass	-	-
FeXANES_fast_fullrange_1s_KE62-3323F_1_InterstitialG_001_merge	8	KE62-3323F	8/5/18	10.45	interstitial melt	-	-
FeXANES_fast_fullrange_1s_KE62-3323F_1_InterstitialG_002_merge	8	KE62-3323F	8/5/18	10.45	interstitial melt	-	-
FeXANES_fast_fullrange_1s_KE62-3323F_5_InterstitialG_001_merge	8	KE62-3323F	8/5/18	10.45	interstitial melt	-	-
FeXANES_fast_fullrange_1s_KE62-3323F_5_InterstitialG_002_merge	8	KE62-3323F	8/5/18	10.45	interstitial melt	-	-
FeXANES_fast_fullrange_1s_KE62-3323F_12_InterstitialG_001_merge	8	KE62-3323F	8/5/18	10.45	interstitial melt	-	-
FeXANES_fast_fullrange_1s_KE62-3323F_12_InterstitialG_002_merge	8	KE62-3323F	8/5/18	10.45	interstitial melt	-	-

Supplementary Table 1C (continued).

Analysis Name	Fissure #	Sample Name	Na2O wt%	SiO2 wt%	CaO wt%	K2O wt%	Al2O3 wt%	FeOT wt%	MgO wt%	TiO2 wt%	MnO wt%
LF8_2	8	LF8	-	-	-	-	-	-	-	-	-
LF8_5	8	LF8	-	-	-	-	-	-	-	-	-
LF8_6	8	LF8	-	-	-	-	-	-	-	-	-
LF8_7	8	LF8	-	-	-	-	-	-	-	-	-
LF8_8	8	LF8	-	-	-	-	-	-	-	-	-
LF8_9	8	LF8	-	-	-	-	-	-	-	-	-
LF8_15	8	LF8	-	-	-	-	-	-	-	-	-
LF8_16c	8	LF8	-	-	-	-	-	-	-	-	-
Fissure 8 late overflow lava, August 4 2018 (REHEATED)											
LF8_rh02_matrixG_133	8	LF8 re-heated	2.14	49.23	8.91	0.54	12.44	14.49	9.71	2.18	0.21
LF8_rh03a_matrixG_141	8	LF8 re-heated	1.83	47.86	8.06	0.45	10.78	15.59	13.25	1.88	0.20
LF8_rh01_126, 127 avg	8	LF8 re-heated	1.96	49.83	9.46	0.35	11.84	11.55	12.75	1.81	0.12
LF8_rh02a_129	8	LF8 re-heated	2.19	50.44	9.37	0.33	12.88	11.55	11.12	1.73	0.14
LF8_rh02b_130	8	LF8 re-heated	2.20	51.40	9.07	0.39	12.46	11.55	11.12	1.41	0.16
LF8_rh03a1_134	8	LF8 re-heated	2.01	50.64	10.75	0.49	13.65	11.53	8.19	2.18	0.16
LF8_rh03a2_135	8	LF8 re-heated	2.16	50.43	10.87	0.44	13.82	11.56	8.19	2.00	0.21
LF8_rh03a3_136	8	LF8 re-heated	2.21	50.39	10.73	0.40	13.53	11.55	8.61	2.09	0.19
Fissure 8 lava flow, August 5 2018											
FeXANES_fast_fullrange_1s_KE62-3323F_MatrixG1_001_merge	8	KE62-3323F	-	-	-	-	-	-	-	-	-
FeXANES_fast_fullrange_1s_KE62-3323F_MatrixG1_002_merge	8	KE62-3323F	-	-	-	-	-	-	-	-	-
FeXANES_fast_fullrange_1s_KE62-3323F_1_InterstitialG_001_merge	8	KE62-3323F	-	-	-	-	-	-	-	-	-
FeXANES_fast_fullrange_1s_KE62-3323F_1_InterstitialG_002_merge	8	KE62-3323F	-	-	-	-	-	-	-	-	-
FeXANES_fast_fullrange_1s_KE62-3323F_5_InterstitialG_001_merge	8	KE62-3323F	-	-	-	-	-	-	-	-	-
FeXANES_fast_fullrange_1s_KE62-3323F_5_InterstitialG_002_merge	8	KE62-3323F	-	-	-	-	-	-	-	-	-
FeXANES_fast_fullrange_1s_KE62-3323F_12_InterstitialG_001_merge	8	KE62-3323F	-	-	-	-	-	-	-	-	-
FeXANES_fast_fullrange_1s_KE62-3323F_12_InterstitialG_002_merge	8	KE62-3323F	-	-	-	-	-	-	-	-	-

Supplementary Table 1C (continued).

Analysis Name	Fissure #	Sample Name	P2O5 wt%	Cl ppm	S ppm	un-normalized total	S/Cl (mass ratio)	non-sulfide corrected S ppm	non-PEC corrected FeOT	melt Mg#	Host Mg#	Host An#
LF8_2	8	LF8	-	-	-	-	-	-	-	-	-	-
LF8_5	8	LF8	-	-	-	-	-	-	-	-	-	-
LF8_6	8	LF8	-	-	-	-	-	-	-	-	-	-
LF8_7	8	LF8	-	-	-	-	-	-	-	-	-	-
LF8_8	8	LF8	-	-	-	-	-	-	-	-	-	-
LF8_9	8	LF8	-	-	-	-	-	-	-	-	-	-
LF8_15	8	LF8	-	-	-	-	-	-	-	-	-	-
LF8_16c	8	LF8	-	-	-	-	-	-	-	-	-	-
Fissure 8 late overflow lava, August 4 2018 (REHEATED)												
LF8_rh02_matrixG_133	8	LF8 re-heated	0.17	28	-2	97.55	-0.1	-2	14.49	54.4	-	-
LF8_rh03a_matrixG_141	8	LF8 re-heated	0.10	48	24	98.20	0.5	24	15.59	60.2	-	-
LF8_rh01_126, 127 avg	8	LF8 re-heated	0.25	85	631	98.84	7.4	631	7.90	66.3	88.3	-
LF8_rh02a_129	8	LF8 re-heated	0.22	98	159	98.98	1.6	159	8.60	63.2	86.8	-
LF8_rh02b_130	8	LF8 re-heated	0.18	113	513	97.91	4.5	513	9.86	63.2	86.8	-
LF8_rh03a1_134	8	LF8 re-heated	0.24	150	1436	99.11	9.6	1436	13.57	55.9	83.0	-
LF8_rh03a2_135	8	LF8 re-heated	0.24	116	603	98.36	5.2	603	15.53	55.8	83.0	-
LF8_rh03a3_136	8	LF8 re-heated	0.23	132	602	101.06	4.6	602	14.37	57.1	83.7	-
Fissure 8 lava flow, August 5 2018												
FeXANES_fast_fullrange_1s_KE62-3323F_MatrixG1_001_merge	8	KE62-3323F	-	-	-	-	-	-	-	-	-	-
FeXANES_fast_fullrange_1s_KE62-3323F_MatrixG1_002_merge	8	KE62-3323F	-	-	-	-	-	-	-	-	-	-
FeXANES_fast_fullrange_1s_KE62-3323F_1_InterstitialG_001_merge	8	KE62-3323F	-	-	-	-	-	-	-	-	-	-
FeXANES_fast_fullrange_1s_KE62-3323F_1_InterstitialG_002_merge	8	KE62-3323F	-	-	-	-	-	-	-	-	-	-
FeXANES_fast_fullrange_1s_KE62-3323F_5_InterstitialG_001_merge	8	KE62-3323F	-	-	-	-	-	-	-	-	-	-
FeXANES_fast_fullrange_1s_KE62-3323F_5_InterstitialG_002_merge	8	KE62-3323F	-	-	-	-	-	-	-	-	-	-
FeXANES_fast_fullrange_1s_KE62-3323F_12_InterstitialG_001_merge	8	KE62-3323F	-	-	-	-	-	-	-	-	-	-
FeXANES_fast_fullrange_1s_KE62-3323F_12_InterstitialG_002_merge	8	KE62-3323F	-	-	-	-	-	-	-	-	-	-

Supplementary Table 1C (continued).

Analysis Name	Fissure #	Sample Name	% PEC (olivine mass)	PEC correction coefficient	Temperature of matrix glass quenching or MI entrapment (°C)	H2O in melt (wt%) (FTIR)	CO2 in melt (ppm) (FTIR)	CO2 in melt + bubble (ppm) (FTIR + Raman)	vapor bubble volume (%)
LF8_2	8	LF8	-	-	-	-	-	103	2%
LF8_5	8	LF8	-	-	-	-	-	449	7%
LF8_6	8	LF8	-	-	-	-	-	8	3%
LF8_7	8	LF8	-	-	-	-	-	49	6%
LF8_8	8	LF8	-	-	-	-	-	150	5%
LF8_9	8	LF8	-	-	-	-	-	7	5%
LF8_15	8	LF8	-	-	-	-	-	94	2%
LF8_16c	8	LF8	-	-	-	-	-	22	5%
Fissure 8 late overflow lava, August 4 2018 (REHEATED)									
LF8_rh02_matrixG_133	8	LF8 re-heated	-	-	1209	-	-	-	-
LF8_rh03a_matrixG_141	8	LF8 re-heated	-	-	1280	-	-	-	-
LF8_rh01_126, 127 avg	8	LF8 re-heated	13.3	0.87	1314	0.15	-		4%
LF8_rh02a_129	8	LF8 re-heated	8.4	0.91	1281	-	-		3%
LF8_rh02b_130	8	LF8 re-heated	6.4	0.93	1284	-	-		2%
LF8_rh03a1_134	8	LF8 re-heated	-17.1	1.22	1204	0.08	-		2%
LF8_rh03a2_135	8	LF8 re-heated	-19.1	1.26	1205	0.05	-		-
LF8_rh03a3_136	8	LF8 re-heated	-16.9	1.22	1216	-	-		-
Fissure 8 lava flow, August 5 2018									
FeXANES_fast_fullrange_1s_KE62-3323F_MatrixG1_001_merge	8	KE62-3323F	-	-	-	-	-	-	-
FeXANES_fast_fullrange_1s_KE62-3323F_MatrixG1_002_merge	8	KE62-3323F	-	-	-	-	-	-	-
FeXANES_fast_fullrange_1s_KE62-3323F_1_InterstitialG_001_merge	8	KE62-3323F	-	-	-	-	-	-	-
FeXANES_fast_fullrange_1s_KE62-3323F_1_InterstitialG_002_merge	8	KE62-3323F	-	-	-	-	-	-	-
FeXANES_fast_fullrange_1s_KE62-3323F_5_InterstitialG_001_merge	8	KE62-3323F	-	-	-	-	-	-	-
FeXANES_fast_fullrange_1s_KE62-3323F_5_InterstitialG_002_merge	8	KE62-3323F	-	-	-	-	-	-	-
FeXANES_fast_fullrange_1s_KE62-3323F_12_InterstitialG_001_merge	8	KE62-3323F	-	-	-	-	-	-	-
FeXANES_fast_fullrange_1s_KE62-3323F_12_InterstitialG_002_merge	8	KE62-3323F	-	-	-	-	-	-	-

Supplementary Table 1C (continued).

Analysis Name	Fissure #	Sample Name	Saturation pressure (bar) (Iacono-Marziano 2012)	Saturation depth (km) (Ryan 1987)	Saturation depth 1σ uncertainy (km)	δ34S (‰)	δ34S 1σ uncertainy (‰)	Fe3+/ΣFe % [Fe-XANES]	ΔQFM [Fe-XANES]	S6+/ΣS % [S-XANES]
LF8_2	8	LF8	197	0.9	0.9	-	-	-	-	-
LF8_5	8	LF8	813	3.5	1.3	-	-	-	-	-
LF8_6	8	LF8	19	0.1	1.0	-	-	-	-	-
LF8_7	8	LF8	97	0.4	3.3	-	-	-	-	-
LF8_8	8	LF8	286	1.3	0.4	-	-	-	-	-
LF8_9	8	LF8	17	0.1	1.0	-	-	-	-	-
LF8_15	8	LF8	182	0.8	0.5	-	-	-	-	-
LF8_16c	8	LF8	46	0.2	1.9	-	-	-	-	-
Fissure 8 late overflow lava, August 4 2018 (REHEATED)										
LF8_rh02_matrixG_133	8	LF8 re-heated	-	-	-	-	-	-	-	-
LF8_rh03a_matrixG_141	8	LF8 re-heated	-	-	-	-	-	-	-	-
LF8_rh01_126, 127 avg	8	LF8 re-heated				-	-	-	-	-
LF8_rh02a_129	8	LF8 re-heated				-	-	-	-	-
LF8_rh02b_130	8	LF8 re-heated				-	-	-	-	-
LF8_rh03a1_134	8	LF8 re-heated				-	-	-	-	-
LF8_rh03a2_135	8	LF8 re-heated				-	-	-	-	-
LF8_rh03a3_136	8	LF8 re-heated				-	-	-	-	-
Fissure 8 lava flow, August 5 2018										
FeXANES_fast_fullrange_1s_KE62-3323F_MatrixG1_001_merge	8	KE62-3323F	-	-	-	-	-	13.7	-0.23	-
FeXANES_fast_fullrange_1s_KE62-3323F_MatrixG1_002_merge	8	KE62-3323F	-	-	-	-	-	13.7	-0.24	-
FeXANES_fast_fullrange_1s_KE62-3323F_1_InterstitialG_001_merge	8	KE62-3323F	-	-	-	-	-	13.3	-0.33	-
FeXANES_fast_fullrange_1s_KE62-3323F_1_InterstitialG_002_merge	8	KE62-3323F	-	-	-	-	-	13.5	-0.27	-
FeXANES_fast_fullrange_1s_KE62-3323F_5_InterstitialG_001_merge	8	KE62-3323F	-	-	-	-	-	13.6	-0.26	-
FeXANES_fast_fullrange_1s_KE62-3323F_5_InterstitialG_002_merge	8	KE62-3323F	-	-	-	-	-	14.4	-0.12	-
FeXANES_fast_fullrange_1s_KE62-3323F_12_InterstitialG_001_merge	8	KE62-3323F	-	-	-	-	-	14.1	-0.16	-
FeXANES_fast_fullrange_1s_KE62-3323F_12_InterstitialG_002_merge	8	KE62-3323F	-	-	-	-	-	13.5	-0.28	-

Supplementary Table 1C (continued).

Analysis Name	Fissure #	Sample Name	Eruption Date	Distance traveled before quench (km)	Glass Type	Host mineral	Sulfide present?
FeXANES_fast_fullrange_1s_KE62-3323F_15_InterstitialG_001_merge	8	KE62-3323F	8/5/18	10.45	interstitial melt	-	-
FeXANES_fast_fullrange_1s_KE62-3323F_15_InterstitialG_002_merge	8	KE62-3323F	8/5/18	10.45	interstitial melt	-	-
FeXANES_fast_fullrange_1s_KE62-3323F_1_MI_001_merge	8	KE62-3323F	8/5/18	10.45	MI	Olivine_MI	-
FeXANES_fast_fullrange_1s_KE62-3323F_4_MI_001_merge	8	KE62-3323F	8/5/18	10.45	MI	Olivine_MI	Inferred
FeXANES_fast_fullrange_1s_KE62-3323F_6_MI_001_merge	8	KE62-3323F	8/5/18	10.45	MI	Olivine_MI	Inferred
FeXANES_fast_fullrange_1s_KE62-3323F_10a_MI_001_merge	8	KE62-3323F	8/5/18	10.45	MI	Olivine_MI	-
FeXANES_fast_fullrange_1s_KE62-3323F_10b_MI_001_merge	8	KE62-3323F	8/5/18	10.45	MI	Olivine_MI	-

Supplementary Table 1C (continued).

Analysis Name	Fissure #	Sample Name	Na2O wt%	SiO2 wt%	CaO wt%	K2O wt%	Al2O3 wt%	FeOT wt%	MgO wt%	TiO2 wt%	MnO wt%
FeXANES_fast_fullrange_1s_KE62-3323F_15_InterstitialG_001_merge	8	KE62-3323F	-	-	-	-	-	-	-	-	-
FeXANES_fast_fullrange_1s_KE62-3323F_15_InterstitialG_002_merge	8	KE62-3323F	-	-	-	-	-	-	-	-	-
FeXANES_fast_fullrange_1s_KE62-3323F_1_MI_001_merge	8	KE62-3323F	-	-	-	-	-	-	-	-	-
FeXANES_fast_fullrange_1s_KE62-3323F_4_MI_001_merge	8	KE62-3323F	-	-	-	-	-	-	-	-	-
FeXANES_fast_fullrange_1s_KE62-3323F_6_MI_001_merge	8	KE62-3323F	-	-	-	-	-	-	-	-	-
FeXANES_fast_fullrange_1s_KE62-3323F_10a_MI_001_merge	8	KE62-3323F	-	-	-	-	-	-	-	-	-
FeXANES_fast_fullrange_1s_KE62-3323F_10b_MI_001_merge	8	KE62-3323F	-	-	-	-	-	-	-	-	-

Supplementary Table 1C (continued).

Analysis Name	Fissure #	Sample Name	P2O5 wt%	Cl ppm	S ppm	un-normalized total	S/Cl (mass ratio)	non-sulfide corrected S ppm	non-PEC corrected FeOT	melt Mg#	Host Mg#	Host An#
FeXANES_fast_fullrange_1s_KE62-3323F_15_InterstitialG_001_merge	8	KE62-3323F	-	-	-	-	-	-	-	-	-	-
FeXANES_fast_fullrange_1s_KE62-3323F_15_InterstitialG_002_merge	8	KE62-3323F	-	-	-	-	-	-	-	-	-	-
FeXANES_fast_fullrange_1s_KE62-3323F_1_MI_001_merge	8	KE62-3323F	-	-	-	-	-	-	-	-	-	-
FeXANES_fast_fullrange_1s_KE62-3323F_4_MI_001_merge	8	KE62-3323F	-	-	-	-	-	-	-	-	-	-
FeXANES_fast_fullrange_1s_KE62-3323F_6_MI_001_merge	8	KE62-3323F	-	-	-	-	-	-	-	-	-	-
FeXANES_fast_fullrange_1s_KE62-3323F_10a_MI_001_merge	8	KE62-3323F	-	-	-	-	-	-	-	-	-	-
FeXANES_fast_fullrange_1s_KE62-3323F_10b_MI_001_merge	8	KE62-3323F	-	-	-	-	-	-	-	-	-	-

Supplementary Table 1C (continued).

Analysis Name	Fissure #	Sample Name	% PEC (olivine mass)	PEC correction coefficient	Temperature of matrix glass quenching or MI entrapment (°C)	H2O in melt (wt%) (FTIR)	CO2 in melt (ppm) (FTIR)	CO2 in melt + bubble (ppm) (FTIR + Raman)	vapor bubble volume (%)
FeXANES_fast_fullrange_1s_KE62-3323F_15_InterstitialG_001_merge	8	KE62-3323F	-	-	-	-	-	-	-
FeXANES_fast_fullrange_1s_KE62-3323F_15_InterstitialG_002_merge	8	KE62-3323F	-	-	-	-	-	-	-
FeXANES_fast_fullrange_1s_KE62-3323F_1_MI_001_merge	8	KE62-3323F	-	-	-	-	-	-	-
FeXANES_fast_fullrange_1s_KE62-3323F_4_MI_001_merge	8	KE62-3323F	-	-	-	-	-	-	-
FeXANES_fast_fullrange_1s_KE62-3323F_6_MI_001_merge	8	KE62-3323F	-	-	-	-	-	-	-
FeXANES_fast_fullrange_1s_KE62-3323F_10a_MI_001_merge	8	KE62-3323F	-	-	-	-	-	-	-
FeXANES_fast_fullrange_1s_KE62-3323F_10b_MI_001_merge	8	KE62-3323F	-	-	-	-	-	-	-

Supplementary Table 1C (continued).

Analysis Name	Fissure #	Sample Name	Saturation pressure (bar) (Iacono-Marziano 2012)	Saturation depth (km) (Ryan 1987)	Saturation depth 1σ uncertainy (km)	δ34S (‰)	δ34S 1σ uncertainy (‰)	Fe3+/ΣFe % [Fe-XANES]	ΔQFM [Fe-XANES]	S6+/ΣS % [S-XANES]
FeXANES_fast_fullrange_1s_KE62-3323F_15_InterstitialG_001_merge	8	KE62-3323F	-	-	-	-	-	13.9	-0.20	-
FeXANES_fast_fullrange_1s_KE62-3323F_15_InterstitialG_002_merge	8	KE62-3323F	-	-	-	-	-	13.8	-0.22	-
FeXANES_fast_fullrange_1s_KE62-3323F_1_MI_001_merge	8	KE62-3323F	-	-	-	-	-	14.5	-0.31	-
FeXANES_fast_fullrange_1s_KE62-3323F_4_MI_001_merge	8	KE62-3323F	-	-	-	-	-	13.9	-0.41	-
FeXANES_fast_fullrange_1s_KE62-3323F_6_MI_001_merge	8	KE62-3323F	-	-	-	-	-	14.3	-0.35	-
FeXANES_fast_fullrange_1s_KE62-3323F_10a_MI_001_merge	8	KE62-3323F	-	-	-	-	-	15.1	-0.21	-
FeXANES_fast_fullrange_1s_KE62-3323F_10b_MI_001_merge	8	KE62-3323F	-	-	-	-	-	13.7	-0.45	-

APPENDIX D

CHAPTER V SUPPLEMENTARY INFORMATION AND FIGURES

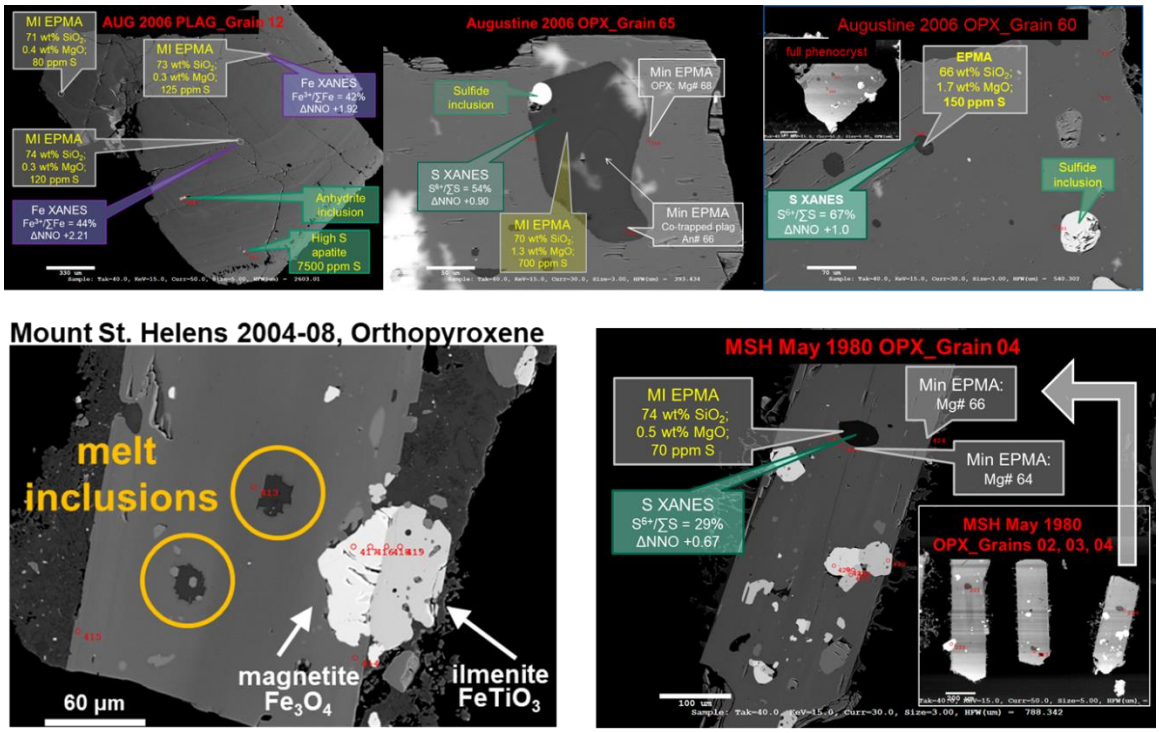

Chapter V, Figure D1. Back scattered electron images of phenocrysts from AUG *(top)* and MSH *(bottom)* showing MI textures, as well as oxide, sulfide, anhydrite and apatite inclusions within the phenocrysts. *(top-middle)* A sulfide is co-trapped within a large melt inclusion in AUG LSA308. Results of multi-parameter analyses are shown, which were conducted on the same MI or on various features within individual grains. Red text indicates location of EPMA measurements of MI or silicate hosts.

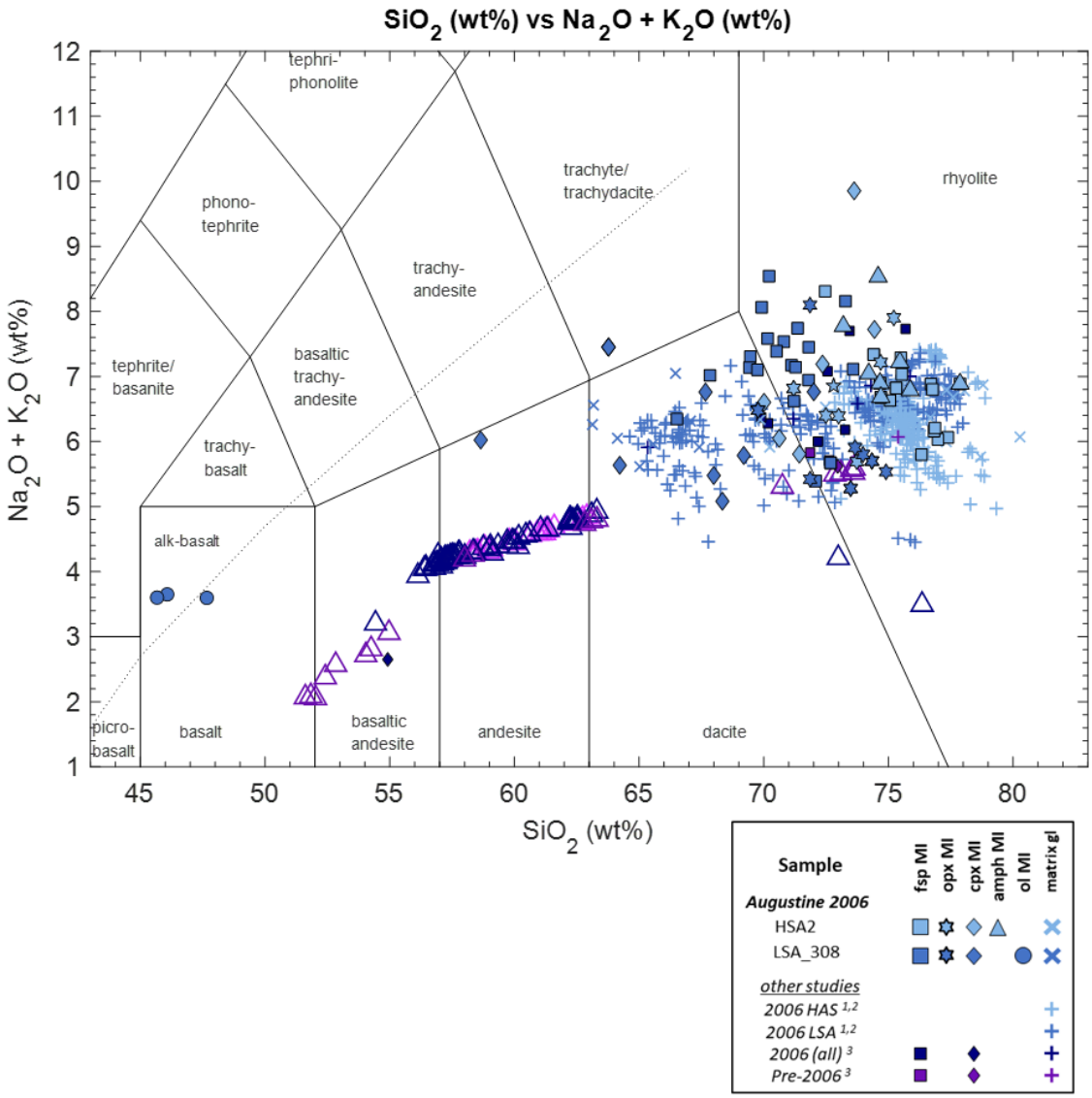

Chapter V, Figure D2. Total alkalis versus silica diagram for MI, matrix glasses, and whole rocks from AUG 2006 (and older samples). Data from other sources are slightly smaller symbols. Other data sources are: [1] Benage et al. (submitted), [2] Larsen et al. (2010), and [3] Webster et al. (2010).

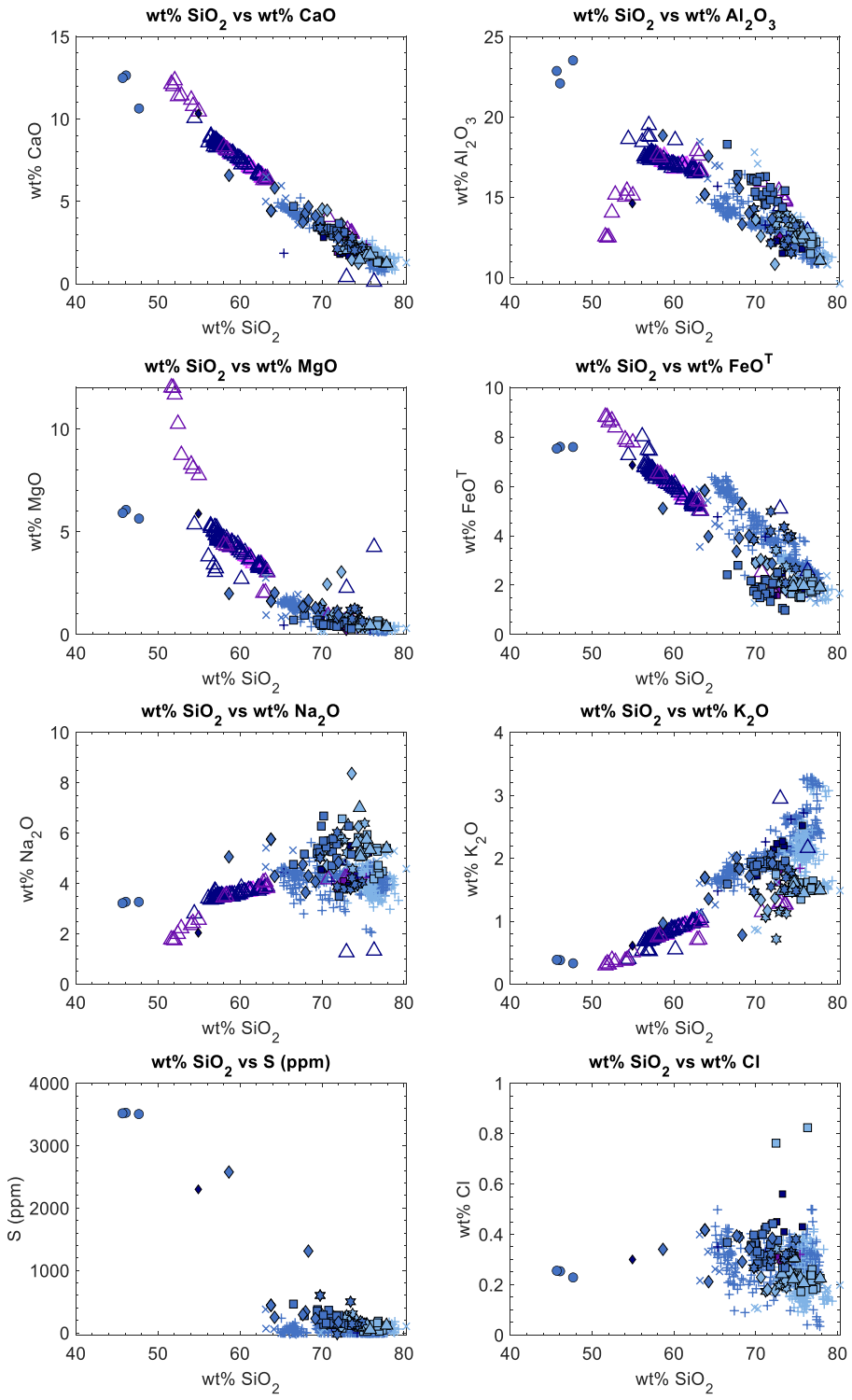

Chapter V, Figure D3. Harker diagrams for MI, matrix glasses, and whole rocks from AUG 2006 (and older samples). Data from other sources are slightly smaller symbols. Other data sources are: Benage et al. (submitted), Larsen et al. (2010), and Webster et al. (2010). Symbology as in Figure D2.

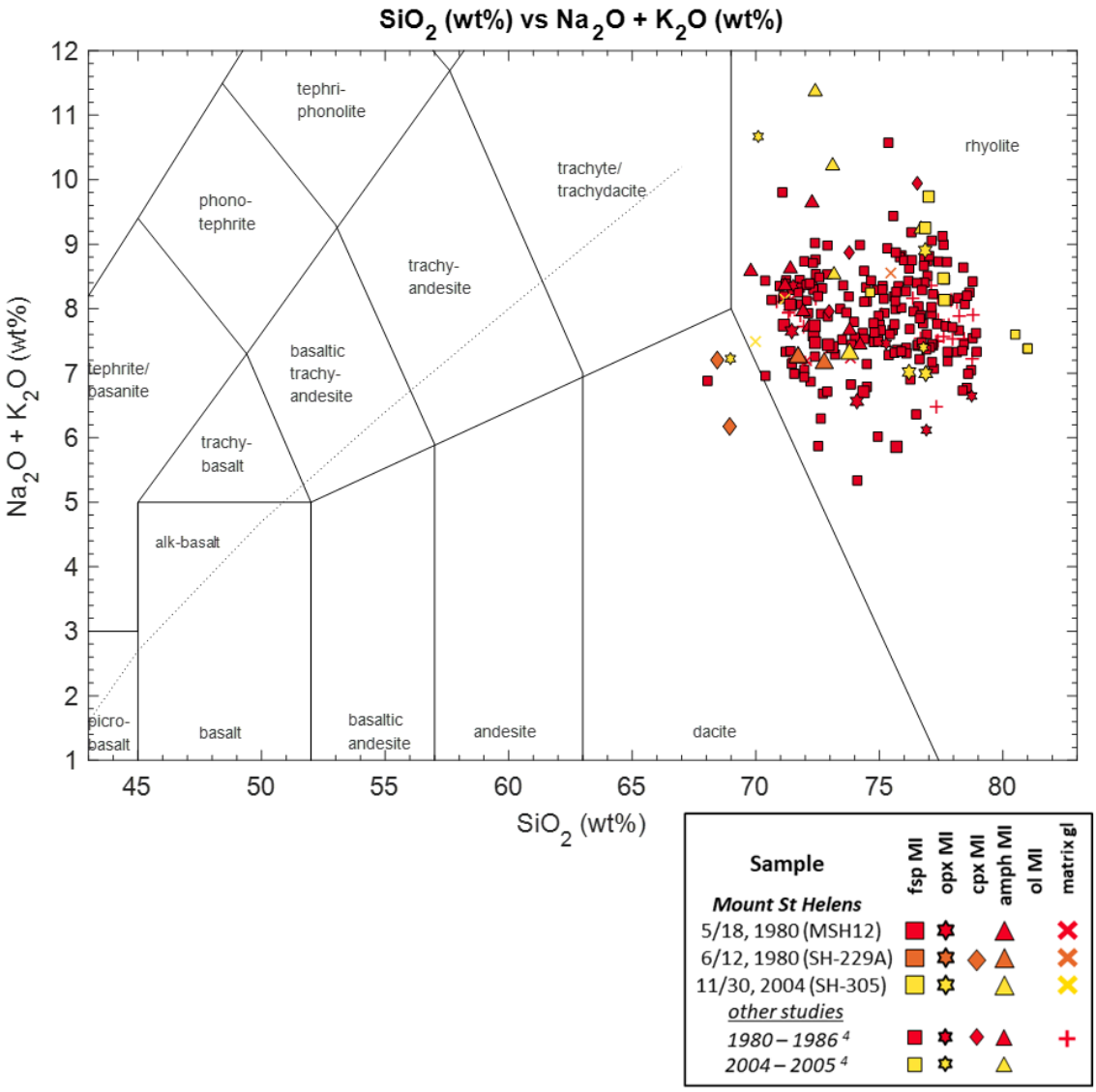

Chapter V, Figure D4. Total alkalis versus silica diagram for MI, matrix glasses, and whole rocks from MSH 1980 – 1986 and 2004 – 2005 eruptions. Data from [4] Blundy et al. (2008) are slightly smaller symbols.

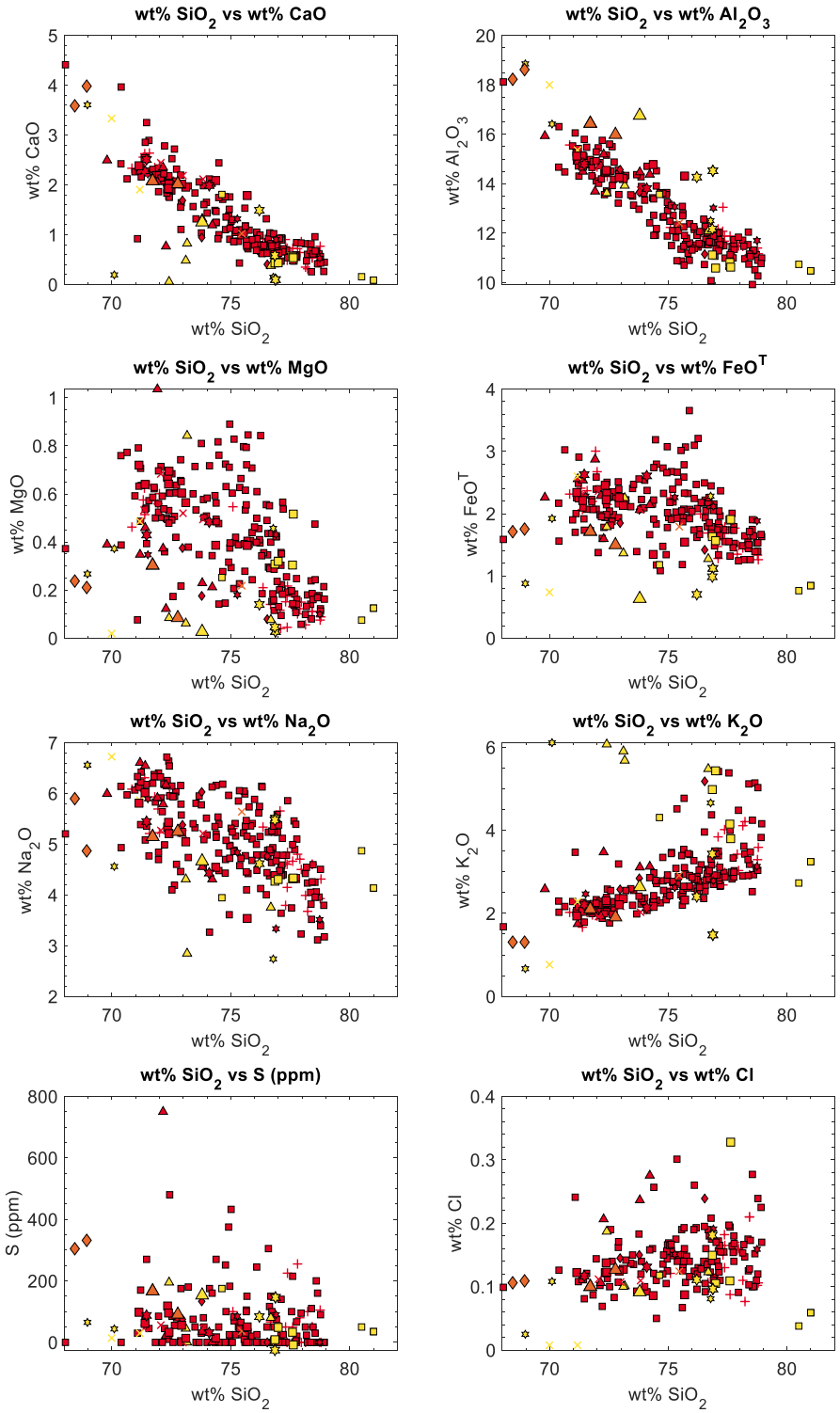

Chapter V, Figure D5. Harker diagrams for MI, matrix glasses, and whole rocks from MSH 1980 – 1986 and 2004 – 2005 eruptions. Data from other sources are slightly smaller symbols. Other data are from Blundy et al. (2008). Symbology as in Supplementary Figure D4.

Supplementary Table 1D. Augustine and Mount St. Helens glass descriptions, major element and volatile concentrations (wt%, ppm, normalized), S-isotopic signatures, and Fe and S speciation.

Analysis Name	Sample Name	Glass Type	Host Mineral	Na2O wt%	SiO2 wt%	CaO wt%	K2O wt%	Al2O3 wt%	FeOT wt%	MgO wt%
AUGUSTINE 2006: Low Silica Andesite (LSA) tephra										
AUG308_plag2_G11_matrixG_176	AUG308	matrix glass	-	5.32	66.46	4.23	1.73	14.71	4.99	1.25
AUG308_plag2_G11_matrixG_182	AUG308	matrix glass	-	5.41	63.17	6.48	1.15	18.45	3.55	0.95
AUG308_small_G65_2_matrixG_162	AUG308	matrix glass	-	4.35	65.03	5.95	1.26	16.99	4.48	0.83
AUG308_small_G170_matrixG_167	AUG308	matrix glass	-	4.43	65.56	5.19	1.54	16.93	4.39	0.89
AUG_308_G06_matrixG_205	AUG308	matrix glass	-	4.27	67.06	3.58	2.04	14.00	5.49	1.95
AUG_308_G06_matrixG_206	AUG308	matrix glass	-	3.91	67.41	3.76	2.01	14.13	5.63	1.60
AUG_308_Ol3_rim_glass_228	AUG308	matrix glass	-	4.43	64.13	4.58	1.62	16.15	5.43	1.98
AUG_308_G02 matrixG	AUG308	matrix glass	-	-	-	-	-	-	-	-
AUG_308_G08 matrixG	AUG308	matrix glass	-	-	-	-	-	-	-	-
AUG_308_Ol3_RE_223	AUG308	re-entrant	ol_RE	4.66	63.13	4.99	1.60	14.83	5.88	2.76
AUG308_plag2_G03_180	AUG308	MI	plag_MI	-	-	-	-	-	-	-
AUG308_plag2_G04_182	AUG308	MI	plag_MI	6.68	70.21	3.21	1.86	15.06	1.94	0.50
AUG308_plag2_G04_183	AUG308	MI	plag_MI	3.78	72.68	3.12	1.90	14.72	2.50	0.62
AUG308_plag2_G09_189	AUG308	MI	plag_MI	5.28	71.11	3.34	1.89	14.60	2.24	0.53
AUG308_plag2_G09_171	AUG308	MI	plag_MI	5.26	71.28	3.37	1.88	14.55	2.18	0.55
AUG308_plag2_G10_190	AUG308	MI	plag_MI	5.69	70.80	3.24	1.85	15.14	1.89	0.48
AUG308_plag2_G11_191	AUG308	MI	plag_MI	5.56	71.81	3.12	1.89	14.84	1.72	0.40
AUG308_plag2_G12_192	AUG308	MI	plag_MI	-	-	-	-	-	-	-
AUG308_plag2_G12_193	AUG308	MI	plag_MI	6.28	73.28	2.34	1.88	14.36	1.06	0.33
AUG308_plag2_G12_194	AUG308	MI	plag_MI	5.15	73.58	2.17	1.96	15.40	0.98	0.27
AUG308_plag2_G13_195	AUG308	MI	plag_MI	3.50	72.09	3.66	1.90	15.30	2.08	0.52
AUG308_plag2_G13_196	AUG308	MI	plag_MI	6.28	69.92	3.51	1.79	15.32	1.82	0.45
AUG308_small_G60_207	AUG308	MI	opx_MI	3.87	71.86	2.99	1.55	12.97	4.98	1.18
AUG308_small_G58_209	AUG308	MI	opx_MI	3.77	73.48	2.51	1.50	12.06	4.35	1.20
AUG308_small_G65_2_212	AUG308	MI	opx_MI	5.01	69.77	3.38	1.47	14.28	3.83	1.29
AUG308_small_G65_2_213	AUG308	MI	opx_MI	4.05	74.90	2.23	1.48	13.23	2.67	0.64
AUG308_small_G102_216	AUG308	MI	cpx_MI	5.06	58.65	6.58	0.97	18.84	5.11	2.00
AUG308_small_G170_217	AUG308	MI	cpx_MI	5.76	63.78	4.43	1.69	15.17	5.83	1.63
AUG308_small_G97_218	AUG308	MI	opx_MI	3.93	74.33	2.08	1.78	11.52	4.00	1.19
AUG308_small_G97_other_220	AUG308	MI	opx_MI	6.03	71.85	2.13	2.07	12.11	4.18	0.78
AUG308_small_G97_other2_185	AUG308	MI	opx_MI	3.97	73.98	2.03	1.83	12.35	3.92	1.28
AUG_308_G13_MI88, 189 avg	AUG308	MI	plag_MI	5.78	71.36	2.91	1.96	15.33	1.56	0.49
AUG_308_G04a_MI92, 193 avg	AUG308	MI	cpx_MI	3.65	67.99	4.29	1.83	15.56	3.91	1.36
AUG_308_G04c_MI94	AUG308	MI	cpx_MI	4.75	67.66	3.74	2.01	16.11	3.37	1.36
AUG_308_G08a_MIun2_289	AUG308	MI	plag_MI	5.17	67.84	3.97	1.85	16.41	2.80	0.95
AUG_308_G08b_MI98	AUG308	MI	plag_MI	4.76	66.52	4.70	1.59	18.29	2.42	0.71
AUG_308_G08c_MI00	AUG308	MI	plag_MI	5.39	69.46	3.43	1.91	16.01	2.18	0.70

Supplementary Table 1D (continued).

Analysis #	Glass Type	Host Mineral	TiO2 wt%	MnO wt%	P2O5 wt%	Cl wt%	S ppm	H2O wt% by difference w matrix correction	un-normalized total	Host Mg#	Host An#
AUGUSTINE 2006: Low Silica Andesite (LSA) tephra											
AUG308_plag2_G11_matrixG_176	matrix glass	-	0.97	-	-	0.30	-34	1.19	98.81	-	-
AUG308_plag2_G11_matrixG_182	matrix glass	-	0.62	-	-	0.22	69	-2.07	102.07	-	-
AUG308_small_G65_2_matrixG_162	matrix glass	-	0.83	-	-	0.26	-5	-2.06	102.06	-	-
AUG308_small_G170_matrixG_167	matrix glass	-	0.80	-	-	0.25	28	1.16	98.84	-	-
AUG_308_G06_matrixG_205	matrix glass	-	0.94	0.14	0.24	0.27	9	1.57	98.43	-	-
AUG_308_G06_matrixG_206	matrix glass	-	0.97	0.11	0.23	0.25	-16	1.71	98.29	-	-
AUG_308_Ol3_rim_glass_228	matrix glass	-	0.98	0.14	0.22	0.33	58	1.67	98.33	-	-
AUG_308_G02 matrixG	matrix glass	-	-	-	-	-	-	-	-	-	-
AUG_308_G08 matrixG	matrix glass	-	-	-	-	-	-	-	-	-	-
AUG_308_Ol3_RE_223	re-entrant	ol_RE	1.34	0.14	0.23	0.40	377	-0.94	100.94	-	-
AUG308_plag2_G03_180	MI	plag_MI	-	-	-	-	-	-	-	-	53.7
AUG308_plag2_G04_182	MI	plag_MI	0.22	-	-	0.28	137	2.60	97.40	-	-
AUG308_plag2_G04_183	MI	plag_MI	0.28	-	-	0.38	148	1.74	98.26	-	57.8
AUG308_plag2_G09_189	MI	plag_MI	0.44	-	-	0.42	248	3.35	96.65	-	76.9
AUG308_plag2_G09_171	MI	plag_MI	0.45	-	-	0.43	180	2.09	97.91	-	76.9
AUG308_plag2_G10_190	MI	plag_MI	0.43	-	-	0.40	361	1.19	98.81	-	54.8
AUG308_plag2_G11_191	MI	plag_MI	0.25	-	-	0.36	180	2.53	97.47	-	51.8
AUG308_plag2_G12_192	MI	plag_MI	-	-	-	-	-	-	-	-	54.7
AUG308_plag2_G12_193	MI	plag_MI	0.16	-	-	0.27	126	2.33	97.67	-	46.0
AUG308_plag2_G12_194	MI	plag_MI	0.14	-	-	0.27	119	1.02	98.98	-	48.3
AUG308_plag2_G13_195	MI	plag_MI	0.44	-	-	0.44	282	2.10	97.90	-	62.8
AUG308_plag2_G13_196	MI	plag_MI	0.48	-	-	0.37	258	2.13	97.87	-	50.0
AUG308_small_G60_207	MI	opx_MI	0.23	-	-	0.30	137	3.44	96.56	67.3	-
AUG308_small_G58_209	MI	opx_MI	0.68	-	-	0.30	499	1.48	98.52	-	-
AUG308_small_G65_2_212	MI	opx_MI	0.50	-	-	0.27	600	1.92	98.08	68.0	64.8
AUG308_small_G65_2_213	MI	opx_MI	0.36	-	-	0.38	174	5.43	94.57	-	-
AUG308_small_G102_216	MI	cpx_MI	1.79	-	-	0.34	2577	6.52	93.48	73.3	-
AUG308_small_G170_217	MI	cpx_MI	1.16	-	-	0.42	442	2.95	97.05	74.3	-
AUG308_small_G97_218	MI	opx_MI	0.79	-	-	0.33	121	1.43	98.57	-	-
AUG308_small_G97_other_220	MI	opx_MI	0.51	-	-	0.32	-23	-0.58	100.58	-	-
AUG308_small_G97_other2_185	MI	opx_MI	0.28	-	-	0.32	146	3.32	96.68	-	-
AUG_308_G13_MI88, 189 avg	MI	plag_MI	0.22	0.05	0.04	0.29	130	3.16	96.84	-	51.2
AUG_308_G04a_MI92, 193 avg	MI	cpx_MI	0.84	0.09	0.06	0.39	339	5.74	94.26	77.4	-
AUG_308_G04c_MI94	MI	cpx_MI	0.45	0.07	0.06	0.39	291	6.21	93.79	-	-
AUG_308_G08a_MIun2_289	MI	plag_MI	0.44	0.09	0.06	0.39	275	4.71	95.29	-	70.6
AUG_308_G08b_MI98	MI	plag_MI	0.44	0.07	0.10	0.37	462	3.76	96.24	-	70.6
AUG_308_G08c_MI00	MI	plag_MI	0.36	0.07	0.08	0.36	373	5.42	94.58	-	70.6

Supplementary Table 1D (continued).

Analysis #	Glass Type	Host Mineral	% PEC (olivine mass)	PEC correction coefficient	Temperature of MI entrapment (°C) (Petrolog3)	H2O in melt (wt%) (FTIR)	CO2 in melt (ppm) (FTIR)	δ34S (‰)	δ34S 1σ uncertainy (‰)
AUGUSTINE 2006: Low Silica Andesite (LSA) tephra									
AUG308_plag2_G11_matrixG_176	matrix glass	-	-	-	-	-	-	-	-
AUG308_plag2_G11_matrixG_182	matrix glass	-	-	-	-	-	-	-	-
AUG308_small_G65_2_matrixG_162	matrix glass	-	-	-	-	-	-	-	-
AUG308_small_G170_matrixG_167	matrix glass	-	-	-	-	-	-	-	-
AUG_308_G06_matrixG_205	matrix glass	-	-	-	-	-	-	-	-
AUG_308_G06_matrixG_206	matrix glass	-	-	-	-	-	-	-	-
AUG_308_Ol3_rim_glass_228	matrix glass	-	-	-	-	-	-	-	-
AUG_308_G02 matrixG	matrix glass	-	-	-	-	-	-	-	-
AUG_308_G08 matrixG	matrix glass	-	-	-	-	-	-	-	-
AUG_308_Ol3_RE_223	re-entrant	ol_RE	-	-	-	-	-	-	-
AUG308_plag2_G03_180	MI	plag_MI	-	-	-	-	-	-	-
AUG308_plag2_G04_182	MI	plag_MI	-	-	-	-	-	-	-
AUG308_plag2_G04_183	MI	plag_MI	-	-	-	-	-	-	-
AUG308_plag2_G09_189	MI	plag_MI	-	-	-	-	-	-	-
AUG308_plag2_G09_171	MI	plag_MI	-	-	-	-	-	-	-
AUG308_plag2_G10_190	MI	plag_MI	-	-	-	-	-	-	-
AUG308_plag2_G11_191	MI	plag_MI	-	-	-	-	-	-	-
AUG308_plag2_G12_192	MI	plag_MI	-	-	-	-	-	-	-
AUG308_plag2_G12_193	MI	plag_MI	-	-	-	-	-	-	-
AUG308_plag2_G12_194	MI	plag_MI	-	-	-	-	-	-	-
AUG308_plag2_G13_195	MI	plag_MI	-	-	-	-	-	-	-
AUG308_plag2_G13_196	MI	plag_MI	-	-	-	-	-	-	-
AUG308_small_G60_207	MI	opx_MI	-	-	-	-	-	-	-
AUG308_small_G58_209	MI	opx_MI	-	-	-	-	-	-	-
AUG308_small_G65_2_212	MI	opx_MI	-	-	-	-	-	-	-
AUG308_small_G65_2_213	MI	opx_MI	-	-	-	-	-	-	-
AUG308_small_G102_216	MI	cpx_MI	-	-	-	-	-	-	-
AUG308_small_G170_217	MI	cpx_MI	-	-	-	-	-	-	-
AUG308_small_G97_218	MI	opx_MI	-	-	-	-	-	-	-
AUG308_small_G97_other_220	MI	opx_MI	-	-	-	-	-	-	-
AUG308_small_G97_other2_185	MI	opx_MI	-	-	-	-	-	-	-
AUG_308_G13_MI88, 189 avg	MI	plag_MI	-	-	-	3.61	26	4.5	1.1
AUG_308_G04a_MI92, 193 avg	MI	cpx_MI	-	-	-	1.91	bdl	5.2	0.5
AUG_308_G04c_MI94	MI	cpx_MI	-	-	-	-	-	-	-
AUG_308_G08a_MIun2_289	MI	plag_MI	-	-	-	1.10	bdl	4.9	0.6
AUG_308_G08b_MI98	MI	plag_MI	-	-	-	1.12	bdl	8.4	0.5
AUG_308_G08c_MI00	MI	plag_MI	-	-	-	-	-	-	-

Supplementary Table 1D (continued).

Analysis #	Glass Type	Host Mineral	Fe3+/ΣFe % [Fe-XANES]	ΔQFM [Fe-XANES]	S6+/ΣS % [S-XANES]
AUGUSTINE 2006: Low Silica Andesite (LSA) tephra					
AUG308_plag2_G11_matrixG_176	matrix glass	-	-	-	-
AUG308_plag2_G11_matrixG_182	matrix glass	-	-	-	-
AUG308_small_G65_2_matrixG_162	matrix glass	-	-	-	-
AUG308_small_G170_matrixG_167	matrix glass	-	-	-	-
AUG_308_G06_matrixG_205	matrix glass	-	18.0	-0.35	-
AUG_308_G06_matrixG_206	matrix glass	-	19.8	-0.05	-
AUG_308_Ol3_rim_glass_228	matrix glass	-	-	-	-
AUG_308_G02 matrixG	matrix glass	-	18.9	-0.19	49.6
AUG_308_G08 matrixG	matrix glass	-	18.0	-0.33	-
AUG_308_Ol3_RE_223	re-entrant	ol_RE	-	-	-
AUG308_plag2_G03_180	MI	plag_MI	-	-	73.1
AUG308_plag2_G04_182	MI	plag_MI	-	-	-
AUG308_plag2_G04_183	MI	plag_MI	-	-	78.4
AUG308_plag2_G09_189	MI	plag_MI	-	-	76.0
AUG308_plag2_G09_171	MI	plag_MI	-	-	-
AUG308_plag2_G10_190	MI	plag_MI	-	-	81.9
AUG308_plag2_G11_191	MI	plag_MI	-	-	-
AUG308_plag2_G12_192	MI	plag_MI	-	-	66.9
AUG308_plag2_G12_193	MI	plag_MI	-	-	42.6
AUG308_plag2_G12_194	MI	plag_MI	-	-	-
AUG308_plag2_G13_195	MI	plag_MI	-	-	73.4
AUG308_plag2_G13_196	MI	plag_MI	-	-	61.8
AUG308_small_G60_207	MI	opx_MI	-	-	66.7
AUG308_small_G58_209	MI	opx_MI	-	-	43.9
AUG308_small_G65_2_212	MI	opx_MI	-	-	54.0
AUG308_small_G65_2_213	MI	opx_MI	-	-	-
AUG308_small_G102_216	MI	cpx_MI	-	-	68.2
AUG308_small_G170_217	MI	cpx_MI	-	-	27.6
AUG308_small_G97_218	MI	opx_MI	-	-	33.4
AUG308_small_G97_other_220	MI	opx_MI	-	-	-
AUG308_small_G97_other2_185	MI	opx_MI	-	-	-
AUG_308_G13_MI88, 189 avg	MI	plag_MI	34.6	1.35	57.7
AUG_308_G04a_MI92, 193 avg	MI	cpx_MI	-	-	83.8
AUG_308_G04c_MI94	MI	cpx_MI	-	-	-
AUG_308_G08a_MIun2_289	MI	plag_MI	25.6	0.48	97.3
AUG_308_G08b_MI98	MI	plag_MI	32.3	1.27	82.2
AUG_308_G08c_MI00	MI	plag_MI	31.4	1.08	91.4

Supplementary Table 1D (continued).

Analysis Name	Sample Name	Glass Type	Host Mineral	Na2O wt%	SiO2 wt%	CaO wt%	K2O wt%	Al2O3 wt%	FeOT wt%	MgO wt%
AUG_308_G08d_MI99	AUG308	MI	plag_MI	5.20	69.42	3.46	1.94	16.20	2.17	0.71
AUG_308_G06a_MI01	AUG308	MI	plag_MI	5.23	69.75	3.84	1.87	16.12	1.75	0.54
AUG_308_G06b_MI02	AUG308	MI	plag_MI	4.71	71.21	3.26	1.91	16.28	1.65	0.43
AUG_308_G06c_MI03	AUG308	MI	plag_MI	5.44	70.51	3.37	1.94	16.25	1.49	0.45
AUG_308_G01_MIw_204	AUG308	MI	cpx_MI	4.30	68.34	4.68	0.78	13.30	5.30	1.67
AUG_308_G10a_MI07	AUG308	MI	plag_MI	5.01	71.80	3.18	1.94	15.61	1.34	0.40
AUG_308_G10b_MI08	AUG308	MI	plag_MI	5.69	70.16	3.35	1.89	15.98	1.61	0.49
AUG_308_Ol2a_MI09, 210 avg	AUG308	MI	ol_MI	3.27	46.08	12.65	0.38	22.09	7.60	6.07
AUG_308_Ol2b_MI11	AUG308	MI	ol_MI	3.21	45.67	12.49	0.39	22.86	7.53	5.92
AUG_308_Ol3_MI22	AUG308	MI	ol_MI	3.27	47.66	10.64	0.33	23.53	7.59	5.65
AUG_308_G15a_MI29	AUG308	MI	cpx_MI	4.84	72.01	2.81	1.92	13.63	2.87	0.96
AUG_308_G15b_MI30	AUG308	MI	cpx_MI	4.07	69.20	4.10	1.71	14.01	4.00	1.31
AUG_308_G14_MI33	AUG308	MI	opx_MI	4.21	73.66	2.81	1.69	13.59	2.09	0.76
AUG_308_G17_MI31, 232 avg	AUG308	MI	cpx_MI	4.28	64.22	5.82	1.35	17.55	3.97	2.02
AUG_308_G09	AUG308	MI	plag_MI	3.25	46.47	11.93	0.37	22.83	7.57	5.88
AUG_308_Ol3b	AUG308	MI	ol_MI	-	-	-	-	-	-	-
AUG_308_Ol10a	AUG308	MI	ol_MI	-	-	-	-	-	-	-
AUG_308_G07	AUG308	MI	plag_MI	-	-	-	-	-	-	-
AUG_308_G12a	AUG308	MI	plag_MI	-	-	-	-	-	-	-
AUG_308_G12b	AUG308	MI	plag_MI	-	-	-	-	-	-	-
AUG_308_G02a	AUG308	MI	cpx_MI	-	-	-	-	-	-	-
AUG_308_G14b	AUG308	MI	opx_MI	-	-	-	-	-	-	-
AUG_308_G16	AUG308	MI	cpx_MI	-	-	-	-	-	-	-
AUGUSTINE 2006: High Silica Andesite (HSA) pyroclastic flow										
AUG_HSA2_G07_matrixG	AUG_HSA2	matrix glass	-	-	-	-	-	-	-	-
AUG_HSA2_G14_matrixG_1	AUG_HSA2	matrix glass	-	-	-	-	-	-	-	-
AUG_HSA2_G14_matrixG_2	AUG_HSA2	matrix glass	-	-	-	-	-	-	-	-
AUG_HSA2_A_G26_matrixG_258	AUG_HSA2	matrix glass	-	5.12	77.60	1.38	1.56	11.48	1.88	0.37
AUG_HSA2_A_G26_matrixG_259	AUG_HSA2	matrix glass	-	4.51	77.32	1.72	1.49	12.19	1.84	0.35
AUG_HSA2_A_G36_matrixG_264	AUG_HSA2	matrix glass	-	5.28	77.33	1.39	1.51	12.34	1.28	0.28
AUG_HSA2_A_G36_matrixG_265	AUG_HSA2	matrix glass	-	5.19	78.05	1.33	1.59	11.50	1.48	0.26
AUG_HSA2_A_G45_matrixG_269	AUG_HSA2	matrix glass	-	5.47	69.86	4.17	0.87	17.80	1.28	0.17
AUG_HSA2_A_G46_matrixG_273	AUG_HSA2	matrix glass	-	5.29	78.79	1.14	1.58	10.81	1.50	0.26
AUG_HSA2_B_G16_matrixG_293	AUG_HSA2	matrix glass	-	4.18	78.70	1.23	1.58	10.79	2.38	0.30
AUG_HSA2_B_G16_matrixG_294	AUG_HSA2	matrix glass	-	5.06	70.24	4.46	0.85	17.09	1.84	0.16
AUG_HSA2_G05_matrixG_249	AUG_HSA2	matrix glass	-	4.88	76.67	1.70	1.48	12.87	1.47	0.28
AUG_HSA2_G15_matrixG_255	AUG_HSA2	matrix glass	-	4.58	80.28	1.28	1.49	9.61	1.67	0.31
AUG_HSA2_G11_RE_251	AUG_HSA2	re-entrant	opx_RE	5.25	74.64	1.78	1.63	13.85	1.69	0.42

Supplementary Table 1D (continued).

Analysis #	Glass Type	Host Mineral	TiO2 wt%	MnO wt%	P2O5 wt%	Cl wt%	S ppm	H2O wt% by difference w matrix correction	un-normalized total	Host Mg#	Host An#
AUG_308_G08d_MI99	MI	plag_MI	0.37	0.06	0.09	0.35	347	5.75	94.25	-	70.6
AUG_308_G06a_MI01	MI	plag_MI	0.36	0.06	0.07	0.40	217	4.15	95.85	-	-
AUG_308_G06b_MI02	MI	plag_MI	0.13	0.04	0.03	0.31	150	5.23	94.77	-	-
AUG_308_G06c_MI03	MI	plag_MI	0.11	0.05	0.03	0.32	156	4.58	95.42	-	-
AUG_308_G01_MIw_204	MI	cpx_MI	0.70	0.13	0.38	0.29	1311	7.27	92.73	-	-
AUG_308_G10a_MI07	MI	plag_MI	0.33	0.05	0.05	0.27	270	4.49	95.51	-	-
AUG_308_G10b_MI08	MI	plag_MI	0.37	0.05	0.04	0.33	285	4.37	95.63	-	-
AUG_308_Ol2a_MI09, 210 avg	MI	ol_MI	1.08	0.11	0.09	0.25	3527	3.95	96.05	85.0	-
AUG_308_Ol2b_MI11	MI	ol_MI	1.04	0.18	0.12	0.26	3518	3.99	96.01	85.0	-
AUG_308_Ol3_MI22	MI	ol_MI	0.59	0.09	0.09	0.23	3507	6.33	93.67	83.5	-
AUG_308_G15a_MI29	MI	cpx_MI	0.42	0.09	0.05	0.38	172	4.58	95.42	-	-
AUG_308_G15b_MI30	MI	cpx_MI	0.97	0.08	0.17	0.34	228	5.73	94.27	-	-
AUG_308_G14_MI33	MI	opx_MI	0.73	0.10	0.01	0.32	142	3.90	96.10	-	-
AUG_308_G17_MI31, 232 avg	MI	cpx_MI	0.34	0.09	0.11	0.21	249	5.70	94.30	-	-
AUG_308_G09	MI	plag_MI	0.90	0.13	0.10	0.25	3517	-	-	-	-
AUG_308_Ol3b	MI	ol_MI	-	-	-	-	-	-	-	-	-
AUG_308_Ol10a	MI	ol_MI	-	-	-	-	-	-	-	-	-
AUG_308_G07	MI	plag_MI	-	-	-	-	-	-	-	-	-
AUG_308_G12a	MI	plag_MI	-	-	-	-	-	-	-	-	-
AUG_308_G12b	MI	plag_MI	-	-	-	-	-	-	-	-	-
AUG_308_G02a	MI	cpx_MI	-	-	-	-	-	-	-	-	-
AUG_308_G14b	MI	opx_MI	-	-	-	-	-	-	-	-	-
AUG_308_G16	MI	cpx_MI	-	-	-	-	-	-	-	-	-
AUGUSTINE 2006: High Silica Andesite (HSA) pyroclastic flow											
AUG_HSA2_G07_matrixG	matrix glass	-	-	-	-	-	-	-	-	-	-
AUG_HSA2_G14_matrixG_1	matrix glass	-	-	-	-	-	-	-	-	-	-
AUG_HSA2_G14_matrixG_2	matrix glass	-	-	-	-	-	-	-	-	-	-
AUG_HSA2_A_G26_matrixG_258	matrix glass	-	0.41	-	-	0.23	-9	-0.75	100.75	-	-
AUG_HSA2_A_G26_matrixG_259	matrix glass	-	0.40	-	-	0.20	31	1.03	98.97	-	-
AUG_HSA2_A_G36_matrixG_264	matrix glass	-	0.40	-	-	0.18	27	0.68	99.32	-	-
AUG_HSA2_A_G36_matrixG_265	matrix glass	-	0.34	-	-	0.20	33	-1.71	101.71	-	-
AUG_HSA2_A_G45_matrixG_269	matrix glass	-	0.26	-	-	0.11	2	1.63	98.37	-	-
AUG_HSA2_A_G46_matrixG_273	matrix glass	-	0.41	-	-	0.19	20	-0.44	100.44	-	-
AUG_HSA2_B_G16_matrixG_293	matrix glass	-	0.64	-	-	0.18	97	0.68	99.32	-	-
AUG_HSA2_B_G16_matrixG_294	matrix glass	-	0.21	-	-	0.10	77	-1.66	101.66	-	-
AUG_HSA2_G05_matrixG_249	matrix glass	-	0.39	0.06	0.04	0.16	25	0.50	99.50	-	-
AUG_HSA2_G15_matrixG_255	matrix glass	-	0.47	0.08	0.03	0.20	105	4.98	95.02	-	-
AUG_HSA2_G11_RE_251	re-entrant	opx_RE	0.35	0.08	0.04	0.24	180	3.47	96.53	-	-

Supplementary Table 1D (continued).

Analysis #	Glass Type	Host Mineral	% PEC (olivine mass)	PEC correction coefficient	Temperature of MI entrapment (°C) (Petrolog3)	H2O in melt (wt%) (FTIR)	CO2 in melt (ppm) (FTIR)	δ34S (‰)	δ34S 1σ uncertainy (‰)
AUG_308_G08d_MI99	MI	plag_MI	-	-	-	1.12	na	8.6	0.6
AUG_308_G06a_MI01	MI	plag_MI	-	-	-	0.37	bdl	9.2	0.7
AUG_308_G06b_MI02	MI	plag_MI	-	-	-	1.94	bdl	-	-
AUG_308_G06c_MI03	MI	plag_MI	-	-	-	2.24	bdl	6.1	1.0
AUG_308_G01_MIw_204	MI	cpx_MI	-	-	-	1.15	139	7.7	2.2
AUG_308_G10a_MI07	MI	plag_MI	-	-	-	2.29	70	5.4	0.6
AUG_308_G10b_MI08	MI	plag_MI	-	-	-	2.16	84	-	-
AUG_308_Ol2a_MI09, 210 avg	MI	ol_MI	11.2	0.9	1006	-	-	6.3	0.6
AUG_308_Ol2b_MI11	MI	ol_MI	-11.7	1.1	1008	-	-	6.2	0.6
AUG_308_Ol3_MI22	MI	ol_MI	13.5	0.9	1002	1.00	bdl	5.9	0.4
AUG_308_G15a_MI29	MI	cpx_MI	-	-	-	-	-	-	-
AUG_308_G15b_MI30	MI	cpx_MI	-	-	-	-	-	5.4	0.6
AUG_308_G14_MI33	MI	opx_MI	-	-	-	-	-	4.9	0.9
AUG_308_G17_MI31, 232 avg	MI	cpx_MI	-	-	-	-	-	3.7	0.6
AUG_308_G09	MI	plag_MI	-	-	-	1.62	55	-	-
AUG_308_Ol3b	MI	ol_MI	-	-	-	1.01	bdl	-	-
AUG_308_Ol10a	MI	ol_MI	-	-	-	0.26	bdl	-	-
AUG_308_G07	MI	plag_MI	-	-	-	-	-	-	-
AUG_308_G12a	MI	plag_MI	-	-	-	-	-	-	-
AUG_308_G12b	MI	plag_MI	-	-	-	-	-	-	-
AUG_308_G02a	MI	cpx_MI	-	-	-	-	-	-	-
AUG_308_G14b	MI	opx_MI	-	-	-	-	-	-	-
AUG_308_G16	MI	cpx_MI	-	-	-	-	-	-	-
AUGUSTINE 2006: High Silica Andesite (HSA) pyroclastic flow									
AUG_HSA2_G07_matrixG	matrix glass	-	-	-	-	-	-	-	-
AUG_HSA2_G14_matrixG_1	matrix glass	-	-	-	-	-	-	-	-
AUG_HSA2_G14_matrixG_2	matrix glass	-	-	-	-	-	-	-	-
AUG_HSA2_A_G26_matrixG_258	matrix glass	-	-	-	-	-	-	-	-
AUG_HSA2_A_G26_matrixG_259	matrix glass	-	-	-	-	-	-	-	-
AUG_HSA2_A_G36_matrixG_264	matrix glass	-	-	-	-	-	-	-	-
AUG_HSA2_A_G36_matrixG_265	matrix glass	-	-	-	-	-	-	-	-
AUG_HSA2_A_G45_matrixG_269	matrix glass	-	-	-	-	-	-	-	-
AUG_HSA2_A_G46_matrixG_273	matrix glass	-	-	-	-	-	-	-	-
AUG_HSA2_B_G16_matrixG_293	matrix glass	-	-	-	-	-	-	-	-
AUG_HSA2_B_G16_matrixG_294	matrix glass	-	-	-	-	-	-	-	-
AUG_HSA2_G05_matrixG_249	matrix glass	-	-	-	-	-	-	-	-
AUG_HSA2_G15_matrixG_255	matrix glass	-	-	-	-	-	-	-	-
AUG_HSA2_G11_RE_251	re-entrant	opx_RE	-	-	-	1.68	bdl	5.9	0.8

Supplementary Table 1D (continued).

Analysis #	Glass Type	Host Mineral	Fe3+/ΣFe % [Fe-XANES]	ΔQFM [Fe-XANES]	S6+/ΣS % [S-XANES]
AUG_308_G08d_MI99	MI	plag_MI	29.4	0.90	93.0
AUG_308_G06a_MI01	MI	plag_MI	33.3	1.26	92.0
AUG_308_G06b_MI02	MI	plag_MI	38.2	1.85	73.9
AUG_308_G06c_MI03	MI	plag_MI	32.0	1.12	86.7
AUG_308_G01_MIw_204	MI	cpx_MI	-	-	92.7
AUG_308_G10a_MI07	MI	plag_MI	31.5	1.12	78.0
AUG_308_G10b_MI08	MI	plag_MI	33.6	1.25	91.1
AUG_308_Ol2a_MI09, 210 avg	MI	ol_MI	-	-	99.8
AUG_308_Ol2b_MI11	MI	ol_MI	-	-	98.2
AUG_308_Ol3_MI22	MI	ol_MI	-	-	100.8
AUG_308_G15a_MI29	MI	cpx_MI	-	-	89.3
AUG_308_G15b_MI30	MI	cpx_MI	-	-	88.4
AUG_308_G14_MI33	MI	opx_MI	-	-	89.2
AUG_308_G17_MI31, 232 avg	MI	cpx_MI	-	-	94.0
AUG_308_G09	MI	plag_MI	-	-	81.4
AUG_308_Ol3b	MI	ol_MI	-	-	-
AUG_308_Ol10a	MI	ol_MI	-	-	-
AUG_308_G07	MI	plag_MI	37.1	1.77	99.6
AUG_308_G12a	MI	plag_MI	33.6	1.43	-
AUG_308_G12b	MI	plag_MI	39.5	1.99	-
AUG_308_G02a	MI	cpx_MI	-	-	90.3
AUG_308_G14b	MI	opx_MI	-	-	83.0
AUG_308_G16	MI	cpx_MI	-	-	76.7
AUGUSTINE 2006: High Silica Andesite (HSA) pyroclastic flow					
AUG_HSA2_G07_matrixG	matrix glass	-	35.2	1.53	-
AUG_HSA2_G14_matrixG_1	matrix glass	-	25.7	0.54	-
AUG_HSA2_G14_matrixG_2	matrix glass	-	33.8	1.39	-
AUG_HSA2_A_G26_matrixG_258	matrix glass	-	-	-	-
AUG_HSA2_A_G26_matrixG_259	matrix glass	-	-	-	-
AUG_HSA2_A_G36_matrixG_264	matrix glass	-	-	-	-
AUG_HSA2_A_G36_matrixG_265	matrix glass	-	-	-	-
AUG_HSA2_A_G45_matrixG_269	matrix glass	-	-	-	-
AUG_HSA2_A_G46_matrixG_273	matrix glass	-	-	-	-
AUG_HSA2_B_G16_matrixG_293	matrix glass	-	-	-	-
AUG_HSA2_B_G16_matrixG_294	matrix glass	-	-	-	-
AUG_HSA2_G05_matrixG_249	matrix glass	-	-	-	-
AUG_HSA2_G15_matrixG_255	matrix glass	-	-	-	-
AUG_HSA2_G11_RE_251	re-entrant	opx_RE	-	-	-

Supplementary Table 1D (continued).

Analysis Name	Sample Name	Glass Type	Host Mineral	Na2O wt%	SiO2 wt%	CaO wt%	K2O wt%	Al2O3 wt%	FeOT wt%	MgO wt%
AUG_HSA2_G11_RE_252	AUG_HSA2	re-entrant	opx_RE	4.91	72.48	2.13	1.62	15.49	2.16	0.48
AUG_HSA2_G12_RE	AUG_HSA2	re-entrant	opx_RE	-	-	-	-	-	-	-
AUG_HSA2_A_G17	AUG_HSA2	MI	quartz_MI	-	-	-	-	-	-	-
AUG_HSA2_A_G25a	AUG_HSA2	MI	amph_MI	-	-	-	-	-	-	-
AUG_HSA2_A_G25b	AUG_HSA2	MI	amph_MI	-	-	-	-	-	-	-
AUG_HSA2_A_G26_75_257	AUG_HSA2	MI	amph_MI	5.59	74.21	2.06	1.45	13.39	2.08	0.54
AUG_HSA2_A_G33_77_261	AUG_HSA2	MI	opx_MI	5.75	71.20	3.02	1.07	14.58	2.97	0.82
AUG_HSA2_A_G34_262	AUG_HSA2	MI	opx_MI	5.68	72.49	2.98	0.72	13.29	3.42	0.56
AUG_HSA2_A_G36_78_263	AUG_HSA2	MI	plag_MI	5.06	75.06	2.27	1.67	13.13	1.80	0.50
AUG_HSA2_A_G40_80_266	AUG_HSA2	MI	plag_MI	4.66	70.23	4.76	1.02	17.48	1.19	0.39
AUG_HSA2_A_G40_80_267	AUG_HSA2	MI	plag_MI	5.37	68.14	5.13	1.00	18.61	1.13	0.36
AUG_HSA2_A_G45_83_268	AUG_HSA2	MI	opx_MI	4.57	73.73	2.67	1.12	13.95	2.76	0.62
AUG_HSA2_A_G45_270	AUG_HSA2	MI	opx_MI	6.38	75.21	1.57	1.52	12.33	1.94	0.35
AUG_HSA2_A_G46_88_271	AUG_HSA2	MI	plag_MI	5.13	75.06	2.11	1.50	13.34	1.73	0.57
AUG_HSA2_A_G46_90_272	AUG_HSA2	MI	plag_MI	5.82	74.41	2.19	1.52	13.33	1.66	0.53
AUG_HSA2_A_G47_92_274	AUG_HSA2	MI	plag_MI	5.24	74.66	1.98	1.66	13.12	2.16	0.68
AUG_HSA2_A_G47_91	AUG_HSA2	MI	plag_MI	5.07	74.70	2.00	1.61	13.34	1.92	0.62
AUG_HSA2_A_G48_95	AUG_HSA2	MI	plag_MI	5.21	75.31	1.99	1.61	13.22	1.52	0.56
AUG_HSA2_A_G48_97_277	AUG_HSA2	MI	plag_MI	5.94	75.50	1.90	1.35	12.96	1.49	0.53
AUG_HSA2_A_G63_102_278	AUG_HSA2	MI	amph_MI	6.29	73.19	2.06	1.48	13.72	2.07	0.55
AUG_HSA2_A_G63_InApatite_279	AUG_HSA2	MI	apatite_MI	5.71	72.80	3.10	1.14	13.91	2.05	0.64
AUG_HSA2_A_G52_101_281	AUG_HSA2	MI	plag_MI	5.54	75.54	2.00	1.49	12.86	1.54	0.52
AUG_HSA2_A_G72_105_282	AUG_HSA2	MI	opx_MI	5.22	73.00	2.48	1.17	13.96	2.58	0.87
AUG_HSA2_A_G72_other_283	AUG_HSA2	MI	opx_MI	5.71	74.69	1.68	1.51	13.15	2.16	0.39
AUG_HSA2_A_G72b_107_284	AUG_HSA2	MI	amph_MI	5.39	77.87	1.25	1.49	11.05	1.92	0.38
AUG_HSA2_A_G89_109_285	AUG_HSA2	MI	cpx_MI	6.25	74.44	1.24	1.47	13.56	2.04	0.38
AUG_HSA2_A_G100_110_286	AUG_HSA2	MI	amph_MI	5.75	75.46	1.75	1.47	12.38	2.03	0.47
AUG_HSA2_A_G107_111_287	AUG_HSA2	MI	amph_MI	7.00	74.59	1.46	1.53	12.34	1.94	0.45
AUG_HSA2_A_G128_113_288	AUG_HSA2	MI	plag_MI	5.40	76.70	1.34	1.49	11.47	2.27	0.64
AUG_HSA2_A_G134_114_289	AUG_HSA2	MI	cpx_MI	5.82	72.36	3.65	1.37	10.82	2.35	3.05
AUG_HSA2_A_G134_lower_290	AUG_HSA2	MI	cpx_MI	8.36	73.63	1.44	1.49	12.07	1.82	0.54
AUG_HSA2_B_G16_292	AUG_HSA2	MI	Fe-Ti oxide_MI	4.28	74.37	2.22	1.47	13.37	3.54	0.31
AUG_HSA2_B_G25_ilmenite_296	AUG_HSA2	MI	Fe-Ti oxide_MI	2.79	74.66	1.91	1.29	12.66	4.10	0.34
AUG_HSA2_B_G25_magnetite_297	AUG_HSA2	MI	Fe-Ti oxide_MI	4.69	74.29	2.46	1.07	12.79	3.51	0.44
AUG_HSA2_B_G26_126_295	AUG_HSA2	MI	amph_MI	5.34	75.87	1.75	1.45	12.63	1.97	0.45
AUG_HSA2_B_G32_other_300	AUG_HSA2	MI	plag_MI	6.57	72.46	2.02	1.74	13.25	2.12	0.72
AUG_HSA2_B_G32_128_304	AUG_HSA2	MI	plag_MI	4.18	76.33	1.68	1.62	12.16	2.46	0.52
AUG_HSA2_G04_MI42,243 avg	AUG_HSA2	MI	cpx_MI	4.64	71.43	2.96	1.17	15.21	2.84	1.03

Supplementary Table 1D (continued).

Analysis #	Glass Type	Host Mineral	TiO2 wt%	MnO wt%	P2O5 wt%	Cl wt%	S ppm	H2O wt% by difference w matrix correction	un-normalized total	Host Mg#	Host An#
AUG_HSA2_G11_RE_252	re-entrant	opx_RE	0.36	0.08	0.04	0.22	255	5.10	94.90	-	-
AUG_HSA2_G12_RE	re-entrant	opx_RE	-	-	-	-	-	-	-	-	-
AUG_HSA2_A_G17	MI	quartz_MI	-	-	-	-	-	-	-	-	-
AUG_HSA2_A_G25a	MI	amph_MI	-	-	-	-	-	-	-	-	-
AUG_HSA2_A_G25b	MI	amph_MI	-	-	-	-	-	-	-	-	-
AUG_HSA2_A_G26_75_257	MI	amph_MI	0.36	-	-	0.25	190	0.10	99.90	69.2	-
AUG_HSA2_A_G33_77_261	MI	opx_MI	0.34	-	-	0.17	294	4.94	95.06	-	-
AUG_HSA2_A_G34_262	MI	opx_MI	0.44	-	-	0.34	246	0.72	99.28	-	-
AUG_HSA2_A_G36_78_263	MI	plag_MI	0.23	-	-	0.24	34	5.20	94.80	-	86.2
AUG_HSA2_A_G40_80_266	MI	plag_MI	0.14	-	-	0.12	22	2.65	97.35	-	81.3
AUG_HSA2_A_G40_80_267	MI	plag_MI	0.15	-	-	0.12	117	5.15	94.85	-	81.3
AUG_HSA2_A_G45_83_268	MI	opx_MI	0.31	-	-	0.19	305	4.34	95.66	69.8	-
AUG_HSA2_A_G45_270	MI	opx_MI	0.42	-	-	0.22	153	-0.54	100.54	-	-
AUG_HSA2_A_G46_88_271	MI	plag_MI	0.28	-	-	0.25	26	6.41	93.59	-	89.0
AUG_HSA2_A_G46_90_272	MI	plag_MI	0.29	-	-	0.22	90	5.55	94.45	-	52.8
AUG_HSA2_A_G47_92_274	MI	plag_MI	0.15	-	-	0.31	134	4.78	95.22	67.5	49.5
AUG_HSA2_A_G47_91	MI	plag_MI	0.44	-	-	0.31	162	6.60	93.40	67.5	49.5
AUG_HSA2_A_G48_95	MI	plag_MI	0.19	-	-	0.20	90	5.51	94.49	-	50.6
AUG_HSA2_A_G48_97_277	MI	plag_MI	0.14	-	-	0.17	29	5.18	94.82	-	57.7
AUG_HSA2_A_G63_102_278	MI	amph_MI	0.34	-	-	0.24	200	0.43	99.57	68.4	-
AUG_HSA2_A_G63_InApatite_279	MI	apatite_MI	0.37	-	-	0.20	253	2.52	97.48	-	-
AUG_HSA2_A_G52_101_281	MI	plag_MI	0.27	-	-	0.22	91	2.54	97.46	-	83.0
AUG_HSA2_A_G72_105_282	MI	opx_MI	0.43	-	-	0.20	283	4.24	95.76	70.8	-
AUG_HSA2_A_G72_other_283	MI	opx_MI	0.41	-	-	0.24	124	0.19	99.81	70.8	-
AUG_HSA2_A_G72b_107_284	MI	amph_MI	0.39	-	-	0.23	120	1.74	98.26	68.4	52.3
AUG_HSA2_A_G89_109_285	MI	cpx_MI	0.34	-	-	0.24	145	2.29	97.71	71.4	-
AUG_HSA2_A_G100_110_286	MI	amph_MI	0.40	-	-	0.22	128	-0.61	100.61	69.6	-
AUG_HSA2_A_G107_111_287	MI	amph_MI	0.43	-	-	0.22	104	-0.97	100.97	68.8	-
AUG_HSA2_A_G128_113_288	MI	plag_MI	0.41	-	-	0.24	84	0.03	99.97	-	90.5
AUG_HSA2_A_G134_114_289	MI	cpx_MI	0.38	-	-	0.18	97	-1.83	101.83	72.2	-
AUG_HSA2_A_G134_lower_290	MI	cpx_MI	0.39	-	-	0.22	157	0.00	100.00	-	-
AUG_HSA2_B_G16_292	MI	Fe-Ti oxide_MI	0.18	-	-	0.19	283	0.70	99.30	-	-
AUG_HSA2_B_G25_ilmenite_296	MI	Fe-Ti oxide_MI	1.95	-	-	0.27	41	2.60	97.40	-	-
AUG_HSA2_B_G25_magnetite_297	MI	Fe-Ti oxide_MI	0.49	-	-	0.17	226	0.26	99.74	-	-
AUG_HSA2_B_G26_126_295	MI	amph_MI	0.32	-	-	0.21	51	3.30	96.70	67.6	-
AUG_HSA2_B_G32_other_300	MI	plag_MI	0.33	-	-	0.76	76	2.29	97.71	-	-
AUG_HSA2_B_G32_128_304	MI	plag_MI	0.21	-	-	0.82	137	2.49	97.51	-	90.4
AUG_HSA2_G04_MI42,243 avg	MI	cpx_MI	0.29	0.15	0.07	0.18	259	5.94	94.06	-	-

Supplementary Table 1D (continued).

Analysis #	Glass Type	Host Mineral	% PEC (olivine mass)	PEC correction coefficient	Temperature of MI entrapment (°C) (Petrolog3)	H2O in melt (wt%) (FTIR)	CO2 in melt (ppm) (FTIR)	δ34S (‰)	δ34S 1σ uncertainy (‰)
AUG_HSA2_G11_RE_252	re-entrant	opx_RE	-	-	-	-	-	-	-
AUG_HSA2_G12_RE	re-entrant	opx_RE	-	-	-	-	-	-	-
AUG_HSA2_A_G17	MI	quartz_MI	-	-	-	-	-	-	-
AUG_HSA2_A_G25a	MI	amph_MI	-	-	-	-	-	-	-
AUG_HSA2_A_G25b	MI	amph_MI	-	-	-	-	-	-	-
AUG_HSA2_A_G26_75_257	MI	amph_MI	-	-	-	-	-	-	-
AUG_HSA2_A_G33_77_261	MI	opx_MI	-	-	-	-	-	-	-
AUG_HSA2_A_G34_262	MI	opx_MI	-	-	-	-	-	-	-
AUG_HSA2_A_G36_78_263	MI	plag_MI	-	-	-	-	-	-	-
AUG_HSA2_A_G40_80_266	MI	plag_MI	-	-	-	-	-	-	-
AUG_HSA2_A_G40_80_267	MI	plag_MI	-	-	-	-	-	-	-
AUG_HSA2_A_G45_83_268	MI	opx_MI	-	-	-	-	-	-	-
AUG_HSA2_A_G45_270	MI	opx_MI	-	-	-	-	-	-	-
AUG_HSA2_A_G46_88_271	MI	plag_MI	-	-	-	-	-	-	-
AUG_HSA2_A_G46_90_272	MI	plag_MI	-	-	-	-	-	-	-
AUG_HSA2_A_G47_92_274	MI	plag_MI	-	-	-	-	-	-	-
AUG_HSA2_A_G47_91	MI	plag_MI	-	-	-	-	-	-	-
AUG_HSA2_A_G48_95	MI	plag_MI	-	-	-	-	-	-	-
AUG_HSA2_A_G48_97_277	MI	plag_MI	-	-	-	-	-	-	-
AUG_HSA2_A_G63_102_278	MI	amph_MI	-	-	-	-	-	-	-
AUG_HSA2_A_G63_InApatite_279	MI	apatite_MI	-	-	-	-	-	-	-
AUG_HSA2_A_G52_101_281	MI	plag_MI	-	-	-	-	-	-	-
AUG_HSA2_A_G72_105_282	MI	opx_MI	-	-	-	-	-	-	-
AUG_HSA2_A_G72_other_283	MI	opx_MI	-	-	-	-	-	-	-
AUG_HSA2_A_G72b_107_284	MI	amph_MI	-	-	-	-	-	-	-
AUG_HSA2_A_G89_109_285	MI	cpx_MI	-	-	-	-	-	-	-
AUG_HSA2_A_G100_110_286	MI	amph_MI	-	-	-	-	-	-	-
AUG_HSA2_A_G107_111_287	MI	amph_MI	-	-	-	-	-	-	-
AUG_HSA2_A_G128_113_288	MI	plag_MI	-	-	-	-	-	-	-
AUG_HSA2_A_G134_114_289	MI	cpx_MI	-	-	-	-	-	-	-
AUG_HSA2_A_G134_lower_290	MI	cpx_MI	-	-	-	-	-	-	-
AUG_HSA2_B_G16_292	MI	Fe-Ti oxide_MI	-	-	-	-	-	-	-
AUG_HSA2_B_G25_ilmenite_296	MI	Fe-Ti oxide_MI	-	-	-	-	-	-	-
AUG_HSA2_B_G25_magnetite_297	MI	Fe-Ti oxide_MI	-	-	-	-	-	-	-
AUG_HSA2_B_G26_126_295	MI	amph_MI	-	-	-	-	-	-	-
AUG_HSA2_B_G32_other_300	MI	plag_MI	-	-	-	-	-	-	-
AUG_HSA2_B_G32_128_304	MI	plag_MI	-	-	-	-	-	-	-
AUG_HSA2_G04_MI42,243 avg	MI	cpx_MI	-	-	-	3.57	54	15.2	4.8

Supplementary Table 1D (continued).

Analysis #	Glass Type	Host Mineral	Fe3+/ΣFe % [Fe-XANES]	ΔQFM [Fe-XANES]	S6+/ΣS % [S-XANES]
AUG_HSA2_G11_RE_252	re-entrant	opx_RE	-	-	-
AUG_HSA2_G12_RE	re-entrant	opx_RE	-	-	61.8
AUG_HSA2_A_G17	MI	quartz_MI	-	-	56.3
AUG_HSA2_A_G25a	MI	amph_MI	-	-	80.2
AUG_HSA2_A_G25b	MI	amph_MI	-	-	36.6
AUG_HSA2_A_G26_75_257	MI	amph_MI	-	-	-
AUG_HSA2_A_G33_77_261	MI	opx_MI	-	-	57.9
AUG_HSA2_A_G34_262	MI	opx_MI	-	-	-
AUG_HSA2_A_G36_78_263	MI	plag_MI	-	-	-
AUG_HSA2_A_G40_80_266	MI	plag_MI	-	-	-
AUG_HSA2_A_G40_80_267	MI	plag_MI	-	-	-
AUG_HSA2_A_G45_83_268	MI	opx_MI	-	-	75.4
AUG_HSA2_A_G45_270	MI	opx_MI	-	-	29.9
AUG_HSA2_A_G46_88_271	MI	plag_MI	-	-	-
AUG_HSA2_A_G46_90_272	MI	plag_MI	-	-	-
AUG_HSA2_A_G47_92_274	MI	plag_MI	-	-	-
AUG_HSA2_A_G47_91	MI	plag_MI	-	-	-
AUG_HSA2_A_G48_95	MI	plag_MI	-	-	-
AUG_HSA2_A_G48_97_277	MI	plag_MI	-	-	-
AUG_HSA2_A_G63_102_278	MI	amph_MI	-	-	-
AUG_HSA2_A_G63_InApatite_279	MI	apatite_MI	-	-	91.3
AUG_HSA2_A_G52_101_281	MI	plag_MI	-	-	-
AUG_HSA2_A_G72_105_282	MI	opx_MI	-	-	81.9
AUG_HSA2_A_G72_other_283	MI	opx_MI	-	-	-
AUG_HSA2_A_G72b_107_284	MI	amph_MI	-	-	-
AUG_HSA2_A_G89_109_285	MI	cpx_MI	-	-	63.9
AUG_HSA2_A_G100_110_286	MI	amph_MI	-	-	-
AUG_HSA2_A_G107_111_287	MI	amph_MI	-	-	-
AUG_HSA2_A_G128_113_288	MI	plag_MI	-	-	-
AUG_HSA2_A_G134_114_289	MI	cpx_MI	-	-	-
AUG_HSA2_A_G134_lower_290	MI	cpx_MI	-	-	-
AUG_HSA2_B_G16_292	MI	Fe-Ti oxide_MI	-	-	23.5
AUG_HSA2_B_G25_ilmenite_296	MI	Fe-Ti oxide_MI	-	-	-
AUG_HSA2_B_G25_magnetite_297	MI	Fe-Ti oxide_MI	-	-	-
AUG_HSA2_B_G26_126_295	MI	amph_MI	-	-	-
AUG_HSA2_B_G32_other_300	MI	plag_MI	-	-	-
AUG_HSA2_B_G32_128_304	MI	plag_MI	-	-	1.0
AUG_HSA2_G04_MI42,243 avg	MI	cpx_MI	-	-	86.2

Supplementary Table 1D (continued).

Analysis Name	Sample Name	Glass Type	Host Mineral	Na2O wt%	SiO2 wt%	CaO wt%	K2O wt%	Al2O3 wt%	FeOT wt%	MgO wt%
AUG_HSA2_G01b_MI44	AUG_HSA2	MI	cpx_MI	5.18	70.01	4.54	1.42	13.59	2.91	1.46
AUG_HSA2_G01a_MI45	AUG_HSA2	MI	cpx_MI	4.71	70.62	4.46	1.34	12.57	3.04	2.45
AUG_HSA2_G05a_MI47	AUG_HSA2	MI	plag_MI	4.49	77.38	1.25	1.58	12.21	1.82	0.52
AUG_HSA2_G05b_MI48	AUG_HSA2	MI	plag_MI	4.39	76.98	1.32	1.64	12.17	2.15	0.59
AUG_HSA2_G05c_MI50	AUG_HSA2	MI	plag_MI	4.62	76.83	1.40	1.54	12.12	2.02	0.67
AUG_HSA2_G15c_MI53	AUG_HSA2	MI	plag_MI	4.72	76.87	1.36	1.49	12.53	1.71	0.48
AUG_HSA2_G15d_MI54	AUG_HSA2	MI	plag_MI	5.28	76.77	1.31	1.52	12.07	1.77	0.45
AUG_HSA2_G01_MI46	AUG_HSA2	MI	cpx_MI	-	-	-	-	-	-	-
AUG_HSA2_G02_MI	AUG_HSA2	MI	cpx_MI	-	-	-	-	-	-	-
AUG_HSA2_G03_MI	AUG_HSA2	MI	cpx_MI	-	-	-	-	-	-	-
AUG_HSA2_G10	AUG_HSA2	MI	plag_MI	-	-	-	-	-	-	-
AUG_HSA2_G15b	AUG_HSA2	MI	plag_MI	-	-	-	-	-	-	-
MOUNT ST. HELENS: May 18, 1980 pumice fall										
MSH12_fines_G11_matrixG	MSH12	matrix glass	-	-	-	-	-	-	-	-
MSH12_fines_G04_matrixG_253	MSH12	matrix glass	-	5.98	71.35	2.24	2.14	14.92	2.30	0.53
MSH12_plag_G58_matrixG_204	MSH12	matrix glass	-	5.21	72.99	2.19	2.17	14.23	2.17	0.52
MSH12_plag_G58_matrixG_205	MSH12	matrix glass	-	5.21	73.83	2.12	2.03	13.74	2.06	0.49
MSH12_plag_G74_matrixG_208	MSH12	matrix glass	-	5.27	72.06	2.44	1.92	14.69	2.36	0.68
MSH12_fines_G03_223	MSH12	MI	opx_MI	5.45	71.46	2.51	2.21	14.79	2.63	0.43
MSH12_fines_G04_224	MSH12	MI	opx_MI	4.43	74.09	1.99	2.14	13.81	2.61	0.48
MSH12_fines_G11_230	MSH12	MI	opx_MI	-	-	-	-	-	-	-
MSH12_plag_G01_266	MSH12	MI	plag_MI	5.05	73.10	1.95	2.36	14.21	2.13	0.56
MSH12_plag_G01_267	MSH12	MI	plag_MI	5.34	72.34	1.92	2.25	14.47	2.46	0.67
MSH12_plag_G37_271	MSH12	MI	plag_MI	5.21	72.40	2.02	2.26	14.51	2.32	0.69
MSH12_plag_G37_other_201	MSH12	MI	plag_MI	5.43	72.38	1.93	2.31	14.54	2.23	0.64
MSH12_plag_G58_273	MSH12	MI	plag_MI	3.54	75.69	1.79	2.32	14.31	1.54	0.39
MSH12_plag_G58_274	MSH12	MI	plag_MI	5.23	72.93	2.02	2.21	14.25	2.26	0.60
MSH12_plag_G58_other_157	MSH12	MI	plag_MI	4.54	74.36	2.09	2.17	14.78	1.35	0.39
MSH12_plag_G74_278	MSH12	MI	plag_MI	6.01	71.39	2.53	2.05	14.71	2.21	0.64
MSH12_plag_G63_279	MSH12	MI	plag_MI	5.81	71.14	2.38	1.94	15.12	2.34	0.72
MOUNT ST. HELENS: June 12, 1980 pyroclastic flow										
SH229A_mafic_G07_matrixG_152	SH229A	matrix glass	-	5.64	75.46	1.02	2.91	12.41	1.79	0.22
SH229A_mafic_G07_126	SH229A	MI	cpx_MI	4.87	68.94	3.98	1.31	18.62	1.75	0.21
SH229A_mafic_G07_127	SH229A	MI	cpx_MI	5.90	68.44	3.59	1.31	18.23	1.71	0.24
SH229A_mafic_G28_M1_130	SH229A	MI	amph_MI	5.15	71.71	2.08	2.10	16.44	1.71	0.30
SH229A_mafic_G32_M1_132	SH229A	MI	amph_MI	5.25	72.77	2.02	1.91	15.99	1.50	0.08

Supplementary Table 1D (continued).

Analysis #	Glass Type	Host Mineral	TiO2 wt%	MnO wt%	P2O5 wt%	Cl wt%	S ppm	H2O wt% by difference w matrix correction	un-normalized total	Host Mg#	Host An#
AUG_HSA2_G01b_MI44	MI	cpx_MI	0.42	0.13	0.04	0.27	290	13.36	86.64	-	-
AUG_HSA2_G01a_MI45	MI	cpx_MI	0.43	0.12	0.03	0.23	151	4.11	95.89	-	-
AUG_HSA2_G05a_MI47	MI	plag_MI	0.45	0.06	0.05	0.19	44	2.38	97.62	-	-
AUG_HSA2_G05b_MI48	MI	plag_MI	0.46	0.08	0.04	0.18	29	2.56	97.44	-	-
AUG_HSA2_G05c_MI50	MI	plag_MI	0.45	0.08	0.04	0.21	107	3.01	96.99	-	-
AUG_HSA2_G15c_MI53	MI	plag_MI	0.44	0.07	0.05	0.26	189	3.45	96.55	-	-
AUG_HSA2_G15d_MI54	MI	plag_MI	0.44	0.08	0.06	0.24	161	2.05	97.95	-	-
AUG_HSA2_G01_MI46	MI	cpx_MI	-	-	-	-	-	-	-	-	-
AUG_HSA2_G02_MI	MI	cpx_MI	-	-	-	-	-	-	-	-	-
AUG_HSA2_G03_MI	MI	cpx_MI	-	-	-	-	-	-	-	-	-
AUG_HSA2_G10	MI	plag_MI	-	-	-	-	-	-	-	-	-
AUG_HSA2_G15b	MI	plag_MI	-	-	-	-	-	-	-	-	-
MOUNT ST. HELENS: May 18, 1980 pumice fall											
MSH12_fines_G11_matrixG	matrix glass	-	-	-	-	-	-	-	-	-	-
MSH12_fines_G04_matrixG_253	matrix glass	-	0.40	-	-	0.11	46	-0.65	100.65	-	-
MSH12_plag_G58_matrixG_204	matrix glass	-	0.41	-	-	0.11	0	-0.49	100.49	-	-
MSH12_plag_G58_matrixG_205	matrix glass	-	0.37	-	-	0.11	47	-4.00	104.00	-	-
MSH12_plag_G74_matrixG_208	matrix glass	-	0.42	-	-	0.11	56	0.28	99.72	-	-
MSH12_fines_G03_223	MI	opx_MI	0.36	-	-	0.12	88	6.39	93.61	64.4	-
MSH12_fines_G04_224	MI	opx_MI	0.30	-	-	0.13	32	7.23	92.77	64.1	-
MSH12_fines_G11_230	MI	opx_MI	-	-	-	-	-	-	-	-	-
MSH12_plag_G01_266	MI	plag_MI	0.46	-	-	0.13	13	5.56	94.44	-	-
MSH12_plag_G01_267	MI	plag_MI	0.39	-	-	0.12	118	6.13	93.87	-	57.7
MSH12_plag_G37_271	MI	plag_MI	0.43	-	-	0.12	33	5.95	94.05	-	56.6
MSH12_plag_G37_other_201	MI	plag_MI	0.34	-	-	0.14	95	5.11	94.89	-	-
MSH12_plag_G58_273	MI	plag_MI	0.30	-	-	0.09	50	5.19	94.81	-	45.2
MSH12_plag_G58_274	MI	plag_MI	0.34	-	-	0.12	55	4.00	96.00	-	45.6
MSH12_plag_G58_other_157	MI	plag_MI	0.22	-	-	0.09	14	3.63	96.37	-	-
MSH12_plag_G74_278	MI	plag_MI	0.32	-	-	0.11	62	4.43	95.57	-	40.4
MSH12_plag_G63_279	MI	plag_MI	0.42	-	-	0.12	98	3.78	96.22	-	58.9
MOUNT ST. HELENS: June 12, 1980 pyroclastic flow											
SH229A_mafic_G07_matrixG_152	matrix glass	-	0.40	-	-	0.12	37	-0.44	100.44	-	-
SH229A_mafic_G07_126	MI	cpx_MI	0.31	-	-	0.11	332	7.46	92.54	77.2	-
SH229A_mafic_G07_127	MI	cpx_MI	0.41	-	-	0.11	304	5.56	94.44	77.2	-
SH229A_mafic_G28_M1_130	MI	amph_MI	0.38	-	-	0.10	167	6.14	93.86	66.6	-
SH229A_mafic_G32_M1_132	MI	amph_MI	0.35	-	-	0.13	91	2.03	97.97	-	-

Supplementary Table 1D (continued).

Analysis #	Glass Type	Host Mineral	% PEC (olivine mass)	PEC correction coefficient	Temperature of MI entrapment (°C) (Petrolog3)	H2O in melt (wt%) (FTIR)	CO2 in melt (ppm) (FTIR)	δ34S (‰)	δ34S 1σ uncertainy (‰)
AUG_HSA2_G01b_MI44	MI	cpx_MI	-	-	-	-	-	-	-
AUG_HSA2_G01a_MI45	MI	cpx_MI	-	-	-	-	-	-	-
AUG_HSA2_G05a_MI47	MI	plag_MI	-	-	-	0.58	bdl	-	-
AUG_HSA2_G05b_MI48	MI	plag_MI	-	-	-	-	-	-	-
AUG_HSA2_G05c_MI50	MI	plag_MI	-	-	-	1.01	14	7.0	1.0
AUG_HSA2_G15c_MI53	MI	plag_MI	-	-	-	1.02	na	8.3	1.0
AUG_HSA2_G15d_MI54	MI	plag_MI	-	-	-	-	-	6.8	0.7
AUG_HSA2_G01_MI46	MI	cpx_MI	-	-	-	-	-	-	-
AUG_HSA2_G02_MI	MI	cpx_MI	-	-	-	-	-	-	-
AUG_HSA2_G03_MI	MI	cpx_MI	-	-	-	-	-	-	-
AUG_HSA2_G10	MI	plag_MI	-	-	-	-	-	-	-
AUG_HSA2_G15b	MI	plag_MI	-	-	-	1.93	na	-	-
MOUNT ST. HELENS: May 18, 1980 pumice fall									
MSH12_fines_G11_matrixG	matrix glass	-	-	-	-	-	-	-	-
MSH12_fines_G04_matrixG_253	matrix glass	-	-	-	-	-	-	-	-
MSH12_plag_G58_matrixG_204	matrix glass	-	-	-	-	-	-	-	-
MSH12_plag_G58_matrixG_205	matrix glass	-	-	-	-	-	-	-	-
MSH12_plag_G74_matrixG_208	matrix glass	-	-	-	-	-	-	-	-
MSH12_fines_G03_223	MI	opx_MI	-	-	-	-	-	-	-
MSH12_fines_G04_224	MI	opx_MI	-	-	-	-	-	-	-
MSH12_fines_G11_230	MI	opx_MI	-	-	-	-	-	-	-
MSH12_plag_G01_266	MI	plag_MI	-	-	-	-	-	-	-
MSH12_plag_G01_267	MI	plag_MI	-	-	-	-	-	-	-
MSH12_plag_G37_271	MI	plag_MI	-	-	-	-	-	-	-
MSH12_plag_G37_other_201	MI	plag_MI	-	-	-	-	-	-	-
MSH12_plag_G58_273	MI	plag_MI	-	-	-	-	-	-	-
MSH12_plag_G58_274	MI	plag_MI	-	-	-	-	-	-	-
MSH12_plag_G58_other_157	MI	plag_MI	-	-	-	-	-	-	-
MSH12_plag_G74_278	MI	plag_MI	-	-	-	-	-	-	-
MSH12_plag_G63_279	MI	plag_MI	-	-	-	-	-	-	-
MOUNT ST. HELENS: June 12, 1980 pyroclastic flow									
SH229A_mafic_G07_matrixG_152	matrix glass	-	-	-	-	-	-	-	-
SH229A_mafic_G07_126	MI	cpx_MI	-	-	-	-	-	-	-
SH229A_mafic_G07_127	MI	cpx_MI	-	-	-	-	-	-	-
SH229A_mafic_G28_M1_130	MI	amph_MI	-	-	-	-	-	-	-
SH229A_mafic_G32_M1_132	MI	amph_MI	-	-	-	-	-	-	-

Supplementary Table 1D (continued).

Analysis #	Glass Type	Host Mineral	Fe3+/ΣFe % [Fe-XANES]	ΔQFM [Fe-XANES]	S6+/ΣS % [S-XANES]
AUG_HSA2_G01b_MI44	MI	cpx_MI	-	-	-
AUG_HSA2_G01a_MI45	MI	cpx_MI	-	-	-
AUG_HSA2_G05a_MI47	MI	plag_MI	52.9	3.24	88.8
AUG_HSA2_G05b_MI48	MI	plag_MI	-	-	-
AUG_HSA2_G05c_MI50	MI	plag_MI	-	-	-
AUG_HSA2_G15c_MI53	MI	plag_MI	-	-	-
AUG_HSA2_G15d_MI54	MI	plag_MI	-	-	-
AUG_HSA2_G01_MI46	MI	cpx_MI	-	-	78.3
AUG_HSA2_G02_MI	MI	cpx_MI	-	-	91.7
AUG_HSA2_G03_MI	MI	cpx_MI	-	-	90.9
AUG_HSA2_G10	MI	plag_MI	-	-	92.1
AUG_HSA2_G15b	MI	plag_MI	-	-	-
MOUNT ST. HELENS: May 18, 1980 pumice fall					
MSH12_fines_G11_matrixG	matrix glass	-	-	-	70.5
MSH12_fines_G04_matrixG_253	matrix glass	-	-	-	-
MSH12_plag_G58_matrixG_204	matrix glass	-	-	-	-
MSH12_plag_G58_matrixG_205	matrix glass	-	-	-	-
MSH12_plag_G74_matrixG_208	matrix glass	-	-	-	-
MSH12_fines_G03_223	MI	opx_MI	-	-	27.0
MSH12_fines_G04_224	MI	opx_MI	-	-	28.8
MSH12_fines_G11_230	MI	opx_MI	-	-	64.7
MSH12_plag_G01_266	MI	plag_MI	-	-	-
MSH12_plag_G01_267	MI	plag_MI	-	-	47.0
MSH12_plag_G37_271	MI	plag_MI	-	-	-
MSH12_plag_G37_other_201	MI	plag_MI	-	-	-
MSH12_plag_G58_273	MI	plag_MI	-	-	23.8
MSH12_plag_G58_274	MI	plag_MI	-	-	47.1
MSH12_plag_G58_other_157	MI	plag_MI	-	-	-
MSH12_plag_G74_278	MI	plag_MI	-	-	34.8
MSH12_plag_G63_279	MI	plag_MI	-	-	29.0
MOUNT ST. HELENS: June 12, 1980 pyroclastic flow					
SH229A_mafic_G07_matrixG_152	matrix glass	-	-	-	-
SH229A_mafic_G07_126	MI	cpx_MI	-	-	75.3
SH229A_mafic_G07_127	MI	cpx_MI	-	-	-
SH229A_mafic_G28_M1_130	MI	amph_MI	-	-	60.0
SH229A_mafic_G32_M1_132	MI	amph_MI	-	-	47.5

Supplementary Table 1D (continued).

Analysis Name	Sample Name	Glass Type	Host Mineral	Na2O wt%	SiO2 wt%	CaO wt%	K2O wt%	Al2O3 wt%	FeOT wt%	MgO wt%
MOUNT ST. HELENS: Nov 30, 2004 lava dome										
SH305_fines_G65_matrixG_256	SH305	matrix glass	-	6.72	69.99	3.33	0.77	18.00	0.74	0.02
SH305_med_G13_matrixG_194	SH305	matrix glass	-	5.87	71.17	1.91	2.28	15.36	2.60	0.49
SH305_fines_G53_234	SH305	MI	opx_MI	-	-	-	-	-	-	-
SH305_fines_G55_238	SH305	MI	opx_MI	-	-	-	-	-	-	-
SH305_fines_G65a_239	SH305	MI	amph_MI	4.67	73.79	1.25	2.64	16.76	0.63	0.03
SH305_fines_G65b	SH305	MI	amph_MI	-	-	-	-	-	-	-
SH305_fines_G88_245	SH305	MI	opx_MI	-	-	-	-	-	-	-
SH305_fines_G103a_252	SH305	MI	opx_MI	5.51	76.88	0.10	1.48	14.52	1.12	0.03
SH305_fines_G103b	SH305	MI	opx_MI	-	-	-	-	-	-	-
SH305_fines_G105_253	SH305	MI	plag_MI	-	-	-	-	-	-	-
SH305_med_G10_255	SH305	MI	plag_MI	4.32	77.59	0.56	4.15	10.81	1.90	0.30
SH305_med_G17_257	SH305	MI	plag_MI	-	-	-	-	-	-	-
SH305_med_G17_258	SH305	MI	plag_MI	4.27	76.85	0.43	4.98	11.12	1.63	0.31
SH305_med_G15_259	SH305	MI	plag_MI	4.33	77.63	0.54	3.80	10.63	1.91	0.52
SH305_med_G13_261	SH305	MI	plag_MI	4.30	76.99	0.44	5.43	10.59	1.57	0.32
SH305_med_G23_263	SH305	MI	amph_MI	4.67	76.06	0.73	2.52	15.08	0.72	0.06
SH305_med_G22_264	SH305	MI	opx_MI	4.62	76.20	1.49	2.40	14.27	0.70	0.14
SH305_med_G22_other_196	SH305	MI	opx_MI	5.48	76.85	0.58	3.43	12.17	0.99	0.05

Supplementary Table 1D (continued).

Analysis #	Glass Type	Host Mineral	TiO2 wt%	MnO wt%	P2O5 wt%	Cl wt%	S ppm	H2O wt% by difference w matrix correction	un-normalized total	Host Mg#	Host An#
MOUNT ST. HELENS: Nov 30, 2004 lava dome											
SH305_fines_G65_matrixG_256	matrix glass	-	0.40	-	-	0.01	14	-1.07	101.07	-	-
SH305_med_G13_matrixG_194	matrix glass	-	0.30	-	-	0.01	30	0.71	99.29	-	-
SH305_fines_G53_234	MI	opx_MI	-	-	-	-	-	-	-	-	-
SH305_fines_G55_238	MI	opx_MI	-	-	-	-	-	-	-	71.7	-
SH305_fines_G65a_239	MI	amph_MI	0.11	-	-	0.09	153	1.56	98.44	-	-
SH305_fines_G65b	MI	amph_MI	-	-	-	-	-	-	-	-	-
SH305_fines_G88_245	MI	opx_MI	-	-	-	-	-	-	-	-	-
SH305_fines_G103a_252	MI	opx_MI	0.19	-	-	0.10	146	2.12	97.88	64.5	-
SH305_fines_G103b	MI	opx_MI	-	-	-	-	-	-	-	-	-
SH305_fines_G105_253	MI	plag_MI	-	-	-	-	-	-	-	-	-
SH305_med_G10_255	MI	plag_MI	0.25	-	-	0.11	33	2.48	97.52	-	42.7
SH305_med_G17_257	MI	plag_MI	-	-	-	-	-	-	-	-	44.4
SH305_med_G17_258	MI	plag_MI	0.24	-	-	0.15	9	2.07	97.93	-	32.7
SH305_med_G15_259	MI	plag_MI	0.31	-	-	0.33	-8	-1.15	101.15	-	59.2
SH305_med_G13_261	MI	plag_MI	0.20	-	-	0.11	49	0.23	99.77	-	41.8
SH305_med_G23_263	MI	amph_MI	0.02	-	-	0.13	47	3.96	96.04	61.9	-
SH305_med_G22_264	MI	opx_MI	0.04	-	-	0.11	84	4.97	95.03	71.0	-
SH305_med_G22_other_196	MI	opx_MI	0.25	-	-	0.18	-25	-1.00	101.00	68.1	-

Supplementary Table 1D (continued).

Analysis #	Glass Type	Host Mineral	% PEC (olivine mass)	PEC correction coefficient	Temperature of MI entrapment (°C) (Petrolog3)	H2O in melt (wt%) (FTIR)	CO2 in melt (ppm) (FTIR)	δ34S (‰)	δ34S 1σ uncertainy (‰)
MOUNT ST. HELENS: Nov 30, 2004 lava dome									
SH305_fines_G65_matrixG_256	matrix glass	-	-	-	-	-	-	-	-
SH305_med_G13_matrixG_194	matrix glass	-	-	-	-	-	-	-	-
SH305_fines_G53_234	MI	opx_MI	-	-	-	-	-	-	-
SH305_fines_G55_238	MI	opx_MI	-	-	-	-	-	-	-
SH305_fines_G65a_239	MI	amph_MI	-	-	-	-	-	-	-
SH305_fines_G65b	MI	amph_MI	-	-	-	-	-	-	-
SH305_fines_G88_245	MI	opx_MI	-	-	-	-	-	-	-
SH305_fines_G103a_252	MI	opx_MI	-	-	-	-	-	-	-
SH305_fines_G103b	MI	opx_MI	-	-	-	-	-	-	-
SH305_fines_G105_253	MI	plag_MI	-	-	-	-	-	-	-
SH305_med_G10_255	MI	plag_MI	-	-	-	-	-	-	-
SH305_med_G17_257	MI	plag_MI	-	-	-	-	-	-	-
SH305_med_G17_258	MI	plag_MI	-	-	-	-	-	-	-
SH305_med_G15_259	MI	plag_MI	-	-	-	-	-	-	-
SH305_med_G13_261	MI	plag_MI	-	-	-	-	-	-	-
SH305_med_G23_263	MI	amph_MI	-	-	-	-	-	-	-
SH305_med_G22_264	MI	opx_MI	-	-	-	-	-	-	-
SH305_med_G22_other_196	MI	opx_MI	-	-	-	-	-	-	-

Supplementary Table 1D (continued).

Analysis #	Glass Type	Host Mineral	Fe3+/ΣFe % [Fe-XANES]	ΔQFM [Fe-XANES]	S6+/ΣS % [S-XANES]
MOUNT ST. HELENS: Nov 30, 2004 lava dome					
SH305_fines_G65_matrixG_256	matrix glass	-	-	-	-
SH305_med_G13_matrixG_194	matrix glass	-	-	-	-
SH305_fines_G53_234	MI	opx_MI	-	-	86.1
SH305_fines_G55_238	MI	opx_MI	-	-	81.0
SH305_fines_G65a_239	MI	amph_MI	-	-	-
SH305_fines_G65b	MI	amph_MI	-	-	39.8
SH305_fines_G88_245	MI	opx_MI	-	-	84.1
SH305_fines_G103a_252	MI	opx_MI	-	-	82.4
SH305_fines_G103b	MI	opx_MI	-	-	35.4
SH305_fines_G105_253	MI	plag_MI	-	-	77.7
SH305_med_G10_255	MI	plag_MI	-	-	-
SH305_med_G17_257	MI	plag_MI	-	-	14.2
SH305_med_G17_258	MI	plag_MI	-	-	18.3
SH305_med_G15_259	MI	plag_MI	-	-	-
SH305_med_G13_261	MI	plag_MI	-	-	-
SH305_med_G23_263	MI	amph_MI	-	-	-
SH305_med_G22_264	MI	opx_MI	-	-	64.7
SH305_med_G22_other_196	MI	opx_MI	-	-	-

REFERENCES CITED

Chapter II

Acocella, V. (2007). Understanding caldera structure and development: An overview of analogue models compared to natural calderas. *Earth-Science Reviews*, *85*(3–4), 125–160.

Aizawa, K., Koyama, T., Hase, H., Uyeshima, M., Kanda, W., Utsugi, M., et al. (2014). Three-dimensional resistivity structure and magma plumbing system of the Kirishima Volcanoes as inferred from broadband magnetotelluric data. *Journal of Geophysical Research: Solid Earth*, *119*(1), 198–215.

Amante, C., & Eakins, B. W. (2009). ETOPO1 1 arc-minute global relief model procedures, data sources and analysis: NOAA Technical Memorandum NESDIS NGDC-24. *National Geophysical Data Center, NOAA*, *10*(V5C8276M).

Annen, C., & Sparks, R. S. J. (2002). Effects of repetitive emplacement of basaltic intrusions on thermal evolution and melt generation in the crust. *Earth and Planetary Science Letters*, *203*(3), 937–955. https://doi.org/10.1016/S0012-821X(02)00929-9

Aoki, Y., Takeo, M., Ohminato, T., Nagaoka, Y., & Nishida, K. (2013). Structural controls on magma pathways beneath Asama Volcano, Japan. *Geol. Soc. London Spec. Publ*, *380*, 67–84.

Argus, D. F., Gordon, R. G., & DeMets, C. (2011). Geologically current motion of 56 plates relative to the no-net-rotation reference frame. *Geochemistry, Geophysics, Geosystems*, *12*(11).

Bohnenstiehl, D. R., Howell, J. K., White, S. M., & Hey, R. N. (2012). A modified basal outlining algorithm for identifying topographic highs from gridded elevation data, Part 1: Motivation and methods. *Computers & Geosciences*, *49*, 308–314.

Calvert, A. T., Fierstein, J., & Hildreth, W. (2018). Eruptive history of Middle Sister, Oregon Cascades, USA–Product of a late Pleistocene eruptive episode. *Geosphere*, *14*(5), 2118–2139.

Carn, S. A., Fioletov, V. E., McLinden, C. A., Li, C., & Krotkov, N. A. (2017). A decade of global volcanic SO2 emissions measured from space. *Scientific Reports*, *7*, 44095.

Castruccio, A., Diez, M., & Gho, R. (2017). The influence of plumbing system structure on volcano dimensions and topography. *Journal of Geophysical Research: Solid Earth*, *122*(11), 8839–8859.

Chaussard, E., & Amelung, F. (2012). Precursory inflation of shallow magma reservoirs at west Sunda volcanoes detected by InSAR. *Geophysical Research Letters*, *39*(21). https://doi.org/10.1029/2012GL053817

Chave, A. D., & Jones, A. G. (2012). The magnetotelluric method: Theory and practice. Cambridge University Press.

Comeau, M. J., Unsworth, M. J., Ticona, F., & Sunagua, M. (2015). Magnetotelluric images of magma distribution beneath Volcán Uturuncu, Bolivia: Implications for magma dynamics. *Geology*, *43*(3), 243–246.

Cooper, K. M., & Kent, A. J. (2014). Rapid remobilization of magmatic crystals kept in cold storage. *Nature*, *506*(7489), 480–483.

Dzurisin, D., & Lu, Z. (2007). Interferometric synthetic-aperture radar (InSAR). In D. Dzurisin (Ed.), *Volcano Deformation: Geodetic Monitoring Techniques* (pp. 153–194). Springer.

Ebmeier, S. K., Andrews, B. J., Araya, M. C., Arnold, D. W. D., Biggs, J., Cooper, C., et al. (2018). Synthesis of global satellite observations of magmatic and volcanic deformation: implications for volcano monitoring & the lateral extent of magmatic domains. *Journal of Applied Volcanology*, *7*(1), 2. https://doi.org/10.1186/s13617-018-0071-3

Ewert, J. W., Diefenbach, A. K., & Ramsey, D. W. (2018). 2018 update to the U.S. Geological Survey national volcanic threat assessment (U.S. Geological Survey Scientific Investigations Report No. 2018–5140) (p. 40). U.S. Geological Survey. Retrieved from https://doi.org/10.3133/ sir20185140

Flusser, J., Suk, T., & Zitová, B. (2016). 2D and 3D image analysis by moments. John Wiley & Sons.

Fournier, R. O. (1999). Hydrothermal processes related to movement of fluid from plastic into brittle rock in the magmatic-epithermal environment. *Economic Geology*, *94*(8), 1193–1211. https://doi.org/10.2113/gsecongeo.94.8.1193

Galland, O., Cobbold, P. R., de Bremond d'Ars, J., & Hallot, E. (2007). Rise and emplacement of magma during horizontal shortening of the brittle crust: Insights from experimental modeling. *Journal of Geophysical Research: Solid Earth*, *112*(B6). https://doi.org/10.1029/2006JB004604

Grosse, P., Euillades, P. A., Euillades, L. D., & de Vries, B. van W. (2014). A global database of composite volcano morphometry. *Bulletin of Volcanology*, *76*(1), 1–16.

Heuret, A., & Lallemand, S. (2005). Plate motions, slab dynamics and back-arc deformation. *Physics of the Earth and Planetary Interiors*, *149*(1–2), 31–51.

Hildreth, W. (2007). Quaternary magmatism in the Cascades: Geologic perspectives (U.S. Geological Survey Professional Paper No. 1744) (p. 125). US Geological Survey. Retrieved from http://pubs.usgs.gov/pp/pp1744

Hill, G. J., Bibby, H. M., Ogawa, Y., Wallin, E. L., Bennie, S. L., Caldwell, T. G., et al. (2015). Structure of the Tongariro Volcanic system: Insights from magnetotelluric imaging. *Earth and Planetary Science Letters*, *432*, 115–125.

Huber, C., Townsend, M., Degruyter, W., & Bachmann, O. (2019). Optimal depth of subvolcanic magma chamber growth controlled by volatiles and crust rheology. *Nature Geoscience*, 1–7.

Hurwitz, S., & Manga, M. (2017). The fascinating and complex dynamics of geyser eruptions. *Annual Review of Earth and Planetary Sciences*, *45*, 31–59.

Jaxybulatov, K., Koulakov, I., Ibs-von Seht, M., Klinge, K., Reichert, C., Dahren, B., & Troll, V. R. (2011). Evidence for high fluid/melt content beneath Krakatau volcano (Indonesia) from local earthquake tomography. *Journal of Volcanology and Geothermal Research*, *206*(3), 96–105.

Jay, J., Costa, F., Pritchard, M., Lara, L., Singer, B., & Herrin, J. (2014). Locating magma reservoirs using InSAR and petrology before and during the 2011–2012 Cordón Caulle silicic eruption. *Earth and Planetary Science Letters*, *395*, 254–266.

Karlstrom, L., Dufek, J., & Manga, M. (2009). Organization of volcanic plumbing through magmatic lensing by magma chambers and volcanic loads. *Journal of Geophysical Research: Solid Earth*, *114*(B10). https://doi.org/10.1029/2009JB006339

Karlstrom, L., Paterson, S. R., & Jellinek, A. M. (2017). A reverse energy cascade for crustal magma transport. *Nature Geoscience*, *10*(8), 604.

Karlstrom, L., Richardson, P. W., O'Hara, D., & Ebmeier, S. K. (2018). Magmatic landscape construction. *Journal of Geophysical Research: Earth Surface*, *123*(8), 1710–1730.

Kiser, E., Levander, A., Zelt, C., Schmandt, B., & Hansen, S. (2018). Focusing of melt near the top of the Mount St. Helens (USA) magma reservoir and its relationship to major volcanic eruptions. *Geology*, *46*(9), 775–778.

Lees, J. M. (2007). Seismic tomography of magmatic systems. *Journal of Volcanology and Geothermal Research*, *167*(1–4), 37–56. https://doi.org/10.1016/j.jvolgeores.2007.06.008

Lerner, A. H. (2020). Supplemental data for "The Prevalence and Significance of Offset Magma Reservoirs at Arc Volcanoes" [Data set]. Harvard Dataverse. https://doi.org/10.7910/DVN/LHD1HY

Lipman, P. W. (1997). Subsidence of ash-flow calderas: relation to caldera size and magma-chamber geometry. *Bulletin of Volcanology*, *59*(3), 198–218.

Lisowski, M., Dzurisin, D., Denlinger, R. P., & Iwatsubo, E. Y. (2008). Analysis of GPS-measured deformation associated with the 2004-2006 dome-building eruption of Mount St. Helens, Washington. In D. R. Sherrod, W. E. Scott, & P. H. Stauffer (Eds.), *A volcano rekindled: The renewed eruption of Mount St. Helens, 2004-2006* (pp. 281–300). US Geological Survey Professional Paper 1750.

Lu, Z., & Dzurisin, D. (2014). InSAR imaging of Aleutian volcanoes. In *InSAR Imaging of Aleutian Volcanoes* (pp. 87–345). Springer.

Lundgren, P., Samsonov, S. V., López Velez, C. M., & Ordoñez, M. (2015). Deep source model for Nevado del Ruiz Volcano, Colombia, constrained by interferometric synthetic aperture radar observations. *Geophysical Research Letters*, *42*(12), 4816–4823.

Maccaferri, F., Bonafede, M., & Rivalta, E. (2011). A quantitative study of the mechanisms governing dike propagation, dike arrest and sill formation. *Journal of Volcanology and Geothermal Research*, *208*(1–2), 39–50.

Magee, C., Muirhead, J. D., Karvelas, A., Holford, S. P., Jackson, C. A., Bastow, I. D., et al. (2016). Lateral magma flow in mafic sill complexes. *Geosphere*, *12*(3), 809–841.

Massol, H., Jaupart, C., & Pepper, D. W. (2001). Ascent and decompression of viscous vesicular magma in a volcanic conduit. *Journal of Geophysical Research: Solid Earth*, *106*(B8), 16223–16240.

McTigue, D. F. (1987). Elastic stress and deformation near a finite spherical magma body: resolution of the point source paradox. *Journal of Geophysical Research: Solid Earth*, *92*(B12), 12931–12940.

McTigue, D. F., & Segall, P. (1988). Displacements and tilts from dip-slip faults and magma chambers beneath irregular surface topography. *Geophysical Research Letters*, *15*(6), 601–604.

Mogi, K. (1958). Relations between the eruptions of various volcanoes and the deformations of the ground surfaces around them, *36*, 99–134.

Moran, S. C., Freymueller, J. T., LaHusen, R. G., McGee, K. A., Poland, M. P., Power, J. A., et al. (2008). Instrumentation recommendations for volcano monitoring at US volcanoes under the National Volcano Early Warning System. *U.S. Geological Survey Scientific Investigations Report*, *5114*.

NASA JPL. (2013). NASA Shuttle Radar Topography Mission Global 1 arc second [Data set]. NASA LP DAAC. Retrieved from https://doi.org/10.5067/MEaSUREs/SRTM/SRTMGL1.003

Pinel, V., & Jaupart, C. (2000). The effect of edifice load on magma ascent beneath a volcano. *Philosophical Transactions of the Royal Society of London. Series A: Mathematical, Physical and Engineering Sciences*, *358*(1770), 1515–1532.

Pinel, V., & Jaupart, C. (2003). Magma chamber behavior beneath a volcanic edifice. *Journal of Geophysical Research: Solid Earth*, *108*(B2), 2072. https://doi.org/10.1029/2002JB001751

Pinel, V., & Jaupart, C. (2004). Magma storage and horizontal dyke injection beneath a volcanic edifice. *Earth and Planetary Science Letters*, *221*(1–4), 245–262.

Rivalta, E., Taisne, B., Bunger, A. P., & Katz, R. F. (2015). A review of mechanical models of dike propagation: Schools of thought, results and future directions. *Tectonophysics*, *638*, 1–42.

Roman, A., & Jaupart, C. (2014). The impact of a volcanic edifice on intrusive and eruptive activity. *Earth and Planetary Science Letters*, *408*, 1–8.

Smithsonian Institution. (2013). Volcanoes of the World, v. 4.3.4 [Data set]. Global Volcanism Program.

Sparks, R. S. J., Biggs, J., & Neuberg, J. W. (2012). Monitoring volcanoes. *Science*, *335*(6074), 1310–1311.

Syracuse, E. M., Maceira, M., Zhang, H., & Thurber, C. H. (2015). Seismicity and structure of Akutan and Makushin Volcanoes, Alaska, using joint body and surface wave tomography. *Journal of Geophysical Research: Solid Earth*, *120*(2), 1036–1052.

Taisne, B., & Jaupart, C. (2009). Dike propagation through layered rocks. *Journal of Geophysical Research: Solid Earth*, *114*(B9).

Tamura, J., & Okada, T. (2016). Ambient noise tomography in the Naruko/Onikobe volcanic area, NE Japan: implications for geofluids and seismic activity. *Earth, Planets and Space*, *68*(1), 1.

University of Washington. (1963). Pacific Northwest Seismic Network. International Federation of Digital Seismograph Networks [Data set]. Dataset/Seismic Network. https://doi.org/10.7914/sn/uw

Vandemeulebrouck, J., Sohn, R. A., Rudolph, M. L., Hurwitz, S., Manga, M., Johnston, M. J., et al. (2014). Eruptions at Lone Star geyser, Yellowstone National Park, USA: 2. Constraints on subsurface dynamics. *Journal of Geophysical Research: Solid Earth*, *119*(12), 8688–8707.

Vargas, C. A., Koulakov, I., Jaupart, C., Gladkov, V., Gomez, E., El Khrepy, S., & Al-Arifi, N. (2017). Breathing of the Nevado del Ruiz volcano reservoir, Colombia, inferred from repeated seismic tomography. *Scientific Reports*, *7*, 46094.

Wallace, P. J. (2005). Volatiles in subduction zone magmas: concentrations and fluxes based on melt inclusion and volcanic gas data. *Journal of Volcanology and Geothermal Research, 140*(1), 217–240.

White, R., & McCausland, W. (2016). Volcano-tectonic earthquakes: A new tool for estimating intrusive volumes and forecasting eruptions. *Journal of Volcanology and Geothermal Research*, *309*, 139–155.

Wicks, C., de La Llera, J. C., Lara, L. E., & Lowenstern, J. (2011). The role of dyking and fault control in the rapid onset of eruption at Chaitén volcano, Chile. *Nature, 478*(7369), 374–377.

Chapter III

Anderson, A. T., & Wright, T. L. (1972). Phenocrysts and glass inclusions and their bearing on oxidation and mixing of basaltic magmas, Kilauea Volcano, Hawaii. American Mineralogist, 57(1–2), 188–216.

Anzures, B. A., Parman, S. W., Milliken, R. E., Lanzirotti, A., & Newville, M. (2020). XANES spectroscopy of sulfides stable under reducing conditions. American Mineralogist, 105(3), 375–381. https://doi.org/10.2138/am-2020-7146

Baker, D. R., & Moretti, R. (2011). Modeling the solubility of sulfur in magmas: a 50-year old geochemical challenge. Reviews in Mineralogy and Geochemistry, 73(1), 167–213.

Barnes, J. D., Prather, T. J., Cisneros, M., Befus, K., Gardner, J. E., & Larson, T. E. (2014). Stable chlorine isotope behavior during volcanic degassing of H2O and CO2 at Mono Craters, CA. Bulletin of Volcanology, 76(3), 805.

Barth, A., Newcombe, M., Plank, T., Gonnermann, H., Hajimirza, S., Soto, G. J., et al. (2019). Magma decompression rate correlates with explosivity at basaltic volcanoes - Constraints from water diffusion in olivine. Journal of Volcanology and Geothermal Research, 387, 106664.

Berry, A. J., Danyushevsky, L. V., O'Neill, H. S. C., Newville, M., & Sutton, S. R. (2008). Oxidation state of iron in komatiitic melt inclusions indicates hot Archaean mantle. Nature, 455(7215), 960.

Berry, A. J., Stewart, G. A., O'Neill, H. S. C., Mallmann, G., & Mosselmans, J. F. W. (2018). A re-assessment of the oxidation state of iron in MORB glasses. Earth and Planetary Science Letters, 483, 114–123. https://doi.org/10.1016/j.epsl.2017.11.032

Borisov, A., Behrens, H., & Holtz, F. (2018). Ferric/ferrous ratio in silicate melts: A new model for 1 atm data with special emphasis on the effects of melt composition. Contributions to Mineralogy and Petrology, 173(12), 98.

Brounce, M., Stolper, E., & Eiler, J. (2017). Redox variations in Mauna Kea lavas, the oxygen fugacity of the Hawaiian plume, and the role of volcanic gases in Earth's oxygenation. Proceedings of the National Academy of Sciences, 114(34), 8997–9002.

Brounce, M., Boyce, J., McCubbin, F. M., Humphreys, J., Reppart, J., Stolper, E., & Eiler, J. (2019). The oxidation state of sulfur in lunar apatite. American Mineralogist, 104(2), 307–312.

Brounce, M. N., Kelley, K. A., & Cottrell, E. (2014). Variations in Fe3+/∑ Fe of Mariana Arc basalts and mantle wedge fO2. Journal of Petrology, 55(12), 2513–2536.

Bucholz, C. E., Gaetani, G. A., Behn, M. D., & Shimizu, N. (2013). Post-entrapment modification of volatiles and oxygen fugacity in olivine-hosted melt inclusions. Earth and Planetary Science Letters, 374, 145–155.

Burgisser, A., Alletti, M., & Scaillet, B. (2015). Simulating the behavior of volatiles belonging to the C–O–H–S system in silicate melts under magmatic conditions with the software D-Compress. Computers & Geosciences, 79, 1–14.

Callegaro, S., Geraki, K., Marzoli, A., Min, A. D., Maneta, V., & Baker, D. R. (2020). The quintet completed: The partitioning of sulfur between nominally volatile-free minerals and silicate melts. American Mineralogist, 105(5), 697–707. https://doi.org/10.2138/am-2020-7188

Carroll, M., & Rutherford, M. J. (1988). Sulfur speciation in hydrous experimental glasses of varying oxidation state–results from measured wavelength shifts of sulfur X-rays. American Mineralogist, 73(7), 845–9.

Chen, Y., Provost, A., Schiano, P., & Cluzel, N. (2011). The rate of water loss from olivine-hosted melt inclusions. Contributions to Mineralogy and Petrology, 162(3), 625–636.

Chowdhury, P., & Dasgupta, R. (2019). Effect of sulfate on the basaltic liquidus and Sulfur Concentration at Anhydrite Saturation (SCAS) of hydrous basalts–Implications for sulfur cycle in subduction zones. Chemical Geology, 522, 162–174.

Cottrell, E., & Kelley, K. A. (2011). The oxidation state of Fe in MORB glasses and the oxygen fugacity of the upper mantle. Earth and Planetary Science Letters, 305(3), 270–282. https://doi.org/10.1016/j.epsl.2011.03.014

Cottrell, E., Birner, S., Brounce, M. N., Davis, F. A., Waters, L. E., & Kelley, K. A. (in press). Oxygen Fugacity Across Tectonic Settings. In D. R. Neuville & R. Moretti (Eds.), Redox variables and mechanisms in magmatism and volcanism. Wiley.

Cottrell, E., Kelley, K. A., Lanzirotti, A., & Fischer, R. A. (2009). High-precision determination of iron oxidation state in silicate glasses using XANES. Chemical Geology, 268(3), 167–179.

Cottrell, E., Lanzirotti, A., Mysen, B., Birner, S., Kelley, K. A., Botcharnikov, R., et al. (2018). A Mössbauer-based XANES calibration for hydrous basalt glasses reveals radiation-induced oxidation of Fe. American Mineralogist, 103(4), 489–501. https://doi.org/10.2138/am-2018-6268

Danyushevsky, L. V., & Plechov, P. (2011). Petrolog3: Integrated software for modeling crystallization processes. Geochemistry, Geophysics, Geosystems, 12(7).

Danyushevsky, L. V., Della-Pasqua, F. N., & Sokolov, S. (2000). Re-equilibration of melt inclusions trapped by magnesian olivine phenocrysts from subduction-related magmas: petrological implications. Contributions to Mineralogy and Petrology, 138(1), 68–83.

Danyushevsky, L. V., McNeill, A. W., & Sobolev, A. V. (2002). Experimental and petrological studies of melt inclusions in phenocrysts from mantle-derived magmas: An overview of techniques, advantages and complications. Chemical Geology, 183(1), 5–24.

Dauphas, N., Roskosz, M., Alp, E. E., Neuville, D. R., Hu, M. Y., Sio, C. K., et al. (2014). Magma redox and structural controls on iron isotope variations in Earth's mantle and crust. Earth and Planetary Science Letters, 398, 127–140.

Demouchy, S., & Mackwell, S. (2006). Mechanisms of hydrogen incorporation and diffusion in iron-bearing olivine. Physics and Chemistry of Minerals, 33(5), 347–355.

Di Genova, D., Sicola, S., Romano, C., Vona, A., Fanara, S., & Spina, L. (2017). Effect of iron and nanolites on Raman spectra of volcanic glasses: A reassessment of existing strategies to estimate the water content. Chemical Geology, 475, 76–86. https://doi.org/10.1016/j.chemgeo.2017.10.035

Di Genova, D., Caracciolo, A., & Kolzenburg, S. (2018). Measuring the degree of "nanotilization" of volcanic glasses: Understanding syn-eruptive processes recorded in melt inclusions. Lithos, 318, 209–218.

Dixon, J. E., Stolper, E., & Delaney, J. R. (1988). Infrared spectroscopic measurements of CO2 and H2O in Juan de Fuca Ridge basaltic glasses. Earth Planet. Sci. Lett, 90(1), 87–104.

Dixon, J. E., Stolper, E. M., & Holloway, J. R. (1995). An experimental study of water and carbon dioxide solubilities in mid-ocean ridge basaltic liquids. Part I: calibration and solubility models. Journal of Petrology, 36(6), 1607–1631.

Dyar, M. D., McCanta, M., Breves, E., Carey, C. J., & Lanzirotti, A. (2016). Accurate predictions of iron redox state in silicate glasses: A multivariate approach using X-ray absorption spectroscopy. American Mineralogist, 101(3), 744–747.

Elam, W. T., Ravel, B. D., & Sieber, J. R. (2002). A new atomic database for X-ray spectroscopic calculations. Radiation Physics and Chemistry, 63(2), 121–128.

Ferriss, E., Plank, T., Newcombe, M., Walker, D., & Hauri, E. (2018). Rates of dehydration of olivines from San Carlos and Kilauea Iki. Geochimica et Cosmochimica Acta, 242, 165–190.

Fiege, A., Behrens, H., Holtz, F., & Adams, F. (2014). Kinetic vs. thermodynamic control of degassing of H2O–S ± Cl-bearing andesitic melts. Geochimica et Cosmochimica Acta, 125, 241–264. https://doi.org/10.1016/j.gca.2013.10.012

Fiege, A., Holtz, F., Shimizu, N., Mandeville, C. W., Behrens, H., & Knipping, J. L. (2014). Sulfur isotope fractionation between fluid and andesitic melt: An experimental study. Geochimica et Cosmochimica Acta, 142, 501–521.

Fiege, A., Ruprecht, P., Simon, A. C., Bell, A. S., Göttlicher, J., Newville, M., et al. (2017). Calibration of Fe XANES for high-precision determination of Fe oxidation state in glasses: Comparison of new and existing results obtained at different synchrotron radiation sources. American Mineralogist, 102(2), 369–380.

Fleet, M. E., Liu, X., Harmer, S. L., & King, P. L. (2005). Sulfur K-edge XANES spectroscopy: Chemical state and content of sulfur in silicate glasses. The Canadian Mineralogist, 43(5), 1605–1618.

Gaetani, G. A., O'Leary, J. A., Shimizu, N., Bucholz, C. E., & Newville, M. (2012). Rapid reequilibration of H2O and oxygen fugacity in olivine-hosted melt inclusions. Geology, 40(10), 915–918.

Galoisy, L., Calas, G., & Arrio, M. A. (2001). High-resolution XANES spectra of iron in minerals and glasses: structural information from the pre-edge region. Chemical Geology, 174(1–3), 307–319.

Gansecki, C., Lee, R. L., Shea, T., Lundblad, S. P., Hon, K., & Parcheta, C. (2019). The tangled tale of Kīlauea's 2018 eruption as told by geochemical monitoring. Science, 366(6470).

Gerlach, T. M., Roeder, P. L., Thornber, C., & Grant, A. (2004). Comment on paper:'Morphology and compositions of spinel in Pu'u'ō'Ō lava (1996-1998), Kilauea volcano, Hawaii': enigmatic discrepancies between lava and gas-based fO2 determinations of Pu'u'ō'Ō lava. Authors' reply. Journal of Volcanology and Geothermal Research, 134(3), 241–244.

Graz, Y., Scaillet, B., Pichavant, M., & Gaillard, F. (2007). The effect of sulfur on the Fe2+/Fe3+ ratio of MORB and its implications for the redox state of the mantle.

Grocke, S. B., Cottrell, E., de Silva, S., & Kelley, K. A. (2016). The role of crustal and eruptive processes versus source variations in controlling the oxidation state of iron in Central Andean magmas. Earth and Planetary Science Letters, 440, 92–104.

Guilbaud, M.-N., Blake, S., Thordarson, T., & Self, S. (2007). Role of syn-eruptive cooling and degassing on textures of lavas from the AD 1783–1784 Laki eruption, South Iceland. Journal of Petrology, 48(7), 1265–1294. https://doi.org/10.1093/petrology/egm017

Hartley, M. E., Neave, D. A., Maclennan, J., Edmonds, M., & Thordarson, T. (2015). Diffusive over-hydration of olivine-hosted melt inclusions. Earth and Planetary Science Letters, 425, 168–178.

Hartley, M. E., Shorttle, O., Maclennan, J., Moussallam, Y., & Edmonds, M. (2017). Olivine-hosted melt inclusions as an archive of redox heterogeneity in magmatic systems. Earth and Planetary Science Letters, 479, 192–205.

Hauri, E. (2002). SIMS analysis of volatiles in silicate glasses, 2: isotopes and abundances in Hawaiian melt inclusions. Chemical Geology, 183(1), 115–141.

Head, E., Lanzirotti, A., Newville, M., & Sutton, S. (2018). Vanadium, sulfur, and iron valences in melt inclusions as a window into magmatic processes: A case study at Nyamuragira volcano, Africa. Geochimica et Cosmochimica Acta, 226, 149–173.

Helz, R. T., & Thornber, C. R. (1987). Geothermometry of Kilauea Iki lava lake, Hawaii. Bulletin of Volcanology, 49(5), 651–668.

Helz, R. T., Cottrell, E., Brounce, M. N., & Kelley, K. A. (2017). Olivine-melt relationships and syneruptive redox variations in the 1959 eruption of Kīlauea Volcano as revealed by XANES. Journal of Volcanology and Geothermal Research, 333, 1–14.

Hughes, E. C., Buse, B., Kearns, S. L., Blundy, J. D., Kilgour, G., Mader, H. M., et al. (2018). High spatial resolution analysis of the iron oxidation state in silicate glasses using the electron probe. American Mineralogist: Journal of Earth and Planetary Materials, 103(9), 1473–1486.

Jarosewich, E., Nelen, J. A., & Norberg, J. A. (1980). Reference samples for electron microprobe analysis. Geostandards Newsletter, 4(1), 43–47.

Jugo, P. J. (2009). Sulfur content at sulfide saturation in oxidized magmas. Geology, 37(5), 415–418.

Jugo, P. J., Wilke, M., & Botcharnikov, R. E. (2010). Sulfur K-edge XANES analysis of natural and synthetic basaltic glasses: Implications for S speciation and S content as function of oxygen fugacity. Geochimica et Cosmochimica Acta, 74(20), 5926–5938.

Kądziołka-Gaweł, M., Adamczyk, Z., & Kalinowski, L. (2019). Mössbauer study of changes in olivine after heating in air. The Canadian Mineralogist, 57(1), 105–115.

Kelley, K. A., & Cottrell, E. (2009). Water and the oxidation state of subduction zone magmas. Science, 325(5940), 605–607. https://doi.org/10.1126/science.1174156

Kelley, K. A., & Cottrell, E. (2012). The influence of magmatic differentiation on the oxidation state of Fe in a basaltic arc magma. Earth and Planetary Science Letters, 329–330, 109–121. https://doi.org/10.1016/j.epsl.2012.02.010

Kent, A. J. (2008). Melt inclusions in basaltic and related volcanic rocks. Reviews in Mineralogy and Geochemistry, 69(1), 273–331.

Kern, C., Lerner, A. H., Elias, T., Nadeau, P. A., Holland, L., Kelly, P. J., et al. (2020). Quantifying gas emissions associated with the 2018 rift eruption of Kīlauea Volcano using ground-based DOAS measurements. Bulletin of Volcanology, 82(7), 55. https://doi.org/10.1007/s00445-020-01390-8

Klimm, K., Kohn, S. C., O'Dell, L. A., Botcharnikov, R. E., & Smith, M. E. (2012). The dissolution mechanism of sulphur in hydrous silicate melts. I: Assessment of analytical techniques in determining the sulphur speciation in iron-free to iron-poor glasses. Chemical Geology, 322, 237–249.

Klimm, K., Kohn, S. C., & Botcharnikov, R. E. (2012). The dissolution mechanism of sulphur in hydrous silicate melts. II: Solubility and speciation of sulphur in hydrous silicate melts as a function of fO2. Chemical Geology, 322, 250–267.

Knafelc, J., Filiberto, J., Ferré, E. C., Conder, J. A., Costello, L., Crandall, J. R., et al. (2019). The effect of oxidation on the mineralogy and magnetic properties of olivine. American Mineralogist, 104(5), 694–702.

Kohlstedt, D. L., Goetze, C., Durham, W. B., & Vander Sande, J. (1976). New technique for decorating dislocations in olivine. Science, 191(4231), 1045–1046.

Konecke, B. A., Fiege, A., Simon, A. C., Parat, F., & Stechern, A. (2017). Co-variability of S6+, S4+, and S2- in apatite as a function of oxidation state: Implications for a new oxybarometer. American Mineralogist, 102(3), 548–557.

Kress, V. C., & Carmichael, I. S. (1991). The compressibility of silicate liquids containing Fe2O3 and the effect of composition, temperature, oxygen fugacity and pressure on their redox states. Contributions to Mineralogy and Petrology, 108(1–2), 82–92.

Lanzirotti, A., Lee, L., Head, E., Sutton, S. R., Newville, M., McCanta, M., et al. (2019). Direct measurements of copper speciation in basaltic glasses: understanding the relative roles of sulfur and oxygen in copper complexation in melts. Geochimica et Cosmochimica Acta, 267, 164–178.

Lee, R. L., Gansecki, C., Lundblad, S., Mills, P., Adams, D. T., Conrey, R., & Wagoner, L. (2019). Whole-rock and glass chemistry of lava samples collected during the 2018 Lower East Rift Zone eruption of Kilauea (U.S. Geological Survey data release). U.S. Geological Survey. Retrieved from https://doi.org/10.5066/P9LVY7GV

Lloyd, A. S., Plank, T., Ruprecht, P., Hauri, E. H., & Rose, W. (2013). Volatile loss from melt inclusions in pyroclasts of differing sizes. Contributions to Mineralogy and Petrology, 165(1), 129–153.

Mackwell, S. J., & Kohlstedt, D. L. (1990). Diffusion of hydrogen in olivine: implications for water in the mantle. Journal of Geophysical Research, 95(B4), 5079–5088.

Manceau, A., & Nagy, K. L. (2012). Quantitative analysis of sulfur functional groups in natural organic matter by XANES spectroscopy. Geochimica et Cosmochimica Acta, 99, 206–223. https://doi.org/10.1016/j.gca.2012.09.033

Masotta, M., & Keppler, H. (2015). Anhydrite solubility in differentiated arc magmas. Geochimica et Cosmochimica Acta, 158, 79–102.

Matjuschkin, V., Blundy, J. D., & Brooker, R. A. (2016). The effect of pressure on sulphur speciation in mid-to deep-crustal arc magmas and implications for the formation of porphyry copper deposits. Contributions to Mineralogy and Petrology, 171(7), 66.

McCanta, M. C., Dyar, M. D., Rutherford, M. J., Lanzirotti, A., Sutton, S. R., & Thomson, B. J. (2017). In situ measurement of ferric iron in lunar glass beads using Fe-XAS. Icarus, 285, 95–102.

McCanta, M. C., Dyar, M. D., Lanzirotti, A., Newville, M., & Breitenfeld, L. B. (2019). In-situ mapping of ferric iron variations in lunar glasses using X-ray absorption spectroscopy. American Mineralogist, 104(3), 453–458. https://doi.org/10.2138/am-2019-6863

Métrich, N., & Wallace, P. J. (2008). Volatile abundances in basaltic magmas and their degassing paths tracked by melt inclusions. Reviews in Mineralogy and Geochemistry, 69(1), 363–402.

Métrich, N., Berry, A. J., O'Neill, H. S. C., & Susini, J. (2009). The oxidation state of sulfur in synthetic and natural glasses determined by X-ray absorption spectroscopy. Geochimica et Cosmochimica Acta, 73(8), 2382–2399.

de Moor, J. M., Fischer, T. P., Sharp, Z. D., King, P. L., Wilke, M., Botcharnikov, R. E., et al. (2013). Sulfur degassing at Erta Ale (Ethiopia) and Masaya (Nicaragua) volcanoes: Implications for degassing processes and oxygen fugacities of basaltic systems. Geochemistry, Geophysics, Geosystems, 14(10), 4076–4108.

Mourey, A., Shea, T., Costa Rodriguez, F., Shiro, B., Lee, R. L., Gansecki, C. A., & Oalmann, J. (2019). Diffusion timescales in olivine from the 2018 eruption at Kilauea Volcano reveal syn-eruptive (months) and long term (years) magma mixing processes. In AGU Fall Meeting (Vol. 2019, pp. V43C–0208).

Moussallam, Y., Oppenheimer, C., Scaillet, B., Gaillard, F., Kyle, P., Peters, N., et al. (2014). Tracking the changing oxidation state of Erebus magmas, from mantle to surface, driven by magma ascent and degassing. Earth and Planetary Science Letters, 393, 200–209.

Moussallam, Y., Edmonds, M., Scaillet, B., Peters, N., Gennaro, E., Sides, I., & Oppenheimer, C. (2016). The impact of degassing on the oxidation state of basaltic magmas: A case study of Kīlauea volcano. Earth and Planetary Science Letters, 450, 317–325.

Moussallam, Y., Longpré, M.-A., McCammon, C., Gomez-Ulla, A., Rose-Koga, E. F., Scaillet, B., et al. (2019). Mantle plumes are oxidised. Earth and Planetary Science Letters, 527, 115798. https://doi.org/10.1016/j.epsl.2019.115798

Myers, M. L. (2017). Storage, ascent, and release of silicic magma in caldera-forming eruptions (PhD Thesis). University of Oregon.

Myers, M. L., Wallace, P. J., Wilson, C. J., Morter, B. K., & Swallow, E. J. (2016). Prolonged ascent and episodic venting of discrete magma batches at the onset of the Huckleberry Ridge supereruption, Yellowstone. Earth and Planetary Science Letters, 451, 285–297.

Nash, W. M., Smythe, D. J., & Wood, B. J. (2019). Compositional and temperature effects on sulfur speciation and solubility in silicate melts. Earth and Planetary Science Letters, 507, 187–198.

Neal, C. A., & Anderson, K. R. (2020). Preliminary analyses of volcanic hazards at Kīlauea Volcano, Hawai‘i, 2017–2018 (USGS Numbered Series No. 2020–1002) (p. 34). Reston, VA: U.S. Geological Survey. Retrieved from http://pubs.er.usgs.gov/publication/ofr20201002

Neal, C. A., Brantley, S. R., Antolik, L., Babb, J. L., Burgess, M., Calles, K., et al. (2019). The 2018 rift eruption and summit collapse of Kīlauea Volcano. Science, 363(6425), 367–374. https://doi.org/10.1126/science.aav7046

Newville, M. (2013). Larch: An analysis package for XAFS and related spectroscopies. In Journal of Physics: Conference Series (Vol. 430, p. 012007). IOP Publishing.

O’Neill, H. S. C., Berry, A. J., & Mallmann, G. (2018). The oxidation state of iron in Mid-Ocean Ridge Basaltic (MORB) glasses: Implications for their petrogenesis and oxygen fugacities. Earth and Planetary Science Letters, 504, 152–162. https://doi.org/10.1016/j.epsl.2018.10.002

Osborn, E. F. (1959). Role of oxygen pressure in the crystallization and differentiation of basaltic magma. American Journal of Science, 257(9), 609–647. https://doi.org/10.2475/ajs.257.9.609

Papike, J. J., Simon, S. B., Burger, P. V., Bell, A. S., Shearer, C. K., & Karner, J. M. (2016). Chromium, vanadium, and titanium valence systematics in Solar System pyroxene as a recorder of oxygen fugacity, planetary provenance, and processes. American Mineralogist, 101(4), 907–918.

Paris, E., Giuli, G., Carroll, M. R., & Davoli, I. (2001). The valence and speciation of sulfur in glasses by X-ray absorption spectroscopy. The Canadian Mineralogist, 39(2), 331–339. https://doi.org/10.2113/gscanmin.39.2.331

Patrick, M. R., Dietterich, H. R., Lyons, J. J., Diefenbach, A. K., Parcheta, C., Anderson, K. R., et al. (2019c). Cyclic lava effusion during the 2018 eruption of Kīlauea Volcano. Science, 366(6470). https://doi.org/10.1126/science.aay9070

Portnyagin, M., Almeev, R., Matveev, S., & Holtz, F. (2008). Experimental evidence for rapid water exchange between melt inclusions in olivine and host magma. Earth and Planetary Science Letters, 272(3), 541–552. https://doi.org/10.1016/j.epsl.2008.05.020

Ravel, B., & Newville, M. (2005). ATHENA, ARTEMIS, HEPHAESTUS: data analysis for X-ray absorption spectroscopy using IFEFFIT. Journal of Synchrotron Radiation, 12(4), 537–541.

Righter, K., Danielson, L. R., Pando, K., Morris, R. V., Graff, T. G., Agresti, D. G., et al. (2013). Redox systematics of martian magmas with implications for magnetite stability. American Mineralogist, 98(4), 616–628.

Rose-Koga, E. F., & others. (submitted). Silicate melt inclusions in the new millennium: A review of recommended practices for preparation, analysis, and data presentation.

Rowe, M. C., Kent, A. J., & Nielsen, R. L. (2007). Determination of sulfur speciation and oxidation state of olivine hosted melt inclusions. Chemical Geology, 236(3–4), 303–322.

Schreiber, H. D., Merkel Jr, R. C., Schreiber, V. L., & Balazs, G. B. (1987). Mutual interactions of redox couples via electron exchange in silicate melts: models for geochemical melt systems. Journal of Geophysical Research: Solid Earth, 92(B9), 9233–9245.

Shorttle, O., Moussallam, Y., Hartley, M. E., Maclennan, J., Edmonds, M., & Murton, B. J. (2015). Fe-XANES analyses of Reykjanes Ridge basalts: Implications for oceanic crust's role in the solid Earth oxygen cycle. Earth and Planetary Science Letters, 427, 272–285.

Sobolev, A. V., & Danyushevsky, L. V. (1994). Petrology and geochemistry of boninites from the north termination of the Tonga Trench: constraints on the generation conditions of primary high-Ca boninite magmas. Journal of Petrology, 35(5), 1183–1211.

Sutton, S. R., Lanzirotti, A., Newville, M., Rivers, M. L., Eng, P., & Lefticariu, L. (2017). Spatially resolved elemental analysis, spectroscopy and diffraction at the GSECARS Sector at the Advanced Photon Source. Journal of Environmental Quality, 46(6), 1158–1165.

Sutton, S. R., Lanzirotti, A., Newville, M., Dyar, M. D., & Delaney, J. (2020). Oxybarometry and valence quantification based on microscale X-ray absorption fine structure (XAFS) spectroscopy of multivalent elements. Chemical Geology, 531, 119305.

Swanson, D. A., & Fabbi, B. P. (1973). Loss of volatiles during fountaining and flowage of basaltic lava at Kilauea Volcano, Hawaii. Journal of Research of the U.S. Geological Survey, 1(6), 649–658.

Tassara, S., Reich, M., Cannatelli, C., Konecke, B. A., Kausel, D., Morata, D., et al. (2020). Post-melting oxidation of highly primitive basalts from the southern Andes. Geochimica et Cosmochimica Acta, 273, 291–312.

Wallace, P. J., & Carmichael, I. S. E. (1992). Sulfur in basaltic magmas. Geochimica et Cosmochimica Acta, 56(5), 1863–1874. https://doi.org/10.1016/0016-7037(92)90316-B

Wallace, P. J., & Carmichael, I. S. E. (1994). S speciation in submarine basaltic glasses as determined by measurements of S Kα X-ray wavelength shifts., 79, 161–167.

Wallace, P. J., Anderson Jr, A. T., & Davis, A. M. (1999). Gradients in H2O, CO2, and exsolved gas in a large-volume silicic magma system: Interpreting the record preserved in melt inclusions from the Bishop Tuff. Journal of Geophysical Research: Solid Earth, 104(B9), 20097–20122.

Wallace, P. J., Dufek, J., Anderson, A. T., & Zhang, Y. (2003). Cooling rates of Plinian-fall and pyroclastic-flow deposits in the Bishop Tuff: inferences from water speciation in quartz-hosted glass inclusions. Bulletin of Volcanology, 65(2–3), 105–123.

Watkins, J. M., Gardner, J. E., & Befus, K. S. (2017). Nonequilibrium degassing, regassing, and vapor fluxing in magmatic feeder systems. Geology, 45(2), 183–186.

Weaver, S. L., Wallace, P. J., & Johnston, A. D. (2011). A comparative study of continental vs. intraoceanic arc mantle melting: Experimentally determined phase relations of hydrous primitive melts. Earth and Planetary Science Letters, 308(1–2), 97–106.

Wilke, M., Partzsch, G. M., Bernhardt, R., & Lattard, D. (2004). Determination of the iron oxidation state in basaltic glasses using XANES at the K-edge. Chemical Geology, 213(1–3), 71–87.

Wilke, M., Farges, F., Partzsch, G. M., Schmidt, C., & Behrens, H. (2007). Speciation of Fe in silicate glasses and melts by in-situ XANES spectroscopy. American Mineralogist, 92(1), 44–56.

Wilke, M., Jugo, P. J., Klimm, K., Susini, J., Botcharnikov, R., Kohn, S. C., & Janousch, M. (2008). The origin of S4+ detected in silicate glasses by XANES. American Mineralogist, 93(1), 235–240.

Zhang, H. L., Hirschmann, M. M., Cottrell, E., Newville, M., & Lanzirotti, A. (2016). Structural environment of iron and accurate determination of Fe3+/ΣFe ratios in andesitic glasses by XANES and Mössbauer spectroscopy. Chemical Geology, 428, 48–58.

Zhang, H. L., Cottrell, E., Solheid, P. A., Kelley, K. A., & Hirschmann, M. M. (2018). Determination of Fe3+/ΣFe of XANES basaltic glass standards by Mössbauer spectroscopy and its application to the oxidation state of iron in MORB. Chemical Geology, 479, 166–175.

Chapter IV

Anderson, A. T., & Brown, G. G. (1993). CO2 contents and formation pressures of some Kilauean melt inclusions. *American Mineralogist*, *78*(7–8), 794–803.

Anderson, A. T., & Wright, T. L. (1972). Phenocrysts and glass inclusions and their bearing on oxidation and mixing of basaltic magmas, Kilauea Volcano, Hawaii. *American Mineralogist*, *57*(1–2), 188–216.

Anderson, K. R., & Poland, M. P. (2017). Abundant carbon in the mantle beneath Hawai‘i. *Nature Geoscience*, *10*(9), 704–708.

Anderson, K. R., Johanson, I. A., Patrick, M. R., Gu, M., Segall, P., Poland, M. P., et al. (2019). Magma reservoir failure and the onset of caldera collapse at Kīlauea Volcano in 2018. *Science*, *366*(6470).

Aster, E. M., Wallace, P. J., Moore, L. R., Watkins, J., Gazel, E., & Bodnar, R. J. (2016). Reconstructing CO2 concentrations in basaltic melt inclusions using Raman analysis of vapor bubbles. *Journal of Volcanology and Geothermal Research*, *323*, 148–162.

Barth, A., Newcombe, M., Plank, T., Gonnermann, H., Hajimirza, S., Soto, G. J., et al. (2019). Magma decompression rate correlates with explosivity at basaltic volcanoes - Constraints from water diffusion in olivine. *Journal of Volcanology and Geothermal Research*, *387*, 106664.

Beattie, P. (1993). Olivine-melt and orthopyroxene-melt equilibria. *Contributions to Mineralogy and Petrology*, *115*(1), 103–111.

Beaudry, P., Longpré, M.-A., Economos, R., Wing, B. A., Bui, T. H., & Stix, J. (2018). Degassing-induced fractionation of multiple sulphur isotopes unveils post-Archaean recycled oceanic crust signal in hotspot lava. *Nature Communications*, *9*(1), 1–12.

Behrens, H., & Stelling, J. (2011). Diffusion and redox reactions of sulfur in silicate melts. *Reviews in Mineralogy and Geochemistry*, *73*(1), 79–111.

Beirle, S., Hörmann, C., Penning de Vries, M., Dörner, S., Kern, C., & Wagner, T. (2014). Estimating the volcanic emission rate and atmospheric lifetime of SO_2 from space: A case study for Kīlauea volcano, Hawai`i. *Atmospheric Chemistry and Physics*, *14*(16), 8309–8322. https://doi.org/10.5194/acp-14-8309-2014

Brounce, M., Stolper, E., & Eiler, J. (2017). Redox variations in Mauna Kea lavas, the oxygen fugacity of the Hawaiian plume, and the role of volcanic gases in Earth's oxygenation. *Proceedings of the National Academy of Sciences*, *114*(34), 8997–9002.

Bucholz, C. E., Gaetani, G. A., Behn, M. D., & Shimizu, N. (2013). Post-entrapment modification of volatiles and oxygen fugacity in olivine-hosted melt inclusions. *Earth and Planetary Science Letters*, *374*, 145–155.

Burgisser, A., & Scaillet, B. (2007). Redox evolution of a degassing magma rising to the surface. *Nature*, *445*(7124), 194–197.

Burgisser, A., Alletti, M., & Scaillet, B. (2015). Simulating the behavior of volatiles belonging to the C–O–H–S system in silicate melts under magmatic conditions with the software D-Compress. *Computers & Geosciences*, *79*, 1–14.

Burnham, C. W. (1979). The importance of volatile constituents. In H. S. Yoder Jr. (Ed.), *The evolution of the igneous rocks: Fiftieth Anniversary Perspective* (pp. 439–482). Princeton, N.J.: Princeton University Press.

Callegaro, S., Geraki, K., Marzoli, A., Min, A. D., Maneta, V., & Baker, D. R. (2020). The quintet completed: The partitioning of sulfur between nominally volatile-free minerals and silicate melts. *American Mineralogist*, *105*(5), 697–707. https://doi.org/10.2138/am-2020-7188

Carmichael, I. S., & Ghiorso, M. S. (1986). Oxidation-reduction relations in basic magma: A case for homogeneous equilibria. *Earth and Planetary Science Letters*, *78*(2–3), 200–210.

Carroll, M., & Rutherford, M. J. (1988). Sulfur speciation in hydrous experimental glasses of varying oxidation state–results from measured wavelength shifts of sulfur X-rays. *American Mineralogist*, *73*(7), 845–9.

Cervelli, P. F., & Miklius, A. (2003). The shallow magmatic system of Kilauea Volcano. *US Geological Survey Professional Paper*, *1676*, 149–163.

Chen, Y., Provost, A., Schiano, P., & Cluzel, N. (2011). The rate of water loss from olivine-hosted melt inclusions. *Contributions to Mineralogy and Petrology*, *162*(3), 625–636.

Clague, D. A., Moore, J. G., Dixon, J. E., & Friesen, W. B. (1995). Petrology of submarine lavas from Kilauea's Puna Ridge, Hawaii. *Journal of Petrology*, *36*(2), 299–349.

Clor, L. E., Kelly, P. J., Nadeau, P., Lerner, A. H., Elias, T., Kern, C., et al. (2018). Gas composition monitoring with Multi-GAS during the 2018 eruption of Kilauea, Hawai'i. In *AGU Fall Meeting Abstracts*.

Cottrell, E., Kelley, K. A., Lanzirotti, A., & Fischer, R. A. (2009). High-precision determination of iron oxidation state in silicate glasses using XANES. *Chemical Geology*, *268*(3), 167–179.

Cottrell, E., Lanzirotti, A., Mysen, B., Birner, S., Kelley, K. A., Botcharnikov, R., et al. (2018). A Mössbauer-based XANES calibration for hydrous basalt glasses reveals radiation-induced oxidation of Fe. *American Mineralogist*, *103*(4), 489–501. https://doi.org/10.2138/am-2018-6268

Danyushevsky, L. V., & Plechov, P. (2011). Petrolog3: Integrated software for modeling crystallization processes. *Geochemistry, Geophysics, Geosystems*, *12*(7).

Danyushevsky, L. V., Della-Pasqua, F. N., & Sokolov, S. (2000). Re-equilibration of melt inclusions trapped by magnesian olivine phenocrysts from subduction-related magmas: petrological implications. *Contributions to Mineralogy and Petrology*, *138*(1), 68–83.

Danyushevsky, L. V., McNeill, A. W., & Sobolev, A. V. (2002). Experimental and petrological studies of melt inclusions in phenocrysts from mantle-derived magmas: An overview of techniques, advantages and complications. *Chemical Geology*, *183*(1), 5–24.

Delaney, P. T., & McTigue, D. F. (1994). Volume of magma accumulation or withdrawal estimated from surface uplift or subsidence, with application to the 1960 collapse of Kilauea volcano. *Bulletin of Volcanology*, *56*(6), 417–424. https://doi.org/10.1007/BF00302823

Desborough, G. A., Anderson, A. T., & Wright, T. L. (1968). Mineralogy of sulfides from certain Hawaiian basalts. *Economic Geology*, *63*(6), 636–644.

Dietterich, H. R., Diefenbach, A. K., Soule, S. A., Zoeller, M. H., Patrick, M. R., & Lundgren, P. R. (in preparation). Syn-eruptive monitoring of lava effusion rates and erupted volume during the 2018 Kīlauea lower East Rift Zone eruption.

Dixon, J. E., Clague, D. A., & Stolper, E. M. (1991). Degassing history of water, sulfur, and carbon in submarine lavas from Kilauea Volcano, Hawaii. *The Journal of Geology*, *99*(3), 371–394.

Dixon, J. E., Stolper, E. M., & Holloway, J. R. (1995). An experimental study of water and carbon dioxide solubilities in mid-ocean ridge basaltic liquids. Part I: calibration and solubility models. *Journal of Petrology*, *36*(6), 1607–1631.

Edmonds, M., Sides, I. R., Swanson, D. A., Werner, C., Martin, R. S., Mather, T. A., et al. (2013). Magma storage, transport and degassing during the 2008–10 summit eruption at Kilauea Volcano, Hawai'i, *123*, 284–301.

Edmonds, M., Mather, T., & Liu, E. (2018). Tracking metal pathways in magmas using volcanic gas fingerprints. *Nature Geoscience*, *11*, 790–794.

Elias, T., & Sutton, A. J. (2007). *Sulfur Dioxide Emission Rates from Kīlauea Volcano, Hawaii, an Update: 2002-2006*. US Geological Survey.

Elias, T., & Sutton, A. J. (2012). *Sulfur dioxide emission rates from Kilauea Volcano, Hawai'i, 2007-2010* (U.S. Geological Survey Open-File Report No. 2012–1107). Retrieved from http://pubs.usgs.gov/of/2012/1107/

Elias, T., Kern, C., Horton, K. A., Sutton, A. J., & Garbeil, H. (2018a). Measuring SO2 emission rates at Kīlauea Volcano, Hawaii, using an array of upward-looking UV spectrometers, 2014–2017. *Frontiers in Earth Science*, *6*, 214.

Elias, T., Kern, C., Horton, K., Garbeil, H., & Sutton, A. J. (2018b). SO2 emission rates from Kilauea Volcano, Hawaii (2014-2017) [Data set]. U.S. Geological Survey. https://doi.org/10.5066/F7794402

Ellis, W. (1825). *A Journal of a Tour Around Hawaii: The Largest of the Sandwich Islands, by a Deputation from the Mission of Those Islands*. Crocker & Brewster.

Epp, D., Decker, R. W., & Okamura, A. T. (1983). Relation of summit deformation to east rift zone eruptions on Kilauea Volcano, Hawaii. *Geophysical Research Letters*, *10*(7), 493–496.

Farquharson, J. I., & Amelung, F. (2020). Extreme rainfall triggered the 2018 rift eruption at Kīlauea Volcano. *Nature*, *580*(7804), 491–495.

Ferguson, D. J., Gonnermann, H. M., Ruprecht, P., Plank, T., Hauri, E. H., Houghton, B. F., & Swanson, D. A. (2016). Magma decompression rates during explosive eruptions of Kīlauea volcano, Hawaii, recorded by melt embayments. *Bulletin of Volcanology*, *78*(10), 71.

Ferriss, E., Plank, T., Newcombe, M., Walker, D., & Hauri, E. (2018). Rates of dehydration of olivines from San Carlos and Kilauea Iki. *Geochimica et Cosmochimica Acta*, *242*, 165–190.

Fiege, A., Holtz, F., Shimizu, N., Mandeville, C. W., Behrens, H., & Knipping, J. L. (2014). Sulfur isotope fractionation between fluid and andesitic melt: An experimental study. *Geochimica et Cosmochimica Acta*, *142*, 501–521.

Fiege, A., Holtz, F., Behrens, H., Mandeville, C. W., Shimizu, N., Crede, L. S., & Goettlicher, J. (2015). Experimental investigation of the S and S-isotope distribution between H2O–S ± Cl fluids and basaltic melts during decompression. *Chemical Geology*, *393*, 36–54.

Fortin, M.-A., Riddle, J., Desjardins-Langlais, Y., & Baker, D. R. (2015). The effect of water on the sulfur concentration at sulfide saturation (SCSS) in natural melts. *Geochimica et Cosmochimica Acta*, *160*, 100–116.

Gaetani, G. A., O'Leary, J. A., Shimizu, N., Bucholz, C. E., & Newville, M. (2012). Rapid reequilibration of H_2O and oxygen fugacity in olivine-hosted melt inclusions. *Geology*, *40*(10), 915–918.

Gansecki, C., Lee, R. L., Shea, T., Lundblad, S. P., Hon, K., & Parcheta, C. (2019). The tangled tale of Kīlauea's 2018 eruption as told by geochemical monitoring. *Science*, *366*(6470).

Garcia, M. O., Pietruszka, A. J., & Rhodes, J. M. (2003). A petrologic perspective of the summit magma chamber of Kilauea Volcano, Hawai'i. *Journal of Petrology*, *44*, 2313–2339.

Gerlach, T. M. (1986). Exsolution of H2O, CO2, and S during eruptive episodes at Kilauea Volcano, Hawaii. *Journal of Geophysical Research: Solid Earth*, *91*(B12), 12177–12185.

Gerlach, T. M. (1993). Oxygen buffering of Kilauea volcanic gases and the oxygen fugacity of Kilauea basalt. *Geochimica et Cosmochimica Acta*, *57*(4), 795–814. https://doi.org/10.1016/0016-7037(93)90169-W

Gerlach, T. M., & Graeber, E. J. (1985). Volatile budget of Kilauea Volcano. *Nature*, *313*(6000), 273–277.

Gerlach, T. M., McGee, K. A., Elias, T., Sutton, A. J., & Doukas, M. P. (2002). Carbon dioxide emission rate of Kīlauea Volcano: Implications for primary magma and the summit reservoir. *Journal of Geophysical Research: Solid Earth*, *107*(B9), ECV–3.

Gerlach, T. M., Roeder, P. L., Thornber, C., & Grant, A. (2004). Comment on paper:'Morphology and compositions of spinel in Pu'u'ō'Ō lava (1996-1998), Kilauea volcano, Hawaii': enigmatic discrepancies between lava and gas-based fO2 determinations of Pu'u'ō'Ō lava. Authors' reply. *Journal of Volcanology and Geothermal Research*, *134*(3), 241–244.

Greaney, A. T., Rudnick, R. L., Helz, R. T., Gaschnig, R. M., Piccoli, P. M., & Ash, R. D. (2017). The behavior of chalcophile elements during magmatic differentiation as observed in Kilauea Iki lava lake, Hawaii. *Geochimica et Cosmochimica Acta*, *210*, 71–96.

Greenland, L. P., Rose, W. I., & Stokes, J. B. (1985). An estimate of gas emissions and magmatic gas content from Kilauea volcano. *Geochimica et Cosmochimica Acta*, *49*(1), 125–129.

Harris, D. M. (1981). The concentration of CO2 in submarine tholeiitic basalts. *The Journal of Geology*, *89*(6), 689–701.

Hartley, M. E., Neave, D. A., Maclennan, J., Edmonds, M., & Thordarson, T. (2015). Diffusive over-hydration of olivine-hosted melt inclusions. *Earth and Planetary Science Letters*, *425*, 168–178.

Hartley, M. E., Shorttle, O., Maclennan, J., Moussallam, Y., & Edmonds, M. (2017). Olivine-hosted melt inclusions as an archive of redox heterogeneity in magmatic systems. *Earth and Planetary Science Letters*, *479*, 192–205.

Hauri, E. (2002). SIMS analysis of volatiles in silicate glasses, 2: Isotopes and abundances in Hawaiian melt inclusions. *Chemical Geology*, *183*(1–4), 115–141.

Hawaiian Volcano Observatory. (2019, August 15). What does water in Halemaʻumaʻu mean? *Hawaiian Volcano Observatory Volcano Watch*. Retrieved from https://volcanoes.usgs.gov/observatories/hvo/hvo_volcano_watch.html?vwid=1425

Head, E., Lanzirotti, A., Newville, M., & Sutton, S. (2018). Vanadium, sulfur, and iron valences in melt inclusions as a window into magmatic processes: A case study at Nyamuragira volcano, Africa. *Geochimica et Cosmochimica Acta*, *226*, 149–173.

Head, J. W., & Wilson, L. (1987). Lava fountain heights at Pu'u 'O'o, Kilauea, Hawaii: Indicators of amount and variations of exsolved magma volatiles. *Journal of Geophysical Research: Solid Earth*, *92*(B13), 13715–13719. https://doi.org/10.1029/JB092iB13p13715

Helz, R. T., & Thornber, C. R. (1987). Geothermometry of Kilauea Iki lava lake, Hawaii. *Bulletin of Volcanology*, *49*(5), 651–668.

Helz, R. T., & Wright, T. L. (1992). Differentiation and magma mixing on Kilauea's east rift zone. *Bulletin of Volcanology*, *54*(5), 361–384.

Helz, R. T., Clague, D. A., Mastin, L. G., & Rose, T. R. (2015). Evidence for large compositional ranges in coeval melts erupted from Kīlauea's summit reservoir. In *Hawaiian Volcanoes* (pp. 125–145). American Geophysical Union (AGU). https://doi.org/10.1002/9781118872079.ch7

Helz, R. T., Cottrell, E., Brounce, M. N., & Kelley, K. A. (2017). Olivine-melt relationships and syneruptive redox variations in the 1959 eruption of Kīlauea Volcano as revealed by XANES. *Journal of Volcanology and Geothermal Research*, *333*, 1–14.

Holcomb, R. T. (1987). Eruptive history and long-term behavior of Kilauea Volcano. *US Geological Survey Professional Paper*, *1350*(1), 261–350.

Hsieh, P. A., & Ingebritsen, S. E. (2019). Groundwater inflow toward a preheated volcanic conduit: Application to the 2018 eruption at Kīlauea Volcano, Hawai'i. *Journal of Geophysical Research: Solid Earth*, *124*(2), 1498–1506.

Hurwitz, S., & Anderson, K. R. (2019). Temporal variations in scrubbing of magmatic gases at the summit of Kīlauea Volcano, Hawai'i. *Geophysical Research Letters*.

Iacono-Marziano, G., Morizet, Y., Le Trong, E., & Gaillard, F. (2012). New experimental data and semi-empirical parameterization of H2O–CO2 solubility in mafic melts. *Geochimica et Cosmochimica Acta*, *97*, 1–23.

Iacovino, K., & Till, C. B. (2019). DensityX: A program for calculating the densities of magmatic liquids up to 1,627° C and 30 kbar. *Volcanica*, *2*(1), 1–10.

Jugo, P. J. (2009). Sulfur content at sulfide saturation in oxidized magmas. *Geology*, *37*(5), 415–418.

Jugo, P. J., Wilke, M., & Botcharnikov, R. E. (2010). Sulfur K-edge XANES analysis of natural and synthetic basaltic glasses: Implications for S speciation and S content as function of oxygen fugacity. *Geochimica et Cosmochimica Acta*, *74*(20), 5926–5938.

Kądziołka-Gaweł, M., Adamczyk, Z., & Kalinowski, L. (2019). Mössbauer study of changes in olivine after heating in air. *The Canadian Mineralogist*, *57*(1), 105–115.

Kelly, P. J., Clor, L. E., Diefenbach, A. K., Lerner, A. H., Elias, T., Nadeau, P. A., et al. (in preparation). Drone-borne monitoring of volcanic plume compositions during the 2018 rift eruption of Kīlauea Volcano.

Kern, C., Lerner, A. H., Elias, T., Nadeau, P. A., Holland, L., Kelly, P. J., et al. (2020). Quantifying gas emissions associated with the 2018 rift eruption of Kīlauea Volcano using ground-based DOAS measurements. *Bulletin of Volcanology*, *82*(7), 55. https://doi.org/10.1007/s00445-020-01390-8

Klimm, K., Kohn, S. C., & Botcharnikov, R. E. (2012). The dissolution mechanism of sulphur in hydrous silicate melts. II: Solubility and speciation of sulphur in hydrous silicate melts as a function of fO2. *Chemical Geology*, *322*, 250–267.

Knafelc, J., Filiberto, J., Ferré, E. C., Conder, J. A., Costello, L., Crandall, J. R., et al. (2019). The effect of oxidation on the mineralogy and magnetic properties of olivine. *American Mineralogist*, *104*(5), 694–702.

Kohlstedt, D. L., Goetze, C., Durham, W. B., & Vander Sande, J. (1976). New technique for decorating dislocations in olivine. *Science*, *191*(4231), 1045–1046.

Konecke, B. A., Fiege, A., Simon, A. C., Parat, F., & Stechern, A. (2017). Co-variability of S6+, S4+, and S2- in apatite as a function of oxidation state: Implications for a new oxybarometer. *American Mineralogist*, *102*(3), 548–557.

Kress, V. C., & Carmichael, I. S. (1988). Stoichiometry of the iron oxidation reaction in silicate melts. *American Mineralogist*, *73*(11–12), 1267–1274.

Kress, V. C., & Carmichael, I. S. (1991). The compressibility of silicate liquids containing Fe_2O_3 and the effect of composition, temperature, oxygen fugacity and pressure on their redox states. *Contributions to Mineralogy and Petrology*, *108*(1–2), 82–92.

Labidi, J., & Cartigny, P. (2016). Negligible sulfur isotope fractionation during partial melting: Evidence from Garrett transform fault basalts, implications for the late-veneer and the hadean matte. *Earth and Planetary Science Letters*, *451*, 196–207. https://doi.org/10.1016/j.epsl.2016.07.012

Labidi, J., Cartigny, P., Birck, J. L., Assayag, N., & Bourrand, J. J. (2012). Determination of multiple sulfur isotopes in glasses: A reappraisal of the MORB δ34S. *Chemical Geology*, *334*, 189–198.

Lange, R. A., & Carmichael, I. S. (1987). Densities of Na2O-K2O-CaO-MgO-FeO-Fe2O3-Al2O3-TiO2-SiO2 liquids: New measurements and derived partial molar properties. *Geochimica et Cosmochimica Acta*, *51*(11), 2931–2946.

Lee, R. L., Gansecki, C., Lundblad, S., Mills, P., Adams, D. T., Conrey, R., & Wagoner, L. (2019). *Whole-rock and glass chemistry of lava samples collected during the 2018 Lower East Rift Zone eruption of Kilauea* (U.S. Geological Survey data release). U.S. Geological Survey. Retrieved from https://doi.org/10.5066/P9LVY7GV

Lesher, C. E., & Spera, F. J. (2015). Thermodynamic and transport properties of silicate melts and magma. In H. Sigurdsson (Ed.), *The Encyclopedia of Volcanoes (Second Edition)* (pp. 113–141). Amsterdam: Academic Press. https://doi.org/10.1016/B978-0-12-385938-9.00005-5

Li, C., & Ripley, E. M. (2009). Sulfur contents at sulfide-liquid or anhydrite saturation in silicate melts: Empirical equations and example applications. *Economic Geology*, *104*(3), 405–412. https://doi.org/10.2113/gsecongeo.104.3.405

Li, Y., & Liu, J. (2006). Calculation of sulfur isotope fractionation in sulfides. *Geochimica et Cosmochimica Acta*, *70*(7), 1789–1795.

Lloyd, A. S., Plank, T., Ruprecht, P., Hauri, E. H., & Rose, W. (2013). Volatile loss from melt inclusions in pyroclasts of differing sizes. *Contributions to Mineralogy and Petrology*, *165*(1), 129–153.

Longpré, M.-A., Stix, J., Klügel, A., & Shimizu, N. (2017). Mantle to surface degassing of carbon- and sulphur-rich alkaline magma at El Hierro, Canary Islands. *Earth and Planetary Science Letters*, *460*, 268–280. https://doi.org/10.1016/j.epsl.2016.11.043

Lundgren, P. R., Bagnardi, M., & Dietterich, H. (2019). Topographic changes during the 2018 Kīlauea eruption from single-pass airborne InSAR. *Geophysical Research Letters*, *46*(16), 9554–9562. https://doi.org/10.1029/2019GL083501

Maaløe, S., & Hansen, B. (1982). Olivine phenocrysts of Hawaiian olivine tholeiite and oceanite. *Contributions to Mineralogy and Petrology*, *81*(3), 203–211.

Mandeville, C. W., Webster, J. D., Rutherford, M. J., Taylor, B. E., Timbal, A., & Faure, K. (2002). Determination of molar absorptivities for infrared absorption bands of H2O in andesitic glasses. *American Mineralogist*, *87*(7), 813–821.

Mandeville, C. W., Shimizu, N., Kelley, K. A., & Cheek, L. (2008). Sulfur isotope variation in basaltic melt inclusions from Krakatau revealed by a newly developed secondary ion mass spectrometry technique for silicate glasses. In *AGU Fall Meeting Abstracts*.

Marini, L., Moretti, R., & Accornero, M. (2011). Sulfur isotopes in magmatic-hydrothermal systems, melts, and magmas. *Reviews in Mineralogy and Geochemistry*, *73*(1), 423–492.

Mercier, M., Di Muro, A., Métrich, N., Giordano, D., Belhadj, O., & Mandeville, C. W. (2010). Spectroscopic analysis (FTIR, Raman) of water in mafic and intermediate glasses and glass inclusions. *Geochimica et Cosmochimica Acta*, *74*(19), 5641–5656.

Métrich, N., Berry, A. J., O'Neill, H. S. C., & Susini, J. (2009). The oxidation state of sulfur in synthetic and natural glasses determined by X-ray absorption spectroscopy. *Geochimica et Cosmochimica Acta*, *73*(8), 2382–2399.

Miyoshi, T., Sakai, H., & Chiba, H. (1984). Experimental study of sulfur isotope fractionation factors between sulfate and sulfide in high temperature melts. *Geochemical Journal*, *18*(2), 75–84.

Moore, L. R., Gazel, E., Tuohy, R., Lloyd, A. S., Esposito, R., Steele-MacInnis, M., et al. (2015). Bubbles matter: An assessment of the contribution of vapor bubbles to melt inclusion volatile budgets. *American Mineralogist*, *100*(4), 806–823.

Moore, R. B., Helz, R. T., Dzurisin, D., Eaton, G. P., Koyanagi, R. Y., Lipman, P. W., et al. (1980). The 1977 eruption of Kilauea volcano, Hawaii. *Journal of Volcanology and Geothermal Research*, *7*(3–4), 189–210.

Mourey, A., Shea, T., Costa, F., Shiro, B., Lerner, A. H., Wallace, P. J., et al. (submitted). A summit origin for the magma supplying the 2018 Kīlauea eruption.

Mourey, A., Shea, T., Costa Rodriguez, F., Shiro, B., Lee, R. L., Gansecki, C. A., & Oalmann, J. (2019). Diffusion timescales in olivine from the 2018 eruption at Kilauea Volcano reveal syn-eruptive (months) and long term (years) magma mixing processes. In *AGU Fall Meeting* (Vol. 2019, pp. V43C–0208).

Mourey, A. J., & Shea, T. (2019). Forming olivine phenocrysts in basalt: A 3D characterization of growth rates in laboratory experiments. *Frontiers in Earth Science*, *7*. https://doi.org/10.3389/feart.2019.00300

Moussallam, Y., Oppenheimer, C., Scaillet, B., Gaillard, F., Kyle, P., Peters, N., et al. (2014). Tracking the changing oxidation state of Erebus magmas, from mantle to surface, driven by magma ascent and degassing. *Earth and Planetary Science Letters*, *393*, 200–209.

Moussallam, Y., Edmonds, M., Scaillet, B., Peters, N., Gennaro, E., Sides, I., & Oppenheimer, C. (2016). The impact of degassing on the oxidation state of basaltic magmas: A case study of Kīlauea volcano. *Earth and Planetary Science Letters*, *450*, 317–325.

Moussallam, Y., Longpré, M.-A., McCammon, C., Gomez-Ulla, A., Rose-Koga, E. F., Scaillet, B., et al. (2019). Mantle plumes are oxidised. *Earth and Planetary Science Letters*, *527*, 115798. https://doi.org/10.1016/j.epsl.2019.115798

Mungall, J. E., & Su, S. (2005). Interfacial tension between magmatic sulfide and silicate liquids: Constraints on kinetics of sulfide liquation and sulfide migration through silicate rocks. *Earth and Planetary Science Letters*, *234*(1–2), 135–149.

Nash, W. M., Smythe, D. J., & Wood, B. J. (2019). Compositional and temperature effects on sulfur speciation and solubility in silicate melts. *Earth and Planetary Science Letters*, *507*, 187–198.

Neal, C. A., Brantley, S. R., Antolik, L., Babb, J. L., Burgess, M., Calles, K., et al. (2019). The 2018 rift eruption and summit collapse of Kīlauea Volcano. *Science*, *363*(6425), 367–374. https://doi.org/10.1126/science.aav7046

Newville, M. (2013). Larch: An analysis package for XAFS and related spectroscopies. In *Journal of Physics: Conference Series* (Vol. 430, p. 012007). IOP Publishing.

Nichols, A. R., & Wysoczanski, R. J. (2007). Using micro-FTIR spectroscopy to measure volatile contents in small and unexposed inclusions hosted in olivine crystals. *Chemical Geology*, *242*(3–4), 371–384.

Orr, T. R., Poland, M. P., Patrick, M. R., Thelen, W. A., Sutton, A. J., Elias, T., et al. (2015). Kilauea's 5-9 March 2011 Kamoamoa fissure eruption and its relation to 30+ years of activity from Pu'u 'Ō'ō: Chapter 18. *Geophysical Monograph*, *208*, 393–420. https://doi.org/10.1002/9781118872079.ch18

Patrick, M., Swanson, D., & Orr, T. (2019a). A review of controls on lava lake level: Insights from Halema ʻuma ʻu Crater, Kīlauea Volcano. *Bulletin of Volcanology*, *81*(3), 13.

Patrick, M., Orr, T., Anderson, K., & Swanson, D. (2019b). Eruptions in sync: Improved constraints on Kīlauea Volcano's hydraulic connection. *Earth and Planetary Science Letters*, *507*, 50–61.

Patrick, M. R., Dietterich, H. R., Lyons, J. J., Diefenbach, A. K., Parcheta, C., Anderson, K. R., et al. (2019c). Cyclic lava effusion during the 2018 eruption of Kīlauea Volcano. *Science*, *366*(6470). https://doi.org/10.1126/science.aay9070

Patrick, M., Johanson, I., Shea, T., & Waite, G. (2020). The historic events at Kīlauea Volcano in 2018: Summit collapse, rift zone eruption, and Mw 6.9 earthquake: preface to the special issue. *Bulletin of Volcanology*, *82*(6), 46. https://doi.org/10.1007/s00445-020-01377-5

Patrick, Matthew R., Anderson, K. R., Poland, M. P., Orr, T. R., & Swanson, D. A. (2015). Lava lake level as a gauge of magma reservoir pressure and eruptive hazard. *Geology*, *43*(9), 831–834.

Pietruszka, A. J., Heaton, D. E., Marske, J. P., & Garcia, M. O. (2015). Two magma bodies beneath the summit of Kīlauea Volcano unveiled by isotopically distinct melt deliveries from the mantle. *Earth and Planetary Science Letters*, *413*, 90–100. https://doi.org/10.1016/j.epsl.2014.12.040

Pietruszka, A. J., Marske, J. P., Heaton, D. E., Garcia, M. O., & Rhodes, J. M. (2018). An isotopic perspective into the magmatic evolution and architecture of the rift zones of Kīlauea Volcano. *Journal of Petrology*, *59*(12), 2311–2352. https://doi.org/10.1093/petrology/egy098

Poland, M. P., Miklius, A., & Montgomery-Brown, E. K. (2014). Magma supply, storage, and transport at shield-stage Hawaiian volcanoes. In M. P. Poland, T. J. Takahashi, & C. M. Landowski (Eds.), *Characteristics of Hawaiian Volcanoes* (Vol. 1801, pp. 179–234). U.S. Geological Survey Professional Paper 1801.

Poland, M. P., de Zeeuw-van Dalfsen, E., Bagnardi, M., & Johanson, I. A. (2019). Post-collapse gravity increase at the summit of Kīlauea Volcano, Hawaiʻi. *Geophysical Research Letters*.

Portnyagin, M., Almeev, R., Matveev, S., & Holtz, F. (2008). Experimental evidence for rapid water exchange between melt inclusions in olivine and host magma. *Earth and Planetary Science Letters*, *272*(3), 541–552. https://doi.org/10.1016/j.epsl.2008.05.020

Richet, P., Bottinga, Y., & Javoy, M. (1977). A review of hydrogen, carbon, nitrogen, oxygen, sulphur, and chlorine stable isotope fractionation among gaseous molecules. *Annual Review of Earth and Planetary Sciences*, *5*(1), 65–110.

Richter, D. H., Eaton, J. P., Murata, K. J., Ault, W. U., & Krivoy, H. L. (1970). *Chronological narrative of the 1959-60 eruption of Kilauea volcano, Hawaii* (U.S. Geological Survey Professional Paper No. 537- D) (pp. 1–73). U.S. Geological Survey Professional Paper 537-D.

Riker, J. (2005). The 1859 eruption of Mauna Loa Volcano, Hawai'i: Controls on the development of long lava channels (MSc Thesis). University of Oregon.

Roeder, P. L., & Emslie, Rf. (1970). Olivine-liquid equilibrium. *Contributions to Mineralogy and Petrology*, *29*(4), 275–289.

Roeder, P. L., Thornber, C., Poustovetov, A., & Grant, A. (2003). Morphology and composition of spinel in Pu'u'O'o lava (1996–1998), Kilauea volcano, Hawaii. *Journal of Volcanology and Geothermal Research*, *123*(3–4), 245–265.

Roman, D. C., Cashman, K. V., Gardner, C. A., Wallace, P. J., & Donovan, J. J. (2006). Storage and interaction of compositionally heterogeneous magmas from the 1986 eruption of Augustine Volcano, Alaska. *Bulletin of Volcanology*, *68*(3), 240–254.

Rowe, M. C., Kent, A. J., & Nielsen, R. L. (2007). Determination of sulfur speciation and oxidation state of olivine hosted melt inclusions. *Chemical Geology*, *236*(3–4), 303–322.

Rowe, M. C., Thornber, C. R., & Orr, T. R. (2015). Primitive components, crustal assimilation, and magmatic degassing during the early 2008 Kīlauea summit eruptive activity. In R. Carey, V. Cayol, & M. P. Poland (Eds.), *Hawaiian Volcanoes: From Source to Surface* (Vol. 208, pp. 439–455). AGU Geophysical Monograph Series.

Ryan, M. P. (1987). Elasticity and contractancy of Hawaiian olivine tholeiite and its role in the stability and structural evolution of subcaldera magma reservoirs and rift systems. In R. W. Decker, T. L. Wright, & P. H. Stauffer (Eds.), *Volcanism in Hawaii* (Vol. 1350, pp. 1395–1447). U.S. Geological Survey Professional Paper 1350.

Sakai, H., Casadevall, T. J., & Moore, J. G. (1982). Chemistry and isotope ratios of sulfur in basalts and volcanic gases at Kilauea Volcano, Hawaii. *Geochimica et Cosmochimica Acta*, *46*(5), 729–738.

Sides, I. R., Edmonds, M., Maclennan, J., Swanson, D. A., & Houghton, B. F. (2014a). Eruption style at Kīlauea Volcano in Hawai‘i linked to primary melt composition. *Nature Geoscience*, *7*(6), 464–469.

Sides, I., Edmonds, M., Maclennan, J., Houghton, B. F., Swanson, D. A., & Steele-MacInnis, M. J. (2014b). Magma mixing and high fountaining during the 1959 Kīlauea Iki eruption, Hawai‘i. *Earth and Planetary Science Letters*, *400*, 102–112.

Smythe, D. J., Wood, B. J., & Kiseeva, E. S. (2017). The S content of silicate melts at sulfide saturation: new experiments and a model incorporating the effects of sulfide composition. *American Mineralogist*, *102*(4), 795–803.

Sobolev, A. V., & Danyushevsky, L. V. (1994). Petrology and geochemistry of boninites from the north termination of the Tonga Trench: constraints on the generation conditions of primary high-Ca boninite magmas. *Journal of Petrology*, *35*(5), 1183–1211.

Sobolev, A. V., Dmitriev, L. V., Barsukov, V. L., Nevsorov, V. N., & Slutskii, A. B. (1980). The formation conditions of the high-magnesium olivines from the monomineralic fraction of Luna 24 regolith. In *Lunar and Planetary Science Conference Proceedings* (Vol. 11, pp. 105–116).

Sparks, R. S. J. (1978). The dynamics of bubble formation and growth in magmas: A review and analysis. *Journal of Volcanology and Geothermal Research*, *3*(1–2), 1–37. https://doi.org/10.1016/0377-0273(78)90002-1

Steele-Macinnis, M., Esposito, R., & Bodnar, R. J. (2011). Thermodynamic model for the effect of post-entrapment crystallization on the H2O–CO2 systematics of vapor-saturated, silicate melt inclusions. *Journal of Petrology*, *52*(12), 2461–2482.

Stolper, E. (1982). Water in silicate glasses: An infrared spectroscopic study. *Contributions to Mineralogy and Petrology*, *81*(1), 1–17.

Stone, W. E., & Fleet, M. E. (1991). Nickel-copper sulfides from the 1959 eruption of Kilauea Volcano, Hawaii: Contrasting compositions and phase relations in eruption pumice and Kilauea Iki lava lake. *American Mineralogist*, *76*(7–8), 1363–1372.

Sutton, A. J., Elias, T., & Kauahikaua, J. (2003). Lava-effusion rates for the Pu’u’O’o–Kupaianaha eruption derived from SO2 emissions and very low frequency (VLF) measurements. In C. Heliker, D. A. Swanson, & T. J. Takahashi (Eds.), *The Pu’u O’o-Kupaianaha eruption of Kilauea Volcano, Hawai’i: the first 20 years* (pp. 137–148). U.S. Geological Survey Professional Paper 1676.

Sutton, S. R., Lanzirotti, A., Newville, M., Rivers, M. L., Eng, P., & Lefticariu, L. (2017). Spatially resolved elemental analysis, spectroscopy and diffraction at the GSECARS Sector at the Advanced Photon Source. *Journal of Environmental Quality*, *46*(6), 1158–1165.

Swanson, D. A., Duffield, W. A., Jackson, D. B., & Peterson, D. W. (1979). *Chronological narrative of the 1969-71 Mauna Ulu eruption of Kilauea Volcano, Hawaii*. US Geological Survey Professional Paper 1056. Retrieved from 10.3133/pp1056

Swanson, D. A., Rose, T. R., Mucek, A. E., Garcia, M. O., Fiske, R. S., & Mastin, L. G. (2014). Cycles of explosive and effusive eruptions at Kīlauea Volcano, Hawai‘i. *Geology*, *42*(7), 631–634.

Symonds, R. B., Gerlach, T. M., & Reed, M. H. (2001). Magmatic gas scrubbing: Implications for volcano monitoring. *Journal of Volcanology and Geothermal Research*, *108*(1), 303–341.

Tassara, S., Reich, M., Cannatelli, C., Konecke, B. A., Kausel, D., Morata, D., et al. (2020). Post-melting oxidation of highly primitive basalts from the southern Andes. *Geochimica et Cosmochimica Acta*, *273*, 291–312.

Taylor, B. E. (1986). Magmatic volatiles; isotopic variation of C, H and S. *Reviews in Mineralogy and Geochemistry*, *16*, 185–225.

Teplow, W., Marsh, B., Hulen, J., Spielman, P., Kaleikini, M., Fitch, D., & Rickard, W. (2009). Dacite melt at the Puna geothermal venture wellfield, Big Island of Hawaii. *Geothermal Resources Council Transactions*, *33*, 989–994.

Thornber, C. R., Orr, T. R., Heliker, C., & Hoblitt, R. P. (2015). Petrologic testament to changes in shallow magma storage and transport during 30+ years of recharge and eruption at Kılauea Volcano, Hawai‘i. In R. Carey, V. Cayol, & M. P. Poland (Eds.), *Hawaiian Volcanoes: From Source to Surface* (Vol. 208, pp. 147–188). AGU Geophysical Monograph Series.

Tucker, J. M., Hauri, E. H., Pietruszka, A. J., Garcia, M. O., Marske, J. P., & Trusdell, F. A. (2019). A high carbon content of the Hawaiian mantle from olivine-hosted melt inclusions. *Geochimica et Cosmochimica Acta*, *254*, 156–172.

Tuohy, R. M., Wallace, P. J., Loewen, M. W., Swanson, D. A., & Kent, A. J. (2016). Magma transport and olivine crystallization depths in Kīlauea’s east rift zone inferred from experimentally rehomogenized melt inclusions. *Geochimica et Cosmochimica Acta*, *185*, 232–250.

Wallace, P. J., & Anderson Jr, A. T. (1998). Effects of eruption and lava drainback on the H_2O contents of basaltic magmas at Kilauea Volcano. *Bulletin of Volcanology*, *59*(5), 327–344.

Wallace, P. J., & Carmichael, I. S. E. (1992). Sulfur in basaltic magmas. *Geochimica et Cosmochimica Acta*, *56*(5), 1863–1874. https://doi.org/10.1016/0016-7037(92)90316-B

Wallace, P. J., & Carmichael, I. S. E. (1994). S speciation in submarine basaltic glasses as determined by measurements of S Ka X-ray wavelength shifts., *79*, 161–167.

Wallace, P. J., Kamenetsky, V. S., & Cervantes, P. (2015). Melt inclusion CO_2 contents, pressures of olivine crystallization, and the problem of shrinkage bubbles. *American Mineralogist*, *100*(4), 787–794.

Wieser, P. E., Edmonds, M., Maclennan, J., Jenner, F. E., & Kunz, B. E. (2019). Crystal scavenging from mush piles recorded by melt inclusions. *Nature Communications*, *10*(1), 1–11. https://doi.org/10.1038/s41467-019-13518-2

Wieser, Penny E., Edmonds, M., Maclennan, J., & Wheeler, J. (2020a). Microstructural constraints on magmatic mushes under Kīlauea Volcano, Hawai'i. *Nature Communications*, *11*(1), 1–14.

Wieser, P.E., Jenner, F. E., Edmonds, M., Maclennan, J., & Kunz, B. E. (2020b). Chalcophile elements track the fate of sulfur at Kılauea Volcano, Hawai'i. *Geochimica et Cosmochimica Acta*. *282*, 245–275. https://doi.org/10.1016/j.gca.2020.05.018

Wilke, M., Jugo, P. J., Klimm, K., Susini, J., Botcharnikov, R., Kohn, S. C., & Janousch, M. (2008). The origin of S4+ detected in silicate glasses by XANES. *American Mineralogist*, *93*(1), 235–240.

Wilson, L., Parfitt, E. A., & Head, J. W. (1995). Explosive volcanic eruptions—VIII. The role of magma recycling in controlling the behaviour of Hawaiian-style lava fountains. *Geophysical Journal International*, *121*(1), 215–225. https://doi.org/10.1111/j.1365-246X.1995.tb03522.x

Witham, F., Blundy, J., Kohn, S. C., Lesne, P., Dixon, J., Churakov, S. V., & Botcharnikov, R. (2012). SolEx: a model for mixed COHSCl-volatile solubilities and exsolved gas compositions in basalt. *Computers & Geosciences*, *45*, 87–97.

Wolfe, E. W., Garcia, M. O., Jackson, D. B., Koyanagi, R. Y., Neal, C. A., & Okamura, A. T. (1987). The Puu oo eruption of Kilauea volcano, episodes 1–20, January 3, 1983, to June 8, 1984. *US Geol Surv Prof Pap*, *1350*, 471–508.

Wright, T. L., & Klein, F. W. (Eds.). (2014). *Two hundred years of magma transport and storage at Kīlauea Volcano, Hawai'i, 1790-2008*. US Geological Survey Professional Paper 1806.

Wysoczanski, R., & Tani, K. (2006). Spectroscopic FTIR imaging of water species in silicic volcanic glasses and melt inclusions: An example from the Izu-Bonin arc. *Journal of Volcanology and Geothermal Research*, *156*(3–4), 302–314.

Zhang, H. L., Cottrell, E., Solheid, P. A., Kelley, K. A., & Hirschmann, M. M. (2018). Determination of Fe3+/ΣFe of XANES basaltic glass standards by Mössbauer spectroscopy and its application to the oxidation state of iron in MORB. *Chemical Geology*, *479*, 166–175.

Zoeller, M. H., Perroy, R. L., Wessels, R. L., Fisher, G. B., Robinson, J. E., Bard, J. A., et al. (2020). Geospatial database of the 2018 lower East Rift Zone eruption of Kīlauea Volcano, Hawai‘i. https://doi.org/10.5066/P9S7UQKQ

Chapter V

Alt, J. C., Shanks III, W. C., & Jackson, M. C. (1993). Cycling of sulfur in subduction zones: The geochemistry of sulfur in the Mariana Island Arc and back-arc trough. *Earth and Planetary Science Letters*, *119*(4), 477–494.

Andersen, D. J., & Lindsley, D. H. (1988). Internally consistent solution models for Fe-Mg-Mn-Ti oxides; Fe-Ti oxides. *American Mineralogist*, *73*(7–8), 714–726.

Andersen, D. J., Lindsley, D. H., & Davidson, P. M. (1993). QUILF: A pascal program to assess equilibria among Fe-Mg-Mn-Ti oxides, pyroxenes, olivine, and quartz. *Computers & Geosciences*, *19*(9), 1333–1350.

Barth, A., Newcombe, M., Plank, T., Gonnermann, H., Hajimirza, S., Soto, G. J., et al. (2019). Magma decompression rate correlates with explosivity at basaltic volcanoes - Constraints from water diffusion in olivine. *Journal of Volcanology and Geothermal Research*, *387*, 106664.

Bedrosian, P. A., Peacock, J. R., Bowles-Martinez, E., Schultz, A., & Hill, G. J. (2018). Crustal inheritance and a top-down control on arc magmatism at Mount St Helens. *Nature Geoscience*, *11*(11), 865–870.

Behrens, H., Tamic, N., & Holtz, F. (2004). Determination of the molar absorption coefficient for the infrared absorption band of CO2 in rhyolitic glasses. *American Mineralogist*, *89*(2–3), 301–306.

Benage, M., Wright, H. M. N., & Coombs, M. L. (submitted). Eruption of compositionally heterogeneous andesites from a complex storage region during the 2006 eruption of Augustine Volcano.

Bergfeld, D., Evans, W. C., Spicer, K. R., Hunt, A. G., & Kelly, P. J. (2017). Evidence for degassing of fresh magma during the 2004–2008 eruption of Mount St. Helens: Subtle signals from the hydrothermal system. *Journal of Volcanology and Geothermal Research*, *343*, 109–121. https://doi.org/10.1016/j.jvolgeores.2017.06.020

Blundy, J., Cashman, K. V., & Berlo, K. (2008). Evolving magma storage conditions beneath Mount St. Helens inferred from chemical variations in melt inclusions from the 1980-1986 and current (2004-2006) eruptions. In D. R. Sherrod, W. E. Scott, & P. H. Stauffer (Eds.), *A volcano rekindled: The renewed eruption of Mount St. Helens, 2004-2006* (pp. 755–790). U.S. Geological Survey Professional Paper 1750.

Blundy, J., Cashman, K. V., Rust, A., & Witham, F. (2010). A case for CO2-rich arc magmas. *Earth and Planetary Science Letters*, *290*(3–4), 289–301.

Bucholz, C. E., Gaetani, G. A., Behn, M. D., & Shimizu, N. (2013). Post-entrapment modification of volatiles and oxygen fugacity in olivine-hosted melt inclusions. *Earth and Planetary Science Letters*, *374*, 145–155.

Burgisser, A., & Scaillet, B. (2007). Redox evolution of a degassing magma rising to the surface. *Nature*, *445*(7124), 194–197.

Burgisser, A., Alletti, M., & Scaillet, B. (2015). Simulating the behavior of volatiles belonging to the C–O–H–S system in silicate melts under magmatic conditions with the software D-Compress. *Computers & Geosciences*, *79*, 1–14.

Callegaro, S., Geraki, K., Marzoli, A., Min, A. D., Maneta, V., & Baker, D. R. (2020). The quintet completed: The partitioning of sulfur between nominally volatile-free minerals and silicate melts. *American Mineralogist*, *105*(5), 697–707. https://doi.org/10.2138/am-2020-7188

Carn, S. A., Fioletov, V. E., McLinden, C. A., Li, C., & Krotkov, N. A. (2017). A decade of global volcanic SO2 emissions measured from space. *Scientific Reports*, *7*, 44095.

Carroll, M., & Rutherford, M. J. (1988). Sulfur speciation in hydrous experimental glasses of varying oxidation state–results from measured wavelength shifts of sulfur X-rays. *American Mineralogist*, *73*(7), 845–9.

Cashman, K. V., & McConnell, S. M. (2005). Multiple levels of magma storage during the 1980 summer eruptions of Mount St. Helens, WA. *Bulletin of Volcanology*, *68*(1), 57. https://doi.org/10.1007/s00445-005-0422-x

Cervelli, P. F., Fournier, T., Freymueller, J. T., Power, J. A., Lisowski, M., & Pauk, B. (2010). Geodetic constraints on magma movement and withdrawal during the 2006 eruption of Augustine Volcano. In J. A. Power, M. L. Coombs, & J. T. Freymueller (Eds.), *The 2006 eruption of Augustine Volcano, Alaska* (pp. 427–452). U.S. Geological Survey Professional Paper 1769.

Chen, Y., Provost, A., Schiano, P., & Cluzel, N. (2011). The rate of water loss from olivine-hosted melt inclusions. *Contributions to Mineralogy and Petrology*, *162*(3), 625–636.

Coombs, M. L., & Gardner, J. E. (2004). Reaction rim growth on olivine in silicic melts: Implications for magma mixing. *American Mineralogist*, *89*(5–6), 748–758.

Coombs, M. L., Bull, K. F., Vallance, J. W., Schneider, D. J., Thoms, E. E., Wessels, R. L., & McGimsey, R. G. (2010). Timing, distribution, and volume of proximal products of the 2006 eruption of Augustine Volcano. In J. A. Power, M. L. Coombs, & J. T. Freymueller (Eds.), *The 2006 eruption of Augustine Volcano, Alaska* (pp. 145–185). U.S. Geological Survey Professional Paper 1769.

Cottrell, E., Kelley, K. A., Lanzirotti, A., & Fischer, R. A. (2009). High-precision determination of iron oxidation state in silicate glasses using XANES. *Chemical Geology*, *268*(3), 167–179.

Danyushevsky, L. V. (2001). The effect of small amounts of H2O on crystallisation of mid-ocean ridge and backarc basin magmas. *Journal of Volcanology and Geothermal Research*, *110*(3), 265–280. https://doi.org/10.1016/S0377-0273(01)00213-X

Danyushevsky, L. V., & Plechov, P. (2011). Petrolog3: Integrated software for modeling crystallization processes. *Geochemistry, Geophysics, Geosystems*, *12*(7).

Danyushevsky, L. V., Della-Pasqua, F. N., & Sokolov, S. (2000). Re-equilibration of melt inclusions trapped by magnesian olivine phenocrysts from subduction-related magmas: petrological implications. *Contributions to Mineralogy and Petrology*, *138*(1), 68–83.

Danyushevsky, L. V., McNeill, A. W., & Sobolev, A. V. (2002). Experimental and petrological studies of melt inclusions in phenocrysts from mantle-derived magmas: An overview of techniques, advantages and complications. *Chemical Geology*, *183*(1), 5–24.

Dauphas, N., Roskosz, M., Alp, E. E., Neuville, D. R., Hu, M. Y., Sio, C. K., et al. (2014). Magma redox and structural controls on iron isotope variations in Earth's mantle and crust. *Earth and Planetary Science Letters*, *398*, 127–140.

De Angelis, S. H., Larsen, J. F., Coombs, M. L., Utley, J. E., & Dunn, A. (2020). Phase equilibrium of a high-SiO2 andesite at fO2=RRO: implications for Augustine Volcano and other high-fO2 arc andesites. *Contributions to Mineralogy and Petrology*, *175*(3), 1–20.

Ferriss, E., Plank, T., Newcombe, M., Walker, D., & Hauri, E. (2018). Rates of dehydration of olivines from San Carlos and Kilauea Iki. *Geochimica et Cosmochimica Acta*, *242*, 165–190.

Fiege, A., Holtz, F., Shimizu, N., Mandeville, C. W., Behrens, H., & Knipping, J. L. (2014). Sulfur isotope fractionation between fluid and andesitic melt: An experimental study. *Geochimica et Cosmochimica Acta*, *142*, 501–521.

Fiege, A., Holtz, F., Behrens, H., Mandeville, C. W., Shimizu, N., Crede, L. S., & Goettlicher, J. (2015). Experimental investigation of the S and S-isotope distribution between H2O–S ± Cl fluids and basaltic melts during decompression. *Chemical Geology*, *393*, 36–54.

Fiege, A., Ruprecht, P., Simon, A. C., Bell, A. S., Göttlicher, J., Newville, M., et al. (2017). Calibration of Fe XANES for high-precision determination of Fe oxidation state in glasses: Comparison of new and existing results obtained at different synchrotron radiation sources. *American Mineralogist*, *102*(2), 369–380.

Gaetani, G. A., O'Leary, J. A., Shimizu, N., Bucholz, C. E., & Newville, M. (2012). Rapid reequilibration of H_2O and oxygen fugacity in olivine-hosted melt inclusions. *Geology*, *40*(10), 915–918.

Galle, B., Oppenheimer, C., Geyer, A., McGonigle, A. J., Edmonds, M., & Horrocks, L. (2003). A miniaturised ultraviolet spectrometer for remote sensing of SO_2 fluxes: a new tool for volcano surveillance. *Journal of Volcanology and Geothermal Research*, *119*(1), 241–254.

Gerlach, T. M., McGee, K. A., & Doukas, M. P. (2008). Emission rates of CO2, SO2, and H2S, scrubbing, and preeruption excess volatiles at Mount St. Helens, 2004-2005. *US Geological Survey Professional Paper*, (1750), 543–571.

Ghiorso, M. S., & Evans, B. W. (2008). Thermodynamics of rhombohedral oxide solid solutions and a revision of the Fe-Ti two-oxide geothermometer and oxygen-barometer. *American Journal of Science*, *308*(9), 957–1039.

Gust, D. A., & Perfit, M. R. (1987). Phase relations of a high-Mg basalt from the Aleutian Island Arc: Implications for primary island arc basalts and high-Al basalts. *Contributions to Mineralogy and Petrology*, *97*(1), 7–18. https://doi.org/10.1007/BF00375210

Harris, G. W. (1994). The petrology and petrogaphy of lava from the 1986 eruption of Augustine volcano (PhD Thesis). University of Alaska Fairbanks.

Hartley, M. E., Neave, D. A., Maclennan, J., Edmonds, M., & Thordarson, T. (2015). Diffusive over-hydration of olivine-hosted melt inclusions. *Earth and Planetary Science Letters*, *425*, 168–178.

Hartley, M. E., Shorttle, O., Maclennan, J., Moussallam, Y., & Edmonds, M. (2017). Olivine-hosted melt inclusions as an archive of redox heterogeneity in magmatic systems. *Earth and Planetary Science Letters*, *479*, 192–205.

Hauri, E. (2002). SIMS analysis of volatiles in silicate glasses, 2: isotopes and abundances in Hawaiian melt inclusions. *Chemical Geology*, *183*(1), 115–141.

Helz, R. T., Cottrell, E., Brounce, M. N., & Kelley, K. A. (2017). Olivine-melt relationships and syneruptive redox variations in the 1959 eruption of Kīlauea Volcano as revealed by XANES. *Journal of Volcanology and Geothermal Research*, *333*, 1–14.

Ide, S. (2013). The proportionality between relative plate velocity and seismicity in subduction zones. *Nature Geoscience*, *6*(9), 780–784.

Johnston, A. D., & Stout, J. H. (1984). Development of orthopyroxene-Fe/Mg ferrite symplectites by continuous olivine oxidation. *Contributions to Mineralogy and Petrology*, *88*(1–2), 196–202.

Johnston, D. A. (1978). Volatiles, magma mixing, and the mechanism of eruption of Augustine Volcano, Alaska (PhD Thesis). University of Washington.

Jugo, P. J., Wilke, M., & Botcharnikov, R. E. (2010). Sulfur K-edge XANES analysis of natural and synthetic basaltic glasses: Implications for S speciation and S content as function of oxygen fugacity. *Geochimica et Cosmochimica Acta*, *74*(20), 5926–5938.

Kent, A. J. (2008). Melt inclusions in basaltic and related volcanic rocks. *Reviews in Mineralogy and Geochemistry*, *69*(1), 273–331.

Kiser, E., Palomeras, I., Levander, A., Zelt, C., Harder, S., Schmandt, B., et al. (2016). Magma reservoirs from the upper crust to the Moho inferred from high-resolution Vp and Vs models beneath Mount St. Helens, Washington State, USA. *Geology*, *44*(6), 411–414.

Kiser, E., Levander, A., Zelt, C., Schmandt, B., & Hansen, S. (2018). Focusing of melt near the top of the Mount St. Helens (USA) magma reservoir and its relationship to major volcanic eruptions. *Geology*, *46*(9), 775–778.

Klimm, K., Kohn, S. C., & Botcharnikov, R. E. (2012). The dissolution mechanism of sulphur in hydrous silicate melts. II: Solubility and speciation of sulphur in hydrous silicate melts as a function of fO2. *Chemical Geology*, *322*, 250–267.

Kress, V. C., & Carmichael, I. S. (1988). Stoichiometry of the iron oxidation reaction in silicate melts. *American Mineralogist*, *73*(11–12), 1267–1274.

Kress, V. C., & Carmichael, I. S. (1991). The compressibility of silicate liquids containing Fe_2O_3 and the effect of composition, temperature, oxygen fugacity and pressure on their redox states. *Contributions to Mineralogy and Petrology*, *108*(1–2), 82–92.

Lange, R. A., & Carmichael, I. S. (1987). Densities of Na2O-K2O-CaO-MgO-FeO-Fe2O3-Al2O3-TiO2-SiO2 liquids: New measurements and derived partial molar properties. *Geochimica et Cosmochimica Acta*, *51*(11), 2931–2946.

Larsen, J. F., Nye, C. J., Coombs, M. L., Tilman, M., Izbekov, P., & Cameron, C. (2010). Petrology and geochemistry of the 2006 eruption of Augustine Volcano. In J. A. Power, M. L. Coombs, & J. T. Freymueller (Eds.), *The 2006 Eruption of Augustine Volcano, Alaska* (pp. 335–382). U.S. Geological Survey Professional Paper 1769.

Lee, C.-W., Lu, Z., Jung, H.-S., Won, J.-S., & Dzurisin, D. (2010). Surface deformation of Augustine Volcano, 1992-2005, from multiple-interferogram processing using a refined Small Baseline Subset (SBAS) Interferometric Synthetic Aperture Radar (InSAR) approach. In J. A. Power, M. Coombs, & J. T. Freymueller (Eds.), *The 2006 eruption of Augustine Volcano, Alaska* (pp. 453–465). U.S. Geological Survey Professional Paper 1769.

Lerner, A. H., Crowley, P. D., Nicolaysen, K. P., & Hazlett, R. W. (2018). Stratigraphy, distribution, and evidence for mafic triggering of the ca. 8.5 ka Driftwood Pumice eruption, Makushin Volcano, Alaska, USA. *Journal of Volcanology and Geothermal Research*, *357*, 362–377.

Lerner, A. H., O'Hara, D., Karlstrom, L., Ebmeier, S. K., Anderson, K. R., & Hurwitz, S. (2020). The prevalence and significance of offset magma reservoirs at arc volcanoes. https://doi.org/10.1029/2020GL087856

Leschik, M., Heide, G., Frischat, G. H., Behrens, H., Wiedenbeck, M., Wagner, N., et al. (2004). Determination of H2O and D2O contents in rhyolitic glasses. *Physics and Chemistry of Glasses*, *45*(4), 238–251.

Lesne, P., Scaillet, B., & Pichavant, M. (2015). The solubility of sulfur in hydrous basaltic melts. *Chemical Geology*, *418*, 104–116. https://doi.org/10.1016/j.chemgeo.2015.03.025

Lisowski, M., Dzurisin, D., Denlinger, R. P., & Iwatsubo, E. Y. (2008). Analysis of GPS-measured deformation associated with the 2004-2006 dome-building eruption of Mount St. Helens, Washington. In D. R. Sherrod, W. E. Scott, & P. H. Stauffer (Eds.), *A volcano rekindled: The renewed eruption of Mount St. Helens, 2004-2006* (pp. 281–300). US Geological Survey Professional Paper 1750.

Lloyd, A. S., Plank, T., Ruprecht, P., Hauri, E. H., & Rose, W. (2013). Volatile loss from melt inclusions in pyroclasts of differing sizes. *Contributions to Mineralogy and Petrology*, *165*(1), 129–153.

Mandeville, C., Shimizu, N., Kelley, K. A., Métrich, N., Fiege, A., & Behrens, H. (2011). Progress in understanding of sulfur in subduction zone magmas (p. 1396). Presented at the Goldschmidt Conference Abstracts, Goldschmidt Conference Abstracts.

Mandeville, C. W., Shimizu, N., Kelley, K. A., & Cheek, L. (2008). Sulfur isotope variation in basaltic melt inclusions from Krakatau revealed by a newly developed secondary ion mass spectrometry technique for silicate glasses. In *AGU Fall Meeting Abstracts*.

Mandeville, C. W., Webster, J. D., Tappen, C., Taylor, B. E., Timbal, A., Sasaki, A., et al. (2009). Stable isotope and petrologic evidence for open-system degassing during the climactic and pre-climactic eruptions of Mt. Mazama, Crater Lake, Oregon. *Geochimica et Cosmochimica Acta*, *73*(10), 2978–3012.

Masotta, M., & Keppler, H. (2015). Anhydrite solubility in differentiated arc magmas. *Geochimica et Cosmochimica Acta*, *158*, 79–102. https://doi.org/10.1016/j.gca.2015.02.033

Matjuschkin, V., Blundy, J. D., & Brooker, R. A. (2016). The effect of pressure on sulphur speciation in mid-to deep-crustal arc magmas and implications for the formation of porphyry copper deposits. *Contributions to Mineralogy and Petrology*, *171*(7), 66.

McCrory, P. A., Blair, J. L., Oppenheimer, D. H., & Walter, S. R. (2004). Depth to the Juan de Fuca slab beneath the Cascadia subduction margin: A 3-D model for sorting earthquakes, Data Ser. 91. *US Geological Survey Data Series 91*.

McGee, K. A., & Casadevall, T. J. (1994). A compilation of sulfur dioxide and carbon dioxide emission-rate data from Mount St. Helens during 1980-88. US Geological Survey 94-212

McGee, K. A., Doukas, M. P., McGimsey, R. G., Neal, C. A., & Wessels, R. L. (2010). Emission of SO2, CO2, and H2S from Augustine Volcano, 2002-2008. In J. A. Power, M. Coombs, & J. T. Freymueller (Eds.), *The 2006 eruption of Augustine Volcano, Alaska* (pp. 609–627). U.S. Geological Survey Professional Paper 1769.

Métrich, N., & Wallace, P. J. (2008). Volatile abundances in basaltic magmas and their degassing paths tracked by melt inclusions. *Reviews in Mineralogy and Geochemistry*, *69*(1), 363–402.

Miyoshi, T., Sakai, H., & Chiba, H. (1984). Experimental study of sulfur isotope fractionation factors between sulfate and sulfide in high temperature melts. *Geochemical Journal*, *18*(2), 75–84.

Moussallam, Y., Oppenheimer, C., Scaillet, B., Gaillard, F., Kyle, P., Peters, N., et al. (2014). Tracking the changing oxidation state of Erebus magmas, from mantle to surface, driven by magma ascent and degassing. *Earth and Planetary Science Letters*, *393*, 200–209.

Moussallam, Y., Edmonds, M., Scaillet, B., Peters, N., Gennaro, E., Sides, I., & Oppenheimer, C. (2016). The impact of degassing on the oxidation state of basaltic magmas: A case study of Kīlauea volcano. *Earth and Planetary Science Letters*, *450*, 317–325.

Myers, M. L., Wallace, P. J., Wilson, C. J., Morter, B. K., & Swallow, E. J. (2016). Prolonged ascent and episodic venting of discrete magma batches at the onset of the Huckleberry Ridge supereruption, Yellowstone. *Earth and Planetary Science Letters*, *451*, 285–297.

Myers, M. L., Geist, D. J., Rowe, M. C., Harpp, K. S., Wallace, P. J., & Dufek, J. (2014). Replenishment of volatile-rich mafic magma into a degassed chamber drives mixing and eruption of Tungurahua volcano. *Bulletin of Volcanology*, *76*(11), 872.

Nash, W. M., Smythe, D. J., & Wood, B. J. (2019). Compositional and temperature effects on sulfur speciation and solubility in silicate melts. *Earth and Planetary Science Letters*, *507*, 187–198.

Newman, S., & Lowenstern, J. B. (2002). VolatileCalc: a silicate melt–H2O–CO2 solution model written in Visual Basic for Excel. *Computers & Geosciences*, *28*(5), 597–604.

Newville, M. (2013). Larch: An analysis package for XAFS and related spectroscopies. In *Journal of Physics: Conference Series* (Vol. 430, p. 012007). IOP Publishing.

Nichols, A. R., & Wysoczanski, R. J. (2007). Using micro-FTIR spectroscopy to measure volatile contents in small and unexposed inclusions hosted in olivine crystals. *Chemical Geology*, *242*(3–4), 371–384.

Ohmoto, H., & Rye, R. O. (1979). Isotopes of sulfur and carbon. In H. L. Barnes (Ed.), *Geochemistry of Hydrothermal Ore Deposits* (2nd ed., pp. 509–567). New York: John Wiley and Sons.

Oppenheimer, C., Fischer, T. P., & Scaillet, B. (2014). Volcanic degassing: Process and impact. In H. D. Holland & K. K. Turekian (Eds.), *Treatise on Geochemistry* (2nd ed., pp. 111–179). Oxford, UK: Elsevier.

Oppenheimer, C., Scaillet, B., Woods, A., Sutton, A. J., Elias, T., & Moussallam, Y. (2018). Influence of eruptive style on volcanic gas emission chemistry and temperature. *Nature Geoscience*, *11*(9), 678–681. https://doi.org/10.1038/s41561-018-0194-5

Pallister, J. S., Thornber, C. R., Cashman, K. V., Clynne, M. A., Lowers, H. A., Mandeville, C. W., et al. (2008). Petrology of the 2004-2006 Mount St. Helens lava dome-implications for magmatic plumbing and eruption triggering. In D. R. Sherrod, W. E. Scott, & K. V. Stauffer (Eds.), *A volcano rekindled: The renewed eruption of Mount St. Helens, 2004-2006* (pp. 647–702). U.S. Geological Survey Professional Paper 1750.

Panjasawatwong, Y., Danyushevsky, L. V., Crawford, A. J., & Harris, K. L. (1995). An experimental study of the effects of melt composition on plagioclase-melt equilibria at 5 and 10 kbar: Implications for the origin of magmatic high-An plagioclase. *Contributions to Mineralogy and Petrology*, *118*(4), 420–432. https://doi.org/10.1007/s004100050024

Parman, S. W., Grove, T. L., Kelley, K. A., & Plank, T. (2011). Along-arc variations in the pre-eruptive H2O contents of Mariana Arc magmas inferred from fractionation paths. *Journal of Petrology*, *52*(2), 257–278. https://doi.org/10.1093/petrology/egq079

Portnyagin, M., Almeev, R., Matveev, S., & Holtz, F. (2008). Experimental evidence for rapid water exchange between melt inclusions in olivine and host magma. *Earth and Planetary Science Letters*, *272*(3), 541–552. https://doi.org/10.1016/j.epsl.2008.05.020

Power, J. A., Coombs, M. L., & Freymueller, J. T. (Eds.). (2010). *The 2006 eruption of Augustine Volcano, Alaska*. U.S. Geological Survey Professional Paper 1769.

Richet, P., Bottinga, Y., & Javoy, M. (1977). A review of hydrogen, carbon, nitrogen, oxygen, sulphur, and chlorine stable isotope fractionation among gaseous molecules. *Annual Review of Earth and Planetary Sciences*, *5*(1), 65–110.

Riker, J. M., Cashman, K. V., Rust, A. C., & Blundy, J. D. (2015). Experimental constraints on plagioclase crystallization during H2O- and H2O–CO2-saturated magma decompression. *Journal of Petrology*, *56*(10), 1967–1998. https://doi.org/10.1093/petrology/egv059

Roman, D. C., Cashman, K. V., Gardner, C. A., Wallace, P. J., & Donovan, J. J. (2006). Storage and interaction of compositionally heterogeneous magmas from the 1986 eruption of Augustine Volcano, Alaska. *Bulletin of Volcanology*, *68*(3), 240–254.

Rose, W. I., Heiken, G., Wohletz, K., Eppler, D., Barr, S., Miller, T., et al. (1988). Direct rate measurements of eruption plumes at Augustine volcano: a problem of scaling and uncontrolled variables. *Journal of Geophysical Research: Solid Earth*, *93*(B5), 4485–4499.

Rutherford, M. J., & Hill, P. M. (1993). Magma ascent rates from amphibole breakdown: An experimental study applied to the 1980–1986 Mount St. Helens eruptions. *Journal of Geophysical Research: Solid Earth*, *98*(B11), 19667–19685.

Rutherford, M. J., Sigurdsson, H., Carey, S., & Davis, A. (1985). The May 18, 1980, eruption of Mount St. Helens: 1. Melt composition and experimental phase equilibria. *Journal of Geophysical Research: Solid Earth, 90*(B4), 2929–2947.

Sakai, H., Casadevall, T. J., & Moore, J. G. (1982). Chemistry and isotope ratios of sulfur in basalts and volcanic gases at Kilauea Volcano, Hawaii. *Geochimica et Cosmochimica Acta*, *46*(5), 729–738.

Seligman, A. N., Bindeman, I., Van Eaton, A., & Hoblitt, R. (2018). Isotopic insights into the degassing and secondary hydration of volcanic glass from the 1980 eruptions of Mount St. Helens. *Bulletin of Volcanology, 80*(4), 37.

Severs, M. J., Azbej, T., Thomas, J. B., Mandeville, C. W., & Bodnar, R. J. (2007). Experimental determination of H_2O loss from melt inclusions during laboratory heating: evidence from Raman spectroscopy. *Chemical Geology*, *237*(3), 358–371.

Sherrod, D. R., Scott, W. E., & Stauffer, K. V. (Eds.). (2008). *A volcano rekindled; The renewed eruption of Mount St Helens, 2004–2006*. U.S. Geological Survey Professional Paper 1750.

Smythe, D. J., Wood, B. J., & Kiseeva, E. S. (2017). The S content of silicate melts at sulfide saturation: new experiments and a model incorporating the effects of sulfide composition. *American Mineralogist*, *102*(4), 795–803.

Sobolev, A. V., & Danyushevsky, L. V. (1994). Petrology and geochemistry of boninites from the north termination of the Tonga Trench: constraints on the generation conditions of primary high-Ca boninite magmas. *Journal of Petrology*, *35*(5), 1183–1211.

Spencer, K. J., & Lindsley, D. H. (1981). A solution model for coexisting iron–titanium oxides. *American Mineralogist, 66*(11–12), 1189–1201.

Stoiber, R. E., Malinconico, L. L., & Williams, S. N. (1983). Use of the correlation spectrometer at volcanoes. In H. Tazieff & J.-C. Sabroux (Eds.), *Forecasting Volcanic Events* (pp. 425–444). Elsevier.

Stolper, E. (1982). Water in silicate glasses: An infrared spectroscopic study. *Contributions to Mineralogy and Petrology*, *81*(1), 1–17.

Streck, M. J., Broderick, C., Thornber, C., Clynne, M. A., & Pallister, J. (2008). Plagioclase populations and zoning in dacite of the 2004–2005 Mount St. Helens eruption: Constraints for magma origin and dynamics. In *A volcano rekindled: The renewed eruption of Mount St. Helens, 2004-2006* (pp. 791–808). U.S. Geological Survey Professional Paper 1750.

Symonds, R. B., Rose, W. I., Gerlach, T. M., Briggs, P. H., & Harmon, R. S. (1990). Evaluation of gases, condensates, and SO2 emissions from Augustine volcano, Alaska: The degassing of a Cl-rich volcanic system. *Bulletin of Volcanology*, *52*(5), 355–374.

Symonds, R. B., Gerlach, T. M., & Reed, M. H. (2001). Magmatic gas scrubbing: Implications for volcano monitoring. *Journal of Volcanology and Geothermal Research*, *108*(1), 303–341.

Taylor, B. E. (1986). Magmatic volatiles; isotopic variation of C, H and S. *Reviews in Mineralogy and Geochemistry*, *16*, 185–225.

Thornber, C. R., Pallister, J. S., Lowers, H. A., Rowe, M. C., Mandeville, C. W., & Meeker, G. P. (2008). Chemistry, mineralogy, and petrology of amphibole in Mount St. Helens 2004–2006 dacite. In *A volcano rekindled: The renewed eruption of Mount St. Helens, 2004-2006* (pp. 727–754). U.S. Geological Survey Professional Paper 1750.

Tilman, M. R. (2008). An investigation of symplectite-rimmed olivine and magmatic processes during the 2006 eruption of Augustine Volcano, Alaska (PhD Thesis). University of Alaska Fairbanks.

Toplis, M. J. (2005). The thermodynamics of iron and magnesium partitioning between olivine and liquid: criteria for assessing and predicting equilibrium in natural and experimental systems. *Contributions to Mineralogy and Petrology*, *149*(1), 22–39.

Vallance, J. W., Bull, K. F., & Coombs, M. L. (2010). Pyroclastic flows, lahars, and mixed avalanches generated during the 2006 eruption of Augustine Volcano. In J. A. Power, M. L. Coombs, & J. T. Freymueller (Eds.), *The 2006 eruption of Augustine Volcano, Alaska* (pp. 219–267). U.S. Geological Survey Professional Paper 1769.

Wallace, K. L., Neal, C. A., & McGimsey, R. G. (2010). Timing, distribution, and character of tephra fall from the 2005-2006 eruption of Augustine Volcano. In J. A. Power, M. L. Coombs, & J. T. Freymueller (Eds.), *The 2006 eruption of Augustine Volcano, Alaska* (pp. 187–217). U.S. Geological Survey Professional Paper 1769.

Webster, J. D., & De Vivo, B. (2002). Experimental and modeled solubilities of chlorine in aluminosilicate melts, consequences of magma evolution, and implications for exsolution of hydrous chloride melt at Mt. Somma-Vesuvius. *American Mineralogist*, *87*(8–9), 1046–1061.

Webster, J. D., Mandeville, C. W., Goldoff, B., Coombs, M. L., & Tappen, C. (2010). Augustine Volcano-The influence of volatile components in magmas erupted AD 2006 to 2,100 years before present. In J. A. Power, M. L. Coombs, & J. T. Freymueller (Eds.), *The 2006 eruption of Augustine Volcano, Alaska* (pp. 383–423). U.S. Geological Survey Professional Paper 1769.

Webster, J. D., Vetere, F., Botcharnikov, R. E., Goldoff, B., McBirney, A., & Doherty, A. L. (2015). Experimental and modeled chlorine solubilities in aluminosilicate melts at 1 to 7000 bars and 700 to 1250 °C: Applications to magmas of Augustine Volcano, Alaska. *American Mineralogist*, *100*(2–3), 522–535. https://doi.org/10.2138/am-2015-5014

Wilke, M., Jugo, P. J., Klimm, K., Susini, J., Botcharnikov, R., Kohn, S. C., & Janousch, M. (2008). The origin of S4+ detected in silicate glasses by XANES. *American Mineralogist*, *93*(1), 235–240.

Wysoczanski, R., & Tani, K. (2006). Spectroscopic FTIR imaging of water species in silicic volcanic glasses and melt inclusions: An example from the Izu-Bonin arc. *Journal of Volcanology and Geothermal Research*, *156*(3–4), 302–314.

Yamashita, S., Kitamura, T., & Kusakabe, M. (1997). Infrared spectroscopy of hydrous glasses of arc magma compositions. *Geochemical Journal*, *31*(3), 169–174.

Zimmer, M. M. (2009). Water in Aleutian magmas: Its origins in the subduction zone and its effects on magma evolution (Ph.D. Thesis). Boston University.

Zimmer, M. M., Plank, T., Hauri, E. H., Yogodzinski, G. M., Stelling, P., Larsen, J., et al. (2010). The role of water in generating the calc-alkaline trend: new volatile data for Aleutian magmas and a new tholeiitic index. *Journal of Petrology*, *51*(12), 2411–2444.